Energy and Electron Transfer Studies

of Triarylamine-based

Dendrimers and Cascades

Dissertation zur Erlangung des

naturwissenschaftlichen Doktorgrades

der Julius-Maximilians-Universität Würzburg

vorgelegt von

Fabian Zieschang

aus Georgsmarienhütte

Würzburg 2014

Eingereicht bei der Fakultät für Chemie und Pharmazie am

10.07.2014

Gutachter der schriftlichen Arbeit

1. Gutachter: Prof. Dr. Christoph Lambert

2. Gutachter: Prof. Dr. Tobias Brixner

Prüfer des öffentlichen Promotionskolloquiums

1. Prüfer: Prof. Dr. Christoph Lambert

2. Prüfer: Prof. Dr. Tobias Brixner

3. Prüfer: Prof. Dr. Matthias Lehmann

Datum des öffentlichen Promotionskolloquiums

14.08.2014

Doktorurkunde ausgehändigt am

Mein besonderer Dank gilt

Herrn Prof. Dr. Christoph Lambert

für die Überlassung dieser spannenden und abwechslungsreichen Themen, der intensiven mit vielen Anregungen und Diskussionen verbundenen Betreuung und der Förderung während dieser Arbeit.

CONTENTS

Abbreviations

CT	charge transfer
CS	charge separated
CV	cyclic voltammetry
dba	dibenzylideneacetone
DIPEA	*N*,*N*-diisopropylethylamine
DMAP	*N*,*N*´-dimethylethylenediamine
DSC	differential scanning calorimetry
EA	ethyl acetate
EnT	energy transfer
ESI	electrospray ionisation
ET	electron transfer
Fc	ferrocene
GPC	gel permeation chromatography
IV-CT	intervalence charge transfer
LED	light-emitting diode
MALDI	matrix assisted laser desorption/ionisation
MV	mixed valence
NDI	1,4,5,8-naphthalene diimide
OD	optical density
OFET	organic field effect transistor
OLED	organic light-emitting diode
OPV	organic photovoltaic device
PE	petrol ether
SOA	sucrose octaacetate
TAA	triarylamine
TBAHFP	tetrabutylammonium hexafluorophosphate

TIPS	tri-*i*-propylsilyl
TIPSA	tri-*i*-propylsilylacetylene
TMS	trimethylsilyl
TMSA	trimethylsilylacetylene

COPYRIGHTS REMARKS

Parts (indicated) of the present thesis have already been published in the following article:

Solvent Controlled Energy Transfer Processes in Triarylamine-Triazole Based Dendrimers, Zieschang, F.; Schmiedel, A.; Holzapfel, M.; Ansorg, K.; Engels, B.; Lambert, C. *J. Phys. Chem. C* **2013**, *117*, 19816-19831.

And in the following theses:

Beiträge zur Synthese und Charakterisierung von triarylaminhaltigen Dendrimeren über die Kupfer(I)-katalysierte 1,3-Huisgen-Cycloaddition, Diploma Thesis of Fabian Zieschang, Würzburg **2009**.

Synthese triarylaminhaltiger Redoxkaskaden, Bachelor Thesis of Maximilian Schreck, Würzburg **2011**. (under supervision of Fabian Zieschang)

Chapter 1

MOTIVATION

"Wenn wir die Natur auf das reduzieren, was wir verstanden haben,
sind wir nicht überlebensfähig – If we reduce nature to what we understand, then we are
not capable of survival"

Hans-Peter Dürr (*1929-2014)

The German nuclear physicist *Hans-Peter Dürr* was laureate of the Right Livelihood Award and member of the Club of Rome and the Pugwash Group (*Nobel* Peace Prize in 1995). He was a vehement and lifelong adversary of nuclear technology for energy production. *Dürr* was convinced that this technology is grossly inefficient, extremely hazardous and hardly manageable by the human being. Nuclear disasters in Tschernobyl (26. April 1986) and Fukushima (11. March 2011) gave compelling evidence for his continuous and alerting concerns. The occurrences in Japan demonstrated once again that the development of alternative ways to gain energy from a safe, clean and renewable source is one of our most pressing challenges in the 21st century.

Dürr argued that in this context the sun is the only source that provides us unlimited energy without depleting our planet. The amount of energy reaching earth every day is about 120000 TW.[1] Conversion and storage of at least a few percent of the total amount would meet all of our energetic needs at a stroke. Furthermore, sun power bears the potential to supply all terrestrials with energy because of its near omnipresence which would tremendously advance the living standard/living conditions of indigent people.

Mankind has to learn how to convert light into convenient energy forms which essentially requires a profound understanding of the fundamental processes during the light harvesting process. Energy and electron transfer plays a crucial rule in natural photosynthesis. In the natural chlorophyll the absorbed solar energy is highly efficiently transferred from the light harvesting antenna chromophores to the "special pair" in the reaction centre, where charge separation is induced.

The presented work is strongly motivated by the aim to achieve a deeper understanding of the factors that determine the fundamental processes in (artificial) light harvesting and energy conversion – the energy transfer and charge separation processes. To address this issue novel

macromolecules and redox cascades are constructed using a straight forward building block synthesis and their photophysical and electrochemical properties are investigated by a number of spectroscopic methods *e.g.* transient absorption spectroscopy and emission anisotropy measurements.

The introductory chapter will equip the reader with the theoretical framework of energy and electron transfer and give an overview over recent energy and electron transfer studies on related systems. Chapter 2 outlines the aim of this work, followed by the presentation of obtained results and a detailed discussion in chapter 3. This includes the synthesis and photophysical and electrochemical investigations of dendritic structures and small donor-acceptor systems. The thesis completes with a summary and the experimental section.

    "*If chemist succeed to create an artificial photosynthetic process*,"…*life and civilization will continue as long as the sun shines*", but "…*nature is not in a hurry and mankind is*"[2].

(*Ciamician*, in Science 1912)

Chapter 2

INTRODUCTION

2.1 Theory

In this section the reader will be equipped with the theoretical framework of energy and electron transfer theory that is needed for a profound understanding of the issue of photoinduced dynamics in complex organic materials. Furthermore, the theory of emission anisotropy measurement will be presented, which is a powerful tool to investigate energy transfer processes.

2.1.1 Energy Transfer Theory

When a donor chromophore is excited into its electronically excited state, the excitation energy might be transferred to an accepting chromophore. Before this transfer, the donor is in the electronic excited state and the acceptor in the electronic ground state. During the energy transfer event the donor returns into the electronic ground state and the acceptor is excited to the electronic excited state. From the excited state, the acceptor chromophore might emit a photon or relaxes by internal conversion into the electronic ground state.

$$\Psi_f = \frac{1}{\sqrt{2}}(\phi_D(1)\phi_{A^*}(2) - \phi_D(2)\phi_{A^*}(1))$$

$$\Psi_i = \frac{1}{\sqrt{2}}(\phi_{D^*}(1)\phi_A(2) - \phi_{D^*}(2)\phi_A(1))$$
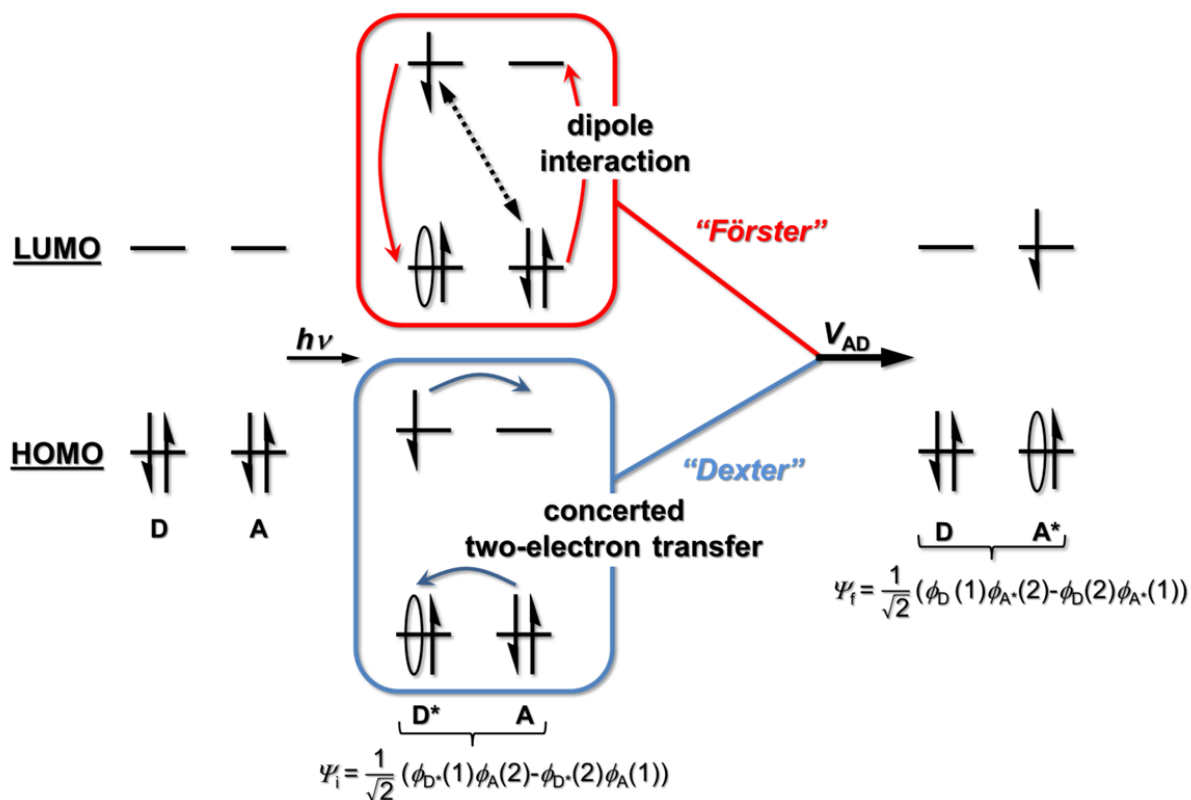
Scheme 1: **Schematic presentation of possibly energy transfer mechanism. After excitation the excited donor chromophore (D*, the asterisk indicates electronically excited states) may transfer its excitation energy to an acceptor chromophore (A) in the electronic ground state. Thereby, the donor returns to its electronic ground state and the acceptor gets in the excited state. In the weak coupling regime, the energy transfer might follow a *Förster* (dipole interaction) or a *Dexter* (exchange interaction) mechanism. The given wave functions refer only to the two electrons that are involved in the energy transfer since the residual electrons remain unaffected during the energy transfer.**

The energy transfer from the excited donor to the acceptor is promoted by the coupling between the initial (Ψ_i) and the final state (Ψ_f) and described by the coupling matrix element V_{DA}. Because only two electrons are involved in the energy transfer and the residual electrons remain unaffected, the system can be sufficiently described by two-electron wave functions (the asterisk indicates electronically excited states). These two-electron asymmetric and orthogonal wave functions of the appropriated states are given in Scheme 1 (1 and 2 denote the two individual electrons in *e.g.* the donor ground (ϕ_D) or excited state (ϕ_{D^*})) and thus V_{DA} is given by (for clarity the integral are written in the Dirac notation):[3]

$$V_{DA} = \langle \Psi_i \,|\, \hat{V} \,|\, \Psi_f \rangle$$

$$= \left\langle \frac{1}{\sqrt{2}}(\phi_{D^*}(1)\phi_A(2) - \phi_{D^*}(2)\phi_A(1)) \,\middle|\, \hat{V} \,\middle|\, \frac{1}{\sqrt{2}}\phi_D(1)\phi_{A^*}(2) - \phi_D(2)\phi_{A^*}(1) \right\rangle$$

$$= \textcolor{red}{\left\langle (\phi_{D^*}(1)\phi_A(2) \,\middle|\, \hat{V} \,\middle|\, \phi_D(1)\phi_{A^*}(2) \right\rangle} - \textcolor{blue}{\left\langle (\phi_{D^*}(1)\phi_A(2) \,\middle|\, \hat{V} \,\middle|\, \phi_D(2)\phi_{A^*}(1) \right\rangle} \tag{1}$$

where

$\hat{V} = \dfrac{e^2}{r_{DA}}$ (= interaction operator) is the perturbation part of the total Hamiltonian $\hat{H} = \hat{H}_D + \hat{H}_A + \hat{V}$, with e as the elementary charge.

In the first integral term (red) of this solution the electrons remain at their original chromophore and only the excitation energy migrates from the donor to the acceptor promoted by *Coulomb* interaction (*Coulomb* integral). In the second integral term (blue) both, the excitation energy **and** the electron exchange between the chromophores and therefore, this integral is called exchange integral. Reasonably, the exchange integral is only non-vanishing when direct orbital overlap between the donor and acceptor exists and thus at larger distances between the donor and the acceptor only the *Coulomb* term operates.[3]

If energy transfer is promoted by *Coulomb* interactions the energy transfer can be described by the *Förster* theory, while describted by the *Dexter* theory in cases where the exchange integral is dominating V_{DA} (see Scheme 1)

2.1.1.1 *Förster* Theory

At distances larger than the dimension of the involved donor and acceptor system no overlap interaction is present and assuming that $\hat{V} \approx \hat{V}_{Coul}$ is reasonable.[4] The *Coulomb* interaction operator $\hat{V}_{Coul,m,n}$ between the donor state n and the acceptor state m is given by the multipole expansion:[3,5]

$$\hat{V}(E)_{Coul,m,n} = \frac{1}{4\pi\varepsilon_0\varepsilon}\left(\underbrace{\frac{q_D q_A}{r_{DA}}}_{\hat{V}_{mono\text{-}mono}} + \underbrace{\frac{q_D\vec{\mu}_{D,n}\cdot\vec{r}}{r_{DA}^3} - \frac{q_A\vec{\mu}_{A,m}\cdot\vec{r}}{r_{DA}^3}}_{\hat{V}_{mono\text{-}dipol}} + \underbrace{\frac{\vec{\mu}_{D,n}\,\vec{\mu}_{A,m}\cdot\vec{r}^2 - 3(\vec{\mu}_{D,n}\cdot\vec{r})(\vec{\mu}_{A,m}\cdot\vec{r})}{r_{DA}^5}}_{\hat{V}_{dipol\text{-}dipol}} + \cdots\right) \quad (2)$$

where

ε_0 is the vacuum permittivity, ε is the permittivity of the surrounding medium (commonly approximated by $\varepsilon = \varepsilon_\infty = n^2$, with *n* as the refractive index) r_{DA} is the distance between the donor and the acceptor, q_D and q_A are the charges of the donor and acceptor, respectively, $\vec{r}$ is an unit vector along the line connecting the donor and the acceptor, $\vec{\mu}_{D,n}$ is the transition moment from the donor ground state to state n and the same for $\vec{\mu}_{A,m}$.

The first three terms, the monopole-monopole and the monopole-dipole interactions, vanish since both, the donor and the acceptor, are uncharged and in addition the expansion is terminated after the dipole-dipole term, neglecting higher interaction terms (dipole-dipole approximation):[3,5]

$$\hat{V}(E)_{Coul,m,n} = \frac{1}{4\pi\varepsilon_0 n^2}\left(\frac{\vec{r}^2\cdot\vec{\mu}_{D,n}\cdot\vec{\mu}_{A,m}}{r_{DA}^{53}} - \frac{3(\vec{\mu}_{D,n}\cdot\vec{r})(\vec{\mu}_{A,m}\cdot\vec{r})}{r_{DA}^5}\right)$$

$$= \frac{1}{4\pi\varepsilon_0 n^2 r_{DA}^3}\left(\vec{\mu}_{D,n}\cdot\vec{\mu}_{A,m} - \frac{3(\vec{\mu}_{D,n}\cdot\vec{r})(\vec{\mu}_{A,m}\cdot\vec{r})}{r_{DA}^2}\right)$$

$$\text{with } \vec{a}\cdot\vec{b} = |\vec{a}||\vec{b}|\cdot\cos\theta$$

$$\hat{V}(E)_{Coul,m,n} = \frac{1}{4\pi\varepsilon_0 n^2 r_{DA}^3}\left(|\vec{\mu}_{D,n}|\cdot|\vec{\mu}_{A,m}|\cos\theta_{AD} - \frac{3|\vec{\mu}_{D,n}|\cdot|\vec{r}|\cos\theta_D\,|\vec{\mu}_{A,m}|\cdot|\vec{r}|\cos\theta_A)}{r_{DA}^2}\right) \quad (3)$$

where

θ_{DA} is the angle between the transition moments of the donor and the acceptor and θ_D and θ_A are the angles between the z-axis and the transition moments of the donor and the acceptor, respectively (see Scheme 2, p: 8).

Insertion of equation (3) in the *Coulomb* integral of equation (1), p: 5, and establishing of the orientation factor κ (see Scheme 2)[6,7] gives the coupling matrix element $V(E)_{dd,m,n}$ between the state n of the donor and the state m of the acceptor as

$$V(E)_{dd,m,n} = \left\langle \phi_{D^*}\phi_A \left| \hat{V}_{dd,m,n} \right| \phi_D\phi_{A^*} \right\rangle = \frac{|\mu_{D,n}| \cdot |\mu_{A,m}|}{4\pi\varepsilon_0 n^2 r_{DA}^3}\kappa \quad |: h \tag{4}$$

$$V(\nu)_{dd,m,n} = \frac{|\mu_{D,n}| \cdot |\mu_{A,m}|}{4\boldsymbol{h}\pi\varepsilon_0 n^2 r_{DA}^3}\kappa \qquad |: c \tag{5}$$

$$V(\tilde{\nu})_{dd,m,n} = \frac{|\mu_{D,n}| \cdot |\mu_{A,m}|}{4\boldsymbol{hc}\pi\varepsilon_0 n^2 r_{DA}^3}\kappa \tag{6}$$

$$\text{with } \kappa = \cos\theta_{DA} - 3\cos\theta_D \cdot \cos\theta_A \text{ and} \tag{7}$$

$$|\mu_{D,n}| = \left\langle \phi_{D^*}\phi_A \left| \vec{\mu}_{D,n} \right| \phi_D\phi_{A^*} \right\rangle \text{ and } |\mu_{A,m}| = \left\langle \phi_{D^*}\phi_A \left| \vec{\mu}_{A,m} \right| \phi_D\phi_{A^*} \right\rangle$$

where

h is the *Planck* constant, c is the speed of light, $V(E)$ coupling matrix element in J, $V(\nu)$ is the coupling matrix element in s^{-1} and $V(\tilde{\nu})$ is the coupling matrix element in cm^{-1}.

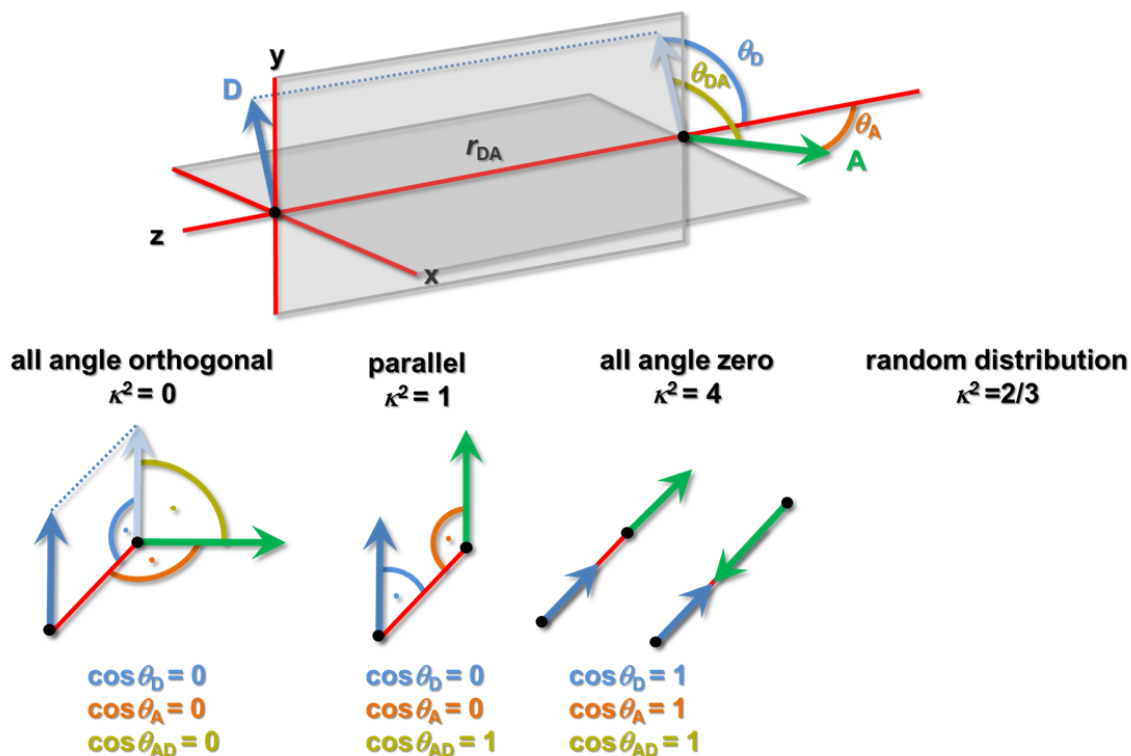Since $\vec{\mu}_{D,n}$ is not operating on ϕ_A and ϕ_{A^*} and because the wave functions are orthonormalised:

$$|\mu_{D,n}| = \left\langle \phi_{D^*}\phi_A \left| \vec{\mu}_{D,n} \right| \phi_D\phi_{A^*} \right\rangle = \left\langle \phi_{D^*} \left| \vec{\mu}_{D,n} \right| \phi_D \right\rangle \left\langle \phi_A \mid \phi_{A^*} \right\rangle = \left\langle \phi_{D^*} \left| \vec{\mu}_{D,n} \right| \phi_D \right\rangle \tag{8}$$

Scheme 2: **Geometric constitution of the transition moments of the donor and acceptor chromophores, indicating the relevant geometric values needed for the estimation of κ. Below are given κ values for same exemplary dipole compositions. (r_{DA} is the distance between the donor and the acceptor, θ_{DA} is the angle between the transition moments of the donor and the acceptor and θ_D and θ_A are the angles between the z-axis and the transition moments of the donor and the acceptor, respectively.)[8]**

Appling the *Born-Oppenheimer* approximation allows separation of the wave functions into their electronic and vibronic parts (and the same for $|\mu_{A,m}|$):

$$\left\langle \phi_{D^*} \left| \vec{\mu}_{D,n} \right| \phi_D \right\rangle = \left\langle \psi_{el,D^*} \left| \vec{\mu}_{D,n} \right| \psi_{el,D} \right\rangle \left\langle \chi_{vib,D^*} \middle| \chi_{vib,D} \right\rangle = \left\langle \psi_{el,D^*} \left| \vec{\mu}_{D,n} \right| \psi_{el,D} \right\rangle \cdot S_n$$

$$\left\langle \phi_A \left| \vec{\mu}_{A,m} \right| \phi_{A^*} \right\rangle = \left\langle \psi_{el,A} \left| \vec{\mu}_{A,m} \right| \psi_{el,A^*} \right\rangle \left\langle \chi_{vib,A} \middle| \chi_{vib,A^*} \right\rangle = \left\langle \psi_{el,A} \left| \vec{\mu}_{A,m} \right| \psi_{el,A^*} \right\rangle \cdot S_m$$

(9)

where

S_n and S_m are the *Franck-Condon* integrals, ψ_{el} are the electronic wave functions and χ_{vib} are the vibronic wave functions.

The rate constant for excitation energy transfer between the state n of the donor and state m of the acceptor ($k_{m,n}$) can be estimated according to first order perturbation theory by a classical *Fermi´s* Golden Rule expression:[9]

$$k_{m,n} = \frac{4\pi^2}{h} V(E)^2_{dd,m,n} \, \delta(E_n - E_m) \tag{10}$$

where

h is the *Planck* constant and E_n and E_m are the energies of the state n of the donor and of state m of the acceptor.

In this equation the *Dirac* δ-function ensures energetic equality between the two states n and m (resonant transitions, see Scheme 3).
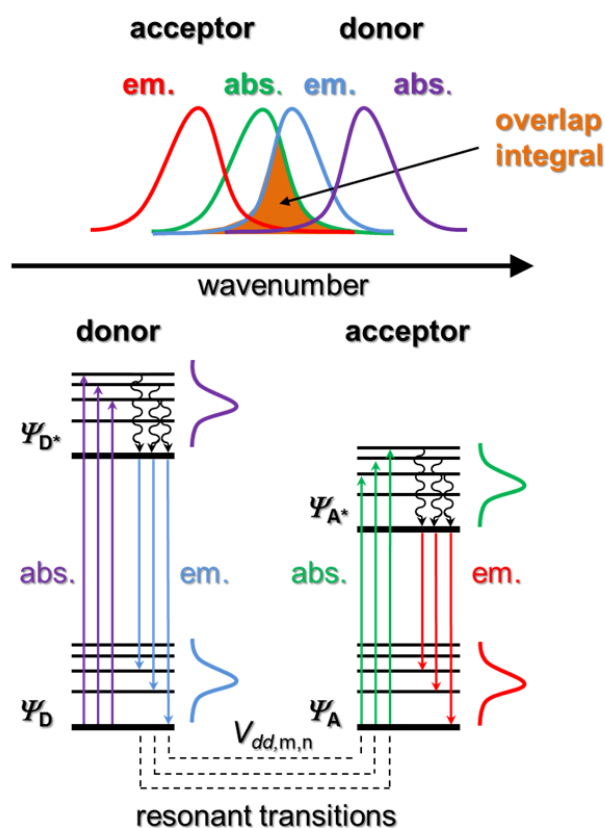
Scheme 3:   Schematic energy state diagram of the donor and the acceptor. Energy transfer takes place by resonant transitions between the deactivation of the donor and simultaneous excitation of the acceptor. Due to energy conservation the acceptor must absorb exactly the energy that the donor emits. Also shown are the spectroscopic characterisations of absorption and emission and the spectral overlap between the emission of the donor and the absorption of the acceptor, which strongly influences *Förster* energy transfer kinetics.[3,10]

Since equation (10) gives the rate constant from the vibrational state n of the donor to the vibrational state m of the acceptor it seem reasonable to use the frequency expression for $k_{m,n}$ (equation (11)).

$$k_{mn} = 4\pi^2 V(\nu)_{dd,m,n}^2 \delta(\nu_n - \nu_m) \tag{11}$$

Substitution of equation (5), p: 7, into equation (11) gives:

$$k_{mn} = 4\pi^2 \left(\frac{\left\langle \psi_{el,D^*} \left| \vec{\mu}_{D,n} \right| \psi_{el,D} \right\rangle \left\langle \psi_{el,A} \left| \vec{\mu}_{A,m} \right| \psi_{el,A^*} \right\rangle S_m S_n \ \kappa}{h\, 4\pi\varepsilon_0 n^2\, r_{DA}^3} \right)^2 \delta(\nu_n - \nu_m) \tag{12}$$

where

ν_n and ν_m are the frequencies of the n state of the donor and the m state of the acceptor, respectively.

Subsequent, summation over all m and n gives k_{FT}, the total rate constant for *Förster* energy transfer.[11]

$$k_{FT} = \frac{4\pi^2 \kappa^2}{h^2\, 8\pi^2 \varepsilon_0^2 n^4\, r_{DA}^6} \sum_{n,m} \mu_D^2 S_n^2 \mu_A^2 S_m^2 \delta(\nu_n - \nu_m) \tag{13}$$

Expressed in the integral form of the *Dirac δ*-function:

$$k_{FT} = \frac{4\pi^2 \kappa^2}{h^2 8\pi^2 \varepsilon_0^2 n^4\, r_{DA}^6} \int d\nu \sum_{n,m} \mu_D^2 S_n^2 \delta(\nu_n - \nu) \mu_A^2 S_m^2 \delta(\nu_m - \nu) \tag{14}$$

Substitution of the normalised fluorescence spectrum of the donor (equation (15)) and the acceptor´s absorption spectrum (equation (16))[11]

$$\mu_D^2 \cdot \sum_n S_n^2 \delta(\nu_n - \nu) = \frac{3hc^3 \varepsilon_0 \phi_D}{16\pi^3 n\nu^3 \tau_D} \cdot \bar{I}_{fl,D}(\nu) \tag{15}$$

$$\mu_A^2 \cdot \sum_m S_m^2 \delta(\nu_m - \nu) = \frac{3000hc\, \ln10\, n\varepsilon_0}{2\pi^2 N_A \nu} \cdot \varepsilon_A(\nu) \tag{16}$$

where

τ_D is the donors excited state lifetime in the absence of the acceptor, ϕ_D is donors quantum yield in the absence of the acceptor, h is the *Planck* constant, c is the speed of light, n is the refractive index of the solvent, N_A is *Avogadro*´s constant, $\bar{I}_{fl,D}$ is the area normalised fluorescence spectrum of the donor and ε_A is the absorption spectrum of the acceptor,

in equation (14) leads to equation (17) in which the energy consistency is expressed by spectroscopic values. Finally, changing integration variable from ν to $\tilde{\nu}$ gives the famous equation for *Förster* Resonance Energy Transfer (FRET) (equation (18)):[12,13]

$$k_{FT} = \frac{9000 \ln 10 \, \phi_D \kappa^2 c^4}{128 \pi^5 N_A n^4 \tau_D \, r_{DA}^6 \, \nu^4} \cdot \int \bar{I}_{fl,D}(\nu) \varepsilon_A(\nu) \frac{d\nu}{\nu^4} \tag{17}$$

$$k_{FT} = \frac{9000 \ln 10 \, \phi_D \kappa^2}{128 \pi^5 N_A n^4 \tau_D \, r_{DA}^6} \cdot \int \bar{I}_{fl,D}(\tilde{\nu}) \varepsilon_A(\tilde{\nu}) \frac{d\tilde{\nu}}{\tilde{\nu}^4}$$

or, $\tag{18}$

$$k_{FT} = \frac{9000 \ln(10) \phi_D \kappa^2}{128 \pi^5 N_A n^4 \tau_D \, r_{DA}^6} \cdot J$$

with $J = \int \bar{I}_{fl,D}(\tilde{\nu}) \varepsilon_A(\tilde{\nu}) \frac{d\tilde{\nu}}{\tilde{\nu}^4}$ $\tag{19}$

Accordingly, energy transfer is effective in cases of strong overlapping of donor emission and acceptor absorption.

Frequently, the *Förster* formula can be found in its R_0 form:

$$k_{FT} = \frac{1}{\tau_D} \left[\frac{R_0}{r_{DA}} \right]^6 \tag{20}$$

with

$$R_0 = \frac{9000 \ln(10) \phi_D \kappa^2 J}{128 \pi^5 N_A n^4}$$

Herein, R_0 is the *Förster* distance and in cases where the donor-acceptor distance matches the value of R_0, the energy transfer rate is equal to the fluorescence decay rate of the donor leading to an energy transfer efficiency of 50 %. As apparent from equation (17) and (20) the energy transfer rate is strongly distance dependent with $1/r^6$. Therefore and because *Förster* transfer occurs predominantly at donor-acceptor distances of ca. 10 – 100 Å, FRET became an useful tool to determined donor-acceptor distances especially in biological studies. Thus, FRET is often entitled a "spectroscopic ruler".[14,15] Energy transfer following the *Förster* mechanism is depressed only in cases where the transition moments are all orthogonal ($\kappa^2 = 0$, see Scheme 2, p: 8) or where the overlap integral is zero. Furthermore, *Förster* energy transfer is only operating when the involved transitions are allowed by selection rules.

2.1.1.2   *Dexter* Theory

In cases where one of the two (or both) transitions from the excited state to the ground state (or *vice versa*) are forbidden energy transfer by *Förster* mechanism is prohibited since at least one of the transition moments becomes zero and thus the coupling matrix element in equation (10), p: 9, vanishes. Therefore, FRET is basically constricted to singlet-singlet transitions.

If the donor-acceptor distance allows direct orbital overlap and the *Förster* mechanism is not allowed, energy transfer takes place by direct electron exchange, which theoretical background was worked out by *Dexter*.[16] In the *Dexter* mechanism the excited electron of the donor is transferred from the donor LUMO to the LUMO of the acceptor while simultaneously an electron from the acceptor ground state is transferred to the donor ground state. As a result, the excitation energy is transferred from the donor to the acceptor. Therefore, energy transfer by the *Dexter* mechanism is the result of a concerted two electron transfer (see Scheme 4).
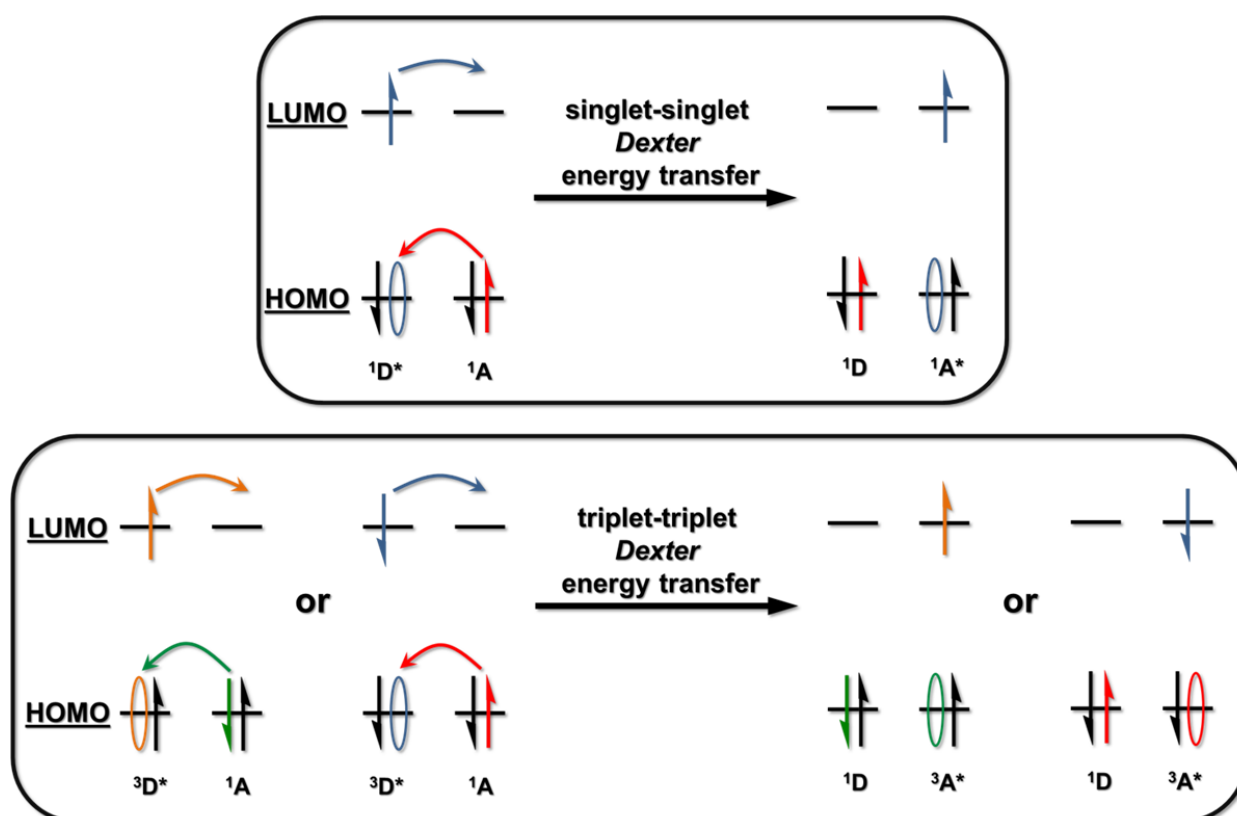
Scheme 4:   Schematic energy state diagram for the exchange energy transfer mechanism (*Dexter* transfer). The excitation energy is transferred by a concerted two-electron transfer. The colours of the arrows indicate the origin of the electrons and the ovals represent the associated holes. In contrast to *Förster* transfer, *Dexter* transfer also works for triplet-triplet energy transfer.

Neglecting the *Coulomb* integral (red) in equation (1), p: 5, leaves only the exchange integral (blue) and with $\widehat{V} = \frac{e^2}{r_{DA}}$ (= interaction operator) the coupling matrix element V_{DA} can be written as (separating the wave function into an electronic and a vibronic part, analogous to equation (8) and (9), p: 7):

$$
\begin{aligned}
V_{AD} &= \left\langle \left(\phi_{D^*}(1)\phi_A(2) \;\middle|\; \widehat{V} \;\middle|\; \phi_D(2)\phi_{A^*}(1)\right)\right\rangle = \left\langle \left(\phi_{D^*}(1)\phi_A(2) \;\middle|\; \frac{e^2}{r_{DA}} \;\middle|\; \phi_D(2)\phi_{A^*}(1)\right)\right\rangle \\
&= \left\langle \left(\psi_{el,D^*}(1)\psi_{el,A}(2) \;\middle|\; \frac{e^2}{r_{DA}} \;\middle|\; \psi_{el,D}(2)\psi_{el,A^*}(1)\right)\right\rangle \sum_{n,m} S_n^2 S_m^2
\end{aligned}
\tag{21}
$$

where

r_{DA} is the distance between the donor and the acceptor, e is the elementary charge and S_n and S_m are the *Franck-Condon* integrals.

Similar to *Förster* theory the rate constant for *Dexter* energy transfer (k_{De}) follows *Fermi*´s Golden Rule expression with the normalised overlap integral $\widetilde{J}$ and an orientation factor K (in the frequency regime).[3]

$$
k_{De} = 4\pi^2 \cdot Z^2 \sum_{n,m} S_n^2 S_m^2 \delta(\nu_n - \nu_m)
\tag{22}
$$

with Z as the electronic exchange integral

$$
Z = \left\langle \left(\psi_{el,D^*}(1)\psi_{el,A^*}(1) \;\middle|\; \frac{e^2}{r_{DA}} \;\middle|\; \psi_{el,D}(2)\psi_{el,A^*}(2)\right)\right\rangle
$$

With the approximation of Z by hydrogen-like orbitals and the introduction of the exchange interaction integral $\tilde{J}$ of the spectral overlap between donor fluorescence and acceptor absorption spectra, *Dexter* gave the rate constant for exchange interaction mediated energy transfer k_{De} (in its wavenumber expression) as:[3,9,16]

$$k_{De} = 4\pi^2 c\, K\, e^{\frac{-2r_{AD}}{L}} \cdot \tilde{J}$$

(23)

with

$$\tilde{J} = \int \bar{I}_{fl,D}(\tilde{v})\varepsilon_A(\tilde{v})d\tilde{v} \text{ where } \int \bar{I}_{fl,D}(\tilde{v})d\tilde{v} = \int \varepsilon_A(\tilde{v})d\tilde{v} = 1$$

where

K is an orientation factor, taking the geometric orbital interactions into account, L is the average *Bohr* radius and $\tilde{J}$ is the overlap integral of the normalised absorption of the acceptor and the emission of the donor.

Apparently, the distance dependence of k_{De} is exponential, which is reasonable as the electron densities of orbitals are related to $e^{-1/R}$ (R is the distance between the particular atom centres). *Dexter* energy transfer requires a direct orbital overlap between the donor and the acceptor and thus typically occurs below 10 Å. As a concerted two-electron transfer the *Dexter* energy transfer mechanism is not restricted to singlet-singlet energy transfer but also triplet-triplet energy transfer is allowed because the acceptor features two electrons with different spin orientation to balance the electron receipt from the excited donor (see Scheme 4).

2.1.1.3   Exciton Coupling Theory

The energy transfer theories presented in the last two preceding sections are only applicable in cases of weak electronic coupling between the initial and the final state. In the present section the situation of strong interaction between the donor and the acceptor as well as the concept of exciton coupling will be briefly discussed but for a more detailed description the reader is referred to the literature of *Kasha[17-19]* and *Eisfeld[20,21]*.

A strong coupling between to chromophores is observed at very small distances and if the chromophores exhibit large transition moments.[19] In such cases the coupling influences the energy eigenvalues of the system and alters the absorption and emission spectra of the involved chromophores. Due to excitonic coupling the excitations are no longer localised at individual chromophore units but have to be seen as a single quasiparticle (electron-hole pair). Thus, the excited states split with an energy splitting of ΔE_{ex} = 2·V_{ex} into two states depending on the direction of the involved transition moments (see Scheme 5). The exciton coupling V_{ex} strongly depends on the relative orientation and strength of the coupled transition moments as apparent from equation (24) (exchange interaction has been disregarded).[20]

$$V(\tilde{\nu})_{ex} = V(\tilde{\nu})_{dd} = \frac{1}{hc4\pi\varepsilon_0} \frac{\mu_D\mu_A}{r_{DA}{}^3} \kappa \qquad (24)$$

where

r_{DA} is the distance between the transition moments of the donor and the acceptor, κ is the orientation factor elucidated in Scheme 2, p: 8, and μ_D and μ_A are the transition moments of the donor and the acceptor, respectively.

Generally, the coupled chromophores are classified by the orientation of the transition moments. Excitons with parallel oriented transition moments are called H-type excitons (the H indicates the **h**ypsochromic shift in the absorption) while those with inline transition moments are termed J-type excitons (named after *Edwin E. **J**elley*[22]).[20,23] The special case of identical donor and acceptor chromphores is in reality not an exception but common.
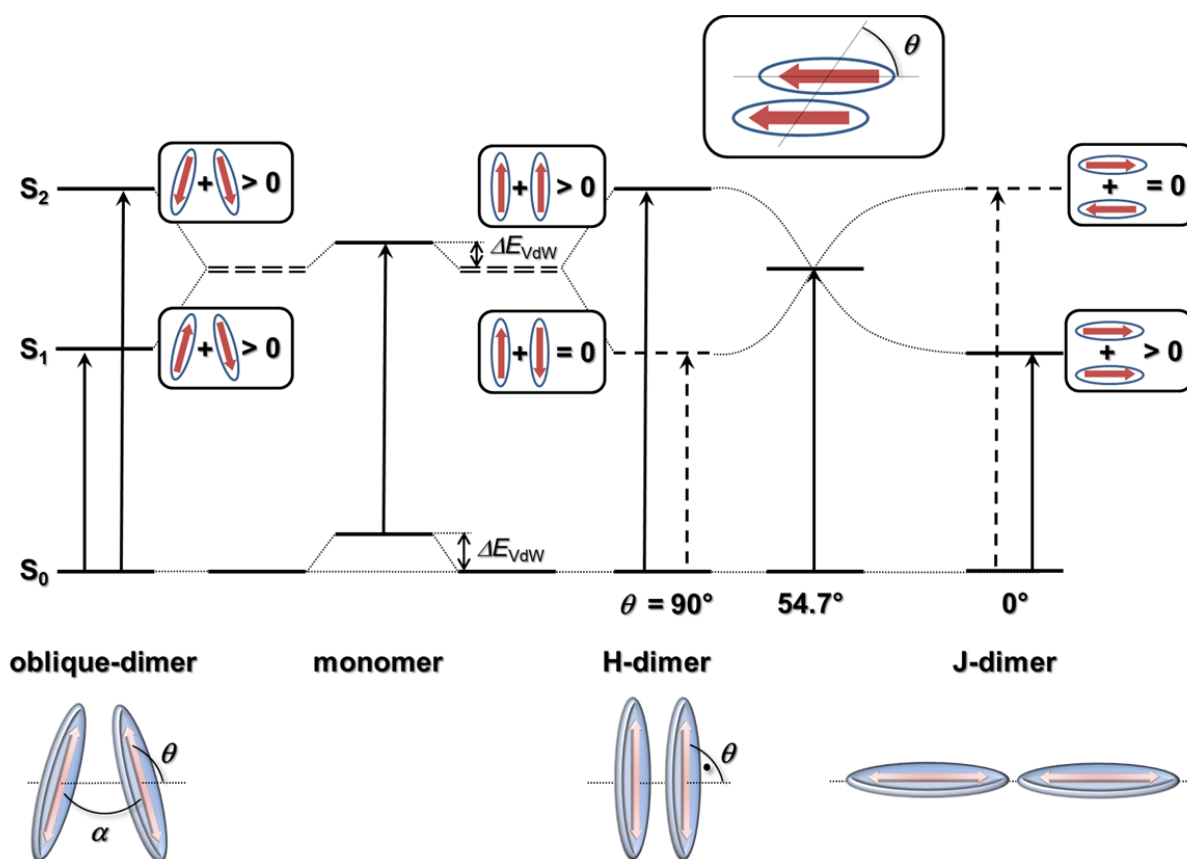

Scheme 5:   **Energy state diagram of homo-dimers and orientation dependence of the exciton coupling between the associated transition moments (red arrows). Transitions into the particular state are only allowed if the sum of the transition moments is non-vanishing. Solid arrows indicate allowed transitions and dashed lines indicate forbidden transitions. θ is the angle of between the transion moment and the vector connecting the two monomers. At an angle of 54.7° (the "magic angle") the transition moments sum up to only one allowed transition. For oblique dimers both transitions become allowed and a band splitting in the absorption is observed. The stabilisation of two interacting chromophores by *Van-der-Waals* interaction (ΔE_{VdW}) might be larger in the electronic ground state but the shown values may not be real.** [19,24] **Note: For organic compounds the *van-der-Waals* interaction in the ground and the excited state is expected to be very similar because the polarisability in the ground state and the excited state is also expected to be similar.**[25]

As apparent from Scheme 5, for J-dimers excitation into the higher lying state is forbidden while it is allowed in the energetic lower state. The situation is reversed for the excitation of H-dimers. Thus, J-dimers absorb at lower energy compared to the monomer (J-band) and the absorptions of H-dimers are hypsochromically shifted compared to the monomer (H-band). This trend continues over tetramers to larger aggregates and, consequently a red shift for J-aggregates and a blue shift for H-aggregates in the absorption can be observed (see Scheme 6).

Generally, H-aggregates are not (or at least only weakly) fluorescent because after allowed excitation the system relaxes into the lowest excited state from which emission normally takes place (*Kasha*´s rule). In H-aggregates the oscillator strength at this lowest state vanishes and thus the system relaxes into the electronic ground state by internal conversion.

On the other hand, in the emission of J-aggregates an effect might be observed, which is called "superradiant effect". The total oscillator strength of the coupled chromophores behave additive in a few states only. Most excitonic states are not accessible by absorption and consequently, the rate of emission k_f from the lowest-lying state is strongly enhanced (k_f depends on the square of the transition moment) compared to the uncoupled chromophores.[26]
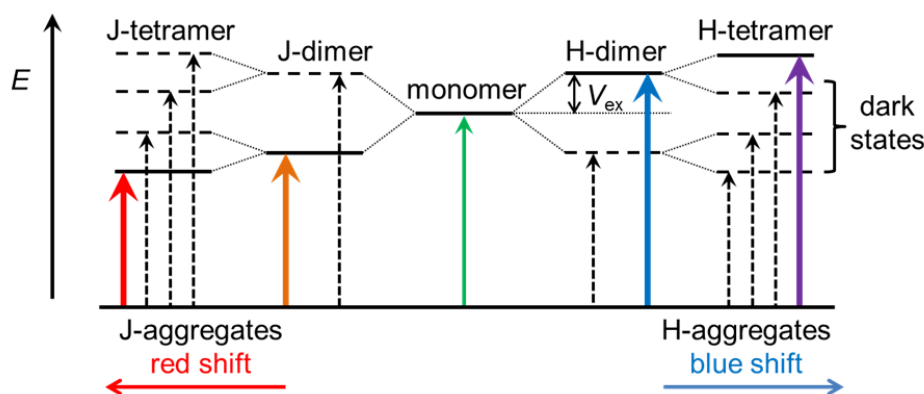
Scheme 6: **Schematic energy diagram going from monomers *via* J/H-dimers to J/H-aggregates. The different colours of the solid arrows indicate a red, respectively, blue shift of the allowed absorption. Dashed arrows mean forbidden transitions into dark states. For clarity, energetic stabilisation of the aggregates compared to the monomer by *Van-der-Waals* interaction is disregarded here.[17]**

The rate constant for energy transfer between the respective chromophores is much faster than the vibrational relaxation of the system (ca. 10^{-12} s). In such cases the excitation energy is delocalised between the individual chromophores and the excitation is a coherent process[17].

Notably, although the exciton coupling is frequently applied to molecular dimers and larger aggregates, it is also valid for coupling transition moments in single molecules as polymers or dendrimers as long as the transition moments are sufficiently strongly coupled.

2.1.1.4   Emission Anisotropy

This section will give an introduction into emission anisotropy theory and its benefits for energy transfer studies. The anisotropy r is defined as the ratio of the polarised light intensity I_{pol} to the total intensity I_{total} (in contrast to the closely related term of polarisation).[8]

$$r = \frac{I_{pol}}{I_{total}} \tag{25}$$

For understanding the concept of anisotropy it is reasonable to assume a light beam, polarised along the z-axis of a *Cartesian* coordinate system as illustrated in Scheme 7.
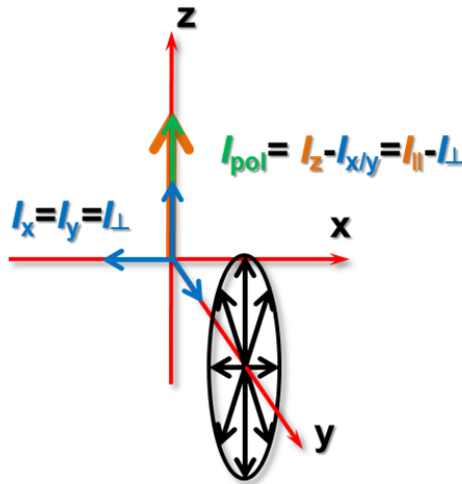
Scheme 7:   **Segmentation of a z-polarised light beam into the three spatial x, y and z-directions. The arrow lengths indicate the light intensity in the given direction. The polarised light intensity I_{pol} is the difference of the total intensity in z-direction and the average intensity in each direction.**

Reasonable, the total intensity corresponds to the intensities in each spatial direction and the intensity in x-direction correlates with the intensity in y-direction (see equation (26)). Furthermore, I_x and I_y are perpendicular to the polarisation direction (= $I_\perp$) and I_z is parallel (= $I_\parallel$).

$$I_{total} = I_z + I_y + I_x = I_\parallel + I_\perp + I_\perp = I_\parallel + 2I_\perp \tag{26}$$

The polarised light intensity in z-direction is the excess of intensity in this direction compared to the intensities in the other two directions.

$$I_{pol} = I_z - I_{x/y} = I_\parallel - I_\perp \tag{27}$$

Insertion of equation (26) and (27) in equation (25) results in equation (28), the frequently used equation for light anisotropy.

$$r = \frac{I_\parallel - I_\perp}{I_\parallel + 2I_\perp} \qquad (28)$$

Several reasons may result in depolarisation of the fluorescence light of a given sample:

After excitation with polarised light the molecule is in an electronically excited state. Assuming the excited state is the lowest excited state, after a certain time the molecule will emit a photon, which is polarised in the same direction as the excitation light since the transition moment for excitation and emission of the same electronic states are expected to be nearly collinear. This would lead to highly polarised emission and therefore to a large anisotropy value.

In another scenario the excitation energy is transferred from the initially excited state to a different state and emission takes place from there. If the transition moment vector of the second state exhibits an angle to the excitation polarisation, than the emitted light is to some extent depolarised.

Even in cases, where the excitation and the emission transition moments are parallel, depolarisation is observed when the measurement is performed in solution. Assuming an excited state lifetime of several ns, which is reasonable for many organic chromophores, the excited molecule features enough time to rotate around its molecular axes displacing the emission dipole moment prior to fluorescence. Thus, the emitted light is at least partially depolarised by the rotational diffusion. This effect gives the upper limit of anisotropy decays in time resolved anisotropy measurements in solution while in steady-state measurements rotational diffusion leads to complete depolarisation of the monitored light, which erases any useful information.

Fortunately, this situation can be prevented by measuring solids or compounds embedded in transparent matrixes (and in special cases compounds in viscous solvent). However, the problem of rotational diffusion will be neglected for the following considerations.[8]
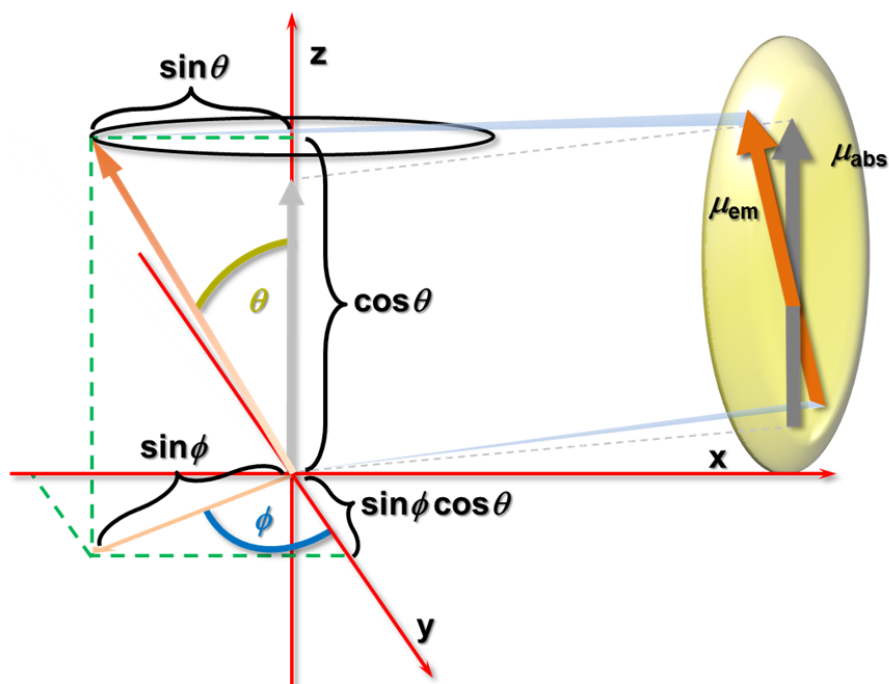
Scheme 8: Geometric orientation of the transition moments of absorption (μ_{abs}) and emission (μ_{em}) in a *Cartesian* coordinate system with the z-axis coinciding with μ_{abs}. Both transition moments were set in the origin of the coordination system. θ is the angle between μ_{em} and the z-axis (μ_{abs}) and ϕ is the angle between μ_{em} and the y-axis.[8]

For a sound understanding of anisotropy studies it seems reasonable to have a look on its derivation. Therefore, a molecule is set in a *Cartesian* coordinate system in such a way that the projection of the transition moment of absorption is congruent with the z-axis. In addition, the transition moment of emission shows an angle θ with the z-axis and an angle ϕ to the y-axis. Assuming excitation of the molecule occurs with light polarised along the z-axis leads to a preferential orientation of the excitation population along this axis. As indicated in Scheme 8, the emission intensities parallel and perpendicular are proportional to the projection of the transition moment on the axes:[8,27,28]

$$I_{\parallel}(\theta,\phi) = \cos^2\theta$$
$$I_{\perp}(\theta,\phi) = \sin^2\phi \sin^2\theta$$

(29)

For random distributed molecules excited with z-polarised light the excitation probability for molecules polarised along the z-axis is equal for all molecules with an identical angle ϕ with the y-axis. Thus, the population of excited molecules is symmetrically distributed around the z-axis with

ϕ values reaching from 0 to 2π (with equal probability). Integration of $\sin^2\phi$ over all ϕ values divided by the integral over ϕ gives 1/2 as the average value of $\sin^2\phi$:

$$<\sin^2\phi> = \frac{\int_0^{2\pi}\sin^2\phi\,d\phi}{\int_0^{2\pi}d\phi} = \frac{1}{2} \qquad (30)$$

This results in expressions for $I_\parallel$ and $I_\perp$ that are not dependent on ϕ anymore:

$$I_\parallel(\theta) = \cos^2\theta$$
$$I_\perp(\theta) = \frac{1}{2}\sin^2\theta \qquad (31)$$

The observed intensities $I_\parallel$ and $I_\perp$ for an assemble of z-oriented molecules are given as

$$I_\parallel = <\cos^2\theta> \qquad (32)$$
$$I_\perp = \frac{k}{2}<\sin^2\theta> \qquad (33)$$

Utilising that $\sin^2\theta = 1 - \cos^2\theta$ and insertion of the equations (32) and (33) in equation (28), p: 19, yields equation (34) for the anisotropy, which corresponds to the average value of $\cos^2\theta$.

$$r = \frac{3<\cos^2\theta> - 1}{2} \qquad (34)$$

However, this equation is only valid for molecules that are z-symmetric and therefore an expression for molecules with random orientation is needed:

When a molecule is illuminated with polarised light, preferentially transitions with a dipole moment parallel to the electric vector of the light are excited. However, for an excitation the transition moment does not to be exactly parallel to the lights electric vector but it needs a significant projection on the polarisation axis. Hereby, the probability for excitation is proportional to $\cos^2\Theta$, where Θ is the angle between the transition moment of absorption and the polarisation direction of the exciting light (z-axis). Although some excited molecules transition moments might be in the x-y-plane, most transition moments are oriented along the z-axis and thus the excited state population is aligned symmetrically around the z-axis.[29]
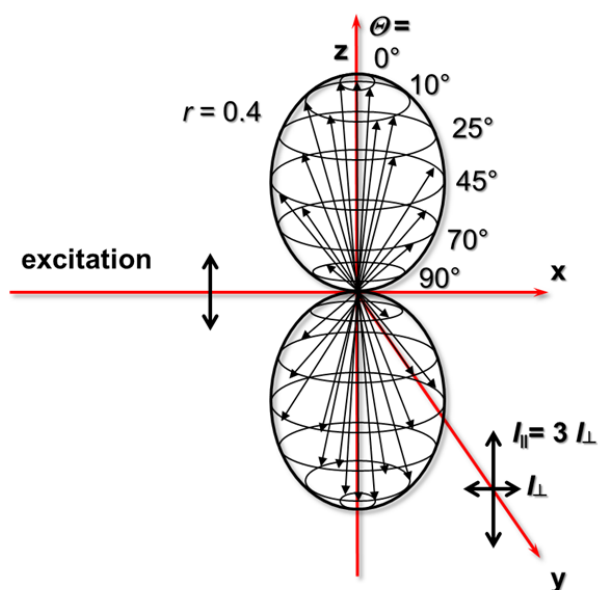
Scheme 9:   **Symmetric distribution of excited-state population around the direction of polarisation of the excitation light. Also molecules with transition moments that exhibit an angle to the polarisation orientation of the excitation light (Θ) possess an excitation probability ($\propto \cos^2\Theta$) and thus due to photoselection the maximum anisotropy value for a single-photon excitation is 0.4.[8]**

This photoselection of excitation gives a probability of excitation of random distributed transition moments of 3/5 for a single-photon excitation. The observed anisotropy is a linear combination of the anisotropy as a result of angular displacement of dipole moments (equation (34)) and of the anisotropy due to photoselection (1 – 3/5 = 2/5).

$$r = \frac{2}{5}\left(\frac{3\cos^2\theta - 1}{2}\right) \tag{35}$$

According to equation (35) the maximum anisotropy value, which is for totally collinear absorption and emission transition moments, is 0.4. The determined anisotropy values can be assigned to the angle θ between the transition moments of absorption and emission. Some crucial values are given in Table 1.

Table 1: Selection of same Crucial Anisotropy Values *r* and the Assigned Angle θ between the Transition Moments of Absorption and Emission. The Arrows Illustrate the Transition Moment Orientations for the given Anisotropy.

The value $r = 0$ refers to complete three-dimensional depolarisation, which is assigned to $\theta = 54.7°$, the magic angle. Measurements with a polariser adjusted in this angle to the polarisation of the excitation light are completely polarisation independent.

Multiphotonic excitation and coherent excitation of several states lead to different excitation probabilities than 2/5 and thus the highest anisotropy value may exceed 0.4. And indeed anisotropy values of up to 0.7 have been predicted and also been found experimentally.[30-34]

If a sample consists of more than one single species, the average (observed) anisotropy is determined by the anisotropies (r_i) of the individual species weighed by the relative amount (f_i).

$$\bar{r} = \sum_i f_i r_i \tag{36}$$

One major advantage of steady-state emission anisotropy measurements is the ease with which useful information can be gained about the orientation of the transition moments of absorption and emission and hence on possible mechanism altering this orientation (*e.g.* energy transfer, relaxation, *et cetera*). For this purpose only a fluorescence spectrometer and two polarisers are required. A commonly used L-format set-up for fluorescence anisotropy measurements is illustrated in Scheme 10.[35,36]
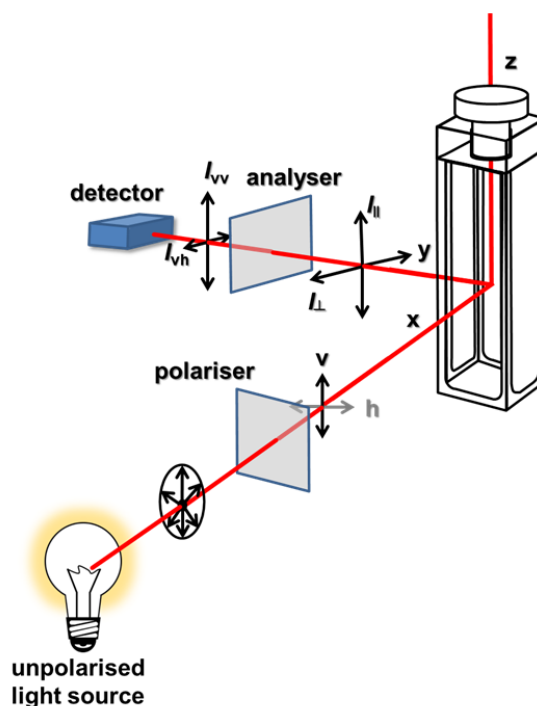
Scheme 10:   Schematic illustration of an L-format emission anisotropy measurement set-up. The observation axis is perpendicular to the excitation beam. One polariser in the excitation light beam provides polarised excitation light even from an unpolarised light source. A second polariser prior to the detector is used to analyse the polarisation of the emission parallel and perpendicular to the polarisation of the excitation light. Two additional measurements are required to determine the hardware factor *G* (explanation in the text).[35,36]

The light source in commercial fluorometers is usually unpolarised. Thus, a polariser prior to the sample ensures z-polarised excitation light while an adjustable analyser allows detection of the emission intensity parallel and perpendicular to the orientation of the excitation beam.[35,36]

However, for most monochromators the transmission efficiencies differ for the two polarisations and thus the detected intensities are not $I_∥$ and $I_⊥$ but I_{vv} and I_{vh}, respectively (the first subscript denotes the orientation of the polariser and the second subscript that of the analyser (v = vertical, h = horizontal)).

Still, the desired intensities are proportional to the measured intensity, the appropriate transmission (T_v and T_h) and a constant k taking the quantum efficiency of the chromophore and other polarisation independent instrument factors into account.[35]

$$I_{vv} = kT_v I_{\parallel}$$
$$I_{vh} = kT_h I_{\perp}$$

(37)

Consequently, the ratio of $I_{\parallel}$ and $I_{\perp}$ leads to the introduction of the hardware factor G.

$$\frac{I_{vv}}{I_{vh}} = \frac{kT_v I_{\parallel}}{kT_h I_{\perp}} = G\frac{I_{\parallel}}{I_{\perp}}$$

(38)

To ascertain the G factor two additional measurements with horizontally orientated polariser are required to obtain the intensities I_{hv} and I_{hh}. Both intensities are supposed to be equal (and proportional to $I_{\perp}$) because the population of excited molecules is now turned alongside the observation axis and are therefore perpendicular to the orientation of the excitation beam. Any difference between the two measured intensities must be the result of the different transmission efficiencies of the monochromator:[8,35]

$$\frac{I_{hv}}{I_{hh}} = \frac{T_v I_{\perp}}{T_h I_{\perp}} = \frac{T_v}{T_h} = G$$

(39)

Accordingly, the "real" intensity ratio of parallel and perpendicular orientation is

$$\frac{I_{\parallel}}{I_{\perp}} = \frac{I_{vv}}{G I_{vh}} = \frac{I_{vv} I_{hh}}{I_{vh} I_{hv}}$$

(40)

and the anisotropy is given as

$$r = \frac{\frac{I_{\parallel}}{I_{\perp}} - 1}{\frac{I_{\parallel}}{I_{\perp}} + 2}$$

(41)

or in its more comment expression:

$$r = \frac{I_{vv} - 2G I_{vh}}{I_{vv} + 2G I_{hv}}$$

(42)

If a given chromophore is excited into its lowest excited state, from which emission is expected according to *Kasha's* rule, then the transition moments of absorption and emission belong to the same electronic transition and are virtually collinear. Because this situation is usually settled at the lowest energy region of the absorption spectrum the highest anisotropy values are found here. After

excitation at higher energies relaxation to the lowest excited state takes place and the transition moments of absorption and emission are generally displaced leading to somewhat lower anisotropy values.

For these reasons the anisotropy of a sample is in the majority of cases dependent on the excitation wavelength and steady-state anisotropy measurements are normally performed as excitation anisotropy spectra. All processes faster than the fluorescence lifetime that alter the orientation of the emission and the absorption transition moments result in a loss of observed anisotropy. The loss by rotational diffusion can be sufficiently suppressed by measuring in *e.g.* viscous solvents, and thus the remaining decrease of anisotropy might be the result of intramolecular energy transfer and molecular relaxation processes.

Unlike to the steady-state anisotropy measurements, which are generally excitation anisotropy spectra, the time resolved anisotropy measurements supply emission anisotropy decay curves at specific emission wavelength and by excitation with a distinct energy.

Therefore, a sample is excited by polarised light pulses and the time dependent emission intensities $I_{\parallel}(t)$ and $I_{\perp}(t)$ are recorded. Thus, the anisotropy at the distinct time t after time zero is given as:

$$r(t) = \frac{I_{\parallel}(t) - I_{\perp}(t)}{I_{\parallel}(t) + 2I_{\perp}(t)} \tag{43}$$

The experimental anisotropy traces show multiexponential decays, which can be fitted assuming independent exponentials (see equation (44)).[37,38] A detailed analysis of the different lifetimes, amplitudes and anisotropy values may provide information about the different depolarisation mechanism (relaxation, energy transfer, *et cetera*). Because such investigations are generally performed in solution the depolarisation caused by rotational diffusion gives the limiting time resolution and only processes faster than the rotational diffusion are observable.[39-42]

$$r(t) = r(0) \cdot (a_1 e^{-t/\tau_1} + a_2 e^{-t/\tau_2} + a_3 e^{-t/\tau_3} + \ldots) \tag{44}$$

where

$r(t)$ is the time-resolved anisotropy, $r(0)$ is the limiting anisotropy in the absence of rotational diffusion, τ_x are the individual correlation times and a_x are the fractional amplitudes of each correlation time in the anisotropy decay ($\Sigma a_x = 1$).

2.1.2   Electron Transfer Theory

Besides the above discussed scenarios of energy transfer, an excited donor molecule features another deactivation pathway. The excited electron might be transferred from the donor to the acceptor. Unlike to the *Dexter* mechanism of excitation energy transfer, no back electron transfer from the acceptor ground state to the donor occurs but the system relaxes into the electronic ground state of the system, where the donor is oxidised and the acceptor is reduced. This section outlines the most important aspects of electron transfer theory.

2.1.2.1   *Marcus* Theory

The *Marcus* theory describes thermally induced electron transfer (ET) from a donor towards an acceptor.[43-48] It is based on the assumption of two intersecting harmonic diabatic free energy surfaces representing the reactant and the product state. In the region of the intersection point both surfaces interact and avoid intersection resulting in an energy gap of $2 \cdot V_{AB}$, see Figure 1.[49]

V_{AB} is the electronic coupling between the reactant and the product states, which is mainly determined by the electronic "communication" between the donor and the acceptor. This allows migration from one energy surface into the other. The *Marcus* theory works strictly only in cases where the interaction between the two states is smaller than the thermal energy ($V_{AB} < k_B T$). Thus, the *Marcus* theory remains a completely diabatic electron transfer theory.
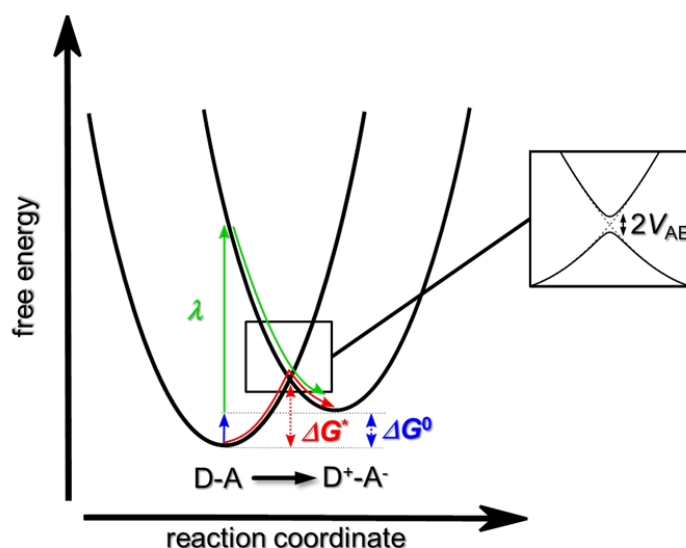
Figure 1: Diabatic free energy surfaces of a non-degenerated donor-acceptor system. ΔG^0 is the ground state energy difference between the two states. ΔG^* is the activation barrier for a thermally induced electron transfer (red arrow). The sum of the (vertical) green and blue arrows represents the energy for an optical induced electron transfer. The inset shows the situation at the intersection between both surfaces. (V_{AB} is the electronic coupling between the two states).[50]

Within this theory, the activation barrier ΔG^* for the thermal electron transfer depends on the energy difference ΔG^0 between the reactant and the product state and the total reorganisation energy λ (equation (45)).[51]

$$\Delta G^* = \frac{(\lambda + \Delta G^0)^2}{4\lambda} \tag{45}$$

with $\lambda = \lambda_o + \lambda_v$

The total reorganisation energy λ is the energy that is needed to bring the system geometry from the reactant to the product state and that can be separated in the inner reorganisation energy λ_v, which characterises the changes in bond length and angles, and the outer reorganisation energy λ_o which refers to the reorientation of the surrounding solvent molecules.[52] λ_v is a solvent independent molecule specific constant and cannot be calculated in an easy way (*cf.* by quantum chemical calculations *via* neutral in cation geometry (NICG)).[43,53,54] In contrast, λ_o is strongly solvent dependent and can be estimated by the *Born* equation (46) taking the solvent as a dielectric continuum.[55-57]

$$\lambda_o = \frac{e^2}{4\pi\,\varepsilon_0}\left(\frac{1}{2r_D} + \frac{1}{2r_A} - \frac{1}{d_{DA}}\right)\cdot\left(\frac{1}{n^2} - \frac{1}{\varepsilon}\right)$$ (46)

where

r_A, r_D are the radii of the donor and acceptor chromophores, respectively, d_{DA} is the centre to centre distance between the donor and the acceptor, n is the refractive index of the solvent and ε is the permittivity of the solvent.

According to *Marcus*, the rate for electron transfers follows equation (47).[43,51]

$$k_{ET} = 4\pi^2\,hc^2V_{AB}^2\sqrt{\frac{1}{4\pi\,hc\lambda\,k_B T}}\,\exp\left(-\frac{hc(\lambda + \Delta G^0)^2}{4\lambda_o k_B T}\right)$$ (47)

where

h is the *Planck* constant, c is the speed of light, k_B is the *Boltzmann* constant, λ is the reorganisation energy, T is the temperature, V_{AB} is the electronic coupling in cm^{-1} and ΔG^0 is the free energy difference of the two states.

The rate for ET becomes higher when the reaction is more exergonic until ΔG^0 reaches the value of λ. In this situation the reaction exhibits no activation barrier and the rate constant is maximal (optimal conditions). From there on, the rate constant start to decline with increasing free energy difference, as a result of an arising activation barrier because the intersection point between both states now climes along the left flank of the reactant state (see Scheme 11).
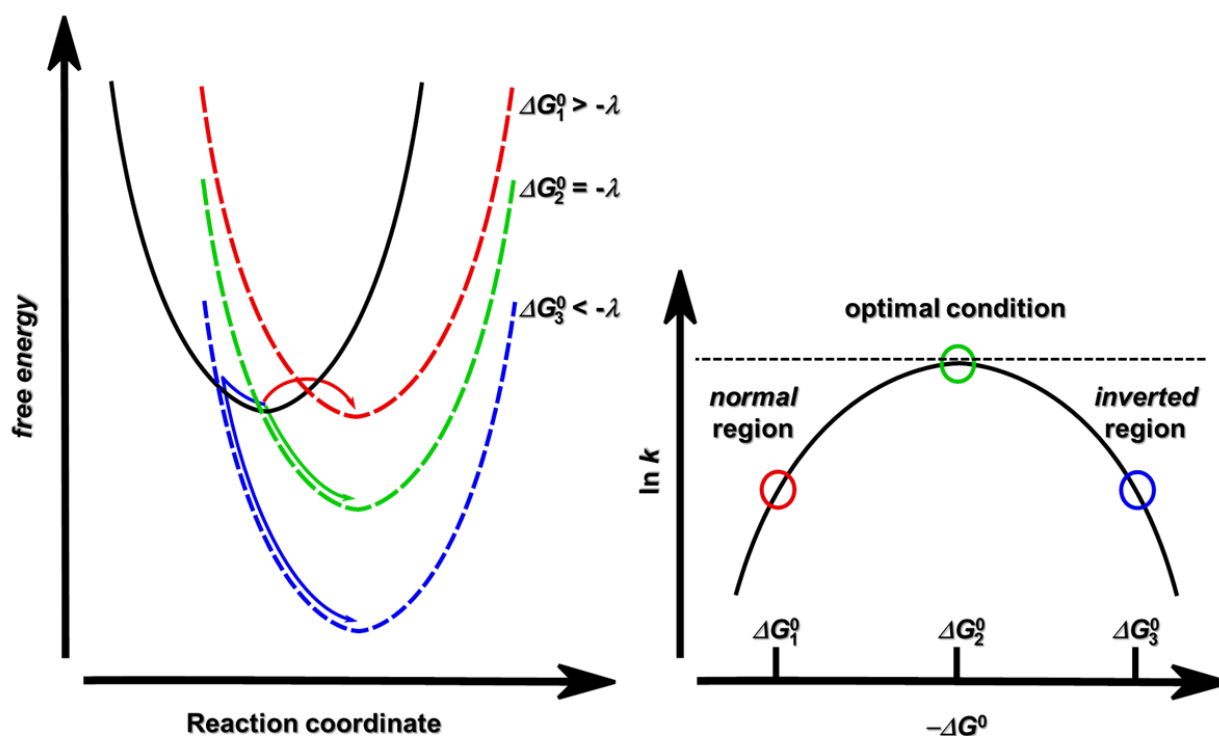
Scheme 11:   Left: Free energy surfaces with decreasing ΔG^0 values representing electron transfer reactions in the *Marcus normal* region (red), under optimal conditions (green) and in the *Marcus inverted* region (blue). Right: Plot of ln k_{ET} versus the reaction driving force (-ΔG^0).[45].

This *inverted* region prediction is certainly the most famous conclusion of the *Marcus* theory[44] (from 1956). Although *Marcus* predicted its existence in 1960[47] it took till 1984 when *Miller et al.*[58] proved his assumption experimentally and in 1992 *Marcus* was honoured with the *Nobel* prize in Chemistry "*for his contribution to the theory of electron transfer reactions in chemical systems*"[a] [45,46].

Until today, the *inverted* region has been observed many times but while the classical *Marcus* theory rather accurately describes ETs in the normal region, it overestimates the *inverted* region effect. According to *Marcus*, the driving force dependence of the rate constant follows a parabolic behaviour but the flank in the *inverted* region has been found complanate.[59]

The situation in the *inverted* region is much better described by semi-classical *Marcus* theories that introduce nuclear tunnelling effects, which are considerably important in the *inverted* region. Thus, thermally activation is no longer required and ET is a non-radiative transition between the two

---

[a]   "The Nobel Prize in Chemistry 1992". *Nobelprize.org.* Nobel Media AB 2013. Web. 29 May 2014. <http://www.nobelprize.org/nobel_prizes/chemistry/laureates/1992/>

states. In the *Bixon-Jortner* theory the rate constant for ET is again based on *Fermi*'s Golden Rule expression (equation (48)).[48,60,61]

$$k_{ET} = 4\pi^2 c V_{AB}^2 \cdot FCWD \qquad (48)$$

where

V_{AB} is the electronic coupling in cm^{-1} and *FCWD* is the *Franck-Condon* weighted density of states at the intersection point of the reactant and the product energy surface.
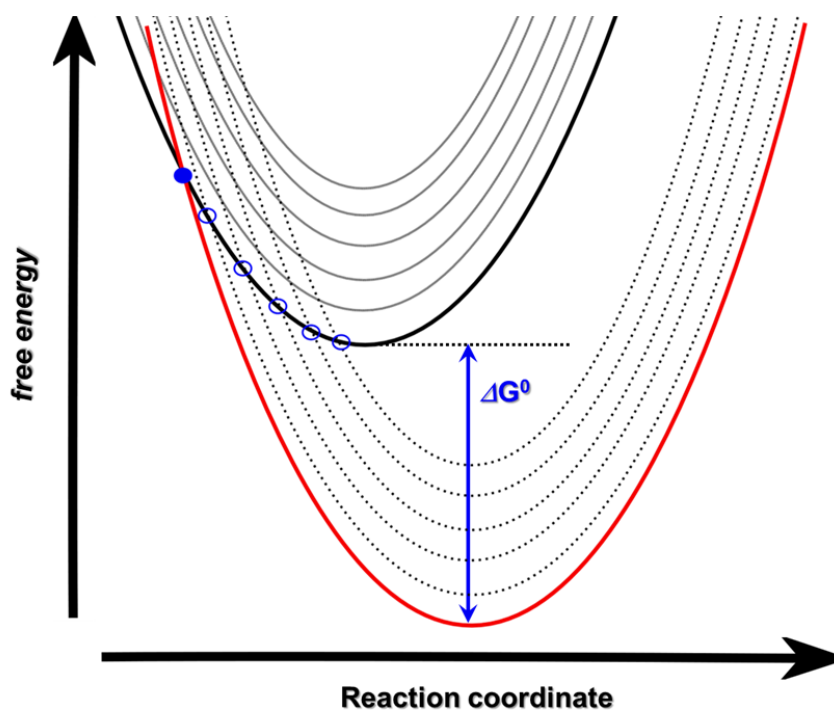
Scheme 12: **Diabatic potentials of the reactants (black) and the products (red) state consisting of several vibrational modes in the *Marcus inverted* region (grey and dotted, respectively). Taking higher vibrational modes into account in the *Bixon-Jortner* theory gives access to additional transition channels (o) in contrast to the single transition channel in the classical *Marcus* theory (•).[62].**

Taking higher-energetic molecular vibrations (following the *Franck-Condon* progression) into account opens additional ET channels (see Scheme 12). *Bixon* and *Jortners* merit was to find an expression that replaces the *FCWD* by a relatively simple algebraic term.[63] They introduced the *Huang-Rhys* factor *S*, which is the ratio of the inner reorganisation energy and the averaged molecular vibration mode ($\tilde{v}_v$) that replaces the quantity of high-energetic molecular vibrations by a single value (equation (49)).[63-66]

$$k_s = 4\pi^2 hc^2 V_{AB}^2 \sum_{j=0}^{\infty} \frac{e^{-S} S^j}{j!} \sqrt{\frac{1}{4\pi hc\lambda_o kT}} \exp\left[-\frac{hc(j\tilde{v}_v + \lambda_o + \Delta G^0)^2}{4\lambda_o kT}\right] \tag{49}$$

$$\text{with } S = \frac{\lambda_v}{\tilde{v}_v}$$

where

h is the *Planck* constant, *c* is the speed of light, *k* is the Boltzmann constant, *T* is the temperature, V_{AB} is the electronic coupling in cm^{-1}, $\tilde{v}_v$ is the averaged molecular vibration mode, ΔG_{CS}^0 is the free energy between the two states, λ_o and λ_v are the outer and inner reorganization energy, respectively.

The *Bixon-Jortner* theory has been applied to determine the important ET parameter V_{AB}, λ_v and λ_o from experimental data but since the theory is adiabatic in nature, it is strictly only valid for weakly coupled systems.

For ET in systems with a strong electronic coupling between the two states, the *Bixon-Jortner* theory is complemented by the *Marcus-Hush* theory or rather by the *Mulliken-Hush* theory.[67-70]

For systems, which can reasonably be described by the *Marcus-Hush* theory, the electronic coupling is much larger than the thermal energy ($V_{AB} \gg k_B T$). The strong diabaticity reduces the activation barrier for the thermally induced ET given in the *Marcus* theory by equation (45), p: 28, to equation (50).[43,71,72]

$$\Delta G^* = \frac{(\lambda + \Delta G^0)^2}{4\lambda} - V_{AB} + \frac{V_{AB}^2}{\lambda} \tag{50}$$

where

$\frac{V_{AB}^2}{\lambda}$ is the resonance delocalisation energy of the adiabatic electronic ground state.

Systems with such a strong electronic coupling feature charge transfer (CT) bands in their absorption spectra as a result of an optically induced CT. An analysis of this band gives excess to V_{AB} according to equation (51).[43]

$$V_{AB} = \frac{\mu_{trans}}{\Delta\mu_{12}} \, \widetilde{\nu}_{max} \tag{51}$$

where

$\Delta\mu_{12}$ is the diabatic dipole moment difference of the ground and excited state, $\Delta\mu_{trans}$ is the transition moment and $\widetilde{\nu}_{max}$ is the maximum of the CT band.

The transition moment (μ_{trans}) can be calculated with the aid of the integral of the CT band and equation (52).[67,68,73,74]

$$\mu_{trans} = \sqrt{\frac{3hc\varepsilon_0 \ln 10}{2000\pi^2 N_A} \cdot \frac{9n}{(n^2+2)^2} \cdot \int \frac{\varepsilon_{CT}}{\widetilde{\nu}} \mathrm{d}\widetilde{\nu}} \tag{52}$$

where

n is the refractive index of the solvent (for the correction term see *Chako et al.*[73]), ε_0 is the vacuum permittivity, h is the *Planck* constant, c is the speed of light, N_A is *Avogadro*'s constant and $\int \frac{\varepsilon_{CT}}{\widetilde{\nu}} \mathrm{d}\widetilde{\nu}$ is the integral of the reduced CT band.

The major drawback of the *Mulliken-Hush* theory is the need of the diabatic dipole moment difference between the electronic ground and the excited state ($\Delta\mu_{12}$), which cannot be obtained directly. Thus, the adiabatic dipole moment difference is commonly used instead. This difference can be estimated geometrically as $e\cdot r$, where r means the effective electron transfer distance and e is the elementary charge.[43,75,76] However, in many cases the mean distance between the redox centres is used, which is obviously inaccurate, since the effective electron transfer distance is generally shorter than the mean distance and especially organic redox centres are certainly no point charges.[77,78] Moreover, a *Mulliken-Hush* analysis allows no distinct determination of λ_v and λ_o and for compounds exhibiting non-degenerated states ($\Delta G^0 \neq 0$), λ and ΔG^0 are not separable.

2.1.2.2 *Robin-Day* Classes

Mixed valence (MV) compounds or generally donor-acceptor systems can be divided in three classes according to *Robin* and *Day*, depending on the strength of the electronic coupling V_{AB} (see Scheme 13).[79,80]

In the *Robin-Day*-class I, the coupling is absent or insignificant and thus the two redox centres can be seen as isolated units. No electron or charge transfer can be observed, neither optically nor thermally induced. Due to the absent of an electronic interaction, only diabatic potential exist.

Completely different are compounds of the *Robin-Day* class III, in which the electron coupling is that strong, that the two diabatic potentials become two adiabatic ones, with one single minimum. Here, an electron transfer is also not observed since the charge is completely delocalised over both redox centres. (ΔG^* is smaller than the zero-point energy).

In between these extreme cases the *Robin-Day* class II is located. The two diabatic potentials split into two adiabatic potentials, where the electronic ground state features a double minimum. Electron transfer occurs either optically induced by light with the energy of λ (+ ΔG^0) or thermally by with the activation energy ΔG^*. The observation of an intervalence charge transfer (IV-CT) band in the absorption spectra of many MV compounds is the result of such an optically induced charge transfer.
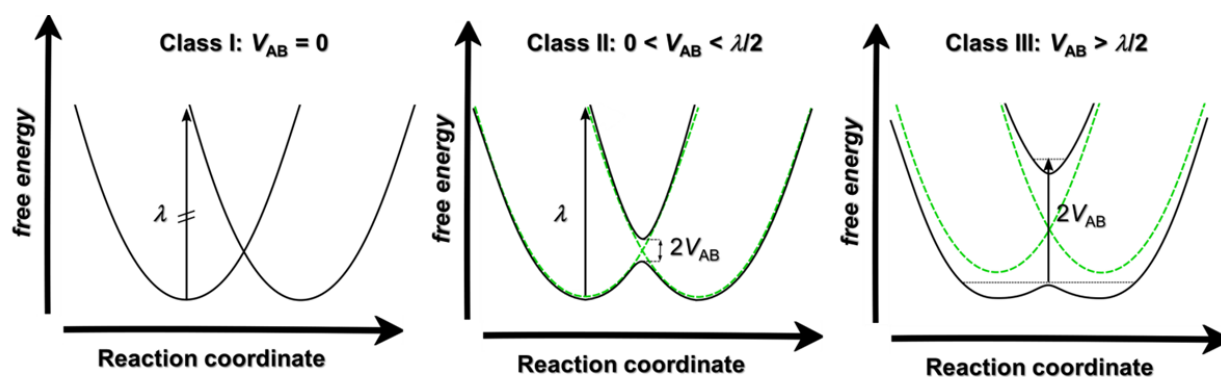
Scheme 13: **Classification of donor-acceptor compounds by means of the electron coupling between the reactant and the product state according to *Robin* and *Day*.**[81,82]

2.1.2.3 Electron Transfer Mechanism

Generally, two different mechanisms may underlie the transfer of an electron from the donor to the acceptor in which the bridge unit plays a crucial role. The electron is either transferred by incoherent hopping, where the electron is for a short time located on the bridge, or by a coherent "superexchange", where the electron is transferred in one single step (see Scheme 14).[83-85]
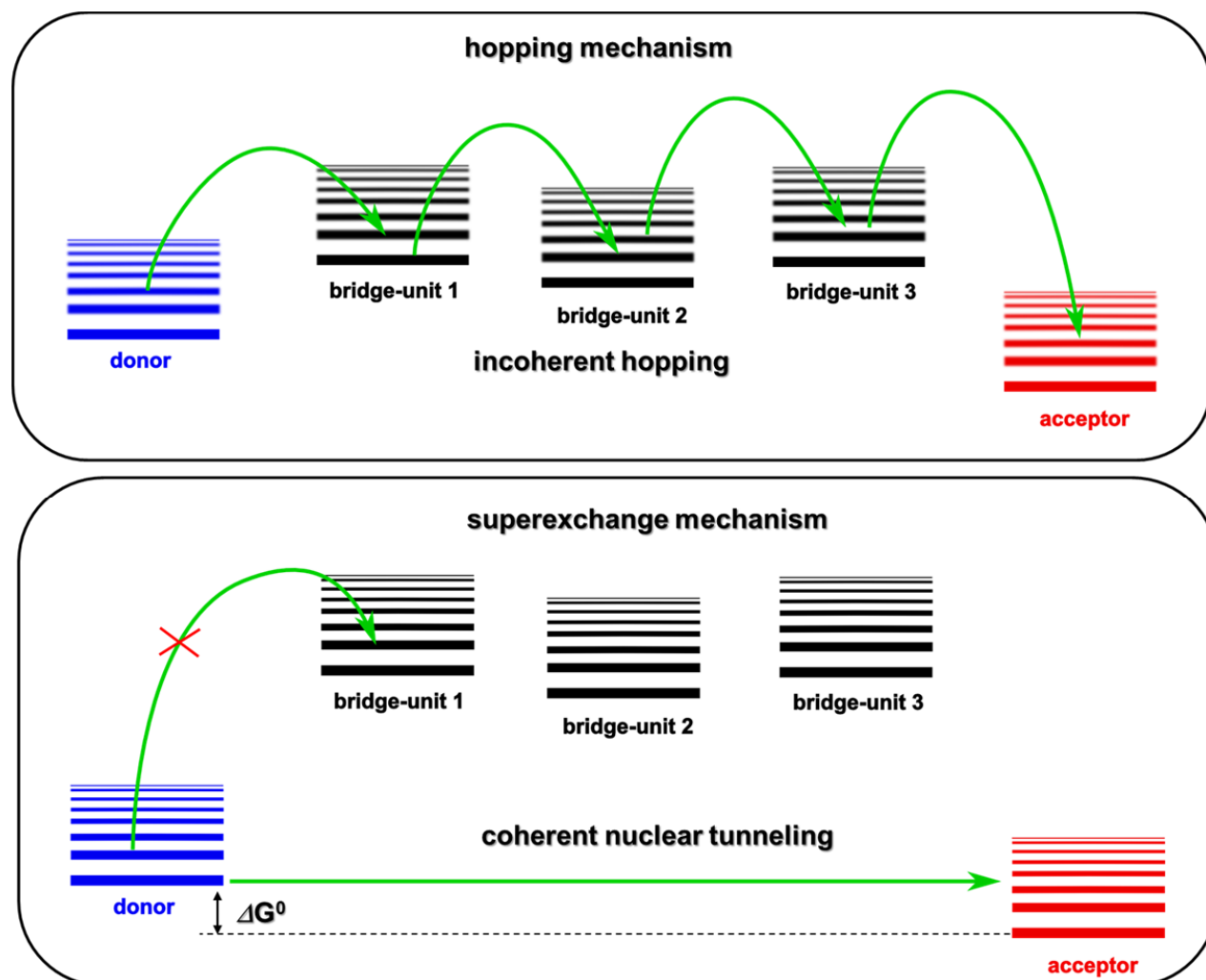
Scheme 14: **Energy state diagram for an ET from a donor to an acceptor *via* several bridging units. If the bridging units possess energetically accessible states the electron transfer takes place by an incoherent hopping process but if the states of the bridge are too high (or to low) in energy, the electron is transferred by one single coherent nuclear tunnelling process from the donor to the acceptor.**[83]

If the bridge possesses energetically suitable states of the bridging unit (and the electronic coupling is relatively small), the electron is transferred in one step from the donor on the bridge and in a second step from the bridge to the acceptor (or to another bridging unit). The situation, where the electron is located on the bridge may be seen as a kind of intermediate, which in principle (if the lifetime is long enough) can be observed by spectroscopy.

The superexchange mechanism is a nuclear tunnel process, which takes place in systems with inaccessible, high-lying bridge states (and with a relatively strong electronic coupling). Although the electron is transferred in one single step and never localised on the bridging unit, the energy of the bridge state strongly influences the electronic coupling according to the *McConnell* model[86,87] (equation (53)) and thus, the electron transfer rate.

$$V_{DA} = \frac{V_{DB} \cdot V_{BA}}{\Delta G^0_{DB}} \qquad (53)$$

where

V_{DA} is the electronic coupling between the acceptor and the donor, V_{DB} and V_{BA} are the electronic couplings between the donor and the bridging unit and between the bridging unit and the acceptor, respectively, and ΔG^0_{DB} is the free energy difference between the donor and the bridging unit.

However, in a given system one electron transfer mechanism may dominate but to some extent both mechanisms operate at the same time and the electron transfer rate is the sum of both fractions.

2.2   State of the Art

The previous section introduced the reader to the theoretical background of energy and electron transfer. This present section will give a basic overview about selected studies concerning energy and electron transfer properties of dendrimers and small donor-acceptor systems.

2.2.1   Photophysical Studies on Dendrimers

One major part of this work is based on the concept of dendritic structures. Dendrimers (from the Greek: *dendron* – tree and *meros* – part) are perfectly hyper-branched self-similar macromolecules with a high density of functional units *e.g.* chromophores (see Figure 2).[88,89]
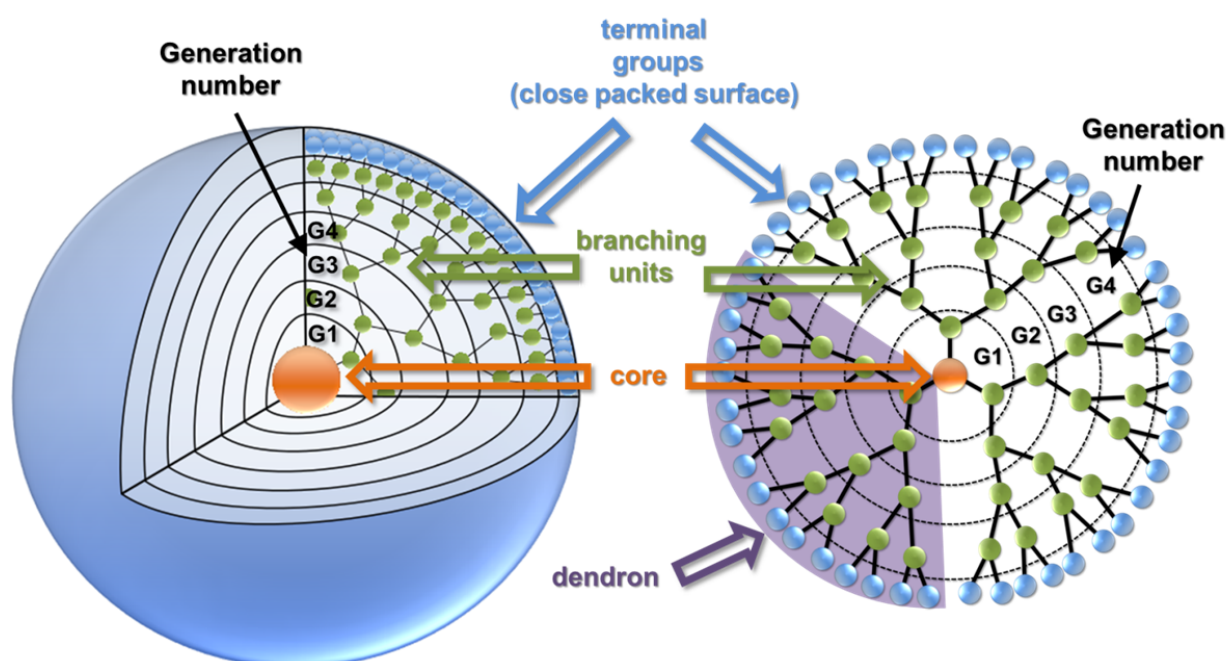

Figure 2:   **Illustration of a dendrimer and its basic components.**

The core in the centre of the dendrimer (or starburst polymer) shapes the system´s three-dimensional structure. The individual dendrons, which are composed of branched repeating units (branching units), are connected to the core. Each layer of branching units is called generation and the number of chromophores increases exponentially from one generation to the next. Consequently, with increasing generation number of the dendrimer the periphery gets more and more crowded and thus the global structure turns into a sphere. The outer layer of the dendrimer is formed by end or terminal groups on which no further growth occurs. Layer-by-layer construction of dendrimers opens the unique opportunity to fully control the arrangement of a large number of chromophores in a rather rigid structure. In contrast to polymers, (ideal) dendrimers are further

characterised by a monodispersive structure and hence they are attractive systems for photophysical investigations.

In general, dendrimer synthesis can be accomplished by two different strategies:

Convergent approach:[90]

Following a convergent synthesis, the dendrimer is synthesised from the outer sphere to the inner core. The individual dendrons are generated stepwise and the lower generation dendron is attached to one at least bifunctional branching unit leading to the next generation dendron. The synthesis is completed by connecting the single dendrons to a focal core (see Scheme 15).
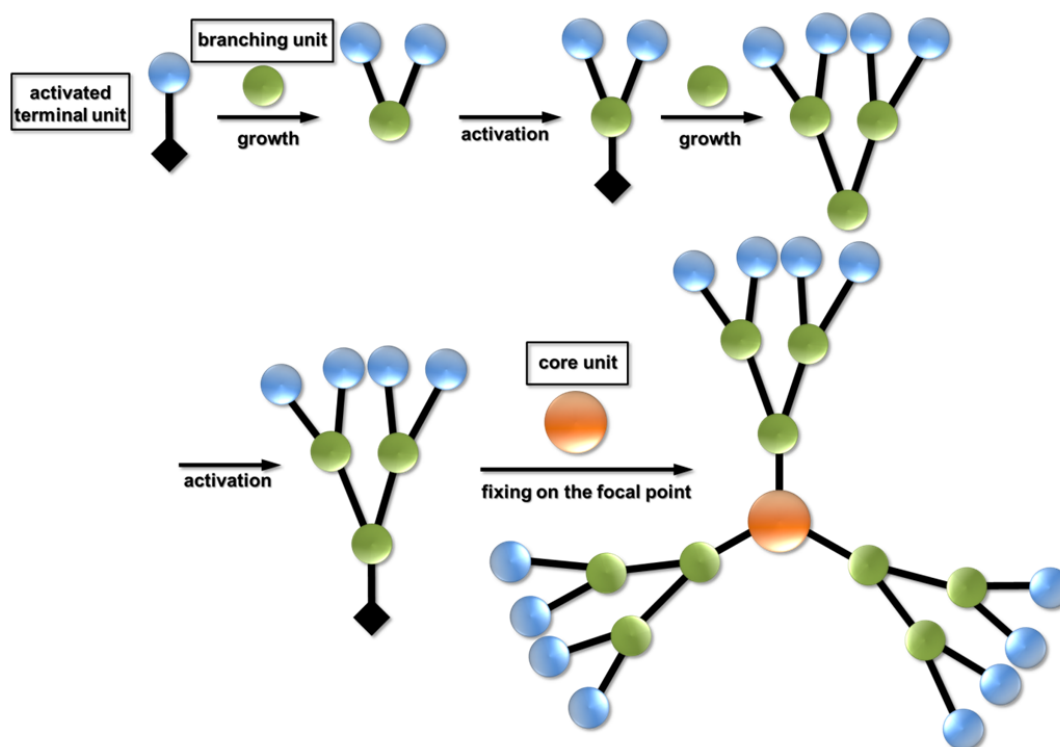
Scheme 15:   **Schematic presentation of a dendrimer synthesis within the converted approach.**

Divergent approach:[91-94]

In contrast to the convergent route, divergent dendrimer synthesis starts from a multifunctional initiator core and grows to the periphery. The dendrimer is constructed by successively treating the evolving dendrimer with branching units. In a concluding step the terminal groups are attached to the dendrimer scaffold to provide the envisioned dendrimer (see Scheme 16).
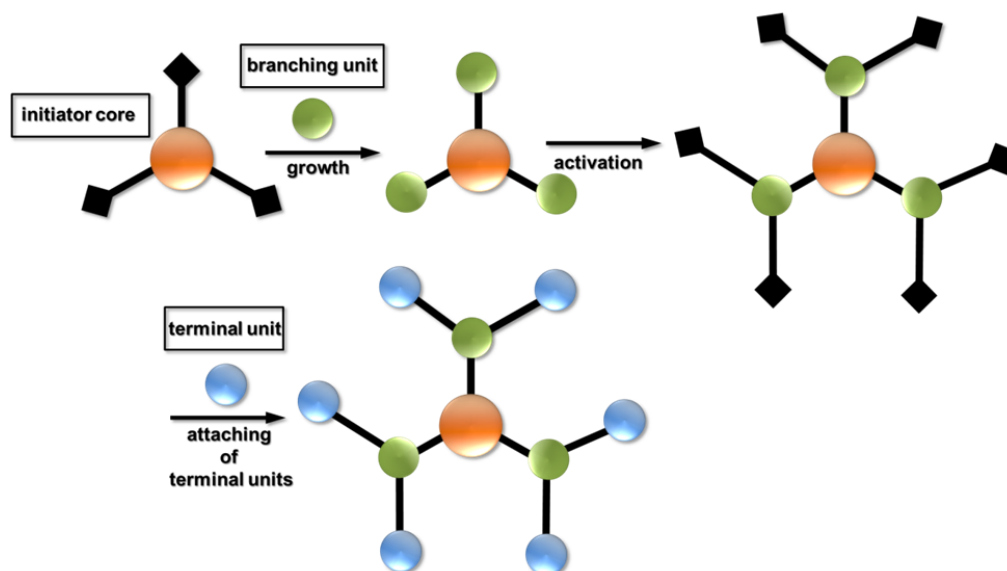
Scheme 16: **Schematic illustration of a dendrimer synthesis following the divergent approach.**

Since in the convergent approach the growing component is connected to a single branching unit per step, resulting dendrimers are generally considered to be more monodispersive than those yielded by a divergent route, where multiple reactive sites have to react within a single reaction step. Thus, dendrimer syntheses conducted by a divergent strategy usually demand highly reliable and quantitative reactions (*e.g.* "click reactions", *vide infra*).

The convergent approach is usually limited to low generation dendrimers as the focal point becomes considerable congested when attaching sterically demanding dendrons. Moreover, convergent syntheses generally require considering amounts of starting material.[95]

So far, several groups have elaborated with dendritic structures to mimic photosynthesis in nature and to study photoinduced dynamics such as energy transfer and electron transfer. Due to the large number of chromophores dendrimers have been of special interest in the field of artificial light harvesting and light emitting devices but there are also widespread biological and medical applications. Moreover, they are potential candidates for nonlinear optical studies.[40,96]

To elucidate energy transfer processes in branched macromolecules *Hartwig et al.* investigated conjugated triarylamine dendrimers up to the third generation (Chart 1) by fs-time resolved emission anisotropy measurements.[39]
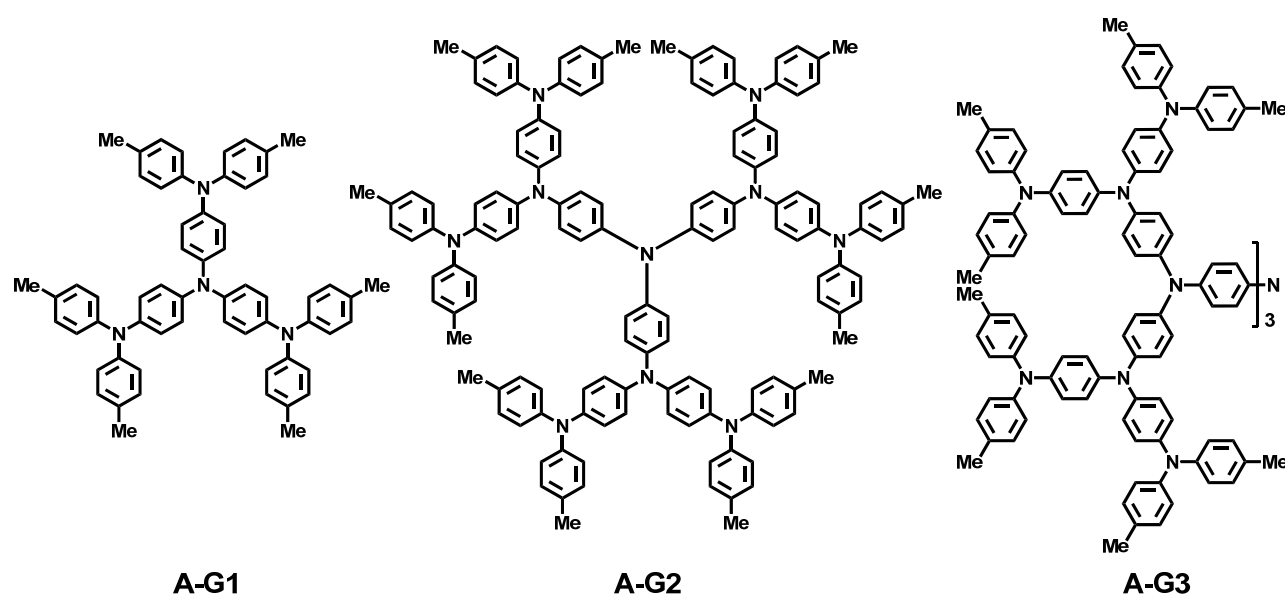

A-G1   A-G2   A-G3

Chart 1:   **Molecular structures of the dendrimers A-G1, A-G2 and A-G3.**[39]

The authors observed very fast initial anisotropy decays during the first 100 fs after excitation (τ(**A-G1**) = 90 ± 50 fs, τ(**A-G2**) = 60 ± 20 fs, τ(**A-G3**) = 30 ± 10 fs). However, the dendrimers possess some residual anisotropy that persists into the ps-time region and becomes smaller with increasing generation number due to an increasing number of accessible dipole moment orientations in the nonplanar dendrimers (see Figure 3). The rapid depolarisation in the sub-picosecond time regime was explained by coherent excitation energy transfer domains in the dendrimers. This effect is caused by intramolecular chromophore clustering and the remainder of anisotropy decay is attributed to incoherent intercluster energy hopping. However, such an energy hopping is not indicated by the anisotropy decays and thus the coherent domains were supposed to range over wide fractions even of the largest dendrimer. This finding might be a result of strong interactions between the chromophores over large distances.[39]
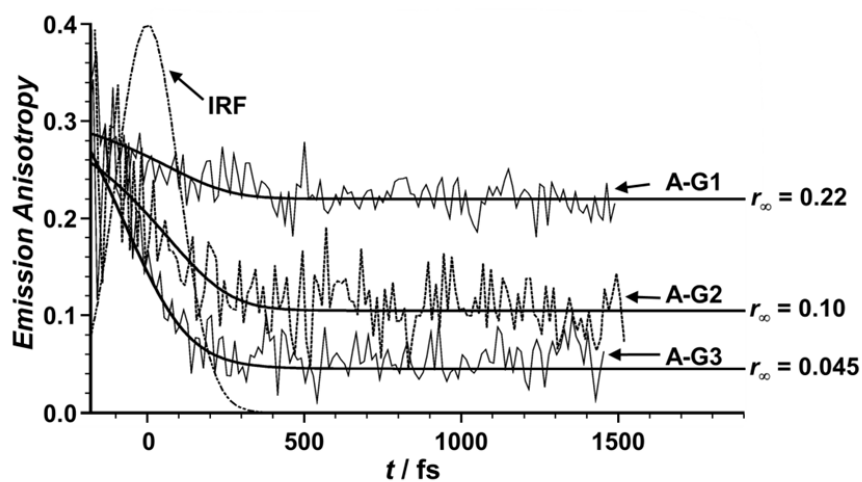
Figure 3: Emission anisotropy decays of A-G1, A-G2 and A-G3 in THF. The arrows mark the experimental data and the solid lines are fits to the experimental curves. r_∞ is the residual anisotropy and IRF means instrument response function. Excitation at 25600 cm^{-1} (390 nm). Emission at 20800 cm^{-1} (480 nm).[a]

Triarylamine chromophore-based dendrimers that are linked by larger π-systems are rather rare. *Blanchard-Desce et al*. investigated the dendrimers **B-G1**, **B-G2** and **B-G3** composed of rigid tolane linear building blocks (Chart 2).[97]
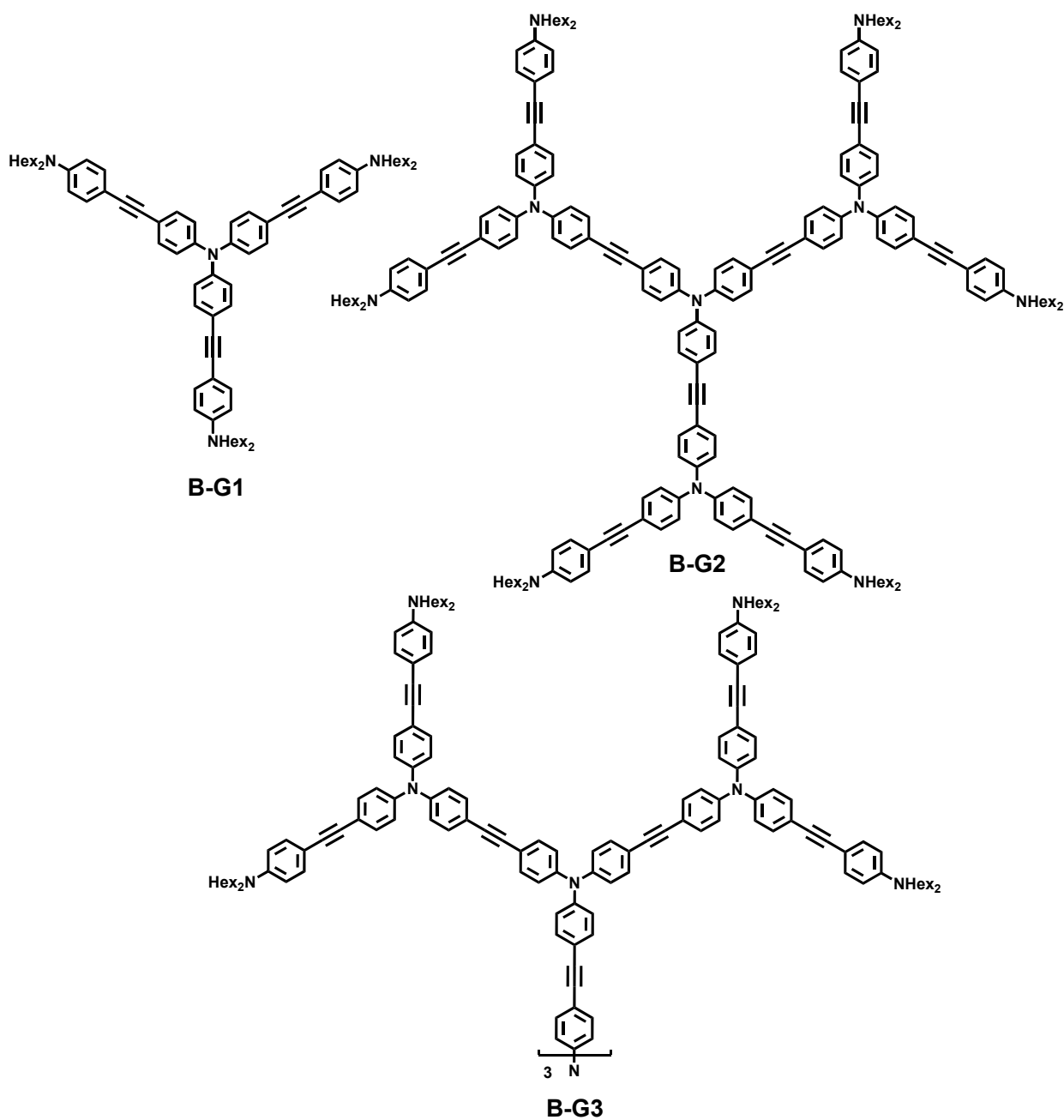

Chart 2: **Molecular structures of the dendrimers B-G1, B-G2 and B-G3.**[97]

The excitation energy transfer in the dendrimers was proposed to occur by incoherent hopping. The authors adopted the concept of "spectroscopic units" as used for linear polymers, for dendrimers in which the excitation is delocalised over a larger section than the size of one linear segment of the branches.[98-100] If the "spectroscopic unit" is not extended over the entire molecule, the dendrimer might be considered as a congregation of those and energy distribution over the dendrimer takes place by incoherent hopping between these units. The energy migration in the dendrimers was monitored by ultrafast emission anisotropy measurements (see Figure 4). The authors classified the anisotropy decay into three regions: At the beginning ultrafast depolarisation caused by coherent energy distribution with a time constant of ca. 30 ps leads to a residue anisotropy of ca. 0.125 within the instrument response function. This process was followed by incoherent excitation energy hopping between the "spectroscopic units". The slowest decay was assigned by starting displacement of the emission transition moment by rotation of the molecule.[97]

Figure 4:   Top: Emission anisotropy decays of B-G1 in toluene. The arrows mark the experimental data and the solid lines are fits to the experimental curve at λ_{em} = 480 nm. Excitation at 25600 cm^{-1} (390 nm). Emission wavelengths are indicated in the figure. Inset: Emission anisotropy in the first ps at $\lambd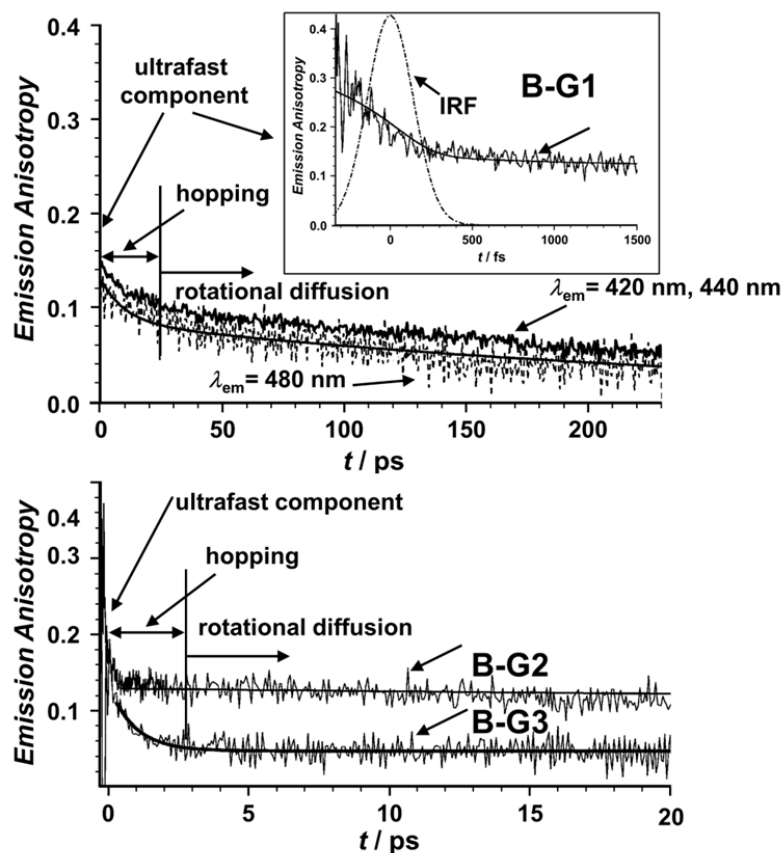a_{em}$ = 480 nm. IRF means instrument response function. Bottom: Emission anisotropy decays of B-G2 and B-G3 in toluene. The arrows mark the experimental data and the solid lines are fits to the experimental curves. Excitation at 24400 cm^{-1} (410 nm). Emission at 22700 cm^{-1} (440 nm).[a]

In a different study *Goodson III et al.* found that the nature of the focal point (N, P and C), to which the branches are connected, plays a significant role on the energy transfer process due to its influence on planarity and electronic coupling in dendrimers (Chart 3).[101]
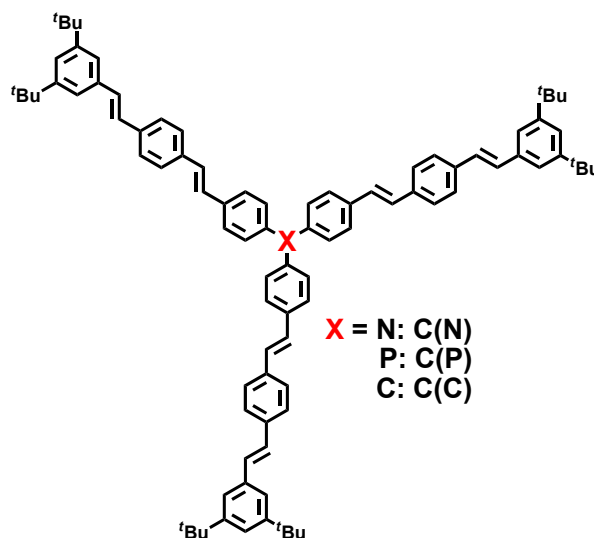

Chart 3: **Molecular structures of the dendrimers C(N), C(P) and C(C).**[101]

The authors measured time resolved emission anisotropy decays by fluorescence up-conversion from the distyrylbenzene dendrimers **C(N)**, **C(P)** and **C(C)**. While the linear model system (not shown) presents no significant anisotropy decay in the monitored time window, the dendrimers demonstrate a strong anisotropy decrease in the first ps (see Figure 5). Remarkably, the anisotropy of **C(N)** decays clearly monoexponentially with a short lifetime of 57 fs. In contrast the **C(P)** and **C(C)** anisotropy decays were reproduced by a biexponential function consisting of a rather short time constant slightly smaller than that found for **C(N)** and a longer lifetime of roughly 1 ps (**C(P)**: τ_1 = 51 fs, τ_2 = 702 fs and **C(C)**: τ_1 = 37 fs, τ_2 = 960 fs). Obviously, the fast depolarisation observed for **C(N)** is related to a coherent energy migration process while the longer lifetime in the decay of **C(P)** and **C(C)** was explained by incoherent excitation energy hopping between the individual branches and serves as a proof for a weaker electronic coupling between the branches in **C(P)** and **C(C)** compared to **C(N)**. In contrast, it is also imaginable that coherent energy migration may occur, as indicated by the fast time constant similar to the one found for **C(N)**.

Moreover, the progression of the electronic communication between the branches in the order **C(N)** > **C(P)** > **C(C)** was explained by the different geometries of the dendrimers centre, which is trigonal planar for **C(N)**, pyramidal for **C(P)** and tetrahedral for the **C(C)** derivative. For this reason the delocalisation of the lone pair is more effective in **C(N)** than in **C(P)** and absent in **C(C)** which is substantiated by an increasing blue shift in the absorption going from **C(P)** to **C(N)**. Furthermore, in the pyramidal geometry of **C(P)** the branches are allowed to come into closer contact than in the

tetrahedral conformation of **C(C)** leading to a faster energy hopping. Additionally, the different geometries and thus the different orientations of the transition moments are reflected in the residual anisotropies before rotational diffusion commences.[101]
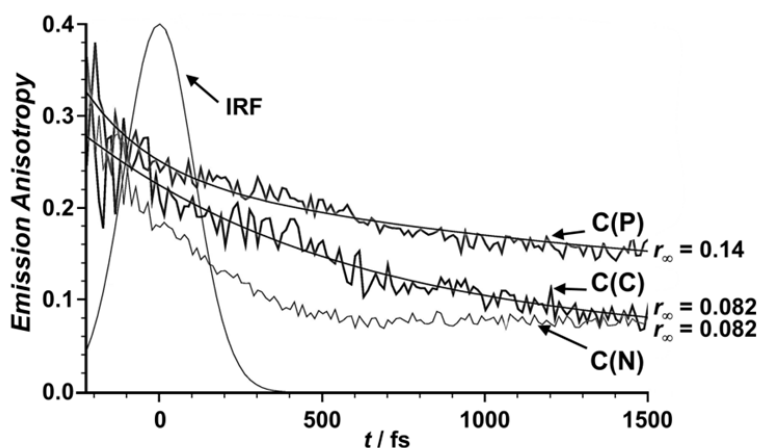

Figure 5:   **Emission anisotropy decays of C(N), C(P) and C(C) in CHCl$_3$. The arrows mark the experimental data and the solid lines are the biexponential fits. r_∞ is the residual anisotropy and IRF means instrument response function. Excitation at 25600 cm^{-1} (390 nm). Emission at 20800 cm^{-1} (480 nm).[a]**

During the process of light harvesting the chromophores at the dendrimers periphery are excited by absorption of solar light and the excitation energy is transported unidirectionally to the centre of the dendrimer, where the energy is converted into chemical or photon energy.

The dendrimers **A-G1**–**A-G3**, **B-G1**–**B-G3**, **C(N)**, **C(P)** and **C(C)** mainly present energy migration between individual (more or less identical) chromophore branches ("spectroscopic units").

In theoretical work *Klafter* and co-workers demonstrated that vectored energy transfer through a carefully adjusted energy gradient from the dendrimer surface to the core may be more efficient in energy funnel dendrimers than "random work" energy transfer by nearest-neighbour jumps.[102-104]

To achieve such an energy gradient the outmost chromophores have to exhibit a large HOMO-LUMO gap which decreases from the periphery to the core. Then, the excitation energy would migrate from the surface *via* a sequence of chromophores with gradual smaller HOMO-LUMO gaps to the centre, where an adequate chromophore either stores the energy or converts it into a convenient form.[105]

Moore et al. investigated energy transfer performances in a series of phenylacetylene-based monodendrons with a terminated perylene-core as an energy "sink" (Chart 4). In the monodendron **D*-5** an inherent energy gradient was realised through decreasing conjugation length of the linear phenylacetylene segments between the meta-substituted benzene branching points from the centre to the outersphere. The authors analysed the energy transfer efficiencies of the monodendrons **D-1**–**6** with varying generation number and further evaluated the influence of the described energy gradient by comparing monodendron **D*-5** with symmetrically grown **D-5** of similar magnitude.[106]
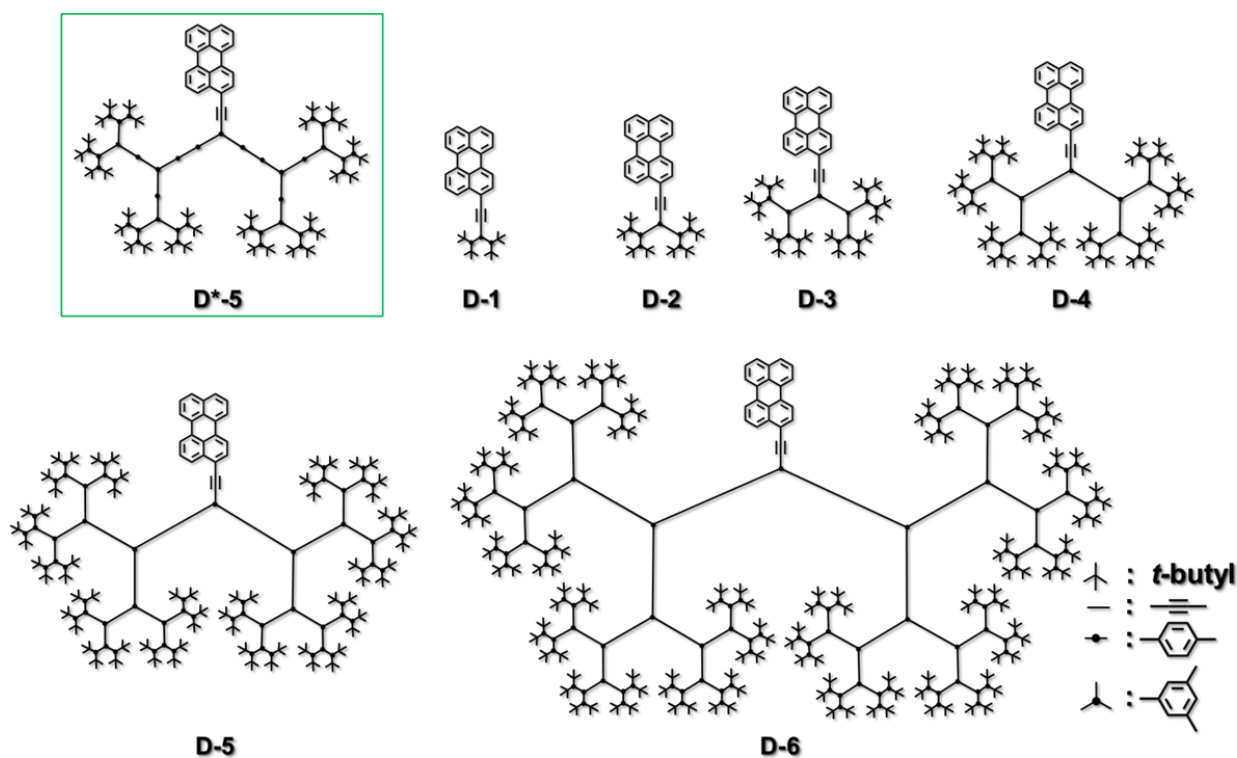
Chart 4: Illustration of the monodendrons D-1 to D-6 and of the monodendron D*-5 (highlighted by the green box) characterised by an energy gradient.[106]

Irradiation of the monodendrons with energy of 32300 cm^{-1} (310 nm) predominantly excites the phenylacetylene groups and statistically the terminal chromophores. Afterwards, the energy is transferred from the periphery to the perylene-core by incoherent energy hopping (*Förster* mechanism) and fluorescence emission occurs from the locally excited perylene moiety. The emission maxima of the perylene at ca. 20800 cm^{-1} (480 nm) and 19600 cm^{-1} (510 nm) are well-separated from the emission maxima of reference monodendrons devoid of a perylene core at ca. 27800 cm^{-1} (360 nm). Thus, the fluorescence quantum yields of the perylene emission from **D1**–**D6** and of the reference systems serve to assess the energy transfer efficiencies in **D1**–**D6**. The authors observed that the energy transport to the perylene-core is significantly less efficient with

increasing generation number. This finding can be explained in context of the *Förster* theory by the larger energy transfer distance in extended monodendrons.[a] However, the monodendrons become more and more efficient in photon-harvesting with growing size as determined by excitation spectroscopy (*cf.* Figure 6).

Most intriguingly, the energy transfer in the monodendron **D*-5** is far more efficient than in **D-5**, a monodendron of similar size, and the rate constant is two orders of magnitude larger for **D*-5** than for **D-5**. This result was explained by the directed energy gradient in **D*-5**. However, the authors added in this regard that **D*-5** exhibits a larger overlap between the absorption of the acceptor and the emission of the donor. Furthermore, uncertainties of rate determining factors (*e.g.* energy transfer distance distributions, non-excluded orbital overlap contributions) in the data of the monodendrons complicated an accurate energy transfer (mechanism) analysis.[96,106]
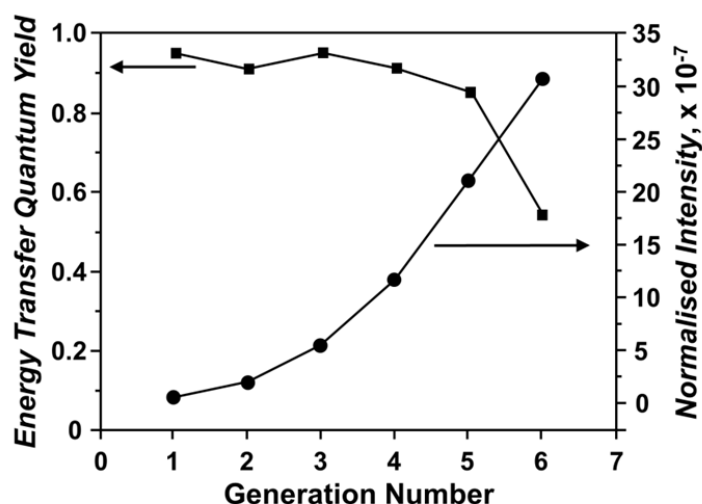

Figure 6: Energy transfer quantum yield and intensities at 32300 cm^{-1} (310 nm) of the normalised excitation spectra of the monodendrons D-1 to D-6 in DCM plotted against the generation number.[106]

---

[a] The energy transfer rate according to a *Förster* mechanism decreases with $1/r^{-6}$.

Beside their unique energy transfer properties dendrimers feature some remarkable characteristics concerning the electron transfer. The accurate control of the redox-chromophore arrangement gives access to arrays with redox-gradients and allows adjusting electron transfer pathways, which predestines these systems for charge capturing or controlled charge transport applications.[107-109]

Selby and *Blackstock* presented a polyarylamine dendrimer in which the arylamino groups on the periphery are more difficult to oxidise then the phenylenediamino groups in the interior of the dendrimer leading to a radial surface-to-core redox gradient (see Scheme 17). Furthermore, the charged core is supposed to be protected from reduction by the dendritic chromophore shell. The authors envision an application as a three-dimensional charge funnel, directing charges from the surface to the core, where the charges might be "stored".[110]
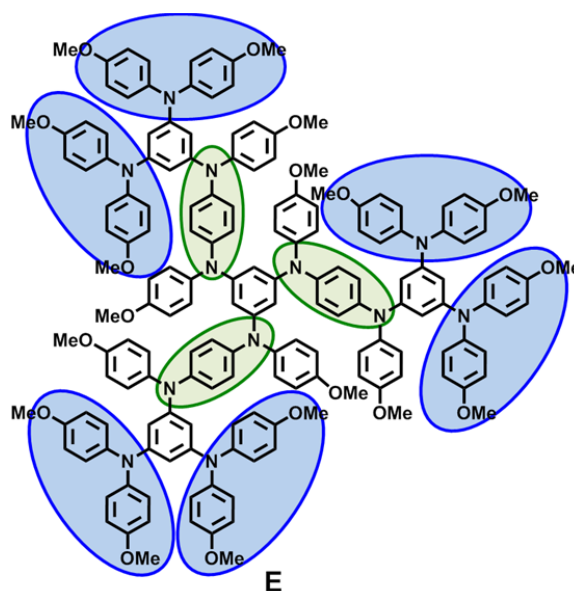
Scheme 17:   **Molecular structure of the dendrimer E with a redox gradient from the periphery to the core. The arylamino groups on the periphery (blue) are more difficult to oxidise then the phenylenediamino groups in the interior (green).**[110]

In natural photosynthesis the absorbed solar energy is efficiently transferred within the light harvesting assembly followed by a sequence of charge/electron transfer processes resulting in a conversion of the excitation energy into chemical energy. Many efforts have been made in the synthesis of dendrimers imitating either the energy or the electron transfer processes of natural light harvesting. However, synthetic approaches that combine both aspects within a single molecule are rare and still of significant importance to understand the natural process of photosynthesis.

Dendrimers in which energy transfer from an excited donor to an acceptor is followed by an electron transfer from the donor to the excited acceptor (Scheme 18) were introduced by *Bardeen et al.*[111]
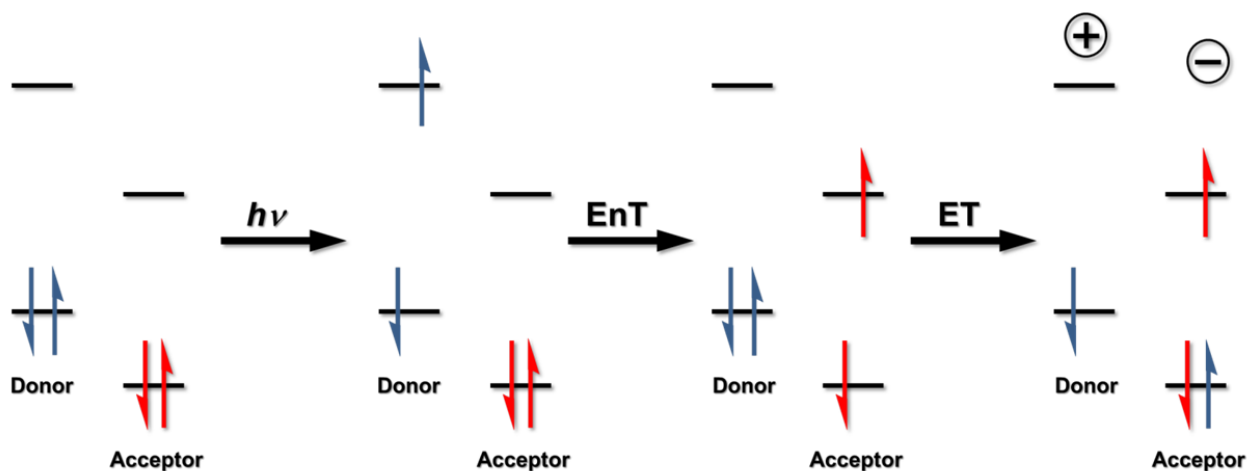
Scheme 18:   **Schematic illustration of the energy state diagram of a donor-acceptor dendrimer. Upon photoexcitation energy is transferred from the donor to the acceptor unit followed by an electron transfer.**[111]

The authors investigated non-conjugated dendrimers bearing a benzthiadiazole energy/electron acceptor core terminated by triarylamine end groups and observed energy transfer processes in the ps-time regime with efficiencies of 80 – 90 % followed by a charge transfer. The individual layers of the macromolecule were built up by meta-substituted benzyl ethers.
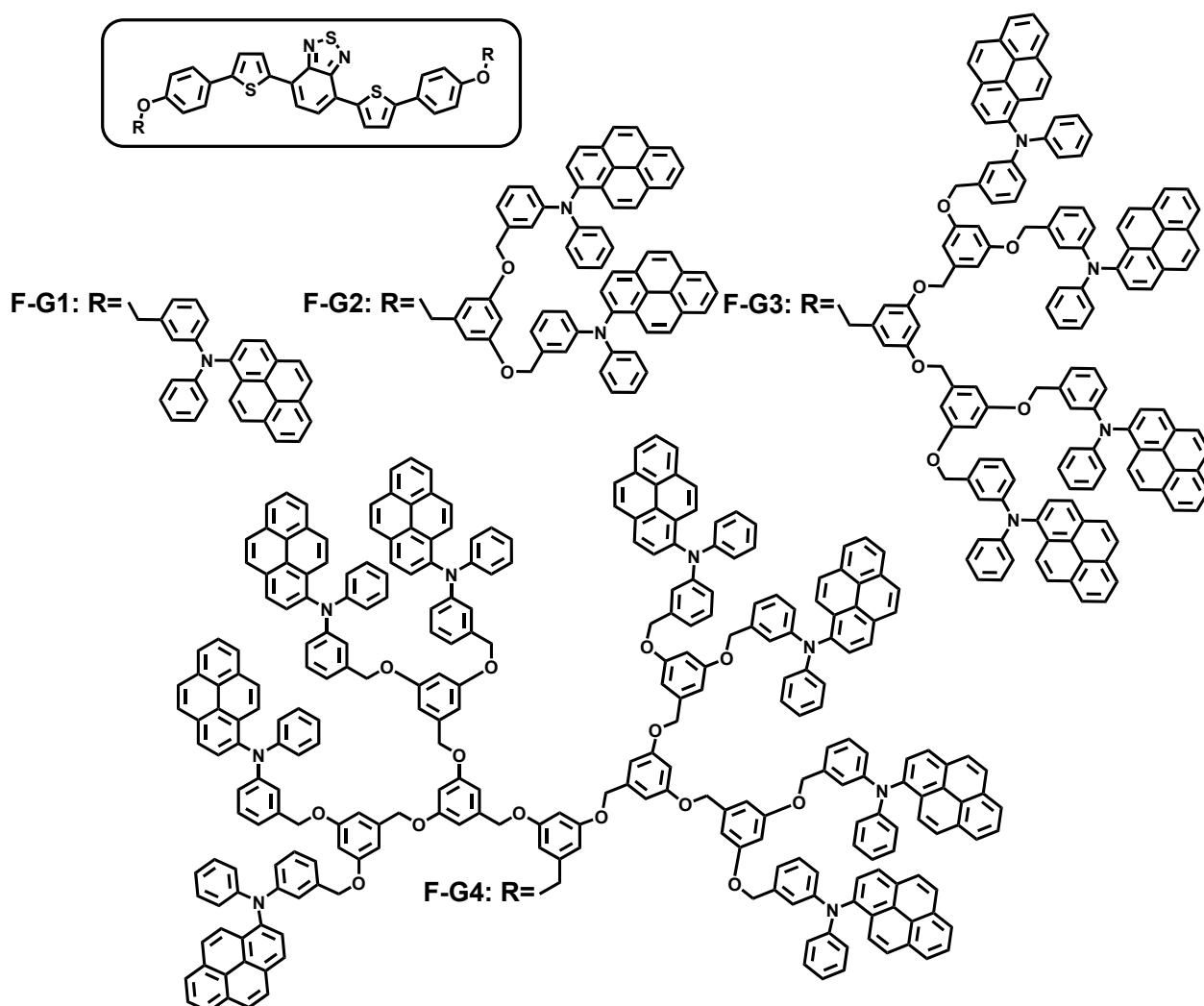
Chart 5:   **Molecular structures of a series of light-harvesting dendrimers investigated by *Bardeen et al.*[111]**

Upon excitation of the dendrimers emission occurs predominantly from the benzthiadiazole core in an excitation wavelength independent manner suggesting efficient energy transfer from the periphery of the dendrimer to the core. The lifetimes in the ps-time regime of the benzthiadiazole fluorescence increase with rising generation number. Similar to *Moore et al.*,[106] the authors explained this finding by the enhanced energy transfer distance in the larger dendrimers leading to a decelerated energy transfer. Concomitantly, emission from the excited core is quenched by an intramolecular electron transfer from the triarylamine donors to the benzthiadiazole acceptor according to time resolved transient absorption measurements. In agreement with that the charge transfer quenching was found to be more rapid in polar solvents such as DMF compared to non-polar toluene while the quenching rate appeared to be independent of the dendrimer size. Although this observation seems to be rather unexpected at the first glance, the authors argued that the CT rate (unlike to the energy transfer rate) is mainly dictated by the distance to the nearest electron

donor, which might be the same for all dendrimers due to backfolding of some chromophore branches in the larger dendrimers, bringing the outersphere donor groups into close contact with the excited core.[111]

Figure 7:   Top: Donor fluorescence decays of F-G1 to F-G4 in DMF. Experimental data are shown in black and the red lines represent the biexponential fits of the experimental data. Excitation at 25000 cm^{-1} (400 nm). The authors do not comment on the emission energy (probably at 21600 cm^{-1} (465 nm)). Bottom: Acceptor fluorescence decay of F-G4 in DMF. Experimental data are shown in black and the red line indicates the biex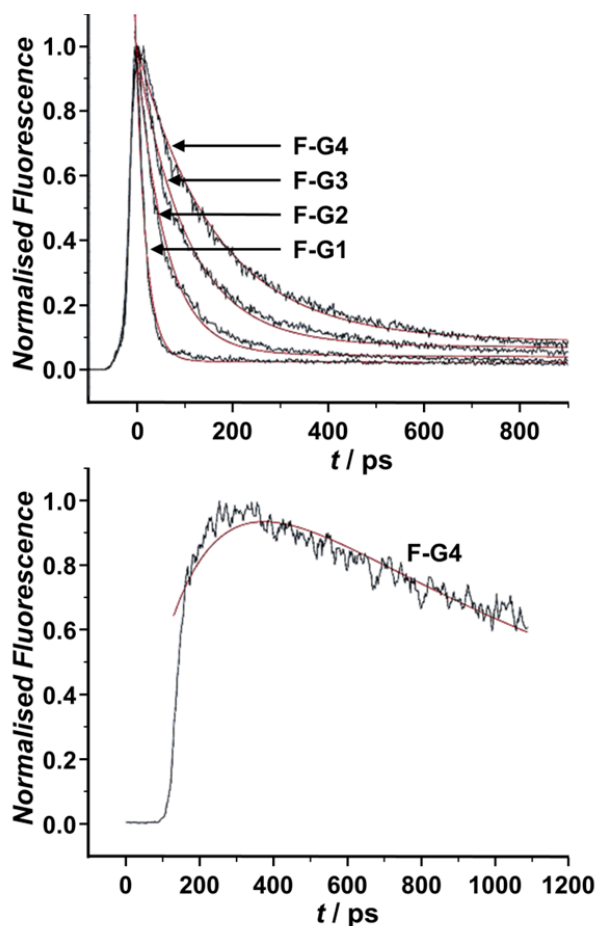ponential fits of the experimental data. Excitation at 25000 cm^{-1} (400 nm). The authors do not comment on the emission energy (probably at 16600 cm^{-1} (600 nm)).[a]

2.2.2 Artificial Systems for Long-Lived Charge Separated States

Donor-acceptor systems are an alternative concept compared to large macromolecules and present simple models to mimic and investigate artificial light harvesting. Beside advantages concerning the production of small molecules such as low-cost synthesis and simple variation of structural components, their reduced complexity facilitates an accurate analysis of structure-property relationships of the key processes for the conversion of solar light – charge separation and charge recombination.

Upon absorption of light an electron is transferred from the donor to the acceptor unit leading to a charge separated (CS) state in which the donor is oxidised and the acceptor is reduced (see Scheme 19) – a prerequisite for converting (solar) light into chemical energy as in natural photosynthesis. A certain lifetime of the resulting CS state is fundamental for using the converted energy. Several groups have developed concepts to guarantee long-lived CS states in artificial light harvesting systems and examined the factors that control charge separation and charge recombination. In the following part the terminal donor chromophores are coloured in blue and the terminal acceptors in red. Intermediate chromophores are coloured according to their donor or acceptor strength, respectively.
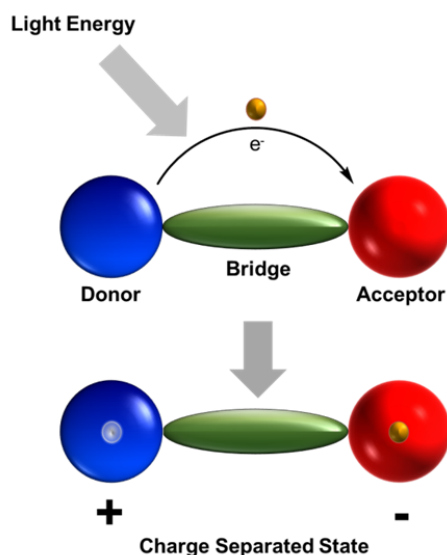
Scheme 19: **Schematic illustration of a donor-acceptor system. Upon absorption of light energy an electron is transferred from the donor (blue) to the acceptor (red) leading to a charge separated (CS) state, in which the donor is oxidised (indicated by the "hole" on the donor) and the acceptor is reduced (indicated by the "electron" (orange)). The bridge (green) may consist of multiple chromophores with an adjusted electron transfer gradient.**

The smallest and simplest artificial system for charge separation represents a dyad comprising one electron donor chromophore and a suitable electron acceptor chromophore that are connected by a bridging unit. An often encountered drawback of donor-acceptor dyads is a fast charge recombination, which certainly limits their application for solar energy conversion.

This drawback is exactly what *Flamigni et al.* found for the TAA electron donor – Ir(III) electron acceptor dyad **G** (see Figure 8). Time resolved transient absorption measurements on **G** in MeCN revealed that photoexcitation with light of an energy of 28200 cm^{-1} (355 nm) at which 30 % of the photons is absorbed by the TAA and 70 % by the Ir(III), leads to charge separation within the instrument resolution (~ 20 ps). The end of pulse spectrum presents a strong transient absorption band at 13100 cm^{-1} (765 nm) with a broad shoulder between 17500 cm^{-1} (570) and 14300 cm^{-1} (700 nm) which the authors attributed to the CS state in which the TAA is oxidised and the Ir(III) reduced. No evidence for either the ^{3}Ir or ^{1}Ir component was provided and thus the lowest value for charge separation processes is supposed to be 5 x 10^{10} s^{-1}. However, the CS state is by far not long-lived with a lifetime of only 70 ps.[112]
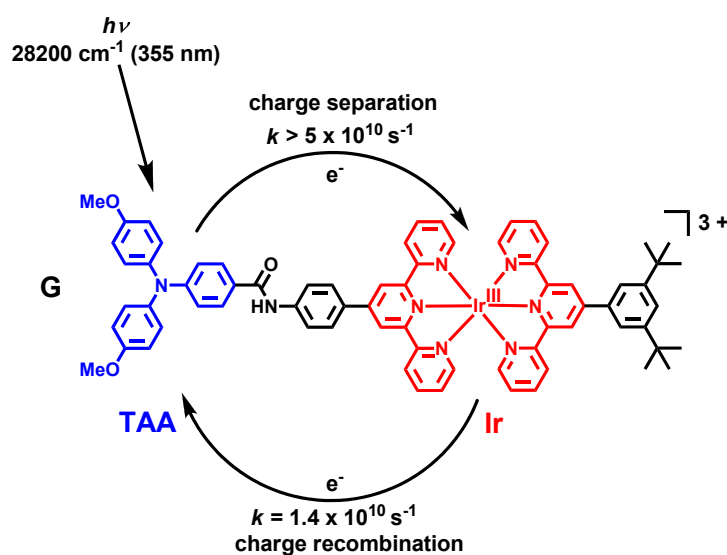
Figure 8:   **Molecular structure of the donor-acceptor dyad G and illustration of photoinduced charge separation followed by a rapid charge recombination taking place in the donor-acceptor dyad G upon excitation with energy at 28200 cm^{-1} (355 nm) in MeCN.**

One approach to prolong the lifetime of CS states is to enhance the distance between the two charges. The prolonged distance might slow down charge recombination as the electronic coupling, which determines the charge recombination rates (*cf*. equation (47), p: 29), strongly decreases with the distance. However, a reduced electronic coupling would not only decelerate the charge recombination but also the charge separation process. This issue might be addressed by the use of

multiple chromophore systems in which a number of subsequent, relatively fast electron transfer steps between accurately adjusted chromophores leads to large overall charge separation. In the charge recombination step, the back electron transfer from the terminal acceptor to the donor (or *vice versa*) has to occur in one single step since the multiple step pathway would be an energetically disfavoured uphill process. As a result, the CS state lifetime will increase.
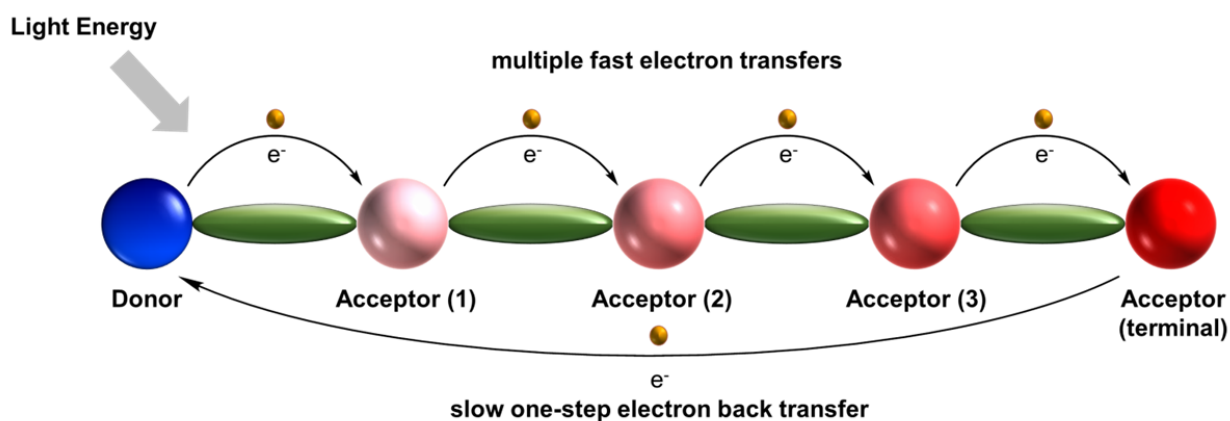
Scheme 20: **Illustration of donor-(multiple)acceptor system with intermediate acceptor chromophores possessing a downhill electron transfer gradient (represented by the saturation of the red colour). After excitation a number of multistep fast electron transfers ensure large spatial charge separation. One-step electron back transfer from the fully CS state is hampered by the small electronic coupling.**

In another study *Flamigni et al.* impressively applied this concept on dyad **G** by attaching an NDI unit adjacent to the Ir(III) as an additional stronger electron acceptor chromophore to yield the triad **H**. Excitation of **H** in MeCN with 28200 cm^{-1} (355 nm) resulted in a similar end-of-pulse spectrum as found for dyad **G** with a pronounced maximum at 13100 cm^{-1} (765 nm) and comprised two additional bands at ca. 20800 cm^{-1} (480 nm) and 16400 cm^{-1} (610 nm). Apparently, the spectrum consists of two different CS state components. As the ratio of the band intensities evolve over time, the authors extracted a time constant for the electron transfer from the Ir(III) to the NDI of $k = 2.4 \times 10^9$ s^{-1} from the rise time of the transient absorption decay at 16400 cm^{-1} (610 nm). Additional transient absorption measurements in the ns to μs time regime reveal a CS state lifetime of ca. 100 μs.
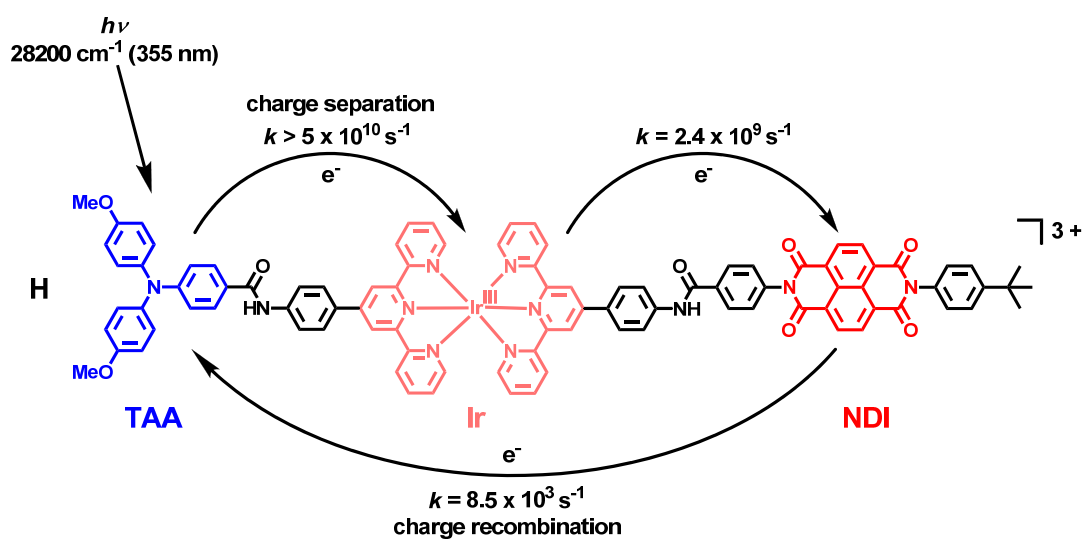
Figure 9: Molecular structure of the donor-acceptor-acceptor triad **H**. The electron transfer processes predominant occur upon excitation of **H** at 28200 cm^{-1} (355 nm) in MeCN.[1,113]

Although the lifetime of the CS state in **H** is significantly enhanced compared to **G**, the efficiency of the second electron transfer step from the Ir(III) to the NDI is dramatically lower compared to the efficiency of the charge separation step. Furthermore, the fully CS state (TAA$^+$-Ir-NDI$^-$) is 0.3 eV lower in energy than the intermediate CS state (TAA$^+$-Ir$^-$-NDI), which indicates a less efficient energy conversion.[1,113]
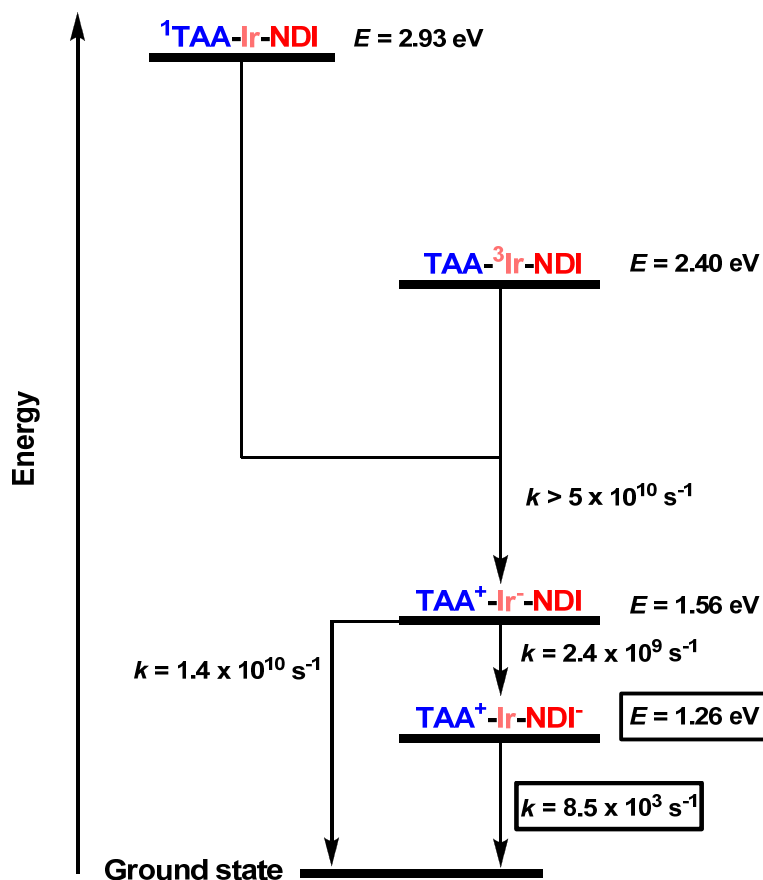
Figure 10: Energy state diagram of the donor-acceptor-acceptor triad H. The triplet state energy was obtained from the maximum of luminescence in butyronitrile at 77 K (excitation at 23300 cm^{-1} (430 nm)), the singlet state energy was obtained from the maximum of luminescence of a model compound in butyronitrile at 77 K (excitation at 24400 cm^{-1} (410 nm)), rate constants were extracted from transient absorption measurements in MeCN, state energies of the CS states were estimated from the redox potentials obtained by cyclic voltammetry in MeCN without further correction.[113]

The multistep charge separation approach obviously prolongs CS state lifetimes up to the sub-second time regime. However, the increasing number of individual steps multiplies the number of deactivation pathways and this in turn reduces the overall efficiency of the CS state population.[114-116] Furthermore, the required downhill electron transfer direction inevitable leads to CS states of lower energy.

According to the *Marcus* theory photoinduced electron transfer dynamics are strongly influenced by relative state energies, reorganisation energies and the electronic coupling between the corresponding states.[59] With an increasing energy difference between two states the rate constant for an electron transfer becomes larger in the *Marcus normal* region but is retarded in the *Marcus inverted* region (*cf.* 2.1.2.1, p: 27).

Crossley et al. investigated donor-acceptor dyads that exhibit charge separation in the *Marcus normal* region and charge recombination in the *Marcus inverted* region. Considering that smaller reorganisation energies will result in faster charge separation (in the *normal* region) and decelerated charge recombination (*inverted* region) the authors designed dyad **I** constituting of a zinc imidazoporphyrin as electron donor and a fullerene as electron acceptor. Both moieties feature minimal small reorganisation energies.[117-119] The existence of a CS state was observed by transient absorption measurements in the ps- and ns-time regime upon excitation of **I** in PhCN with an energy of 18800 cm^{-1} (532 nm) and 17900 cm^{-1} (560 nm). The signal of the CS state was found to decay monoexponentially with a lifetime of 260 μs – a remarkable value taking into account the size of the dyad and experimental conditions (298 K, in solution (310 μs at 278 K)).[118]
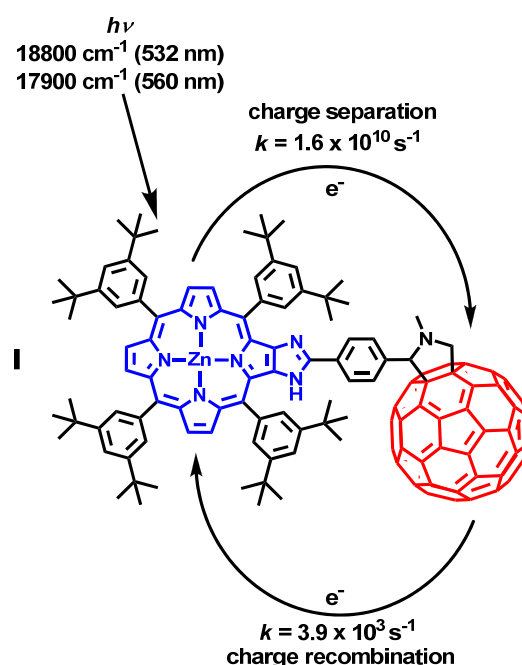
Figure 11:   **Molecular structure of the donor-acceptor dyad I. After excitation of the dyad with 17900 cm^{-1} (560 nm) in PhCN a rapid charge separation in the ps-time regime was observed. The CS state was monitored in the ns-time regime after excitation with 18800 cm^{-1} (532 nm).[118]**

However, the above reported results for dyad **I** were critically reviewed by *Verhoeven et al.* and an alternative explanation was given. The authors supposed that the small rate for charge recombination is not the result of a strong *inverted* region effect but of the generation of a long-lived ^{3}CT state.[51]

The use of spin control is an alternative elegant way towards long-lived CS states in small donor-acceptor systems as the population of triplet CS states (^{3}CS) can significantly enhance the CS state lifetime.[120-122] Charge recombination from ^{3}CS states to the electronic ground state is forbidden by the spin conversion rule and in the absence of heavy atoms there is usually no sufficient spin orbital coupling to overcome this rule. However, it is essential that the ^{3}CS state is the energetically lowest triplet state to prevent spin-allowed charge recombination into localised triplet states.
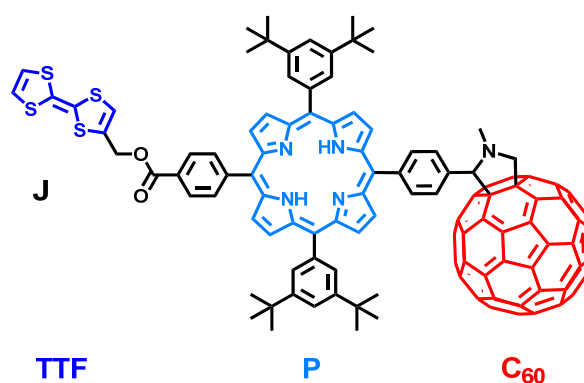
Chart 6:   **Molecular structure of the donor-donor-acceptor triad J.**[123]

By investigation of triad **J** composes of a fullerene electron acceptor and a tetathiafulvalene electron donor connected *via* a free porphyrine, *Gust* el al. observed the generation of a fully CS state after excitation with 16600 cm^{-1} (600 nm) in 2-MeTHF by ns-flash-photolysis. This CS state is energetically lower lying than the localised triplet states and decays within 660 ns into the electronic ground state.[123]
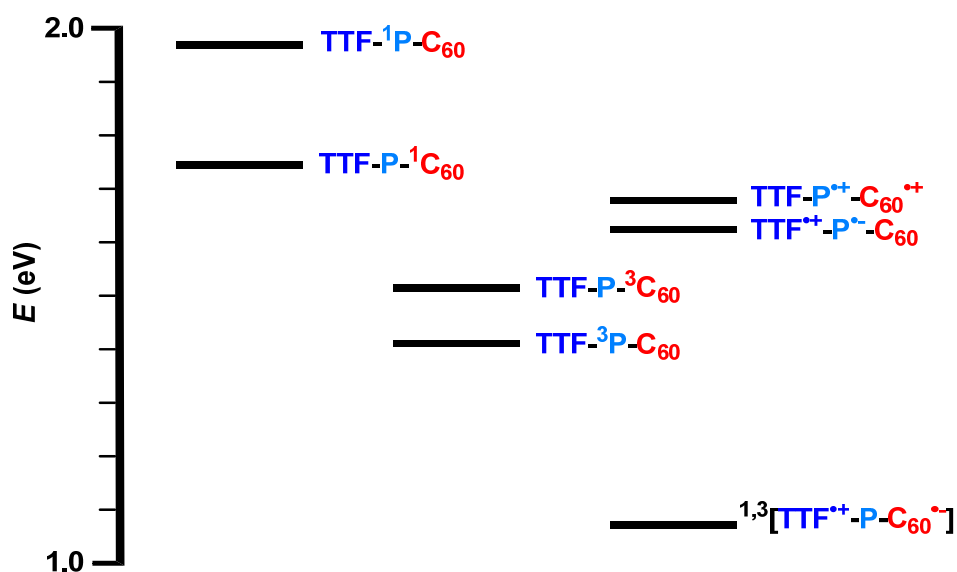
Figure 12: Energy state diagram of the triad J. The energies of the charge separated states were estimated from the cyclic voltammetry data in PhCN and the energies of the singlet states were taken as the wavelength average of the longest-wavelength absorption and the shortest-wavelength emission maxima of J and appropriate model compounds in 2-MeTHF (excitation at 16900 cm^{-1} (590 nm)). The authors do not comment on the derivation of the energies of the triplet states.[123,124]

Carbonera et al. showed by time resolved electron paramagnetic resonance studies (excitation at 18800 cm^{-1} (532 nm)) that refrigerating of **J** in 2-MeTHF to a cryogenic temperature of 10 K, where 2-MeTHF forms an isotropic glass, significantly prolongs the CS state lifetime (~ 8 μs). Moreover, the authors reported the existence of two CS state components with lifetimes of > 1μs and of ~7 μs, which were assigned to the ^{1}CS and the ^{3}CS state, respectively, for **J** embedded and oriented in the nematic phase of the liquid crystal E-7 (LC, Merck) at 295 K.[124]

2.2.3   CuAAC: The Crop of the Cream

In their landmark report in 2001 *Sharpless et al.* coined the concept of "click chemistry" – a class of reactions that are highly selective, wide in scope, occur in quantitative yields and allow product isolation by standard purification strategies.[125]

Beyond a number of identified "click reactions", the copper(I) catalysed 1,3-dipolar alkyne-azide cycloaddition (CuAAC) leading to 1,2,3-triazoles is most prominent and has evolved to a key reaction in numerous synthesis strategies.

First described by *Michael*[126] in the late 19th century, *Huisgen et al.* were the first to systematically study the uncatalysed, thermal reaction in the 1960 – 70s.[127-129] The reaction product, a 1*H*-1,2,3-triazole is a planar aromatic heterocycle that is chemically inert even under harsh reaction conditions. Furthermore, the triazoles exhibit a dipole moment of ca. 5 D and feature hydrogen bond accepting abilities, which makes them a hydrolytically-stable replication of the amide bond in *e.g.* peptides.[130-132]

However, the uncatalysed reaction suffers from high reaction temperatures and a lack of regioselectivity (yielding the 1,5- and the 1,4-regioisomers in nearly equal ratio, see Scheme 21).
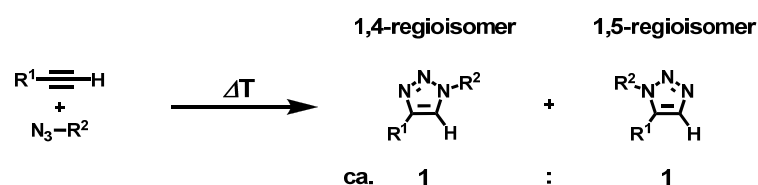
Scheme 21:   Reaction scheme of the thermal, uncatalysed 1,3-dipolar alkyne-azide cycloaddition and the observed ratio of the two possible regioisomers.

In pioneering work *Sharpless* and *Meldal* independently found in 2002 that catalytic amounts of copper(I) significantly improve the reaction performance (therefore, the CuAAC is also known as *Fokin-Sharpless-Meldal* reaction). Since its discovery, the CuAAC enjoys great popularity in diverse research fields not least due to the various approaches for preparation of organic alkynes and azides, such as Pd-catalysed cross reactions.[133,134]

In contrast to the thermal reaction, the reaction rate of the CuAAC is enhanced by a factor of 10^5 and the 1,4-regioisomer is exclusively formed in excellent yields.[135] The reaction can be performed at temperatures from below 0°C up to 160°C in media reaching from aqueous to complete non-polar solvents and is mostly independent of the pH (ca. 4 – 12).[135] Furthermore, the reaction tolerates a wide range of steric and electronic demands at both the azide and the acetylene, is orthogonal and occurs exclusively upon activation by the copper(I) catalyst.[136]

For these reasons *Sharpless* called the CuAAC "as good as a reaction can be"[125] and the "cream of the crop"[125] of "click reactions".[137,138]

The enhanced reaction rates in the presence of copper(I) can be attributed to the course of the reaction mechanism. In case of the thermal reaction a concerted mechanism is supposed for which *Sharpless et al*. calculated an insignificant difference between the activation barrier for the 1,4- and the 1,5-regioisomer, explaining the observed product ratio.[135] For the metal catalysed reaction the authors suggested a stepwise catalytic cycle with a significant decrease of activation barrier leading to the observed 10^5 rate acceleration compared to the thermal reaction. Although the basic steps of the catalytic cycle are fairly understood, the role and appearance of the active copper acetylene species is still subject of current research.[139] Supported by their DFT calculations *Sharpless et al*. assumed a mononuclear copper-acetylene complex with "end-on" orientation of the copper to the triple bond.[135] This "end-on" orientation was questioned by *Meldal* and *Tornøe*, who argued that at least two copper atoms are participating in the transition state considering kinetic studies and the comparison of a series of Cu(I)-acetylene complexes from the Cambridge Crystal database. In addition the azide was proposed to coordinate *via* its terminal nitrogen towards a copper atom with a bond angle of ca 180° and coordination of the carbon linked nitrogen seems to demand further directing coordination affirming the involvement of a second copper atom.[130]

Hein and *Fokin* in turn refuted this mechanism by DFT computations, which revealed that the azide coordination supposed by *Meldal et al*. might be energetically unfavourable. However, the authors added that the consideration of a second copper atom in the proposed catalytic mechanism has a positive effect on the activation barrier.[131] Recently, *Fokin et al*. performed a series of stoichiometric copper isotope (^{65}Cu : ^{63}Cu) crossover studies to elucidate the respective role of two independent copper species in the crucial cycloaddition steps.[136] Their investigation resulted in the state of the art catalytic cycle depicted in Scheme 22.
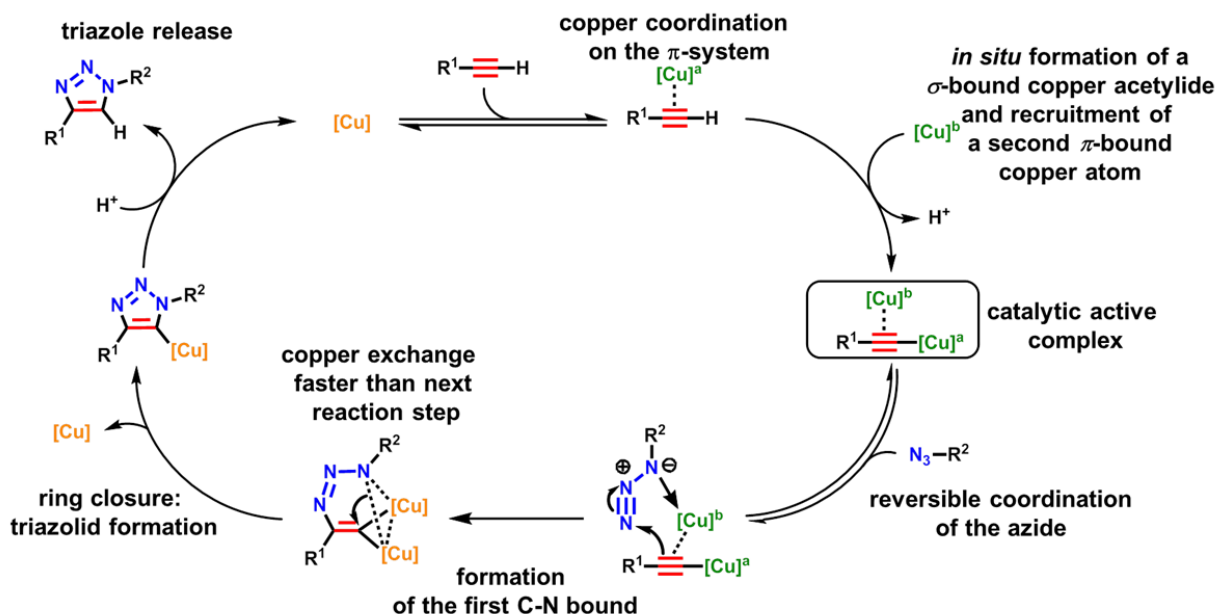
Scheme 22:   Proposed catalytic cycle of the CuAAC reaction including to two independent copper(I) atoms. **[Cu]^a** denotes Cu(I) with natural isotope distribution (^{63}Cu / ^{65}Cu = 69:31), **[Cu]^b** denotes isotopically pure ^{63}Cu(I). The authors used an isotopically pure ^{63}Cu(I) catalyst and a Cu(I) acetylide with a naturally isotopic distribution (^{63}Cu / ^{65}Cu = 69:31). After reaction an isotopic distribution of ^{63}Cu / ^{65}Cu = 85:15 was found (indicated as **[Cu]**). Ligands attached to the coppers are omitted for clarity.[136]

Scheme 22 highlights that the formation of the catalytically active complex (framed in Scheme 22) restricts the CuAAC to the use of terminal acetylenes with few exceptions such as iodo-acetylenes.[131,140] For the sake of completeness it is mentioned that the regioselective synthesis of 1,5-disubstituted 1,2,3-triazoles can be accomplished by Ru(II) catalysis, however, this reaction is by far less established and will not be discussed in this context.[141]

Since 2002, the CuAAC has found entrance in various research areas reaching from classical organic synthesis[142-145] over biological and medical applications[146-149] to advanced materials.[150-152]

With regard to biomedical applications *Bertozzi et al*. presented a fascinating approach for non-invasive *in vivo* imaging of developing zebrafish. The authors fed the embryos with artificial azido-sugars to metabolically engineer glycan structures of cell surfaces. Following application of cyclooctyne-substituted fluorescence markers led to a strain-promoted *in vivo* (copper-free) "click reaction" and permitted to follow glycan formation and degradation during embryonic development by three-colour fluorescence imaging (see Figure 13).[153]
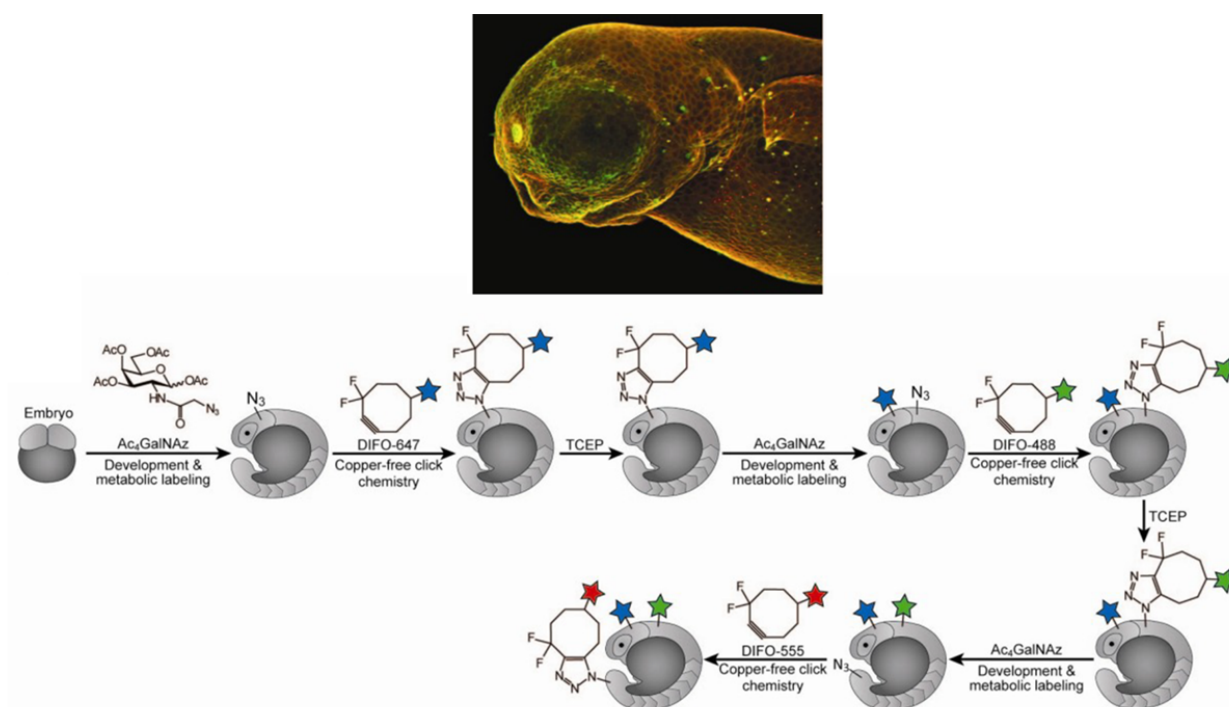
Figure 13:   Top: Three-colour fluorescence image of developing zebrafish. Bottom: Strategy for three-colour labelling of zebrafish with different fluorophore markers (represented by the coloured stars).[a]

Beside such remarkable biological applications, CuAAC has been applied for synthesis of conjugated polymers, dendrimers and donor-acceptor compounds.

In a series of porphyrine-fullerene donor-acceptor systems *Guldi et al*. implemented triazoles as bridging unit to mediate photoinduced electron transfer from the porphyrine to the fullerene acceptor. Transient absorption studies of the compounds depicted in Chart 7 revealed that triazoles present useful aromatic bridging units for investigations on electron transfer processes.[154]
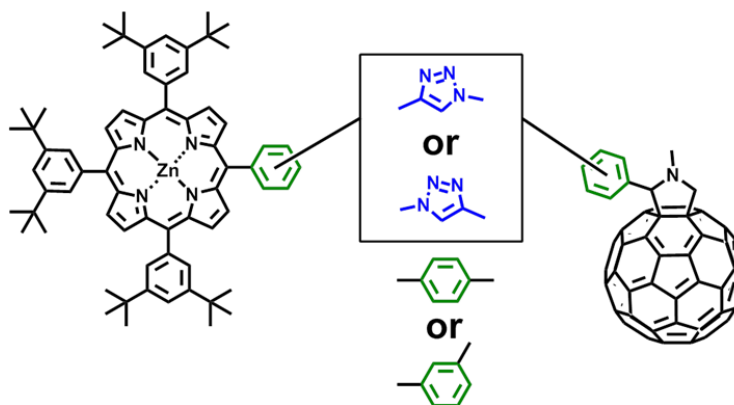
Chart 7: **Molecular structures of Zn-porphyrine-ferrocene dyads with 1,4-disubstituted 1H-1,2,3-triazoles as electron transfer bridges.**[154].

Sharpless et al. were one of the first to use CuAAC for the synthesis of dendrimers. In a convergent approach they constructed dendrons by a repetitive two-step process consisting of a "click reaction" and a nucleophilic substitution of chloride by azide to regenerate the "clickable" functionality after each circle. Attaching the azido-dendrons to a multialkynyl provided dendrimers up to the fourth generation with no chromatography required for purification.[155]

Shortly afterwards *Hawker et al.* also implemented the CuAAC in a divergent dendrimer synthesis. Starting from a bisazido core the dendrons were grown by repetitive sequences of "click reactions" followed by transforming the outer hydroxyl groups into the essential azido-moieties. The efficiency of the CuAAC led to 3rd generation dendrimers and only required extraction and precipitation as purification steps.[156]

Due to its generally high yields, the CuAAC is also suited for post-modification of dendrimers as *Astruc et al.* impressively demonstrated. An 81-fold "click reaction" with ethynylferrocene produced the macromolecular structure given in Scheme 23 with remarkable 56 % yield (more than 99 % per single reaction).[157]
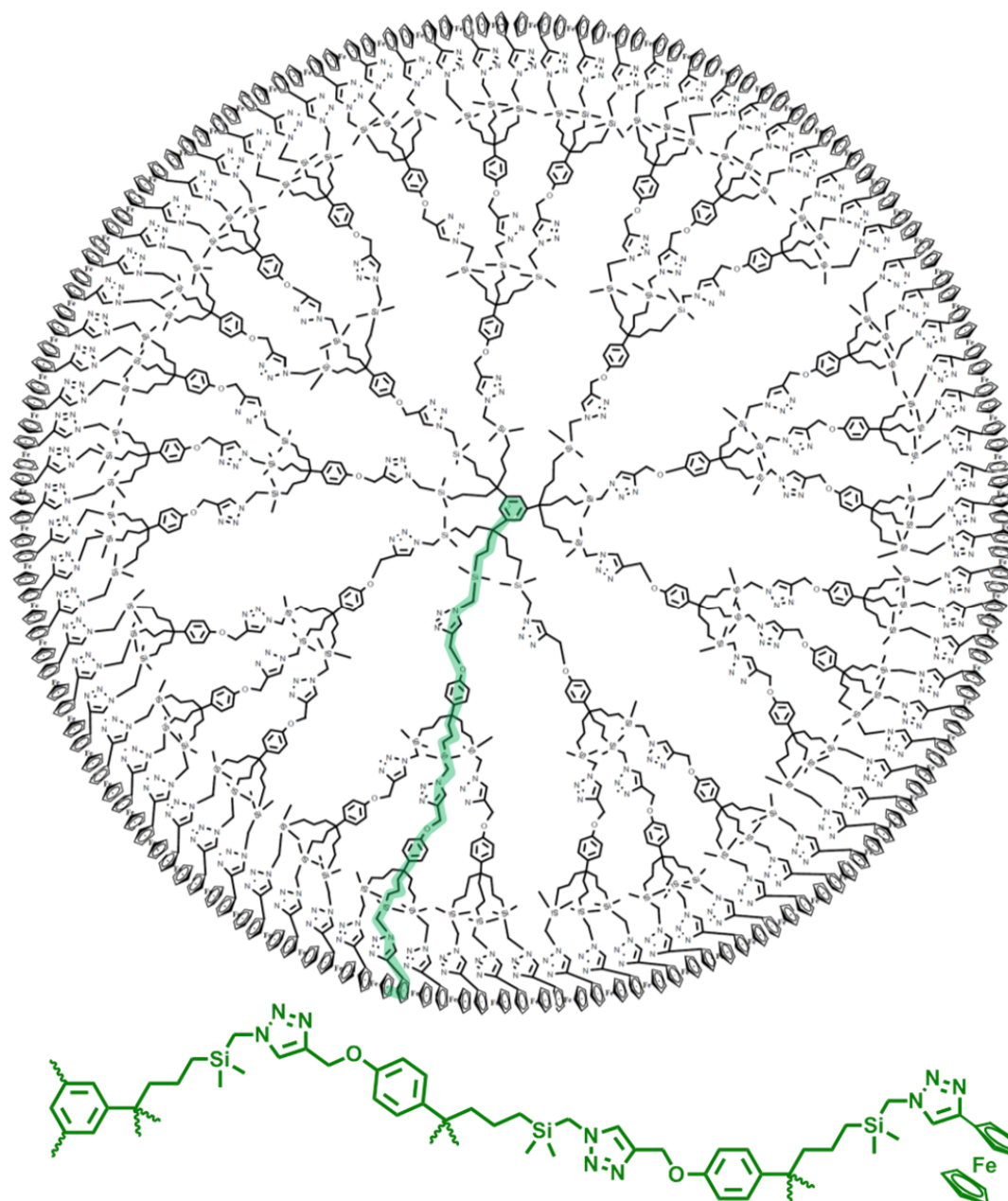
Scheme 23:   **Molecular structure of the dendrimer by *Astruc et al*. In a single step 81 ferrocene groups were introduced by CUAAC. The green structure represents an individual arm, as indicated by the green line in the macromolecule.[a]**

Unequivocally, the CuAAC is a powerful and reliable tool for the synthesis of dendrimers either by a convergent or a divergent approach.[158] However, to date the reaction has not been used for the

synthesising π-conjugated dendrimers larger than the first generation (*e.g.* by *Parent et al.*,[159] see Chart 8) and systematic investigation of the 1,4-disubstituted 1,2,3-triazoles as bridging unit in electron or charge transfer reactions remain to be performed (*vide infra*).
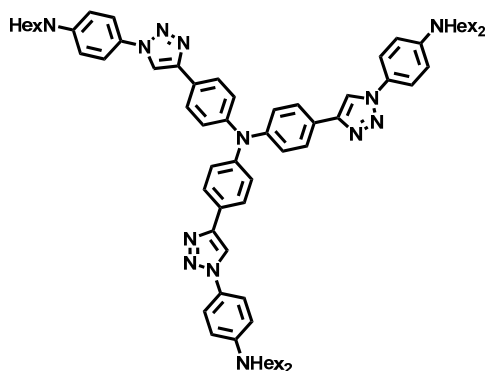
Chart 8:   **Molecular structure of a first generation dendrimer based on a TAA and synthesised using CuAAC.**[159]

2.3   Scope of the Work

This work aims at contributing to a better understanding of the fundamental aspects that dictate energy and electron transfer processes in organic compounds. A control about the relevant parameters is essential for an implementation and application in optoelectronic devices.

In this context both complex dendritic structures as well as small redox cascades (dyads and triads) based on triarylamine (TAA) chromophores (and NDI acceptors), which are linked by triazoles units are promising structures for the investigation of energy transfer and electron transfer processes.

To prepare the envisioned systems, a building block concept on the basis of the CuAAC will be implemented, which provides the unique opportunity to interexchange all basic components of the dendrimers – the core, the terminal units and the branching units (*cf.* Figure 14).
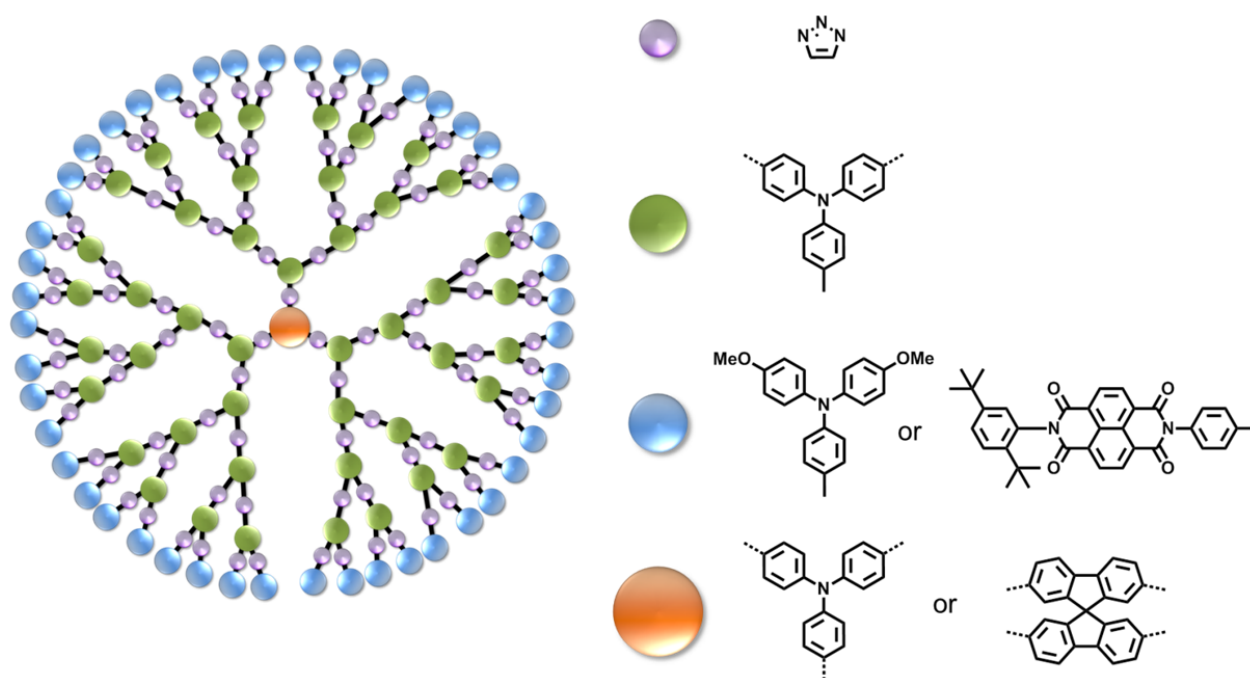
Figure 14:   **Illustration of the modular building block approach to the envisioned dendrimers.**

The investigation of energy transfer processes focuses on dendrimers exclusively composed of TAAs and linked by triazoles. This architecture implicates that the core, the terminal units and the branching units are all formed by TAA chromophores (see Scheme 24).
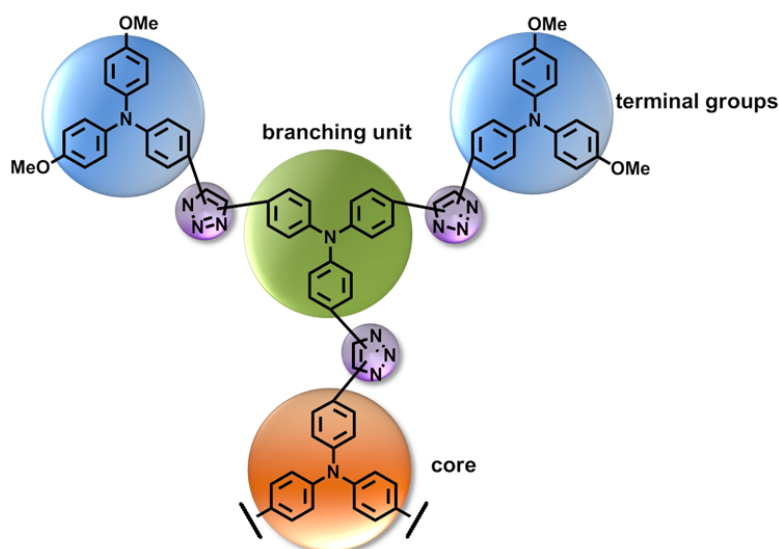
Scheme 24:   **Schematic illustration of the molecular structure of an envisioned dendrimer, in which all basic components are based on TAA chromophores. Note: the linkage of the TAAs on the triazoles is not specified yet.**

Furthermore, a series of redox cascades will be synthesised and investigated for their electron transfer dynamics upon photoexcitation. The cascade experiments extend studies about dendrimers and intend to examine photoinduced electron transfer processes and the factors determining charge separation and charge recombination rates. Crucial structural components of the TAA dendrimer units will be integrated in the construction of the cascades. In more detail, the cascades are a "linear" structure and may be considered as an arm of the dendrimer, in which the core is exchanged by an NDI acceptor and one substituent of the branching unit is exchanged by a variable substituent X (see Scheme 25). Therefore, in a modified synthetic approach the interchange of the branching unit will lead towards the desired series of redox cascades.
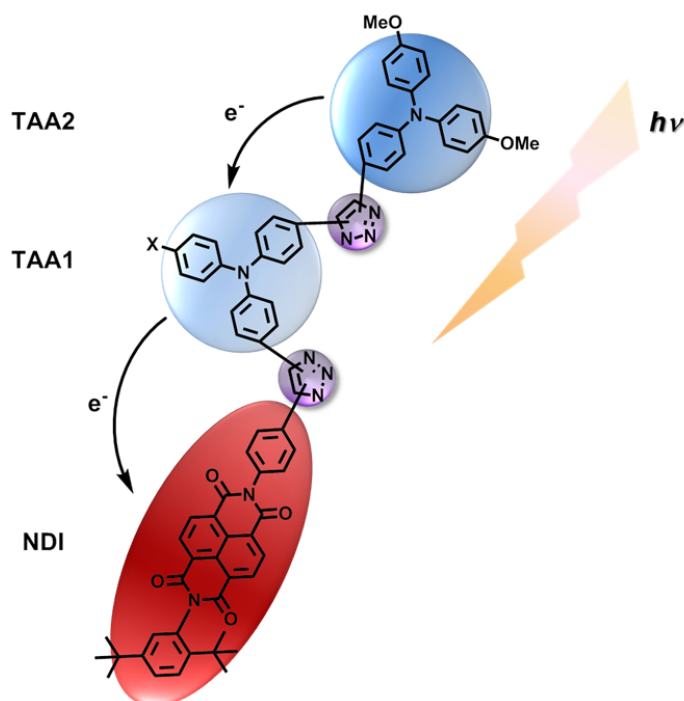
Scheme 25: **Illustration of the envisioned redox cascades, which show the structural parallels to a "linear" segment of an individual chromophore branch in the dendrimers (*cf.* Scheme 24).**

Furthermore, the synthesis of smaller model compounds will be performed, which may facilitate to understand the photophysical and electrochemical properties of the dendrimers and the cascades.

Structural Considerations about Donor and Acceptor Units

The modular building block concept is mainly based on TAAs because **TAAs** are excellent **donor units** and one of the key players in hole transfer applications, such as organic field effect transistors (OFETs), organic light-emitting diodes (OLEDs) and organic photovoltaic devices (OPVs).[160-163] TAAs are predestined as electron donor units, since they are known for their relatively small reorganization energies.[164-166] Furthermore, *p*-substituted TAAs form very stable radical cations with characteristic strong and sharp absorption bands between ca. 13000 cm^{-1} (770 nm) and 15000 cm^{-1} (670 nm).[167-169] These absorption bands are generally not overlapped by other transitions, such as the absorption of neutral TAA, which makes TAAs ideal candidates for the investigation of photoinduced electron transfer. Moreover, their redox potential can easily be tuned by different *p*-substituents, which opens the prospect to generate a downhill-directed redox gradient in the cascades.[168,170-172]

1,4,5,8-naphthalene diimides (NDI) are strong **electron acceptor** and possess two reversible reduction potentials at ca. -1.1 V and ca. -1.5 V.[173] *N*-alkyl substituted NDIs are well-known to experience fast ISC into the locally excited triplet state ($1/k \approx 10$ ps in chloroform).[174] In contrast *N*-aryl substituted NDIs rapidly form a CT state where the positive charge is located at the aryl substituent and the negative charge at the NDI core ($1/k \approx 500$ fs in chloroform).[120,174,175] With regard to this work, *N*-aryl substituted NDIs are excellent complementary chromophores to the TAAs because their radical anions exhibit characteristic strong and intensive absorption bands in the visible and near-infrared. Moreover, the bands do not overlap significantly with the TAA radical cation band.[173] Additionally, *N*-aryl substituted NDIs show weak electronic interaction when linked *via* the second nitrogen atom to another chromophore for two reasons. First, NDIs exhibit a nodal plane along the molecular long axis going through the nitrogens in the π-LUMO as well as in the π-HOMO. Second, the aryl substituent is twisted out-of-plane by almost 90°, which reduces orbital interaction with the NDI core.[176-178]

Energy Transfer Processes in TAA Dendrimers

Homotransfer between the chromophores by incoherent hopping (*Förster* transfer) is expected to be fast if the overlap integral between the excited donor emission and the acceptor absorption is sufficiently large. In case of a homotransfer a relatively small *Stokes* shift is required for effective energy transfer as both, the emission and absorption characteristics are equal. Thus, a small reorganisation energy is required. Therefore, excitation into a distinct charge transfer state generally prohibits efficient transfer of the excitation energy, especially in more polar solvents.[179] Consequently, most dendrimers that have been investigated for their energy transfer dynamics feature chromophores with locally excited non-polar states. In this work, the influence of the introduced charge transfer states on the energy transfer processes in the dendrimers will be examined. The energy transfer dynamics are expected to be strongly solvent dependent as the excited states of the dendrimers are more stabilised by polar solvents. By connecting TAAs *via* triazoles in the dendrimers a charge transfer state is expected upon excitation. Due to their electron deficient character, triazoles act as weak electron acceptors and form a donor-acceptor motif when combined with a strong TAA electron donor (see Scheme 26).[159]
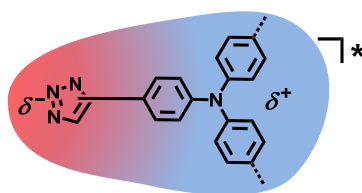
Scheme 26: Illustration of a charge transfer excited state in a donor-acceptor motif consisting of a TAA donor and a triazole acceptor.

The energy transfer properties of the dendrimers will be investigated by steady-state and time resolved emission anisotropy measurements, which are powerful tools for monitoring energy transfer processes (*cf.* section 2.1.1.4, p: 18). Furthermore, the influence of the solvent will be examined by measurements in various solvents with different polarity, from non-polar toluene to polar MeCN, and by measuring the dynamic *Stokes* shift of the emission.

Influence of the Global Shape

A change of the TAA core to a 2,2',7,7'-tetrasubstituted-9,9'-spirobi[9*H*-fluorene] (spirobifluorene) core affects the overall shape of the dendrimers from a more disc-like to an almost global-like constitution. The perpendicular orientation of the two fluorene subunits prevents a direct interaction of the two conjugated π-systems and thus *Dexter*-type energy transfer is expected to be suspended in these systems (see Scheme 27).[180] The structural aspects may influence the energy transfer performance of the spiro dendrimers compared to the "pure" TAA dendrimers.
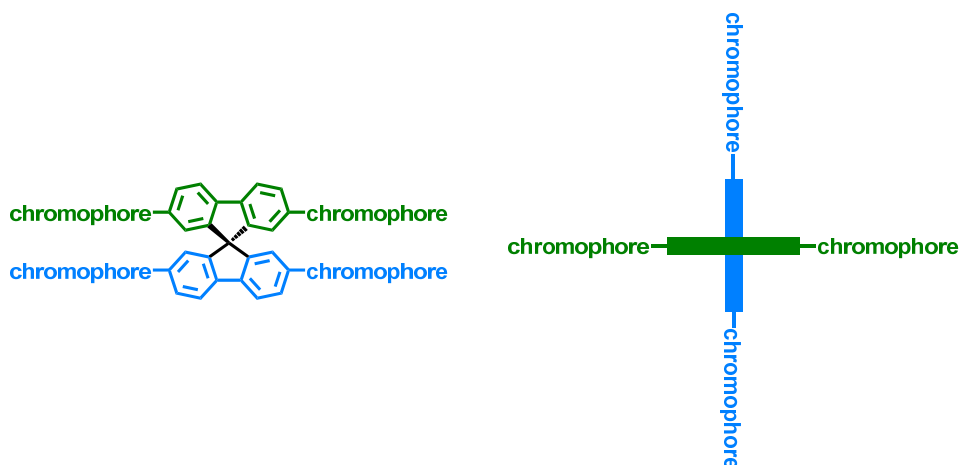
Scheme 27: Illustration of the geometric arrangement of chromophores in spirobifluorene systems. The top view (right) illustrates the perpendicular arrangement of the two fluorene subunits.

Furthermore, the electron transfer properties of the radical cations of the dendrimers will be investigated by steady-state absorption spectroscopy. In addition to the photophysical properties, the morphology of the dendrimers might also be influenced by the overall shape of the dendrimers. Due to the more global shape of the spiro dendrimers the glass transition temperature of the spiro dendrimers is probably enhanced compared to the TAA dendrimers.[181,182] The glass transition temperature reflects the stability of amorphous phases, which is an important factor in optoelectronic devices (*vide infra*).

Cascades

A series of redox cascades will be obtained according to the synthetic considerations outlined earlier in this section, in particular dyads and triads of A-D and A-D1-D2 type, respectively, possessing a downhill-directed redox gradient from TAA1 to TAA2. Such systems are expected to undergo charge separation by a number of successive relatively fast, electron transfers leading to large overall charge separation. In contrast charge recombination is slowed down by the very weak electronic coupling in the CS state (*cf.* 2.2.2, p: 53).

The photoinduced electron transfer dynamics are strongly influenced by relative state energies, reorganization energies and the electronic coupling between the corresponding states. Recently *Lambert et al*. reported about the investigation of compact cyclophane-bridged TAA-NDI dyads. The authors showed that the population of triplet CS states (^{3}CS) can significantly enhance the CS state lifetime.[120] Charge recombination from the ^{3}CS state to the electronic ground state is forbidden by spin conversion rules and, in the absence of heavy atoms, there is no sufficient spin orbital coupling to overcome this rule. To effectively populate the ^{3}CS state, the charge separation process has to be faster than the charge recombination process by a ~10^4 factor. Then the ^{1}CS state can undergo intersystem crossing (ISC) before reaching the electronic ground state.[49,59] For the envisioned cascades the charge separation step is expected to be in the *Marcus normal* region, while charge recombination should occur in the *inverted* region.
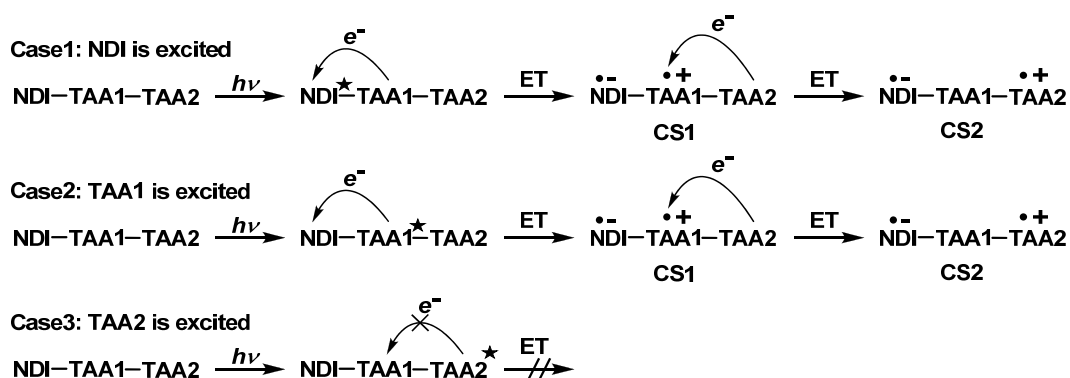
Scheme 28: Schematic representation of the three possible excited states of the triads. The star marks the locally excited group.

Upon excitation of the NDI or the TAA1 (cases 1 and 2 in Scheme 28), a stepwise electron transfer (ET) is expected. First leading to the CS state (CS1) where the negative charge is localised on the NDI and at first the intermediate TAA1 is oxidised (**NDI**⁻–Tz–**TAA1**⁺–Tz–TAA2). Then, the charge is transferred to the terminal TAA2 and the fully CS state (CS2) is generated (**NDI**⁻–Tz–TAA1–Tz–**TAA2**⁺). Consequently, the charges are much more distant in the CS2 state of the triads than in the CS state of the dyads, which consist of an NDI and a single MeO-TAA. Furthermore, the CS2 state of the triads is energetically lower than the CS state of the dyads (the charged chromophores are identical in both fully CS states). Thus, a smaller rate for the recombination process is expected for the triads compared to the dyads. The required downhill state progressions will be examined amongst others by fs- and ns-time resolved transient absorption spectroscopy. A different scenario is presented by case 3 (Scheme 28). The terminal TAA2 is excited and subsequent electron transfer to the TAA1 is prevented.

Donor-Acceptor Dendrimers

Exchange of the terminal groups in the TAA dendrimers by NDI acceptors, combining the concept of redox-cascades and dendrimers, leads to donor-acceptor dendrimers with an electron transfer gradient from the core to the periphery. Resulting structures are promising for effective light harvesting applications.

Chapter 3

RESULTS AND DISCUSSION

This section starts with the presentation of the accomplished syntheses towards the compounds envisioned in the preceding section followed by the investigations concerning their photophysical and electrochemical properties. Sections about synthesis and spectroscopy are subdivided in parts for dendrimers and cascades.

3.1   Synthesis

This section discusses the applied synthesis to the desired cascades, dendrimers and model compounds. As mentioned above, the dendrimers as well as the cascades were built up by the CuAAC "click reaction" leading to systems in which the chromophores are connected *via* 1,4-disubstituted 1,2,3-triazoles.

One main requirement for the synthetic realisation was to develop a concept that allows the modular exchange of all basic components of the dendrimers (core, branching and terminal unit). As outlined in the scope of this work, a trisubstitiuted TAA and a tetrasubstituted spirobifluorene served as core units while a TAA and an NDI served as terminal units. The interior and thus the branching unit was planned to consist of TAAs only and those building blocks gave rise to plain TAA dendrimers, TAA dendrimers with a 3-dimentional structure caused by the spirobifluorene core and donor-acceptor dendrimer composed of TAA donors as the core unit and as the interior and of several NDI acceptors on the surface.

Accordingly, cascade syntheses were achieved by taking a donor-acceptor dendrimer and replacing the tri-functionalised TAA core by a mono-substituted TAA derivative. Furthermore, the branching units were substituted by appropriate bivalent building blocks, in which one substituent for dendritic growth of the former branching unit is exchanged by a variable (redox determining) substituent. This will lead to a linear TAA connection with an adjustable redox gradient.

3.1.1   Dendrimers

As already mentioned, dendrimer synthesis can generally be achieved either by a convergent or a divergent approach (*cf.* 2.2.137). The decision, for one of the two approaches does not necessarily depend on the advantages or disadvantages of the convergent or divergent concept, but rather on practical synthetic considerations such as synthetic effort for the building blocks, purification methods *et cetera*.

The terminal as well as the core unit demand for one distinct type of connecting group either the acetylene or the azide functional group (which one depends on the synthetic strategy), see Chart 9. The synthesis of the terminal and the core unit allows for both strategies and thus has less influence on the decision for either the convergent or divergent approach.
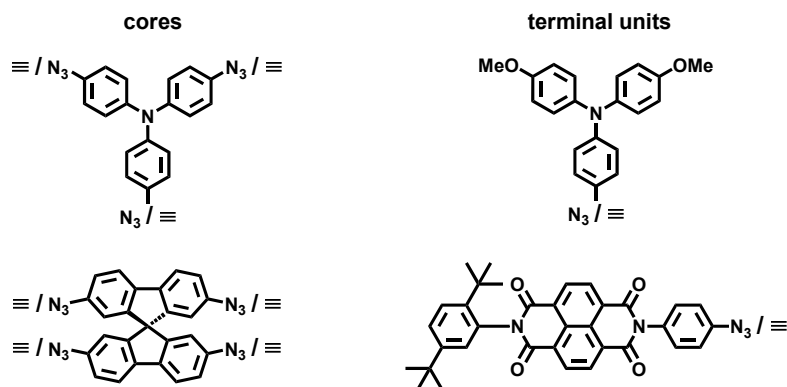
Chart 9:   **Possible substitution pattern of cores and terminal units in a modular building block synthesis towards the envisioned dendrimers.**

In contrast, the branching unit in either a convergent or a divergent synthesis has to be equipped with both functionalities within a single molecule independent of the dendrimer approach (see Chart 10). The challenge to prevent uncontrolled growth demands for the use of rational protecting groups.
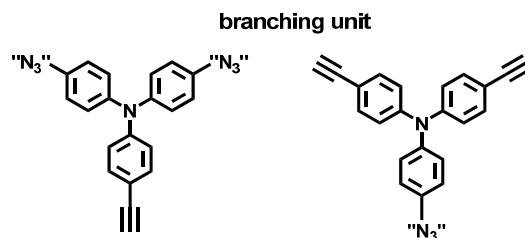
Chart 10:   **Possible substitution pattern of branching units in a modular building block synthesis towards the envisioned dendrimers ("N₃" denotes an azido function or a precursor function leading to an azido function).**

A wide range of protecting groups has been reported for acetylenes of which the alkylsilyl groups are certainly the most common ones.[183-187] Within the scope of this work the tri-*i*-propylsilyl (TIPS) group seems to be well-suited for the branching unit because it is stable even under demanding conditions, the bulky geometry might prevent unwanted thermal cycloadditions and cleavage succeeds under mild conditions with tetra-*n*-butylammonium fluoride (TBAF).[186]

Yet, there are no protecting groups for azides and thus their precursor functionalities (commonly halides) had to be used instead. The transformation of halides into azides can be realised by substitution with sodium azide and therefore the solubility of the aryl halide and alkali azide had to be taken into account.

This consideration precluded a convergent synthesis in which the azide would have to be activated after each growing step. Extended halide substituted dendrons are not expected to be soluble under the same conditions as sodium azide. Furthermore, arylazides are known to be susceptible to photodegradation, exploited in commercial applications such as lithography, and thus an introduction of multiple azides involves the risk of losing some reactive functionalities, which in turn may result in structural defects.[188,189]

For these reasons the dendrimer syntheses were accomplished by a divergent approach with a branching unit consisting of two protected alkynes and one azide. The branching units were attached to the lower generation dendrimer precursors *via* the azide.

First, the synthesis of the building blocks will be discussed followed by the synthesis of the dendrimers and several model compounds.

3.1.1.1   Building Block Syntheses

TAA core 2

In Scheme 29, the straight-forward synthesis of the TAA core **2** is shown.[190] Thereby, tris(4-bromophenyl)amine was transformed by a Pd-catalysed *Sonogashira-Hagihara* cross coupling with trimethylsilylacetylene (TMSA) in 1,4-dioxane into the trimethylsilylacetylene derivative **1**.[191] Subsequently, deprotection with TBAF in DCM provided the free alkyne TAA core **2** in excellent yields. Noteworthy, although deprotection of alkynes in THF supplemented with TBAF solved in THF is a standard reaction in literature, these reaction conditions were found to be unreliable in the deprotection reactions presented in this work. In some cases the reaction did not lead to the desired product but an insoluble solid was formed instead. This problem was solved by adding solid TBAF to solutions of the protected alkynes in DCM.
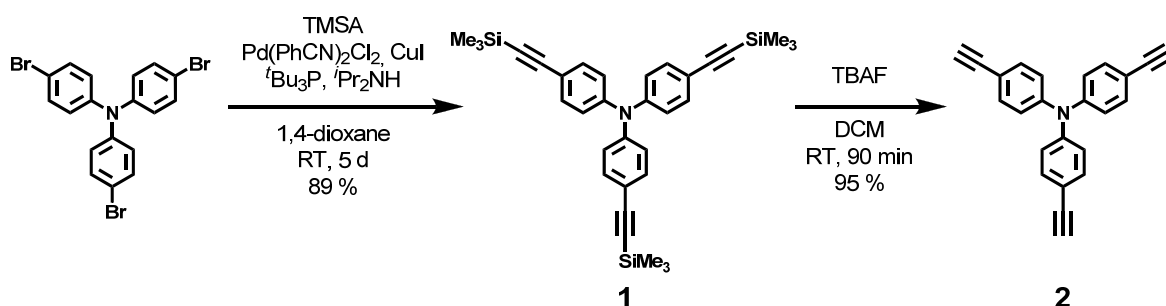
Scheme 29: Syntheses of TAA core **2**.

Spirobifluorene core 4

The synthesis of the spirobifluorene core **4** was accomplished by a reaction sequence according to *Yu et al.*[192] First **3** was synthesised by a *Sonogashira-Hagihara* reaction of 2,2',7,7'-tetrabromo-9,9'-spirobi[9*H*-fluorene] with TMSA in triethylamine with Pd(PhCN)$_2$Cl$_2$ as catalyst. Final deprotection with TBAF in THF resulted in **4** in excellent yields (Scheme 30).
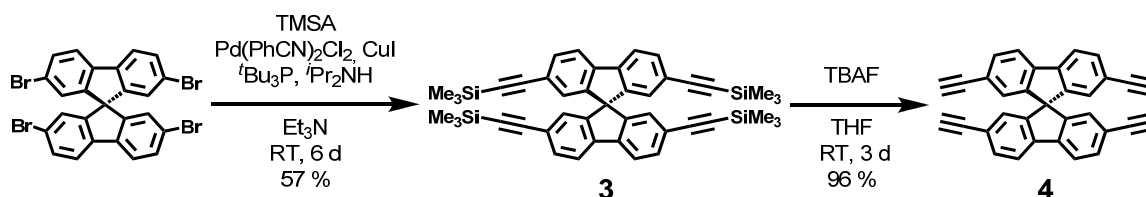
Scheme 30: Syntheses of spirobifluorene core **4**.

Terminal TAA azide 6[a]

As outlined in Scheme 31, the synthesis of **6** started with an Cu(I)-catalysed *Ullmann* reaction of 4-bromo-aniline and 4-iodoanisole in the presence of 1,10-phenanthroline in toluene, leading to the bromo-substituted TAA **5**.[193] In a next step the bromide was substituted by an azido group. Several attempts to achieve this substitution *via* metalation with (*n*-, *sec*-, *t*-) butyl lithium followed by addition of either sodium azide or tosyl azide left the starting material unaffected.

Finally, **6** was obtained under *Ullmann*-type reaction conditions with sodium azide and CuI as a catalyst reported by *Liang et al.*[194] Herein, the usage of *N,N´*-dimethylethylenediamine (DMEDA) as co-catalyst and *L*(+)-sodium ascorbate as mild reducing agent guaranteed high concentration of Cu(I). As reaction medium a mixture of ethanol and water (7:3) was used to address the issue of solubility of the precursor as well as of the sodium azide.

---

[a] Parts of this section have already been published in *Beiträge zur Synthese und Charakterisierung von triarylaminhaltigen Dendrimeren über die Kupfer(I)-katalysierte 1,3-Huisgen-Cycloaddition*, Diploma Thesis of Fabian Zieschang, Würzburg 2009.
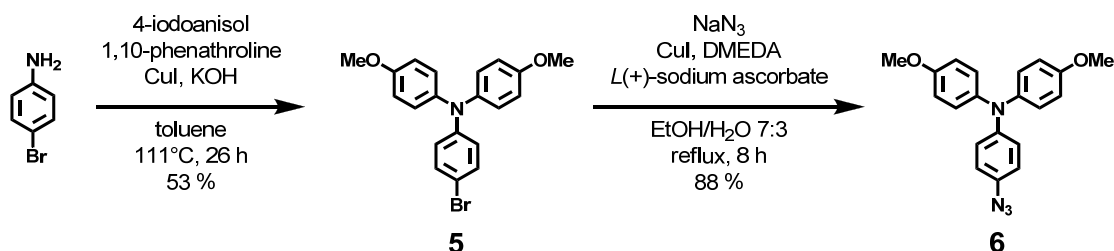
Scheme 31:   Synthesis of the terminal TAA azide 6.

Terminal NDI azide 8

In the first reaction step towards **8**, the bromo substituted NDI derivative **7** was obtained by microwave-assisted condensation of 1,4,5,8-naphthalenetetracarboxylic dianhydride with 2,5-di-*tert*-butylaniline and 4-bromo-aniline in dry pyridine in 26 % yield.[120,195] Therefore, a mixture of 1,4,5,8-naphthalenetetracarboxylic dianhydride and 2,5-di-tert-butylaniline was heated at 145°C for 90 min to generate the monoimide, that was converted *in situ* with 4-bromo-aniline at 145 °C for further 90 min. 2,5-Di-*tert*-butylaniline was employed to increase the solubility of **7** compared to its unsubstituted phenyl derivative. However, in the following azidation even **7** showed poor solubility in the solvent mixture (EtOH/H$_2$O) recommended in literature. Thus, the solvent mixture was changed to ^{i}PrOH/H$_2$O 9:2, which provided at least moderate solubility. Therefore, the reaction time had to be extended to 16 h compared to the synthesis of **6** to gain **8** in reasonable yields (Scheme 32).
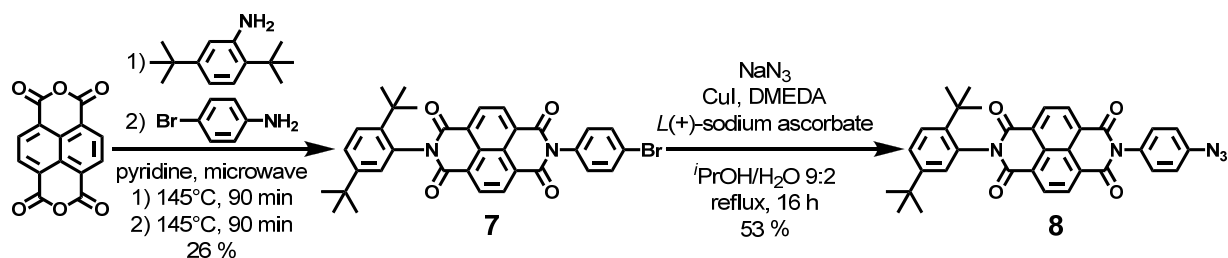
Scheme 32:   Synthesis of the terminal azido NDI derivative 8.

Branching unit 11

As mentioned above, the branching unit had to be equipped with two protected acetylene and one azido moiety to allow **controlled** dendritic growth. First, the bisarylamine **9** was generated by introducing the tri-*i*-propylsilylacetylene (TIPSA) substituents into bis(4-bromophenyl)amine *via* a *Sonogashira-Hagihara* reaction using Pd(CN)$_2$Cl$_2$ as Pd-catalyst in 1,4-dioxane (see Scheme 33).[191] The subsequent arylation of **9** to the TAA **10** emerged to be most challenging. Several attempts to transform the bisarylamine **9** into **10** by a Pd-catalysed *Buchwald-Hartwig* cross coupling with different catalyst/ligand/base/solvent combinations failed (see Table 2). This finding

might be explained by the electron deficient character of amine **9** (TIPSA exhibits an –I-effect) or by high sterical hindrance.[196-199] Hence, several *Ullmann* coupling[200,201] reactions using Cu(I) were tested and indeed CuI in the presence of 1,10-phenanthroline in toluene with potassium carbonate as base yielded at least traces of **10**.[193]

Table 2: Amination Reactions with Different Bases, Catalysts, Ligands and Reaction Conditions.

catalyst	ligand	base	solvent	T	t	%
Pd$_2$(dba)$_3$·CHCl$_3$	^{t}Bu$_3$P	KO^{t}Bu	toluene	60°C	8 d	-
Pd$_2$(dba)$_3$·CHCl$_3$	^{t}Bu$_3$P	KO^{t}Bu	toluene	110°C	11 d	-
Pd$_2$(dba)$_3$·CHCl$_3$	^{t}Bu$_3$P	NaO^{t}Bu	toluene	110°C	14 d	-
Pd$_2$(dba)$_3$·CHCl$_3$	^{t}Bu$_3$P	NaO^{t}Bu	1,4-dioxane	90°C	10 d	-
Pd$_2$(dba)$_3$·CHCl$_3$	dppf	NaO^{t}Bu	toluene	110°C	8 d	-
Pd$_2$(dba)$_3$·CHCl$_3$	dppf	NaO^{t}Bu	1,4-dioxane	80°C	9 d	-
Cu$_2$O[193]	-	-	DMAC	170°C	4 d	-
CuI	1,10-phenanthroline	KOH	toluene	105°C	7 d	traces
Cu	18-crown-6	K$_2$CO$_3$	*o*-DCB	179°C	3 d	49 %

Harsher *Ullmann* reaction conditions, that is activated Cu in *o*-DCB at ca. 180°C, yielded **10** in 49 %.[202] Particularly in this reaction step, the extreme stability of the TIPS group against strongly basic and high temperature conditions compared to the standard TMS group were beneficial.

Remarkably, the use of 1,4-dibromobenzene instead of 1-bromo-4-iodobenzene under the same reaction conditions provided only traces of **10**. This result might be explained by polarisation effects in 1-bromo-4-iodobenzene as iodide is more polarisable than bromide. However, this hypothesis has not been proven experimentally.

Azidation according to *Liang et al*. finished the synthesis of the branching unit **11**.[194] Therein, the solvent was changed to ^{i}PrOH/H$_2$O with regard to the solubility of **10** and sodium azide similar to the azidation leading to **8**. The more branched TIPS group were respected to confer higher solubility than the TMS group – another advantage of TIPS compared to standard TMS.
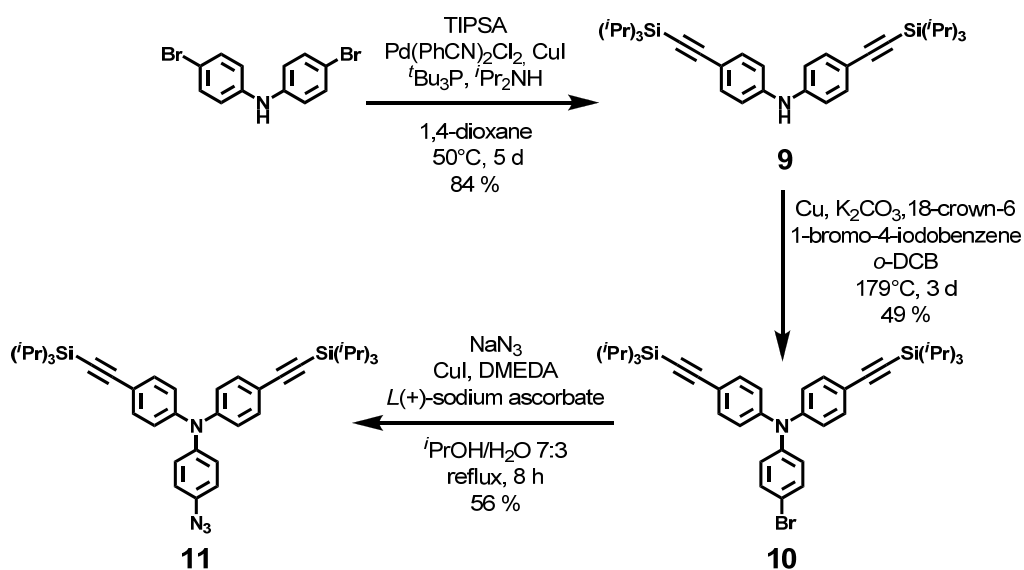
Scheme 33: Synthesis of the branching unit 11.

3.1.1.2 Dendrimer Syntheses

All dendrimers were constructed by divergent synthetic routes, in which the dendrons were subsequently built up by "click reactions" from the core to the periphery. The experimental procedure involved repetitive synthetic steps consisting of a "click reaction" and a deprotection step to activate the alkynes for next the next round. All "click reactions" were performed with *N,N*-diisopropylethylamine (DIPEA) as non-nucleophilic base with (PPh₃)₃CuBr as organo-soluble Cu(I) source.[203] THF was chosen as solvent and the reactions accomplished in the dark. After each reaction step, purification using recycling GPC was essential to remove both by-products and unreacted starting material. Thus, isolation and characterisation by complete assigning of ¹H- and ¹³C-NMR signals of precursors and final products guaranteed monodispersity of the dendrimers. Furthermore, the precursors were characterised by high resolution mass spectrometry. Few dendrimers showed an unexpected behaviour in the high resolution mass spectrometry experiments that will be discussed in more detail later on.

TAA Dendrimers G1–G3[a]

Synthesis of the dendrimers **G1**–**G3** was accomplished by the repetitive synthetic approach described above. This cascading reaction sequence shown in Scheme 34 started from the TAA core unit **2**. Direct attachment of terminal units **6** to **2** by "click reaction" resulted in the 1st generation dendrimer **G1** in a yield of 79 %.

Using **11** instead of **6** in the reaction converted **2** into the 1st generation precursor dendrimer **12** and following deprotection of the alkynes with TBAF led to the activated dendrimer **13**. "Click reaction" of **13** with **6** provided the 2nd generation dendrimer **G2** in 83 % yield, which is the first dendrimer in this series that consists of the core, the branch and the terminal units.

Following the progressive synthesis by treating **13** with **11** gave rise to the 2nd generation precursor dendrimer **14**. The largest dendrimer, that is the 3rd generation dendrimer **G3**, was obtained from **14** through deprotection of the TIPSA groups with TBAF and following CuAAC with **6**. Since **G3** proved to be exclusively soluble in chlorinated hydrocarbons, syntheses of higher generation dendrimers were not accomplished.

Increased reaction times of the CuAAC dramatically improved the yields and therefore some "click reactions" were performed longer than 20 d. Remarkable, the yields per reaction centre were at least 93 % (**G1**: 93 %; **12**: 97 %; **G2**: 97 %, **14**: 95 %, **G3**: 93 %).

---

[a] Parts of this section have already been published in *Beiträge zur Synthese und Charakterisierung von triarylaminhaltigen Dendrimeren über die Kupfer(I)-katalysierte 1,3-Huisgen-Cycloaddition*, Dploma Thesis of Fabian Zieschang, Würzburg 2009.
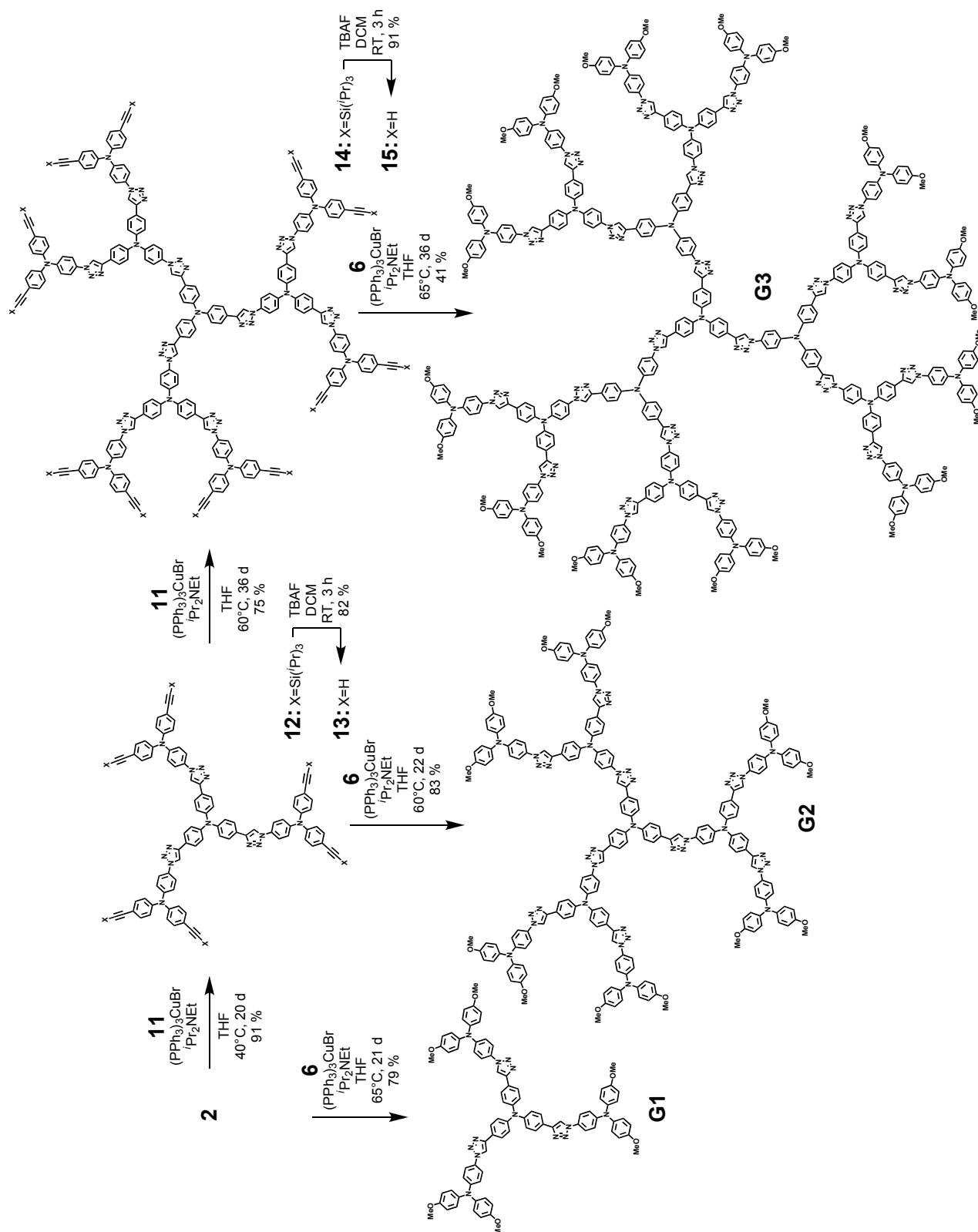
Scheme 34: Cascading synthesis sequence yielding the TAA dendrimers G1–G3.

Spiro Dendrimers spiro-G1 and spiro-G2

Spiro dendrimers were prepared similar to the plain TAA dendrimers **G1–G3** (see Scheme 35). The reaction sequence started with the spirobifluorene core **4**. In a "click reaction" of **4** with **6** the 1st generation spiro dendrimer **spiro-G1** was obtained in 23 % yield, while in a second reaction **4** was converted with **11** to the 1st generation precursor spiro dendrimer **16**. Subsequent deprotection of the alkylsilyl acetylenes with TBAF resulted in the precursor dendrimer **17**, which gave rise to the 2nd generation spiro dendrimer **spiro-G2** *via* "click reaction" with **6**. **Spiro-G2** and **G3** show a similar solubility behaviour, which prevented the synthesis of higher generation spiro dendrimers. Compared to the syntheses of the plain TAA dendrimers the yields of the "click reactions" for the spiro dendrimers are significantly lower, which might be a result of the different global structure.
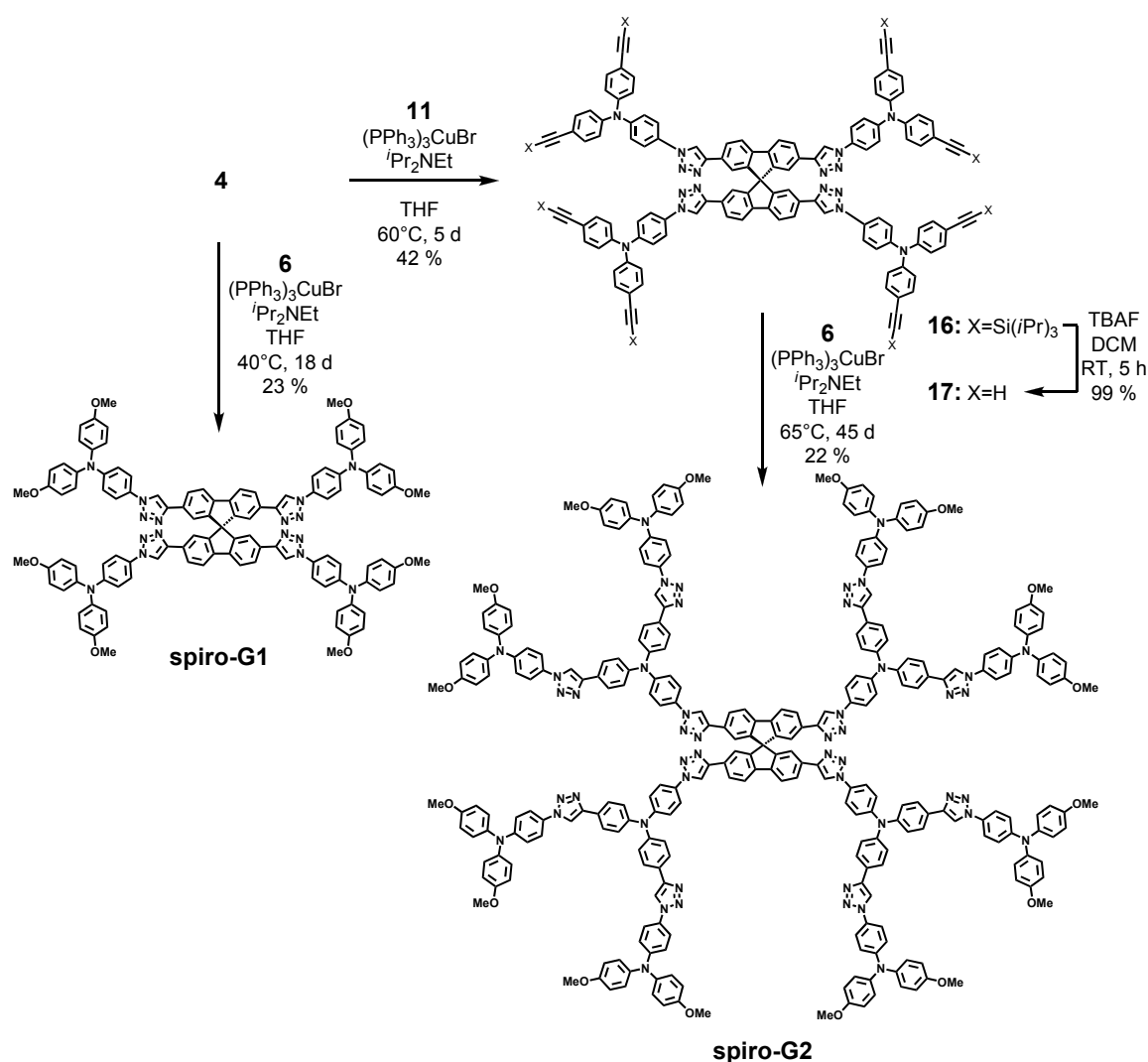
Scheme 35:   Cascading synthesis sequence yielding the spiro dendrimers spiro-G1 and spiro-G2.

Donor-Acceptor Dendrimer D-A-G1

Besides replacing the core of the dendrimer structure, as realised in the spiro dendrimer synthesis, the terminal units were substituted with an NDI. The conversion of the TAA core **2** (electron donor) with the NDI derivatives **8** (electron acceptor) gave access to the 1st generation donor-acceptor dendrimer **D-A-G1** by in moderate yields (see Scheme 36).
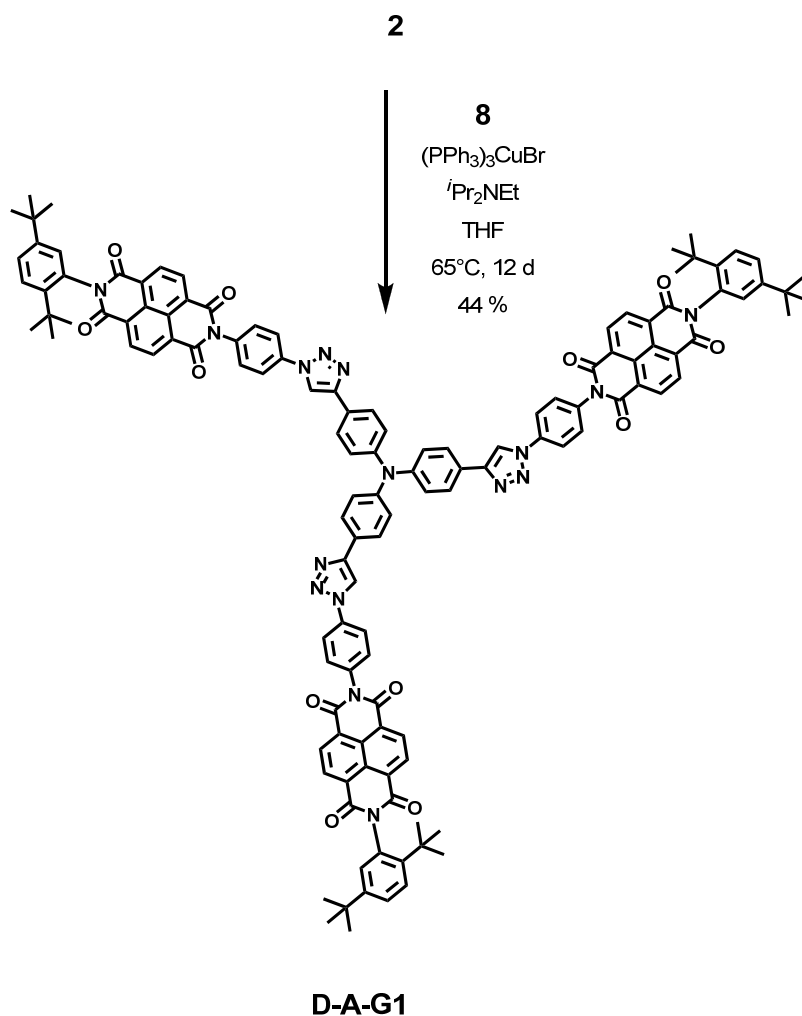
D-A-G1

Scheme 36: **Synthesis of the 1st generation donor-acceptor dendrimer D-A-G1.**

3.1.1.3   Model Compound Syntheses[a]

In addition to the different dendritic structures several smaller model compounds were synthesised in order to achieve a better understanding of the spectroscopic properties of the dendrimers´. Therefore, the acetylene counterpart **19** of the terminal unit **6** was synthesised by introducing an acetylene moiety into **5** *via Sonogashira-Hagihara* reaction in 1,4-dioxane with TMSA followed by deprotection with TBAF (Scheme 37).[191,203]
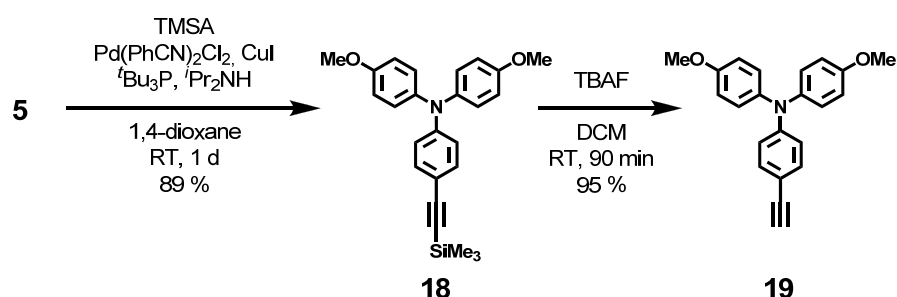
Scheme 37:   Syntheses of the alkyne TAA derivative **19**.

Conversion of **6** and **19** with the phenyl counterparts provided **N-M** and **C-M**, respectively, which differ in the connection mode to the triazole (Scheme 38). Furthermore, the bis-TAA model compound **M** was prepared *via* "click reaction" of **6** and **19**.[204]
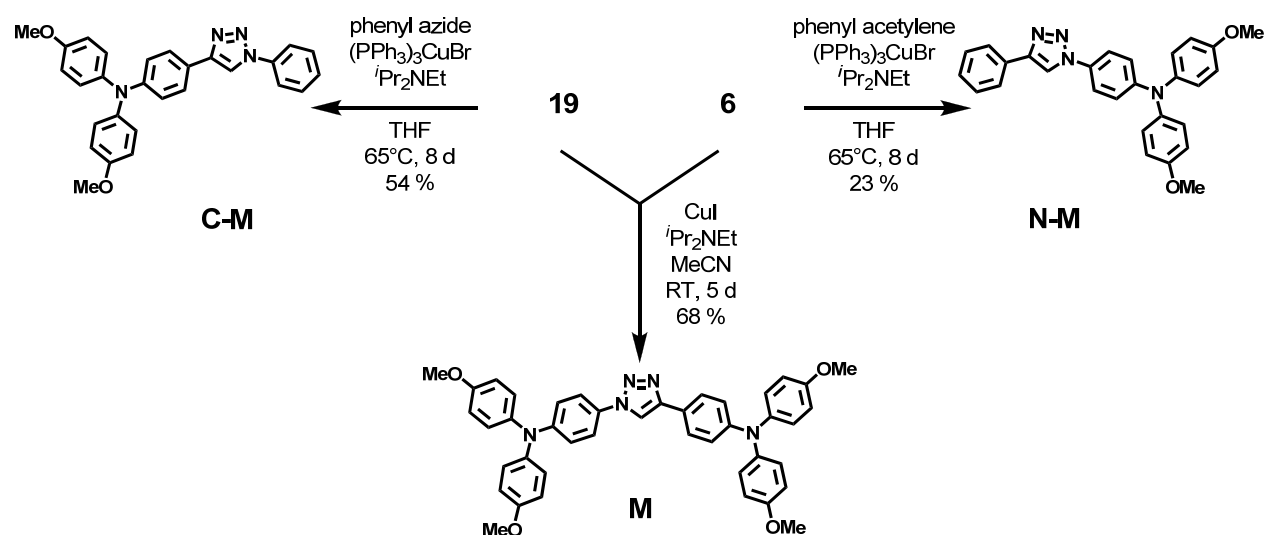
Scheme 38:   Synthesis of the model compounds C-M, N-M and M.

---

[a] Parts of this section have already been published in *Beiträge zur Synthese und Charakterisierung von triarylaminhaltigen Dendrimeren über die Kupfer(I)-katalysierte 1,3-Huisgen-Cycloaddition*, Diploma Thesis of Fabian Zieschang, Würzburg 2009.

Two further mono-TAAs were synthesised to mimic the substitution pattern of the core and the branch TAA unit. Reaction of **2** with phenyl azide yielded the "core model" **core-M** in 65 % yield (Scheme 39).
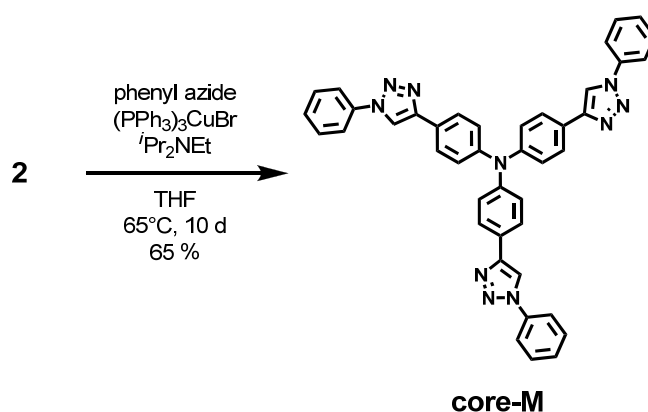
core-M

Scheme 39:   **Synthesis of the "core model "core-M.**

Preparation of the "branch model" **branch-M** required a more elaborated synthetic route. **Branch-M** was prepared in a three step synthesis starting from the branching unit **11**. In a first reaction step, phenyl acetylene was treated with the azide function of **11** leading to compound **20** in moderate yields. Subsequently, the trialkylsilyl protecting groups in **20** were cleaved with TBAF and provided compound **21** in nearly quantitative yields. A final "click reaction" with phenyl azide resulted in the desired product **branch-M** (Scheme 40).
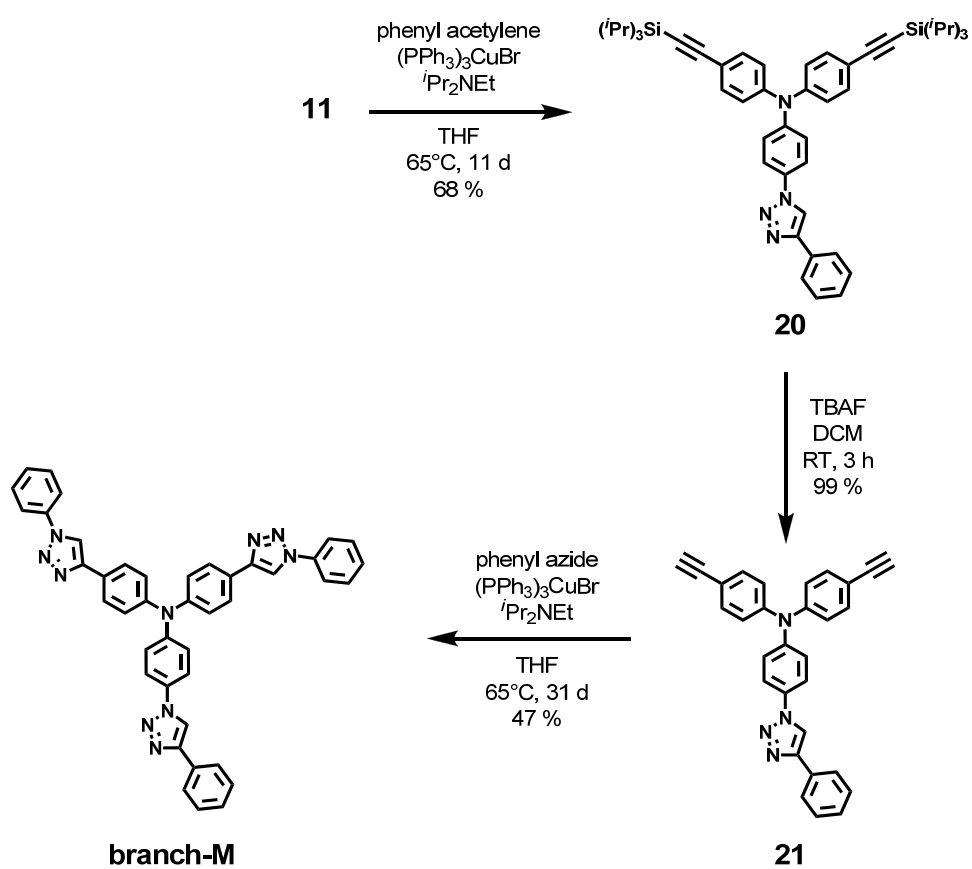
Scheme 40:   Synthesis of the "branch model" **branch-M**.

3.1.1.4 Mass Spectrometry

In this section the mass spectrometry experiments (ESI/MALDI) of the compounds presented in the preceding section will be discussed. For nearly all triazole containing compounds the appearance of additional signals in the mass spectra was observed. Those signals were assigned to species lacking one N_2-molecule per triazole. This phenomenon is well-known from literature and probably results from a thermal decomposition of the triazole during the mass spectrometry experiment.[205-208] Presumably, the elimination of N_2 generates the singlet iminocarbene **A**, which transfoms into the unstable ketenimine **B** *via* a hetero-*Wolff*-rearrangement. **B** can undergo subsequent reactions with *e.g.* H_2O (reaction path I in Scheme 41).[207] Alternatively, **A** follows a ring closing reaction to the 1*H*-azirines **C** as reactive intermediate (reaction path II in Scheme 41) and further evolves to *e.g.* indole **D**.[207,208] Since those species are all isomers a discrimination is not possible by mass spectrometry.
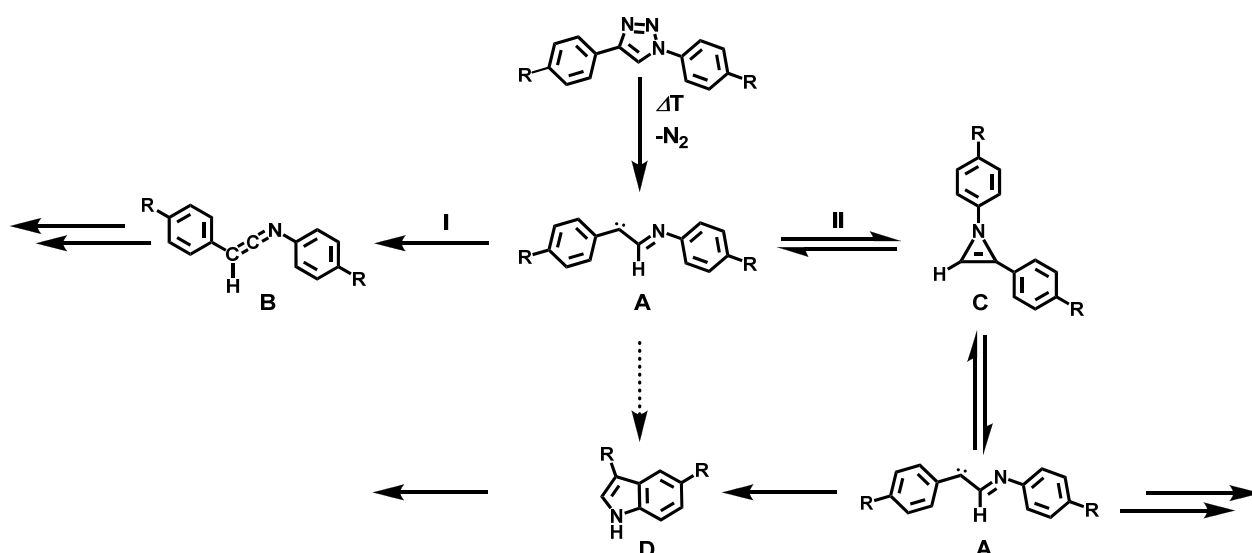
Scheme 41: **Possible thermal decomposition pathways of triazoles.**

While ESI masses were obtained for the smallest dendrimers **G1** and **spiro-G1** as well as for the model compounds, this technique failed for the larger dendrimers **G2**, **G3** and **spiro-G2**. However, ESI mass spectrometry provided data for their protected (**12**, **14** and **16**) and deprotected (**13**, **15** and **17**) precursors even though it had become more and more sophisticated to obtain useful data for molecules with increasing molecular weight. *E.g.* **15** shows the $M^{\bullet 2+}$- 9 x N_2 peak as basic peak. Obviously, the introduction of MeO-substituted TAAs in **G2**, **G3** and **spiro-G2** is responsible for the observed performance of the larger dendrimers **G2**, **G3** and **spiro-G2**. This finding might be explained by the large influence of the MeO-substituted TAAs as cyclic voltammetry measurements revealed that these TAAs exhibit the lowest oxidation potential. However, MALDI mass experiments

were successfully performed for **G1**–**G3**, **spiro-G1** and **spiro-G2**. Due to an increased nitrogen elimination during the MALDI measurements in combination with the isotopic distributions of all present species, the spectra of **G2**, **G3** and **spiro-G2** became more and more complex. Thus, an assignment to a distinct species was impossible. Furthermore, these structures showed cluster formation resulting in a series of peaks with constant mass intervals and decreasing intensity. Further investigations would be necessary to fully understand the properties of **G2**, **G3** and **spiro-G2** in mass spectrometry experiments.

3.1.2   Cascades[a]

In this section the syntheses to the envisioned dyads and triads are presented. The dyads can be generated by an one step reaction with the related building blocks. The preparation of the triads involved a modified synthetic approach of the modular dendrimer synthesis.

The redox centres of the presented cascades are linked *via* triazole heterocycles. Such triazoles are formed by CuAAC between terminal alkynes and azides.[204] As an unsymmetric bridge the triazole can be either connected *via* the carbon or *via* the nitrogen to the NDI acceptor. Therefore, in addition to the azide substituted NDI **8** (synthesis shown in Scheme 32; p: 81) also the alkyne substituted NDI **22** was synthesised. This was achieved by one-step microwave-assisted condensation of 1,4,5,8-naphthalenetetracarboxylic dianhydride with the arylamines in dry DMF. Similar to the synthesis of **7**, the monoimide was generated from 1,4,5,8-naphthalenetetracarboxylic dianhydride and 2,5-di-tert-butylaniline by heating of both components in DMF at 145°C for 60 min. Subsequent addition of 4-ethynyl-aniline to the mixture and heating at 145°C for further 90 min led directly to **22** in 25 % yield (see Scheme 43).[120]
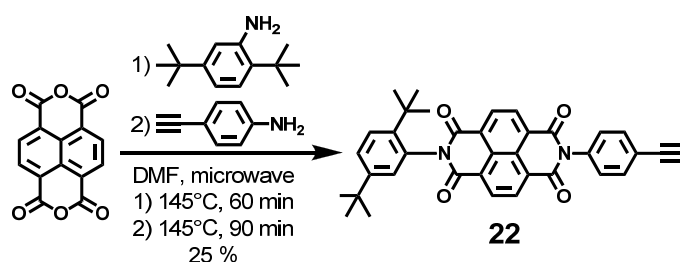
Scheme 42:   Synthesis of the alkyne substituted naphthalene diimide derivative 22.

Hence, "click reaction" of **8** or **22** and its alkyne- (**19**) or azido -substituted (**6**) TAA counterpart, gave access to the two different dyads **Da** and **Db**, which differ in the connection mode to the triazole (see Scheme 43). However, the enhanced reaction times in the synthesis of **Db** did not improve the yields as observed for the dendrimer.

---

[a] Parts of this section have already been published in *Synthese triarylaminhaltiger Redoxkaskaden*, Bachelor Thesis of Maximilian Schreck, Würzburg **2011**.
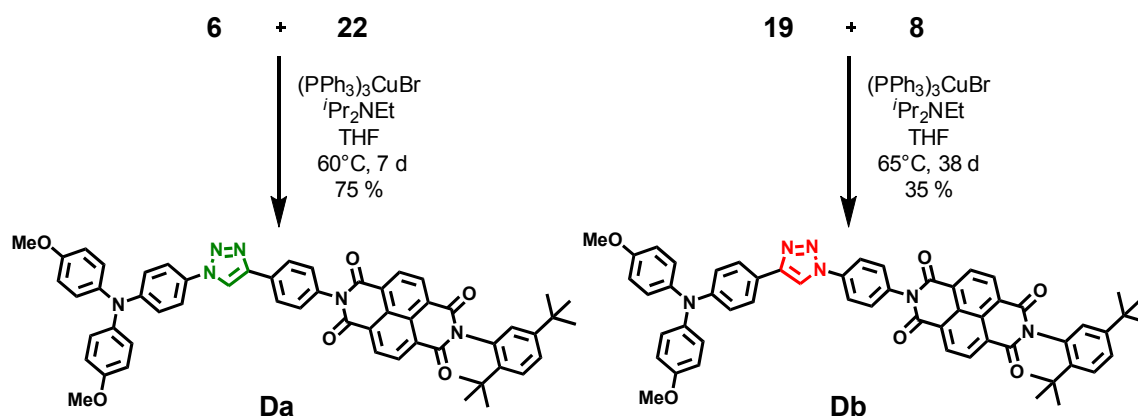
Scheme 43: Synthesis of the two dyads Da and Db that differ in the connection mode to the triazole, indicated by the green and red colour, respectively.

The larger cascades consisted of two different TAA donors featuring a downhill-directed redox gradient. Accordingly, the redox potentials of the TAAs were tuned *via* substituents in *p*-position. The bivalent TAAs possess only one functionalisable position because the other two are involved in the construction of the cascades´ backbone (Scheme 44).
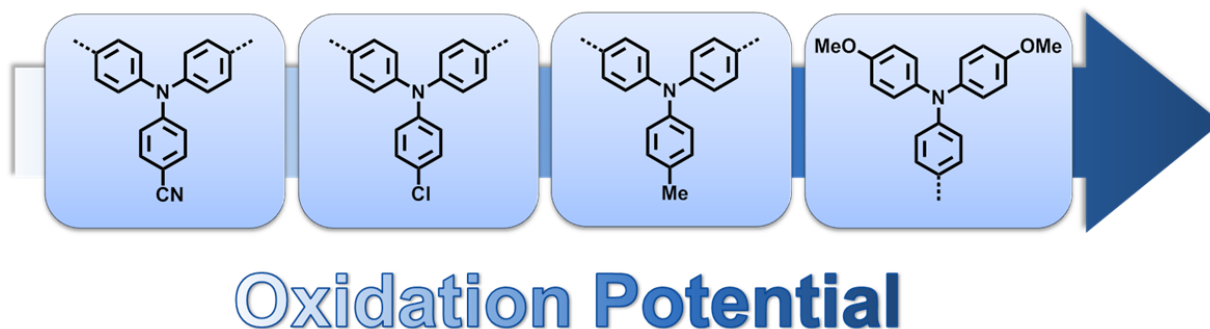
Scheme 44: The downhill redox potential of the TAAs is determined by the substitution pattern.

Starting from either **19** or **22** gave rise to two different series of redox cascades differing in the junction of the triazoles, see Scheme 45.
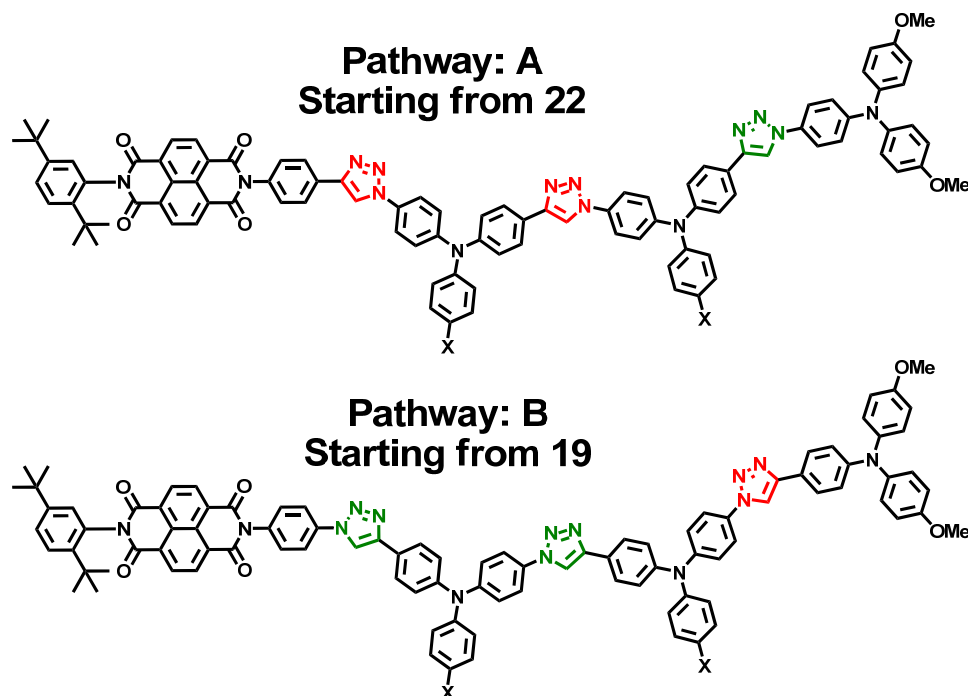
Scheme 45:   Illustration of the different cascade backbones defined by the use of the starting compounds. X denotes different substituents that determine the oxidation potential.

For both series the same bivalent building blocks were required, that include an azido, an (protected) acetylene and an oxidation potential affecting function **X**. The straightforward synthesis of **35**, **36** and **37** is outlined in Scheme 46 and is inspired by the synthesis introduced for the branching unit in the dendrimer section (*cf.* Scheme 33, p: 83).

The synthesis of the building blocks **35**, **36** and **37** started with the generation of the *p*-substituted diarylamines **23**, **24** and **25** by a Pd-catalysed *Buchwald-Hartwig*[199,209-212] cross coupling of aniline with 4-iodotoluene and 4-bromobenzonitrile, respectively, or of iodobenzene with 4-chloroaniline.

Next, the diarylamines were selectively brominated in *p*-position using tetra-*n*-butylammonium tribromide (TBATB)[107] in CHCl$_3$ as bromination reagent, which had two major advantages over classical bromide. First, TBATB is a solid, that is easy to handle and much more environmentally benign. Second, it allows mild bromination conditions and is less oxidizing than bromide.[213]

Sonogashira-Hagihara[191] cross coupling reactions of **26-28** with TIPSA in 1,4-dioxane with reaction times of several days provided the bisarylamine derivatives **29-31** in yields over 80 %. TIPS protecting groups were employed for the benefits outlined in the dendrimer section.

Similarly to the synthesis of **11** the following *Ullmann* coupling reactions of **29**-**31** with 1-bromo-4-iodobenzene leading to the TAAs **32**-**34** were performed in *o*-DCB with activated copper and potassium carbonate as base.[202]

Finally, substitution of the bromides in **32**-**34** with sodium azide and CuI in a mixture of ^{i}PrOH/H_2O 7:3 gave rise to the desired bivalent TAA reagents **35**-**37**. Thereby, the low solubility of the precursors might have accounted for the relatively low yields of **36** and **37**. Another reason might be their electron poor character of **36** and **37**.[194] One major drawback of this synthetic route is the determination of **X** in the first reaction step but all attempts to find an alternative strategy in which the substituent is introduced at a later time of the reaction failed.
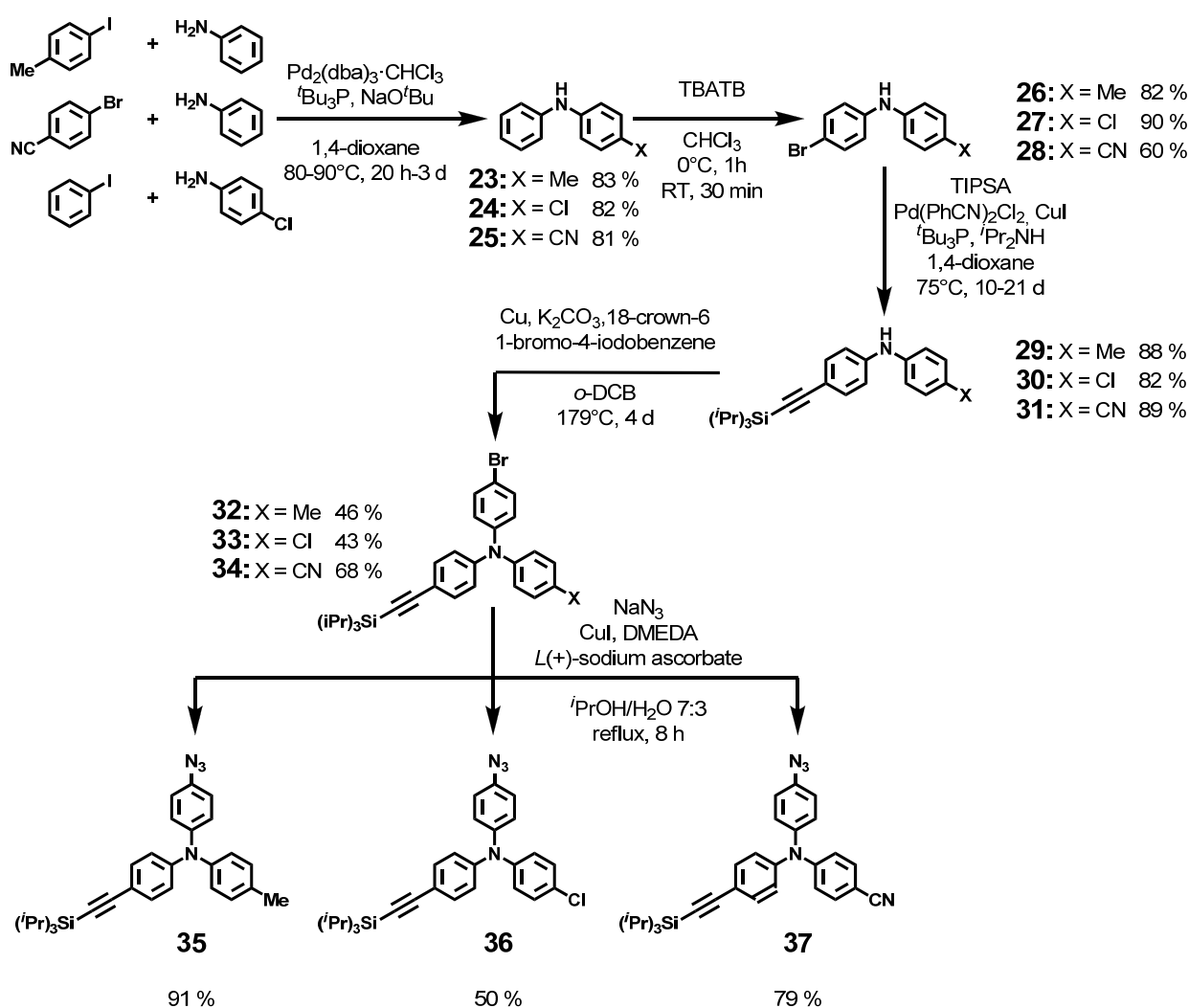
Scheme 46: Synthesis of the bivalent building blocks 35, 36 and 37.

With precursors **35**-**37** in hands, the synthesis of both series of cascades **A** and **B** was approached. In pathway **A** the synthesis started with a "click reaction" of **22** and the three bivalent TAA building blocks **35**-**37**, respectively, leading to the three TAA-NDI derivatives **38**-**40**. However, subsequent deprotections with TBAF failed for all derivatives and led to a complete degradation of the starting material (see Scheme 47).

Fluoride ions show an extraordinary affinity to NDIs as reported for several applications in literature ranging from fluoride detection[214,215] to regioselective brominations[216]. Although fluoride is expected to be a much too weak reduction agent to reduce NDIs, several reports in literature indicate that the fluoride reduces the NDI to its radical anion NDI˙⁻, which may undergo irreversible consecutive reactions.[215,217] To address this issue, several fluoride sources and solvent combinations were tested. However, degradation occurred much faster than the deprotection of the TIPS group in all cases and prevented the synthesis of this series of cascades.
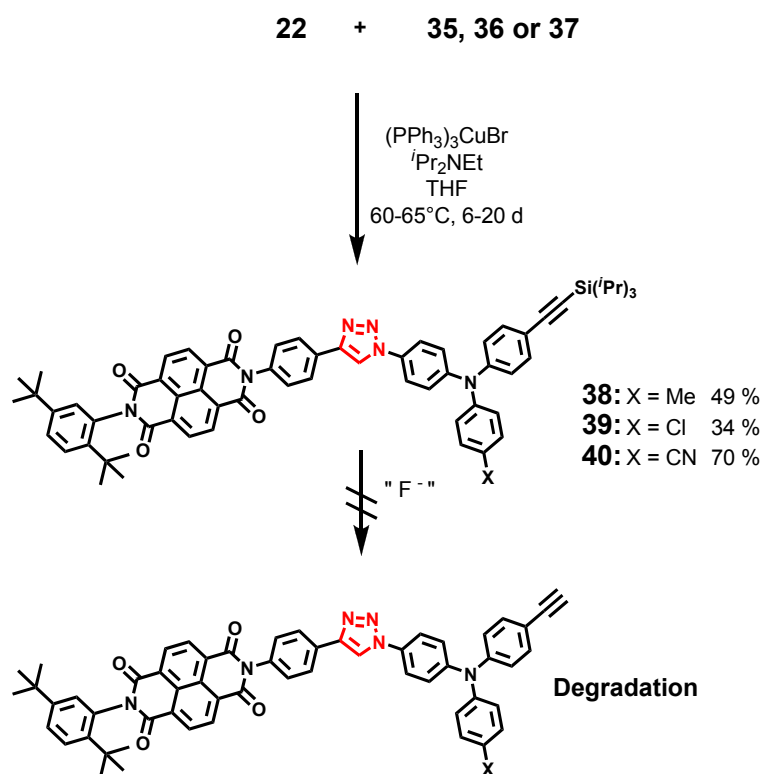
Scheme 47: Abortive synthesis of the cascades by synthetic pathway A.

Contrarily, the cascade synthesis applying pathway **B** started from **19** which has proved to be stable under optimised deprotection conditions. The three triads **T-Me**, **T-Cl** and **T-CN** were prepared in three-step reactions, shown in Scheme 48, starting with a "click reaction" of **19** with **35**, **36** and **37**, respectively, which resulted in the compounds **41**, **42** and **43** in moderate yields.

Following deprotections with TBAF in DCM led to the deprotected bis-triarylamines **44**-**46** in good to excellent yields.

A complete removal of TBAF trihydrate was essential to avoid degradation of **8** in the subsequent "click reactions" leading to the desired three triads **T-Me**, **T-Cl** and **T-CN**.[203] Although reaction times were varied, yields could not be improved any further and experimental data indicated that reaction times of ca. 13-15 d provide the best results.

19 + 35, 36 or 37

(PPh₃)₃CuBr
ⁱPr₂NEt
THF
65°C

41: X = Me   16 d, 28 %
42: X = Cl   15 d, 51 %
43: X = CN   9 d, 16 %

TBAF
DCM
RT, 2 h

44: X = Me   86 %
45: X = Cl   >99 %
46: X = CN   98 %

8
(PPh₃)₃CuBr
ⁱPr₂NEt
THF
65°C

T-Me: X = Me   13 d, 39 %
T-Cl : X = Cl   13 d, 68 %
T-CN: X = CN   34 d, 39 %
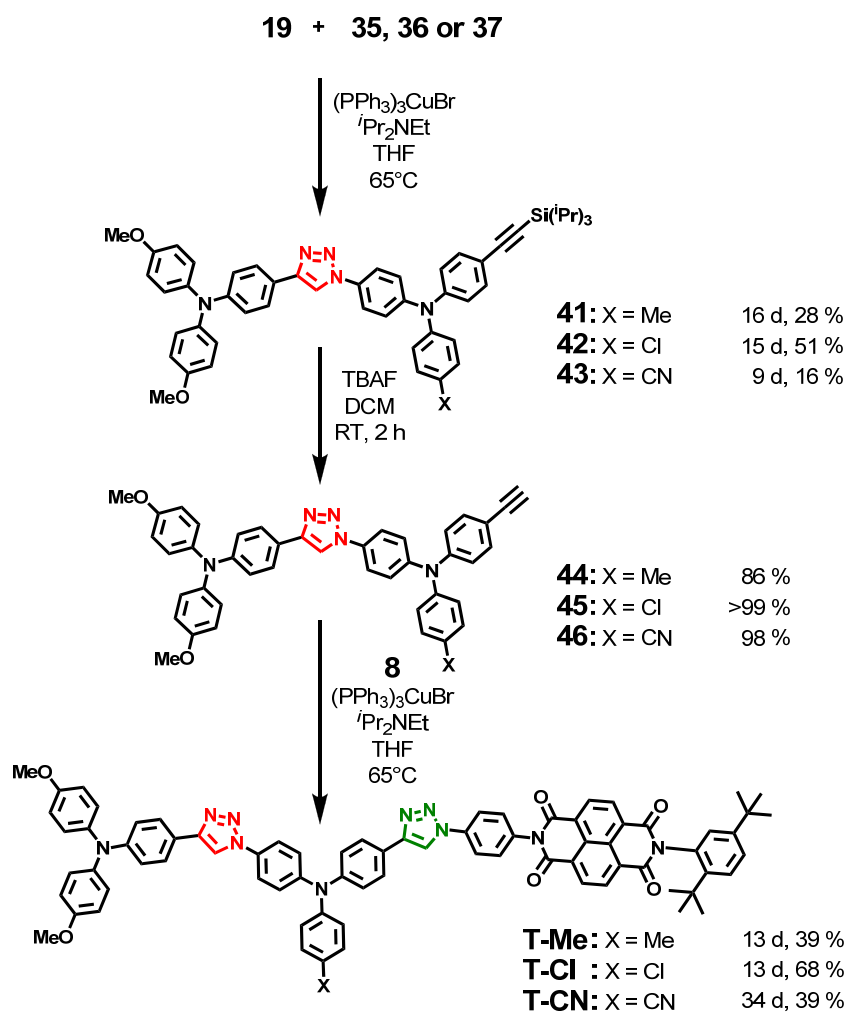
Scheme 48:   **Synthesis of the triads T-Me, T-Cl and T-CN by synthetic pathway B.**

Although this building block concept would allow the design of more complex cascades, the synthesis of larger cascades is not promising because absorption spectroscopy of **T-Me**, **T-Cl** and **T-CN** already showed overlapping absorption bands.

The five obtained cascades are summarised in Chart 11.

Dyads

Triads
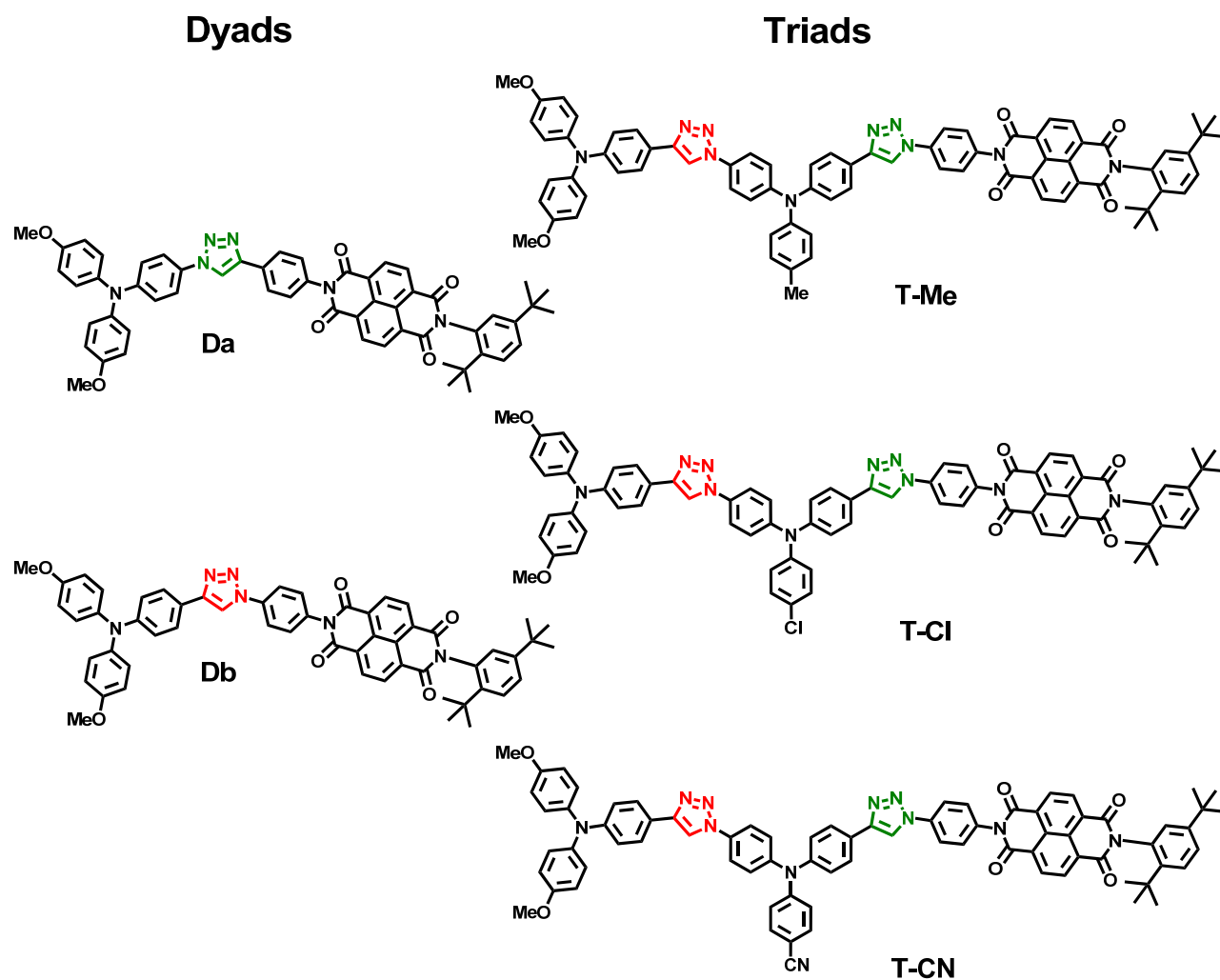
Chart 11: Summary of the redox cascades synthesised and investigated in this thesis.

3.2   Spectroscopy

In the following section the optical and electrochemical properties of the synthesised dendrimers (and model compounds) and cascades are reported. First the dendrimers will be discussed followed by the cascades. However, the donor-acceptor dendrimer **D-A-G1** will be examined after the cascades since it features more parallels to the cascades as to the "only donor comprising" dendrimers.

3.2.1   TAA Dendrimers

3.2.1.1   Cyclic Voltammetry[a]

Cyclic voltammetry (CV) was performed to investigate the electrochemical properties of the dendrimers **G1**–**G3** as well as of the model compounds **C-M**, **N-M**, **M**, **core-M** and **branch-M** (see Figure 15). All measurements were performed in DCM under argon atmosphere with TBAHFP (~ 0.2 M) as supporting electrolyte, referenced against the ferrocene/ferrocenium redox couple (Fc/Fc$^+$) and CVs that exhibit at least two different potentials were digital simulated with DigiSim[218] to obtain reliable $E_{1/2}$ values (see Figure 15 and Table 3).

---

[a] Parts of this section have already been published in *Beiträge zur Synthese und Charakterisierung von triarylaminhaltigen Dendrimeren über die Kupfer(I)-katalysierte 1,3-Huisgen-Cycloaddition*, Diploma Thesis of Fabian Zieschang, Würzburg **2009**.
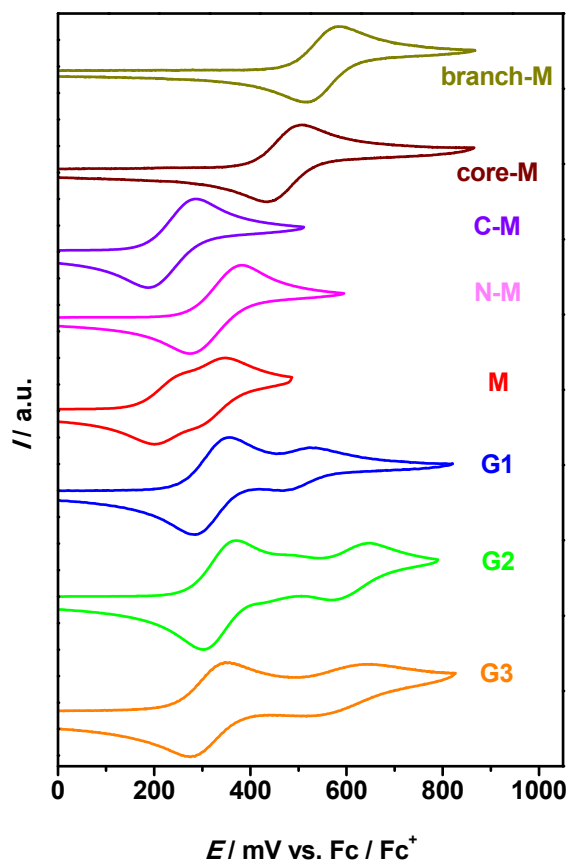
Figure 15:   Cyclic voltammograms of branch-M, core-M, C-M, N-M, M and G1–G3 measured in DCM with TBAHFP (~ 0.2 M) as supporting electrolyte and referenced against the Fc/Fc$^+$ redox couple.

In the CV experiment **C-M** and **N-M** present reversible oxidation waves at 240 mV and 330 mV, respectively. Both compounds differ in their linkage towards the triazole only and this linkage strongly influences the redox potentials. Accordingly, triazoles connected *via* the carbon to the TAA act as an electron-donating-group (EDG) while nitrogen-linked triazoles act as an electron-withdrawing-group (EWG).[159,219,220] This EWG behaviour of *N*-linked triazoles might be a result of the incorporation of the nitrogen lone pair into the aromatic π-system, which precludes a +M-effect and thus, only the –I-effect due to the nitrogen electronegativity remains.

The CV of **M** provides $E_{1/2}$ values of 240 mV and of 340 mV and thus appears as a superposition of the CVs of **C-M** and **N-M** since the two TAAs in **M** possess the same substitution pattern as **C-M** and **N-M**. The assignment of the first oxidation to the carbon-linked and the second to the nitrogen-linked TAA was also supported by two-dimensional redox NMR-measurements.[221] The values found might indicate less electronic communication of the two TAAs *via* the triazole and thus the potentials are defined only by the EWG/EDG behaviour of the triazoles.

This ambivalent potential defining behaviour of the triazoles also extensively influences the CVs of **G1**–**G3**, hence all TAAs, except for the terminal TAAs, are substituted exclusively by triazoles.

Thus, the first oxidation waves for **G1**–**G3** at ca. 330 mV are assigned to the oxidation of the terminal TAAs because the donor strength of the MeO-substituents is considerably larger than any influence of the triazole. The following oxidations at ca. 480 mV refer to the core-TAAs, which feature three EDGs (carbon linked triazoles) whereas the branch TAAs (only in **G2** and **G3**) possess the most positive oxidation potentials at ca. 600 mV as a result of two EWGs and one EDG. Moreover, these assignments of the oxidation waves were also supported by CVs of **core-M** ($E_{1/2}$ = 470 mV) and **branch-M** ($E_{1/2}$ = 550 mV).

Table 3: Half-Wave Potentials ($E_{1/2}$) of G1–G3 and of the Model Compounds branch-M, core-M, C-M, N-M and M. All $E_{1/2}$ Values were Estimated by Cyclic Voltammetry in DCM/TBAHFP (~0.2 M) at RT and Referenced against the Fc/Fc$^+$ Redox Couple.

	$E_{1/2}^{terminal}$ /mV	$E_{1/2}^{branch}$ /mV	$E_{1/2}^{core}$ /mV
core-M[c]	-	-	470
branch-M[b]	-	550	-
N-M[b]	330	-	-
C-M[b]	240	-	-
M[a, b]	245, 340	-	-
G1[a, d]	295, 320, 340	-	500
G2[a, b]	300, 305, 330, 340, 360, 370	580, 615, 620	465
G3[a, c]	250, 270, 280, 300, 305, 320, 320, 335, 340, 360, 370, 390	510, 540, 570, 590, 615, 635, 665, 715, 800	440

[a] $E_{1/2}$ values obtained by digital simulation of the related CV with DigiSim.[218] [b] Measured with a scan rate of 250 mVs^{-1}. [c] Measured with a scan rate of 500 mV s^{-1}. [d] Measured with a scan rate of 1000 mVs^{-1}.

3.2.1.2   Steady-State Absorption Spectroscopy[a]

In order to obtain information about the electronic ground state of the dendrimers, steady-state absorption spectra of **N-M**, **C-M**, **M** and **G1** were recorded in solvents of different polarity (ranging from nonpolar cyclohexane to polar MeCN). The obtained data are listed in Table 4. From **G2** and **G3** only spectra in DCM could be obtained because of the high insolvability in other then medium polar solvents. In DCM **C-M** and **N-M** show a broad absorption band at 30300 cm^{-1} (330 nm) with a small shoulder at 33000 (300 nm) that was present in all systems (Figure 16).

For **M**, the wide and structureless absorption band is shifted ca. 1100 cm^{-1} to about 29200 cm^{-1} (340 nm). The shoulder remains at ca. 33000 cm^{-1} (300 nm) and is slightly decreased compared to **N-M** and **C-M**.

For the dendrimers, the main absorption band is shifted about 1100 cm^{-1} to ca. 28200 cm^{-1} (355 nm) and the shoulder decreases with increasing generation number (see Figure 16). With assumed C_3-symmetry **G1** ends up with a set of E-symmetric excited states with lower energy and one higher energy state with A-symmetry.[18,19,222] The selection rules forbid optical excitation into the later, but allow it in into the E-symmetric states. However, such selection rules can be lifted by symmetry breaking caused by the solvent and leading to somewhat non-degenerated states.[18,19,222] However, the identical position of the lowest energy transition of the individual dendrimers is an evidence for poor if at all exciton interaction of **M** motifs, which are more distant in the higher generation dendrimers. Similar 00-energies of **C-M**, **N-M**, **M** and the dendrimers are indicated by the fact that all compounds show very similar onsets of the absorption bands. This is also proved by the small energy differences in the fluorescence maxima between **M** and **G1** (about 200 cm^{-1}, see section 3.2.1.3). The extinction coefficients of the dendrimers approximately reflect the number of **M** units in the systems (see Table 4, p: 107).
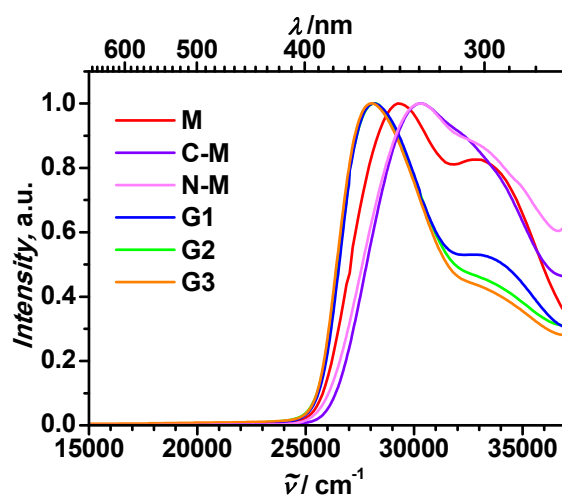
Figure 16: Normalised absorption spectra of C-M, N-M, M and G1–G3 in DCM.

3.2.1.3 Emission Spectroscopy[a]

In the absorption spectra there is weak solvatochromism for all dendrimers but the emission bands are strongly solvent dependent (shown for **G1** in Figure 17 (right)). All bands are broad and featureless and the maxima shift bathochromic with increasing solvent polarity (about 5300 cm^{-1} going from cyclohexane to MeCN). This is a typical behaviour for the emission from a charge transfer state. The apparently symmetric donor-acceptor-donor (TAA-triazole-TAA) structure of **M** allows no polar excited state but due to the asymmetric triazole-spacer the two TAAs become differently strong donors and this asymmetry could result in small changes of dipole moments after excitation.[223] Additionally, systems analogous to **M**, composed of *e.g.* two TAA donors linked *via* an aromatic bridge exhibiting acceptor character (*e.g.* anthracene), have proved to shift electron density from the two donors towards the bridging acceptor and thus the excited quadrupolar state will be stabilised in polar solvents comparable to dipolar excited states of pure donor-acceptor systems.[167,224,225]

Remarkably, in the emission **C-M** shows a clear difference to the other systems. While for **N-M**, **M** and **G1**–**G3** the emission spectra are all similar in related solvents, the emission of **C-M** is shifted to higher energy for most solvents (cf. emission in DCM shown in Figure 17 (left)). This finding and the lower emission energy in MeCN compared to the all other compounds indicates a more polar excited state in **C-M**.
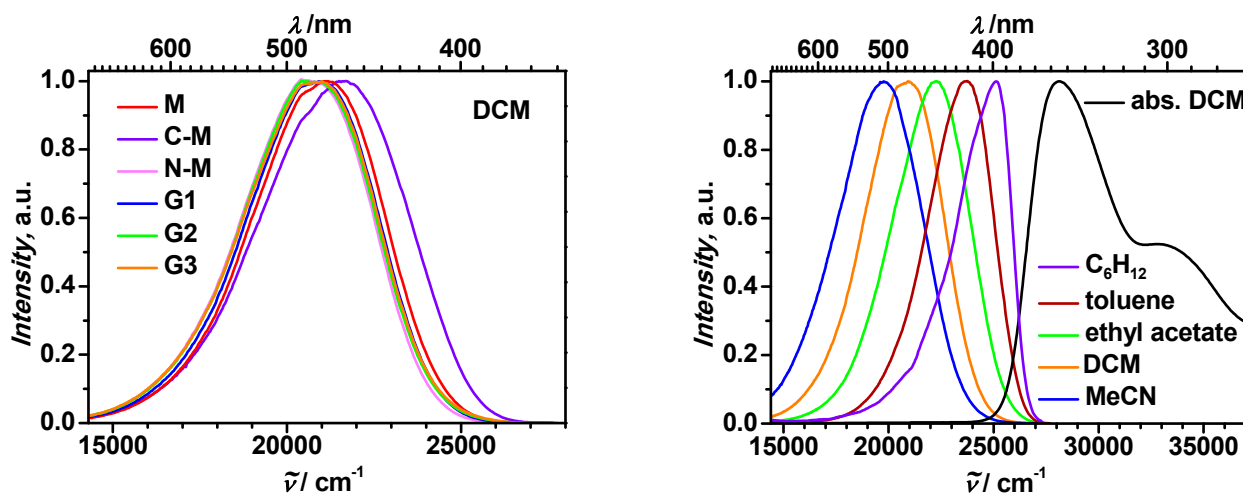
Figure 17: Normalised emission spectra of C-M, N-M, M and G1–G3 in DCM (left) and normalised absorption in DCM and emission spectra of G1 in different solvents (right). Excitation at 28200 cm^{-1} (355 nm).

For **N-M**, **M** and all dendrimers, the fluorescence quantum yields, determined using quinine sulfate in H$_2$SO$_4$ as a quantum yield standard (ϕ = 0.55), are in the range of 50 – 60% and of 20 – 40% for **C-M** with a maximum in moderately polar solvents. Also similar for all compounds are the excited state lifetimes τ_f with values around 5 ns in DCM, 6 ns in MeCN and 2 ns in toluene (see Table 4). With these data and equation, (54) the rate of radiative decay k_f was determined and applying the *Strickler-Berg* equation (55) the fluorescence transition moments μ_f were estimated to be roughly 4 D.

$$k_f = \frac{\phi_f}{\tau_f} \tag{54}$$

$$k_f = \frac{16 \cdot 10^6 \, \pi^3}{3h\varepsilon_0} \cdot \frac{n(n^2+2)^2}{9} \cdot \frac{g_g}{g_e} \langle \tilde{\nu}_f^{-3} \rangle_{av}^{-1} \mu_f^2 \tag{55}$$

where

ϕ_f the fluorescence quantum yield, τ_f is the excited state lifetime, n is the refractive index of the solvent, ε_0 is the vacuum permittivity, h is the *Planck* constant, g_g and g_e are the degree of degeneracy (= 1) in the ground and excited state, respectively, and $\langle \tilde{\nu}_f^{-3} \rangle_{av}^{-1} = \int I_f \mathrm{d}\tilde{\nu} / \int \tilde{\nu}^{-3} I_f \mathrm{d}\tilde{\nu}$ is the average cubic fluorescence energy.

No superradiant effect can be observed in the narrow range of the fluorescence transition moments and thus exciton coupling may be neglected in the vibronically and solvent-relaxed excited emissive state.

Table 4: **Absorption and Fluorescence Data of N-M, C-M, M and G1–G3**

		$\widetilde{\nu}_{max}$ /cm^{-1}	ε_{max} /M^{-1} cm^{-1}	$\widetilde{\nu}_f$ /cm^{-1}	ϕ_f	τ_f /ns	k_f /10^7 s^{-1}	μ_{fl} /D
N-M	MeCN	30950	22900	19600	0.54	6.1	9	4.4
	ethyl acetate	30550	23100	22000	0.61	4.8	13	4.3
	DCM	30300	21000	20600	0.65	6.2	10	3.9
	toluene	30100	21300	23400	0.40	2.7	15	3.7
	cyclohexane	30250	-	24800	-	-	-	-
C-M	MeCN	30950	25700	19000	0.21	6.6	3	2.6
	ethyl acetate	30500	25200	23000	0.39	3.2	12	3.8
	DCM	30300	24200	21500	0.34	5.2	7	3.1
	toluene	29900	22900	24400	0.27	1.8	15	3.5
	cyclohexane	29750	-	25400	-	-	-	-
M	MeCN	29900	41300	20000	0.52	6.0	9	4.3
	ethyl acetate	29450	41400	22400	0.62	3.6	17	4.8
	DCM	29200	38800	21100	0.64	5.1	13	4.4
	toluene	29000	38600	24000	0.45	1.6	28	4.9
	cyclohexane	29200	-	25300	-	-	-	-
G1	MeCN	28500	-	19800	0.45	5.7	8	4.1
	ethyl acetate	28300	112000	22200	0.67	4.2	16	4.7
	DCM	28100	103000	20900	0.57	5.0	11	4.1
	toluene	27900	112000	23800	0.49	1.8	27	4.9
	cyclohexane	27700	-	25100	-	-	-	-
G2	MeCN	-	-	19800	-	-	-	-
	ethyl acetate	28200	-	22000	0.54	4.2	13	4.3
	DCM	28100	288000	20500	0.67	4.8	14	4.6
	toluene	27900	-	23500	0.38	2.5	15	3.7
G3	ethyl acetate	-	-	22300	-	-	-	-
	DCM	28000	613000	21000	0.48	4.6	10	3.9

3.2.1.4   Steady-State Emission Anisotropy Measurements[a]

Steady-state emission anisotropy measurements were performed for **C-M**, **N-M**, **M** and **G1**–**G3** to get a closer view on the relative orientation of the transition moments of absorption and emission. For the investigations the compounds were embedded in a solid glass matrix of sucrose octaacetate (SOA) to avoid molecular motions. The fluorescence anisotropy r (*cf.* equation (35), p: 22 and equation (42), p: 25) is defined as the ratio of the polarised component to the total intensity, see equation (56). The anisotropy values can be assigned to the angle θ, which is the angle between the transition moments of absorption and emission. If the transition moments are parallel r gives a value of 0.4, if they are perpendicular the anisotropy value is -0.2. For completely depolarised transition moments, the value is 0.[8,167,224-227] The value 0.1 refers to a 2-dimensional depolarisation of the transition moments, which is expected if energy transfer takes place between the chromophore branches in the dendrimers. However, r values up to 0.7 were predicted and also measured for coherent excitation of two states.[30-34]

$$r = \frac{I_{vv} - 2GI_{vh}}{I_{vv} + 2GI_{hv}} = \frac{2}{5}\left(\frac{3\cos^2\theta - 1}{2}\right) \tag{56}$$

where

I_{vv} and I_{vh} are the fluorescence intensities with excitation and emission polariser set vertically or perpendicular, respectively, and G is a hardware correction factor (*cf.* 2.1.1.4, p: 24).

The excitation anisotropies of **C-M**, **N-M**, **M** and **G1**–**G3** can be found in Figure 18. At the start at 24000 cm^{-1} (415 nm) the anisotropy of all compounds is about 0.33. A reason why this value is a little lower than the expected value of r = 0.4 for parallel transition moments may be some remaining flexibility even in the solid glass matrix. Another reason could be very fast relaxation processes, which result in a rearrangement of the orientation of the transition moments, which would lead to a lower anisotropy in the beginning. For **M**, this high anisotropy value stays in the area of the main absorption band (down to 27000 cm^{-1} (370 nm)) and then decreases with an increasing overlap with the higher energy absorption band to r = 0.25 at 31000 cm^{-1} (320 nm). The transition moment of this band is obviously in a different orientation and thus the anisotropy with r = 0 at 35000 cm^{-1} (290 nm) converges near the value for complete depolarisation. The lowest energy transition in **M** is polarised along the molecular axis as predicted by time-dependent DFT calculations using B3LYP/6-31G*[228] level of theory with a COSMO solvation model for DCM. The anisotropy behaviour of **C-M** and **N-M** corresponds to the one of **M**. This observation reveals that

either no energy transfer takes place in **M** or that the energy transfer leads only to a small change of the anisotropy values due to the small angle between the transition moments.
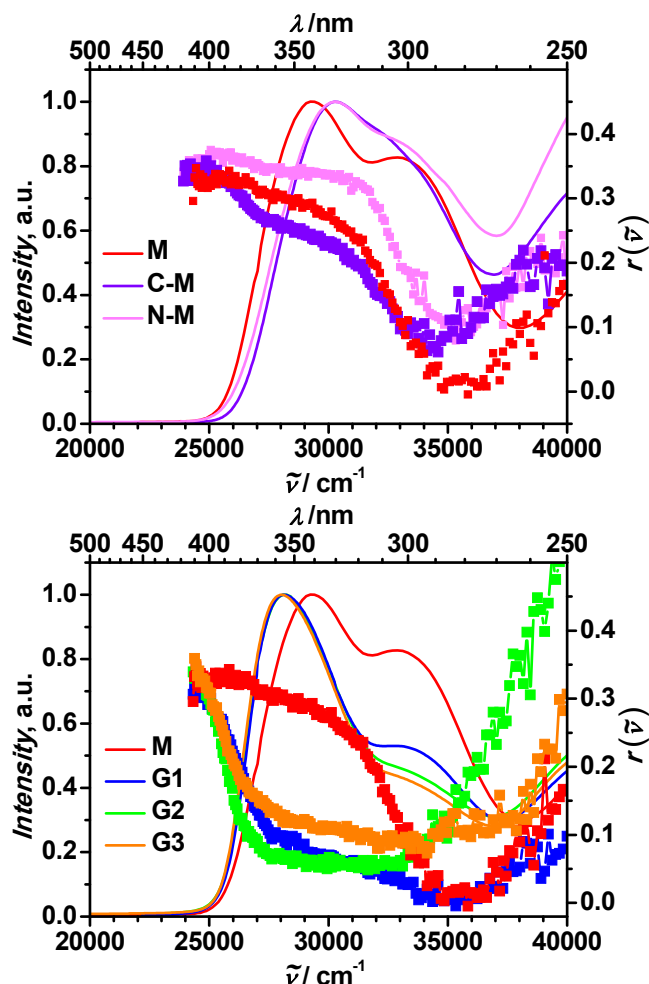
Figure 18: Normalised absorption spectra (—) in DCM and fluorescence excitation polarisation anisotropy spectra $r(\tilde{v})$ (-■-) of C-M, N-M and M (top) and M and G1–G3 (bottom) in sucrose octaacetate at RT.

However, the situation is different for the dendrimers. The high anisotropy at the beginning at 24000 cm^{-1} (415 nm) readily drops to a value about 0.05 – 0.10 between 28200 cm^{-1} (355 nm) and 33000 cm^{-1} (300 nm). The low anisotropy in this region is caused by energy transfer between the chromophore branches within the excited state lifetime of about 5 ns. Hence, the high anisotropy values for **G1**-**G3** at the low energy side of the S$_0$-S$_1$ absorption are remarkable. In this region the emission is more polarised than in the range of the absorption maxima. This instance has to be explained by the so called "red edge excitation effect".[229-235] The chromophores are symmetry broken by an inhomogeneous environment (when not inherently asymmetric). This includes the solvent configuration as well as intramolecular geometric interaction and leads to a slightly different

stabilisation of the branches and the former degenerated states split. On the red side of the spectra only the lowest energy state can be excited and no energy transfer occurs as the other states are too high in energy. Thus, the transition moments of absorption and emission are oriented almost parallel and the anisotropy becomes high. At excitation with higher energies also the higher excited states can be populated and after photoexcitation the energy is transferred to the lowest energy state and following *Kasha´s* rule fluorescence occurs from this state with lower anisotropy.

The observation of a red edge excitation effect is a proof for energy transfer. In order to gain information about the dynamics of the energy transfer occurring in the dendrimers, time resolved emission spectroscopy using a fluorescence up-conversion technique was performed.

3.2.1.5   Photophysics and Solvation Dynamics of M[a]

As the smallest unit that shows excitation delocalisation, **M** operates as a "spectroscopic unit" in **G1**–**G3**.[97] Reasonably, the photophysics of **M** will be delighted at first (the photophysics of **C-M** and **N-M** are expected to be similar and will not be an issue anymore). This will be the basic for a further understanding of the more complicated processes in the dendrimers. In the up-conversion measurement the compounds were excited at the low energy flank of the absorption band by a 26300 cm^{-1} (380 nm) laser pulse to prevent excitation of electronically higher excited states. Details about the up-conversion experiments as well as the data processing can be found in the experimental section. Figure 19 shows the fluorescence decay of **M** at 20800 cm^{-1} (480 nm) under magic angle conditions. A fit of this decay leads to three lifetimes: a short risetime with 0.4 ps, a medium long decay of 31 ps and a lifetime related to the depopulation of the excited state with 5.0 ns (see Table 5, p: 116). The depopulation lifetime obtained from the up-conversion setup is in good agreement with that from the ns setup (discussed above), which seems to be the more accurate result due to the limited delay stage length (0 – 3.3 ns) in the up-conversion setup.

---

[a] Adapted or reproduced (or reproduced in parts) from *Solvent Controlled Energy Transfer Processes in Triarylamine-Triazole Based Dendrimers*, Zieschang, F.; Schmiedel, A.; Holzapfel, M.; Ansorg, K.; Engels, B.; Lambert, C. *J. Phys. Chem. C* **2013**, *117*, 19816-19831. Copyright 2013 American Chemical Society.
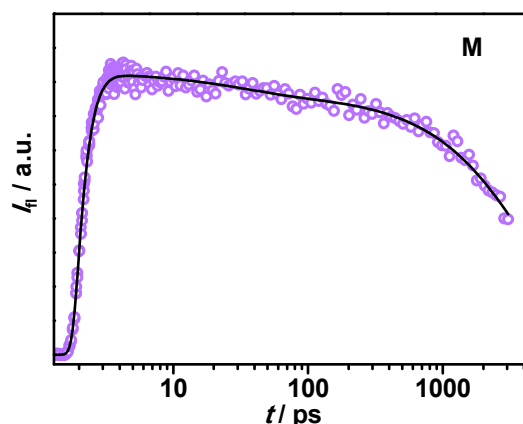
Figure 19:   Fluorescence decay of M in DCM measured by fluorescence up-conversion under magic angle conditions. The black line is the multiexponential fit of the experimental data (purple circles) convoluted by the instrument response. Excitation at 26300 cm^{-1} (380 nm), fluorescence at 20800 cm^{-1} (480 nm).

Additionally, fs-time resolved fluorescence anisotropy r(t) was determined to get a closer view on the changes of the orientation of the transition moments. Therefore measurements were performed with the excitation beam polarised perpendicular and parallel to the gate beam. With equation (57) the experimental anisotropy R(t) can be obtained from the experimental intensities $I_\perp(t)$ and $I_\parallel(t)$. The experimental intensities are convoluted with the instrument response and the same is true for the anisotropy R(t).
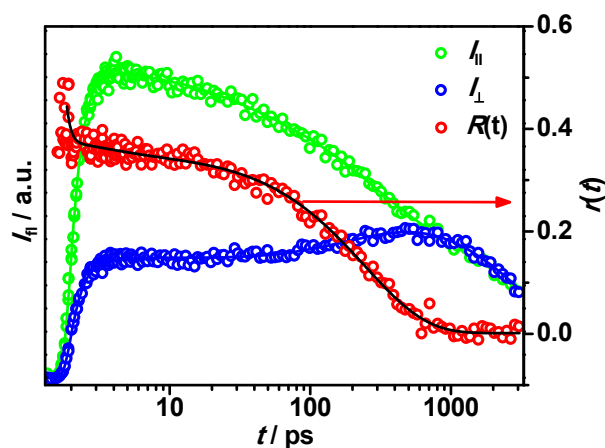
Figure 20:   Fluorescence decay at 20800 cm^{-1} (480 nm) of M in DCM with pump pulse oriented parallel (green circles) and perpendicular (blue circles), global fit (green or blue line, respectively), experimental anisotropy $R(t)$ (red circles) and fitted anisotropy $r(t)$ (black line). Note: r(t) is calculated from the global deconvolution fits of $I_\perp(t)$ and $I_\parallel(t)$ and not a fit of the experimental anisotropy.

Unfortunately, it is difficult to deconvolute $R(t)$[236,237] and thus the experimental intensities $I_\perp(t)$ and $I_\parallel(t)$ were deconvoluted with up to five exponentials using the GLOTARAN-software[238],[239] This leads to the deconvoluted intensities $i'_\perp(t)$ and $i'_\parallel(t)$ with time zero being the maximum of the Gaussian shaped instrument response. Subsequently, $i'_\perp(t)$ and $i'_\parallel(t)$ were tail-matched to allow for the different intensities of parallel and perpendicular pump measurements. Using the resulting intensities ($i_\perp(t)$ and $i_\parallel(t)$) and equation (58) the deconvolute anisotropy $r(t)$ was obtained. However, the deconvoluted intensities $I_\perp(t)$ and $I_\parallel(t)$ have to be shifted for some 10 fs prior to global fitting to agree for an initial rise of the curves. Otherwise artificially high anisotropies with fast decays of several 10 fs were obtained.

$$R(t) = \frac{I_\parallel(t) - I_\perp(t)}{I_\parallel(t) + 2I_\perp(t)} \tag{57}$$

$$r(t) = \frac{i_\parallel(t) - i_\perp(t)}{i_\parallel(t) + 2i_\perp(t)} \tag{58}$$

The anisotropy decay of **M** shows a high value of $r = 0.44$ at the beginning. This is close to the value of $r = 0.4$, which is the value for parallel orientation of the transition moments of absorption and emission. Some reasons are responsible that the anisotropy at time zero is hardly to ascertain:

- moderate shifts of the parallel and the perpendicular intensities towards each other yield in large differences of the initial anisotropy
- initial decays, faster than the time resolution of the setup possibly give an apparently lower initial anisotropy
- coherent excitation of two states may result in an initial anisotropy up to $r = 0.7$[30-34]
- simultaneous absorption of multiple photons effects the initial anisotropy ($r(0) = 2/5$ for one-photon absorption, $r(0) = 4/7$ for two-photon absorption and $r(0) = 2/3$ for three-photon absorption)[8]
- at the rise of the fluorescence the signal to noise ratio is bad and therefore the anisotropy is noisy too

Thus, an interpretation of the anisotropy in the very first two picoseconds is sophisticating and the following discussion will focus on the processes occurring after 2 ps. After the first 2 ps the anisotropy of **M** drops to a value of about 0.36 with $\tau_1 = 0.13$ ps ($a_1 = 0.067$). There it remains some ten picoseconds ($r = 0.34$ at $t = 10$ ps) with $\tau_2 = 2.6$ ps ($a_2 = 0.023$) until it again decreases after 100 ps to $r = 0.23$ with $\tau_3 = 250$ ps ($a_3 = 0.35$). The last process is related to rotational diffusion of **M** in DCM, with a typical lifetime for a system of such size in DCM.[8] This assignment is also indicated by the fact that this component is completely missing in the isotropic decay.
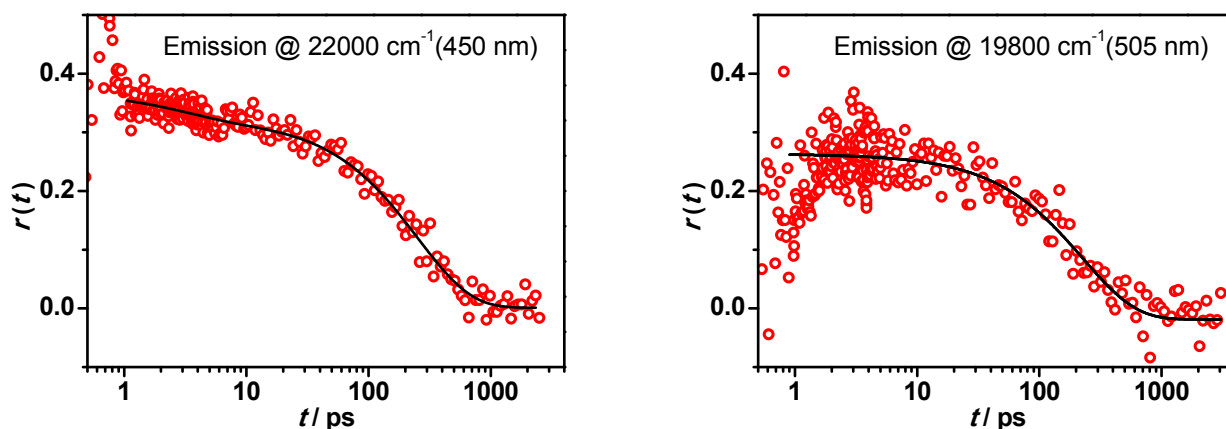
Figure 21: Experimental anisotropy $R(t)$ (red circles) and fitted anisotropy $r(t)$ (black line) of **M** in DCM at 22000 cm^{-1} (450 nm) (left) and 19800 cm^{-1} (505 nm) (right). Note: $r(t)$ is calculated from the global deconvolution fits of $I_{\perp}(t)$ and $I_{\parallel}(t)$ and not a fit of the experimental anisotropy.

Apparently, **M** loses some anisotropy in the first two picoseconds but most loss is caused by rotational diffusion. In a fit of the anisotropy decay at 22000 cm^{-1} (455 nm) τ_2 has a net higher amplitude and in the fit of anisotropy measurement at 19800 cm^{-1} (505 nm) τ_2 is entire missing (excitation still at 26300 cm^{-1} (380 nm)), see Figure 21. At higher emission energies fast relaxation processes can be followed, while at lower emission energies fast relaxations are already completed and only slower processes are observed (Table 5, p: 116). Obviously, relaxation processes strongly influence the anisotropy decay of **M**. Therefore, a complete map of time resolved emission spectra (TRES) was measured to use the dynamic *Stokes* shift (DSS) to obtain insight in the solvent and relaxation processes of the first picoseconds.[240]
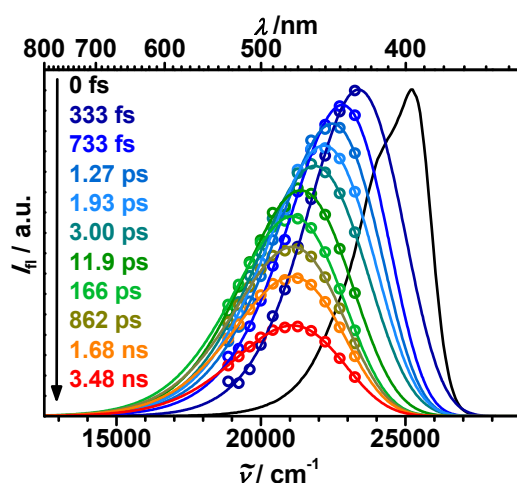
Figure 22: **TRES of M in DCM at different delay times. Note: the lines are log-normal fits of the data points (circles) that were obtained from a global fit of the experimental data and therefore already include a fit model. An emission spectrum in cyclohexane serves as the time-zero spectrum.**

This was done by measuring fluorescence decays at different energies from 23300 cm^{-1} (430 nm) to 18900 cm^{-1} (530 cm^{-1}) in 10 nm steps. Deconvolution of the resulting $I(\lambda,t)$ map was achieved by global fitting with multiple exponentials and correction for the time zero wavelength dependence, which gives the deconvoluted map $i(\lambda,t)$. The intensity of the steady-state emission spectrum of **M** in DCM and the intensity of the longest time delay was matched to allow for correction of the wavelength dependence. Each time correlated emission spectrum, obtained by slicing the corrected map at discrete delay times, was fitted by a log-normal function (Figure 22). From the maxima of this functions $\tilde{\nu}_{max}(t)$ and using equation (59) the normalised solvent spectra response function $S(t)$ were calculated, which is a correlation of the *Stokes* shift vs. time, see Figure 23.[241,242]

$$S(t) = \frac{\tilde{\nu}_{max}(t) - \tilde{\nu}_{max}(\infty)}{\tilde{\nu}_{max}(0) - \tilde{\nu}_{max}(\infty)} \tag{59}$$

where

$\tilde{\nu}_{max}(\infty)$ is the wavenumber at infinite time and $\tilde{\nu}_{max}(0)$ is the wavenumber at time zero.
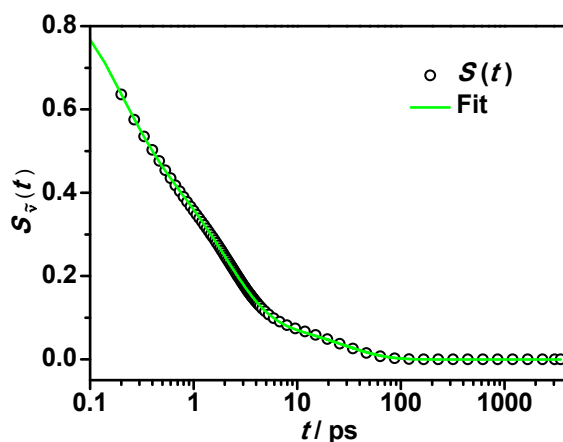
Figure 23: Normalised solvent spectral response function $S(t)$ of M in DCM calculated from the maxima of the log-normal functions presented in Figure 22 applying equation (59) and fit of this function yielding the lifetimes and amplitudes given in Table 5.

The time zero spectrum is hard to measure due to a large overlap with stray light from the second harmonic of the fundamental of the laser at 12500 cm^{-1} (800 nm). Therefore, the steady-state fluorescence spectrum of **M** in cyclohexane seems to be the best alternative since it is accepted to be almost free of solvent relaxation effects.[243] A fit of $S(t)$ leads to three lifetimes, where $\tau_1 = 0.17$ ps and $\tau_2 = 1.9$ ps are analogous to the ones *Maroncelli et al.* already reported for coumarin in DCM ($\tau_1 = 0.144$ ps and $\tau_2 = 1.02$ ps; $a_1 \approx a_2$) and are assigned to solvent relaxation of the chromophores.[244] But the lifetime of 27 ps, which can also be found in the isotropic decay of **M**, can directly be linked to molecular relaxation processes in the molecule.

Table 5:   **Time Constants τ (ps) and Amplitudes a of Fluorescence Up-conversion Measurements under Magic Angle Conditions (MA), Anisotropy ($r(t)$), Solvent Spectral Response Function ($S(t)$) and Global Fit of TRES of M in DCM.**

	τ_1	a_1	τ_2	a_2	τ_3	a_3	τ_4	a_4	τ_5	a_5
MA[a]	0.40	-0.94			31	0.075			5.0×10^3	0.93
@455 nm			2.9	0.032			253	0.31		
$r(t)$[a] @480 nm	0.13	0.067	2.6	0.023			250	0.35		
@505 nm							227	0.28		
$S(t)$[b]	0.17	0.46	1.9	0.44	27	0.10				
global fit[b]	0.38		1.7		22					

[a] Pump at 26300 cm^{-1} (380 nm), fluorescence at 20800 cm^{-1} (480 nm). [b] Pump at 26300 cm^{-1} (380 nm), emission between 23300 cm^{-1} (430 nm) and 18900 cm^{-1} (530 nm) in 10 nm steps.

Furthermore, a global analysis of the TRES leads to evolution associated spectra (EAS) and to likely more accurate time constants (see Table 5). Obviously, the lifetimes of the TRES global fit and of $S(t)$ are in good agreement but the EAS and the TRES exhibit considerably different spectral shapes. This might be a result of the different restrictions in the analyses. While spectral shapes in the TRES were accepted to follow log-normal functions, in the global analysis no such restrictions on the spectral shape were incorporated. As a result considerable intensities at about 24000 cm^{-1} (415 nm) are obtained for early delay times and it can be assumed that the spectral shapes of the EAS are distorted. Thus the results from the TRES and $S(t)$ seem more reliable.
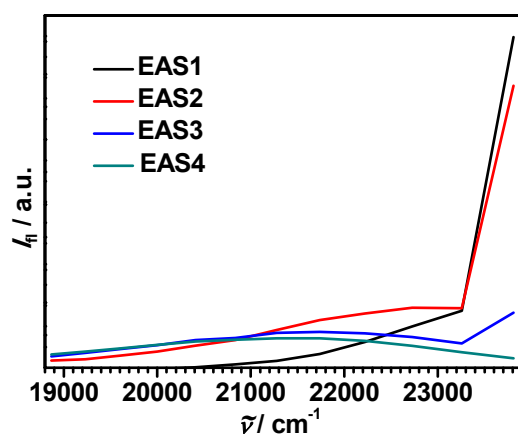
Figure 24:   **Evolution associated spectra (EAS) from a global fit of the TRES of M in DCM.**

A comparison of the results from the $S(t)$ with those from the isotropic and anisotropy decay leads to the following picture after excitation of **M** (see Figure 25). A DSS observed by the short rise time of 0.40 ps and the two short lifetimes in $S(t)$ support the conclusion that the first two picoseconds after photoexcitation are solvent controlled. But there must also occur a molecular, possibly vibronic, relaxation process in this time range, because the anisotropy also decreases with $\tau_1 = 0.13$ ps and a change of the orientation of the transition moments can hardly be caused by solvent relaxation alone.[245] To ascertain if this molecular relaxation is induced by the solvent relaxation, further detailed solvent dependent investigations would be necessary. The 20 – 30 ps lifetime can be found in all decay curves except in the anisotropy one. Therfore, it can be supposed that slow torsional modes lead to a relaxed excited state geometry, while the orientation of the transition moments is not altered. *Glasbeek et al.*[240,245,246] has found a comparable behaviour for auramine[247] and *Michler*'s ketone and *Ernsting et al.*[248] for dimethylanilinopyridinium. To confirm the assumption that aryl twist angles change the molecular geometry of **M** in the excited state, the ground and first excited CT state were optimised using time-dependent DFT calculation at B3LYP/6-31G* level of theory with a COSMO solvation model (to include solvent dependences).^{a} The geometries show a planarisation of the angle between the triazole plane and the *N*-phenyl ring from 33° to -2° during relaxation of the *Franck-Condon* state to the CT state. Furthermore the diansylamino group increases its dihedral angle to the *N*-phenyl ring (27° → 72°). The calculated energy of the *Franck-Condon* state of 26985 cm^{-1} corresponds well with the steady-state absorption maximum of **M** in cyclohexane at 29200 cm^{-1}. The same is true for the energy of the relaxed CT state (19743 cm^{-1}) and the fluorescence energy of **M** in cyclohexane (21100 cm^{-1}).

---

^{a} Although the B3LYP functional is known to underestimate the energy of CT states, the usually better suited long range corrected functional CAM-B3LYP fails completely for **M** and overestimates the CT energies.[M. J. G. Peach *JCP* **2008**, 128, 044118] Thus, the B3LYP functional was used anyway as it reproduces the experimental energies quite well in this case.
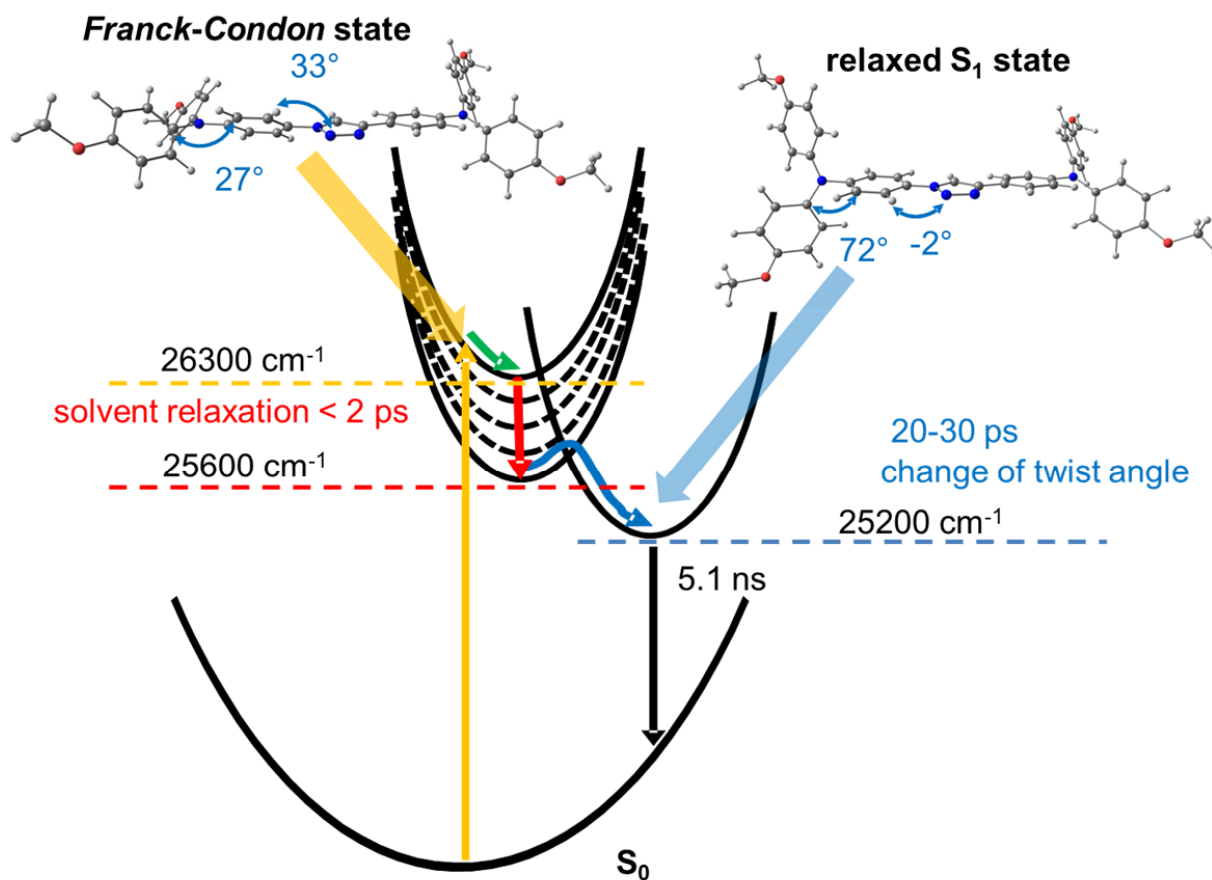
Figure 25: Potential energy diagram indicating the processes after excitation of M and calculated structures of the *Franck-Condon* and the completely relaxed S_1 state at TD-B3LYP/6-31G* level of theory applying the COSMO model for DCM. The 00-energies were obtained from the intersection of the normalised absorption and emission bands in DCM and cyclohexane, respectively. The energy of the solvent relaxed state was estimated from the *Stokes* shift of $S(t)$. However, the energy barrier between the solvent and the fully relaxed S_1 state is not accurate.

3.2.1.6 Photophysics and Solvation Dynamics of G1–G3[a]

The acquired information about the photophysical and solvent relaxation dynamics of **M** will lead to an easier understanding of the dynamics emerging in **G1**–**G3**. Up-conversion measurements were performed using the same setup than for **M**. Due to the large amount of excitable chromophores in the dendrimers, multiphoton excitation may cause exciton annihilation, resulting in distorted kinetics. Thus, to prevent multiphoton excitation, the excitation probability of one isolated chromophore calculated by equation (60) was ensured to be smaller than 10 %.[249] For **G3** this yields with ε = 15000 M^{-1} cm^{-1} at 26300 cm^{-1} (380 nm), D = 140 μm and E = 8 nJ an excitation probability of p = 0.014.

$$p = 1 - \exp\left[-\frac{E\lambda \ln(10) \cdot 0.1 \cdot \varepsilon}{hc\pi N_A \left(\frac{D}{2}\right)^2}\right] \tag{60}$$

where

E is the pump energy, λ is the excitation wavelength, D is the pump spot diameter, h is the *Planck* constant, c is the speed of light, N_A is *Avogadro*'s constant and ε is the molar extinction coefficient at the pump wavelength.

The probability of multiexcitations $P(k)$ up to the third excitation of **G3** (with p = 0.014 ($\frac{1000}{14}$) was evaluated by the hypergeometric distribution in equation (61).

$$P(k) = \frac{\binom{14}{k}\binom{1000-14}{n-k}}{\binom{1000}{n}} \tag{61}$$

with k = 0 – 3 (the number of simultaneous excitations) and n = 21 (the number of chromophores in **G3**) equation (61) gives

$P(0)$ = 0.74
$P(1)$ = 0.22
$P(2)$ = 0.03
$P(3)$ = 0.002

These results indicate that besides 22 % monoexcitation only up to ca. 3 % multiexcitation takes place in the up-conversion experiments of **G3** and even less in **G1** and **G2**. Thus, exciton annihilation can be neglected.

The obtained isotropic fluorescence decays of the dendrimers, presented in Figure 26, were treated analogous to the one described for **M**. Fits of the deconvoluted curves lead to four lifetimes for each dendrimer. The risetimes of about 0.4 ps can be ascribed to solvation processes just as found for **M**. This is in good agreement with the characteristics *Chou et al.*[250] and *Fakis et al.*[251] found for different star-shaped chromophores, which they also interpreted as solvation processes. Contrary to **M**, **G1**–**G3** each show two medium long lifetimes with about 5 – 7 ps and about 60 – 90 ps. These lifetimes are assigned to torsional modes analogous to the 20 – 30 ps lifetimes for **M**. This assignment is also in agreement with picosecond lifetimes measured in conjugated polymers and explained by torsional changes in the excited state.[252-255] The excited state depopulation lifetimes of about 4 – 5 ns are again in good agreement with those obtained in the ns-experiment.
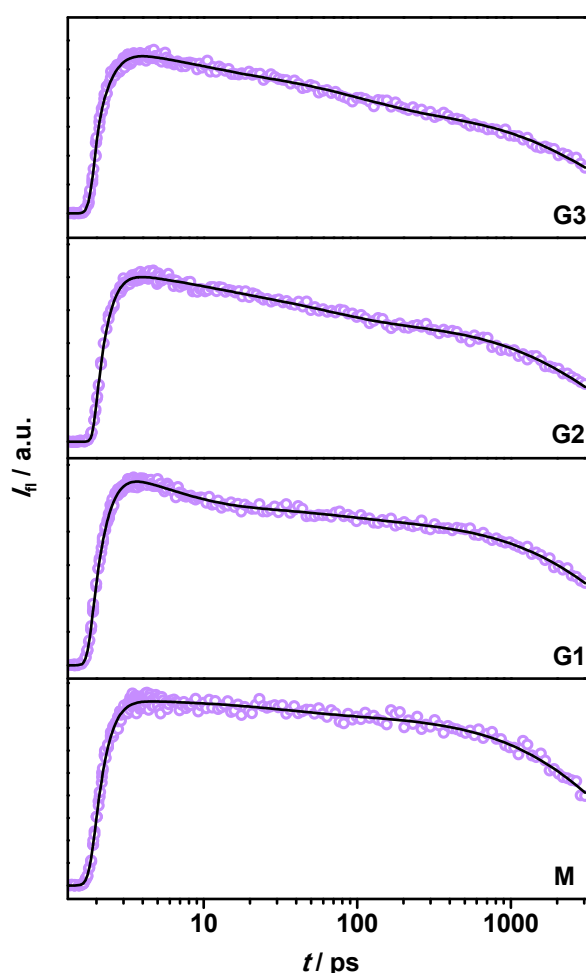
Figure 26:   **Fluorescence decays of M and G1–G3 in DCM measured by fluorescence up-conversion under magic angle conditions. Presented are the multiexponential fits (black lines) of the experimental data (purple circles) convoluted by the instrument response. Excitation at 26300 cm^{-1} (380 nm), emission at 20800 cm^{-1} (480 nm).**

Fits of the anisotropy curves of **G1**–**G3** lead to lifetimes in the sub-picosecond regime (ca. 0.2 – 0.3 ps), which are similar to the 0.13 ps found for **M**. The larger dendrimers **G2** and **G3** show two medium long anisotropy decays, one of about 4 – 5 ps (with small amplitudes) and another of ca. 20 – 60 ps, which can also be found for **G1** and are in a similar time range as their magic angle complements. **G1** and **G2** show reasonable rotational diffusion lifetimes of τ_{rot} = 440 ps (**G1**) and τ_{rot} = 760 ps (**G2**) while this lifetime is remarkably too short for **G3** (τ_{rot} = 650 ps) compared with an approximation taking the molecular weight (as a parameter equivalent to the hydrodynamic volume) and τ_{rot} = 250 ps for **M** into account (τ_{rot} = 2 – 3 ns for **G3**).[250]

Beside the possibility that the 650 ps are inaccurate due to the limited delay stage length in the up-conversion setup (3.3 ps), another reason might be a different overall globally shape of **G2** and **G3**, which would complicate comparing rotational diffusion lifetimes of the systems. Individual subunits of the dendrimers may show rotational diffusion process faster than the rotation of the entire molecule leading to somewhat shorter averaged rotational diffusion lifetimes. Hence, the extracted lifetimes represent average lifetimes with contributions from several conformations, which is especially true for the larger dendrimers **G2** and **G3**. Therefore, several decays with different lifetimes overlap in the curves of the dendrimers and furthermore amplitudes might compensate modified lifetimes in multiexponential fits and vis-à-vis.[8]

Thus, the obtained lifetimes are intrinsically inaccurate and it seems more effective to discuss anisotropy values of **M** and **G1**–**G3** after discrete delay times (2 ps, 10 ps and 100 ps) after time zero and not the specific lifetimes. After t = 2 ps the anisotropy for the dendrimers is much lower than for **M** (r = 0.36) while the larger the dendrimer is, the lower is the anisotropy after 2 ps (r = 0.25 for **G1** and r = 0.22 for **G3**). This drop-off of anisotropy values between **M** and **G1**–**G3** can be explained by energy migration from on excited TAA-triazole-TAA branch to the next in **G1** (and a similar energy transfer process in **G2** and **G3**). But for a complete two-dimensional depolarisation the expected anisotropy value is 0.1 and this is obviously not the case for **G1** (and also not for **G2** and **G3**).

Therefore, it can be supposed that after the energy is transferred from the initially excited chromophore branch to the next, the excitation is localised within 2 ps and this avoids further fast energy transfer. As seen in the preceding section, solvent relaxation in **M** also takes place in 2 ps and thus the excitation localisation in **G1** should also be solvent relaxation correlated. The anisotropy values after 2 ps of **G2** (r = 0.25) and **G3** (r = 0.22) are comparable to the one of **G1**. Consequently, similar energy transfer and relaxation processes might proceed in the larger dendrimers, in which the terminal chromophores are excited preferably due to their larger number.
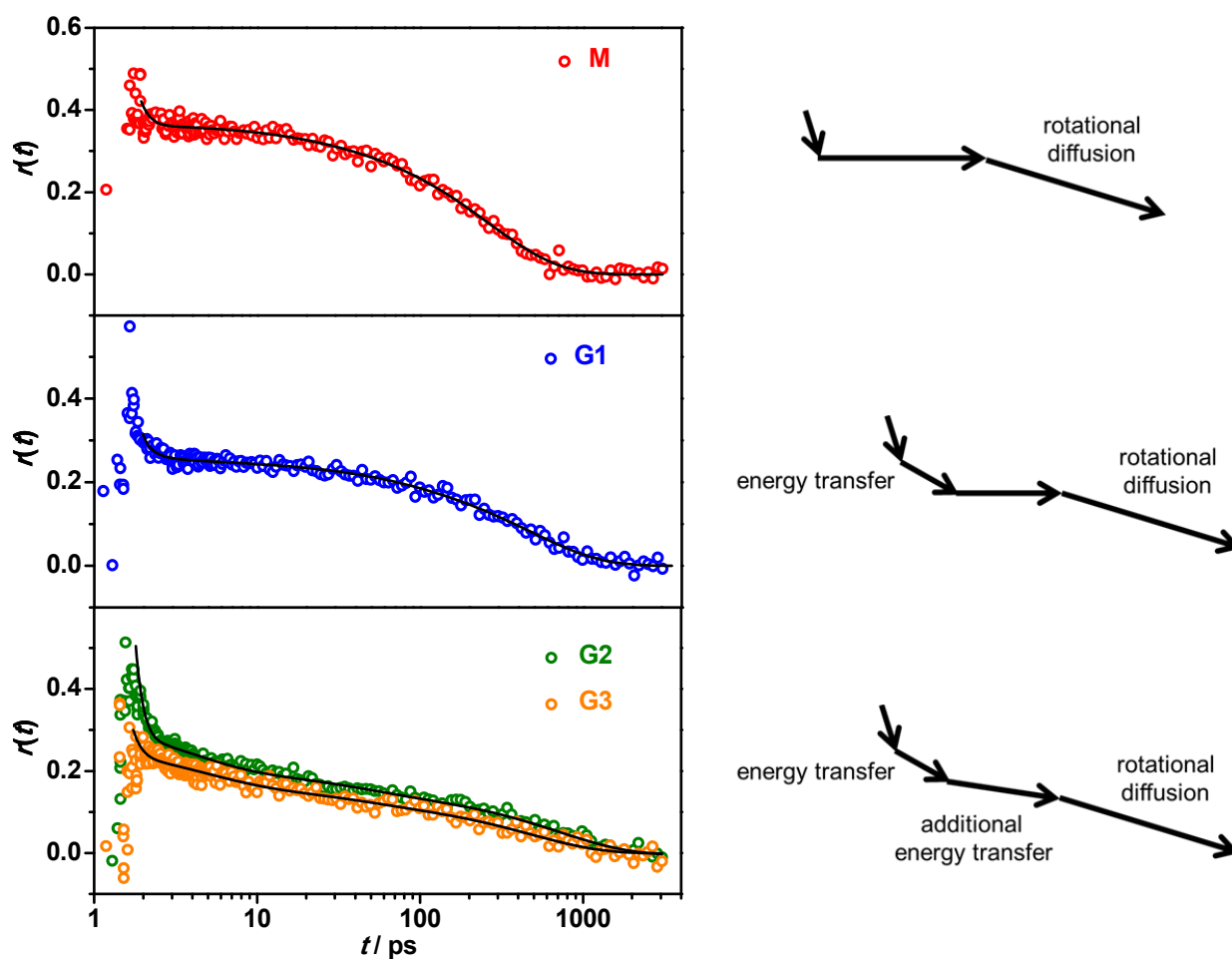
Figure 27: Left: Experimental anisotropy $R(t)$ (circles) and fitted anisotropy $r(t)$ (black lines) of M and G1–G3 in DCM. Note: $r(t)$ is calculated from the global deconvolution fits of $I_\perp(t)$ and $I_\parallel(t)$ and not a fit of the experimental anisotropy. The beginning of the fits represents time zero since it is not identical for all measurements. Right: Illustration of the processes altering the decay curve progression.

After $t = 10$ ps the anisotropy of **G1** decays only insignificantly ($r(2$ ps$) = 0.25 \rightarrow r(10$ ps$) = 0.24$) but the anisotropies of **G2** and **G3** decline by 0.05 and this indicates an additional energy transfer only possible in the larger dendrimers. Finally, the decrease between $t = 10$ and $t = 100$ ps is caused by the rotational diffusion process for all compounds.

Moreover, the solvent dependence of the anisotropy and thereby of the energy transfer properties was investigated by recording anisotropy decays of **G1** in MeCN, PhCN and toluene. At the first glance, the curve progression shows only slight differences between the diverse solvents but the decay in toluene is considerably more shallow (at $t = 10$ ps less than at $t = 100$ ps) in contrast to the other solvents. The obtained lifetimes and amplitudes of the magic angle and fluorescence anisotropy measurements are listed in Table 6.
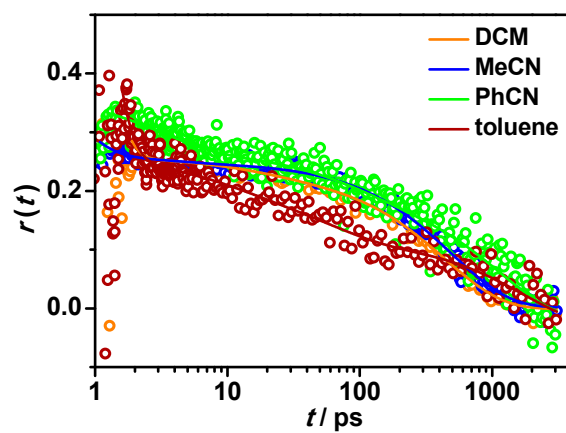
Figure 28: Experimental anisotropy $R(t)$ (circles) and fitted anisotropy $r(t)$ (lines) G1 in different solvents. Note: $r(t)$ is calculated from the global deconvolution fits of $I_\perp(t)$ and $I_\parallel(t)$ and not a fit of the experimental anisotropy. The beginning of the fits represents time zero since it is not identical for all measurements.

Table 6:   **Time Constants τ (in ps) and Amplitudes[a] a obtained from Deconvolution Fits of the Fluorescence Up-conversion Measurements under Magic Angle Conditions (MA) and of the Fluorescence Anisotropies ($r(t)$) of M and G1–G3 in different Solvents.**

		M		G1		G2		G3	
		τ	a	τ	a	τ	a	τ	a
MeCN[b]									
MA	$\tau_1\,(a_1)$			0.23	(-0.97)				
	$\tau_2\,(a_2)$			2.2	(0.41)				
	$\tau_3\,(a_3)$			34	(0.15)				
	$\tau_4\,(a_4)$			4.1 x10^3	(0.44)				
$r(t)$	$\tau_1\,(a_1)$			0.38	(0.024)				
	$\tau_2\,(a_2)$			3.0	(0.011)				
	$\tau_3\,(a_3)$								
	$\tau_4\,(a_4)$			500	(0.25)				
DCM[c]									
MA	$\tau_1\,(a_1)$	0.40	(-0.94)	0.43	(-1.00)	0.39	(-0.98)	0.47	(-0.61)
	$\tau_2\,(a_2)$			4.9	(0.19)	7.1	(0.09)	7.0	(0.12)
	$\tau_3\,(a_3)$	31	(0.075)	65	(0.067)	57	(0.20)	92	(0.24)
	$\tau_4\,(a_4)$	5.0x10^3	(0.93)	5.2x10^3	(0.74)	3.8x10^3	(0.71)	3.7x10^3	(0.64)
$r(t)$	$\tau_1\,(a_1)$	0.13	(0.067)	0.30	(0.030)	0.23	(0.081)	0.22	(0.063)
	$\tau_2\,(a_2)$	2.6	(0.023)			5.4	(0.085)	3.7	(0.065)
	$\tau_3\,(a_3)$			17	(0.025)	61	(0.045)	39	(0.056)
	$\tau_4\,(a_4)$	250	(0.35)	440	(0.23)	760	(0.15)	650	(0.13)
toluene[d]									
MA	$\tau_1\,(a_1)$	0.52	(-0.18)	0.30	(-0.67)				
	$\tau_2\,(a_2)$	6.8	(-0.15)						
	$\tau_3\,(a_3)$			80	(0.093)				
	$\tau_4\,(a_4)$	1.6x10^3	(1.00)	1.8x10^3	(0.91)				
$r(t)$	$\tau_1\,(a_1)$	0.63	(0.031)	0.35	(0.13)				
	$\tau_2\,(a_2)$			9.0	(0.042)				
	$\tau_3\,(a_3)$	19	(0.010)	56	(0.092)				
	$\tau_4\,(a_4)$	380	(0.37)	1.7x10^3	(0.15)				
PhCN[e]									
MA	$\tau_1\,(a_1)$			0.90	(-0.23)				
	$\tau_2\,(a_2)$			20	(0.41)				
	$\tau_3\,(a_3)$			160	(0.24)				
	$\tau_4\,(a_4)$			3.2x10^3	(0.35)				
$r(t)$	$\tau_1\,(a_1)$			3.0	(0.066)				
	$\tau_2\,(a_2)$								
	$\tau_3\,(a_3)$			84	(0.068)				
	$\tau_4\,(a_4)$			1.1x10^3	(0.22)				

[a] Negative amplitudes denote a rise time. [b] Pump at 26300 cm^{-1} (380 nm), fluorescence at 20600 cm^{-1} (485 nm). [c] Pump at 26300 cm^{-1} (380 nm), fluorescence at 20800 cm^{-1} (480 nm). [d] Pump at 26300 cm^{-1} (380 nm), fluorescence at 23500 cm^{-1} (425 nm). [e] Pump at 26300 cm^{-1} (380 nm), fluorescence at 20400 cm^{-1} (490 nm).

3.2.1.7   Energy Transfer in G1–G3[a]

To put the results discussed above into context, an analysis of possible energy transfer mechanisms and their related rates seems reasonable.[3,4,256-259] Typically, the energy transfer mechanism depends on the time scale of local vibrational or solvent relaxation and the time of the actual energy transfer. Of course, these rates in turn depend on the interaction energy in-between chromophores and the interaction energy between chromophores and the solvent.[260] Consequently, the exciton coupling energy V_{dd} between an excited donor branch and an acceptor branch in **G1** can be evaluated by the point-dipole approximation (equation (24); p: 15).

$$V(\tilde{\nu})_{ex} = V(\tilde{\nu})_{dd} = \frac{1}{hc4\pi\varepsilon_0}\frac{\mu_D\mu_A}{r_{DA}{}^3}\kappa \tag{24}$$

where

$\kappa = \cos\theta_{AD} - 3\cos\theta_D \cdot \cos\theta_A$ (= 1.75 for an 120° angle, *cf.* Scheme 2; p: 8), *h* is the *Planck* constant, *c* is the speed of light, ε_0 is the vacuum permittivity, μ_D and μ_A are the transition moments of the donor and acceptor branch, respectively, and r_{DA} is the distance of the transition moments.

Using $\mu_D = \mu_A$ = 4.4 D (as determined for **M** using the *Strickler-Berg* equation (55), p: 33) and r_{AD} = 11 x 10^{-10} m (estimated from a MM2 modelling of **G1**)[b] taking the C(H) atom in the triazoles as the centre of the transition moment, equation (24) yields an exciton coupling energy of 128 cm^{-1}. This value is comparable to the emission energy difference between **G1** and **M** (200 cm^{-1}) and thus the given approximation seems reasonable.

While the foregoing estimate of electronic coupling corresponds to the excited state after solvent relaxation, time dependent DFT calculations of the electronic interaction at B3LYP/6-31G* level of theory with the COSMO solvation model for introducing solvent effects of DCM cover the C_3-symmetric *Franck-Condon* state in **G1**. Such computations lead to the energies of the states already mentioned in the discussion of the steady-state absorption spectra. These are two degenerate *E*-symmetric states at 25960 cm^{-1} and one energetic higher lying state with *A*-symmetry (excitation forbidden) at 27187 cm^{-1} with singlet configuration and two degenerate *E*-symmetric states at 21875 cm^{-1} and one energetically higher lying state with *A*-symmetry (excitation forbidden) at 22387 cm^{-1} with triplet configuration. From these state energies the exciton coupling energies V_{DFT}[18,19,222] can be evaluated by equation (62).

---

[a] Adapted or reproduced (or reproduced in parts) from *Solvent Controlled Energy Transfer Processes in Triarylamine-Triazole Based Dendrimers*, Zieschang, F.; Schmiedel, A.; Holzapfel, M.; Ansorg, K.; Engels, B.; Lambert, C. *J. Phys. Chem. C* **2013**, *117*, 19816-19831. Copyright 2013 American Chemical Society.
[b] Calculations was performed by means of MM2 in ChemBio3D Ultra 12.0.2, CambridgeSoft **2010**.

$$V_{DFT} = \frac{E_{LUMO+1} - E_{LUMO}}{n} \tag{62}$$

where

E_{LUMO} and E_{LUMO+1} are the energies of the two states and n is the number of coupled states.

Thereby the coupling energy obtained by the singlet state energies (V_{DFT}(singlet) = 409 cm^{-1}) comprises *Coulomb* as well as exchange interactions while the coupling energy obtained from the triplet state energies (V_{DFT}(triplet) = 171 cm^{-1}) includes only exchange interactions.[260-262] Obviously, for systems with close proximity between the chromophores as in **G1**, the delocalisation by direct orbital overlap must be taken into account. In the point-dipole approximation used above, the delocalisation is not included and the estimated interaction of 128 cm^{-1} is clearly too low.

The ratio of the interaction energy V_{dd} and the homogenous linewidth Γ gives the crossover between coherent and incoherent energy transfer.[263,264] The homogenous linewidth is not available but the emission spectrum of **G1** in cyclohexane gives a total linewidth of 3000 cm^{-1}. A fit of this spectrum according to *Bixon-Jortner* theory[65,66,265-267] leads to $\tilde{\nu}_v$ = 1320 cm^{-1} for the averaged vibrational energy, λ_v = 1160 cm^{-1} for the inner reorganisation energy and λ_o = 940 cm^{-1} for the solvent reorganisation energy. From the solvent reorganisation energy the homogenous linewidth of **G1** can be calculated by equation (63) leading to 500 cm^{-1} as the upper limit.[268,269] Because this linewidth seems to be on the same order of magnitude as the interaction energy, the energy transfer in the *Franck-Condon* state of **G1** is expected to be in the intermediate coupling regime.

$$\Gamma = \frac{\sqrt{4\pi\lambda_o k_B T}}{\pi} \tag{63}$$

where

k_B is the *Boltzmann* constant and T is the temperature.

Although the electronic coupling and the homogeneous linewidth are rather similar, coherent excitation of two electronic states, by name the two *E* states and the *A* state of **G1**, might be the primary photophysical process. For coherent excitation of two chromophores *Knox* and *Gülen*[31,32] reported three requirements:

1: both transition moments should not be oriented parallel

2: to assure an equal population of both states at a particular temperature, they should be energetically close

3: the excitation pulse should be energetically broad enough to excite the two states

With supposed C_3 symmetry for **G1** the transition moments of the two *E* states are oriented perpendicular and thus solvent fluctuations promote the energy transfer between these transition moments.[270] According to that, **G1** might be coherently excited and after excitation fast dephasing, affected by solvent movement, takes place.[271] Although the anisotropy measurements of **G1** show no anisotropy value higher than 0.4, which would indicate coherent excitation,[31,34] this will be taken into consideration in the analysis of possible energy transfer mechanisms.

After photoexcitation and rapid dephasing only one individual chromophore is excited and the starting energy transfer is an incoherent hopping process. This means, before each individual energy transfer the excited donor branch gets into its molecular vibrational relaxed state (not necessarily solvent relaxed state). The *Förster* theory of resonance energy transfer serves to estimate the rate constant k_{FT} for such incoherent energy transfer by equation (18) and (19) (repeated here from the introduction, p: 11) and by the application of readily available spectroscopic data.[12,13]

$$k_{FT} = \frac{9000 \ln(10) \phi_D \kappa^2}{128 \pi^5 N_A n^4 \tau_D r_{DA}^6} \cdot J \tag{18}$$

$$\text{with } J = \int \bar{I}_{fl,D}(\widetilde{\nu}) \varepsilon_A(\widetilde{\nu}) \frac{d\widetilde{\nu}}{\widetilde{\nu}^4} \tag{19}$$

where

ϕ_D is the fluorescence quantum yield of the donor chromophore, κ is an orientation factor (*cf.* Scheme 2, p: 8), *J* is the overlap integral of donor emission and the acceptors absorption, $\bar{I}_{fl,D}(\widetilde{\nu})$ is the area normalised fluorescence spectrum of the donor, $\varepsilon_A(\widetilde{\nu})$ is the absorption spectrum of the acceptor (divided by the number of "spectroscopic units"), *n* is the refractive index of the solvent, N_A is *Avogadro´s* constant, τ_D is the fluorescence lifetime of the donor and r_{DA} is the distance between donor and acceptor.

The used interaction V_{dd} in the *Förster* theory is based on the coupling of transition moments (see equation (24), p: 15 and 125) and thus on the point-dipole approximation, which is only true for small chromophores with large interchromophore distances. In **G1** the size of a spectroscopic unit, given by the *N-N* amine distance, is 13.3 Å, which is obviously smaller than the wavelength of the absorbed photons. The interchromophore distance in **G1** is obviously too small as indicated by MM3 force field calculations.[a] These computations yield distances between spectroscopic units, as the distance between the C(H) atoms of the triazole moieties, of 11 – 12 Å in **G1** (depending on the conformer), 10 – 35 Å in **G2** and between ca. 10 and 57 Å in **G3**.

To obtain more reliable information about the structure of **G3**, molecular dynamic (MD) simulations were performed in cooperation with the group of Prof. *Engels*.[42] In the initial structure of **G3**, shown in Figure 29, no close contact between the chromophore branches can be observed but during MD the energy reaches a local minimum and the related structure of **G3** shows intramolecular interactions.
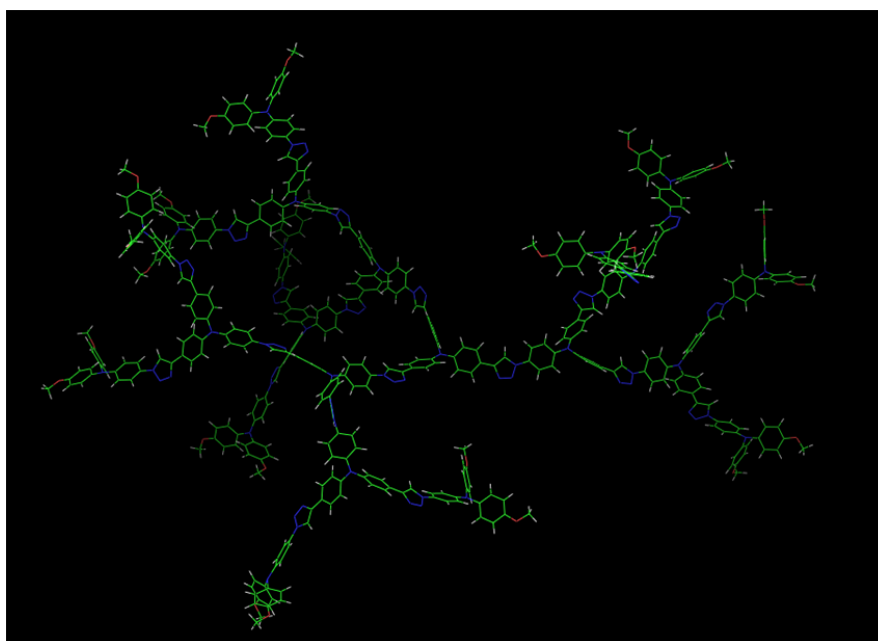
Figure 29:   **Initial structure of G3 for MD build up by PyMOLE[272] and optimised using PM6DH2[273,274].b**

As apparent from Figure 30, the chromophores in the outer sphere in **G3** are able to aggregate with interchromophore distances between the terminal TAA and the triazole of another branch being actually shorter than in **G1** or **G2**. A *Mulliken* charge analysis indicates that this clustering is mainly caused by electrostatic interactions and this alters the supposed globular shape into a highly

---

[a] Calculations was performed by means of MM2 in ChemBio3D Ultra 12.0.2, CambridgeSoft **2010**.
[b] Adapted or reproduced (or reproduced in parts) from *Solvent Controlled Energy Transfer Processes in Triarylamine-Triazole Based Dendrimers*, Zieschang, F.; Schmiedel, A.; Holzapfel, M.; Ansorg, K.; Engels, B.; Lambert, C. *J. Phys. Chem. C* **2013**, *117*, 19816-19831. Copyright 2013 American Chemical Society.

asymmetric structure. For more detailed information see Supporting Information of the related publication.[42]
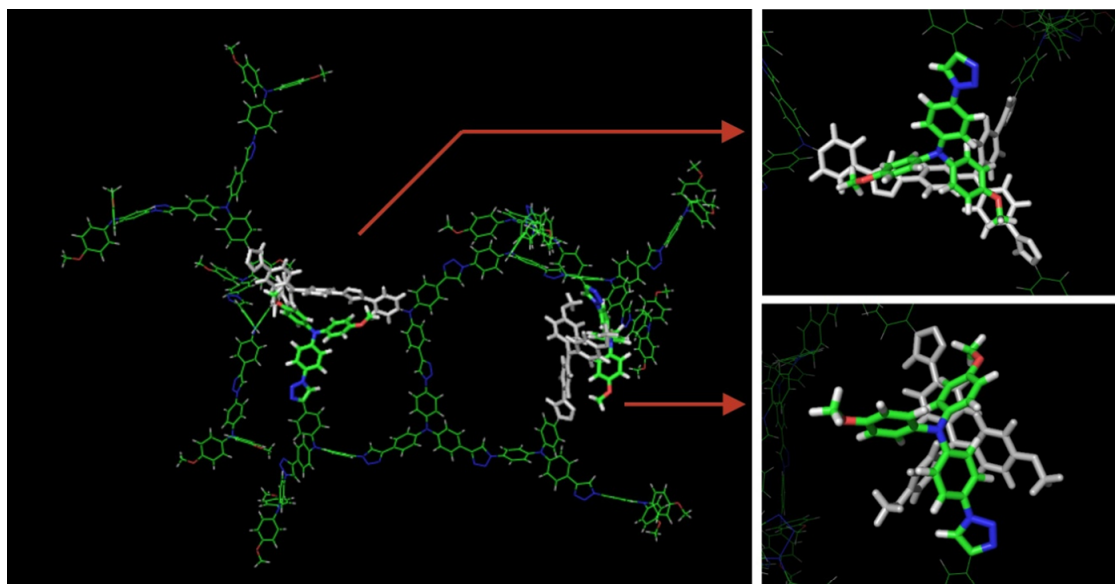
Figure 30:   **Left: Optimised structure of G3. Right: Details of the intermolecular interactions. Upper right: End-centre interaction. Bottom right: End-end interaction. Obtained by MD simulation using the PM6-DH2 method[273,274] employing the MOZYME[275] approximation.[a]**

To calculate the rate constants for an incoherent energy transfer by equation (18) (p: 11 and 127) the orientation factor κ = 1.75 (for a 120° angle as in **G1**) was also taken for **G2** and **G3**. Although this is obviously not accurate, it seems sufficient since the impact of κ is rather small (κ = 2/3 for a random distribution of orientations) and the obtained rates should only be compared by their magnitude. Taking n = 1.4242 (DCM), ϕ_D = 0.64 (of **M**), τ_D = 5.0 ns and J = 1.24 x 10^{-17} dm^3 mol^{-1} cm^3, equation (18) yields

$1/k_{FT}$ = 1.7 ns for 11 Å (the shortest distance in **G1**),

$1/k_{FT}$ = 1.8 μs for 35 Å (the widest distance in **G2**),

$1/k_{FT}$ = 1.0 ns for 10 Å (the shortest distance in **G3**) and

$1/k_{FT}$ = 33 μs for 57 Å (the widest distance in **G3**).

The rates estimated by *Förster* theory are related to only one energy transfer from one excited donor branch to one acceptor branch, but in order to compare the calculated with the experimental data, the time dependent relative population of the different braches has to be taken into account. In **G1**, as a system with threefold rotational symmetry, there are three different branches i = 1 – 3,

---

whose time dependent relative population $P_i(t)$ is influenced by the rate of energy transfer between the branches k_{EN} and the fluorescence lifetime τ_f. In this consideration the rate of energy transfer between all branches is identical and the energy transfer is much faster than the rotational diffusion process, as illustrated in Scheme 49. The incoherent energy hopping between the branches can be described by a set of *Pauli* master differential equations (64). If branch 1 is primarily excited the *Pauli* equations give the solution equations (65).[276-279]
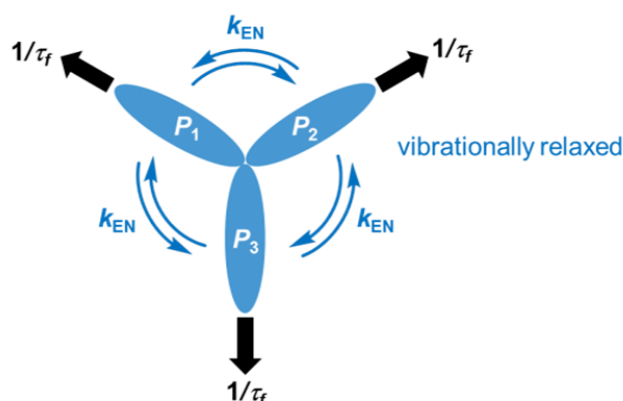
Scheme 49:   **Energy transfer pathways in G1. k_{EN} denotes the energy transfer rate in the vibrationally relaxed state, τ_f is the excited state lifetime and P_1–P_3 are the relative populations of a particular vibrationally relaxed branch.**

$$\frac{dP_1(t)}{dt} = -\frac{1}{\tau_f + 2k_{EN}}P_1 + k_{EN}P_2 + k_{EN}P_3$$

$$\frac{dP_2(t)}{dt} = -\frac{1}{\tau_f + 2k_{EN}}P_2 + k_{EN}P_1 + k_{EN}P_3 \tag{64}$$

$$\frac{dP_3(t)}{dt} = -\frac{1}{\tau_f + 2k_{EN}}P_3 + k_{EN}P_2 + k_{EN}P_1$$

$$P_1(t) = \frac{e^{-\frac{t}{\tau_f}}P_1(0)}{3}(1 + 2e^{-3k_{EN}t})$$

$$P_{2,3}(t) = \frac{e^{-\frac{t}{\tau_f}}P_1(0)}{3}(1 - e^{-3k_{EN}t}) \tag{65}$$

where

k_{EN} denotes the rate constant for energy transfer, τ_f is the excited state lifetime, t is the time and $P_1(t) - P_3(t)$ are the time dependent relative populations of a particular branch.

Applying the law of addition, the total time dependent anisotropy $r(t)$ (depolarisation by rotational diffusion is excluded) is the quotient of the sum of all independent spectroscopic unit contributions with r_1 = 0.4 (0°) and $r_{2,3}$ = -0.05 (120°) weighted by their time dependent relative populations $P_i(t)$ and the total population of all excited states, see equation (66).

$$r(t) = \frac{\sum\limits_{i=1}^{3} r_i P_i(t)}{\sum\limits_{i=1}^{3} P_i(t)} \qquad (66)$$

With the help of equation (65) this gives the simple expression equation (67) for the time-dependent anisotropy $r(t)$ (contributions due to rotational diffusion are neglected).

$$r(t) = 0.1 + 0.3e^{-3k_{EN}t} \qquad (67)$$

In the reasonable consideration that $1/\tau_f \ll k_{EN}$ the energy transfer between all three spectroscopic units leads to a monoexponential anisotropy decay with a time constant k_{dep} = 3 x k_{EN}. Hence, to match the experimental rates for depolarisation, the calculated rates based on *Förster* theory ($k_{EN} = k_{FT}$) have to be taken three times. The fast anisotropy decay in the very first 2 ps after excitation is not even explained by a calculated rate of $1/(3k_{EN}(\mathbf{G1}))$ = 0.37 ns. The rotational diffusion process can be seen as the limiting factor for anisotropy detection. Since all calculated energy transfer rates are slower than the rotational diffusion process (except of the shortest distance in **G3**) all processes should not be observable in the anisotropy measurement setup used here.

As indicated in section 3.2.1.5, p: 110, solvent relaxation might strongly influence the energy transfer properties in the dendrimers and the above given discussion based on the *Förster* theory refers to solvent relaxed states. The overlap integral between the emission of the donor and the absorption of the acceptor is an important factor for the energy transfer rate constant according to *Förster*. This integral gets smaller with the dynamic *Stokes* shift (see Figure 22, p: 114) and thus the *Franck-Condon* factor of fluorescence and absorption processes at a specific common energy gets also smaller, leading to a decrease of the energy transfer rate (see Figure 31). In the solvent relaxed state **G1** shows only an insignificant integral overlap of emission and absorption spectra in DCM as seen in the steady-state spectrum (see Figure 17, p: 106).
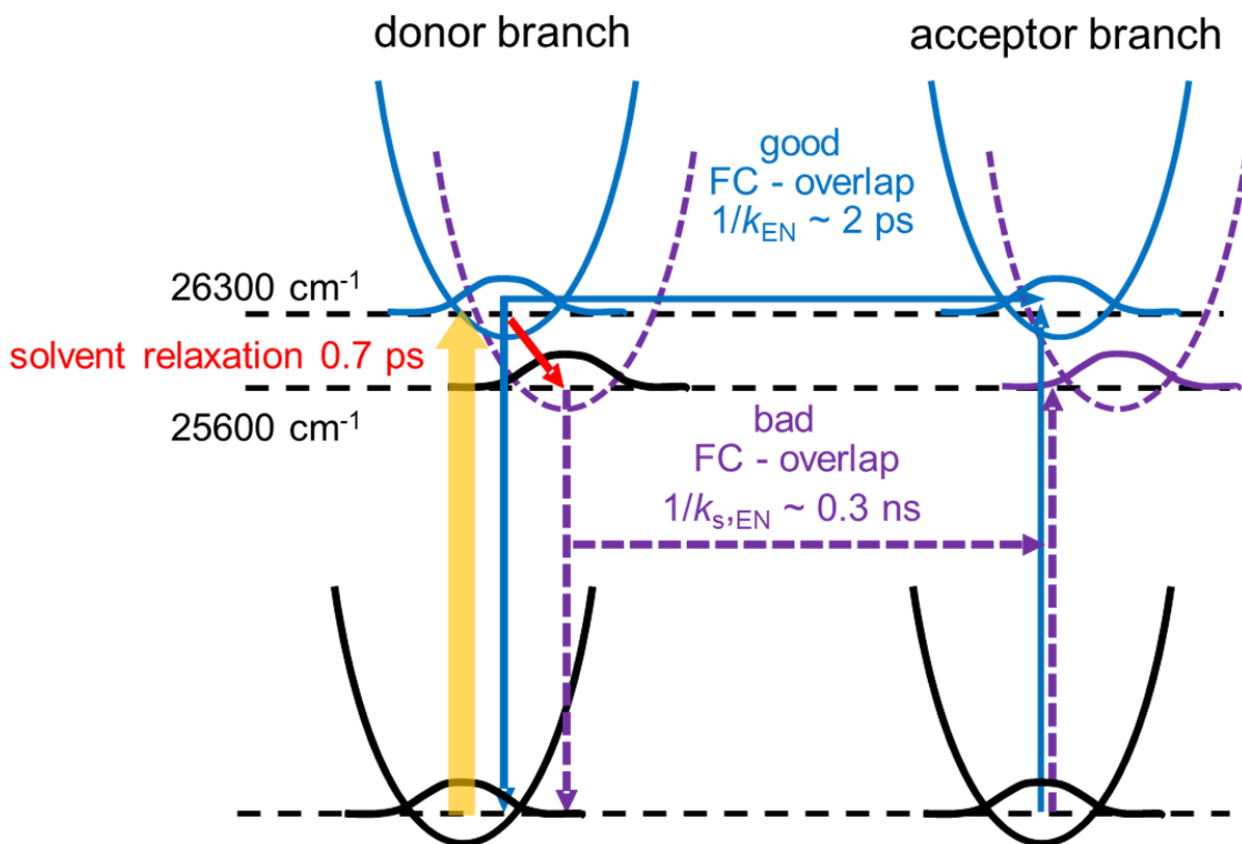
Figure 31:   Potential energy diagram indicating the processes after excitation of G1. The 00-energies were obtained from the intersection of normalised absorption and emission bands in DCM and cyclohexane, respectively. The energy of the solvent relaxed state was estimated from the *Stokes* shift of the $S(t)$ for M. Herein, k_{EN} denotes the energy transfer rate in the vibrationally relaxed state and $k_{s,EN}$ denotes the energy transfer rate in the solvent relaxed state.

This leads to the assumption that energy localisation caused by solvent relaxation is the limiting step for rapid energy transfer. If energy transfer takes place before solvent relaxation proceeds, the overlap integral of absorption and emission at time zero has to be used in equation (19), p: 11 and 127, instead of those of the relaxed system at infinite time. As the time zero spectrum is rather difficult to measure, the steady-state spectrum in cyclohexane serves as an alternative. The overlap integral of this, with the absorption spectrum is obviously larger ($J = 1.9 \times 10^{-15}$ dm^3 mol^{-1} cm^3) than in DCM (see Figure 17, p: 106). With the help of equation (18), p: 11 and 127, this integral leads to $1/k_{FT} = 11$ ps for **G1** and therefore to a rate of $1/k_{dep} = 3.7$ ps, which is certainly in the magnitude of the solvent relaxation in DCM.

However, the estimate by the *Förster* theory given above has some undoubted drawbacks. The interchromophore distance is too short to proper use the point-dipole approximation on which the *Förster* theory is based. Furthermore, the two spectroscopic units in **G1** are connected by one shared TAA and therefore the used interchromophore distance might be incorrect. The shared TAA causes some orbital overlap and this increases the possibility for *Dexter* type through-bond energy transfer. In addition to this, for short interchromophore distances solvent screening by $1/n^4$ is improper.[4,257] Furthermore, the disordered local environment of the three branches results in an inhomogeneous broadening of the absorption and emission spectra and thus the analysed overlap integral corresponds to an average ensemble value quantity and not to the real *Förster* overlap.[4] In other words, in the case of **G1**–**G3** the calculated rates based on *Förster* theory are to some extent untrustworthy.

Thus, incoherent energy transfer before solvent relaxation has to be included in the model of Scheme 49, p: 130, by introducing the rate constant for solvent relaxation (k_s) and the rate constants for energy transfer between vibrational relaxed chromophores before (k_{EN}) and after solvent relaxation ($k_{s,EN}$). The new model for **G1** together with coherent excitation and instantaneous dephasing is shown in Scheme 50.
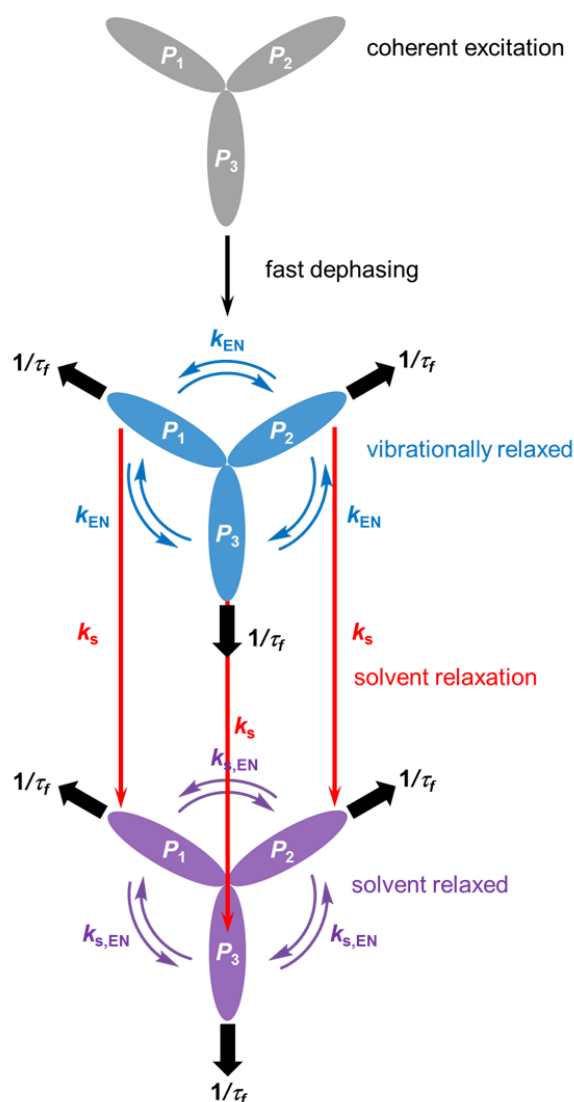
Scheme 50: Energy transfer pathways in G1 taking solvent relaxation into account. k_{EN} denotes the energy transfer rate in the vibrationally relaxed state, k_s the rate constant for solvent relaxation, $k_{s,EN}$ the energy transfer rate in the solvent relaxed state and τ_f is the excited state lifetime. P_1–P_3 are the relative populations of a particular branch. The colours are connected to the states illustrated in Figure 31, p: 132.

The kinetic model given in in Scheme 50 was applied to the deconvoluted anisotropy decays (Figure 28, p: 123) of **G1** in all probed solvents for the first 10 ps with the help of the TENUA[280] program. As mentioned above, coherent excitation might lead to initial anisotropies up to 0.7. In the TENUA-fit the coherent excitation was ignored and thus all decays start with the theoretical value of $r = 0.4$ at time zero. The fits (apparently biexponential) yield k_{EN}, k_s and $k_{s,EN}$, whose inverse values, together with some related data, are given in Table 7. According to these simulations, the initial rapid energy transfer is roughly described by 3 x k_{ET}, while the slow decay is given by $k_{s,EN}$. The amplitude of this slow decay (r ~ 2.5) appears very sensitive to the ratio of the rate constant of the

energy transfer before solvent relaxation and the rate of solvent relaxation itself ($k_{EN}/k_s \sim 1/3$). In addition to this, the data proofs that if $1/k_s \gg 1/k_{EN}$, the two-dimensional depolarisation (theoretical value of $r = 0.1$) is reached with $k_{dep} = 3 \times k_{EN}$. The fact that solvation can compete with energy transfer is certainly one of the important conclusions of analysis shown above. This circumstance results in anisotropy values in an intermediate time interval between the theoretical initial $r = 0.4$ and the two-dimensional depolarisation anisotropy of 0.1.

Table 7:   **Inverse Rate Constants Applying the Kinetic Model of Scheme 50 and Solvent Relaxation Times Reported by *Maroncelli et al*. in their Form to Describe the Short (τ_0), the Average ($\tau_{1/e}$) and Long ($<\tau>$) Solvation Components.**[244,281]

	$1/k_{EN}$ /ps	$1/k_s$ /ps	$1/k_{s,EN}$ /ps	τ_0 /ps	$\tau_{1/e}$ /ps	$<\tau>$ /ps	J /dm^3 mol^{-1} cm^3
MeCN	2.6	0.81	380	0.12	0.15	0.26	
DCM	2.0	0.65	260	0.25	0.38	0.56	1.2×10^{-17}
toluene	2.3	0.81	86	0.37	1.35	2.72	3.2×10^{-16}
PhCN	21	5.9	590	0.85	3.2	5.1	

Consequently, a change of the solvent is expected to have a great impact on the energy transfer dynamics of **G1**–**G2**. As mentioned above the overlap integral is an important factor for the rate constant according to *Förster*. In different solvents the rate of energy transfer after solvent relaxation should differ, since the *Stokes* shift is strongly solvent dependent which directly influences J. This is proved by comparing the anisotropy decays of **G1** in DCM and the nonpolar solvent toluene. A fit of the anisotropy curve of **G1** in toluene yields a lifetime of 56 ps, whose amplitude is considerably larger than the amplitudes of comparable lifetime values of either **M** in toluene or **G1** in DCM (see Table 6, p: 124). Hence, this component is provoked by a particular process of **G1** in toluene and not by molecular geometry relaxations as in **M** and **G1**–**G3** in DCM. This can in particular be observed for the anisotropy values after discrete delay times after 10 and 100 ps, see Table 8, p: 137. Applying *Förster* theory on **G1** in toluene ($n = 1.4969$, $\phi_D = 0.49$, $\tau_D = 1.8$ ns and $J = 3.2 \times 10^{-16}$ dm^3 mol^{-1} cm^3) yields $1/k_{EN} = 38$ ps leading to $1/k_{dep} = 13$ ps. Even though this value is clearly too small (ca. factor four) the 56 ps lifetime is supposed to be due to *Förster* transfer between the chromophore branches because, as mentioned above, the pole-dipole approximation is not working accurately here.

Additionally, the solvent influences the depolarisation dynamics by the solvent relaxation time τ_L. In Table 7 the values reported by *Maroncelli et al.*[244,281] are listed in their form to describe the short (τ_0), the average ($\tau_{1/e}$) and long ($<\tau>$) solvation components. The rate constants k_{EN}, k_s and k_{EN} were determined for **G1** in MeCN, PhCN and toluene identically to the ones in DCM (see Table 7).

Thereby, it becomes clear that k_s is qualitatively characterised by ($<\tau>$), which is in good agreement with result reported by *Lochbrunner et al.* for donor-substituted triphenylboranes.[282] The different values of $1/k_{s,EN}$ in DCM and toluene again reveal the strong influence of the overlap integral *J* (see Table 7). The calculated $1/k_{s,EN}$ = 86 ps for toluene can be observed in the experimental anisotropy decay of **G1** (as τ = 56 ps) while the corresponding calculated components of 260 ps in DCM, of 380 ps in MeCN and of 590 ps in PhCN are invisible because these values are obviously in the same time region as the rotational diffusion, which is the limiting factor for the observation of anisotropy processes.

The above developed model for understanding the anisotropy processes of **G1** in several solvents serves now as a basis for a further understanding of the energy transfer properties of the larger dendrimers in DCM. Therefore, the anisotropy values after discrete delay times have to be analysed in more detail (see Table 8). This data show two pronounced drop-offs of anisotropy between *t* = 2 and 10 ps and between *t* = 10 and 100 ps. Especially, the anisotropy differences of 0.06 between 10 and 100 ps are equal for all dendrimers and can be attributed to slow energy hopping as well as to some extent to rotational diffusion.

However, the earlier drop-off of the anisotropy values of the larger dendrimers between *t* = 2 ps and 10 ps may be ascribed to processes related with the stronger branching in **G2** and **G3**. The above mentioned computations reveal that already in **G2** but of course more likely in **G3** two different branches of the periphery may cluster, resulting in shorter interchromphore distances than in **G1**. Due to these close contacts, energy hopping is supposed to be faster in **G2** and **G3** than in **G1** resulting in faster anisotropy decays. Thereby **G2** and **G3** show parallels to conjugated polymers, where interchain hopping is faster than the alternative along a conjugated route (intrachain hopping).[259] In **G3** energy hopping causes an altogether faster anisotropy decrease than in **G1** down to the value for two-dimensional depolarisation of 0.1. In the fluorescence excitation anisotropy measurements in a SOA glass **G3** (as well as **G1** and **G2**) shows anisotropy values of 0.1 over the almost complete range of absorption, which also reveal a basically two-dimensional shape of **G3**.

Table 8:   Fluorescence Anisotropies $r(t)$ of M and G1–G3 at Discrete Delay Times after Time Zero.

	t/ps	M	G1	G2	G3
MeCN	0+2		0.25		
	0+10		0.24		
	0+100		0.20		
DCM	0	0.44	0.29	0.36	0.31
	0+2	0.36	0.25	0.25	0.22
	0+10	0.34	0.24	0.20	0.17
	0+100	0.23	0.18	0.14	0.11
toluene	0+2	0.38	0.24		
	0+10	0.37	0.21		
	0+100	0.28	0.12		
PhCN	0+2		0.30		
	0+10		0.26		
	0+100		0.20		

3.2.1.8   Conclusions – Energy Transfer

In DCM the dendrimers **G1**–**G3** exhibit in the first 2 ps upon excitation a prominent and rapid emission anisotropy decay followed by some residual anisotropy higher than the values for two-dimensional (r = 0.1) or complete depolarisation (r = 0). Investigation of the photophysical processes occurring in the "spectroscopic unit" **M** reveals that solvent relaxation processes also take place in the first 2 ps. The rate constant for incoherent energy migration in the vibrationally relaxed molecule before solvent relaxation commences was determined by the mean of the *Förster* theory and by utilising the emission spectra in cyclohexane as the time-zero spectrum. The resulting values are similar to solvent relaxation, which strongly suggests that incoherent energy hopping takes place shortly after time zero when the system´s vibrational relaxation is mainly completed and solvent relaxation just begins. With proceeding solvent relaxation, the overlap integral between the emission of the donor and the absorption of the acceptor becomes successively smaller (unfavourable *Franck-Condon* overlap) leading to increasingly decelerated energy hopping. When solvent relaxation is terminated, the excitation energy is localised on one individual chromophore branch and energy transfer is remarkably slowed down due to the unfavourable *Franck-Condon* overlap. Since solvent relaxation and energy transfer in the vibrationally relaxed state occur in the same time regime both processes compete and the initial

fast energy transfer does not lead to complete energy distribution over the entire molecule. In the solvent relaxed state slow incoherent energy hopping occurs with a rate constant comparable to rotational diffusion, which is the limiting factor for anisotropy detection. Thus, energy hopping in the solvent relaxed state remains invisible in DCM but can be observed in toluene, where the energy transfer is faster than the rotational diffusion.

Although the presented results do not suggest any *Dexter*-type through-bond energy transfer at $t < 2$ ps, this mechanism cannot be excluded. However, the discussed solvent correlated energy transfer process reasonably explains the rapid energy transfer between the distinct chromophore branches in **G1**–**G3**.

In summary, it is demonstrated that energy transfer can be fast even between identical chromophores (homotransfer), in which a polar excited state leads to a large *Stokes* shift and thus to a small overlap integral between the acceptor absorption and the donor emission, in case where the time zero emission spectrum overlaps significantly with the absorption spectrum. Thus, a strict distinction between energy transfer processes in the *Franck-Condon* state and the solvent relaxed state is crucial.

3.2.1.9 UV/Vis/NIR – Chemical Oxidation[a]

After discussing the optical properties of the neutral compounds **C-M**, **N-M**, **M** and **G1**–**G2** in section 3.2.1.2 to 3.2.1.7, the spectroscopic properties of their cationic species will be elucidated in the following. Therefore, a samples of these compounds in DCM were stepwise oxidised with $SbCl_5$ in DCM and absorption spectra were recorded after each addition of oxidant (Figure 32 - Figure 34).

Figure 32: Evolution of the absorption spectra during chemical oxidation of N-M and C-M by stepwise addition of SbCl₅ in DCM. Early spectra are presented in blue/red, late ones in orange/green colours. The absorption spectra of the neutral compounds are given in black. Further addition of oxidant leaves the spectra unaffected.

The processes occurring during chemical oxidation of **N-M** and **C-M** are similar. With starting oxidation of **N-M** and **C-M** the absorption bands for the neutral TAA at 30300 cm^{-1} (330 nm) (denoted A in Figure 32) vanish and simultaneously the characteristic absorption bands of the TAA radical cation (B and D) at 26500 cm^{-1} (375 nm) and around 13000 cm^{-1} (770 nm) arise.[168,283] In the absorption spectra of **N-M**$^{•+}$ and **C-M**$^{•+}$ band B at 26500 cm^{-1} (375 nm) and 26000 cm^{-1} (385 nm), respectively, might be caused by a SOMO-LUMO transition as illustrated in Scheme 51. Although no exact assignment can be found in the literature to date, the presented attribution is supported by reports on isoelectronic triarylboranes[284] and perchlorotriphenylmethanes[285]. Hence, band D is related to a HOMO-SOMO transition in the TAA radical cation.[168] Remarkably, the extinction coefficient of this band for **C-M**$^{•+}$ (ε = 36300 M^{-1} cm^{-1}) is significantly higher compared to **N-M**$^{•+}$ (ε = 23600 M^{-1} cm^{-1}).

---

[a] Parts of this section have already been published in *Beiträge zur Synthese und Charakterisierung von triarylaminhaltigen Dendrimeren über die Kupfer(I)-katalysierte 1,3-Huisgen-Cycloaddition*, Diploma Thesis of Fabian Zieschang, Würzburg **2009**.

C_3-symmetric C_1-symmetric
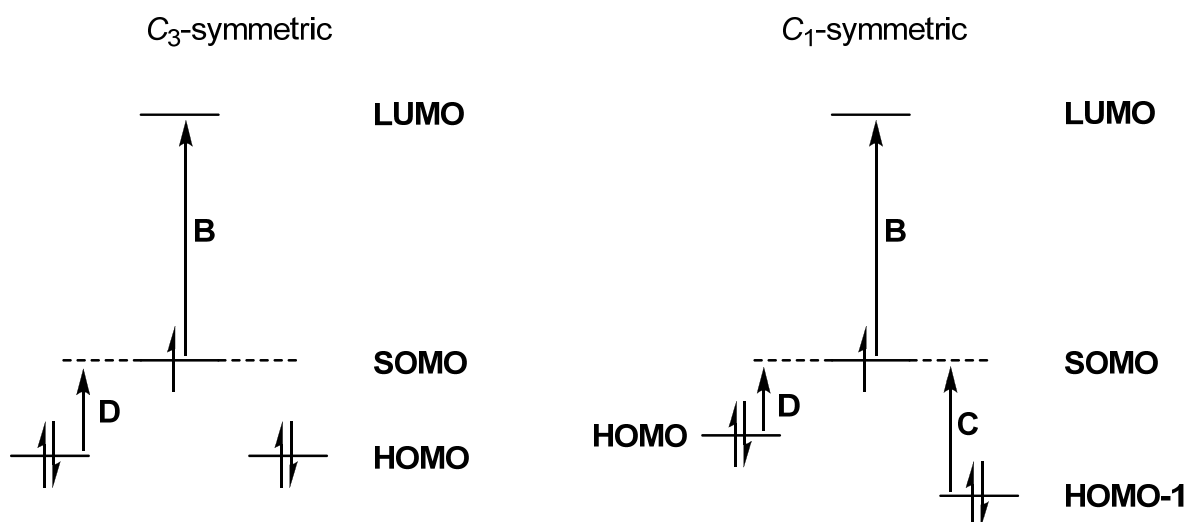
Scheme 51: Configuration diagram for the electronic ground and excited state of a C_3 symmetric (left) and of a symmetry broken (right) TAA radical cation. Energetic relations are arbitrary. Transitions denoted with B-D are related to bands in Figure 32 – Figure 34.[168]

Moreover, the HOMO–SOMO transition band D at ca. 13000 cm^{-1} (770 nm) shows a shoulder on the higher energy side, but the origin remains unclear. According to Scheme 51, the degenerated HOMO levels of a C_3-symmetric TAA radical cation split into a HOMO and a HOMO-1 level by symmetry breaking. The symmetry breaking can be caused by *e.g.* exchanging a substituent, and thus, band C might be related to a HOMO-1-SOMO transition.[168] Band C might also be assigned to a charge transfer from the triazole bridge to the TAA$^{•+}$ centre, however, an accurate assignment is not supported by the available data.[283,286,287] While for **N-M$^{•+}$** this band is considerably broadened with a maximum at 15800 cm^{-1} (630 nm), it is red shifted to ca. 15200 cm^{-1} (660 nm) and more narrow for **C-M$^{•+}$**.
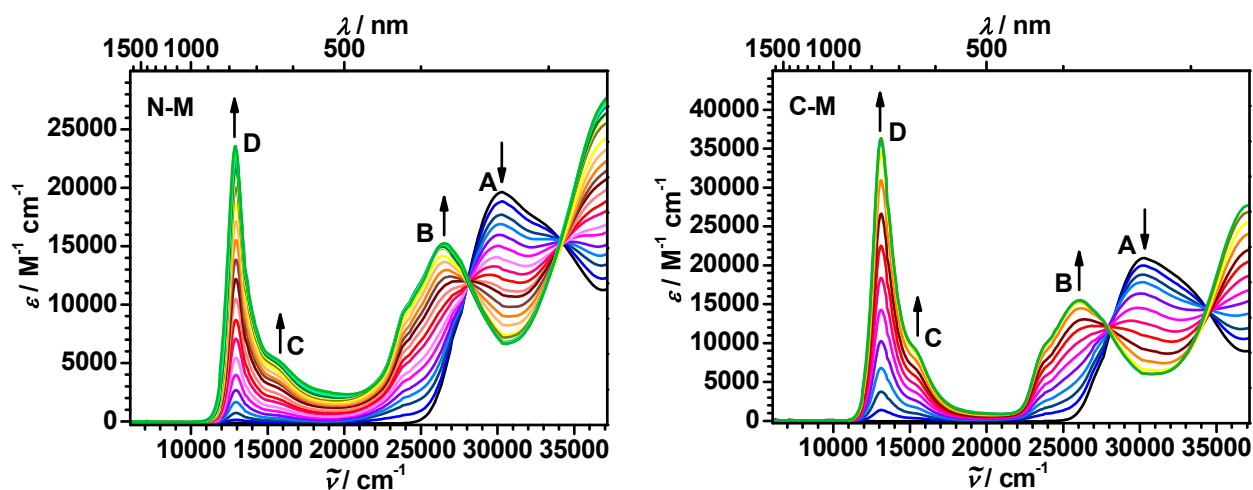
Figure 33: Evolution of the absorption spectra during chemical oxidation of **M** by stepwise addition of SbCl₅ in DCM. Early spectra are presented in blue/red, late ones in orange/green colours. The absorption spectra of the neutral compounds are given in black. Further addition of oxidant leaves the spectra unaffected.

During the oxidation of **M**, the occurring processes are analogous to those observed for **N-M** and **C-M**. The decrease of the neutral TAA bands (A) at 29200 cm⁻¹ (340 nm) and 33000 cm⁻¹ (300 nm) and subsequent rise of the characteristic TAA radical cation bands (B and D) at 13000 cm⁻¹ (770 nm) and 26500 cm⁻¹ (375 nm) and of band C at 15500 cm⁻¹ (650 nm) were observed.[168,283] Band D starts to emerge at 13300 cm⁻¹ (750 nm), but when the band has reached approximately half of its final intensity, the maximum starts to shift until it reaches its final position at 13000 cm⁻¹ (770 nm). This finding is explained by the fact, that **M•⁺** exhibits its band D maximum at 13300 cm⁻¹ (750 nm) and the diradical dication **M²⁽•⁺⁾** at 13000 cm⁻¹ (770 nm). Thus, with increasing concentration of **M²⁽•⁺⁾**, the maximum of band D shifts towards the maximum of the diradical dication at 13000 cm⁻¹ (770 nm).

More interestingly, the weak and very broad absorption band E emerges at 8600 cm⁻¹ (1200 nm), which is absent in the chemical oxidation experiment of **N-M** and **C-M**. This band first increases with progressing oxidation while mainly **M•⁺** is generated and decreases again with continuing oxidation to **M²⁽•⁺⁾**. The mono radical cation **M•⁺** is a mixed valence (MV) compound, which are known to exhibit intervalence charge transfer (IV-CT) bands caused by an optically induced charge transfer from the neutral TAA centre to the TAA radical cation (*cf.* 2.1.2.2, p: 34).[287,288] As long as the addition of an oxidant leads to higher concentrations of **M•⁺** the IV-CT band increases, but with starting oxidation of **M•⁺** to **M²⁽•⁺⁾** the IV-CT band begins to decrease. In **M²⁽•⁺⁾** also the second TAA donor is oxidised and thus optically induced charge transfer is precluded (see Scheme 52, top, p: 143). However, the low intensity of the IV-CT band indicates a weak electronic coupling between the TAA moieties.[289]
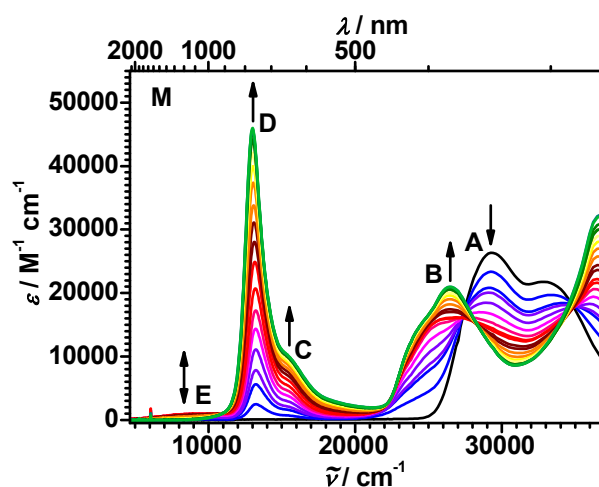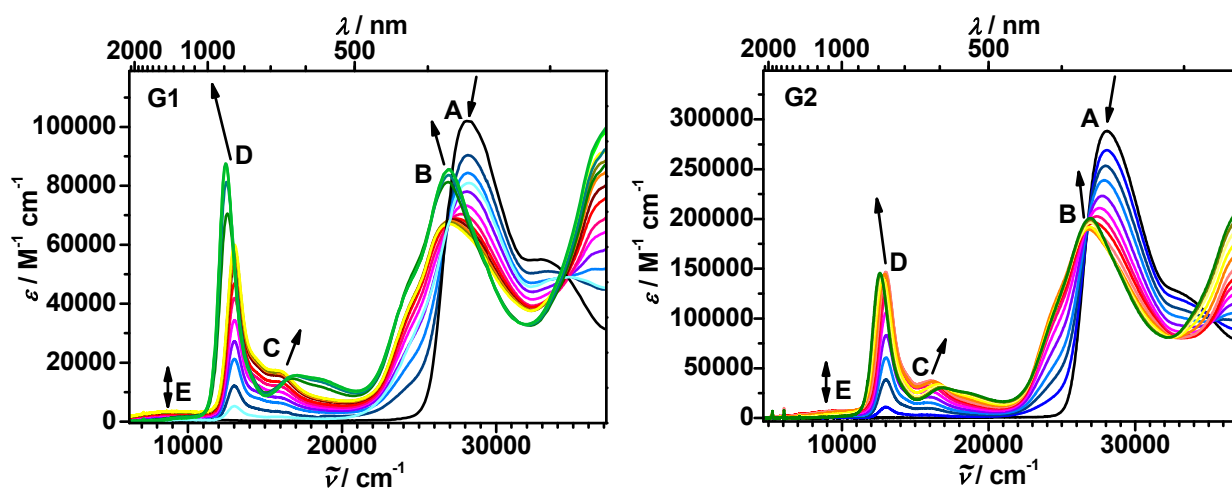
Figure 34: Evolution of the absorption spectra during chemical oxidation of G1 and G2 by stepwise addition of SbCl₅ in DCM. Early spectra are presented in blue/red, late ones in orange/green colours. The absorption spectra of the neutral compounds are given in black. Further addition of oxidant leaves the spectra unaffected.

As expected, during the chemical oxidation experiments of **G1** and **G2** the typical absorptions (A) of the neutral compound at 27800 cm⁻¹ (360 nm) and 33000 cm⁻¹ (300 nm) vanish while the bands of the TAA radical cation (B, D) at ca. 13000 cm⁻¹ (770 nm), the band C at ca. 16200 cm⁻¹ (620 nm) and the IV-CT band (E) at ca. 9300 cm⁻¹ (1080 nm) rise.[168,283]

At the beginning of the oxidation process, band D starts to rise for both compounds with its maximum at 13000 cm⁻¹ (770 nm) and further the small shoulder C on the higher energy side emerges similarly for **G1** and **G2** at 16200 cm⁻¹ (620 nm). When the IV-CT band reaches approximately its highest intensity, the observed band maximum of band D starts to shift to ca. 12500 cm⁻¹ (800 nm). In contrast the maximum of band C shifts towards higher energies (16800 cm⁻¹ (600 nm)) and becomes considerably broader.

As apparent from Scheme 52 (bottom) the IV-CT band of **G1** is a result of three different MV species and even more processes have to be taken into account for the IV-CT band of **G2** (*cf.* Figure 37, p: 147). Therefore, a detailed analysis of the IV-CT band in the chemical oxidation experiment of **G2** was prevented.

Astonishingly, the radical cations of the model compounds feature a band D with obviously higher intensities compared to band A of the related neutral compounds. However with increasing number of TAA moieties in the compounds, the relative intensity of the radical cation band D decreases. Hence, the intensity of band D of the radical cation of **G1** is slightly and of **G2** is significantly smaller than band A of neutral **G1** and **G2**, respectively. This might be explained by the existence of diverse TAAs in **G1** and **G2**, which all contribute with different absorption characteristics to the

observed spectra. This assumption is further supported by the fact that even **N-M•+** and **C-M•+** possess remarkably different intensities for band D although both compounds only differ in the junction *via* the triazole.

However, an incomplete oxidation of **G1** or **G2** may not be responsible for the less intense band D because the IV-CT band of both **G1** and **G2** entirely disappears during the chemical oxidation experiment. This in turn reveals that no IV-CT pathway is present at the end of the chemical oxidation experiment of **G1** and **G2** – all TAAs are oxidised.
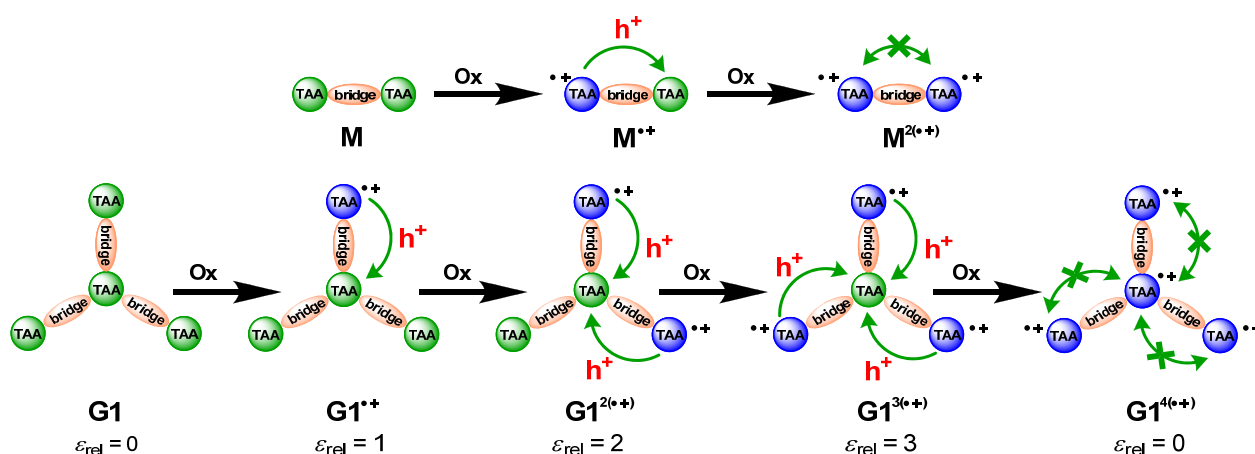
Scheme 52:   Possible electron transfer pathways during the chemical oxidation process of M (top) and G1 (bottom). ε_{rel} is the relative absorbance of the IV-CT band.

3.2.1.10   Electron Transfer in M and G1[a]

Mulliken-Hush analysis of the IV-CT bands of $\mathbf{M}^{\bullet+}$, and $\mathbf{G1}^{x(\bullet+)}$ gives access to the electronic coupling (V_{AB}) according to equation (51), p: 33.[283,288] Therefore, first the transition moment (μ_{trans}) has to be estimated using equation (52), p: 33).

$$V_{AB} = \frac{\mu_{trans}}{\Delta\mu_{12}}\, \widetilde{\nu}_{max} \tag{51}$$

$$\mu_{trans} = \sqrt{\frac{3hc\varepsilon_0 \ln 10}{2000\pi^2 N_A} \cdot \frac{9n}{(n^2+2)^2} \cdot \int \frac{\varepsilon_{CT}}{\widetilde{\nu}}\,d\widetilde{\nu}} \tag{52}$$

where

n is the refractive index of the solvent, $\int \frac{\varepsilon_{CT}}{\widetilde{\nu}}\,d\widetilde{\nu}$ is the integral of the reduced (IV-)CT band, h is the *Planck* constant, N_A is *Avogadro´s* constant, c is the speed of light, ε_0 is the vacuum permittivity, $\Delta\mu_{12}$ is the diabatic dipole moment difference of the ground and excited state and $\widetilde{\nu}_{max}$ is the maximum of the IV-CT band.

For determination of μ_{trans}, the extinction coefficient of the IV-CT band has to be determined but at no time the concentration of $\mathbf{M}^{\bullet+}$ is equal to the starting concentration c_0 of $\mathbf{M}$. Hence, first the comproportionation constant (K) was estimated from the redox potentials given in Table 3, p: 103, applying the *Nernst* equation (68), followed by calculation of the equilibrium concentration c_{eq} using equation (69).[290,291]

$$K = e^{\frac{|\Delta E|F}{RT}} \tag{68}$$

$$c_{eq} = c_0\, \frac{\sqrt{K}}{2+\sqrt{K}} \tag{69}$$

where

ΔE is the redox potential difference, F is the *Faraday* constant, R is the universal gas constant and T is the temperature.

The equilibrium concentration c_{eq} represents the concentration of $\mathbf{M}^{\bullet+}$, at which the IV-CT band exhibits its highest intensity. With c_{eq} and the spectrum presenting the most intense IV-CT band,

---

[a] Parts of this section have already been published in *Beiträge zur Synthese und Charakterisierung von triarylaminhaltigen Dendrimeren über die Kupfer(I)-katalysierte 1,3-Huisgen-Cycloaddition*, Diploma Thesis of Fabian Zieschang, Würzburg 2009.

the extinction coefficient of the IV-CT band of $M^{\bullet+}$ was estimated. The spectrum was reduced and then the bands were fitted by three *Gauss* functions to obtain the reduced spectral integral ($J = \int \frac{\varepsilon_{\text{IV-CT}}}{\tilde{\nu}} d\tilde{\nu}$) of the IV-CT band (see Figure 35).
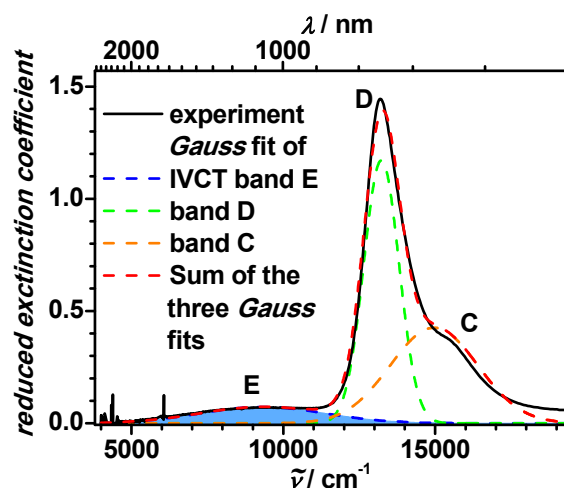
Figure 35: Reduced absorption spectrum of $M^{\bullet+}$ at maximal absorbance in DCM (black, solid) and *Gauss* fits of the IV-CT band (E) (blue, dashed), the HOMO-SOMO transition band (D) (green, dashed) and the band C (orange, dashed). The reduced spectral integral *J* was taken from the blue fit curve.

Using equation (52), p: 33 and p: 144, μ_{trans} was calculated to 2.18 D. With μ_{trans} and equation (51), p: 33 and 144, V_{AB} was determined to be 300 cm^{-1}. Herein, the diabatic dipole moment difference $\Delta\mu_{12}$ was approximated as $e \cdot r$, where the effective electron transfer distance (*r*) was taken as the mean distance ($r \approx 13.2$ Å) [a] between the two chromophore centres obtained by DFT calculations using B3LYP/6-31G*[228] level of theory.[43]

However, the situation is even more complicated for the *Mulliken-Hush* treatment of the IV-CT band of **G1**. As apparent from Scheme 52, p: 143 (bottom), the observed IV-CT band is the superposition of the IV-CT bands of up to three MV-species (**G1$^{\bullet+}$**, **G1$^{2(\bullet+)}$** and **G1$^{3(\bullet+)}$**). Therefore, an accurate determination of V_{AB} requires a deconvolution of the IV-CT band into the contributions of **G1$^{\bullet+}$**, **G1$^{2(\bullet+)}$** and **G1$^{3(\bullet+)}$** in respect of their relative concentrations and relative absorptivities ε_{rel} (*cf.* Figure 36 and Scheme 52, p: 143). Thus, their relative concentrations were calculated using the coupled *Nernst* equation (70) and plotted together with their relative absorbance against the "applied" potential (the "applied" potential represents the concentration of oxidant in the sample solution), see Figure 36.[290]

---

[a] This approximation underestimates the electron transfer distance and thus $\Delta\mu_{12}$, see section 2.1.2.1, p: 33.

$$c_0(\mathbf{G1}^{m(\bullet+)}) = \frac{c_0(\mathbf{G1}) \cdot \displaystyle\prod_{m=1}^{i}\left[\exp\left(\frac{F(E-E_m)}{RT}\right)\right]}{\displaystyle\sum_{j=1}^{m+1}\left\{\prod_{m=1}^{j}\left[\exp\left(\frac{F(E-E_m)}{RT}\right)\right]\right\}} \tag{70}$$

where

E_m is the redox potential for the $\mathbf{X}^{m-1(+)}/\mathbf{X}^{m(+)}$ process, F is the *Faraday* constant, R is the universal gas constant, T is the temperature.
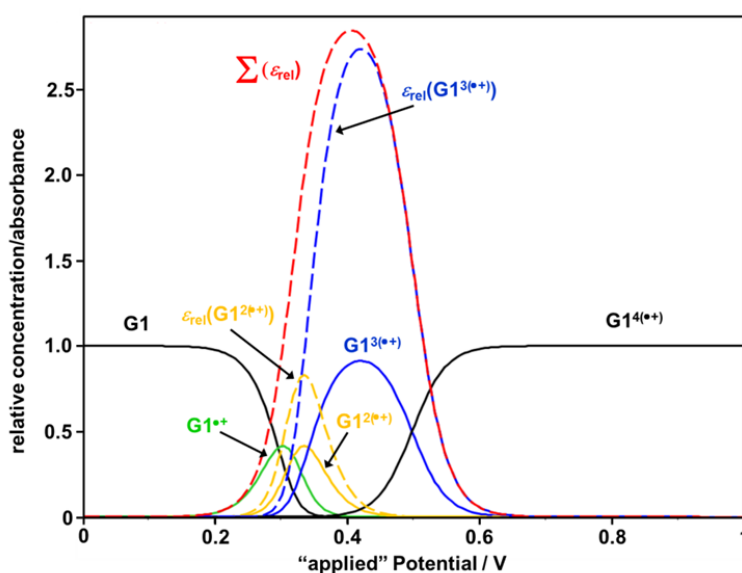
Figure 36: Relative concentrations (solid lines) of G1 (black), G1$^{\bullet+}$ (green), G1$^{2(\bullet+)}$ (yellow), G1$^{3(\bullet+)}$ (blue) and G1$^{4(\bullet+)}$ (black) and the relative absorbance ε_{rel} (dashed lines) of G1$^{\bullet+}$, G1$^{(\bullet+)_2}$, G1$^{(\bullet+)_3}$ and their sum (red) vs "applied" potential. (The relative absorbance of G1$^{\bullet+}$ equals its relative concentration).

Accordingly, the most intense IV-CT band is predominantly caused by $\mathbf{G1}^{3(\bullet+)}$ due to its high molar fraction and high relative absorbance ($\varepsilon_{rel}(\mathbf{G1}^{3(\bullet+)}) = 3$) compared to the other MV species ($\varepsilon_{rel}(\mathbf{G1}^{2(\bullet+)}) = 2$ and $\varepsilon_{rel}(\mathbf{G1}^{\bullet+}) = 1$). Thus, the IV-CT band is most intense when the equilibrium concentration $c_{eq}(\mathbf{G1}^{(\bullet+)_3})$ reaches its maximum and thus further evaluation of the transition moment ($\mu_{trans} = 2.49$) was performed analogously to **M** utilising $c_{eq}(\mathbf{G1}^{3(\bullet+)})$.
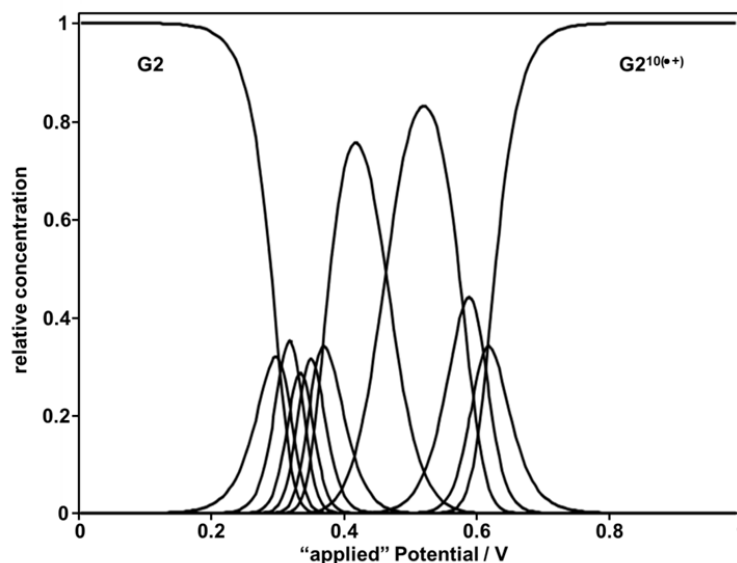
Figure 37: Relative concentrations of the oxidised species of G2 vs "applied" potential.

For the calculation of V_{AB} according to equation (51), p: 33 and p: 144, the centre-to-centre distance r in **G1**$^{3(\bullet+)}$ was supposed to differ only insignificantly from the value for **M**$^{\bullet+}$. However, for systems, which are not linear, the introduction of a symmetry factor $1/\sqrt{s}$ is required, taking the dimension of the system into account.[290-292] Since **G1** possesses a superficial trigonal structure, s for **G1** is 3 and thus the electronic coupling was multiplied by $1/\sqrt{3}$ to yield $V_{AB} = 220$ cm^{-1}. An analysis of the IV-CT band arising during the oxidation of **G2** was not carried out due to a multiple number of possible electron transfer pathways and thus IV-CT species (*cf.* Figure 37). The data obtained by *Mulliken-Hush* analyses are summarised in Table 9.

Table 9: Optical Data for the IV-CT Band of G1$^{3(\bullet+)}$ and M$^{\bullet+}$.

	$\widetilde{\nu}_{max}$ / cm^{-1}	μ_{trans} / D	$\varepsilon_{IV\text{-}CT}$ / M^{-1}cm^{-1}	V_{AB} / cm^{-1}
M	8600	2.18	900	300
G1	9300	2.49	2240	220

3.2.1.11   Conclusions – Electron Transfer

The obtained values for the electronic coupling in **M** and **G1** are in the same order of magnitude. While in **M** the electron is transferred from a TAA linked *via* the triazole nitrogen to a TAA linked *via* the triazole carbon, the electron transfer direction in **G1** is opposite. This might be the reason for the somewhat different V_{AB} for **M** and **G1**. This assumption is additionally supported by previously conducted studies that showed that the linkage towards the triazole strongly influences the electron transfer properties.[154,293]

Although triazoles have been of eminent interest as suitable bridges for electron transfer studies in recent years, their role as electron transfer mediator remains unclear.[154,159,219,293-296] The results both, experimental and theoretical studies, are diverse and controversial. Thereby, triazoles were characterised as electron acceptors[159,297] as well as electron donors[219]. This finding might be reasonably explained by the ambivalent behaviour of the triazoles depending on the connection mode as found in the CV experiments. Triazoles are further described as having "neither electron-donating nor electron-withdrawing character"[295]. Furthermore, for some authors triazoles feature excellent electronic communication between the electron donor and the electron acceptor, which results in rapid and efficient electron transfer,[154] while other investigations led to the opposite conclusion.[298]

However, the statements found in literature are not results of systematic studies. For example, the asymmetric behaviour of triazoles concerning electron transfer was explained by the distinction between oxidative and reductive electron transfer,[296] by the diverging influence of the triazole linkage mode on the HOMO-LUMO gap[154] and by differences in the dimension of torsional angles with neighbouring phenyl rings on both sides of the triazole[295].

Hence, the reason for this diversity of interpretations might be on one hand the very delicate response of the triazole properties on *e.g.* substitution modifications. On the other hand, the generalisation of findings, obtained by sometimes very specialised studies, may lead to overrated conclusions. For example: The donor character of triazoles was concluded by changes of the coumarin emission provoked by a triazole introduction.[219] In contrast, transient absorption spectroscopy studies, where charge separation or recombination processes were monitored, served as the fundament of several statements concerning the electronic coupling of triazoles[154].

This reflection out previously conducted studies does not intend to rather question the reported results, but illustrates the issue of gaining reliable statements. Thus, the properties concerning triazoles found in this thesis are not to be understood as general but compound specific and no classification into "good" or "bad" electron transfer mediators will be given.

In order to assess the electronic couplings obtained by *Mulliken-Hush* analyses of the IV-CT bands of **M** (and **G1**), couplings will be compared to those of related MV compounds with diverse bridging units (see Chart 12).
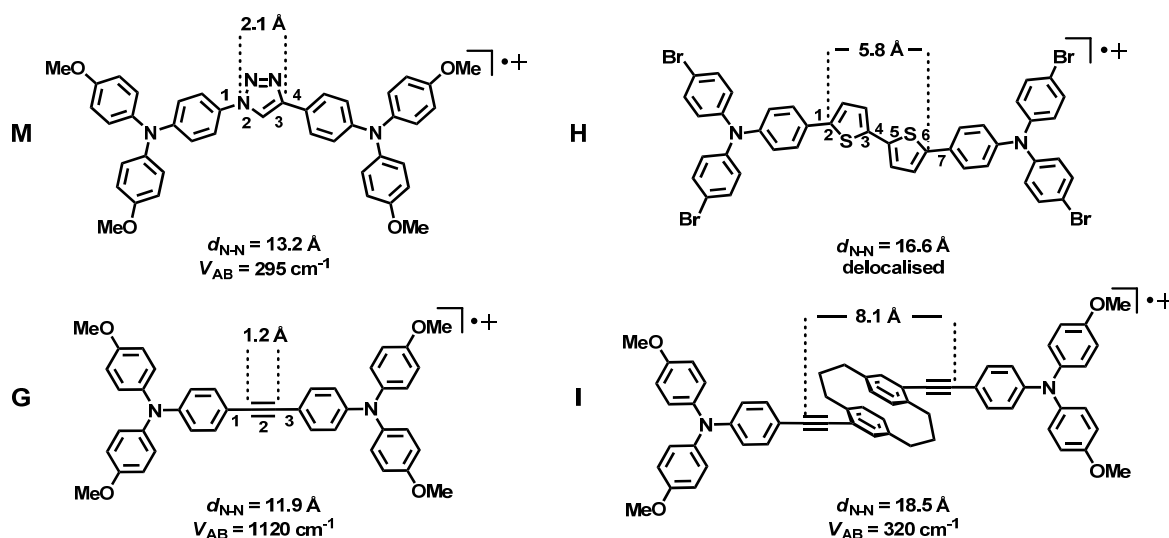
Chart 12: Structure, electronic coupling V_{AB}, *N-N* distance d_{N-N} and dimension of the bridging unit of M and of the compounds G[50], H[299] and I[288].

Bis(triarylamine) radical cations with different bridging units are one of the most intensive studied MV compounds to date.[43] In the following a selection of compounds with bridges that show either structural parallels or a similar electronic coupling compared to **M** is presented. The *N-N* distance, the number of bonds between the TAAs and the size of the bridge were considered as relevant factors to review the electronic communication between the chromophores.

The data presented in Chart 1 reveal that the triazole bridge in **M** is significantly larger and the electrons have to travel over more bonds and over a longer distance compared to the tolane bridge in compound **G**. Consequently, the significantly larger electronic coupling in **G** (V_{AB} = 1120 cm^{-1}) seems reasonable but even the clearly longer 2,2′-bithiophene bridge in **H** allows a strong electronic communication between the TAAs.[50] In fact, the positive charge in **H** is completely delocalised over the entire molecule.[299] Thus, the electronic coupling over its π-system is considerably small although, the triazole is a five membered aromatic ring system comparable to thiophene. The orbital interaction between the TAAs and the triazole is disrupted by the large twist angle between the triazole and the phenylen group of ca. 30 – 40°.[295] This might be one reason why **M** exhibits a relatively small electronic coupling comparable to the value found for **I**, where the two TAAs are connected by a [3,3]-paracyclophane moiety. Therein, the electron transfer takes place through-space and not through-bonds as in **M**, **G** and **H**.[288,300]

In conclusion, the use of triazole as bridging units leads to a considerably reduced coupling between the adjacent chromophores, which is remarkable for such a small aromatic heterocycle. Thus, the redox potentials of the distinct TAAs in **C-M**, **N-M**, **M** and **G1**–**G3** are essentially determined by the attached substituents. Triazoles connected *via* the carbon act as an EDG while nitrogen-linked triazoles act as an EWG.[159,219,220] However, the triazole still possesses sufficient electronic coupling to allow for an effective electron transfer from one chromophore to the other.

3.2.2 Spiro dendrimers

3.2.2.1 Cyclic Voltammetry

The redox potentials of **spiro-G1** and **spiro-G2** were determined by CV (see Figure 38 and Table 10). Measurements were performed in DCM solution under argon atmosphere with TBAHFP (~ 0.2 M) as supporting electrolyte and the obtained values were referenced against the Fc/Fc$^+$ redox couple.
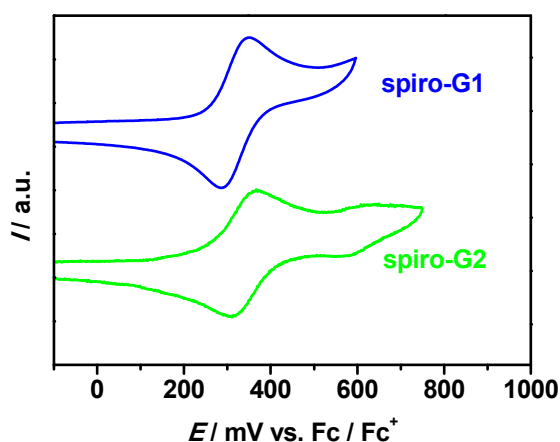
Figure 38: Cyclic voltammograms of spiro-G1 and spiro-G2 measured in DCM with TBAHFP (~ 0.2 M) as supporting electrolyte and referenced against the Fc/Fc$^+$ redox couple.

The CV of **spiro-G1** is characterised by one reversible oxidation wave at 320 mV that comprises the oxidation of all four individual MeO-TAAs. This finding is in good agreement with the obtained $E_{1/2}$ values for the terminal TAAs in **G1**–**G3** and for **N-M**, and proves no detectably effect from the spirobifluorene on the redox potentials.

To date, no analyses of redox properties of 9,9´-spirobifluorenes have been reported.[301] In publications with the spirobifluorene as a structural motif, including electrochemical considerations, oxidation or reduction potentials of spirobifluorene have not been mentioned. Presumably, spirobifluorene is neither oxidised nor reduced at the potential generally applied in electrochemical measurements.

In the CV experiment **spiro-G2** exhibits two reversible oxidation waves that consequently are assigned to the oxidation of the terminal TAAs (340 mV) and of the branch TAAs (600 mV). These values are very similar to the values found for **G2** and **G3** (*cf.* Table 3, p: 103, and Figure 15, p: 102). An interaction between terminal TAAs and branch TAAs through the triazole might be negligible and thus the redox potential is determined exclusively by the substitution pattern, analogously to **G1**–**G3** (*cf.* section 3.2.1.1, p: 101).

Table 10: Half Wave Potentials ($E_{1/2}$) of spiro-G1[a] and spiro-G2[b]. All $E_{1/2}$ Values were Estimated by Cyclic Voltammetry in DCM/TBAHFP (~0.2 M) at RT and Referenced Against the Fc/Fc$^+$ Redox Couple.

	$E_{1/2}^{terminal}$ /mV	$E_{1/2}^{branch}$ /mV
spiro-G1	320	-
spiro-G2	340	600

[a] Measured with a scan rate of 250 mVs^{-1}. [b] Measured with a scan rate of 500 mVs^{-1}.

3.2.2.2   Steady-State Absorption Spectroscopy

To obtain information about the characteristics of the spiro dendrimers electronic ground state, steady-state absorption spectra were recorded in solvents with different polarity. However, **spiro-G2** proved to be in soluble only in DCM. The spectra of **spiro-G1** and **spiro-G2** in DCM are shown in Figure 39 together with the spectra of the relative TAA dendrimers **G1** and **G2**, which proved to be rather similar. For **spiro-G1** no solvent dependence was observed, indicating a nonpolar electronic ground state. This is assumed to be similar for **spiro-G2**, although an experimental proof cannot be given. **Spiro-G1** exhibits a broad and featureless absorption maximum at 28400 cm^{-1} (350 nm) with a shoulder at about 33300 cm^{-1} (300 nm) and an additional weak band indicated at about 31000 cm^{-1} (320 nm). For **spiro-G2**, the main absorption band is red-shifted by ~ 200 cm^{-1} to ca. 28200 cm^{-1} (355 nm). Exciton coupling between the terminal TAAs in the individual chromophore branches might be responsible for this shift. However it is also possible that this shift is caused by introduced branch TAAs with different absorption characteristics.

Remarkably, the spectrum of **spiro-G2** is much broader than the one of **spiro-G1** (and **G1**–**G2**), which might be explained by conformational disorder in the more expanded dendrimer. The two dendrimers exhibit very similar 00-energies, as indicated by the comparable onset of absorption. Similar to **G1**–**G3** the intensity of the higher energy shoulder decreases with increasing generation number (*cf.* section 3.2.1.2, p: 104). The absorption characteristics of the spirobifluorene moiety is not pronounced and not resolved due to the overlap with the strong TAA absorptions. The neat spirobifluorene exhibits absorption maxima above 31000 cm^{-1} (320 nm) but an introduction of substituents may shift the absorption maxima below 25000 cm^{-1} (400 nm).[302-306] In literature, no triazole-substituted spirobifluorenes are reported, but it seems obvious that the spirobifluorene moiety has no significant impact on the absorption spectra of **spiro-G1** and in particular of **spiro-G2**.
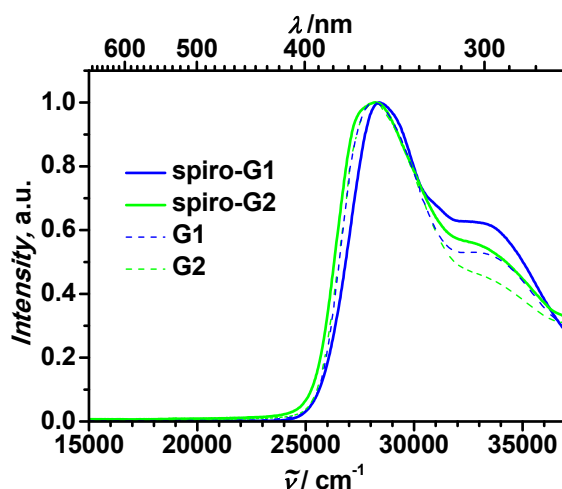
Figure 39: Normalised absorption spectra of spiro-G1 and spiro-G2 in DCM. Spectra of G1 and G2 are given for comparison (dashed lines).

3.2.2.3   Emission Spectroscopy

Information about the characteristics of the excited state of **spiro-G1** and **spiro-G2** were obtained by steady-state and time resolved emission spectroscopy. The emission of **spiro-G1** and **spiro-G2** is mainly determined by the TAA chromophore branches and similar to the absorption no influence of the spirobifluorene was observed.

However, the emission spectra of **spiro-G1** in all solvents are broad and structureless and, unlike to the absorption, the emission of **spiro-G1** shows a strong solvatochromism. The emission maxima shift with increasing solvent polarity towards lower energy, which reveals the emission occurring from a charge transfer state (see Figure 40). While the TAA-triazole-TAA structure in **G1** may lead to excited quadrupolar states that are the reason of polar charge transfer states, the second donor-TAA is absent in **spiro-G1** (*cf.* 3.2.1.3, p: 105). Herein, electron density might be shifted upon excitation from the donor to the triazole acceptor and a classical dipolar excited state results.[159,219]

The quantum yields of **spiro-G1** in diverse solvents, determined using quinine sulfate in H_2SO_4 as a quantum yield standard (ϕ = 0.55), are all in the order of ca. 60 % but with a remarkably high value of 87 % in MeCN. Since **spiro-G1** shows only weak solubilty in MeCN, the high quantum yield might be to some extent inaccurate due to uncertainties in the experiment. For **spiro-G2** in DCM a quantum yield of 33 % was found, which is much lower compared to **spiro-G1**, **G2** (57 %) and **G3** (48 %).

The excited state lifetimes in the diverse solvents are in the range of 2.5 to 5.1 ns with a maximum in medium polar solvents and a minimum in nonpolar toluene. Applying these data to equation (54),

p: 106, yields the rates of the radiative decay k_f and with the *Strickler-Berg* equation (55), p: 106, the fluorescence transition moments μ_f were determined. Values of ca. 4 D were obtained for **spiro-G1** in all solvents except for MeCN. Here an impressive μ_f value of about 8 D was determined. This high value might be caused by the high fluorescence quntum yield and is therefore not trustworth (*c.f.* 3.2.2.3, p: 153). The μ_f value of ca. 3 D for **spiro-G2** in DCM is smaller than for **spiro-G1**, but similar to the values found for **G2** and **G3**. This narrow range of transition moments (disregarding the value in MeCN) indicates the absence of a superradiant effect and thus exciton coupling can be neglected in the excited state. The spectroscopic data of **spiro-G1** and **spiro-G2** are listed in Table 11.
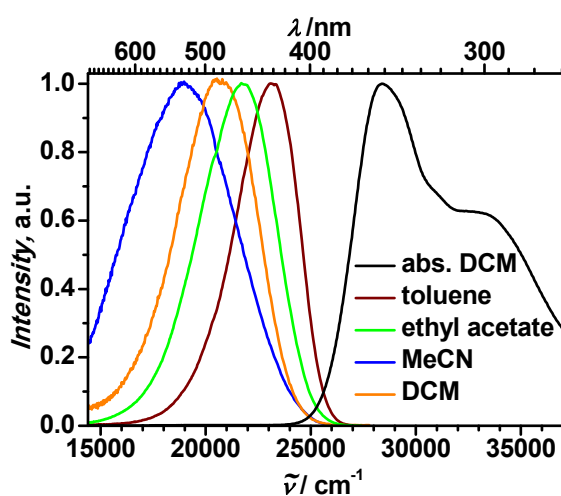
Figure 40:   **Normalised absorption and emission spectra of spiro-G1 in different solvent. Excitation at 28200 cm^{-1} (355 nm).**

Table 11:   **Absorption and Fluorescence Data of spiro-G1 and spiro-G2.**

		$\tilde{\nu}_{max}$ /cm^{-1}	ε_{max} /M^{-1} cm^{-1}	$\tilde{\nu}_f$ /cm^{-1}	ϕ_f	τ_f /ns	k_f /10^7 s^{-1}	μ_{fl} /D
spiro-G1	MeCN	28950	-	19000	0.87	3.5	24	7.8
	EE	28200	-	20650	0.58	4.1	14	4.6
	DCM	28400	161900	21700	0.65	5.1	13	4.3
	toluene	28000	141900	23250	0.56	2.5	22	4.6
spiro-G2	DCM	28400	281000	20500	0.33	4.8	7	3.3

3.2.2.4   Steady-State Emission Anisotropy Measurements

In order to get a closer view on the relative orientation of the transition moments of absorption and emission in **spiro-G1** and **spiro-G2**, fluorescence excitation polarisation anisotropy measurements were performed. Both dendrimers were investigated in a rigid glass matrix of SOA at RT to prevent molecular motions. The excitation anisotropies of **spiro-G1** and **spiro-G2** are shown in Figure 41.
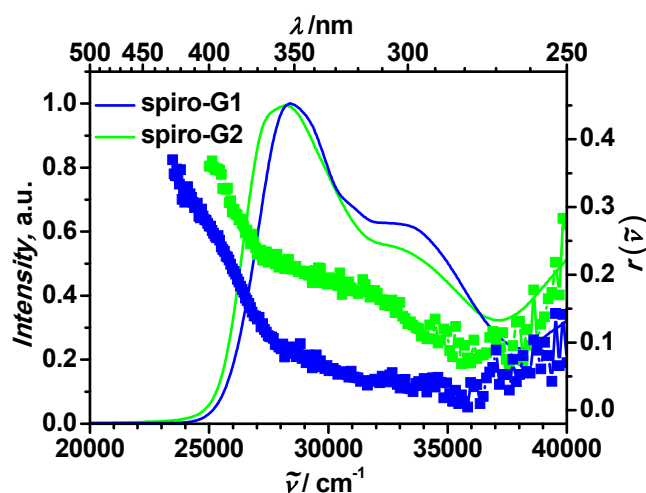
Figure 41:   Normalised absorption spectra in DCM and fluorescence excitation polarisation anisotropy spectra $r(\tilde{v})$ of spiro-G1 and spiro-G2 in SOA at RT.

The anisotropy for **spiro-G1** starts with a high value of 0.35 at the beginning at 23700 cm^{-1} (420 nm), which immediately decreases to a value of ca. 0.05 at 30300 cm^{-1} (330 nm). From there, the anisotropy slightly decreases with an increasing overlap with the higher energy transitions. The observed value of ca. 0.05 over the area of the main absorption band is between the expected value for three-dimensional ($r = 0$) and two-dimensional ($r = 0.1$) depolarisation. Since the exact global structure of **spiro-G1** is unknown, it is supposed that upon photoexcitation the energy is equally distributed over the entire molecule.

The high anisotropy at the beginning is a result of a "red-edge excitation effect" similar to the one observed for **G1**–**G3** (3.2.1.4, p: 108).[229-235] This is a clear proof for an energy transfer between the chromophore branches in **spiro-G1**.

The wavelength dependent anisotropy course of **spiro-G2** shows clear parallels to the one of **spiro-G1**. The high anisotropy at the start of 0.35 at 25000 cm^{-1} (400 nm) readily decays to a value of 0.24 at 27000 cm^{-1} (370 nm) from where the anisotropy only moderately decreases in the range of the main absorption band. An increasing overlap of the high energy transitions results in a clearly stronger decrease of anisotropy above ca. 32300 cm^{-1} (310 nm). Thus, the overall progression of the anisotropy spectra of **spiro-G1** and **spiro-G2** are comparable. On the low energy side of the main absorption band both anisotropy spectra exhibit a strong anisotropy decline as a result of a

"red-edge excitation effect" caused by an inhibited energy transfer between chromophores in the symmetry broken systems (*cf.* 3.2.1.4, p: 108).[229-235] In the area of the main absorption band the anisotropy decreases only slightly with values of ca. 0.05 and ca. 0.2 for **spiro G1** and **spiro-G2**, respectively. Remarkably, the anisotropy of **spiro-G2** is higher over the complete spectrum than that of **spiro-G1**. Further the value of ca. 0.2 in the area of the main absorption band is significantly larger than the expected value for either three-dimensional ($r = 0$) or two-dimensional ($r = 0.1$) depolarisation.

The question arises, why the emission in **spiro-G2** is more polarised than in **spiro-G1** and why the energy is not completely distributed over the entire molecule.

Homoenergy transfer between the chromophore branches certainly takes place by a *Förster*-like mechanism since the chromophores in **spiro-G1** as well as in **spiro-G2** are too distant (*N-N* distance of two adjacent terminal TAAs in **spiro-G1** is ca. 16 Å) to allow *Dexter*-type energy transfer, as supported by MM2 force field calculations in ChemBio3D Ultra[307] (see Figure 42).

For **spiro-G2** energy transfer processes resulting in anisotropies lower than 0.2, especially energy transfer between the individual chromophore branches, seem to play a less important rule compared to those resulting in higher anisotropies. Thus, energy transfer may occur basically in the individual chromophore branches where the terminal TAAs are predominantly excited due to their high relative number. From the terminal TAAs, intrachain energy hopping to the branch TAAs might be related with higher anisotropy values. A distinction between the energy transfer pathways might be possible by time resolved emission anisotropy measurements. A comparison of decays for **spiro-G1** and **spiro-G2** and an analysis of the related time rates of the diverse pathways might provide the decisive information.
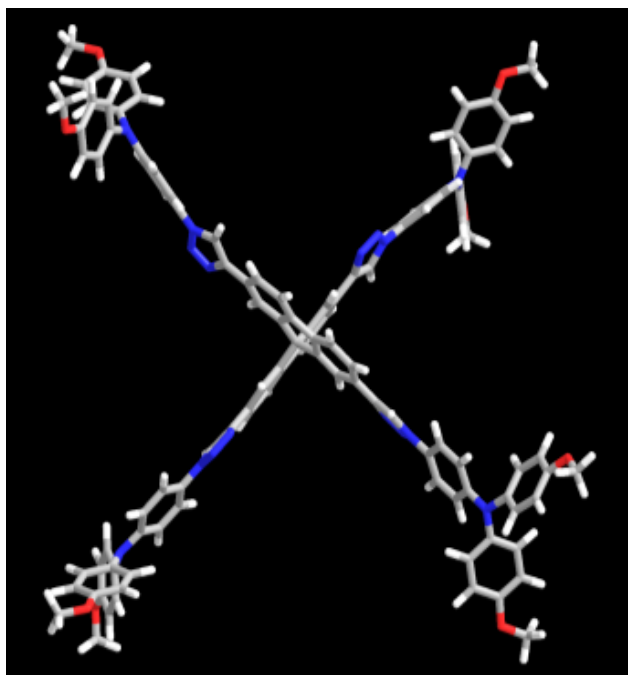
Figure 42: Optimised structure of spiro-G1. Optimisation was performed by means of MM2 force field in ChemBio3D Ultra[307]

3.2.2.5   UV/Vis/NIR – Chemical Oxidation

Steady-state absorption spectra of the radical cations of **spiro-G1** and **spiro-G2** were recorded to investigate their spectroscopic properties. Therefore, chemical oxidation experiments for **spiro-G1** and **spiro-G2** in DCM using $SbCl_5$ in DCM as oxidant were performed analogously to the measurements in section 3.2.1.9, p: 139.

Figure 43:   Evolution of the absorption spectra during chemical oxidation of spiro-G1 by stepwise addition of $SbCl_5$ in DCM. Early spectra are presented in blue/red, late ones in orange/green colours. The absorption spectra of the neutral compounds are given in black. Further addition of oxidant leaves the spectra unaffected.

In Figure 43, the evolution of the absorption spectra of **spiro-G1** during the chemical oxidation with $SbCl_5$ in DCM is shown. The processes that account for rising and vanishing absorption bands are similar to those characterising the chemical oxidation data of **C-M** and **N-M** (*cf.* 3.2.1.9, p: 139). With starting oxidation, band A of the neutral **spiro-G1** at 28400 cm^{-1} (350 nm) begins to decrease and congruently, bands B, C and D at 26700 cm^{-1} (375 nm), 16400 cm^{-1} (610 nm) and 12900 cm^{-1} (775 nm), respectively, arise.[168,283] The assignment of the absorption bands refers to Scheme 51, p: 140. According to that, band B is caused by a SOMO-LUMO transition, while band D is the result of an excitation from the HOMO into the LUMO of the TAA.[168] The origin of band C remains open and a clear attribution to either a HOMO-1 to SOMO transition or to a charge transfer from the bridge to the TAA radical cation is not supported by the available data.

In the neutral **spiro-G1**, the spirobifluorene absorption bands are strongly overlapped by the strong absorbance of the TAAs. However, with proceeding oxidation the strong absorbance of the TAAs declines and the absorption of the spirobifluorene core may become observable. This is also indicated by the fact, that the intensity of the band A of **spiro-G1** is remarkably higher than that of **G1**, which also comprises four absorbing TAA moieties. Thus, the intensities of band D are roughly

identical for **spiro-G1** and **G1**. However, the absorption energy of spirobifluorenes is highly dependent on substituents and therefore the accurate position of the absorption bands cannot be determined.

Crucially, the absence of an IV-CT band proves no (or only insignificant) electronic coupling between the individual TAA moieties neither through the sp³-carbon of the spirobifluorene nor through one fluorene subunit.
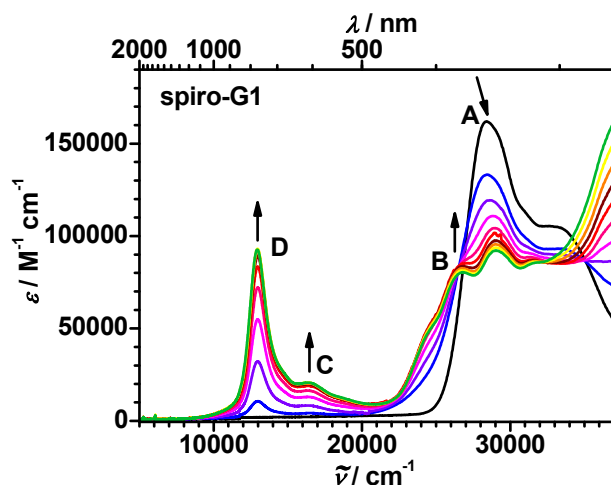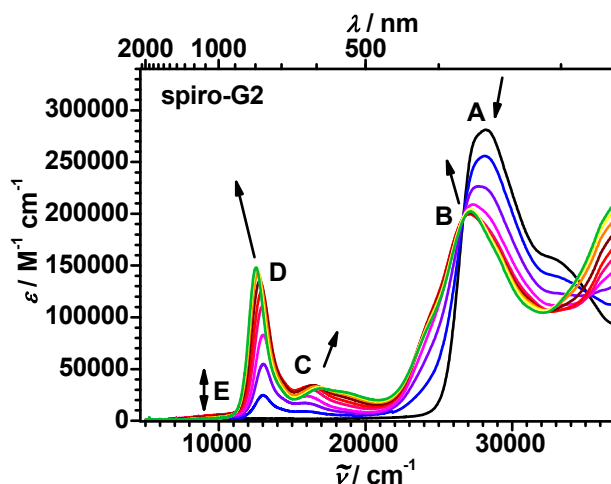

Figure 44: Evolution of the absorption spectra during chemical oxidation of spiro-G2 by stepwise addition of SbCl₅ in DCM. Early spectra are presented in blue/red, late ones in orange/green colours. The absorption spectra of the neutral compounds are given in black. Further addition of oxidant leaves the spectra unaffected.

Spiro-G2 exhibits significant differences in the recorded spectra during oxidation progression compared to **spiro-G1** and shows a rather similar behaviour like **G1**. As expected, with starting oxidation band A of neutral **spiro-G2** decreases, accompanied by a red-shift of the maximum at 28200 cm⁻¹ (355 nm) to 27000 cm⁻¹ (370 nm). This red-shift is caused by the overlap of absorption band A, related to the neutral TAAs in **spiro-G2**, and band B assigned to TAA radical cations. The ratio of these two species changes continuously and dictates the position of the observed band maximum. Due to the high amount of TAA absorption, the absorption of the spirobifluorene core is not observed.

At lower energies bands C and D emerge at 16200 cm⁻¹ (620 nm) and 13000 cm⁻¹ (770 nm), respectively. During the chemical oxidation experiment, also the appearance of the IV-CT band E is observed. Band E is caused by an optically induced charge transfer from a branch TAA to a terminal TAA. The most intense IV-CT band is expected to be the result of a large number of different MV species, which all may feature similar relative absorbances and energies. Therefore a *Mulliken-Hush* analysis was expected to be too complex. Analogously to **G1**, bands D and C start to shift at approximately the same time when the intensity of the IV-CT band E passes its maximum

(*cf.* 3.2.1.9, p: 139). From there on in particular the branch TAAs are oxidised. The radical cations of the branch TAAs feature different absorption characteristics than the terminal TAA radical cations, which results in the observed shift.

3.2.2.6   Conclusions

The spiro dendrimers **spiro-G1** and **spiro-G2** exhibit rather similar spectroscopic properties compared with the dendrimers **G1**–**G3**.

In **spiro-G1** the excitation energy is supposed to be equally distributed, as indicated by the almost completely depolarised steady-state emission. However, the emission of **spiro-G2** is more polarised than for **spiro-G1** and thus the energy is probably not transferred beyond the individual chromophore branch within fluorescence lifetime. Presumably, energy transfer within one distinct chromophore branch is more rapid than between individual chromophore branches.

Energy transfer in **spiro-G1** and **spiro-G2** is expected to be mediated by dipole-dipole interaction according to the *Förster* theory. In contrast *Dexter* transfer would require a direct orbital overlap between the donor and the acceptor branch, which is prevented by the perpendicular arrangement of the branches caused by the spirobifluorene motif.[a]

However, time resolved emission anisotropy measurements and solvent dependent analyses may give a comprehensive understanding of the photophysical dynamics in **spiro-G1** and **spiro-G2**. These studies may further serve as a basis for a more detailed discussion of possible energy transfer mechanisms and pathways in **spiro-G1** and **spiro-G2** in the future.

Concerning electron transfer, the four TAA-triazole moieties of **spiro-G1** behave like individual subunits. The absence of an IV-CT band during the oxidation progression of **spiro-G1** indicates no or a negligible electronic communication between the TAAs. This finding can be reasonably explained by considering the relative small electronic coupling found for **M** (*cf.* Table 9, p: 147) and by the large *N-N* distance (~ 23 Å)[b] between two TAAs along one fluorene subunit. Thus, the IV-CT band detected in the chemical oxidation experiment of **spiro-G2** is attributed to electron transfers between the branch TAAs and the terminal TAAs in the individual chromophore branches.

---

[a] Direct orbital interaction between the two fluorene subunits might be possible due to "spiro-conjugation" in symmetry broken spirobifluorenes.[308-311]

[b] Optimisation was performed by means of MM2 in ChemBio3D Ultra 12.0.2, CambridgeSoft **2010**.

3.2.3   Morphology of the Dendrimers

Compounds that form amorphous films (= glasses) are particularly beneficial for many optoelectronic applications compared to single and polycrystalline materials. In contrast to single crystal growth the amorphous state can be easily achieved *e.g.* by spin coating or vacuum vapour decomposition. Polycrystalline states exhibit grain boundaries between neighbouring microcrystallites that result in charge carrier traps or light scattering and thus in corrupted device performance.[312,313] Furthermore, polycrystalline states are anisotropic and seldom reproducible and therefore their characteristics are laborious to investigate.

Polymers are a class of materials that are commonly found to form amorphous films. However, polymers typically show wide molecular weight distributions and are loaded with aliphatic (non-photoactive) chains to guarantee solubility.[314] That is why low-molecular substances that form stable amorphous phases are in the focus of intensive research. Such molecules can be diversified with relative ease and characterisation and purification is accomplished by common techniques (*e.g.* NMR and chromatography). The stability of the amorphous state is correlated with the glass transition temperature T_g. Beyond T_g intermolecular motions rapidly increase and facilitate the transition into the stable crystalline state. Materials in optoelectronic devices require high T_g values as the surface temperature in e.g. photovoltaics can reach several hundred centigrade.

Some requirements for the synthesis of low-molecular compounds with enhanced T_g were given by *Naito* and *Miura.* They stated that highly symmetric, globular, rigid and dense compounds with large molecular weights and a weak intermolecular cohesion are expected to form stable amorphous states.[181,182] On this basis, several new organic materials with high T_g values were designed. These are in particular starburst systems investigated by *Shirota*[160,314-316] and spiro compounds by *Salbeck*,[180,305,317] in which the globular structure annihilates intramolecular dipoles and reduces the intermolecular cohesion.

The dendrimers presented in this thesis, fulfil these requirements and in the case of the spiro dendrimers, the concepts of starburst and spiro structures are even combined. Therefore, all dendrimers as well as the model compounds were investigated by differential scanning calorimetry (DSC) to characterise the glass forming properties and the dependence of size and structure on T_g.[318,319]

In the DSC plots shown in Figure 45, a glass transition is indicated by a deflection of the baseline and the T_g is defined as the inflexion point at the transition between phases.[320] Two heating-cooling cycles were performed for each compound to assure that all transitions are reversible. Beside the glass transition found for all investigated compounds (disregarding **spiro-G2**, *vide infra*),

the DSC plots of **N-M** and **C-M** present two additional signals. The exothermic process (negative peak) at T_{rec} = 95°C for **N-M** and T_{rec} = 94°C for **C-M** might be assigned to recrystallisation of the sample, while the endothermic process (**N-M**: T_m = 174°C, **C-M**: T_m= 134°C) is caused by melting of the sample.[304,318] The small positive peak at ca. T = 150°C in the DSC plot of **C-M** is caused by an artefact in the measurement.

According to the T_g values listed in Table 12, the T_g significantly increases with molecular weight, size and branching factor of the systems. However, this effect is more significant at lower molecular weights. Thus, the T_g value increases from 69°C for **M** (MW: 675.77 g/mol) to 141°C for **G1** (MW: 1356.53 g/mol) by a factor of around two just like the MW. However, T_g increases from 196°C for **G2** (MW: 3398.80 g/mol) to 231°C for **G3** (MW: 7483.33 g/mol) only by a factor of ca. 1.2 (MW by a factor of ca. 2.2). Therefore, it is assumed that the T_g value reaches an upper limit where higher MWs and increased branching will not enhance T_g any further.

However, introducing spirobifluorene into the dendrimer structure remarkably increases the T_g of **spiro-G1** by ca. 50°C compared to **G1**. The DSC curve of **spiro-G2** possesses no characteristic step up to 350°C indicating an amorphous state transition. The absence of a glassy state seems to be unreasonable, since **spiro-G1** and **G3** are structurally similar to **spiro-G2** but with increasing generation number the observed step becomes less pronounced. Thus, a supposed amorphous state in **spiro-G2** might be indiscernible under the applied measurement conditions.

The use of triazoles as spacer between the TAA and the spirobifluorene results in a 20°C higher T_g for **spiro-G1** compared to **spiro-MeOTAD** (T_g = 121°C; MW: 1225.42 g/mol).[180] The latter is used in a great diversity of optoelectronic devises. If this enhancement is caused by the angulated nature of the triazole spacer, leading to a somewhat different global structure, or by the higher molecular weight cannot be stated.
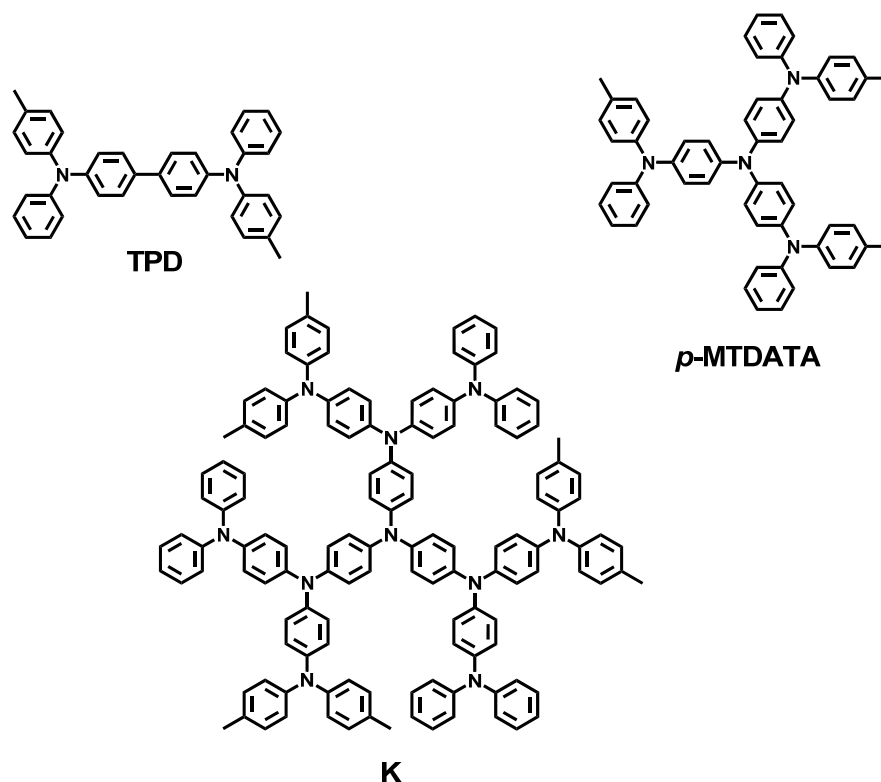
Chart 13: **Molecular structures of the compounds TTB, *p*-MTDATA and K.**

However, both **G1** and **G2** feature improved T_g values compared to the structural related dendrimers ***p*-MTDATA** (T_g = 80°C; MW: 789.01)[314] and **K** (T_g = 169°C; MW: 1834.33)[160,321] which comprise no triazoles. Contrarily **M** shows no significant shift of T_g compared to **TPD** (T_g = 62°C; MW: 516.67)[317]. In brief, all presented compounds exhibit slightly higher MWs than their literature-known counterparts and considerably higher T_g values.

Table 12: **Molecular Weight and Glass Transition Temperature Extracted from DSC Measurements.**

	N-M	C-M	M	G1	G2	G3	spiro-G1	spiro-G2
MW	448.52	448.52	675.77	1356.53	3398.80	7483.33	1798.01	4521.03
T_g	46°C	43°C	69°C	141°C	196°C	231°C	181°C	-
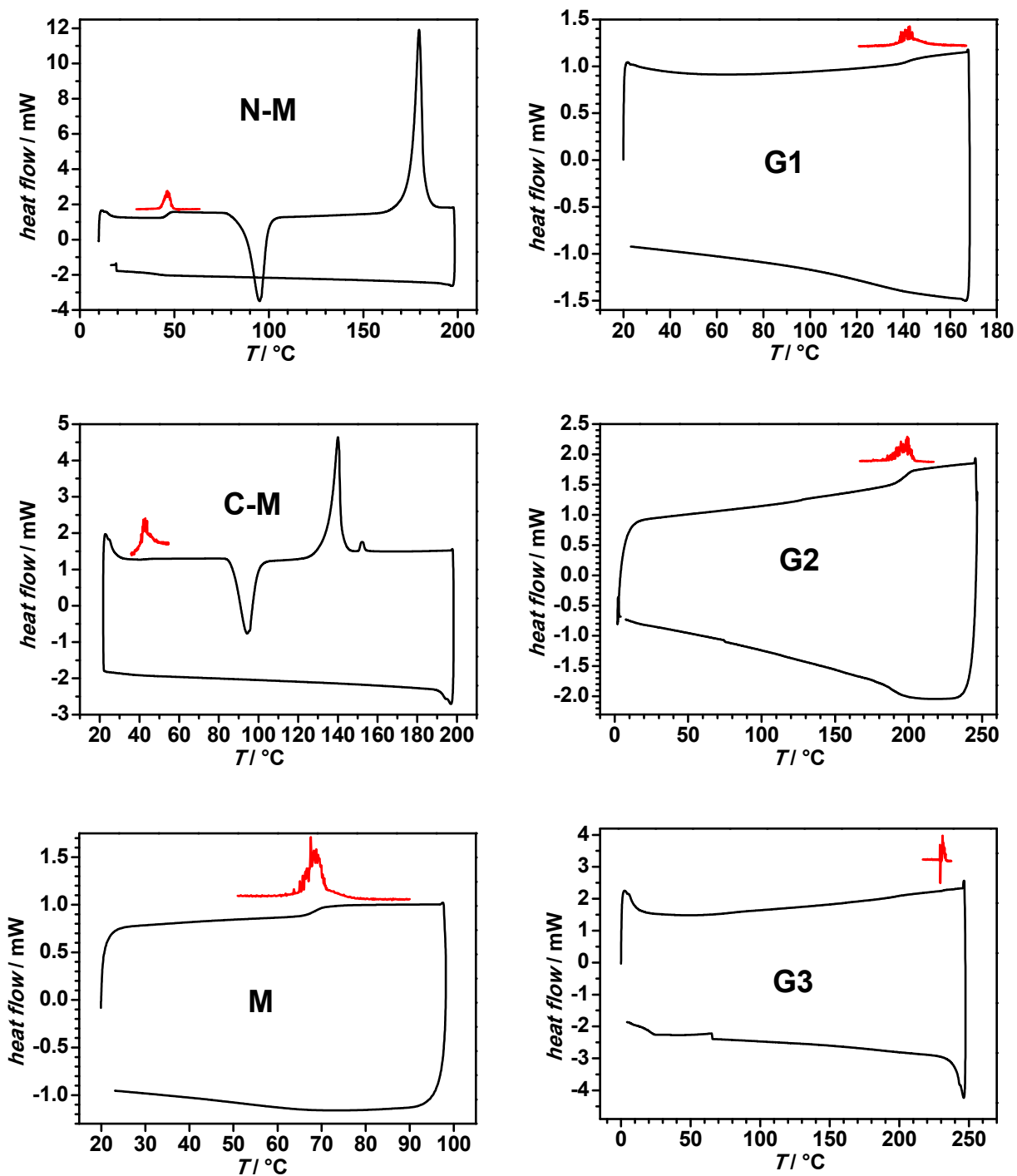
Figure 45: Continued
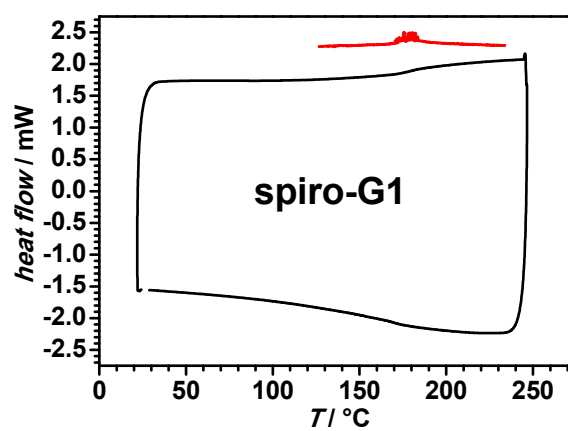
Figure 45: Differential scanning calorimetry curves of N-M, C-M, M, G1–G3 and spiro-G1. The maximum of the first derivative of the curve (red) indicates the glass transition temperature (T_g).

3.2.4 Cascades

3.2.4.1 Results

3.2.4.1.1 Cyclic Voltammetry

Cyclic voltammetry measurement were performed for all TAA-NDI cascades in order to determine the redox potentials of the incorporated chromophores in the cascades, and to estimate the energies of various charge separated states upon photoexcitation. The measurements were realised in DCM with TBAHFP as supporting electrolyte and the potentials were referenced against the Fc/Fc$^+$ redox couple. In this measurement the NDI acceptor is reduced and up to two TAA donors are oxidised (see Figure 46 and Table 13). Multiple thin-layer measurements proved the reduction of the NDI as well as the oxidation of the TAAs to be fully reversible.
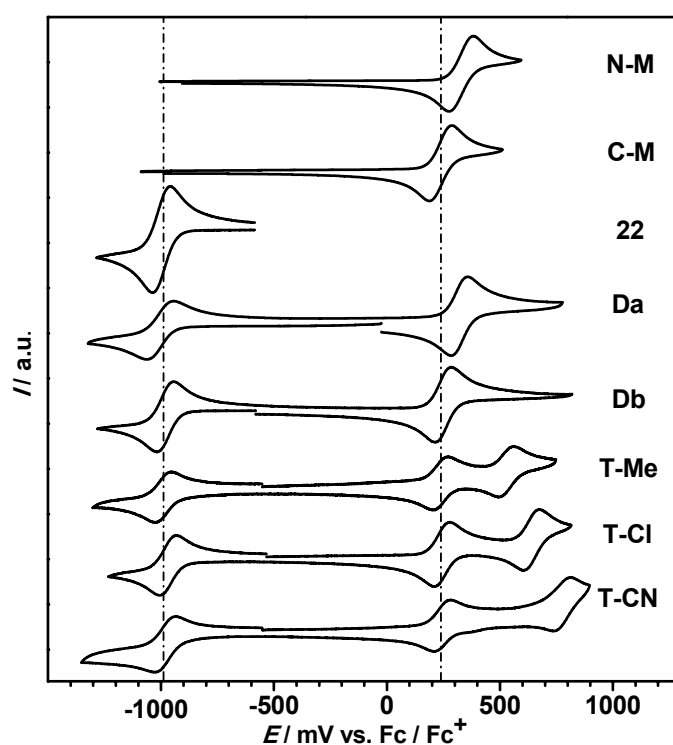
Figure 46: Cyclic voltammograms in DCM/TBAHFP (~ 0.2 M) of C-M[a], C-M[a], 22[a], the dyads[a] and the triads[b] vs. Fc/Fc$^+$. [a] Measured with a scan rate of 250 mV s^{-1}. [b] Measured with a scan rate of 1000 mV s^{-1}.

Similar to the redox potentials found for the dendrimers, the triazoles show an ambivalent influence on the oxidation of the adjacent triarylamines, inasmuch as triazoles connected *via* the carbon to the TAA act as an electron-donating-group (EDG) while nitrogen-linked triazoles act as an electron-withdrawing-group (EWG), see section 3.2.1.1, p: 101.

As a result, in **Da** the oxidation of the MeO-substituted TAA connected *via* the nitrogen to the triazole is observed at 320 mV, almost at the same position as in **N-M** ($E_{1/2}$ = 330 mV). Analogously, in **Db** the oxidation potential of the MeO-substituted TAA connected *via* the carbon to the triazole is found at 250 mV, which is very similar to the value found for **C-M** ($E_{1/2}$ = 240 mV).

As apparent from Figure 46, p: 170, the reduction potential of the NDI in **Da** and **Db** is rather similar to the value found for **22** (about -1000 mV) and thus, only marginally influenced by the connection mode to the triazole, which suggests electronic decoupling of the NDI from the *N*-aryl substituents. Consequently, in the triads the NDIs are reduced at ca. 1000 mV and the oxidation of the MeO-substituted TAAs (TAA2) corresponds to the lowest oxidation wave at ca. 250 mV, which is similar to the values found for **Db**. All triads exhibit an additional oxidation wave with more positive potential caused by the oxidation of the intermediate TAA1. These oxidation potentials are determined by the substituent (Me < Cl < CN) at the TAA1. Thus, the CV experiment proved a downhill-directed redox gradient between TAA1 and TAA2 in all triads.

Table 13: Half-Wave Potentials ($E_{1/2}$) of the Dyads[a], the Triads[b] and of some Model Compounds[a]. All $E_{1/2}$ Values were Estimated by Cyclic Voltammetry in DCM/TBAHFP (~0.2 M) at RT and Referenced Against the Fc/Fc[+] Redox Couple.

	$E_{1/2}^{red}$ /mV	$E_{1/2}^{ox1}$ /mV	$E_{1/2}^{ox2}$ /mV
N-M		330	
C-M		240	
22	-1000		
Da	-1000	320	
Db	-980	250	
T-Me	-1000	240	530
T-Cl	-970	250	640
T-CN	-980	240	780

[a] Measured with a scan rate of 250 mV s^{-1}. [b] Measured with a scan rate of 1000 mV s^{-1}.

3.2.4.1.2 Steady-State Absorption Spectroscopy

UV/Vis steady-state absorption spectra of all cascades were recorded in polar MeCN and nonpolar toluene to investigate potential ground state interactions between the TAA donor and the NDI acceptor. The two dyads **Da** and **Db** exhibit very similar absorption characteristics.

In MeCN both compounds exhibit a sharp absorption band at 26500 cm^{-1} (375 nm) with nearly identical extinction coefficients of ca. 35200 M^{-1} cm^{-1}. The main absorption band is at 27800 cm^{-1} (360 nm) and is more intense for **Db** (ε = 40900 M^{-1} cm^{-1}) compared to **Da** (ε = 37200 M^{-1} cm^{-1}). At the higher energy side there are two small bands at 29200 cm^{-1} (340 nm) and ca. 31000 cm^{-1} (320 nm) with decreasing intensity.

In MeCN and toluene the spectra of **Da** and **Db** are considerably different. While in MeCN many bands are sharp and resolved, they become broad and featureless in toluene. As apparent from Figure 47, D, the absorption spectrum of **N-M** is sharper in MeCN than in toluene but for **22** the same trend as for the dyads is observed. This indicates that the broadening is caused by the NDI, probably due to aromatic solvent-specific effects such as exciplex formation.[322,323]

Remarkably, **Da** shows an additional very weak and broad absorption band in MeCN and toluene (see Figure 47, B) between ca. 16900 cm^{-1} (590 nm) and 25000 cm^{-1} (400 nm), which is absent in the spectra of **Db**. In toluene excitation into this band results in a weak fluorescence at 15600 cm^{-1} (640 nm) while in MeCN no emission could be observed. This band might be caused be a charge transfer (CT) from the NDI to the triazole or might be related to an *n-π** transition in the triazole. A distinct assignment as either a CT band or an *n-π** band is not possible. However, this transition is not recognised in any other cascade probably due to the different connection mode *via* the triazole.

Only weak solvatochromism is indicated by the observed shift of the main absorption band from MeCN to toluene of ca. 200 cm^{-1}, while the onset of the absorption in toluene (24800 cm^{-1}) compared to that MeCN (25800 cm^{-1}) indicates smaller 00-energies for both compounds in toluene estimated by applying a tangent on the flank of the lowest energy transition (disregarding the "CT" band for **Db**).

As shown for **Da** in MeCN, the absorption spectrum of the dyads are roughly the sum of the absorption spectra of the TAA and the NDI fragments (see Figure 47, C), which indicates little, if at all, electronic interaction between the NDI and the TAA in the electronic ground state.
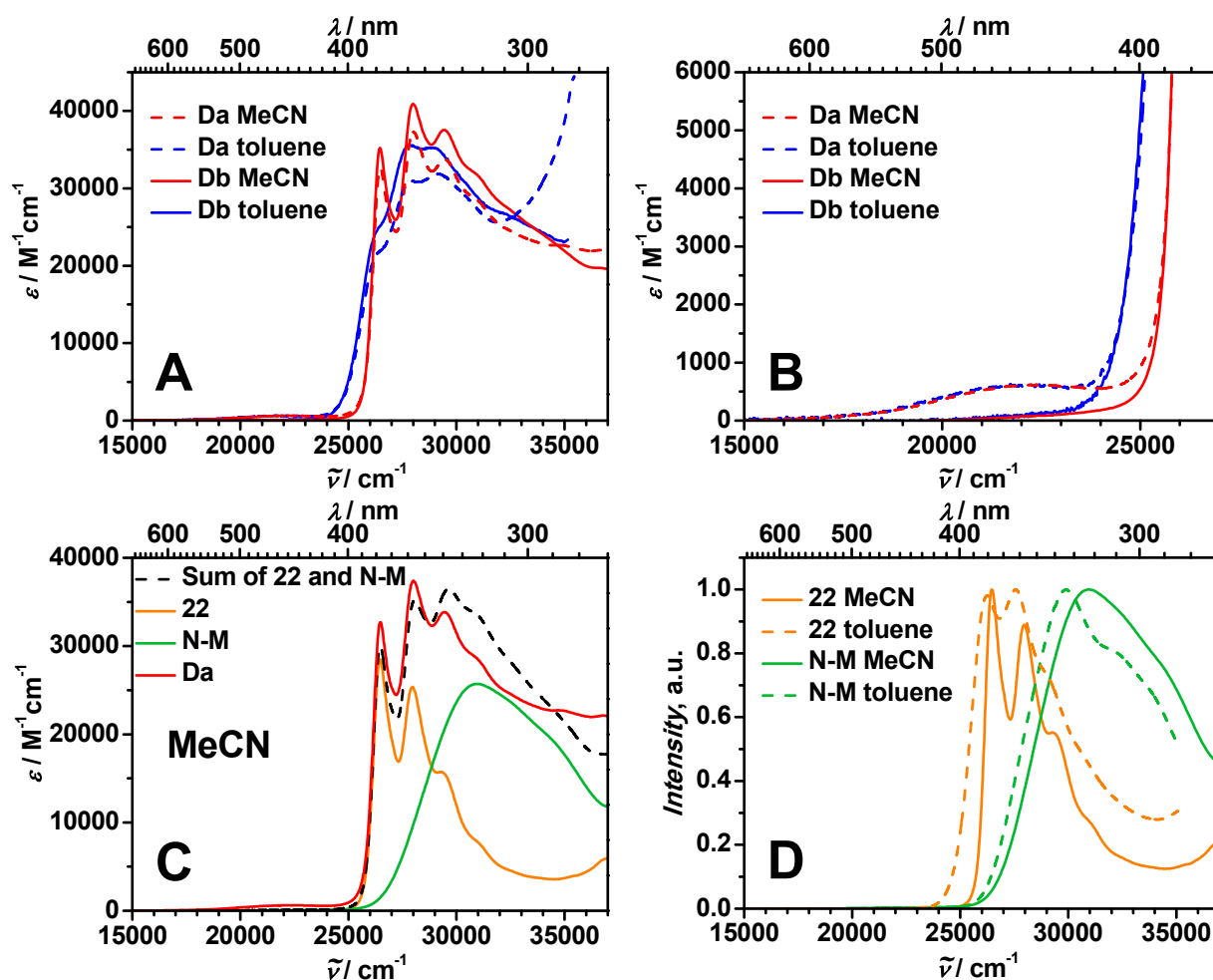
Figure 47:   **A: Absorption spectra of the dyads Da and Db in MeCN and toluene. B: Magnification of A showing the n-π^* band of Da. C: Normalised absorption spectra of Da, 22, N-M and the sum of 22 and N-M in MeCN. D: Normalised absorption spectra of 22 and N-M in MeCN and toluene.**

A complete assignment of the absorption bands to either the NDI or the TAA chromophore seems complicated, however the sharp bands are certainly caused by the π-π^* transitions of the NDI moiety with its typical vibronic features. It is obvious that the strong overlap of the NDI and the TAA absorption precludes an exclusive excitation of either the NDI or the TAA (in MeCN at 28200 cm^{-1} (355 nm) ca. 50 % and at 26300 cm^{-1} (380 nm) ca. 10 % TAA excitation).
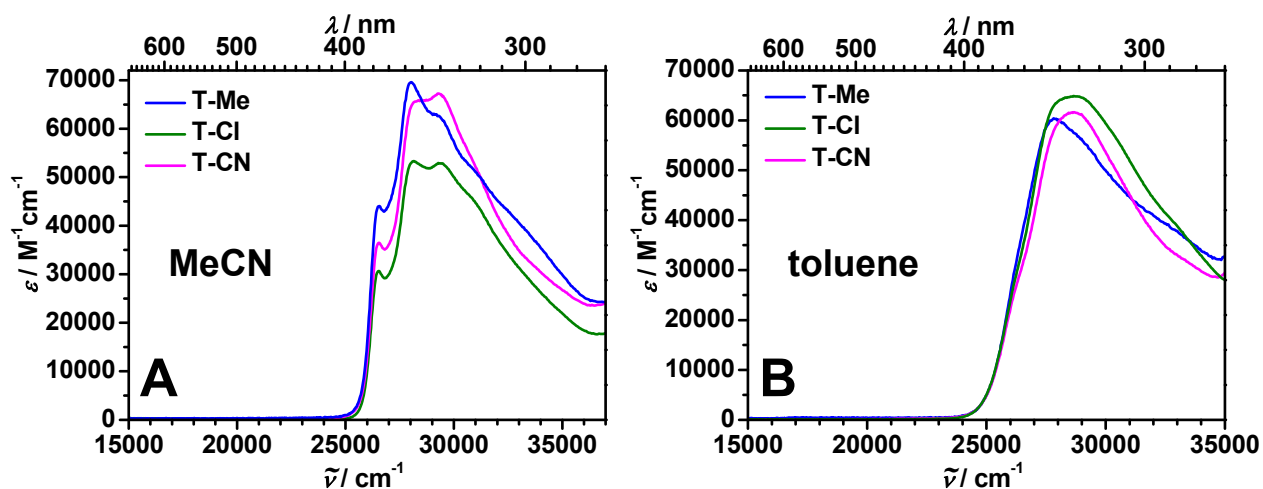
Figure 48: Absorption spectra of T-Me, T-Cl and T-CN in MeCN (A) and toluene (B).

The absorption spectra of the triads are even much broader compared to the spectra of the dyads (see Figure 48). This finding can be explained by the present of a second TAA donor in the triads, TAAs being characterised by relatively broad absorption bands.

In MeCN all triads possess three absorption bands at 26500 cm^{-1} (375 nm), 27800 cm^{-1} (360 nm) and 29200 cm^{-1} (340 nm) with a tiny shoulder at ca. 30700 cm^{-1} (325 nm). The intensities of the three bands vary between the triads, which can be explained by the different absorption characteristics of the intermediate TAA1 in the triads.

The absorption bands of **T-Me**, **T-Cl** and **T-CN** in toluene are very broad and present only a single maximum. For **T-Me** this maximum is at 27800 cm^{-1} (360 nm) in agreement with the most intense absorption band in MeCN. For **T-Cl** and **T-CN** the maxima are at 28400 cm^{-1} (350 nm) and thus in-between the two absorption bands 27800 cm^{-1} (360 nm), and 29200 cm^{-1} (340 nm) found in MeCN. Similar to the dyads a shift of ca. 210 – 230 cm^{-1} is observed in the spectra changing the solvent from MeCN to toluene. The onsets of absorption are similar for all compounds in MeCN and toluene, respectively, and indicate very similar 00-energies to those found for the dyads. Similar to the dyads, neither the NDI acceptor nor the TAA donors of the triads can be selectively excited and the TAA/NDI ratio might be reflected in the excitation.

3.2.4.1.3   Transient Absorption Spectroscopy

All presented cascades do not exhibit any fluorescence due to the quenching of the excited state by photoinduced electron transfer. In order to elucidate the dynamics of electron transfer processes in the excited state, and of other nonradiative processes upon photoexcitation, transient absorption spectroscopy measurements were performed in the ns- as well as in the fs-time regime. Therefore, two different pump-probe setups were used. While the latter enables examinations of processes

from ca. 100 fs up to 8 ns, the former enables investigations from 2 ns to several μs. The dynamics following the photoexcitation will be described step by step until relaxation to the electronic ground state. Thus, the results of the fs-measurements will be discussed first, which should comprise the charge separation process and an analysis of the ns-measurements will than describe the charge recombination processes and ISC.

fs-Transient Absorption

To shed light on the possible CT and CS state formation processes in the cascades, fs-measurements in toluene and MeCN were performed for **Db** and **T-CN** and for **T-Cl** in MeCN only. All cascades were excited with 140 fs pulses at 26300 cm^{-1} (380 nm) to prevent population of higher excited states. The optical changes were probed by a white light continuum (140 fs) between 12500 cm^{-1} (800 nm) and 25000 cm^{-1} (400 nm). The transient absorption spectra corrected for white light dispersion (chirp) given in Figure 49 – Figure 51 consist exclusively of excited state absorption (ESA) and evolve in time.

For **Db** in toluene, the rise of a broad band is found first extending from 12500 cm^{-1} (800 nm) up to 25000 cm^{-1} (400 nm) with a pronounced maximum at 21100 cm^{-1} (470 nm). After ca. 1.5 ps, the spectra sharpens and the characteristic bands of the NDI radical anion[173,324] at ca. 21000 cm^{-1} (475 nm) and ca. 16400 cm^{-1} (610 nm) emerge. A third weak and broad band at ca. 13500 cm^{-1} (740 nm) might be partly caused by the NDI radical anion but also by the absorption of a TAA radical cation.[167] All these bands rise within the first 10 ps and from then on decrease.

In MeCN **Db** behaves rather differently. At first an intensive band at ca. 16900 cm^{-1} (590 nm) rises. This band has its maximum intensity at ~1.3 ps and is caused by the ^{1}NDI state. This band is replaced by an even stronger one at 16600 cm^{-1} (600 nm) together with a very intense band at 21100 cm^{-1} (470 nm). Similar to the pump-probe measurements in toluene these two bands are assigned to the NDI radical anion. In parallel a broad band around 14300 – 12500 cm^{-1} (700 – 800 nm) rises, which is caused by the TAA radical cation.

Thus, a CS state is formed which decays within ~100 ps and gives rise to weak and broad ESA around 22200 cm^{-1} (450 nm), which were assigned to a ^{3}NDI state.

The spectra of **T-CN** in toluene develop quite similarly to **Db** in toluene except that all bands are marginally broader for **T-CN** (see Figure 49 and Figure 50). Also in MeCN the evolution of the spectra of **T-CN** and **T-Cl** are nearly identical to the ones of **Db** in MeCN.

Figure 49: fs-Transient absorption spectra corrected for chirp and scattered light of Db in MeCN (A) and toluene (B) at 26300 cm^{-1} (380 nm) pump energy and related transient absorption decays at 21100 cm^{-1} (470 nm) in MeCN (C) and toluene (D). Early spectra are given in dark blue, later spectra in red.

Figure 50: fs-Transient absorption spectra corrected for chirp and scattered light of T-CN in MeCN (E) and toluene (F) at 26300 cm⁻¹ (380 nm) pump energy and related transient absorption decays at 21100 cm⁻¹ (470 nm) in MeCN (G) and toluene (H). Early spectra are given in dark blue, later spectra in red.

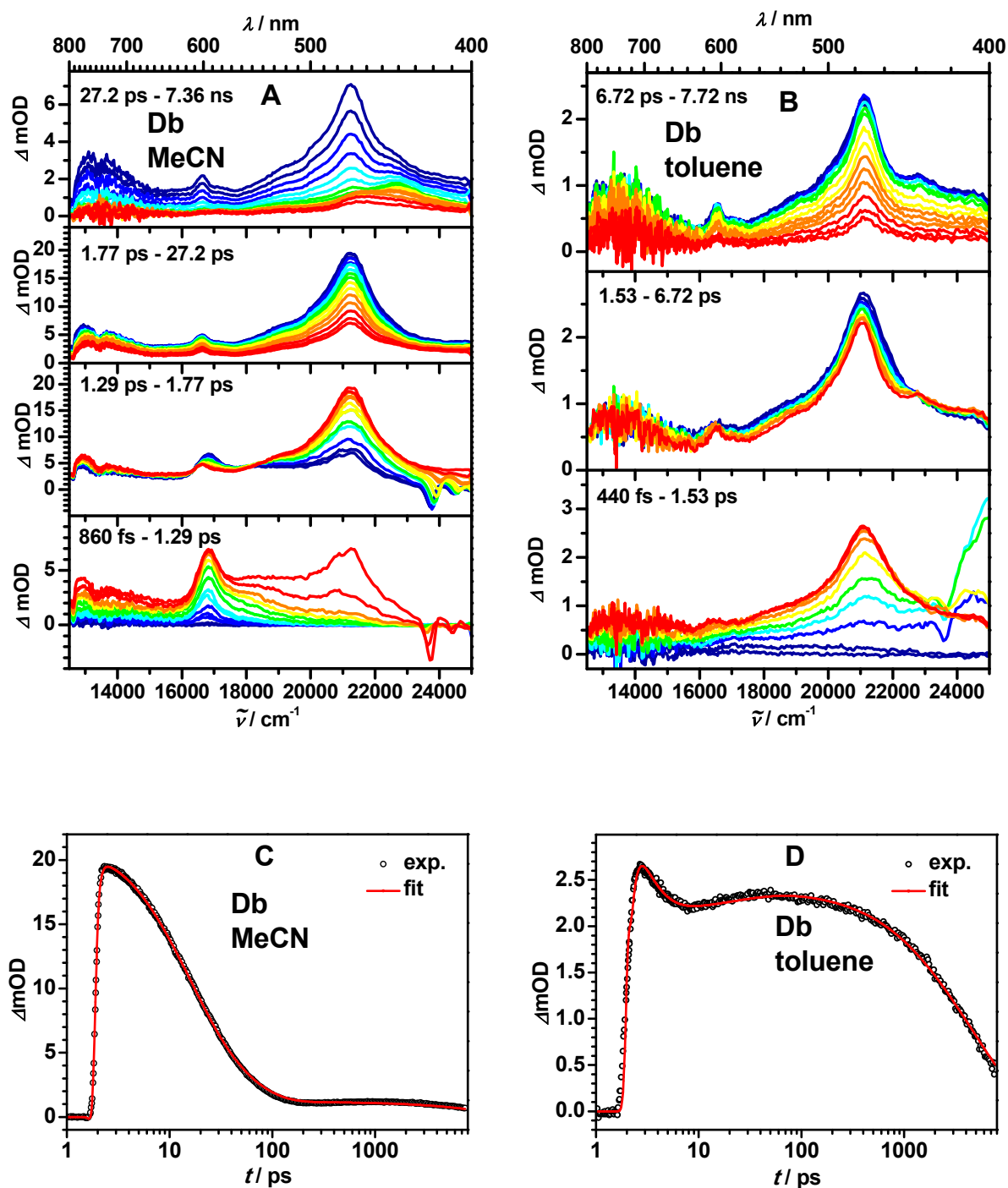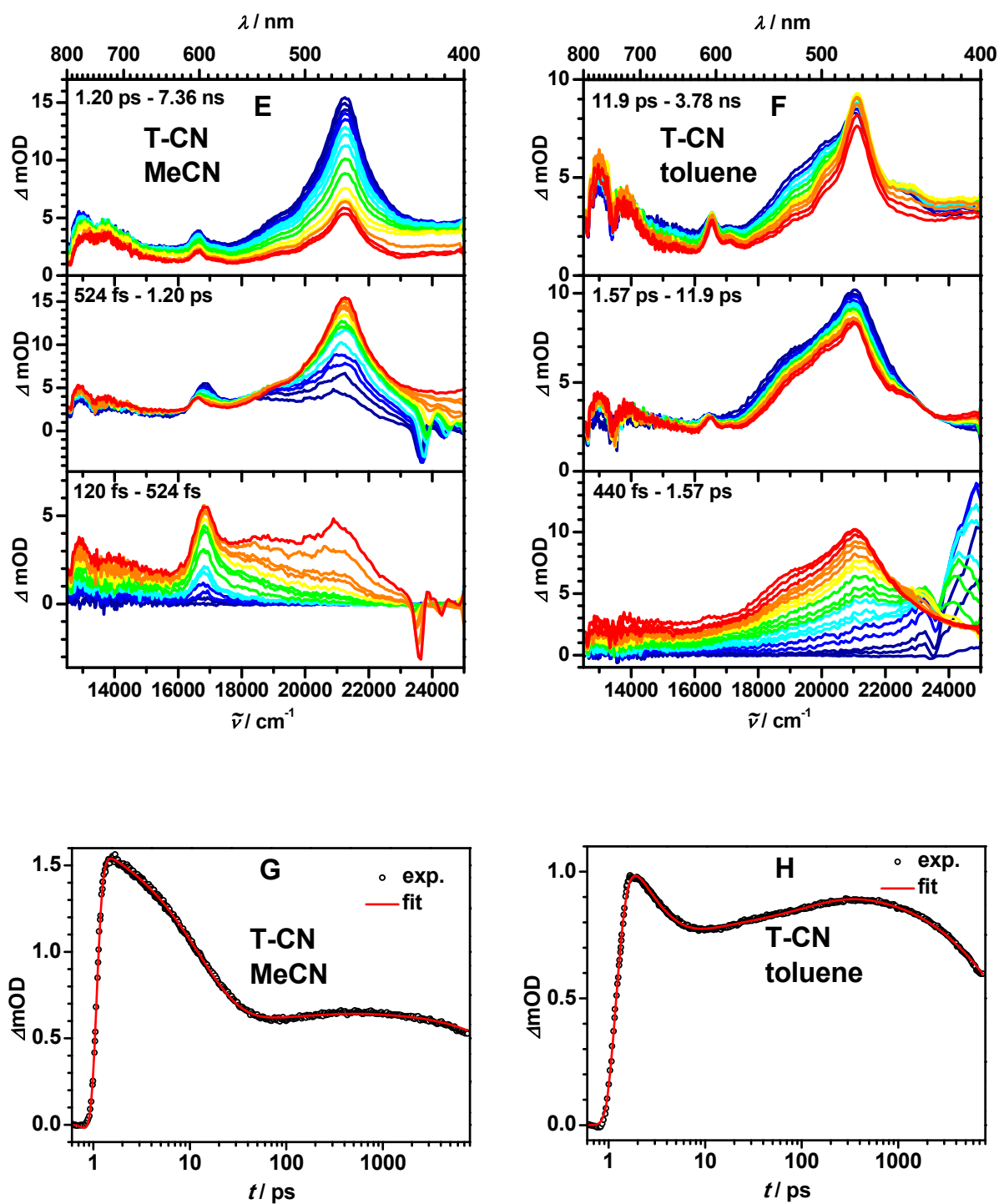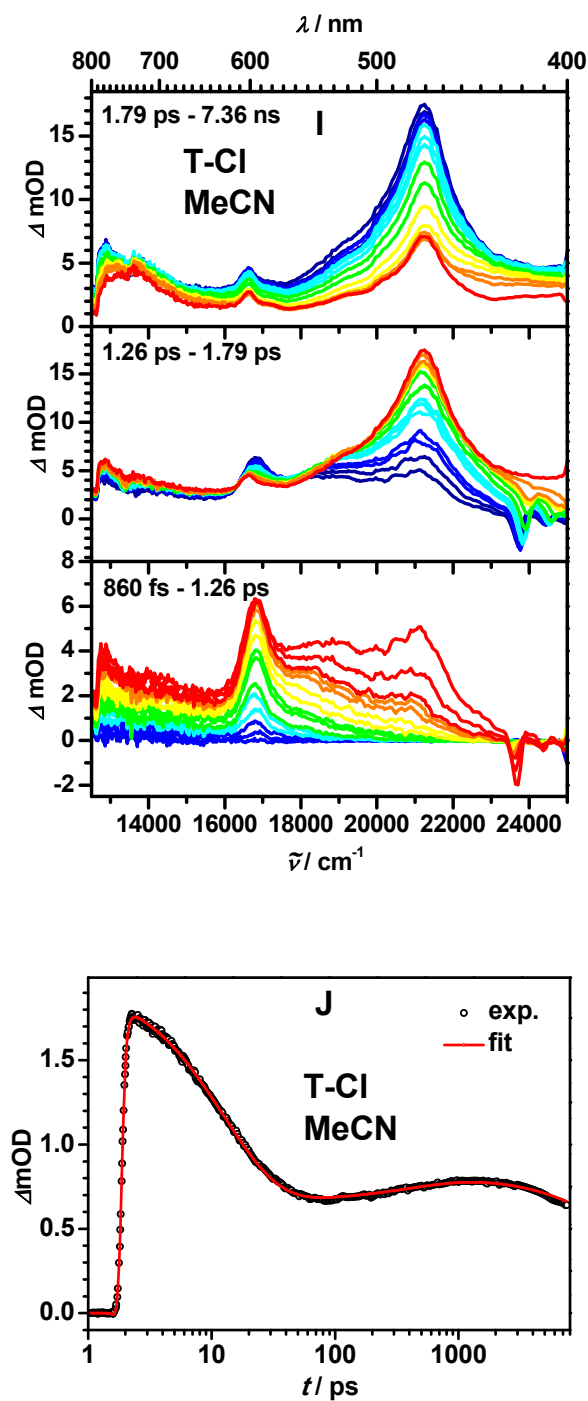**Figure 51:** fs-Transient absorption spectra corrected for chirp and scattered light of T-Cl in MeCN (I) at 26300 cm^{-1} (380 nm) pump energy and related transient absorption decay (J) at 21100 cm^{-1} (470 nm). Early spectra are given in dark blue, later spectra in red.

ns-Transient Absorption

In the ns-measurements the cascades were excited with an 8 ns laser pulse at 28200 cm^{-1} (355 nm) and the excited state dynamics were probed by a Xenon flash lamp white light continuum between 12500 cm^{-1} (800 nm) and 25000 cm^{-1} (400 nm). For all dyads and triads in MeCN and toluene the ESA rise with the instrument response (~ 9 ns) and decrease rapidly (see Figure 52). The spectra are dominated by a sharp and intensive band at about 21000 cm^{-1} (475 nm), together with a smaller and less pronounced band at ca. 16400 cm^{-1} (610 nm) related to the NDI radical anion.[173,324] The broad absorption band at ca. 13200 cm^{-1} (760 nm) is assigned to a TAA radical cation but may also features some of the NDI radical anion absorption.[167]

According to the fs-measurements in MeCN, **Db** shows ^{3}NDI state characteristics at the end of the time window (8 ns). Due to signal-to-noise ratio limitations of the ns-measurements this cannot be fully elucidated but it seems reasonable to consider that the dynamics of **Db** in the ns-measurement in MeCN consist of the CS and the ^{3}NDI state since the spectra at least at the beginning clearly show the NDI anion and the TAA cation features. This might be caused by the long instrument response function of the ns-set-up, which is ca. 9.6 ns. Thus, the lifetimes of the fs-measurements are considered to be more accurate.

To compare the result from the fs-transient absorption measurement with those from the ns-transient absorption measurement, the normalised transient absorption spectra at t = 0 and after longer delay times, where only the long-lived specie persists, are presented in Figure 60 and Figure 60, p: 194.
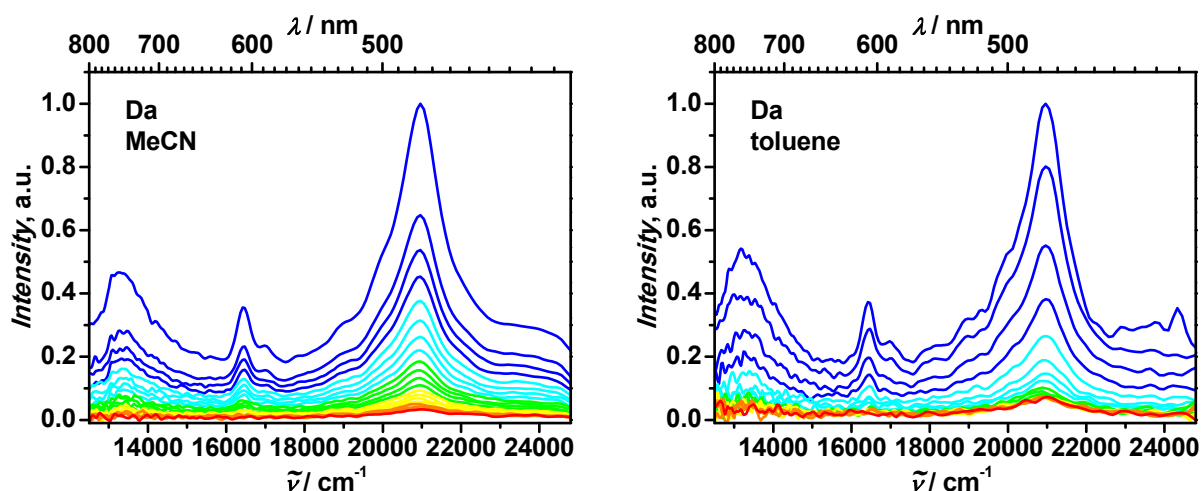
Figure 52: Continued
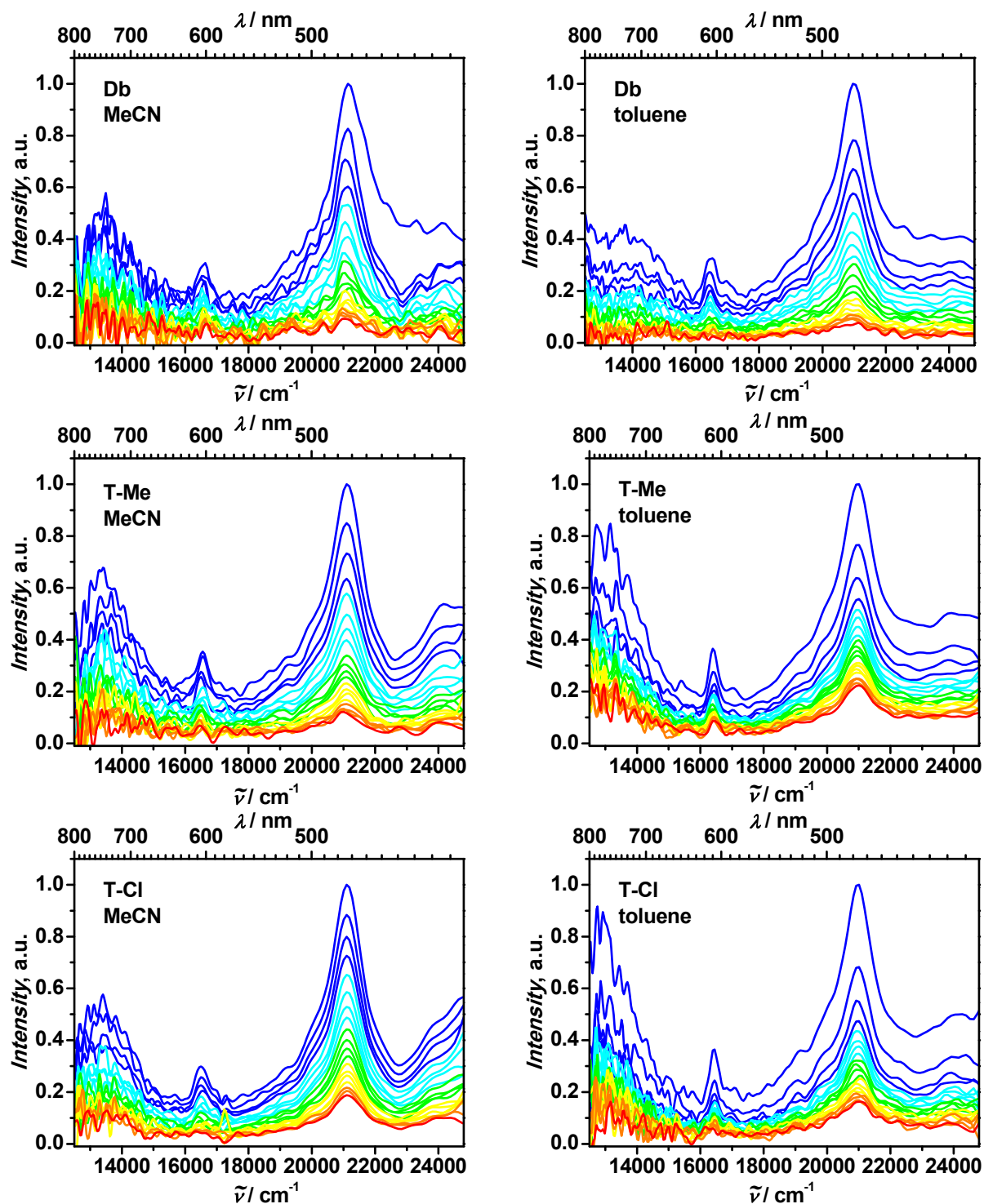
Figure 52: Continued
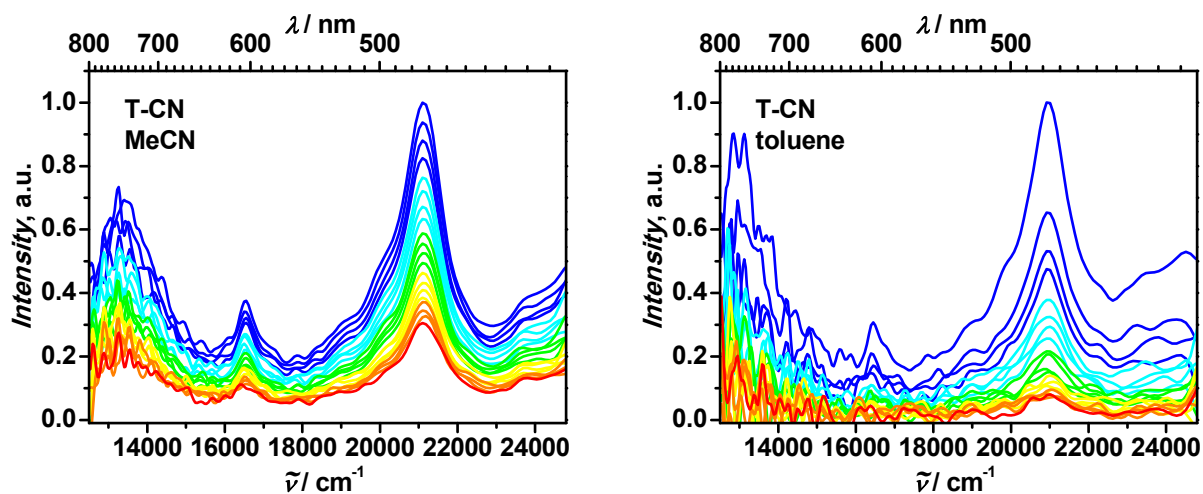
Figure 52: Normalised ns-transient absorption spectra in MeCN and toluene of the cascades at 28200 cm^{-1} (355 nm) pump energy. Early spectra are given in dark blue, later spectra in red.

The lifetimes extracted from the biexponential tail and reconvolution fits at 21000 cm^{-1} (475 nm) (see Figure 53) are listed in Table 14 and Table 15. In toluene the transient absorption bands all decay biexponentially with almost identical time constants for both dyads, a long one (τ_{long}) in the μs-time regime, which is strongly oxygen sensitive and a short one (τ_{short}) in the ns-time regime, which is only slightly influenced by remaining oxygen in the sample. That might be a hint to the existence of singlet and triplet species, which will be discussed below. For the triads in toluene both lifetimes are in the ns-time regime with τ_{short} around 20 – 50 ns and τ_{long} around 300 – 600 ns. In MeCN both lifetimes are quite similar with a slightly shorter lifetime of ca. 100-300 ns and a longer lifetime of ca. 350 – 800 ns.
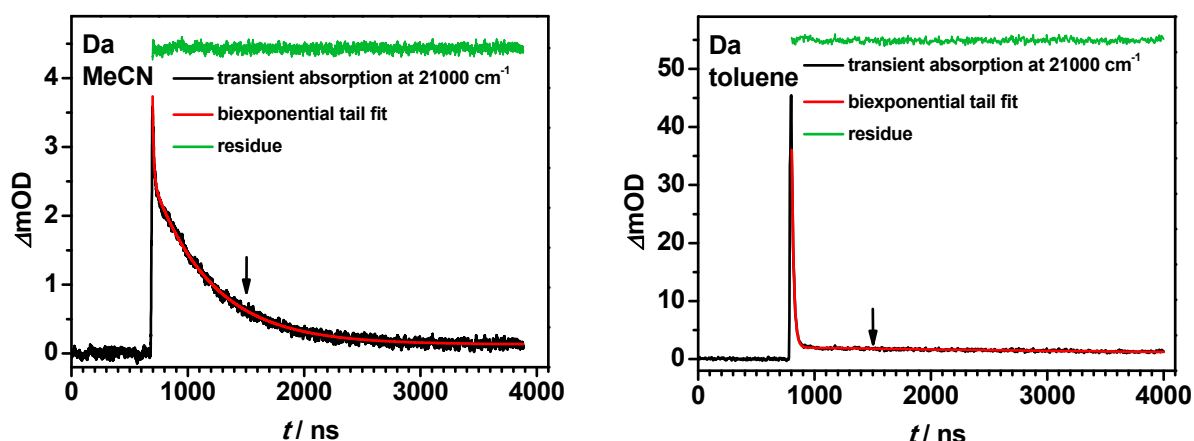
Figure 53: Continued
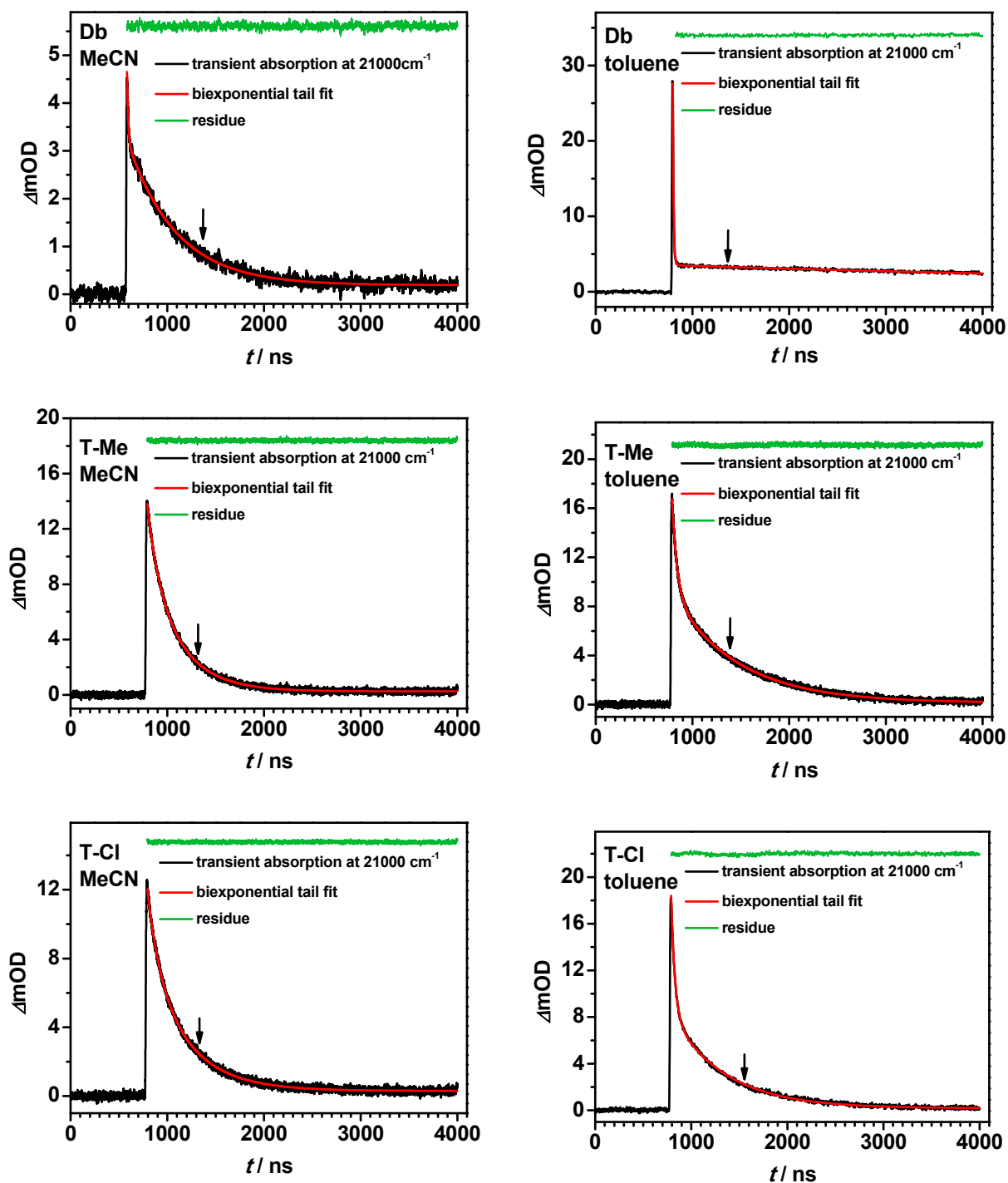
Figure 53: Continued
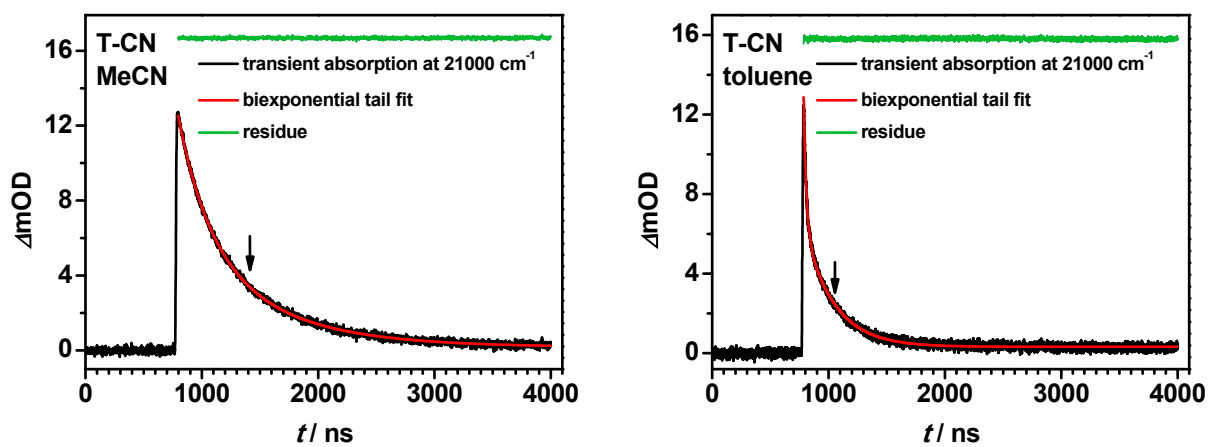
Figure 53: Biexponential tail fits of the ns-transient absorption kinetics of the dyads and triads in MeCN and toluene pumped at 28200 cm^{-1} (355 nm) and probed at 21000 cm^{-1} (475 nm). The arrows mark the delay times after which the normalised transient absorption spectra in Figure 59 and Figure 60, p: 194, are taken.

Table 14: **Lifetimes and Ratio of Amplitudes of ns-Transient Absorption Experiments of the Dyads at a given Concentration and Laser Pulse Energy at 28200 cm^{-1} (355 nm), Assuming an Independent Biexponential Decay at 21000 cm^{-1} (475 nm).**

	c	E	a_{long}/a_{short}	τ_{long}	τ_{short}
	/M	/mJ		/ns	/ns
toluene					
Da	2.5 x 10^{-5}	1.2	0.079	5.9 x 10^3	18
	1.1 x 10^{-5}	1.2	0.025	6.7 x 10^3	18
	5.9 x 10^{-6}	1.2	0.035	7.7 x 10^3	19
	2.9 x 10^{-6} [a]	1.2	0.032	8.6 x 10^3	19
MeCN					
	8.9 x 10^{-6}	1.2	0.99	510	12
	9.4 x 10^{-6}	1.2	0.99	490	12
	7.2 x 10^{-6}	1.2	1.2	490	16
	6.6 x 10^{-6}	1.2	0.91	490	12
toluene					
Db	1.1 x 10^{-5}	1.2	0.069	7.8 x 10^3	8.7
	1.0 x 10^{-5}	1.2	0.078	8.5 x 10^3	6.1
	5.3 x 10^{-6}	1.2	0.069	9.8 x 10^3	6.1
	3.1 x 10^{-6}	1.2	0.063	1.0 x 10^4	6.8
	2.1 x 10^{-6} [a]	1.2	0.057	1.2 x 10^4	7.8
MeCN					
	7.7 x 10^{-6}	1.0	1.0	510	9.3
	9.7 x 10^{-6}	1.0	0.78	500	8.8
	4.7 x 10^{-6}	1.0	0.79	520	8.9
	4.7 x 10^{-6}	1.0	0.80	510	8.6

[a] used for the simulation with the TENUA[280] program to obtain the rate constants k_S and k_{ST}

Table 15: Lifetimes and Ratio of Amplitudes of ns-Transient Absorption Experiments of the Triads at a given Concentration and Laser Pulse Energy at 28200 cm^{-1} (355 nm), Assuming an Independent Biexponential Decay at 21000 cm^{-1} (475 nm).

	c /M	E /mJ	a_{long}/a_{short}	τ_{long} /ns	τ_{short} /ns
			toluene		
T-Me	5.5 x 10^{-6} [a]	0.80	0.84	710	51
	5.4 x 10^{-6} [a]	0.80	0.92	700	49
	4.0 x 10^{-6} [a]	0.80	0.82	720	52
	3.6 x 10^{-6} [a]	0.80	0.85	680	48
			MeCN		
	5.9 x 10^{-6} [a]	0.80	2.1	340	150
	5.9 x 10^{-6} [a]	0.80	2.0	340	130
	1.8 x 10^{-6} [a]	0.80	1.1	390	150
	1.7 x 10^{-6} [a]	0.80	3.4	300	70
			toluene		
T-Cl[a]	6.0 x 10^{-6} [a]	0.80	0.57	540	36
	5.9 x 10^{-6} [a]	0.80	0.57	540	37
	3.1 x 10^{-6} [a]	0.80	0.56	540	36
	3.0 x 10^{-6} [a]	0.80	0.54	540	35
			MeCN		
	6.7 x 10^{-6} [a]	0.80	1.8	420	130
	6.6 x 10^{-6} [a]	0.80	2.0	460	220
	3.2 x 10^{-6} [a]	0.80	0.81	380	110
	3.0 x 10^{-6} [a]	0.80	1.5	410	120
			toluene		
T-CN[a]	6.4 x 10^{-6} [a]	0.80	0.60	260	21
	6.3 x 10^{-6} [a]	0.80	0.63	260	22
	3.8 x 10^{-6} [a]	0.80	0.51	300	22
	3.7 x 10^{-6} [a]	0.80	0.56	260	21
			MeCN		
	5.5 x 10^{-6} [a]	0.80	0.81	770	290
	5.2 x 10^{-6} [a]	0.80	0.92	740	270
	3.0 x 10^{-6} [a]	0.80	0.99	750	260
	2.9 x 10^{-6} [a]	0.80	3.5	670	220

[a] used for the simulation with the TENUA[280] program to obtain the rate constants k_S and k_{ST}

No concentration dependence was found for the dyads in MeCN and triads in MeCN and toluene, but the sample concentration could not significantly varied due to the signal-to-noise ratio of the ns-transient absorption setup used here. However, for the dyads in toluene a decrease of τ_{long} up to ~35 % with increasing concentration (2.1 x 10^{-6} M to 1.0 x 10^{-5} M) is observed (see Table 14). A reasonable explanation for this finding is a bimolecular deactivation process. Thus τ_{long} consists of two rate constants k_{di} (rate constant for diluted concentrations) and k_{da} (rate constant for bimolecular deactivation). Indeed, a plot of $1/\tau_{long}$ as a function of concentration leads to a linear correlation. The slope of the linear regression gives k_{da} and the intersection with the $1/\tau_{long}$ axis yields k_{di} ((k_{di}(**Da**): 1.0 x 10^7 s^{-1}, k_{di}(**Db**): 7.7 x 10^8 s^{-1}). The values of k_{da} (k_{da}(**Da**): 4.7 x 10^9 s^{-1}, k_{da}(**Db**): 4.3 x 10^9 s^{-1}) are in the typical range for a diffusion controlled bimolecular deactivation process (see Figure 54).[120]
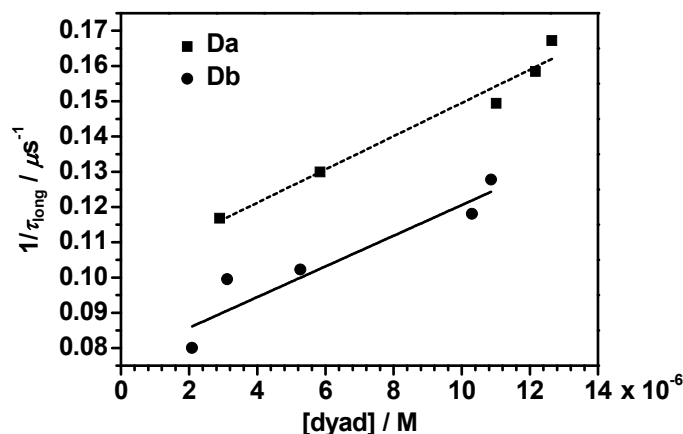
Figure 54: Plot of $1/\tau_{long}$ vs concentration of **Da** and **Db** in toluene from linearisation of $\tau_{long} = 1/(k_{di}+k_{da}[dyad])$ for a bimolecular deactivation process.

As suspected from the O_2-sensitivity of the excited state lifetimes, the dynamics of the cascades are strongly influenced by singlet-triplet interactions and therefore magnetic field dependent transient absorption spectroscopy were performed for **Db** and **T-CN** in toluene. Upon stepwise increase of the magnetic field from 0 to ca. 2000 mT, no significant effect could be observed for **Db**. However, the transient absorption decay of **T-CN** is strongly magnetic field dependent (see Figure 55). From 0 mT to 2000 mT all transient absorption decays show biexponential kinetics but the corresponding lifetimes τ_{short} and τ_{long} are change with increasing magnetic field. With an applied magnetic field of 1 mT τ_{short} becomes significantly longer and τ_{long} becomes only slightly longer compared to the zero-field lifetimes. From then on τ_{short} starts to decrease while τ_{long} simultaneously starts to increase with increasing field until changes of the decay become insignificant at higher fields (>30 mT).

Figure 55:   **Normalised biexponential reconvolution fits of the ns-transient absorption decays of T-CN in toluene 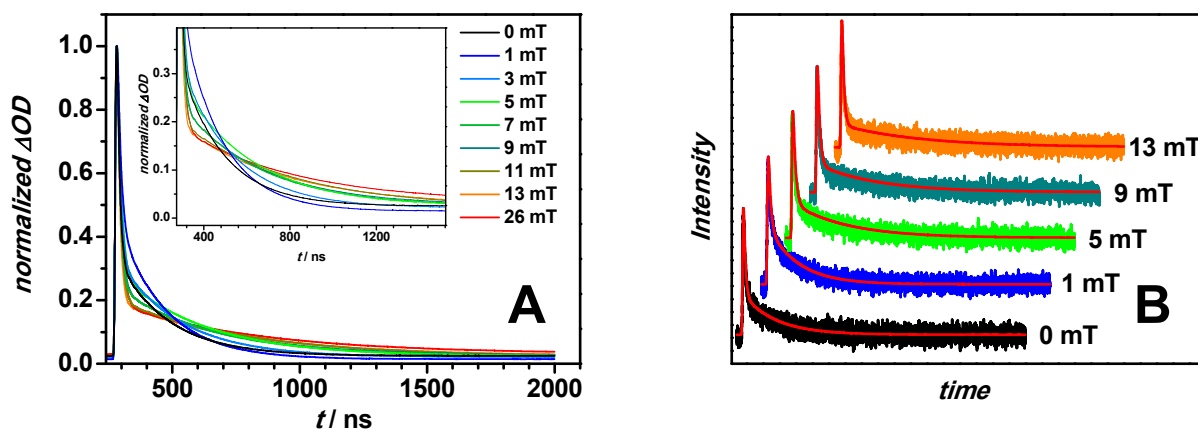with increasing magnetic field (A) and of related experimental decays with biexponential reconvolution fits for selected magnetic fields (B).**

3.2.4.2   Discussion

From the results presented in the preceding section, it is obvious that upon photoexcitation of the cascades an electron is transferred from the TAA to the NDI. This leads to the formation of CS states with lifetimes of several ns to μs.

Before the diverse photophysical processes in the dyads and triads can be discussed, estimating of the relative state energies is required, as these data will determine the ET dynamics to a large extent.

The energies of the CS state formed in the dyads are expected to be somewhat different, as the redox potentials of the TAA in **Da** and **Db** differ, which in turn leads to different ΔG^0_{CS} values. These ΔG^0_{CS} values of the CS states were calculated using the redox potentials derived from the CV experiment (Table 13, p: 168) and the *Weller* equation (71)[325].

$$\Delta G^0_{CS} = \frac{N_A z e}{1000}(E^{ox}_{1/2} - E^{red}_{1/2}) - \frac{N_A e^2}{4000 \pi \varepsilon_0}\left(\left(\frac{1}{2r_D} + \frac{1}{2r_A}\right)\left(\frac{1}{\varepsilon_r} - \frac{1}{\varepsilon_s}\right) + \frac{1}{\varepsilon_s d_{DA}}\right) \quad\quad (71)$$

where

N_A is *Avogadro's* constant, e is the elementary charge, ε_0 is the is vacuum permittivity, ε_s is the permittivity of the solvent used for spectroscopic measurements, ε_r is the permittivity of the solvent used in the electrochemical measurements, z is the number of transferred electrons, r_D and r_A are the radii of the donor and the acceptor, respectively, and d_{DA} is the electron transfer distance.

The radii of the donor r_D (= 4.81 Å) and the acceptor r_A (= 3.97 Å) were estimated from the Connolly Molecular Surfaces of the moieties using the ChemBio3D Ultra[307] software. For the electron transfer distances d_{DA} the distance between the chromophore centres were used, which were determined by calculating the geometries of the cascades using at B3LYP/6-31G* level of theory (see Figure 56).[a]

The triads may form two different CS states, in which either the intermediate TAA1 (CS1) or the terminal TAA2 (CS2) are oxidised and the NDI is reduced. As a result of the very similar $E_{1/2}$ values for the reduction of the NDI and for the oxidation of the MeO-TAA, the CS2 states of all triads possesses almost the same free energy (ΔG_{CS}^0). The higher energy CS1 states differ in the free energies between the triads according to the different substituents (Me, Cl, CN) attached to the TAA1.

For estimating of the ΔG_{CS}^0 values of the CS1 states the distance obtained for the dyads (d_{AD} = 16.7 Å) was used. Because the CS2 energies are strongly distance dependent and since the triads are flexible in solution, the CS2 energies were calculated assuming two different conformers (see Figure 56). One of these conformers is highly bent and has a chromophore-distance of 22.5 Å and the other is elongated with a distance of 28.0 Å. The two structures may serve to estimate the smallest and the largest possible distance and, thus, the range of possible CS2 energies. The corresponding free energies of all states are listed in Table 16.

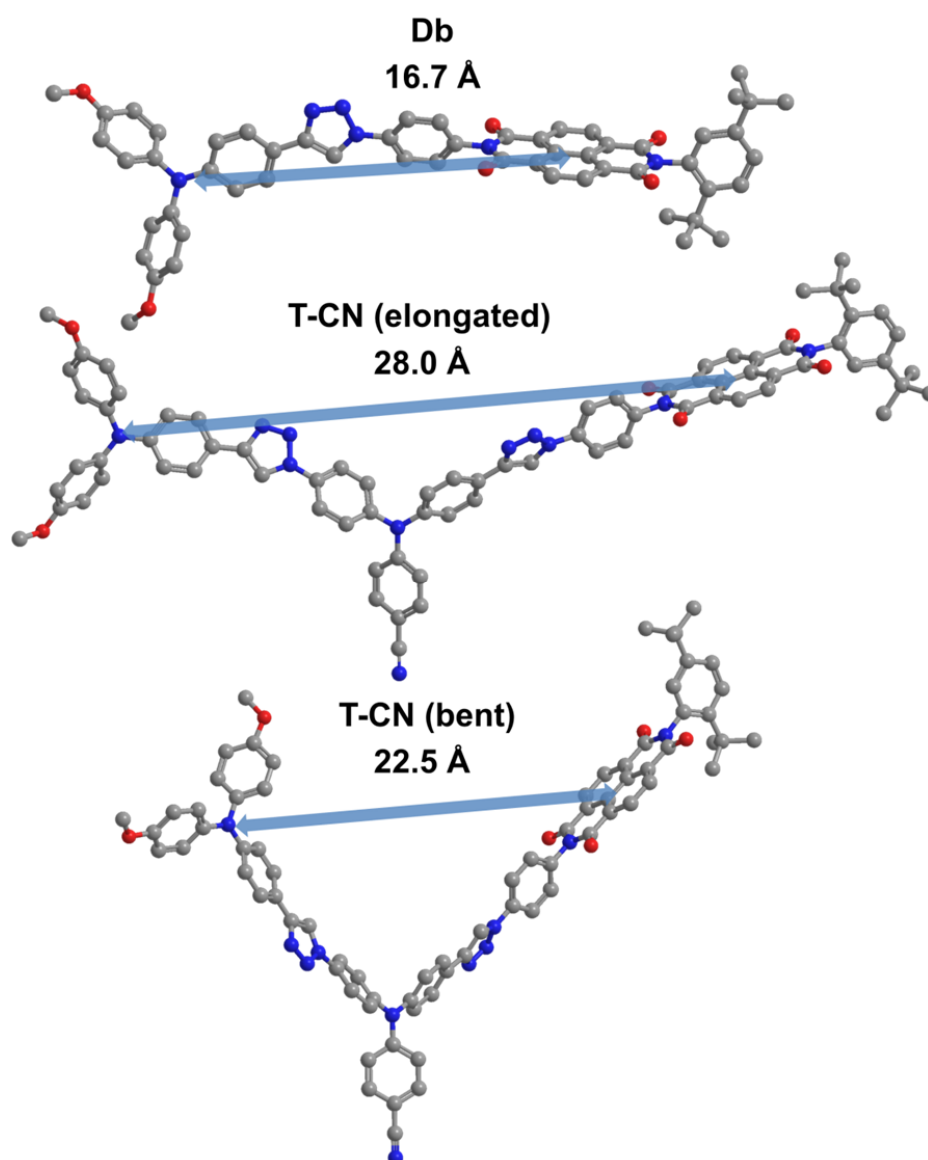[a] Calculations were performed in our group by *M. Holzapfel*.

Figure 56: Optimised structure of Db and T-CN in an elongated and a strongly bent conformation using DFT at B3LYP/6-31G* level of theory.

Table 16:   **Free Energies ΔG_{CS}^0 of the CS States Estimated by *Weller* Equation and the $E_{1/2}$ Values given in Table 13, p: 168.**

			ΔG_{CS}^0 / eV	
			toluene	MeCN
Da			1.97	1.01
Db			1.88	0.93
T-Me	CS1		2.18	1.23
	CS2	*bent*	1.99	0.94
		elongated	2.04	0.95
T-Cl	CS1		2.26	1.30
	CS2	*bent*	1.97	0.92
		elongated	2.02	0.93
T-CN	CS1		2.41	1.46
	CS2	*bent*	1.97	0.92
		elongated	2.02	0.93

Next, the photophysical processes monitored by fs-transient absorption will be discussed. For this reason the number of individual spectral components *n* were determined from the transient (wavenumber x time) maps by singular value decomposition. Subsequently the time resolved spectra were globally fitted with GLOTARAN[238] employing the target models presented in Figure 57, the IRF was treated as a Gaussian shaped function (ca. 150 fs), corrected for the white light dispersion (chirp) and the coherent artefact (the models used have the time characteristics of the IRF) at time zero to give species associated difference spectra (SADS) and their related time constants (Figure 58 and Table 17, p: 191). In this target model the efficiencies were adjusted in order to obtain equal absorption intensity of the NDI radical anion at 21000 cm^{-1} (475 nm).
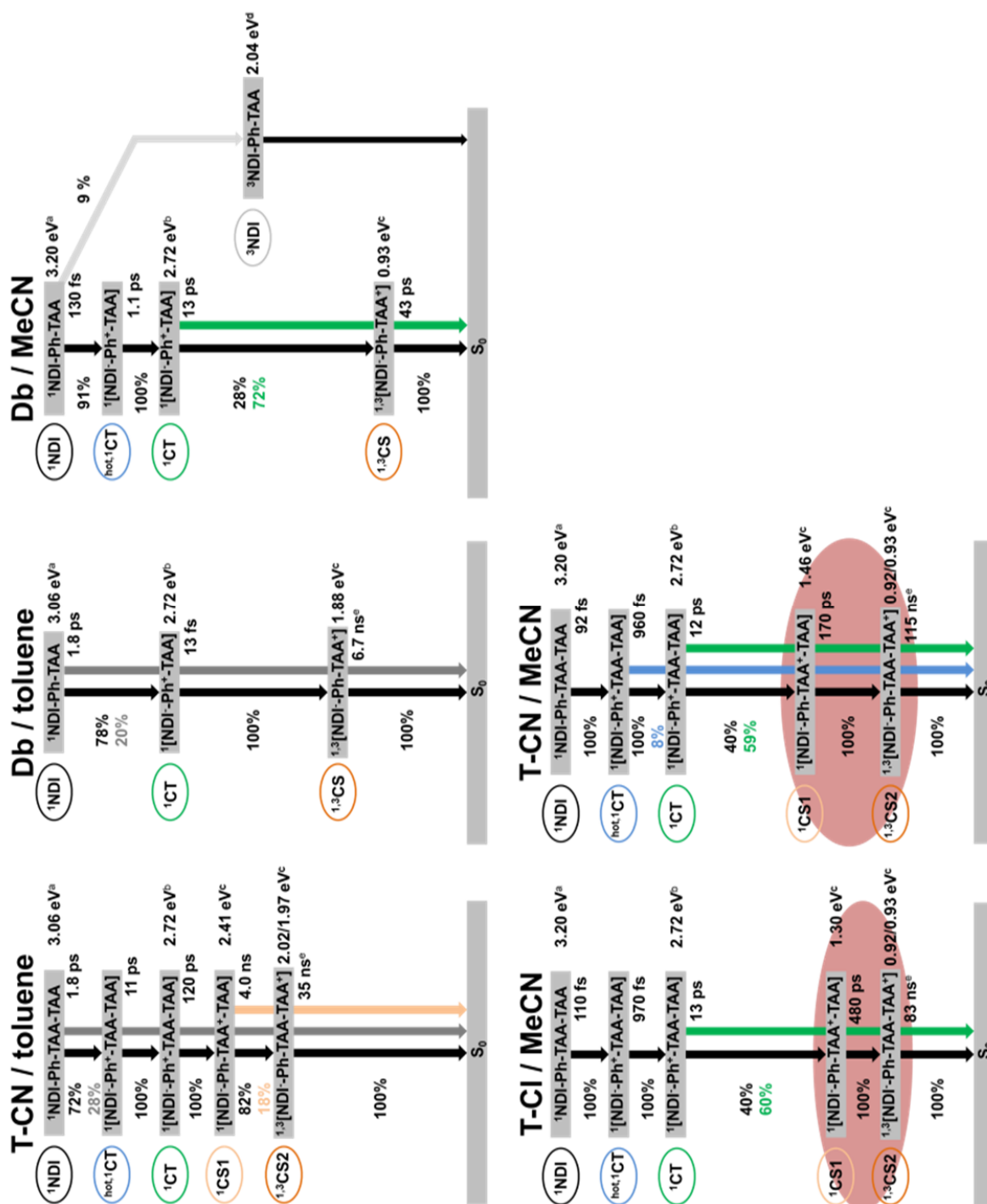
Figure 57: Energy schemes and dynamics of the photophysical processes upon excitation at 26300 cm^{-1} (380 nm) of Db, T-Cl and T-CN in MeCN and of Db and T-CN in toluene. [a] Taken from the rising edge of the absorption band of 22 in MeCN or toluene. [b] Taken from the rising edge of the high energy side of the fluorescence band of NDI.[175] [c] State energies estimated by the *Weller* approach (Table 16). [d] Taken as the average of the triplet energy of NDI in in EtOH at 77 K (2.03 eV)[326] and in 2-methyltetrahydofuran at 77 K (2.05 eV)[327]. [e] Lifetimes estimated as 1/k_s, extracted from TENUA[280] fits of the ns-measurements.

Before the photophysics of the triads could be discussed, first the process occurring in **Db** need to be elucidated to provide the basis for a better understanding of the processes taking place in the triads.

In MeCN **Db** gives five SADS corresponding to five lifetimes. The first SADS with a lifetime of 130 fs exhibits the typical features of the NDI singlet excited state (^{1}NDI), a distinct maximum at 16900 cm^{-1} (590 nm) with a shoulder at 18200 cm^{-1} (550 nm) and a broad band at ca. 21750 cm^{-1} (460 nm).[174] Thus, although both NDI and TAA absorb to some extend at the pump energy, only the NDI is excited, which probably is a consequence of ultrafast energy transfer from the TAA to the NDI within the instrument response time. The ^{1}NDI is followed by a SADS presenting an intense absorption at 21100 cm^{-1} (470 nm) and a weaker is at 16400 cm^{-1} (610 nm), respectively, that decays within 1.1 ps into a very similar SADS but with obviously sharper absorption. These signals are characteristic of the NDI radical anion[173,324] and those SADS can be assign to a hot charge transfer (^{hot}CT) state where the negative charge is located on the NDI and the positive charge on one of the phenyl groups attached to the nitrogens, relaxing in 1.1 ps into the vibrational CT ground state (^{cool}CT).[175]

At this point it has to be stressed that while there is a strong evidence for the NDI radical anion formation, on the position of the corresponding positive charge in the CT states can only be speculated. From the phenyl group the positive charge is then transferred with τ = 13 ps to the TAA forming a charge separated state, which is indicated by the appearance of a broad TAA radical cation band at ca. 13300 cm^{-1} (750 nm), well-described in literature.[167] From this CS state charge recombination occurs in 43 ps. The longest lasting SADS with an (in the fs-experiment) infinitely long lifetime is related to the triplet NDI state, with its typical double absorption maxima at 22700 cm^{-1} (440 nm) and 21750 cm^{-1} (460 nm), populated *via* an additional pathway directly starting from the ^{1}NDI state.[175] According to this target model, the CS state is formed in only 25 % quantum yield.

In toluene **Db** possesses three SADS. The first SADS features a broad absorption band which reaches up to 12500 cm^{-1} (800 nm) but exhibits a pronounced maximum at 21100 cm^{-1} (470 nm). This SADS can be assigned to the localised excited NDI, which appears to have a different spectral characteristic in toluene compared to MeCN. Within 1.8 ps the ^{1}NDI is transformed into a CT state, as indicated by the rise of the typical NDI radical anion band at 21000 cm^{-1} (475 nm) and the weaker absorption at 16400 cm^{-1} (610 nm). This CT state has a lifetime of only 13 ps, then the charge is transferred to the TAA and a CS state with a lifetime of 4.6 ns is populated. This is suggested by the small shift of the weak NDI radical anion band from 16400 cm^{-1} (610 nm) to 16600 cm^{-1} (600 nm) and by the increased intensity of the broad band at ca. 13000 cm^{-1} (770 nm).
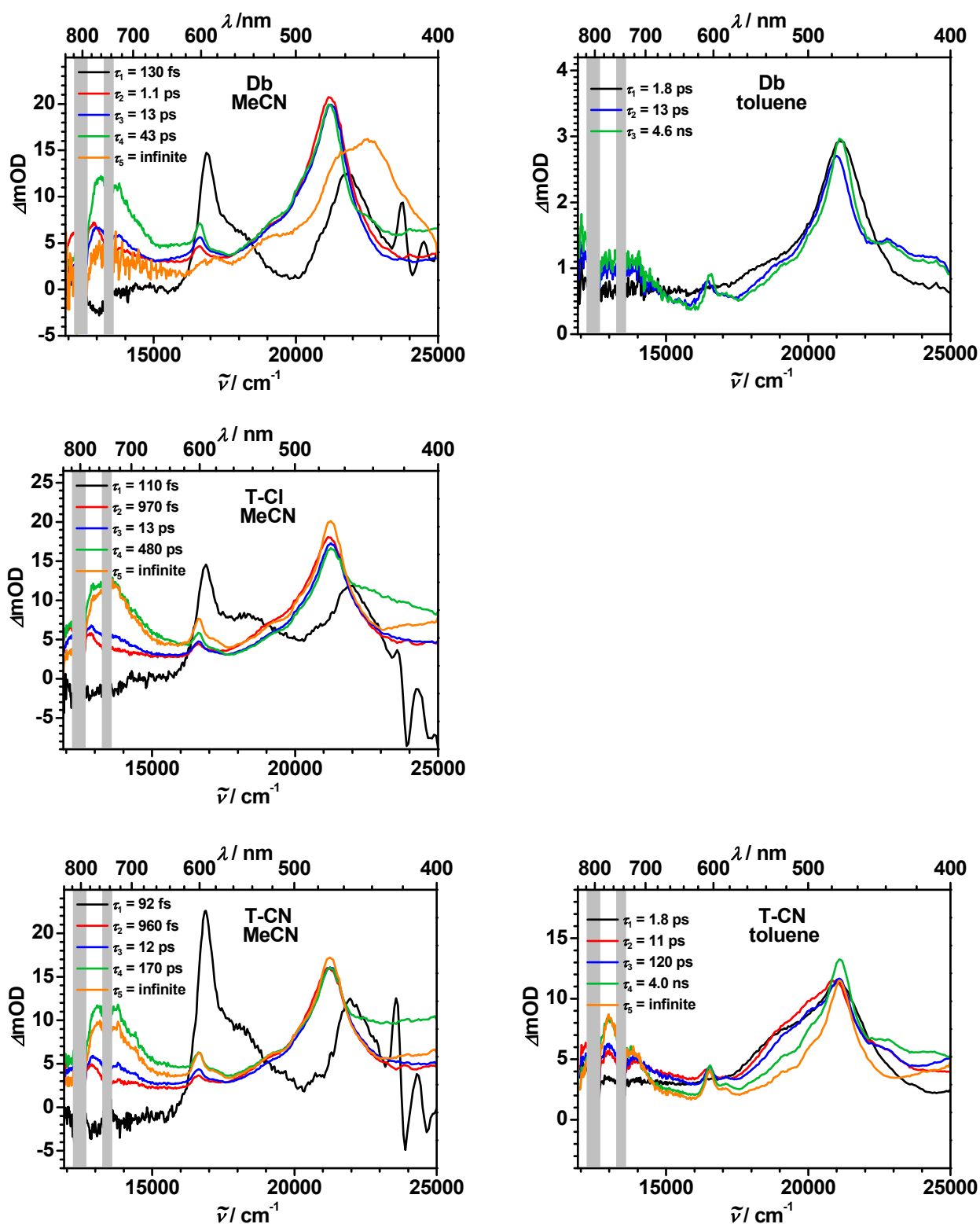
Figure 58: Species associated difference spectra (SADS) of Db, T-CN and T-Cl in MeCN and of Db and T-CN in toluene at 26300 cm^{-1} (380 nm) pump energy. The grey bars hide stray light of the fundamental wavenumber of the laser at 12500 cm^{-1} (800 nm) and the second order signal from the pump pulse at 13200 cm^{-1} (760 nm).

With this information at hand, now the processes occurring in the triads can be discussed. Similar to **Db**, the first SADS for **T-CN** in MeCN is assigned to the ^{1}NDI that decays with a lifetime of 93 fs into a ^{hot}CT followed by relaxation (τ = 960 fs) to the vibrational CT ground state. This state has a lifetime of 12 ps and goes into the CS1 state by transferring the positive charge from the phenyl group to the intermediate TAA1. This process can be monitored by the rise of the TAA radical cation absorption at ca. 13300 cm^{-1} (750 nm). Additional hole transfer with τ = 170 ps to the terminal TAA2 yields the SADS of the CS2 that lives up to the ns-time regime.

The development of SADS spectra of **T-Cl** in MeCN is essentially the same to that of **T-CN**, besides the lifetime for the CS1 state, which is with 480 ps, much longer than in **T-CN** (τ = 170 ps). The redox potentials of the TAA1s are considerably different for **T-CN** and **T-Cl** and thus the differences of the free energies between the CS1 and CS2 states (*cf.* Table 16, p: 187). Accordingly, the CS1–CS2 transition in **T-CN** possesses a higher driving force (ca. 0.14 eV) than in **T-Cl**, resulting in a much shorter lifetime of the CS1 state for **T-CN** compared to **T-Cl**.

Exciting **T-CN** in toluene with 26300 cm^{-1} (380 nm) pump energy first populates the ^{1}NDI similar to the situation in **Db**. This ^{1}NDI has a lifetime of 1.8 ps and decays into a ^{hot}CT, which then relaxes with τ = 11 ps into the ^{cool}CT. From there the CS1 state is populated with τ = 120 ps and finally the CS1 state decays with τ = 4.0 ns into the CS2 state, which has an infinitely long lifetime in the fs-experiment.

From the data given in Table 17, it is obvious that the lifetimes of the particular species of **T-CN** in toluene are significantly larger (by ca. one order of magnitude) compared to those in MeCN.

Table 17: Lifetimes of the SADS Obtained by Global Analysis of the fs-Transient Absorption Map.

		τ_1 (^{1}NDI) /ps	τ_2 (^{hot}CT) /ps	τ_3 (^{cool}CT) /ps	τ_4 (CS1) /ps	τ_5 (CS2) /ns
Db	MeCN	0.13	1.1	13	43	∞[a]
	toluene	1.8	-	13	4.6 x 10^3	-
T-Cl	MeCN	0.11	0.97	13	480	∞
T-CN	MeCN	0.092	0.96	12	170	∞
	toluene	1.8	11	120	4.0 x 10^3	∞

[a] ^{3}NDI state

A comparison of the results from the fs-transient absorption measurement with the normalised transient absorption spectra at t = 0 and after longer delay times from the ns-transient absorption measurement revealed that the first spectra of the triads in MeCN and toluene and of the dyads in toluene show very similar characteristics than the fs-transient absorption spectra after infinite time (see Figure 60 and Figure 60). These are a sharp and intense absorption at ca. 20800 cm^{-1} (480 nm) and a weaker band at 16400 cm^{-1} (610 nm), which are related to the NDI radical anion, and a much broader band at ca. 13200 cm^{-1} (760 nm), related to the TAA radical cation. Thus, the t = 0 spectra of the ns-measurement are related to the lowest energy CS states in the cascades.

The fs-measurements of **Db** in MeCN show a lifetime of 43 ps for the CS state while in the ns-measurement a biexponential decay of the CS state of 9 ns and 500 ns is observed. It is assumed that the shorter component with τ = 9 ns is caused by convolution of the 48 ps with the instrument response (τ ~ 9 ns) and the larger component (τ = 500 ns) is invisible in the fs-measurements because of its small amplitude.

Figure 59: Normalised ns-transient absorption spectra of the dyads in MeCN and toluene at $t = 0$ and after longer time, at which the short component only insignificantly contributes to the spectra (indicated in Figure 53, p: 180). The fs-transient absorption spectra at infinite time are shown for comparison (for Db).
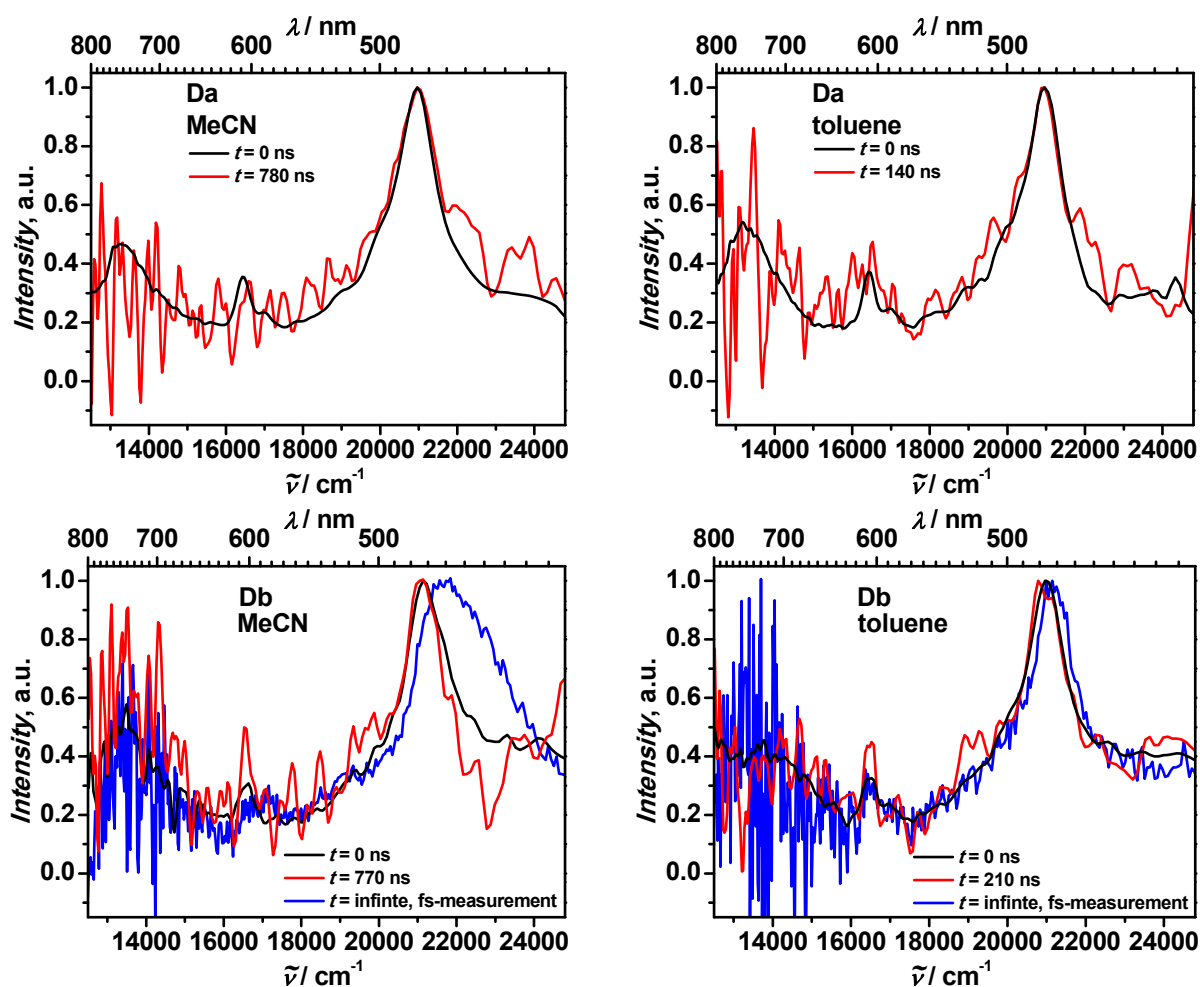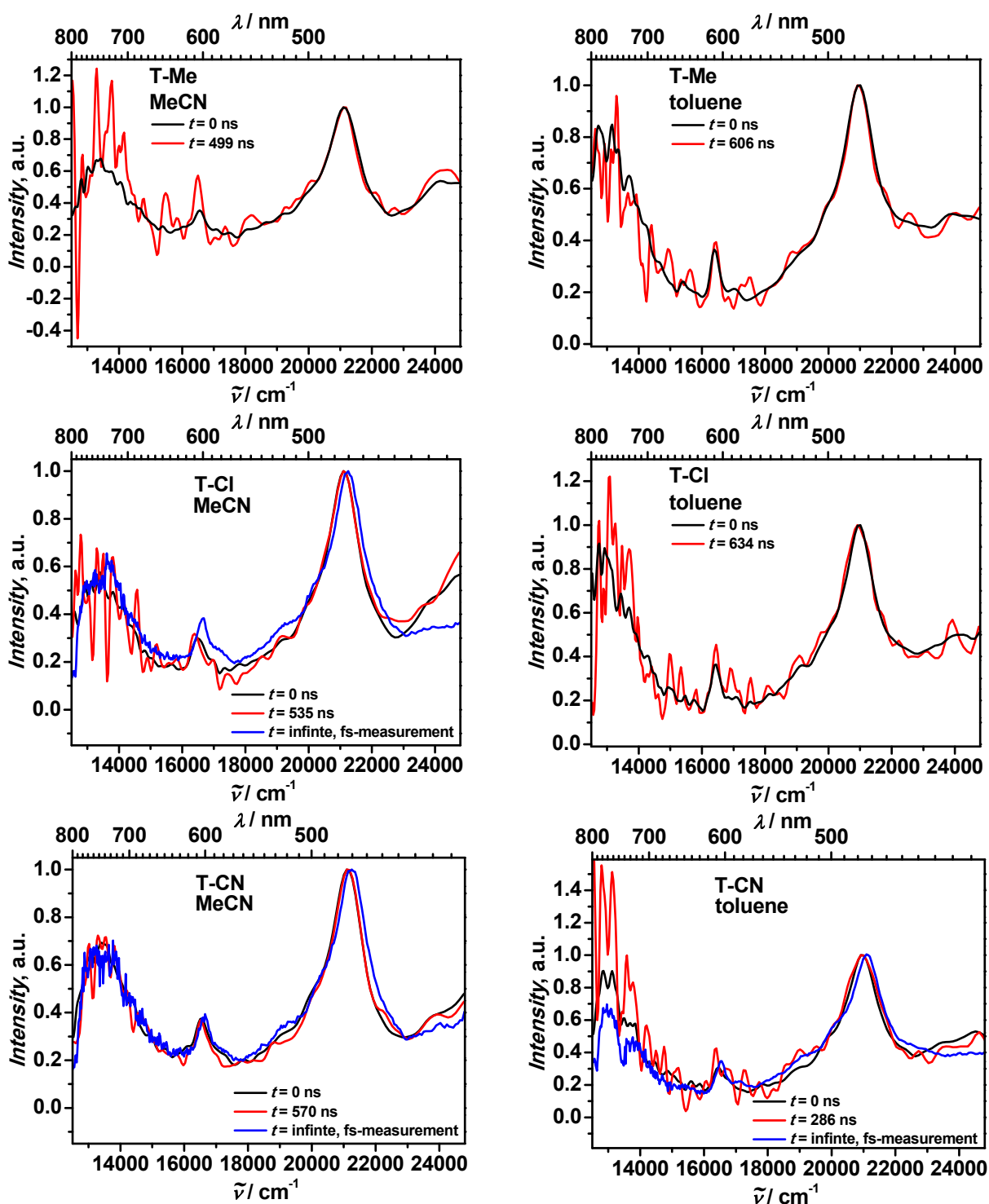
Figure 60: Normalised ns-transient absorption spectra of the triads in MeCN and toluene at $t = 0$ and after longer time, at which the short component only insignificantly contributes to the spectra (indicated in Figure 53, p: 180). The fs-transient absorption spectra at infinite time are shown for comparison (for T-CN in toluene and for T-Cl and T-Me in MeCN).

The sometimes bad signal-to-noise ratio of the spectra at longer delay times complicates an analysis. But it seems obvious that even after delay times, when the short component contributes only insignificantly to the observed spectra, the spectra show similar bands to the spectra at $t = 0$ and are, therefore, also related to a CS state species.

Accordingly, it can be assumed that primarily only the ^{1}CS state is populated, which than undergoes ISC into the ^{3}CS state. Charge recombination to the S_0 state from the ^{3}CS state is spin forbidden and, thus, charge recombination should only take place *via* the ^{1}CS state. This ^{1,3}CS equilibrium is expected to be strongly influenced by a magnetic field since the triplet sublevel start to split at $B > 0$ (see Figure 61).

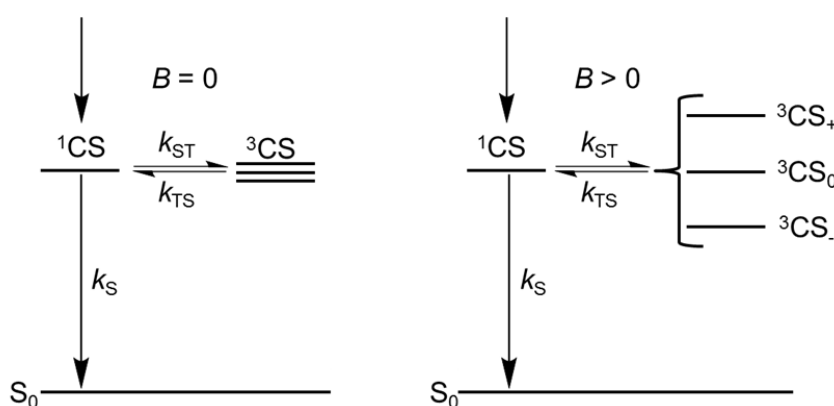**Figure 61:** **Illustration of the singlet-triplet dynamics in a zero magnetic field and a B > 0 situation.**

The spectra of the ^{1}CS and ^{3}CS are indistinguishable and the two states are practically degenerated because of the large distance between the two radical centres.

Appling the kinetic scheme of Figure 61, the deconvoluted decays of all dyads and triads were simulated using the TENUA[280] program and the mechanism given in the appendix, p: 315, to obtain the rate constant for charge recombination k_S and ISC (^{1}CS→^{3}CS) k_{ST}. Herein $k_{ST} = 3k_{TS}$ was set to account for spin statistics of degenerated states.[325] Furthermore, it was assumed that the ^{1}CS state is initially populated. The resulting data are listed in Table 18.

It becomes obvious that k_S is up to one order of magnitude smaller in the triads than in the dyads in toluene (three orders of magnitude in MeCN) whereas k_{ST} in toluene is two orders of magnitude higher. While for **Db** the k_S rate constant differs strongly between MeCN and toluene, for the triads the k_S rates are very similar in both solvents. This might be fortuitous because charge recombination in toluene takes place in the *Marcus inverted* region and in MeCN in the *Marcus normal* region (*vide infra*).

The much slower k_{ST} for the dyads compared to the triads is expected to arise from singlet–triplet splittings (ΔSTs) being larger in the dyads than in the triads (*vide infra*).

Table 18:   Rate Constants of the Charge Recombination (k_S) and the Intersystem Crossing (k_{ST}) Obtained from Simulating the ns-Transient Absorption Decays with TENUA[280].

	toluene		MeCN	
	k_S / s^{-1}	k_{ST} / s^{-1}	k_S / s^{-1}	k_{ST} / s^{-1}
Da	5.3×10^7	3.5×10^5	-	-
Db	1.5×10^8	2.5×10^5	2.3×10^{10a}	-
T-Me[b]	$1.2 \pm 0.01 \times 10^7$	$7.2 \pm 0.06 \times 10^6$	$1.5 \pm 0.23 \times 10^7$	$6.7 \pm 2.51 \times 10^7$
T-Cl[b]	$1.7 \pm 0.01 \times 10^7$	$8.0 \pm 0.16 \times 10^6$	$1.2 \pm 0.10 \times 10^7$	$6.2 \pm 0.19 \times 10^7$
T-CN[b]	$2.9 \pm 0.05 \times 10^7$	$2.0 \pm 0.10 \times 10^7$	$8.7 \pm 0.18 \times 10^6$	$4.7 \pm 0.18 \times 10^7$

[a] k_S for **Db** in MeCN is calculated as $1/\tau_4$, extracted from the fs-measurement. [b] average value of the corresponding fits (given together with the standard deviation (four values)).

The supposed kinetic model of Figure 61 leads to the observed biexponential decay if either ^{1}CS is primarily populated (so-called "relaxation mechanism")[223,328-331] or if ^{3}CS is populated in parallel to ^{1}CS but not if ^{3}CS is primarily populated. In order to support this mechanism, the magnetic field dependent measurements may help.
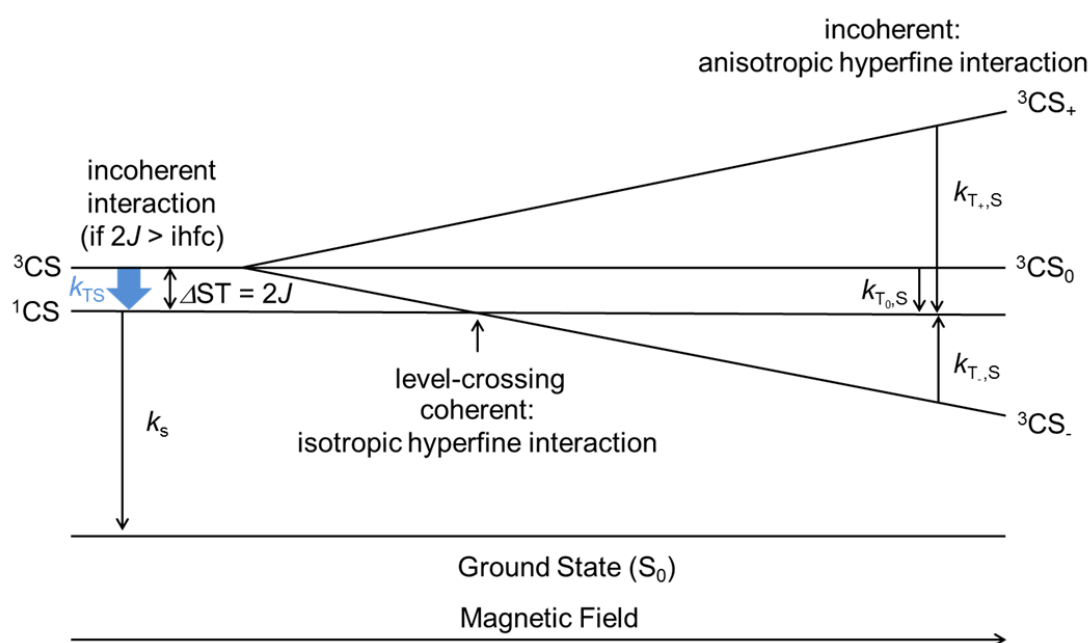

Figure 62:   Singlet and triplet energy levels of the triads as a function of the magnetic field *B*. At applied magnetic field k_{TS} is an average value of the contribution of the rate constants $k_{T_0,S}$, $k_{T_+,S}$ and $k_{T_-,S}$.

In general, in the zero magnetic field situation, the three triplet states are degenerated as long as zero field splitting for organic radicals are neglected. The triplet states are higher in energy by twice the exchange interaction J compared to the ^{1}CS state (the relative energetic position of the ^{3}CT state with respect to the ^{1}CS state was estimated by TD-DFT computations (*vide infra*)). With increasing magnetic fields, the ^{3}CS$_0$ state is unaffected while the ^{3}CS$_+$ and ^{3}CS$_-$ states start to split in energy with $\Delta E = g\beta B$, where g is the electronic g-factor, β *Bohr´*s magneton, and B the magnetic field (see Figure 62).

Although the considerations given below reasonably explain the observed magnetic field effects, there might be other interpretations as well. A more detailed analysis of the magnetic field dependent measurements and of the relevant singlet triplet interactions is currently in progress.

At medium field the ^{3}CS$_-$ comes close to the ^{1}CS in energy and thus k_{S,T_-} increases caused by coherent spin-interconversion mediated by the isotropic hyperfine interaction (ihfc) (level-crossing), simultaneously ^{3}CS$_+$ rises in energy and ihfc becomes suppressed from this state.

At even higher fields, ihfc is no longer effective and other incoherent processes (mainly anisotropic hyperfine interaction (ahfc)) are operating for the interconversion of ^{1}CS with ^{3}CS$_-$ or ^{3}CS$_+$.[332]

As apparent from Figure 55, p: 184, the transient absorption decays of **T-CN** show a strong magnetic field dependence at rather low magnetic fields while higher fields result in insignificant changes of the lifetimes. Thus, in the case of the triad, it can be assumed that the ΔST splitting is very small and the level-crossing occurs at very low magnetic field (B < 1 mT) and thus escapes the measurements. On the other side, **Db** does not exhibit any change of either the lifetimes or the amplitudes of the biexponential transient absorption decay during magnetic field dependent measurements. For **Db** the ΔST is probably so large that the necessary field to accomplish the level-crossing is not reached and therefore no magnetic field effect is observed. This hypothesis was supported by DFT computations of **Db** and **T-CN** at CAM-B3LYP/6-31G* level of theory in the gas phase.[a] These computations yielded ΔST = 7.2 cm^{-1} for **Db** and ΔST = 0.026 cm^{-1} for **T-CN** and also show that the ^{3}CS state is higher in energy that the ^{1}CS state. Thus, the level crossing is expected at 27 mT for the triads and at 7700 mT for the dyads. The latter is clearly much higher than the applied magnetic field in the magnetic field dependent measurements (B< 2000 mT).

Consequently, the smaller rate constants for ISC between the CS states (k_{ST}) for the dyads compared to the triads reflect the larger ΔST values of the dyads. Furthermore, the ΔSTs of the triads´ CS states seem to be larger in toluene than in MeCN, as indicated by the smaller k_{ST} values in toluene compared to MeCN, see Table 18, p: 196.

---

[a] Calculation where performed in our group by *M. Holzapfel*.

According to the perturbation approximation (equation (72)) given by *Anderson et al.* and applied by many others the ΔST is developed by a sum over states.[120,122,333-335]

$$\Delta ST = E_s - E_T = \left[\sum_n \frac{V_{^1CS\text{-}N_n}^2}{\Delta G_{^1CS\text{-}N_n}}\right]_S - \left[\sum_n \frac{V_{^3CS\text{-}N_n}^2}{\Delta G_{^3CS\text{-}N_n}}\right]_T \tag{72}$$

where

E_s and E_T are the energies of the ^1CS and ^3CS states, respectively, $V_{^{1,3}CS\text{-}N_n}$ are the couplings between the $^{1,3}CS$ states and the surrounding states n and $\Delta G_{^{1,3}CS\text{-}N_n}$ are the energy gaps between the $^{1,3}CS$ states and the states to which they are coupled.

The solvent dependence of the ΔST might be the result of a solvent dependence of the mixing of the $^{1,3}CS$ states with other states. As apparent from equation (72), those states that are next in energy to the $^{1,3}CS$ states have the strongest influence on the ΔST. The energetically position towards the ^3NDI state (2.04 eV)[a] seems to be the most important factor in the determination of the ^3CS state energy and thus on the ΔST, because it is next to the ^3CS state in energy. As apparent from the values given in Figure 57, p: 188, Table 16, p: 187, the ^3CS state closer to the ^3NDI state in MeCN than in toluene resulting in a stronger mixing of these states. This in turn causes a larger ΔST in MeCN compared to in toluene.

---

[a] Taken as the average of the triplet energy of NDI in EtOH at 77 K (2.03 eV)[326] and in 2-MeTHF at 77 K (2.05 eV)[327].

In the triads, the differences of k_S values might be explained by different electronic couplings. Thus, the electronic couplings were estimated by using the semi-classical *Bixon-Jortner* theory which describes the dependence of the charge recombination rates from the ^{1}CS, k_s, are by equation (73) (*cf.* equation (49), p: 32):[63-66]

$$k_s = 4\pi^2 hc^2 V_{AB}^2 \sum_{j=0}^{\infty} \frac{e^{-S} S^j}{j!} \sqrt{\frac{1}{4\pi hc\lambda_o kT}} \exp\left[-\frac{hc(j\tilde{\nu}_v + \lambda_o + \Delta G_{CS}^0)^2}{4\lambda_o kT}\right] \qquad (73)$$

$$\text{with } S = \frac{\lambda_v}{\tilde{\nu}_v}$$

where

h is the *Planck* constant, c is the speed of light, k is the Boltzmann constant, T is the temperature, and $\tilde{\nu}_v$ is the averaged molecular vibration mode (here 1500 cm^{-1} was used as a typical value),[267,335-337] ΔG_{CS}^0 is the free energy of the CS state, λ_o and λ_v are the outer and inner reorganization energy, respectively, and V_{AB} is the electronic coupling.

With the knowledge of k_s (Table 18), λ_o, λ_v, and ΔG_{CS}^0 (Table 16, p: 187), equation (73) can be used to evaluate the electronic coupling V_{AB}. The inner reorganisation energies λ_v of the cascades for the charge separation and charge recombination processes can be estimated by the average λ_v value of TAA (= 0.20 eV, as the average value of tri-*p*-anisylamine (0.27 eV) and tri-tolylamine (0.13 eV))[166] and of NDI (0.39 eV)[176], which yields 0.29 eV. The solvent reorganisation energies λ_o were estimated by the *Born* equation (46)[55], which yields 0.06 eV in toluene and 1.29 eV in MeCN for the dyads.

$$\lambda_o = \frac{e^2}{4\pi\varepsilon_0}\left(\frac{1}{2r_D} + \frac{1}{2r_A} - \frac{1}{d_{DA}}\right) \cdot \left(\frac{1}{n^2} - \frac{1}{\varepsilon}\right) \qquad (46)$$

where

r_A, r_D are the radii of the donor and acceptor chromophores, respectively, d_{DA} is the centre to centre distance between the donor and the acceptor, n is the refractive index of the solvent and ε is the permittivity of the solvent.

Since λ_o is depending on the distance between the two chromophores, for the triads, the λ_o values were estimate for the two given geometries (see Figure 56, p: 186), which are $\lambda_{o-bent} = \lambda_{o-elongated} = 0.07$ eV in toluene and $\lambda_{o-bent} = 1.40$ eV and $\lambda_{o-elongated} = 1.47$ eV in MeCN. Hence, for all cascades ($\lambda_v + \lambda_o$) is smaller than the $|\Delta G_{CS}^0|$ in toluene and larger in MeCN.

Therefore, it is concluded that charge recombination in toluene takes place in the *Marcus inverted* region and in MeCN in the *Marcus normal* region.[45]

For **Db** in MeCN (k_S = 1/τ_4 was used, obtained from the fs-measurements) this results in an electronic coupling of 29 cm^{-1}. This seems reasonable since the NDI possesses a nodal-plane through the nitrogen atoms in the LUMO and exhibits a large twist angle between the NDI and the *N*-aryl substituent, both reducing the electronic interaction. However, calculations for **Db** in toluene yielded an electronic coupling of 172 cm^{-1} which appears to be rather large for two reasons: First, **Db** is not expected to possess such a high V_{AB} value for the reasons mentioned before and second, the electronic coupling does not commonly exhibit such a strong solvent dependence. Similarly, the values estimated for the triads in MeCN and toluene exhibit a strong discrepancy. In order to obtain an independently estimate, the electronic couplings of **Db** and **T-CN** in the gas phase were also evaluated by computational methods:[a] The CS states were optimised by TD-DFT method at CAM-B3LYP/6-31G* level of theory. At this CS geometry the transition moments between the ground state (S$_0$) and the CS state were calculated. Using the *Mulliken-Hush* equation (74) (*cf.* equation (51), section 2.1.2.1, p: 33), then the electronic coupling V_{AB} was evaluated with the calculated input parameter $\tilde{\nu}$ (= energy difference between CS and S$_0$ state at the CS-state geometry (ΔG(S$_0$ − S$_1$) = 2.25 eV for **T-Me**, ΔG(S$_0$ − S$_1$) = 2.26 eV for **T-Cl**, ΔG(S$_0$ − S$_1$) = 2.28 eV for **T-CN** and 2.12 eV for **Db**)), $\Delta \mu$ (= dipole moment difference between CS and S$_0$ ($\Delta \mu$ = 114.9 D for **T-Me**, $\Delta \mu$ = 115.6 D for **T-Cl**, $\Delta \mu$ = 112.7 D for **T-CN** and 70.9 D for **Db**) and μ (= the projection of the transition moments (μ_{eg} = 0.00397 D for **T-Me**, μ_{eg} = 0.00206 D for **T-Cl**, μ_{eg} = 0.00169 D for **T-CN** and 0.0166 D for **Db**) onto $\Delta \mu$).

$$V_{AB} = \frac{\mu}{\Delta \mu} \, \tilde{\nu} \tag{74}$$

This calculation results in V_{AB} = 0.62 cm^{-1} for **T-Me**, V_{AB} = 0.32 cm^{-1} for **T-Cl**, V_{AB} = 0.28 cm^{-1} for **T-CN** and V_{AB} = 4.0 cm^{-1} for **Db**. The accuracy of the method was checked by the SCS ADC(2)/cc-pVDZ method, which gave V_{AB} = 4.2 cm^{-1} for **Db** with ΔG(S$_0$ − S$_1$) = 2.45 eV, $\Delta \mu$ = 73.0 D and $\Delta \mu_{eg}$ = 0.0154 D at the DFT computed geometry. Thus, there is a large discrepance for V_{AB} in the two solvents and compared to the computed values. In the following, the reasons that may account for this discrepance will be discussed.

---

[a] Calculations were performed in our group by *M. Holzapfel*.

It is well known that the *Born* equation (46) strongly underestimates the outer reorganisation energy λ_o in aromatic solvents because their high quadropole moments are not adequately treated by the permittivity ε.[338,339] The outer reorganisation energy enters the *Bixon-Jortner* equation (73) and by this way may influence the evaluation of V_{AB}. Similarly, V_{AB} depends on ΔG^0_{CS}. Both, λ_o and ΔG^0_{CS} depend on the permittivity of the solvent, ε, which enters the *Born* equation (46) and the *Weller* equation (71), p: 184, for estimating λ_o and ΔG^0_{CS}. Therefore ε was varied in both equations to find an empirical value which gives a similar electronic coupling in toluene and MeCN. Using $\varepsilon = 2.8$ yielded the reasonable values $\lambda_o = 0.22$ eV for both dyads, $\Delta G^0_{CS} = 1.82$ eV and $V_{AB} = 25$ cm^{-1} for **Da** and $\Delta G^0_{CS} = 1.73$ eV and $V_{AB} = 29$ cm^{-1} for **Db** in toluene, which agree well with those in MeCN.

However, using $\varepsilon = 2.8$ for the calculation of V_{AB} by equation (73) for the triads in toluene yielded much too large values of V_{AB}. Thus, ε in this case describes not only the permittivity of the solvent but is dependent on both, the solvent and the solute. For the triads an empirical ε value of 4.0 was adjusted for toluene to obtain similar electronic couplings as in MeCN (see Table 19). This yields $\lambda_{o\text{-bent}} = 0.52$ eV for the bent conformer and $\lambda_{o\text{-elongated}} = 0.55$ eV for the elongated conformer for the triads in toluene.

The V_{AB} values in toluene ($\varepsilon = 2.8$) for **Da** and **Db** clearly demonstrate that the orientation of the triazole bridge exhibits only negligible influence on the electronic coupling. Thus, the threefold faster charge recombination rate of **Db** compared to **Da** is a result of the different ΔG^0_{CS} values (*inverted* region effect) which are strongly dependent on the triazole-linkage since this directly affects the redox potentials as proved by cyclic voltammetry.

The situation is far more complicated for the triads. One might expect equal charge recombination rates for all cascades since λ_o, λ_v and the ΔG^0_{CS2} values are in the same range for all cases. However, different k_s were found experimentally for the diverse cascades. Because the redox potential of TAA1 is much higher than that of TAA2, it can be safely assumed that back electron transfer from the CS2 to S_0 occurs by a single step superexchange mechanism. In this case the oxidised TAA1 bridge state mixes in only as a virtual state according to the *McConnell* model[86] (equation (75), *cf.* section 2.1.2.3, p: 33).

$$V_{AB} = \frac{V_{CS2\leftarrow CS1} \cdot V_{CS1\leftarrow S_0}}{\Delta G^0_{CS1} - \Delta G^0_{CS2}} \tag{75}$$

For the estimation of V_{AB} by of the *McConnell* model, a value of 300 cm^{-1} obtained by the *Mulliken-Hush* analysis of the IV-CT-band of **M** (*cf.* Table 9, p: 147) serves as $V_{CS2 \leftarrow CS1}$ and for $V_{CS1 \leftarrow S_0}$ the value estimated by equation (73) from the measurements of k_S of **Db** in MeCN was used, which seems to be the most reliable of all available values. The values for V_{AB} obtained from the *Bixon-Jortner* and the *McConnell* equation are compared in Table 19 (together with ΔG^0_{CS} values calculated assuming $\varepsilon = 2.8$ and 4.0 for toluene, respectively).

Table 19:   **Electronic Coupling V_{AB} Estimated by *Bixon-Jortner* Equation and by *McConnell* Equation and ΔG^0_{CS} Values of the CS States.**

			ΔG^0_{CS} / eV	V_{AB} / cm^{-1}	
				by *Bixon-Jortner*	by *McConnell*
			toluene ($\varepsilon = 2.8$)		
Da			1.82	25	-
			toluene ($\varepsilon = 2.8$)		
Db			1.73	29	
			MeCN		
			0.93	29	-
			toluene ($\varepsilon = 4.0$)		
T-Me	CS1		2.03		
	CS2	bent	1.82	1.0	4.5
		elongated	1.86	0.99	5.2
			MeCN		
	CS1		1.22		
	CS2	bent	0.94	0.99	3.8
		elongated	0.95	1.2	3.9
			toluene ($\varepsilon = 4.0$)		
T-Cl	CS1		1.85		
	CS2	bent	1.51	1.1	3.1
		elongated	1.54	1.1	3.5
			MeCN		
	CS1		1.30		
	CS2	bent	0.92	0.95	2.8
		elongated	0.93	1.2	2.8
			toluene ($\varepsilon = 4.0$)		
T-CN	CS1		2.00		
	CS2	bent	1.51	1.5	2.2
		elongated	1.54	1.4	2.3
			MeCN		
	CS1		1.46		
	CS2	bent	0.92	0.79	2.03
		elongated	0.93	0.98	2.04

Because the values determining the charge recombination rate k_S (λ_v, λ_o and ΔG^0_{CS2}) are expected to be rather similar for all triads, any difference of the k_S rates are assumed to be caused by the electronic coupling V_{AB}. In case of the triads in MeCN according to the *McConnell* model the electronic coupling decreases in the order **T-Me** > **T-Cl** > **T-CN** as a result of the decreasing $(\Delta G^0_{CS1} - \Delta G^0_{CS2})$ values in the same order. The electronic couplings calculated by TD-DFT computations follow the same order and furthermore, this trend can be observed in the k_S values and consequently in the electronic coupling estimated by the *Bixon-Jortner* theory. In toluene the *McConnell* model predicts the same $(\Delta G^0_{CS1} - \Delta G^0_{CS2})$ progression and, thus, of the electronic coupling V_{AB}. However, the experimental k_S values and, therefore, the electronic couplings estimated by the *Bixon-Jortner* theory exhibit a reversed trend.

Even though the errors of the estimated k_S values seem to be small, the corresponding trends of k_S are also minimal. From Table 19 it is obvious that the electronic couplings calculated by the *McConnell* theory show a discrepancy of a factor of 2 – 4 compared to the values obtained by the *Bixon-Jortner* theory and of a factor of ~10 compared to the DFT computations. Although the magnitude of these values are in qualitative agreement with the experimental results, the suggested trends in the electronic coupling between the distinct triads are rather small in respect to the made assumptions for the estimation of V_{AB}. Consequently, the inaccuracy in the estimation of V_{AB} do not allow to clearly conclude that the trends in the k_S values are caused by the electronic coupling.

3.2.4.3   Conclusions

The presently investigated dyads and triads exhibit charge separation upon photoexcitation. As apparent from the fs- and ns-transient absorption measurements, the locally excited triplet NDI state is only populated in **Db** in MeCN. These measurements and the CV measurements reveal a redox gradient and a down-hill oriented progression of CS2 states in the triads. In these triads, first a CS state is formed in which the intermediate TAA1 is oxidised and the NDI is reduced followed by an additional electron transfer to form the fully CS2 state. The signals of the CS states of all triads and dyads feature biexponential decays with a short and a longer component. These biexponential decays were expected to be the result of an ISC from the predominantly populated ^{1}CS state to the ^{3}CS, from which charge recombination into the S_0 state is forbidden by the spin conversion rule. Charge recombination into local triplet states is prevented as the ^{3}CS state is the lowest lying triplet state. This assumption was supported by a strong magnetic field effect found in a magnetic field dependent ns-transient absorption measurement of **T-CN** in toluene. Although the exact singlet-triplet dynamics are not elucidated yet and a detailed analysis of this issue is in progress, it seems that the population of the ^{3}CS state strongly influences the overall lifetime of the CS states.

The charge recombination rate k_s for the recombination of the ^{1}CS state is prolonged in the triads compared to the dyads due to an increased spatial distance between the two charges in the fully CS states in the triads. In all cascades $(\lambda_v + \lambda_o)$ is smaller than the $|\Delta G^0_{CS}|$ in toluene and larger in MeCN. Thus, charge recombination in toluene takes place in the *Marcus inverted* region and in MeCN in the *Marcus normal* region. Indeed, **Db** exhibits a strong *inverted* region effect that places the lifetime of the CS state in MeCN in the ps and in toluene in the ns-time regime. However, for the triads no *inverted* region effect can be observed which is probably because both charge recombination processes are near the vertex of the *Marcus* parabola.

Although rate constants allow a more detailed analysis of the processes in the cascades, for practical applications the overall lifetime of the specific CS state is much more important. Thus, though the charge recombination in the triads is prolonged compared to the dyads, the lifetime of the ^{1,3}CS states is clearly longer in the dyads. This is a result of the larger ΔST in the dyads. A lifetime of tens of ns is a well value for small donor-acceptor dyads but a lifetime of several μs is remarkable for such a small distance separating the two charges. From the ISC rate constants k_{ST} obtained by TENUA simulation of the transient absorption decays, is can be seen that the ΔST in the triads is strongly solvent dependent. In toluene the coupling of the ^{3}CS state to the ^{3}NDI state is more effective than in MeCN which leads to a larger ΔST. Therefore, concerning the ^{1,3}CS states´ free energy it should not only be included that local excited triplet state have to be higher in energy

that the ^{3}CS state to preclude triplet charge recombination but also that higher lying local triplet states influence the $\varDelta$ST and in turn the ^{1,3}CS state dynamics.

Furthermore, the fully CS state is much faster populated in the dyads because in the triads a second electron transfer must occur from the intermediate CS1 state, which also exhibit a certain lifetime. The reasons given above prove that the control of spin correlation and of the $\varDelta$ST is a promising key parameter to achieve long-lived CS states in even small donor-acceptor systems.

The small charge recombination rates for the dyads is a result of weak electronic coupling in the dyads, caused by the large twist angle between the NDI and the *N*-aryl substituent, the nodal plane along the *N-N* axes of the NDI and last, but not least important by the small electronic coupling of the triazole bridge as has been proved in section 3.2.1.10, p: 144. According to the *McConnell* theory the electronic coupling in the triads is strongly influenced by the intermediate CS1 states, which act *via* virtual states as bridges in the superexchange charge recombination process. Although this is reflected in the calculated V_{AB} values using the *McConnell* approach, this effect is not be supported by the trends observed in the estimated rate constants as these trends are too weak pronounced. The analysis is strongly complicated by the influence of the solvent permittivity, which appear in the *Weller* and the *Born* equation. Herein, the polarity of the toluene is underestimated due to its small dipole but large quadropole moment. Therefore, additional solvent dependent measurements are envisioned to resolve this issue.

3.2.5 Donor-Acceptor Dendrimer

3.2.5.1 Results

Cyclic Voltammetry

In order to estimate the redox potentials of the NDIs and the TAA units in **D-A-G1** CV measurements were performed in DCM with TBAHFP (~ 0.2 M) as supporting electrolyte (see Figure 63). All reported potentials were referenced against the Fc/Fc$^+$ redox couple. In its cyclic voltammogram **D-A-G1** exhibits an oxidation process at 480 mV, which can be attributed to the oxidation of the TAA core. This value is in excellent agreement with the potentials found for the dendrimers **G1**–**G3** and the model compound **core-M** (*cf.* Table 3, p: 103). Therefore, it seems obvious that the adjacent NDI chromophores do not feature any perceivable influence on the oxidation potential of the TAA, very similar to the findings in the CV experiment of the cascades (*cf.* 3.2.4.1.1, p: 167). Consequently, the reduction of the NDI is observed at 1000 mV, which is almost identical to the values found of the cascades. Besides, the reduction wave in the CV attributed to the NDIs is three times as large as the oxidation wave assigned to the oxidation of the TAA, which reflects the ratio of the donor and acceptor chromophores in the molecules.
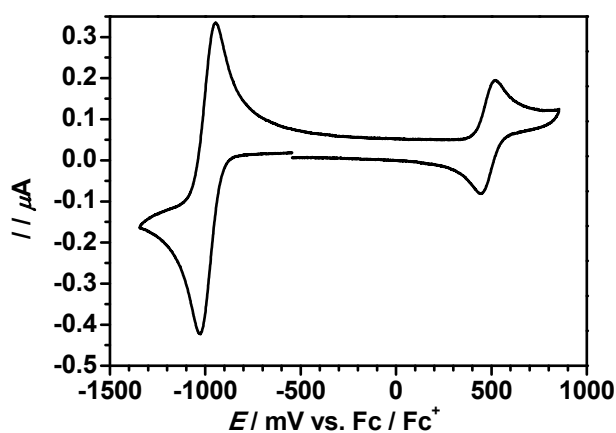
Figure 63: Cyclic voltammogram of D-A-G1 measured with a scan speed of 500 mV s^{-1} in DCM with TBAHFP (~ 0.2 M) as supporting electrolyte and referenced against the Fc/Fc$^+$ redox couple.

Steady-State Absorption Spectroscopy

For the purpose of examination of possible ground state interactions between the TAA donor and the NDI acceptors, UV/Vis steady state absorption spectra were recorded in polar MeCN and nonpolar toluene (see Figure 64). The absorption spectra are mainly dominated by the absorption characteristics of the NDI moieties in respect to the ratio of NDIs and TAAs in **D-A-G1.** In MeCN **D-A-G1** exhibits two sharp maxima at 26500 cm^{-1} (375 nm) and 28200 cm^{-1} (355 nm) while the latter features a small shoulder on the high energy side. Because **D-A-G1** was found to be only weakly soluble in MeCN, estimation of the molecular extinction coefficient was precluded. Similar to the cascades, also the spectrum of **D-A-G1** appears much broader in toluene compared to MeCN. Thus, the absorption spectrum of **D-A-G1** in toluene exhibits a single maximum a 27800 cm^{-1} (360 nm) with an extinction coefficient of 113700 M^{-1} cm^{-1}. Since **D-A-G1** consists of three NDI units, the strong broadening found for **D-A-G1** supports the assumption that this effect is caused by the NDI chromophores, probably due to aromatic solvent-specific effects (*cf.* section 3.2.4.1.2, p: 169).[322,323] As apparent from Figure 64, B, the absorption spectra of **D-A-G1** represent a superposition of the absorption characteristics of the distinct chromophores (the NDIs and the TAA) and no ground state interactions between them are observed. Beside the band broadening in toluene, only weak solvents dependence of the absorption is indicated by the small shift of the absorption maxima of ca. 300 cm^{-1}. However, a smaller onset of the absorption in toluene denotes a smaller 00-energy of **D-A-G1** in toluene (24600 cm^{-1}) compared to MeCN (25700 cm^{-1}), estimated by applying a tangent on the flank of the lowest energy transition. The difference of ca. 1000 cm^{-1} is much larger than that found for the cascades (*cf.* section 3.2.4.1.2, p: 169).
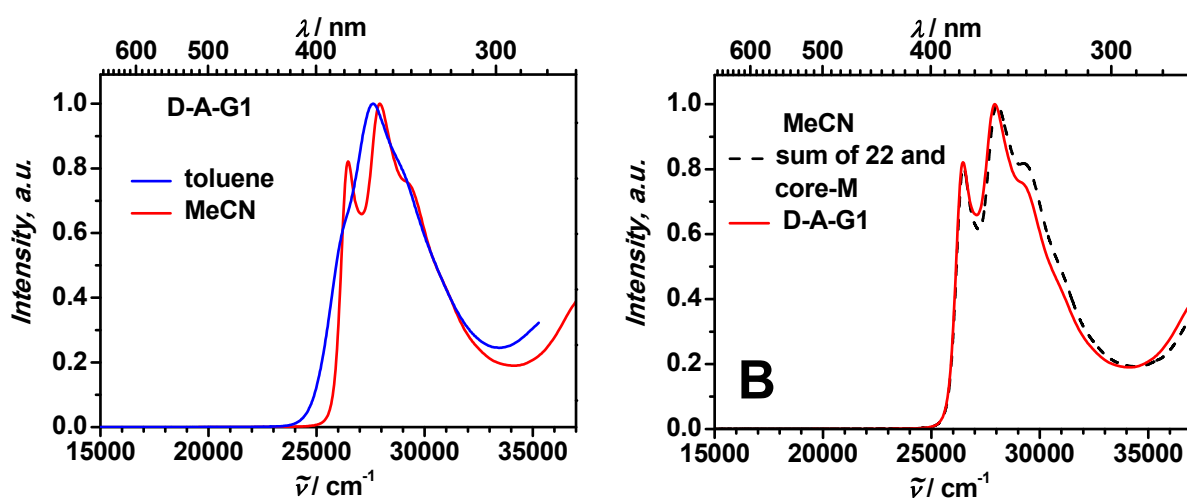

Figure 64: **A: Normalised absorption spectra of D-A-G1 in MeCN and toluene. B: Normalised absorption spectra of D-A-G1 and of the sum of 22 and core-M in MeCN considering the ratio of the NDIs and the TAA in D-A-G1.**

ns-Transient Absorption

Upon excitation of **D-A-G1** the excited state is supposed to be quenched by a photoinduced electron transfer from the TAA core to one on the NDIs on the periphery. This assumption is supported by the fact that **D-A-G1** does not exhibit any emission in either MeCN or toluene. Thus, a CS state might be populated, in which the TAA is oxidised and one of the NDIs is reduced, likewise to the cascades presented in the previous section. To elucidate the CS state dynamics transient absorption spectroscopy in the ns-time regime was performed. However, only processes in toluene will be discussed since the low solubility of **D-A-G1** precludes any transient absorption experiments in MeCN.

D-A-G1 was excited with an 8 ns laser pulse at 28200 cm^{-1} (355 nm) and the excited state dynamics were probed by a white light continuum between 12500 cm^{-1} (800 nm) and 25000 cm^{-1} (400 nm). The transient absorption signal rises within the instrument response and start to decay instantaneously. The transient absorption spectrum of **D-A-G1** is dominated by a strong band at 21000 cm^{-1} (475 nm) along with a smaller one at 16400 cm^{-1} (610 nm), see Figure 65. These bands appear at identical positions than in the cascades (*cf.* Figure 52) and are attributed to the NDI radical anion.[173,324] Furthermore, in the spectrum an intense and broad band at 23700 cm^{-1} (420 nm) can be observed. However, the typical absorption band of the TAA radical cation at ca. 13200 cm^{-1} (760 nm) is not observed. Hence, if an NDI radical anion is present in **D-A-G1**, the positive charge must be localised on the molecule as well. It is supposed that the band of the TAA radical cation is located at lower energy as the probed spectrum maybe caused by the different substituents at the TAA compared to that in the cascades. A small hint for this assumption is the indication of a rising edge of a band at ca. 12500 cm^{-1} (800 nm) at the lowest energy side of the spectrum. Moreover the strong band at 23700 cm^{-1} (420 nm) might be attributed to a SOMO-LUMO transition in the TAA radical cation (*cf.* Scheme 51, p: 140). The steady-state absorption spectrum of **core-M** in DCM (not shown) revealed a hypsochromic shift of the main absorption band of 1500 cm^{-1} compared to **N-M** (*cf.* Figure 16, p: 105).

In the transient absorption spectra of the cascades might be the indication of a similar band at the high energy side of the spectrum (*cf.* Figure 52, p: 178) and a shift of in the range of 1500 cm^{-1} might push the transition of the TAA radical cation into the probe spectral range. Besides, all three transient absorption bands present almost identical kinetics. Although there is no evidence for this assumption, it is likely that a CS state is generated in **D-A-G1** upon excitation in a comparable fashion than in the cascades.
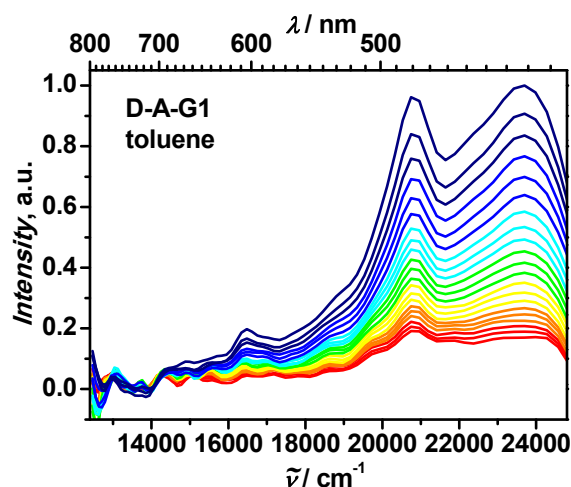
Figure 65:   Normalised ns-transient absorption spectra of D-A-G1 in toluene at 28200 cm^{-1} (355 nm) pump energy. Early spectra are given in dark blue, later spectra in red.

The transient absorption signals of **D-A-G1** in toluene at all three observed band maxima show biexponential decays consistent of a short component of ca. 40 ns and a much longer one of ca. 7.6 μs (Figure 66). As seen from the decays of **Da** and **Db** in toluene in the preceding section (*cf.* 3.2.4.1.3, p: 183), the longer lifetime was supposed to be strongly concentration dependent as a result of a diffusion controlled bimolecular deactivation process. Therefore, **D-A-G1** was measured in the lowest concentration that allows a reasonable signal-to-noise ratio (c = 3.5 x 10^{-7} M). In this diluted solution the longer lifetime was proved to prolong up to 14 μs (see Table 20).
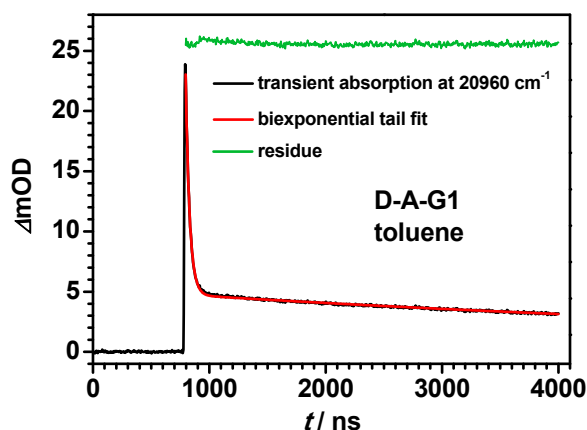
Figure 66:   Biexponential tail fit of the ns-transient absorption kinetic of D-A-G1 in toluene pumped at 28200 cm^{-1} (355 nm) and probed at 21000 cm^{-1} (475 nm).

Table 20: **Lifetimes and Ratio of Amplitudes of ns-Transient Absorption Experiments in Toluene at the given Concentration and Laser Pulse Energy at 28200 cm^{-1} (355 nm), Assuming Independent Biexponential Decay.**

c /M	E /mJ	a_{long}/a_{short}	τ_{long} /ns	τ_{short} /ns
3.4×10^{-6}	1.2	0.10	5.9×10^3	36
3.5×10^{-7a}	1.2	0.060	13.9×10^3	49

[a] used for the simulation with the TENUA[280] program to obtain the rate constants k_S and k_{ST}.

3.2.5.2 Discussion

The presented data of the ns-transient absorption of **D-A-G1** exhibit the generation of a CS state, which decays biexponentially into the ground state. This dynamics are strongly influenced by the relative state energies and reorganisation energy. The CS state motif in **D-A-G1** shows structural parallels to that in **Db**, thus in the estimation of λ_o and ΔG_{CS} the electron transfer distance in **Db** was taken to be identical to the one in **D-A-G1** (d_{DA} = 16.7 Å, *cf.* Figure 56, p: 186). Using the *Weller* approach (equation (71)) and the redox potentials given in section 3.2.5.1, p: 207, results in a ΔG_{CS}^0 value of 2.14 eV.[325]

$$\Delta G_{CS}^0 = \frac{N_A z e}{1000}(E_{1/2}^{ox} - E_{1/2}^{red}) - \frac{N_A e^2}{4000\pi\varepsilon_0}\left(\left(\frac{1}{2r_D} + \frac{1}{2r_A}\right)\left(\frac{1}{\varepsilon_r} - \frac{1}{\varepsilon_s}\right) + \frac{1}{\varepsilon_s d_{DA}}\right) \quad (71)$$

where
N_A is *Avogadro´s* constant, e is the elementary charge, ε_0 is the is vacuum permittivity, ε_s is the permittivity of the spectroscopy solvent, ε_r is the permittivity of the solvent of the electrochemical measurements, z is the number of transferred electrons, r_D and r_A are the radii of the donor (= 4.81 Å)[a] and the acceptor (= 3.97 Å)[a], respectively, and d_{DA} is the electron transfer distance.

Applying the *Born* equation (46)[55] yielded the outer reorganisation energy λ_o = 0.06 eV and 0.29 eV was taken for λ_v, as estimated in the preceding section for a TAA-NDI system (*cf.* section 3.2.4.2, p: 199). From these values it is obvious that charge recombination in **D-A-G1** in toluene takes place in the *Marcus inverted* region ($\lambda_v + \lambda_o < \Delta G_{CS}$).[45]

---

[a] See section 3.2.4.2, p: 176.

$$\lambda_o = \frac{e^2}{4\pi\varepsilon_0}\left(\frac{1}{2r_D} + \frac{1}{2r_A} - \frac{1}{d_{DA}}\right)\cdot\left(\frac{1}{n^2} - \frac{1}{\varepsilon}\right) \tag{46}$$

where

r_A, r_D are the radii of the donor and acceptor chromophores, respectively, d_{DA} is the centre to centre distance between the donor and the acceptor, n is the refractive index of the solvent and ε is the permittivity of the solvent.

Due to the strong analogy of **D-A-G1** with the cascades, the observed biexponential decay is supposed to be the result of an ISC of the predominantly populated ^{1}CS state into the ^{3}CS state, from which charge recombination is spin forbidden. In order to analyse the dynamics of the ^{1,3}CS state in more detail, the rate constant for singlet charge recombination (k_S) and for ISC (k_{ST}) were estimated by simulating the experimental decay in diluted solution with the TENUA[280] program by applying the kinetic mechanism given in Figure 61, p: 195 and using the script given in the appendix. Therein $k_{ST} = 3k_{TS}$ was assumed to take spin statistics of degenerated states into account.[325] This yielded $k_S = 2.0 \times 10^7$ s^{-1} and $k_{ST} = 2.2 \times 10^5$ s^{-1}.

The charge recombination rate of **D-A-G1** is about one order of magnitude smaller than that of **Db** and of the same order of those found for the triads (*cf.* Table 18, p: 196). To elucidate if this is a result of a reduced electronic coupling V_{AB} or of the higher ΔG_{CS} value (*inverted* region) of **D-A-G1** compared to **Db**, V_{AB} was calculated using the *Bixon-Jortner* equation (73).[63-66]

$$k_s = 4\pi^2 hc^2 V_{AB}^2 \sum_{j=0}^{\infty} \frac{e^{-S}S^j}{j!}\sqrt{\frac{1}{4\pi hc\lambda_o kT}}\exp\left[-\frac{hc(j\tilde{\nu}_v + \lambda_o + \Delta G_{CS}^0)^2}{4\lambda_o kT}\right] \tag{73}$$

$$\text{with } S = \frac{\lambda_v}{\tilde{\nu}_v}$$

where

h is the *Planck* constant, c is the speed of light, k is the Boltzmann constant, T is the temperature, and $\tilde{\nu}_v$ is the averaged molecular vibration mode (here 1500 cm^{-1} was used as a typical value),[267,335-337] ΔG_{CS}^0 is the free energy of the CS state, λ_o and λ_v are the outer and inner reorganization energy, respectively, and V_{AB} is the electronic coupling.

This gives for **D-A-G1** an electronic coupling of 178 cm^{-1}. Similar to the situation of the dyads (cf. 3.2.4.2, p: 201) this value is by far too large and could not account for the observed slow charge recombination rate. Thus, the value of the solvent permittivity of toluene was set to 2.8, which is the same value empirical found for **Da** and **Db**. The empirical solvent permittivity enters the *Weller* and the *Born* equation, which give $\Delta G_{CS}^0 = 1.98$ eV and $\lambda_o = 0.22$ eV. Utilising these values in the *Bixon-*

Jortner approach yielded an electronic coupling of 33 cm^{-1}, which is in reasonable agreement with the values found for **Da** and **Db**.

From those results it is expected that the slower charge recombination rate found for **D-A-G1** compared to **Db** is caused by a higher ΔG^0_{CS} value in **D-A-G1** and, in turn, by a more pronounced *inverted* region effect. Moreover, the slightly smaller value for ISC revealed a minimal larger singlet-triplet splitting (ΔST) in **D-A-G1** than in the dyads and triads leading to a prolonged lifetime of the ^{1,3}CS state.

3.2.5.3   Conclusions

The presented results revealed that in **D-A-G1** the excited state populated upon photoexcitation is quenched by an electron transfer from the TAA core to the NDIs on the periphery. In this CS state one NDI is reduced and the TAA is oxidised. Although no evidences for the TAA radical cation are observed, it is supposed that three adjacent triazole units shift the HOMO-SOMO transition in the TAA radical cation out of the probed spectral region. Thus, the strong transient absorption at 23700 cm^{-1} (420 nm) might be attributed to a SOMO-LUMO transition in the TAA radical cation, which is pushed into the observed ns-transient absorption spectrum by the three triazoles.

The rate constants for charge recombination and ISC obtained from TENUA simulation of the experimental decay show a prolonged charge recombination rate for **D-A-G1** compared to **Db**, in which the two charges are separated by the same spatial distance. Furthermore, the electronic coupling in **D-A-G1** is comparable to that found for the dyads. Thus, the smaller charge recombination rate is a result of a higher ΔG_{CS} value in **D-A-G1**, which slows down charge recombination in the *inverted* region. In addition, the rate of ISC in **D-A-G1** is in the same order of magnitude than for the dyads leading to a long lifetime of the CS state of ca. 14 μs.

In conclusion, the donor-acceptor dendrimer exhibits very similar CS state characteristics to the dyads but with a clearly slower charge recombination process. The longer overall CS state lifetime in the μs time regime in combination with the increases CS state free energy value compared to the dyads leads to a beneficial performance for light energy conversion. Moreover, the enhanced number of excitable chromophores (3 x NDI + 1 x TAA, ε = 113700 M^{-1} cm^{-1}), which all might result in the generation of a CS state makes **D-A-G1** a promising key structure for further studies on light harvesting applications.

Chapter 4

SUMMARY AND OUTLOOK

In this work the synthesis of dendritic macromolecules and small redox cascades was reported and studies of their energy and electron transfer properties discussed.

The chromophores in the dendrimers and the redox cascades are linked *via* triazoles, which were built up by CuAAC. Thereby, a synthetic concept based on building blocks was implemented, which allowed the exchange of all basic components. Resulting structures include dendrimers composed exclusively of TAAs (**G1**–**G3**), dendrimers with an incorporated spirobifluorene core (**spiro-G1** and **spiro-G2**) and the donor-acceptor dendrimer **D-A-G1**, in which the terminal groups are exchanged by NDIs.

Furthermore, a series of model compounds was synthesised in order to achieve a better understanding of the photophysical processes in the dendrimers.

A modification of the synthetic concept for dendrimers enabled the synthesis of a series of donor-acceptor triads (**T-Me**, **T-Cl** and **T-CN**) consisting of two TAA donors and one NDI acceptor unit. The intermediate TAA chromophore ensured a downhill redox gradient from the NDI to the terminal TAA, which was proved by cyclic voltammetry measurements. The redox potential of the intermediate TAA was adjusted by different redox determining substituents in the "free" *p*-position of the TAA. Additionally, two dyads (**Da** and **Db**) were synthesised which differ in the junction of the triazole to the TAA or the NDI, respectively. In these cascades a nodal-plane along the *N-N*-axes in the NDI and a large twist angle between the NDI and the *N*-aryl substituent guaranteed a small electronic coupling.

The photophysical investigations of the dendrimers focused on the homo-energy transfer properties in the TAA dendrimers **G1**–**G3**. Steady-state emission spectroscopy revealed that the emission takes place from a charge transfer state. The polar excited state resulted in a strong *Stokes* shift of the emission, which in turn led to a small spectral overlap integral between the absorption of the acceptor and the emission of the donor in the solvent relaxed state. According to the *Förster* theory, the overlap integral strongly determines the energy transfer rate. Fluorescence up-conversion measurements showed a strong and rapid initial fluorescence anisotropy decay and a much slower decrease on the longer time scale. The experiment revealed a fast energy transfer in the first 2 ps

followed by a much slower energy hopping. Time resolved emission spectra (TRES) of the model compound **M** indicated a solvent relaxation on the same time scale as the fast energy transfer.

The *Förster* estimation of energy transfer rates in **G1** explains fast energy transfer in the vibrotionally relaxed state before solvent relaxation starts. Thereby, the emission spectrum of **G1** in cyclohexane served as the time zero spectrum. Thus, solvent relaxation and fast energy transfer compete in the first two ps after excitation and it is crucial to discriminate between energy transfer in the *Franck-Condon* and in the solvent relaxed state. Furthermore, this finding demonstrates that fast energy transfer occurs even in charge transfer systems where a large *Stokes* shift prevents an effective spectral overlap integral if there is a sufficient overlap integral in before solvent relaxation.

Energy transfer upon excitation was also observed in the spiro dendrimers **spiro-G1** and **spiro-G2** and identified by steady-state emission anisotropy measurements. It was assumed that the energy in **spiro-G1** is completely distributed over the entire molecule while the energy in **spiro-G2** is probably distributed over only one individual branch. This finding was based on a more polarised emission of **spiro-G2** compared to **spiro-G1**. This issue has to be ascertained by *e.g.* time resolved emission anisotropy measurements in further energy transfer studies.

Concerning the electron transfer properties of TAA-triazole systems the radical cations of **G1**–**G2**, **spiro-G1** and **spiro-G2** and of the model compound **M** were investigated by steady-state absorption spectroscopy. Experiments showed that the triazole bridge exhibits small electronic communication between the adjacent chromophores but still possesses sufficient electronic coupling to allow an effective electron transfer from one chromophore to the other.

Due to the high density of chromophores, their D-A-D structure and their superficial centrosymmetry, the presented dendrimers are prospective candidates for two-photon absorption applications.[97,159,225,295]

The dyads, triads and the donor-acceptor dendrimer **D-A-G1** were investigated regarding their photoinduced electron transfer properties and the effects that dominate charge separation and charge recombination in these systems.

The steady-state absorption spectra of all cascades elucidated a superposition of the absorption characteristics of the individual subunits and spectra indicated that the chromophores do not interact in the electronic ground state.

Time resolved transient absorption spectroscopy of the cascades was performed in the fs- and ns- time regime in MeCN and toluene as solvent. Measurements revealed that upon with 28200 cm^{-1} (355) nm and 26300 cm^{-1} (380 nm), respectively, an electron is transferred from the TAA towards

the NDI unit yielding a CS state. In the triads at first a CS1 state is populated, in which the NDI is reduced and the intermediate TAA1 is oxidised. Subsequently, an additional electron transfer from the terminal TAA2 to TAA1 led to the fully CS2 state. Fully CS states of the dyads and triads exhibit lifetimes in the ns-time regime. In contrast for **Db** in MeCN, a lifetime of 43 ps was observed for the CS state together with the population of a ^{3}NDI state. The signals of the other CS states decay biexponentially, which is a result of the presence of the ^{1}CS and the ^{3}CS states. While magnetic field dependent measurements of **Db** did not show an effect due to the large singlet-triplet splitting, **T-CN** exhibited a strong magnetic field dependence which is an evidence for the ^{1}CS/^{3}CS assignment. Further analysis of the singlet-triplet dynamics are required and are currently in progress.

Charge recombination occurred in the *Marcus inverted* region for compounds solved in toluene and in the *Marcus normal* region for MeCN as solvent. However, a significant *inverted* region effect was observed only for **Db**. Triads are probably characterised by charge recombination rates in the *inverted* and in the *normal* region near to the vertex of the *Marcus* parabola. Hence the *inverted* region effect is not pronounced and the rate charge recombination rates are all in the same magnitude. However, compared to the charge recombination rate of **Db** the enlarged spatial distance between the terminal TAA and the NDI in the fully CS2 states in the triads resulted in reduced charge recombination rates by ca. one order of magnitude.

More important than a small charge recombination rate is an overall lifetime of the CS states and this lifetime can significantly be enhanced by the population of the ^{3}CS state. The reported results reveal that a larger singlet-triplet splitting in the dyads led to a CS state lifetime in the μs time regime while a lifetime in the ns-time regime was observed in cases of the triads. Moreover, the singlet-triplet splitting was found to be solvent dependent in the triads, which is a promising starting point for further investigations concerning singlet-triplet splitting.

The donor-acceptor dendrimer **D-A-G1** showed similar characteristics to the dyads. The generation of a CS state is assumed due to a clear NDI radical anion band in the transient absorption spectrum. Noteworthy, the typical transient absorption band of the TAA radical cation is absent for **D-A-G1** in toluene. *Bixon-Jortner* analysis yielded a similar electronic coupling in **D-A-G1** compared to the dyads. However, the charge recombination rate is smaller than of **Db** due to a more energetic CS state, which in the *inverted* region slows down charge recombination. In combination a singlet-triplet splitting similar to the dyads prolongs the CS state lifetime up to 14 μs in diluted solution. Both effects result in an even better performance of **D-A-G1** concerning energy conversion. **D-A-G1** is therefore a promising key structure for further studies on light harvesting

applications. In a prospective study a second generation donor-acceptor dendrimer **D-A-G2** might be an attractive structure accessible by "click reaction" of **13** and **8**. **D-A-G2** is expected to exhibit a downhill oriented gradient of CS states as assumed from the CV studies on **G1**–**G3**.

Chapter 5

EXPERIMENTAL SECTION

5.1   Analytical Methods[a]

NMR Spectroscopy

- Bruker Avance 400 FT-Spectrometer (^{1}H: 400.1 MHz, ^{13}C: 100.6 MHz)

- Bruker Avance DMX 600 FT-Spectrometer (^{1}H: 600.1 MHz, ^{13}C: 150.9 MHz)

All ^{1}H- and ^{13}C spectra were measured at 300 K unless otherwise indicated. As internal reference the signal of the respective solvent was used and the chemical shifts are given in ppm (δ-scale) vs. tetramethylsilane. Multiplicities were denoted as s (singulet), d (doublet), dd (doublet of doublets), t (triplet) and m (multiplet). Coupling constants are given in Hz. NMR spectroscopy data is quoted as follows: (chemical shift (multiplicity, coupling constant, number of protons, assignment of signal), Solvents for ^{13}C-NMR spectra were degassed with argon for at least 15 min prior to measurements.

Mass Spectrometry

- Bruker Daltonics micoTOF focus (ESI)

- Bruker Daltonics autoflex II (MALDI)

Mass spectra were recorded at the Institute of Organic Chemistry, University of Würzburg. For ESI-spectra 10 μM solutions of the sample in $CHCl_3$ or DCM were prepared. The software module "Bruker Daltonics IsotopePattern" from the software Compass 1.1 from Bruker Daltonics GmbH, Bremen was used for the calculation of the respective mass values of the isotropic distribution.

---

[a] Adapted or reproduced (or reproduced in parts) from *Solvent Controlled Energy Transfer Processes in Triarylamine-Triazole Based Dendrimers*, Zieschang, F.; Schmiedel, A.; Holzapfel, M.; Ansorg, K.; Engels, B.; Lambert, C. *J. Phys. Chem. C* **2013**, *117*, 19816-19831. Copyright 2013 American Chemical Society.

Infra-red Spectroscopy

- JASCO 410 FT-IR spectrometer with an attenuated total reflectance (ATR) attachement.

Positions of the absorption bands are given in reciprocal centimetres (cm^{-1}) and signals are described by w (weak) and s (strong).

Recycling Gel Permeation Chromatography (GPC)

- Shimadzu Gel Permeation Chromatography System

  - photodiode array detector 190 – 800 nm (SPD-M20A)

  - high precision solvent delivery unit (LC-20AD)

  - card type system controller (CBM-20Alite)

  - high pressure flow channel selection valve (FCV-20AH2)

  - 3-way online degassing unit (DGU-20A3)

  - fraction collector (FRC-10A)

  - software LCsolution (v. 1.0.0.1)

- JASCO Gel Permeation Chromatography System

  - multi wavelength UV/vis detector 200 – 600 nm (UV-2077)

  - intelligent HPLC pump (PU-2080 plus)

  - interface box (LC-Netll-ADC)

  - solvent selection valve unit (LV-2080-03)

  - inline degasser (DG-2080-53)

  - fraction collector (CHF122SC) with software FraColl (v. 3.0.2)

  - software Chrompass (v. 1.8)

All chromatographies were carried out at RT in recycling mode and two SDV columns (PSS SDV preparative 50 Å and 500 Å, dimension 20 x 600 mm, particle size: 10 μm) were operated in line. CHCl$_3$ (HPLC grade) was used as eluent with a flow rate of 4 mL/min.

Differential Scanning Calorimetry (DSC)

- TA Q1000 calorimeter

Differential scanning calorimetry measurements were performed with a heating/cooling rate of 30 K/min unless otherwise indicated. Two heating-cooling cycles were performed consecutively.

Cyclic Voltammetry

- Electrochemical workstation BAS CV-50 W

- Computer controlled GAMRY instruments (Reference 600) potentiostat (Warminister, PA, USA)

Electrochemical experiments were performed under argon atmosphere in dry oxygen-free DCM with tetrabutylammonium hexafluorophosphate (TBAHFP) (ca. 0.2 M) as supporting electrolyte. A three electrode set-up with a platinum disc working electrode (Ø = 1 mm), a platinum wire counter electrode and either a platinum pseudoreference or an Ag/AgCl LEAK FREE reference electrode (Warner Instruments, Hamden, CT, USA) were used in a sealed glass flask purged with argon. Chemical and electrochemical reversibility of the redox processes were tested by multi thin layer measurements and all potentials were measured against the ferrocene/ferrocenium (Fc/Fc^+) redox couple as reference.

Steady-State UV/Vis/NIR Spectroscopy

- JASCO V-670 double beam UV/Vis/NIR spectrometer (software SpectraManager v.2.8.4.1)

- Agilent Technologies Cary 5000 double beam UV/Vis/NIR spectrometer (software Agilent Cary WinUV Analysis and Bio v. 4.2)

The absorption spectra of all compounds were measured in 1 cm quartz cuvettes (Hellma) at RT with pure solvent as reference. The solvents were Uvasol solvent purchased from Merck or of comparable grade. All compounds were investigated in a concentration range from ca. 1.0×10^{-6} M to ca. 5.0×10^{-5} M to exclude aggregation effects.

Steady-State Emission Spectroscopy /
Time-Dependent Fluorescence-Decay

- Photon Technology International QuantaMasterTM model QM-2000-4

  o water-cooled photomultiplier (R928P)

  o xenon short-arc lamp (75 W, Ushio UXL-75XE)

  o software FeliX32TM (v. 1.2.0.56)

Fluorescence measurements were performed using standard 1 cm quartz cuvettes and spectra were recorded in Uvasol solvents from Merck or of comparable grade after purging the samples for 15 min with argon gas. As a fluorescence standard, quinine sulfate in 1 M sulfuric acid (ϕ_f = 0.55)[340] was used and the following equation was applied to determine the quantum yields:

$$\phi_f = \phi_{f,Ref}\left(\frac{I(\widetilde{\nu}) \cdot OD_{Ref} \cdot (n_D)^2}{I(\widetilde{\nu})_{Ref} \cdot OD \cdot (n_{D,Ref})^2}\right)$$

where

ϕ_f and $\phi_{f,Ref}$ are the fluorescence quantum yields, $I(\widetilde{\nu})$ and $I(\widetilde{\nu})_{Ref}$ are the integrated emission bands, OD and OD_{Ref} are the optical densities of the absorption bands at the excitation wavelength, and n_D and $n_{D,ref}$ are the refraction indices of the solvent of the sample and reference, respectively.

- Photon Technology International TimeMasterTM TM-200 LED strobe lifetime spectrofluorometer including a Photon Technology International pulses LED (26500 cm^{-1} (375 nm))

To determine the instrument response a LUDOX AS-30 colloidal silica suspension in de-ionised water was used as scatter solution. Decays were measured under magic angle conditions using a Glan-Thompson-polariser from Photon Technology International. Lifetimes were determined by deconvolution of the experimental decay with the instrument response function and by fitting the decay curves with an exponential decay function using the corresponding spectrometer software. Solvents and cuvette were used as in the steady state fluorescence experiments.

Polarised Steady-State Fluorescence Excitation Spectroscopy

- Photon Technology International QuantaMasterTM model QM-2000-4

    o   water-cooled photomultiplier (R928P)

    o   xenon short-arc lamp (75 W, Ushio UXL-75XE)

    o   software FeliX32TM (v. 1.2.0.56)

For polarised excitation and detection two Glan-Thompson-polarisers from Photon Technology International were used in an L-format setup (cf. Scheme 10, p: 24). The emission was detected at 22000 cm^{-1} (450 nm). For the measurements at RT sucrose octaacetate (SOA) was used as the solid matrix. SOA was purchased from Acros and recrystallised from ethanol. SOA and the analyte were dissolved in DCM (Merck, Uvasol) and filtered through a PTFE-filter (0.2 μm pore size, Whatman). After purging with argon for 10 min, the solution was concentrated in vacuo and a colourless oil was obtained. This oil was filled in a 1 cm quartz cuvette (Hellma) and kept at 100°C for 1 h and at 130°C for 4 h in an oven in order to remove excess of solvent.

fs-Fluorescence Up-conversion[341,342]

A commercial fluorescence up-conversion set-up (Halcyone from Ultrafast Systems) was used for fluorescence up-conversion measurements. The laser system consists of an ultrafast amplified Ti:Sapphire laser (Solstice from Newport-Spectra-Physics) with a central wavenumber of 12500 cm^{-1} (800 nm), a pulse length of 100 fs and a repetition rate of 1 kHz. One part of the output beam was used to pump an optical parametric amplifier (TOPAS from Light Conversion/Newport-Spectra-Physics) as the source for the pump pulse with an attenuated energy of < 250 nJ, a wavenumber of 26300 cm^{-1} (380 nm) and a pulse length of 140 fs. This pump pulse was slightly focussed (spot diameter at 1/e^2 intensity ca. 100 μm) onto a 2 mm path length quartz cuvette (Spectrocell Inc.) with the stirred sample solution (Uvasol solvents, purged with argon). After the quartz cuvette the pump pulse was filtered off by a coloured glass 400 nm longpass filter.

The fluorescence light was collected by a quartz lens (f = 100 mm) and focussed with an identical quartz lens on a 0.5 mm BBO type I crystal for frequency up-conversion with the gate pulse (250 – 500 nJ at 12500 cm^{-1} (800 nm)) from the Solstice laser system. The gate pulse was delayed by a 0 – 3.3 ns delay line in linear 20 fs steps between 0 – 4 ps and in logarithmic steps between 4 – 3200 ps. The up-converted light was focussed onto the entrance slit of a double monochromator, measured by a PMT and subsequently amplified. For polarisation dependent

measurements, both the pump and the gate pulse were polarised by wire grids polarisers (Thorlabs) and the pump pulse polarisation was adjusted by a half-wave-plate either parallel, perpendicular or in magic angle relative to the gate pulse. The instrument response was estimated by measuring stray light or the Raman signals of the pure solvents which gave ca. 260 fs fwhm for DCM, 350 fs for MeCN, 350 fs for toluene and 770 fs for PhCN. However, during the global analysis, the IRF was treated as a Gaussian shaped function with the fwhm as a free floating parameter.

Excitation of the chromophore at 26300 cm^{-1} (380 nm) with 140 fs pulses induces fluorescence at 20800 cm^{-1} (480 nm) in the sample (2 mm cuvette with the respective compound in DCM at ca. *OD* = 0.3) which was up-converted by a 12500 cm^{-1} (800 nm) gate pulse in a 0.5 mm BBO type I crystal. The excitation wavelength 26300 cm^{-1} (380 nm) was chosen because this minimises excitation of electronically higher excited states. The time resolution was measured by up-converting stray light from the OPA at 20800 cm^{-1} (480 nm) which yields an instrument response of 260 fs at fwhm in DCM. The measurements under magic angle conditions were deconvoluted by the instrument response (taken as a Gaussian shaped pulse with fwhm as a free-floating parameter) and fitted by multiple exponentials.

ns-Transient Absorption Spectroscopy

- Edinburgh LP 920 laser flash spectrometer with a 450 W ozone-free Xe arc lamp including a photomultiplier (Hamamatsu R955), digital storage oscilloscope (Tektronix TD3012B) and software (L900 v. 6.5.6.3)

- Continuum Minilite II Nd:YAG laser operating at 10 Hz, 3 – 5 ns pulse duration, pulse energy between 0.2 mJ and 2.0 mJ at 355 nm

For these experiments the substances were dissolved in the same solvent as used for steady-state experiments filled in 1 cm sealed quartz cuvettes (Starna, Pfungstadt, Germany) and the solutions were degassed by bubbling argon through the solution for 60 min prior to measurements. As pump pulse the third harmonic of the fundamental at 28200 cm^{-1} (355 nm) was used and the laser pulse energy was varied between 0.2 mJ and 2.0 mJ with a pulse length of 5 ns. The instrument response function (IRF) (~ 8 ns) was determined by measuring the scatter light using a LUDOX AS-30 colloidal silica suspension in water. The measured transient signal intensity was corrected by the fluorescence intensity obtained from measurements without probe light. Decay traces with lifetimes shorter than 100 ns were deconvoluted with the IRF and decay curves with longer lifetimes were tail-fitted using the corresponding spectrometer software. Residuals and autocorrelation

function (without any significant structure) served as the main criteria in the evaluation of the fits. Decay curves recorded at the three band maxima all present identical biexponential kinetics for a given compound. Excitation with different laser pulse energies had no effect on the dynamics and the transient spectra and thus two-photon processes are excluded.[326]

For the magnetic field dependent measurements the probe beam was redirected by four mirrors through an electromagnet (Model: 5403FG, GMW-Associates) powered by a Sorensen (DLM-E 3kW) power supplier and performing between 0 and 2000 mT. The pulse and the probe beam were oriented perpendicular and met each other in the sample cuvette (see Scheme 53). The magnetic field was measured by a Hall-sensor (Single-Axis Magnetic Field Transductor YM12 2 5-5T, SENIS GmbH) and varied in 1 mT steps (till 20 mT), 4 mT steps (till 100 mT), 10 mT steps (till 500 mT), 50 mT steps (till 1000 mT) and 100 mT steps (till 2000 mT).
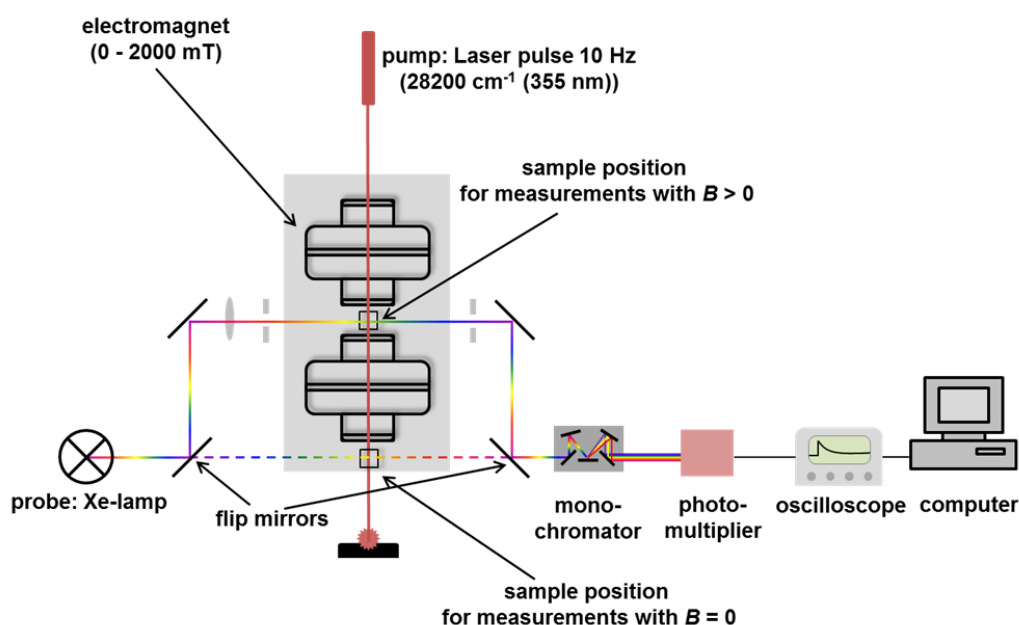
Scheme 53:   **Illustration of the magnetic field dependent ns-transient absorption set-up.**

fs-Transient Absorption Spectroscopy

All pump-probe experiments were performed in a 2 mm quartz cuvette (Spectrocell Inc.) at RT. The sample was dissolved in the same solvent as used in the steady-state experiments ($OD \approx 0.3$ at the excitation energy), degassed with argon for 30 min prior to the measurement and sustained stirred during the measurement. The setup consists of a commercial Helios transient spectrometer from Ultrafast Systems and is driven by an Solstice Ti:sapphire amplifier from Newport-Spectra-Physics (pulse duration of 100 fs) with a central wavenumber of 12500 cm^{-1} (800 nm) and a repetition rate of 1 kHz.

The output beam gained from the Solstice amplifier was split into two parts. One part was used to pump an optical parameter amplifier (TOPAS-C) from Newport-Spectra-Physics as the source for the pump pulses with a pulse length of 140 fs and a wavenumber of 26300 cm^{-1} (380 nm) with an attenuated energy of 150 – 210 nJ. The other, quite small part of the Solstice amplifier output beam was focused into a moving CsF$_2$-plate to generated a white light continuum between 12500 cm^{-1} (800 nm) and 24000 cm^{-1} (415 nm) which was used as the probe pulse. The depolarised excitation pulse was collimated to a spot, which was at least two times larger than the diameter of the spatially overlapping linear polarised probe pulse.

Detection of the probe pulses was achieved using a CMOS sensor (Ultrafast Systems, Helios) with 1.5 nm intrinsic resolution and 350 – 800 nm sensitivity range. A part of the probe light was used to correct for intensity fluctuations of the white light continuum. A mechanical chopper (working at 500 Hz) blocked every second pump pulse, in order to measure I and I_0. The photoinduced change of the optical density can be recorded by comparing the transmitted spectral intensity of consecutive pulses ($I(\lambda, \tau)$, $I_0(\lambda)$) by the following equation:

$$\Delta OD = -\log\left(\frac{I(\lambda, \tau)}{I_0(\lambda)}\right)$$

The relative temporal delay between pump and probe pulses was varied over a maximum range of 8 ns with a motorised, computer-controlled linear stage. While the delay interval between two consecutive data points was 13.3 fs for small delay times, it increased up to 200 ps for very large delay times.

Steady-state absorption measurements of the sample before and after the pump-probe measurements were performed to verify the stability of the sample.

The obtained time resolved spectra were corrected for stray light and the white light dispersion (chirp). The chirp was corrected by fitting a polynomial to the cross phase modulation signal of the pure solvent under otherwise experimental conditions. Further analyses of the spectra using GLOTARAN[238] is described in the respective section (*cf.* 3.2.4.2, p: 187).

5.2 Synthesis

All solvents and reagents were commercially available and were used without further purification unless otherwise denoted. All reactions were performed in standard glass ware. For inert-gas conditions using schlenk techniques flame dried glass ware were used. The nitrogen was dried over Sicapent from Merck and the oxygen was removed by copper catalyst R3-11 from BASF. Solvents were dried according to known literature.[343] Merck silica gel 32-63 μm was used for flash chromatography.

5.2.1 General Procedures

GP1:   Azidation of aryl bromides[194]

Under nitrogen atmosphere the aryl bromide (1.0 equiv.), NaN_3 (2.0 equiv.) and L(+)-sodium ascorbate (0.05 equiv.) were dissolved in the specified solvent and CuI (0.1 equiv.) and N,N'-dimethylethylenediamine (DMAP) (0.15 equiv.) were added while the solution was degassed with nitrogen. The resulting solution was heated to reflux for 8 h in the dark. Then the solution was allowed to cool down to RT and stirred for additional 18 h. The reaction mixture was taken-up by a mixture of brine and EA. The layers were separated and the organic layer was washed twice with water while the aqueous phase was extracted twice with EA. The organic layers were combined, dried over $MgSO_4$ and the solvent was removed under reduced pressure. The crude product was purified by flash-chromatography.

GP2:   *Hagihara-Sonogashira* Coupling with $Pd(PhCN)_2Cl_2$, ${}^tBu_3P$, Copper(I) iodide and ${}^iPr_2NH$
         in 1,4-dioxane[191]

The aryl halide (1 equiv.*) was dissolved in dry 1,4-dioxane and CuI (0.02 equiv.*) and $Pd(PhCN)_2Cl_2$ (0.03 equiv.*) were added while the solution was degassed with nitrogen. After addition of ${}^tBu_3P$ (0.06 equiv.*, 1.0 M solution in toluene), ${}^iPr_2NH$ (1.10 equiv.*) and an excess of the acetylene the resulting solution was stirred at the specified temperature under preclusion of light. The solvent was evaporated *in vacuo*, the residue resolved in DCM and washed twice with a saturated aqueous $Na_2S_2O_3$-solution and three times with water while the aqueous phase was extracted twice with DCM. The organic layers were combined and the solvent was removed under reduced pressure. The crude product was purified by flash-chromatography.

* The data are referenced to one halide functionality in the reactant.

GP3:   Transformation of trialkylsilylacetylenes into terminal acetylenes (deprotection)

The triisopropylsilyl acetylene (1 equiv.*) was dissolved in DCM and solid TBAF trihydrate (1.1 equiv. – 2.5 equiv.*) was added. The solution was stirred for the given period at RT in the dark. More DCM was added to the mixture and the organic layer was washed three times with water while the aqueous phase was extracted twice with DCM. The organic layers were combined and the solvent was removed. Further purification was performed as mentioned below.

* The data are referenced to one of trialkylsilylacetylene functionality in the reactant.

GP4:   Cu catalysed *Ullmann* Coupling of diarylamines with 1-bromo-4-iodobenzene[202]

A solution of the diarylamine (1 equiv.), 1-bromo-4-iodobenzene (1.5 equiv.), dried K_2CO_3 (5 equiv.) and 18-crown-6-ether (0.125 equiv) in *o*-DCB was degassed with nitrogen for 15 min before activated copper[344] (2.5 equiv) was added. The solution was degassed for further 7 min and then heated at 179°C for the given time under preclusion of light. The solid was filtered off and the solvent was evaporated *in vacuo*, the residue resolved in DCM and washed once with a saturated aqueous $Na_2S_2O_3$-solution and twice with water while the aqueous phase was extracted twice with DCM. The organic layers were combined, dried over $MgSO_4$ and the solvent was removed under reduced pressure. The crude product was purified by flash-chromatography.

GP5:   *Buchwald-Hartwig* Amination with $Pd_2(dba)_3 \cdot CHCl_3$, NaO^{t}Bu and ^{t}Bu$_3$P in toluene[210,211]

The bromo-aryl or iodo-aryl derivative (1 equiv.) was dissolved in dry toluene and NaO^{t}Bu (1.5 euiv.) and $Pd_2(dba)_3 \cdot CHCl_3$ (0.04 quiv.) were added while the solution was degassed with nitrogen. After addition of ^{t}Bu$_3$P (0.06 quiv., 1.0 M solution in toluene) and the aniline derivative (1 equiv.) the solution was stirred for the given time at the specified temperature under preclusion of light. The solvent was evaporated *in vacuo*, the residue resolved in DCM and washed once with a saturated aqueous $Na_2S_2O_3$-solution and three times with water while the aqueous phase was extracted twice with DCM. The organic layers were combined and the solvent was removed under reduced pressure. The crude product was purified by flash-chromatography.

GP6: Bromination of diarylamines with TBATB[107]

A solution of the diarylamine (1 equiv.) in CHCl₃ was cooled to 0°C and a solution of TBATB (1 equiv.) in CHCl₃ was added over 3.5 h. After addition the mixture was stirred for 1 h at 0°C and then allowed to warm up to RT. At this temperature the mixture was stirred for additional 30 min until a saturated aqueous $Na_2S_2O_3$-solution was added. This mixture was stirred for 12 h at RT and then washed twice with a saturated aqueous $NaHCO_3$-solution and three times with water. The organic layers were combined and the solvent was removed under reduced pressure. The crude product was purified by flash-chromatography.

5.2.2 Dendrimers

5.2.2.1 Building Blocks

Compound 1
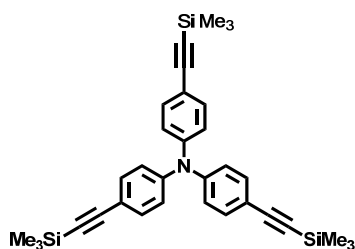
CA: [189178-08-3]

According to general procedure GP2:

Tris(4-bromophenyl)amine (300 mg, 622 μmol), CuI (7.11 mg, 37.0 μmol), Pd(PhCN)$_2$Cl$_2$ (21.0 mg, 56.0 μmol), ^{t}Bu$_3$P (112 μL, 112 mmol, 1.0 M solution in toluene), ^{i}Pr$_2$NH (208 mg, 2.05 mmol), TMSA (excess), 1,4-dioxane (15 mL), 5 d, RT, flash-chromatography (silica gel, PE / DCM = 10:1→ 1:1).

Formula: C$_{33}$H$_{39}$NSi$_3$ [533.93].

Yield: 295 mg (553 μmol) **89 %** of a yellow solid.

^{1}H-NMR (400 MHz, CDCl$_3$): δ / ppm = 7.34 (AA´, 6 H), 6.95 (BB´, 6 H), 0.23 (s, 27 H).

Compound 2
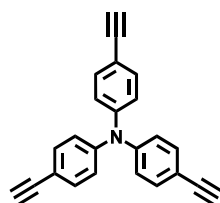
CA: [189178-09-4]

According to general procedure GP3:

1 (500 mg, 936 μmol), TBAF trihydrate (975 mg, 3.09 mmol), DCM (20 mL), 30 min.

Formula: $C_{33}H_{15}N$ [317.38].

Yield: 283 mg (892 μmol) **95 %** of an orange to yellow solid.

^{1}H-NMR (400 MHz, CDCl$_3$): δ / ppm = 7.38 (AA´, 6 H), 7.00 (BB´, 6 H), 3.05 (s, 3 H).

Compound 3[192]
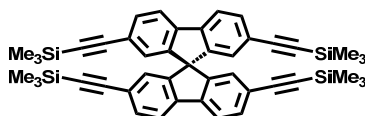
CA: [1103763-96-7]

2,2',7,7'-Tetrabromo-9,9'-spirobi[9H-fluorene] (300 mg, 475 μmol) was dissolved in Et$_3$N (20 mL) and CuI (24.0 mg, 127 μmol), Pd(PhCN)$_2$Cl$_2$ (73.0 mg, 190 μmol), ^{i}Pr$_2$NH (256 mg, 2.53 mmol), ^{t}Bu$_3$P (304 μL, 304 μmol, 1.0 M solution in toluene) and TMSA (excess) were added while the solution was degassed with nitrogen. The resulting solution was stirred at RT for 6 d under preclusion of light. The solvent was removed *in vacuo* and the residue was redissolved in DCM (50 mL). The solution was once washed with water (50 mL) and filtered through silica gel. Next the solution was concentrated and dropped into ethanol. The solid were filtered off and washed with ethanol to obtain the product as an off-white solid.

Formula: $C_{45}H_{48}Si_4$ [701.20].

Yield: 190 mg (271 μmol) **57 %** of an off-white solid.

¹H-NMR (400 MHz, CDCl₃)**:** δ / ppm = 7.73 (dd, ^3J = 7.9, ^5J = 0.68, 4 H), 7.49 (dd, ^3J = 7.9, ^4J = 1.4, 4 H), 6.77 (dd, ^4J = 1.4, ^5J = 0.68, 4 H), 0.16 (s, 36 H).

Compound 4[192]
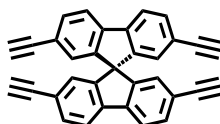
CA: [1103763-99-0]

A solution of **3** (71.0 mg, 101 μmol) and TBAF trihydrat (540 μL, 540 μmol, 1.0 M solution in THF) in THF (20 mL) was stirred for 3 d at RT in the dark. The solvent was evaporated *in vacuo*, the residue was resolved in DCM (50 mL) and washed with water (3 x 30 mL). The solvent was removed under reduced pressure and the crude product was purified by flash-chromatography (silica gel, PE / DCM = 2:1) to obtain a yellow solid.

Formula: C₃₃H₁₆ [412.48].

Yield: 40.0 mg (97.0 μmol) **96 %** of a yellow solid.

¹H-NMR (400 MHz, CDCl₃)**:** δ / ppm = 7.77 (dd, ^3J = 7.9, ^5J = 0.64, 4 H), 7.52 (dd, ^3J = 7.9, ^4J = 1.4, 4 H), 6.83 (dd, ^4J = 1.4, ^5J = 0.64, 4 H), 3.00 (s, 4 H).

Compound 5[193]
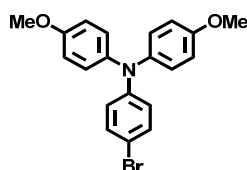
CA: [194416-45-0]

To a solution of 4-iodoanisole (7.00 g, 29.9 mmol), 4-bromoaniline (2.44 g, 14.2 mmol) and 1,10-phenanthroline (102 mg, 568 μmol) in toluene (15 mL) CuI (108 mg, 568 μmol) and dried powdered KOH (6.21 g, 111 mmol) were added while the suspension was degassed with nitrogen. The reaction mixture was heated to 111°C for 26 h. The solvent was evaporated *in vacuo*, the residue was dissolved in DCM (125 mL) and washed with a saturated aqueous Na₂S₂O₃-solution (120 mL) and water (120 mL) while the aqueous phase was extracted twice with DCM (50 mL). The organic layers were combined and the solvent was removed under reduced pressure. The crude

product was purified by flash-chromatography (silica gel, *n*-hexane / DCM = 3:1) to obtain an off-white solid.

Formula: $C_{20}H_{18}BrNO_2$ [384.27].

Yield: 2.89 g (7.52 mmol) **53 %** of an off-white solid.

^{1}H-NMR (400 MHz, $(CD_3)_2CO$)**:** δ / ppm = 7.29 (AA´, 2 H), 7.06 (AA´, 4 H), 6.91 (BB´, 4 H), 6.74 (BB´, 2 H), 3.79 (s, 6 H).

Compound 6[221]
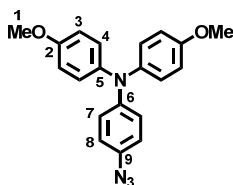
According to general procedure GP1:

5 (1.00 g, 2.60 mmol), NaN_3 (338 mg, 5.20 mmol), *L*(+)-sodium ascorbate (26.0 mg, 130 μmol), CuI (50.0 mg, 260 μmol), DMAP (34.0 mg, 390 μmol), nitrogen degassed $EtOH/H_2O$ 7:3 (80 mL), flash-chromatography (silica gel, PE / EA = 10:1).

Formula: $C_{20}H_{18}N_4O_2$ [346.38].

Yield: 791 mg (2.28 mmol) **88 %** of a brown solid.

^{1}H-NMR (600 MHz, $CDCl_3$)**:** δ / ppm = 7.01 (AA´, 4 H, H-4), 6.93 (AA´, 2 H, H-7), 6.84 (BB´, 2 H, H-8), 6.81 (BB´, 4 H, H-3), 3.79 (s, 6 H, H-1).

^{13}C-NMR (150 MHz, $CDCl_3$)**:** δ / ppm = 155.8 C-2, 146.1 C-6, 141.0 C-5, 132.0 C-9, 126.2 C-4, 122.5 C-7, 119.7 C-8, 114.8 C-3, 55.6 C-1.

IR (ATR): $\tilde{v}$ / cm^{-1}: 2930 (w, C-H aryl), 2100 (s, -N_3).

ESI-MS pos (high resolution): [M$^{\bullet+}$ -N$_2$, -H]

$$\text{calc.} \quad m/z = 317.12845$$
$$\text{found.} \quad m/z = 317.12846 \quad\quad\quad \Delta = 0.03 \text{ ppm}$$

Compound 7[120,195]
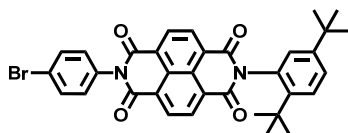
CA: [1163177-10-3]

2,5-Di-tert-butylaniline (766 mg, 3.73 mmol) and 1,4,5,8-naphthalenetetracarboxylic dianhydride (1.00 g, 3.73 mmol) were suspended in dry pyridine (28 mL). The suspension was irradiated with microwaves to heat it to 145°C for 90 min. After cooling down, 4-bromo-aniline (641 mg, 3.73 mmol) was added to the mixture and it was again heated to 145°C for 90 min using microwave irradiation. Afterwards the mixture was cooled to RT, the solid was filtered off and washed with DCM. After removing the solvents under reduced pressure, the residue was purified by flash-chromatography (silica gel, DCM) to obtain the product as a yellow solid.

Formula: C$_{34}$H$_{29}$BrN$_2$O$_4$ [609.51].

Yield: 593 mg (973 μmol) **26 %** of a yellow solid.

^{1}H-NMR (400 MHz, CDCl$_3$): δ / ppm = 8.85 (-, 4 H), 7.72 (AA′, 2 H), 7.61 (d, ^3J = 8.5, 1 H), 7.49 (dd, ^3J = 8.5, ^4J = 2.2, 1 H), 7.22 (BB′, 2 H), 7.01 (d, ^4J = 2.2, 1 H), 1.33 (s, 9 H), 1.27 (s, 9 H).

Compound 8
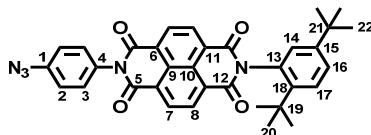
Compound **7** (528 mg, 866 μmol), NaN$_3$ (113 mg, 1.73 mmol) and L(+)-sodium ascorbate (8.58 mg, 43.0 μmol) were dissolved in nitrogen degassed ^{i}PrOH/H$_2$O 9:2 (210 mL) and CuI (269 mg, 1.41 mmol) and DMAP (11.0 mg, 130 μmol) were added while the solution was degassed with nitrogen. The resulting solution was heated to reflux for 16 h under preclusion of light. Then the solution was cooled to RT. The reaction mixture was taken up by a mixture of brine and EA (200 mL). The layers were separated and the organic layer was washed twice with water (100 mL)

while the aqueous phase was extracted twice with EA. The organic layers were combined and the solvent was removed under reduced pressure. The crude product was purified by flash-chromatography (silica gel, DCM / PE = 5:1 → 10:1) to obtain a yellow solid.

Formula: $C_{34}H_{29}N_5O_4$ [571.63].

Yield: 263 mg (460 μmol) **53 %** of a yellow solid.

^{1}H-NMR (600 MHz, $CDCl_3$): δ / ppm = 8.86 (-, 4 H, H-8 a. H-7), 7.61 (d, ^3J = 8.5, 1 H, H-17), 7.49 (dd, ^3J = 8.5, ^4J = 2.0, 1 H, H-16), 7.33 (AA´, 2 H, H-3), 7.24 (BB´, 2 H, H-2), 7.01 (d, ^3J = 2.0, 1 H, H-14), 1.33 (s, 9 H, H-22) 1.27 (s, 9 H, H-20).

^{13}C-NMR (150 MHz, $CDCl_3$): δ / ppm = 163.9 C-12, 163.1 C-5, 150.5 C-15, 143.8 C-18, 141.2 C-1, 132.0 C-13, 131.7 C-7 o. C-8, 131.6 C-7 o. C-8, 131.2 C-4, 130.1 C-3, 129.1 C-17, 127.6 C-14, 127.5 C-9 a. C-10, 127.4 C-6 o. C-11, 127.0 C-16, 126.8 C-6 o. C-11, 120.3 C-2, 35.7 C-19, 34.4 C-21, 31.8 C-22, 31.3 C-20.

MALDI-TOF pos: [M$^{\bullet+}$ -N$_2$]

$$\text{calc.} \quad m/z = 543.215$$
$$\text{found.} \quad m/z = 543.091$$

Compound 9
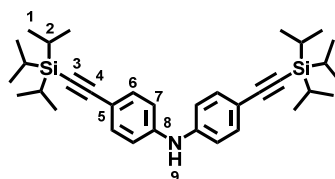
According to general procedure GP2:

Bis(4-bromophenyl)amine (500 mg, 1.52 mmol), CuI (12.0 mg, 61.0 μmol), Pd(PhCN)$_2$Cl$_2$ (35.0 mg, 92.0 μmol), ^{t}Bu$_3$P (183 μL, 183 mmol, 1.0 M solution in toluene), ^{i}Pr$_2$NH (340 mg, 3.36 mmol), TIPSA (excess), 1,4-dioxane (10 mL), 3 d, 50°C, flash-chromatography (silica gel, PE / DCM = 10:1).

Formula: $C_{34}H_{51}NSi_2$ [529.95].

Yield: 672 mg (1.27 mmol) **84 %** of a yellow solid.

^{1}H-NMR (600 MHz, (CD$_3$)$_2$CO)**:** δ / ppm = 7.96 (s, 1 H, H-9), 7.39 (AA′, 4 H, H-6), 7.14 (BB′, 4 H, H-7), 1.14 (-, 42 H, H-1 a. H-2).

^{13}C-NMR (150 MHz, (CD$_3$)$_2$CO)**:** δ / ppm = 144.1 C-8, 144.0 C-8^a, 133.9 C-6, 117.9 C-7, 117.8 C 7^a, 115.72 C-5, 115.70 C-5^a, 108.9 C-4, 88.565 C-3, 88.561 C-3^a, 19.0 C-1, 12.0 C-2.

ESI-MS pos (high resolution)**:** [M$^{•+}$]

              calc.   m/z = 529.35545
              found.   m/z = 529.35543 Δ = 0.04 ppm

Compound 10
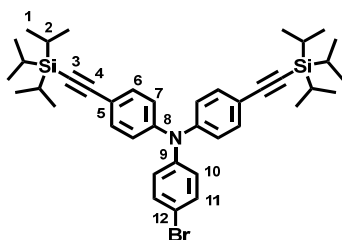
According to general procedure GP4:

9 (300 mg, 566 μmol), 1-bromo-4-iodobenzene (240 mg, 849 μmol), dried K$_2$CO$_3$ (391 mg, 2.83 mmol), 18-crown-6-ether (19.0 mg, 71.0 μmol), activated copper (90.0 mg, 1.42 mmol), *o*-DCB (15 mL), 3 d, flash-chromatography (silica gel, PE).

Formula: C$_{40}$H$_{54}$BrNSi$_2$ [684.94].

Yield: 189 mg (276 μmol) **49 %** of a yellow solid.

^{1}H-NMR (600 MHz, (CD$_3$)$_2$CO)**:** δ / ppm = 7.50 (AA′, 2 H, H-11), 7.43 (AA′, 4 H, H-6), 7.06 (2 x BB′, 4 H + 2 H, H-7 a. H-10), 1.14 (-, 42 H, H-1 a. H-2).

^{13}C-NMR (150 MHz, (CD$_3$)$_2$CO)**:** δ / ppm = 148.0 C-5, 146.9 C-9, 134.0 C-6, 133.5 C-11, 127.6 C-10, 124.5 C-7, 118.7 C-8, 117.1 C-12, 108.1 C-4, 90.2 C-3, 19.0 C-1, 12.0 C-2.

---

^{a} The ^{13}C-signal split is probably caused by a hindered rotation in the phenyl rings.

ESI-MS pos (high resolution)**:** [M$^{•+}$]

<div style="text-align:center">

calc.   m/z = 683.29726

found. m/z = 683.29770 Δ = 0.64 ppm

</div>

Compound 11
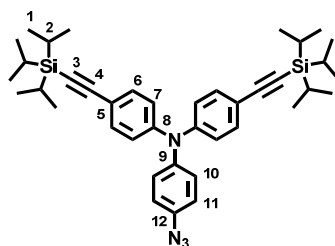
According to general procedure GP1:

10 (643 mg, 938 μmol), NaN$_3$ (122 mg, 1.87 mmol), L(+)-sodium ascorbate (9.29 mg, 47.0 μmol), CuI (18.0 mg, 94.0 μmol), DMAP (12.0 mg, 141 μmol), nitrogen degassed ^{i}PrOH/H$_2$O 7:3 (80 mL), flash-chromatography (silica gel, n-hexane).

Formula: C$_{40}$H$_{54}$N$_4$Si$_2$ [647.05].

Yield: 340 mg (525 μmol) **56 %** of an orange solid.

^{1}H-NMR (600 MHz, (CD$_3$)$_2$CO)**:** δ / ppm = 7.42 (AA´, 4 H, H-6), 7.17 (AA´, 2 H, H-10), 7.09 (BB´, 2 H, H-11), 7.03 (BB´, 4 H, H-7), 1.14 (-, 42 H, H-1 a. H-2).

^{13}C-NMR (150 MHz, (CD$_3$)$_2$CO)**:** δ / ppm = 148.2 C-5, 144.5 C-9, 136.8 C-12, 134.0 C-6, 127.9 C-10, 124.0 C-7, 121.2 C-11, 118.2 C-8, 108.2 C-4, 90.0 C-3, 19.0 C-1, 12.0 C-2.

MALDI-TOF pos: [M$^{•+}$ -N$_2$, + 2 x H]

<div style="text-align:center">

calc.   m/z = 620.397

found. m/z = 620.461

</div>

5.2.2.1.1   Dendrimer Syntheses

Compound 12
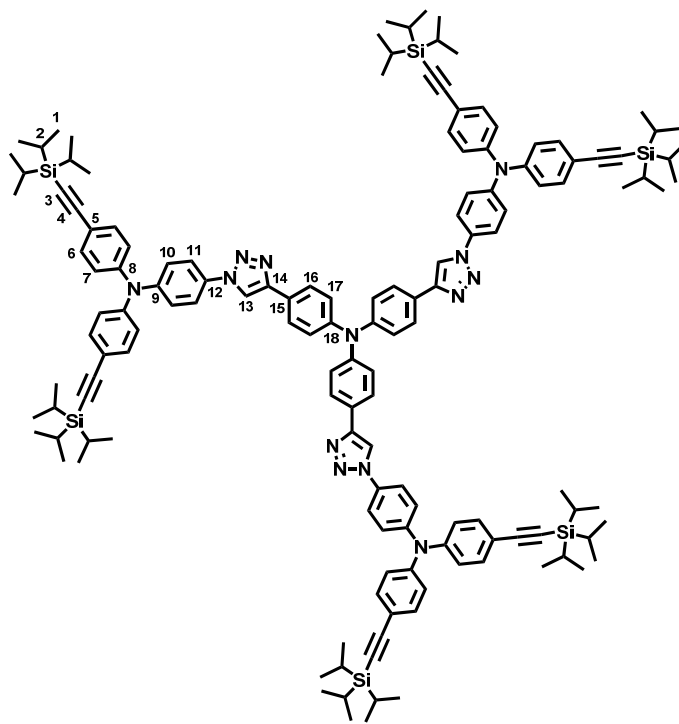
Compound **2** (77.0 mg, 243 μmol) and **11** (843 mg, 1.30 *m*mol) were dissolved in dry THF (25 mL) and (PPh$_3$)$_3$CuBr (50.0 mg, 54.0 μmol) was added while the solution was degassed with nitrogen. After addition of DIPEA (94.0 mg, 728 μmol) the solution was stirred for 20 d at 40°C under preclusion of light. The solvent was evaporated *in vacuo* and the raw product was purified by recycling GPC in CHCl$_3$.

Formula: C$_{144}$H$_{177}$N$_{13}$Si$_6$ [2258.55].

Yield: 496 mg (220 μmol) **90 %** of a brown solid.

^{1}H-NMR (600 MHz, CD$_2$Cl$_2$): δ / ppm = 8.16 (s, 3 H, H-13), 7.84 (AA´, 6 H, H-16), 7.68 (AA´, 6 H, H-11), 7.40 (AA´, 12 H, H-6), 7.26 (BB´, 6 H, H-17), 7.23 (BB´, 6 H, H-10), 7.05 (BB´, 12 H, H-7), 1.12 (-, 126 H, H-1 a. H-2).

^{13}C-NMR (150 MHz, CD$_2$Cl$_2$): δ / ppm = 148.1 C-14, 147.6 C-18, 147.5 C-9, 147.1 C-8, 133.6 C-6, 132.7 C-12, 127.1 C-16, 125.6 C-15, 125.3 C-10, 124.9 C-17, 124.3 C-7, 122.0 C-11, 118.7 C-5, 117.6 C-13, 107.1 C-4, 90.6 C-3, 18.8 C-1, 11.7 C-2.

ESI-MS pos (high resolution)**:** [M$^{•+}$]

$$\text{calc.} \quad m/z = 2256.28600$$
$$\text{found.} \quad m/z = 2256.28566 \qquad \Delta = 0.15 \text{ ppm}$$

Compound 13
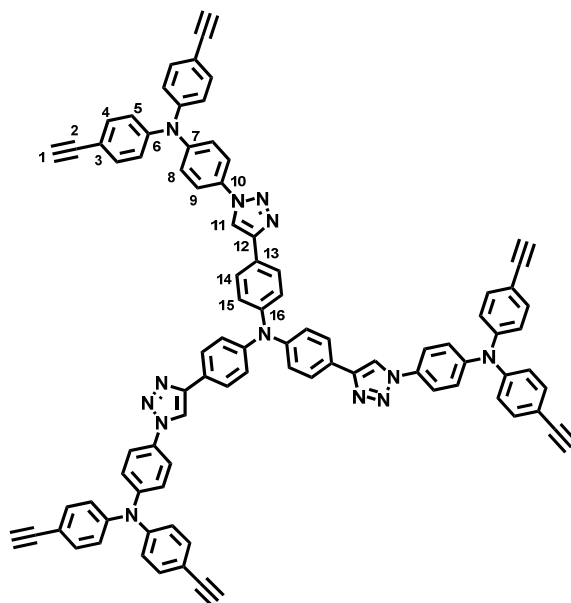
According to general procedure GP3:

12 (137 mg, 61.0 μmol), TBAF trihydrate (126 mg, 400 μmol), DCM (10 mL), 3 h, recycling GPC (CHCl$_3$).

Formula: C$_{90}$H$_{57}$N$_{13}$ [1320.50].

Yield: 66.0 mg (50.0 μmol) **82 %** of a yellow solid.

^{1}H-NMR (600 MHz, CD$_2$Cl$_2$)**:** δ / ppm = 8.17 (s, 3 H, H-11), 7.84 (AA´, 6 H, H-14), 7.70 (AA´, 6 H, H-9), 7.41 (AA´, 12 H, H-4), 7.25 (BB´ + BB´, 12 H, H-8 a. H-15), 7.07 (BB´, 12 H, H-5), 3.12 (s, 6 H, H-1).

^{13}C-NMR (150 MHz, CD$_2$Cl$_2$)**:** δ / ppm = 148.1 C-12, 147.7 C-16, 147.5 C-6, 147.4 C-7, 133.7 C-4, 132.9 C-10, 127.1 C-14, 125.7 C-8, 125.6 C-13, 124.9 C-15, 124.2 C-5, 122.0 C-9, 117.6 C-11, 117.1 C-3, 83.6 C-1, 77.2 C-2.

ESI-MS pos (high resolution)**:** [M$^{\bullet+}$]

$$\text{calc.} \quad m/z = 1319.48544$$

$$\text{found.} \quad m/z = 1319.48558 \qquad \Delta = 0.11 \text{ ppm}$$

Compound 14
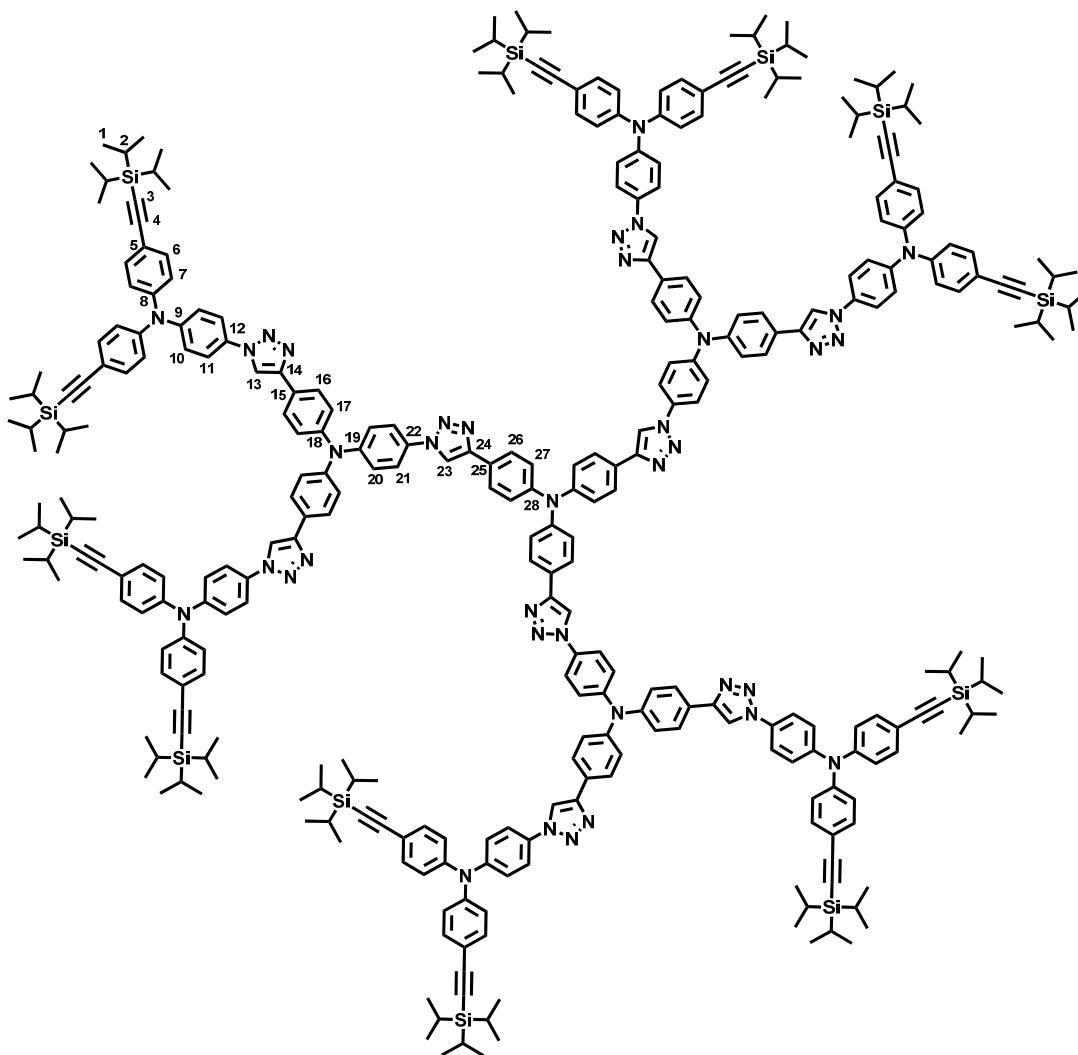
Compound **12** (34.3 mg, 26.0 μmol) and **11** (210 mg, 325 μmol) were dissolved in dry THF (20 mL) and (PPh$_3$)$_3$CuBr (11.0 mg, 12.0 μmol) was added while the solution was degassed with nitrogen. After addition of DIPEA (38.0 mg, 291 μmol) the solution was stirred for 36 d at 60°C under preclusion of light. The solvent was evaporated *in vacuo* and the residue purified by dropping a concentrated solution in DCM into methanol. The solid was filtered off and washed with methanol. The product was further purified by recycling GPC in CHCl$_3$.

Formula: $C_{330}H_{381}N_{37}Si_{12}$ [5202.83].

Yield: 101 mg (19.4 μmol) **75 %** of a brown solid.

¹H-NMR (600 MHz, CD_2Cl_2)**:** δ / ppm = 8.19 (s, 3 H, H-23), 8.18 (s, 6 H, H-13), 7.86–7.83 (AA´ + AA´, 12 H + 6 H, H-16 a. H-20), 7.71–7.67 (AA´ + AA´, 6 H + 12 H, H-26 a. H-11), 7.39 (AA´, 24 H, H-6), 7.30 (BB´, 6 H, H-27), 7.27–7.21 (BB´+ BB´ + BB´, 12 H + 6 H + 12 H, H-17 a. H-21 a. H-10), 7.04 (BB´, 24 H, H-7), 1.12 (-, 252 H, H-1 a. H-2).

¹³C-NMR (150 MHz, CD_2Cl_2)**:** δ / ppm = 148.11 C-28, 148.1 C-24, 148.0 C-14, 147.6 C-19, 147.5 C-9, 147.3 C-18, 147.1 C-8, 133.5 C-6, 132.6 C-12, 132.2 C-25, 127.2 C-16, 127.1 C-20, 126.1 C-15, 125.6 C-22, 125.3 C-10, 125.2 C-17, 124.9 C-21, 124.7 C-27, 124.3 C-7, 122.0 C-11 a. C-26, 118.7 C-5, 117.7 C-13, 117.6 C-23, 107.1 C-4, 90.6 C-3, 18.8 C-1, 11.6 C-2.

ESI-MS pos (high resolution)**:** X+2 [M$^{•2+}$]

                calc.   m/z = 2600.41206

                found. m/z = 2600.41948 Δ = 2.85 ppm

Compound 15
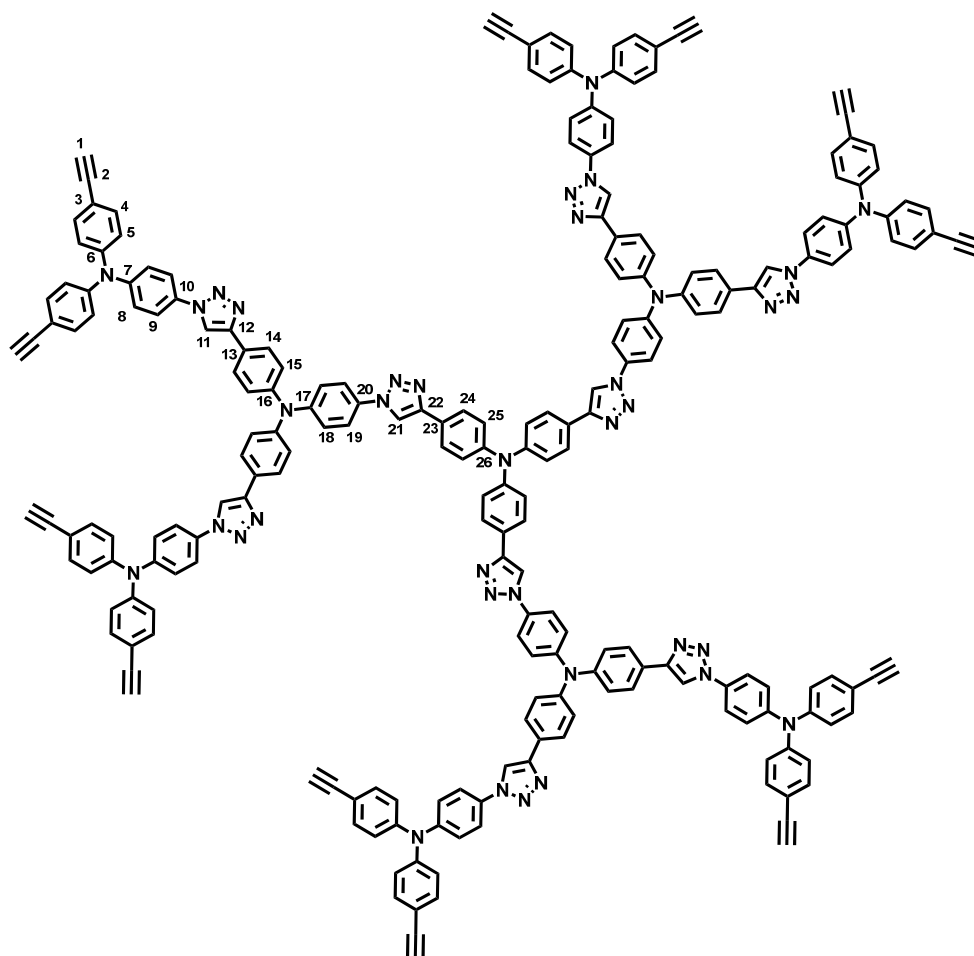
According to general procedure GP3:

14 (50.0 mg, 9.61 μmol), TBAF trihydrate (37.0 mg, 117 μmol), DCM (7 mL) 3 h, recycling GPC (CHCl₃).

Formula: $C_{222}H_{141}N_{37}$ [3326.74].

Yield: 29.2 mg (8.78 μmol) **91 %** of a beige solid.

¹H-NMR (600 MHz, CD_2Cl_2): δ / ppm = 8.19 (s, 3 H, H-21), 8.18 (s, 6 H, H-11), 7.87–7.84 (AA′ + AA′, 12 H + 6 H, H-14 a. H-19), 7.71–7.68 (AA′ + AA′, 6 H + 12 H, H-24 a. H-9), 7.41 (AA′, 24 H, H-4), 7.32 (BB′, 6 H, H-25), 7.28–7.24 (BB′ + BB′ + BB′, 12 H + 6 H + 12 H, H-15 a. H-18 a. H-8), 7.07 (BB′, 24 H, H-5), 3.12 (s, 12 H, H-1).

^{13}C-NMR (150 MHz, CD$_2$Cl$_2$): δ / ppm = 148.0 C-12 a. C-22 a. C-17, (147.5, 147.4, 147.3, C-6 a. C-7 a. C-16 a. C-26), 133.7 C-4, 132.9 C-10 a. C-20 a. C-23, 127.2 C-14, 127.1 C-19, 126.1 C-13, 125.7 C-8, 125.2 C-15, 124.9 C-18, 124.7 C-25, 124.2 C-5, 122.1 C-9, 122.0 C-24, 117.7 C-11 a. C-21, 117.1 C-3, 83.5 C-1, 77.2 C-2.

ESI-MS pos (high resolution): [M$^{\bullet 2+}$- 9 x N$_2$]

$$\text{calc.}\quad m/z = 1536.08031$$
$$\text{found.}\quad m/z = 1536.07953 \qquad \Delta = 0.51\ \text{ppm}$$

Compound 16
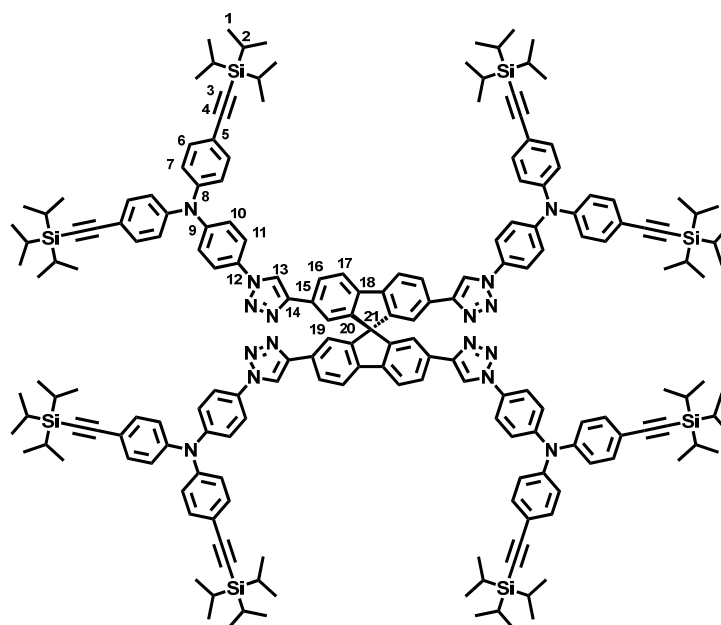
A solution of **4** (40.0 mg, 97.0 μmol), **11** (753 mg, 1.16 $m$mol) and (PPh$_3$)$_3$CuBr (34.0 mg, 37.0 μmol) in dry THF (30 mL) was degassed with nitrogen for 5 min. After addition of DIPEA (50.0 mg, 388 μmol) the solution was stirred for 5 d at 60°C under preclusion of light. The solvent was evaporated *in vacuo* and the residue purified dropping a concentrated DCM solution into 2-propanol. The solid was filtered off and washed with 2-propanol. The product was further purified by recycling GPC in CHCl$_3$.

Formula: C$_{193}$H$_{232}$N$_{16}$Si$_8$ [3000.70].

Yield: 121 mg (40.3 μmol) **42 %** of a yellowish solid.

¹H-NMR (600 MHz, CD$_2$Cl$_2$): δ / ppm = 8.10 (s, 4 H, H-13), 8.01–7.98 (-, 8 H, H-16 a. H-17), 7.53 (AA´, 8 H, H-11), 7.35 (AA´, 16 H, H-6), 7.30 (s, 4 H, H-19), 7.12 (BB´, 8 H, H-10), 6.99 (BB´, 16 H, H-7), 1.11 (-, 168 H, H-1 a. H-2).

¹³C-NMR (150 MHz, CD$_2$Cl$_2$): δ / ppm = 149.6 C-20, 148.0 C-14, 147.3 C-9, 147.0 C-8, 141.9 C-18, 133.4 C-6, 132.4 C-12, 130.6 C-15, 126.1 C-16, 125.1 C-10, 124.2 C-7, 121.7 C-11, 121.4 C-19, 121.2 C-17, 118.6 C-5, 118.0 C-13, 107.1 C-4, 90.6 C-3, 66.2 C-21, 18.7 C-1, 11.6 C-2.

MALDI-TOF neg: X+2 [M$^{\bullet-}$, - 4 x N$_2$, - 2 x H]

$\qquad\qquad\qquad$ calc.$\quad$ m/z = 374.217

$\qquad\qquad\qquad$ found.$\quad$ m/z = 374.215

Compound 17
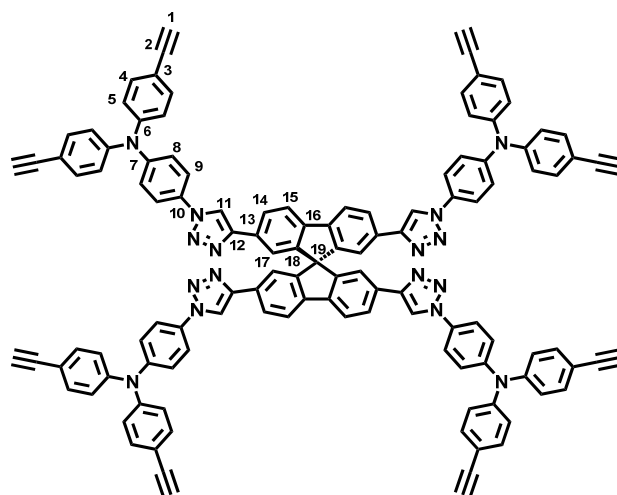
According to general procedure GP3:

16 (45.4 mg, 15.0 μmol), TBAF trihydrate (47.7 mg, 151 μmol), DCM (15 mL), 5 h, flash-chromatography (silica gel, DCM → EA).

Formula: C$_{121}$H$_{72}$N$_{16}$ [1749.97].

Yield: 25.9 mg (14.8 μmol) **99 %** of an off-white solid.

¹H-NMR (400 MHz, CD$_2$Cl$_2$): δ / ppm = 8.09 (s, 4 H, H-11), 8.022–8.020 (-,4 H + 4 H, H-14 a. H-17), 7.56 (AA´, 8 H, H-9), 7.37 (AA´, 16 H, H-4), 7.32 (dd, ^3J = 1.0, ^5J = 1.0, 4 H, H-15), 7.15 (BB´, 8 H, H-8), 7.01 (BB´, 16 H, H-5), 3.10 (s, 8 H, H-1).

¹³C-NMR (100 MHz, CD$_2$Cl$_2$): δ / ppm = 149.8 C-18, 148.2 C-12, 147.5 C-6, 147.3 C-7, 142.0 C-16, 133.7 C-4, 132.8 C-10, 130.7 C-13, 126.2 C-14, 125.6 C-8, 124.2 C-5, 121.9 C-9, 121.6 C-15, 121.3 C-17, 118.1 C-11, 117.2 C-3, 83.6 C-2, 77.2 C-1, 66.4 C-19.

MALDI-TOF pos: [M$^{\bullet+}$ + K]

<div align="center">

calc. m/z = 1787.575

found. m/z = 1787.515

</div>

Compound G1[221]
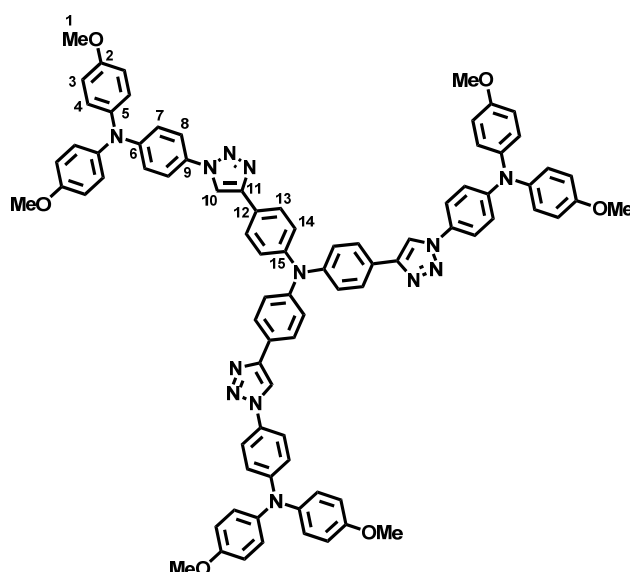
Compound **2** (100 mg, 315 μmol) and **6** (670 mg, 1.93 mmol) were dissolved in dry THF (35 ml) and (PPh$_3$)$_3$CuBr (65.0 mg, 70.0 μmol) was added while the solution was degassed with nitrogen. After addition of DIPEA (122 mg, 945 μmol) the solution was stirred for 21 d at 65°C under preclusion of light. The solvent was evaporated *in vacuo* and the residue purified by dropping a concentrated solution in DCM into methanol. The solid was filtered off and washed with methanol. The product was further purified by recycling GPC in CHCl$_3$.

Formula: C$_{84}$H$_{69}$N$_{13}$O$_6$ [1356.53].

Yield: 336 mg (248 μmol) **79 %** of a beige solid.

¹H-NMR (600 MHz, CD_2Cl_2)**:** δ / ppm = 8.09 (s, 3 H, H-10), 7.81 (AA´, 6 H, H-13), 7.52 (AA´, 6 H, H-8), 7.24 (BB´, 6 H, H-14), 7.10 (AA´, 12 H, H-4), 6.99 (BB´, 6 H, H-7), 6.88 (BB´, 12 H, H-3), 3.79 (s, 18 H, H-1).

¹³C-NMR (150 MHz, CD_2Cl_2)**:** δ / ppm = 157.0 C-2, 149.8 C-6, 148.1 C-11, 147.6 C-15, 140.4 C-5, 129.7 C-9, 127.5 C-4, 127.1 C-13, 125.8 C-12, 124.8 C-14, 121.7 C-8, 120.0 C-7, 117.6 C-10, 115.2 C-3, 55.8 C-1.

ESI-MS (high resolution)**:** $[M^{\bullet+}]$

calc. m/z = 1355.54882

found. m/z = 1355.54885 Δ = 0.02 ppm

Compound G2
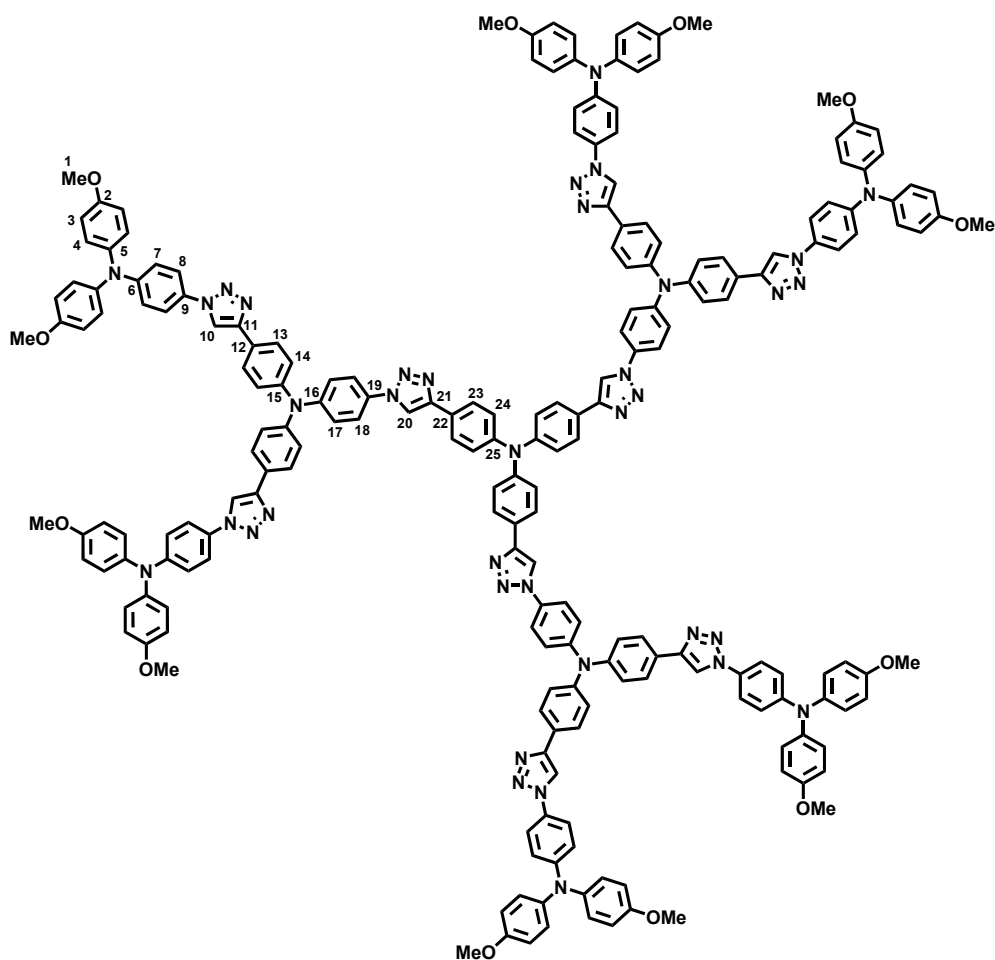
Compound **13** (137 mg, 104 μmol) and **6** (425 mg, 122 mmol) were dissolved in dry THF (40 mL) and (PPh₃)₃CuBr (45.0 mg, 48.0 μmol) was added while the solution was degassed with nitrogen. After addition of DIPEA (148 mg, 1.15 mmol) the solution was stirred for 22 d at 60°C under preclusion of light. The solvent was evaporated *in vacuo* and the residue purified by flash-chromatography (silica gel, PE / EA = 1:1). The product fraction was further purified by recycling GPC in CHCl₃.

Formula: $C_{210}H_{165}N_{37}O_{12}$ [3398.80].

Yield: 295 mg (86.8 μmol) **83 %** of a brown solid.

¹H-NMR (600 MHz, CD₂Cl₂)**:** δ / ppm = 8.18 (s, 3 H, H-20), 8.11 (s, 6 H, H-10), 7.84 (AA′ + AA′, 6 H + 12 H, H-13 a. H-23), 7.68 (AA′, 6 H, H-18), 7.52 (AA′, 12 H, H-8), 7.30 (BB′, 6 H, H-17), 7.25

(BB´ + BB´, 12 H + 6 H, H-14 a. H-24), 7.10 (AA´, 24 H, H-4), 6.98 (BB´, 12 H, H-7), 6.87 (BB´, 24 H, H-3), 3.79 (s, 36 H, H-1).

¹³C-NMR (150 MHz, CD₂Cl₂)**:** δ / ppm = 156.9 C-2, 149.7 C-6, 148.1 C-16, 148.0 C-21, 147.7 C-12, 147.6 C-11, 147.2 C-15 a. C-25, 140.4 C-5, 132.1 C-19, 129.6 C-9, 127.5 C-4, 127.2 C-13, 127.1 C-23, 126.3 C-22, 125.2 C-14 a. C-24, 124.6 C-17, 121.9 C-18, 121.7 C-8, 119.9 C-7, 117.7 C-10, 117.6 C-20, 115.2 C-3, 55.8 C-1.

Compound G3
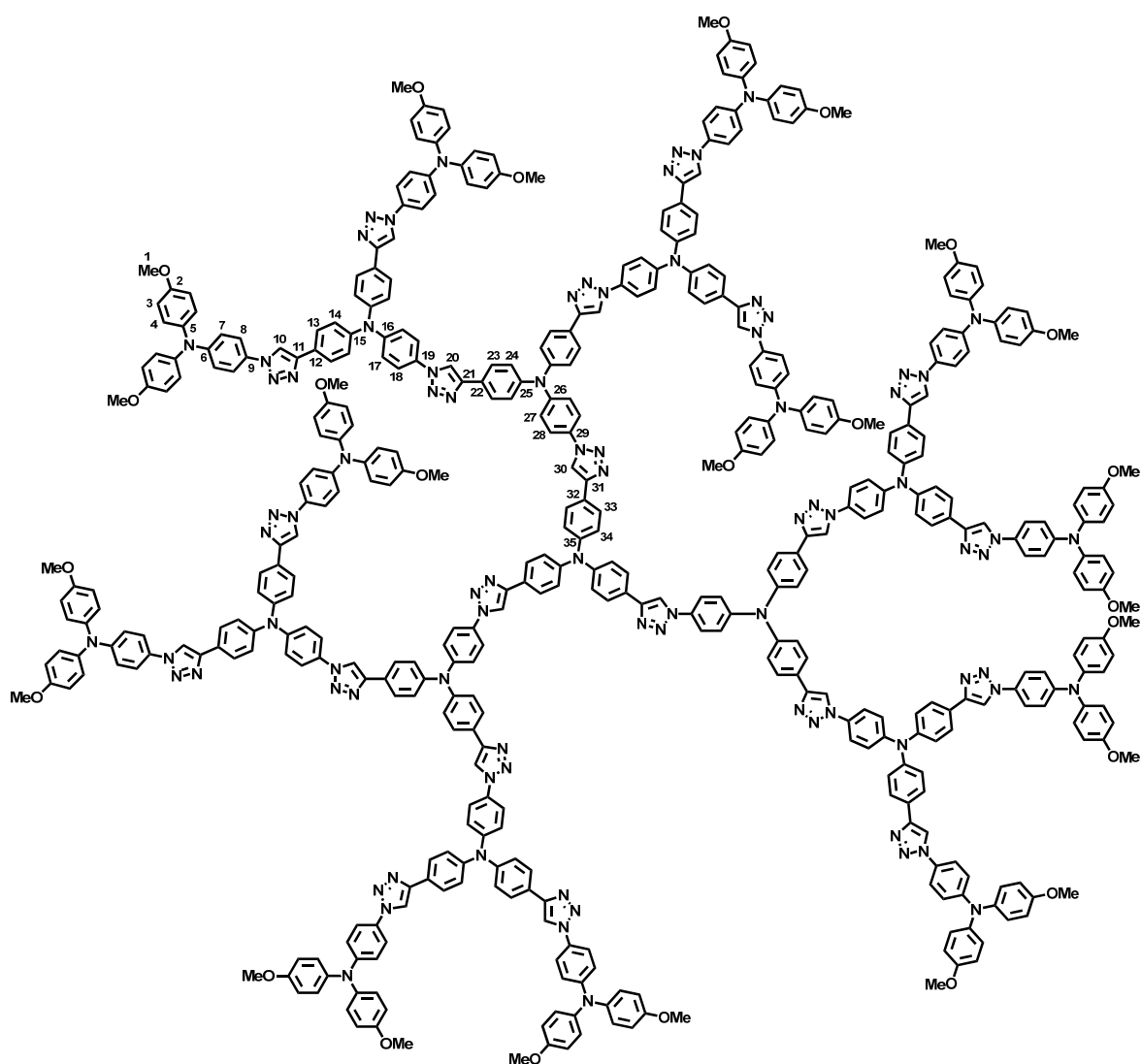
Compound **8** (34.7 mg, 10.4 μmol) and **4** (355 mg, 1.03 mmol) were dissolved in dry THF (15 mL) and (PPh₃)₃CuBr (26.0 mg, 28.0 μmol) was added while the solution was degassed with nitrogen. After addition of DIPEA (88.0 mg, 678 μmol) the solution was stirred for 36 d at 65°C under

preclusion of light. The solvent was evaporated *in vacuo* and the residue purified by dropping a concentrated solution in DCM into methanol. The solid was filtered off and washed with methanol. The product was further purified by recycling GPC in $CHCl_3$.

Formula: $C_{462}H_{357}N_{85}O_{24}$ [7483.33].

Yield: 32.3 mg (4.32 μmol) **42 %** of a beige solid.

^{1}H-NMR (600 MHz, $C_2D_2Cl_4$, 333 K)**:** δ / ppm = 8.06 (s + s, 6 H + 3 H, H-20 a. H-30), 7.98 (s, 12 H, H-10), 7.81–7.77 (AA′ + AA′ + AA′, 6 H + 12 H + 24 H, H-33 a. H-23 a. H-13), 7.63–7.60 (AA′ + AA′, 12 H + 6 H, H-18 a. H-28), 7.44 (AA′, 24 H, H-8), 7.27–7.20 (BB′ + BB′ + BB′ + BB′ + BB′ + BB′, 24 H + 12 H + 12 H + 6 H + 6 H, H-14 a. H-17 a. H-24 a. H-27 a. H-34), 7.05 (AA′, 48 H, H-4), 6.94 (BB′, 24 H, H-7), 6.81 (BB′, 48 H, H-3), 3.74 (s, 72 H, H-1).

^{13}C-NMR (150 MHz, $C_2D_2Cl_4$, 333 K)**:** δ / ppm = 156.8 C-2, 149.8 C-6, 148.1 C-16 a. C-26, 148.0 C-21 a. C-31, 147.7 C-11, (147.2, 147.1, C-25 a. C-35), 147.1 C-15, 140.3 C-5, 132.0 C-32, 131.9 C-22, 129.5 C-9, 127.4 C-13, 127.4 C-4, 127.3 C-23 a. C-33, 126.3 C-12, 126.1 C-19 a. C-29, 125.2 C-14, (124.8, 124.5, 124.4, C-17 a. C-24 a. C-27 a. C-34), 122.1 C-18 a. C-28, 121.8 C-8, 120.1 C-7, 117.7 C-10 a. C-20 a. C-30, 115.4 C-3, 55.9 C-1.

Compound spiro-G1
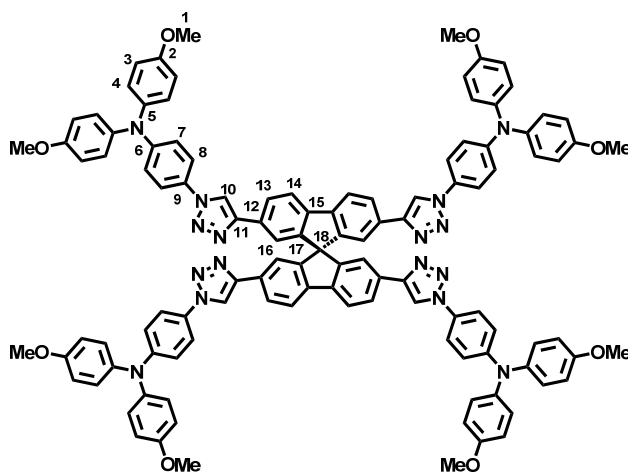
Compound **4** (34.0 mg, 82.0 μmol) and **6** (355 mg, 1.03 mmol) were dissolved in dry THF (20 mL) and (PPh$_3$)$_3$CuBr (34.0 mg, 37.0 μmol) was added while the solution was degassed with nitrogen. After addition of DIPEA (43.0 mg, 330 μmol) the solution was stirred for 18 d at 40°C under

preclusion of light. The solvent was evaporated *in vacuo* and the residue purified by flash-chromatography (silica gel, PE / EA = 7:1 → EA). Afterwards the product fraction was purified by dropping a concentrated solution in DCM into methanol. The solid was filtered off and washed with methanol. The product was further purified by recycling GPC in $CHCl_3$.

Formula: $C_{113}H_{88}N_{16}O_8$ [1798.01].

Yield: 33.5 mg (18.6 μmol) **23 %** of a brown solid.

^{1}H-NMR (600 MHz, CD_2Cl_2): δ / ppm = 8.02 (s, 4 H, H-10), 7.97 (dd, 4 H, ^3J= 8.05 , ^4J= 1.12, H-13), 7.92 (d, 4 H, ^3J= 8.05, H-14), 7.36 (AA´, 8 H, H-8), 7.24 (s, 4 H, H-16), 7.02 (AA´, 16 H, H-4), 6.86 (BB´, 8 H, H-7), 6.82 (BB´, 16 H, H-3), 3.75 (s, 24 H, H-1).

^{13}C-NMR (150 MHz, CD_2Cl_2): δ / ppm = 156.9 C-2, 149.6 C-17, 149.5 C-6, 147.8 C-11, 141.7 C-15, 140.3 C-5, 130.7 C-12, 129.5 C-9, 127.4 C-4, 126.0 C-13, 121.4 C-8, 121.3 C-16, 121.1 C-14, 119.8 C-7, 118.1 C-10, 115.1 C-3, 66.2 C-18, 55.7 C-1.

ESI-MS (high resolution): [M$^{•+}$- 4 x N$_2$]

calc.	m/z =	1684.67193
found.	m/z =	1684.67464

Δ = 1.61 ppm

Compound spiro-G2
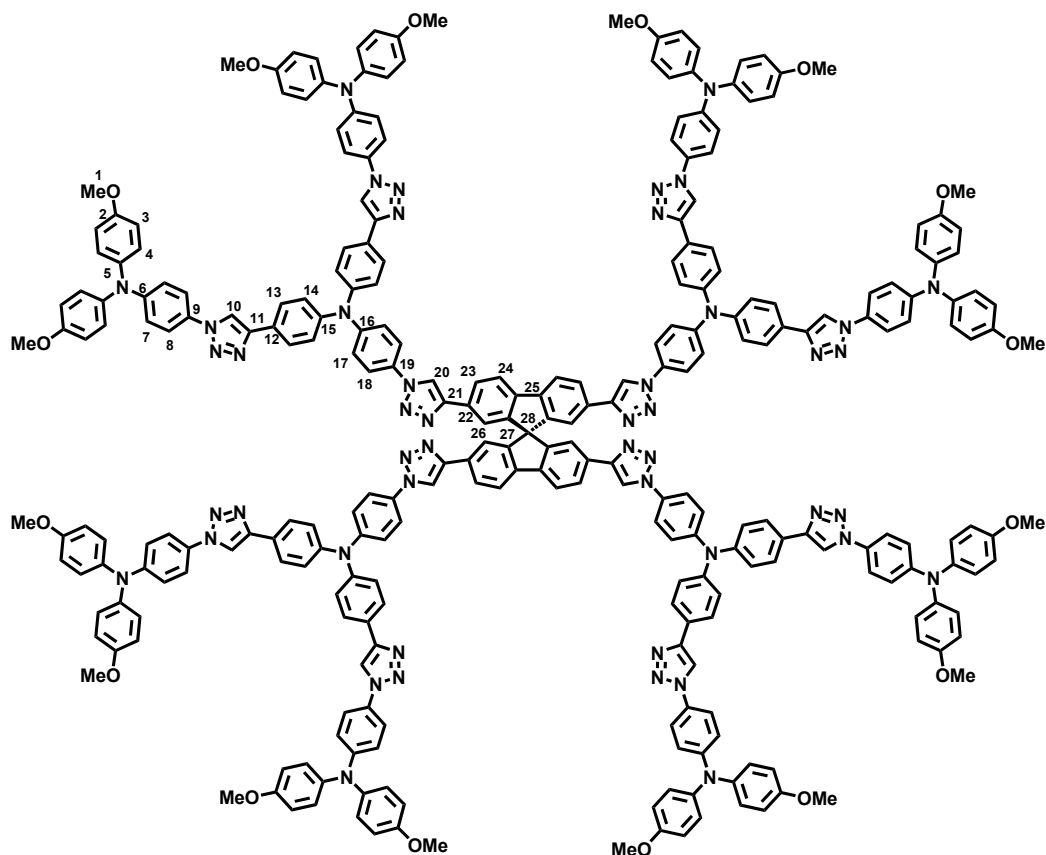
Compound **17** (47.0 mg, 27.0 μmol) and **6** (149 mg, 430 μmol) were dissolved in dry THF (20 mL) and (PPh$_3$)$_3$CuBr (14.0 mg, 15.0 μmol) was added while the solution was degassed with nitrogen. After addition of DIPEA (28.0 mg, 215 μmol) the solution was stirred for 45 d at 65°C under preclusion of light. The solvent was evaporated *in vacuo* and the residue purified by recycling GPC in CHCl$_3$.

Formula: C$_{281}$H$_{216}$N$_{48}$O$_{16}$ [4521.03].

Yield: 26.7 mg (5.91 μmol) **22 %** of a beige solid.

¹H-NMR (600 MHz, C$_2$D$_2$Cl$_4$, 333 K): δ / ppm = 7.98 (-, 4 H + 4 H, H-23 a. H-24), 7.96 (s + s, 4 H + 8 H, H-20 a. H-10), 7.74 (AA′, 16 H, H-13), 7.48 (AA′, 8 H, H-18), 7.43 (AA′, 16 H, H-8), 7.28 (m, 4 H, H-26), 7.16 (BB′ + BB′, 8 H + 16 H, H-17 a. H-14), 7.05 (AA′, 32 H, H-4), 6.93 (BB′, 16 H, H-7), 6.81 (BB′, 32 H, H-3), 3.74 (s, 48 H, H-1).

^{13}C-NMR (150 MHz, $C_2D_2Cl_4$, 333 K)**:** δ / ppm = 156.8 C-2, 149.8 C-6, 149.7 C-27, 148.2 C-16, 148.1 C-21, 147.7 C-11, 147.1 C-15, 141.9 C-25, 140.3 C-5, 131.8 C-19, 130.6 C-22, 129.5 C-9, 127.39 C-4, 127.36 C-13, 126.2 C-23 a. C-12, 125.1 C-14, 124.3 C-17, 122.2 C-18, 121.8 C-8 a. C-26, 121.2 C-24, 120.1 C-7, 118.4 C-20, 117.7 C-10, 115.3 C-3, 62.1 C-28, 55.8 C-1.

Compound D-A-G1
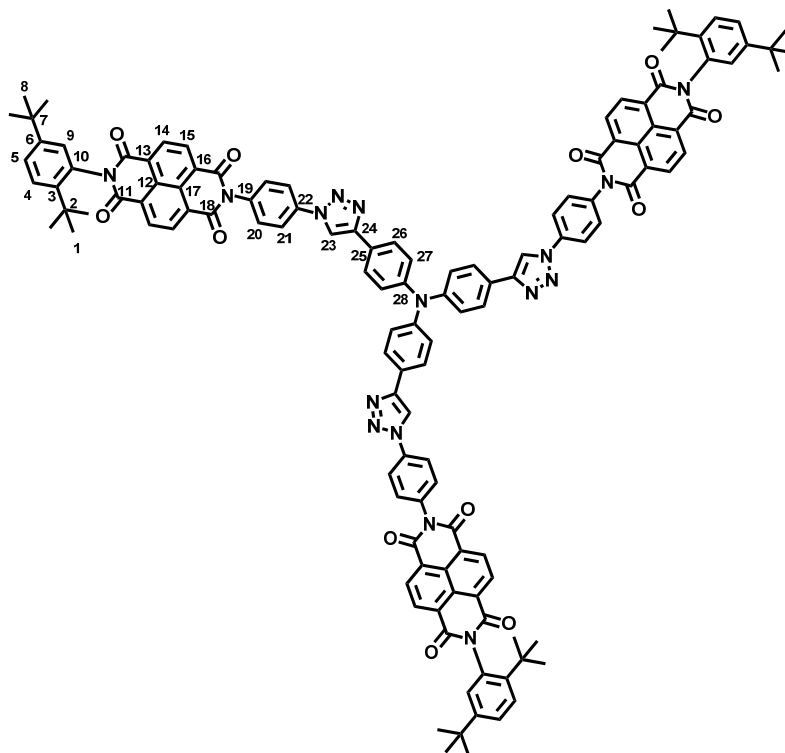
Compound **2** (17.0 mg, 54.0 μmol) and **8** (128 mg, 223 μmol) were dissolved in dry THF (20 mL) and the solution was degassed with nitrogen. After addition of DIPEA (20.7 mg, 161 μmol) and (PPh$_3$)$_3$CuBr (17.0 mg, 18.0 μmol) the solution was stirred for 12 d at 65°C under preclusion of light. The solvent was evaporated *in vacuo* and the residue purified by recycling GPC in CHCl$_3$.

Formula: $C_{126}H_{102}N_{16}O_{12}$ [2032.26].

Yield: 48.6 mg (23.9 μmol) **45 %** of a beige solid.

^{1}H-NMR (600 MHz, CD$_2$Cl$_2$)**:** δ / ppm = 8.87–8.84 (-, 12 H, H-14 a. H-15), 8.34 (s, 3 H, H-23), 8.06 (AA´, 6 H, H-21), 7.91 (AA´, 6 H, H-26), 7.64 (d, ^3J = 8.6, 3 H, H-4), 7.59 (BB´, 6 H, H-20),

7.53 (dd, ^3J = 8.6, ^4J = 2.2, 3 H, H-5), 7.33 (BB´, 6 H, H-27), 7.05 (d, ^4J = 2.2, 3 H, H-9), 1.33 (s, 27 H, H-8), 1.27 (s, 27 H, H-1).

¹³C-NMR (150 MHz, CD$_2$Cl$_2$)**:** δ / ppm = 164.2 C-11, 163.3 C-18, 150.9 C-6, 148.5 C-24. 147.8 C-28, 144.5 C-3, 137.7 C-22, 135.4 C-19, 132.9 C-10, 131.8 C-14 o. C-15, 131.7 C-14 o. C-15, 130.7 C-20, 129.4 C-4, 128.0 C-9, 127.72 C-16 o. C-13, 127.71 C-12 a. C-17, 127.3 C-26, 127.2 C16 o.C13, 126.8 C-5, 125.4 C-25, 124.9 C-27, 121.6 C-21, 117.7 C-23, 35.8 C-2, 34.5 C-7, 21.8 C-1, 31.3 C-8.

ESI-MS (high resolution)**:** [M$^{•+}$]

$$\text{calc.} \quad m/z = 2030.78576$$
$$\text{found.} \quad m/z = 2030.78340 \qquad \Delta = 1.16 \text{ ppm}$$

5.2.2.1.2 Model compounds

Compound 18
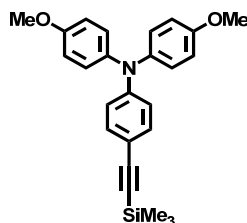
CA: [218608-72-1]

According to general procedure GP2:

5 (300 mg, 781 μmol), CuI (2.97 mg, 16.0 μmol), Pd(PhCN)$_2$Cl$_2$ (8.98 mg, 23.0 μmol), ^{t}Bu$_3$P (47.0 μL, 47.0 μmol, 1.0 M solution in toluene), ^{i}Pr$_2$NH (79.0 mg, 781 μmol), TMSA (excess), 1,4-dioxane (8 mL), 24 h, RT, flash-chromatography (silica gel, PE / DCM = 1:2).

Formula: C$_{25}$H$_{27}$NO$_2$Si [401.57].

Yield: 279 mg (695 μmol) **89 %** of a beige solid.

¹H-NMR (400 MHz, (CD₃)₂CO): δ / ppm = 7.23 (AA´, 2 H), 7.09 (AA´, 4 H), 6.93 (BB´, 4 H), 6.72 (BB´, 2 H), 3.80 (s, 6 H), 0.20 (s, 9 H).

Compound 19

CA: [218608-73-2]

According to general procedure GP3:

18 (1.04 g, 2.60 mmol), TBAF trihydrate (984 mg, 3.12 mmol), DCM (40 mL) 90 min.

Formula: $C_{22}H_{19}NO_2$ [329.39].

Yield: 810 mg (2.46 mmol) **95 %** of a beige solid.

¹H-NMR (400 MHz, (CD₃)₂CO): δ / ppm = 7.26 (AA´, 2 H), 7.09 (AA´, 4 H), 6.93 (BB´, 4 H), 6.73 (BB´, 2 H), 3.80 (s, 6 H), 3.44 (s, 1 H).

Compound 20

Compound **11** (200 mg, 309 μmol) and phenyl acetylene (228 mg, 2.23 mmol) were dissolved in dry THF (30 mL) and the solution was degassed with nitrogen. After addition of DIPEA (40.0 mg, 309 μmol) and (PPh₃)₃CuBr (20.0 mg, 22.0 μmol) the solution was stirred for 11 d at 65°C under

preclusion of light. The solvent was evaporated *in vacuo* and the residue was purified by flash-chromatography (silica gel, PE / DCM = 1:1). The product fraction was further purified by recycling GPC in CHCl$_3$.

Formula: C$_{48}$H$_{60}$N$_4$Si$_2$ [749.19].

Yield: 157 mg (210 μmol) **68 %** of an off-white solid.

^{1}H-NMR (600 MHz, CD$_2$Cl$_2$): δ / ppm = 8.22 (s, 1 H, H-6), 7.92–7.91 (m, 2 H, H-3), 7.68 (AA´, 2 H, H-8), 7.48–7.45 (m, 2 H, H-2), 7.41 (AA´, 4 H, H-13), 7.39–7.36 (m, 1 H, H-1), 7.23 (BB´, 2 H, H-9), 7.06 (BB´, 4 H, H-12), 1.14 (-, 42 H, H-17 a. H-18).

^{13}C-NMR (150 MHz, CD$_2$Cl$_2$): δ / ppm = 148.4 C-5, 147.5 C-10, 147.1 C-11, 133.6 C-13, 132.7 C-7, 130.8 C-4, 129.3 C-2, 128.7 C-1, 126.0 C-3, 125.3 C-9, 124.3 C-12, 122.0 C-8, 118.7 C-14, 118.1 C-6, 107.1 C-15, 90.6 C-16, 18.8 C-18, 11.7 C-17.

MALDI-TOF pos: [M$^{\bullet+}$]

calc.   m/z = 748.435
found. m/z = 748.424

Compound 21
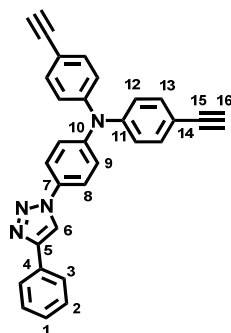
According to general procedure GP3:

20 (61.0 mg, 81.0 μmol), TBAF trihydrate (57.0 mg, 179 μmol), DCM (10 mL), 3 h, recycling GPC (CHCl$_3$).

Formula: C$_{30}$H$_{20}$N$_4$ [436.51].

Yield: 35.3 mg (80.9 μmol) **99 %** of a brownish solid.

^{1}H-NMR (600 MHz, CD$_2$Cl$_2$)**:** δ / ppm = 8.21 (s, 1 H, H-6), 7.92–7.90 (m, 2 H, H-3), 7.70 (AA´, 2 H, H-8), 7.48–7.35 (m + AA´+ m, 2 H + 4 H + 1 H, H-2 a. H-13 a. H-1), 7.24 (BB´, 2 H, H-9), 7.07 (BB´, 4 H, H-12), 3.12 (s, 2 H, H-16).

^{13}C-NMR (150 MHz, CD$_2$Cl$_2$)**:** δ / ppm = 148.5 C-5, 147.5 C-11, 147.4 C-10, 133.7 C-13, 133.0 C-7, 130.8 C-4, 129.3 C-2, 128.7 C-1, 126.1 C-3, 125.7 C-9, 124.3 C-12, 122.1 C-8, 118.1 C-6, 117.3 C-14, 83.6 C-16, 77.2 C-15.

MALDI-TOF pos: [M$^{•+}$]

<div align="center">

calc.   m/z = 436.168

found. m/z = 436.148

</div>

Compound C-M
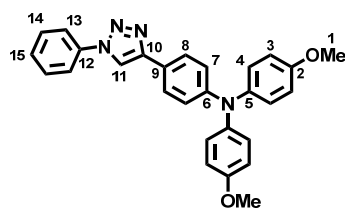
Compound **19** (122 mg, 370 μmol) and phenyl azide (52.9 mg, 444 μmol) were dissolved in dry THF (35 mL) and (PPh$_3$)$_3$CuBr (76.0 mg, 82.0 μmol) was added while the solution was degassed with nitrogen. After addition of DIPEA (57.4 mg, 444 μmol) the solution was stirred for 8 d at 65°C under preclusion of light. Then the solvent was evaporated, the residue was redissolved in DCM and the solution was washed with a saturated aqueous Na$_2$S$_2$O$_5$-solution and three times with water. The solvent was evaporated and the residue was purified by flash-chromatography (silica gel, PE / EA = 3:1). The product was further purified by recycling GPC in CHCl$_3$.

Formula: C$_{28}$H$_{24}$N$_4$O$_2$ [448.52].

Yield: 37.4 mg (83.4 μmol) **23 %** of a beige solid.

^{1}H-NMR (600 MHz, CD$_2$Cl$_2$)**:** δ / ppm = 8.13 (s, 1 H, H-11), 7.79–7.77 (m, 2 H, H-13), 7.68 (AA´, 2 H, H-8), 7.57–7.54 (m, 2 H, H-14), 7.47–7.44 (m, 1 H, H-15), 7.08 (AA´, 4 H, H-4), 6.96 (BB´, 2 H, H-7), 6.86 (BB´, 4 H, H-3), 3.79 (s, 6 H, H-1).

13C-NMR (150 MHz, CD$_2$Cl$_2$)**:** δ / ppm = 155.6 C-2, 149.3 C-9, 148.5 C-10, 140.8 C-5, 137.5 C-12, 130.1 C-14, 128.9 C-15, 127.2 C-4, 126.7 C-8, 122.3 C-6, 120.6 C-13, 120.3 C-7, 117.0 C-11, 115.0 C-3, 55.8 C-1.

ESI-MS pos (high resolution)**:** [M$^{\bullet+}$]

$$\text{calc.} \quad m/z = 448.18937$$
$$\text{found.} \quad m/z = 448.18887 \qquad \Delta = 1.12 \text{ ppm}$$

Compound N-M
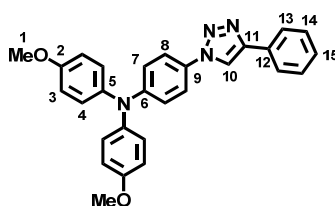
Compound **6** (170 mg, 493 μmol) and phenyl acetylene (42.0 mg, 410 μmol) were dissolved in dry THF (25 mL) and (PPh$_3$)$_3$CuBr (85.0 mg, 91.0 μmol) was added while the solution was degassed with nitrogen. After addition of DIPEA (64.0 mg, 493 μmol) the solution was stirred for 8 d at 65°C under preclusion of light. The solvent was evaporated *in vacuo* and the residue purified by flash-chromatography (silica gel, PE / EA = 3:1). The product fraction was dissolved in DCM, washed with a saturated aqueous Na$_2$S$_2$O$_5$-solution and further purified by recycling GPC in CHCl$_3$.

Formula: C$_{28}$H$_{24}$N$_4$O$_2$ [448.52].

Yield: 99.7 mg (222 μmol) **54 %** of a beige solid.

1H-NMR (600 MHz, CD$_2$Cl$_2$)**:** δ / ppm = 8.14 (s, 1 H, H-10), 7.89–7.87 (m, 2 H, H-13), 7.52 (AA´, 2 H, H-8), 7.47–7.44 (m, 2 H, H-14), 7.37-7.34 (m, 1 H, H-15), 7.11 (AA´, 4 H, H-4), 6.99 (BB´, 2 H, H-7), 6.88 (BB´, 4 H, H-3), 3.79 (s, 6 H, H-1).

13C-NMR (150 MHz, CD$_2$Cl$_2$)**:** δ / ppm = 156.9 C-2, 149.7 C-6, 148.1 C-11, 140.4 C-5, 130.9 C-12, 129.6 C-9, 129.2 C-14, 128.5 C-15, 127.5 C-4, 125.9 C-13, 121.7 C-8, 119.9 C-7, 118.1 C-10, 115.2 C-3, 55.8 C-1.

ESI-MS pos (high resolution)**:** [M$^{\bullet+}$]

calc.   m/z = 448.18937

found.   m/z = 448.18958 Δ = 0.47 ppm

Compound M[221]
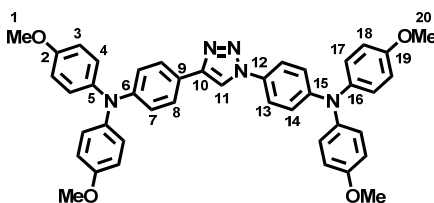
To a solution of **6** (59.0 mg, 170 μmol) and **19** (68.5 mg, 208 μmol) in dry acetonitrile (15 mL) CuI (32.0 mg, 168 μmol) was added. The suspension was degassed with nitrogen and DIPEA (22.0 mg, 170 μmol) was added. The mixture was stirred at RT for 5 d under preclusion of light. Then the solvent was evaporated, the residue was redissolved in DCM and the organic solvent was washed three times with water. The solvent was evaporated and the residue was purified by flash-chromatography (silica gel, PE / EA = 10:1) to obtain an off-white solid.

Formula: $C_{42}H_{37}N_5O_4$ [675.77]

Yield: 78.0 mg (115 μmol) **68 %** of a beige solid.

^{1}H-NMR (600 MHz, CD$_2$Cl$_2$)**:** δ / ppm = 8.01 (s, 1 H, H-11), 7.66 (AA´, 2 H, H-8), 7.50 (AA´, 2 H, H-13), 7.10 (AA´, 4 H, H-17), 7.07 (AA´, 4 H, H-4), 6.97 (BB´, 2 H, H-14), 6.94 (BB´, 2 H, H-7), 6.87 (BB´, 4 H, H-18), 6.85 (BB´, 4 H, H-3), 3.79 (s, 6 H, H-20), 3.78 (s, 6 H, H-1).

^{13}C-NMR (150 MHz, CD$_2$Cl$_2$)**:** δ / ppm = 156.9 C-19, 156.3 C-2, 149.6 C-15, 149.1 C-9, 148.1 C-10, 140.9 C-5, 140.4 C-16, 129.7 C-12, 127.4 C-17, 127.1 C-4, 126.6 C-8, 122.6 C-6, 121.6 C-13, 120.4 C-7, 120.0 C-14, 117.0 C-11, 115.1 C-18, 114.9 C-3, 55.78 C-1 o. C-20, 55.76 C-1 o. C-20.

ESI-MS pos (high resolution)**:** [M$^{\bullet+}$]

calc.   m/z = 675.28400

found.   m/z = 675.28401 Δ = 0.01 ppm

Compound core-M
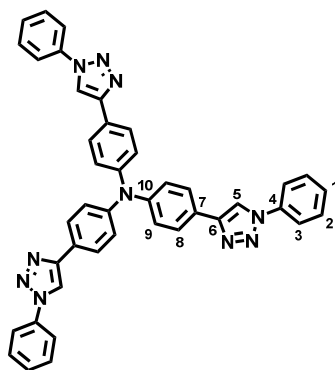
Compound **2** (100 mg, 315 μmol) and phenyl azide (227 mg, 1.90 mmol) were dissolved in dry THF (15 mL) and (PPh$_3$)$_3$CuBr (59.0 mg, 63.0 μmol) was added while the solution was degassed with nitrogen. After addition of DIPEA (122 mg, 945 μmol) the solution was stirred for 10 d at 65°C under preclusion of light. The solvent was evaporated *in vacuo* and the residue purified by recycling GPC in CHCl$_3$.

Formula: C$_{42}$H$_{30}$N$_{10}$ [674.75].

Yield: 138 mg (205 μmol) **65 %** of a beige solid.

^{1}H-NMR (600 MHz, CD$_2$Cl$_2$)**:** δ / ppm = 8.23 (s, 3 H, H-5), 7.85 (AA′, 6 H, H-8), 7.82-7.80 (m, 6 H, H-3), 7.59-7.56 (m, 6 H, H-2), 7.49-7.46 (m, 3 H, H-1), 7.27 (BB′, 6 H, H-9).

^{13}C-NMR (150 MHz, CD$_2$Cl$_2$)**:** δ / ppm = 148.2 C-6, 147.7 C-10, 137.5 C-4, 130.1 C-8, 129.0 C-1, 127.1 C-2, 125.6 C-7, 124.9 C-3, 120.7 C-9, 117.7 C-5.

ESI-MS pos (high resolution)**:** [M$^{•+}$]

        calc.   m/z = 674.26494

        found. m/z = 674.26489 Δ = 0.07 ppm

Compound branch-M
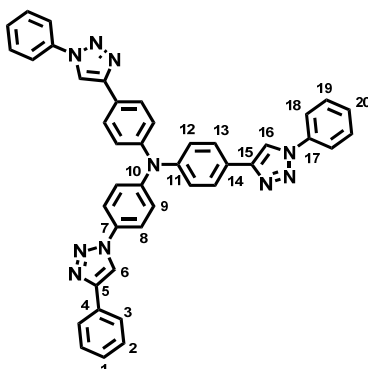
21 (30.0 mg, 69.0 μmol) and phenyl azide (228 mg, 1.91 mmol) were dissolved in dry THF (20 mL) and (PPh$_3$)$_3$CuBr (26.0 mg, 27.0 μmol) was added while the solution was degassed with nitrogen. After addition of DIPEA (18.0 mg, 137 μmol) the solution was stirred for 31 d at 65°C under preclusion of light. The solvent was evaporated *in vacuo* and the residue purified by recycling GPC in CHCl$_3$.

Formula: C$_{42}$H$_{30}$N$_{10}$ [674.75].

Yield: 21.8 mg (32.3 μmol) **47 %** of a beige solid.

^{1}H-NMR (600 MHz, CD$_2$Cl$_2$)**:** δ / ppm = 8.24 (s, 2 H, H-16), 8.23 (s, 1 H, H-6), 7.92–7.90 (m, 2 H, H-3), 7.88 (AA´, 4 H, H-13), 7.82–7.80 (m, 4 H, H-18), 7.70 (AA´, 2 H, H-8), 7.59–7.56 (m, 4 H, H-19), 7.49–7.45 (m + m, 2 H + 2 H, H-2 a. H-20), 7.39–7.36 (m, 1 H, H-1), 7.32 (BB´, 2 H, H-9), 7.28 (BB´, 4 H, H-12).

^{13}C-NMR (150 MHz, CD$_2$Cl$_2$)**:** δ / ppm = 148.3 C-5, 148.14 C-10, 148.11 C-15, 147.3 C-11, 137.4 C 17, 132.2 C-7, 130.8 C-4, 130.1 C-19, 129.2 C-20, 129.1 C-2, 128.6 C-1, 127.3 C-13, 126.1 C-14, 126.0 C-3, 125.2 C-12, 124.7 C-9, 122.0 C-8, 120.7 C-18, 118.2 C-6, 117.8 C-16.

ESI-MS pos (high resolution)**:** [M$^{•+}$]

calc. m/z = 674.26494

found. m/z = 674.26476 Δ = 0.27 ppm

5.2.3 Cascades

5.2.3.1 Building Blocks

Compound 22[120]
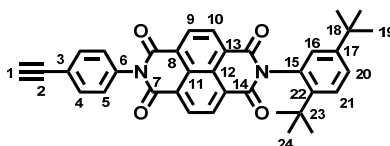
2,5-Di-tert-butylaniline (800 mg, 3.90 mmol) and 1,4,5,8-naphthalenetetracarboxylic dianhydride (1.04 g, 3.90 mmol) were suspended in dry DMF (30 mL). The suspension was irradiated with microwaves to heat it to 145°C for 60 min. After cooling down 4-ethynyl-aniline (458 mg, 3.91 mmol) was added to the mixture and it was again heated to 145°C for 90 min using microwave irradiation. Afterwards the mixture was cooled to RT, the solid was filtered off and washed with DCM. After removing the solvent under reduced pressure, the residue was purified by flash-chromatography (silica gel, DCM) to obtain the product as an off-white solid.

Formula: $C_{36}H_{30}N_2O_4$ [554.63].

Yield: 545 mg (983 μmol) **25 %** of an off-white solid.

¹H-NMR (400 MHz, CDCl₃): δ / ppm = 8.85 (∕, 4 H, H-10 a. H-9), 7.70 (AA′, 2 H, H-5), 7.61 (d, ^3J = 8.6, 1 H, H-21), 7.49 (dd, ^3J = 8.6, ^4J = 2.2, 1 H, H-20), 7.13 (BB′, 2 H, H-4), 7.01 (d, ^4J = 2.2, 1 H, H-16), 3.17 (s, 1 H, H-1), 1.33 (s, 9 H, H-19), 1.28 (s, 9 H, H-24).

¹³C-NMR (100.6 MHz, CDCl₃): δ / ppm = 163.8 (quart.), 162.9 (quart.), 150.5 (quart.), 143.8 (quart.), 134.9 (quart.), 133.4 (tert.), 132.1 (quart.), 131.7 (tert.), 131.6 (tert.), 129.1 (tert.), 128.8 (tert.), 127.6 (tert.), 127.5 (quart.), 127.4 (quart.), 126.9 (2 x quart.), 126.8 (tert.), 123.4 (quart.), 82.8 (tert.), 78.6 (quart.), 35.7 (quart.), 34.4 (quart.), 31.8 (prim.), 31.3 (prim.).

MALDI-TOF pos: [M•⁺]

calc.   m/z = 554.220

found. m/z = 554.217

Compound 23
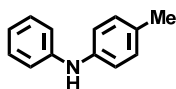
CA: [620-84-8]

According to general procedure GP5:

4-Iodotoluene (3.00 g, 13.7 mmol), NaO^{t}Bu (1.98 g, 20.6 mmol), Pd$_2$(dba)$_3$·CHCl$_3$ (575 mg, 556 μmol), ^{t}Bu$_3$P (826 μL, 826 μmol, 1.0 M solution in toluene), aniline (1.28 mg, 13.7 mmol), toluene (60 mL), 20 h, 90°C, flash-chromatography (silica gel, PE / EA = 50:1).

Formula: C$_{13}$H$_{13}$N [183.25].

Yield: 2.08 g (11.4 mmol) **83 %** of a yellow solid.

^{1}H-NMR (400 MHz, CDCl$_3$): δ / ppm = 7.32–7.28 (m, 2 H), 7.17–7.14 (m, 2 H), 7.09–7.05 (m, 4 H), 6.97–6.93 (m, 1 H), 5.63 (s, 1 H), 2.38 (s, 3 H).

Compound 24
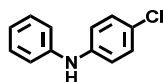
CA: [1205-71-6]

According to general procedure GP5:

Iodobenzene (5.00 g, 24.5 mmol), NaO^{t}Bu (3.53 g, 36.8 mmol), Pd$_2$(dba)$_3$·CHCl$_3$ (1.02 mg, 980 μmol), ^{t}Bu$_3$P (1.47 mL, 1.47 mmol, 1.0 M solution in toluene), 4-chloroaniline (3.13 g, 24.5 mmol), toluene (60 mL), 23 h, 80°C, flash-chromatography (silica gel, PE / EA = 70:1 → 70:2).

Formula: C$_{12}$H$_{10}$ClN [203.67].

Yield: 4.08 g (20.0 mmol) **82 %** of a brown solid.

^{1}H-NMR (400 MHz, CDCl$_3$): δ / ppm = 7.41–7.37 (m, 2 H), 7.31 (m, 2 H), 7.14–7.03 (m, 5 H), 5.69 (s, 1 H).

Compound 25[345]
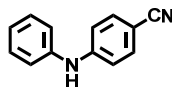
CA: [36602-01-4]

According to general procedure GP5:

4-Bromobenzonitrile (3.00 g, 16.4 mmol), NaO^{t}Bu (2.37 g, 24.7 mmol), Pd$_2$(dba)$_3$·CHCl$_3$ (682 mg, 659 μmol), ^{t}Bu$_3$P (989 μL, 989 μmol, 1.0 M solution in toluene), aniline (1.53 mg, 16.4 mmol), toluene (60 mL), 3 d, 90°C, flash-chromatography (silica gel, PE / EA = 10:1 → 5:1).

Formula: C$_{13}$H$_{10}$N$_2$ [194.23].

Yield: 2.58 g (13.3 mmol) **81 %** of a yellow solid.

^{1}H-NMR (400 MHz, CDCl$_3$): δ / ppm = 7.47 (AA´, 2 H), 7.38–7.34 (m, 2 H), 7.18–7.10 (m, 3 H), 6.97 (BB´, 2 H), 6.06 (s, 1 H).

Compound 26
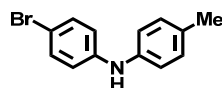
CA: [858516-23-1]

According to general procedure GP6:

23 (1.99 g, 10.8 mmol) in CHCl$_3$ (15 mL), TBATB (5.24 g, 10.8 mmol) in CHCl$_3$ (45 mL), flash-chromatography (silica gel, *n*-hexane / EA = 60:1).

Formula: C$_{13}$H$_{12}$BrN [262.15].

Yield: 2.33 g (8.89 mmol) **82 %** of a white solid.

^{1}H-NMR (400 MHz, CDCl$_3$): δ / ppm = 7.38 (AA´, 2 H), 7.18 (AA´, 2 H), 7.04 (BB´, 2 H), 6.91 (BB´, 2 H), 5.56 (s, 1 H), 2.41 (s, 3 H).

Compound 27
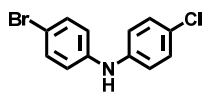
CA: [13676-98-7]

According to general procedure GP6:

24 (4.08 g, 20.0 mmol) in $CHCl_3$ (25 mL), TBATB (9.66 g, 20.0 mmol) in $CHCl_3$ (90 mL), flash-chromatography (silica gel, PE / EA = 60:1 → 30:1).

Formula: $C_{12}H_9BrClN$ [282.56].

Yield: 5.09 g (18.0 mmol) **90 %** of an off-white solid.

^{1}H-NMR (400 MHz, $(CD_3)_2CO$): δ / ppm = 7.62 (s, 1 H), 7.38 (AA´, 2 H), 7.25 (AA´, 2 H), 7.12 (BB´, 2 H), 7.06 (BB´, 2 H).

Compound 28
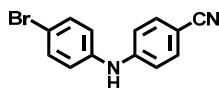
CA: [1019601-02-5]

According to general procedure GP6:

25 (2.58 g, 13.3 mmol) in $CHCl_3$ (20 mL), TBATB (6.42 g, 13.3 mmol) in $CHCl_3$ (60 mL), flash-chromatography (silica gel, PE / EA = 10:1 → 5:1).

Formula: $C_{13}H_9BrN_2$ [273.13].

Yield: 2.19 g (8.02 mmol) **60 %** of a brown solid.

^{1}H-NMR (400 MHz, $CDCl_3$): δ / ppm = 7.49 (AA´, 2 H), 7.45 (AA´, 2 H), 7.04 (BB´, 2 H), 6.95 (BB´, 2 H), 5.97 (s, 1 H).

Compound 29[346]
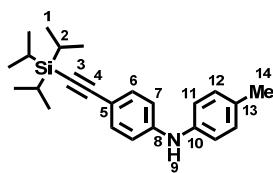
According to general procedure GP2:

26 (1.15 g, 4.42 mmol), CuI (18.0 mg, 93.0 μmol), Pd(PhCN)$_2$Cl$_2$ (51.0 mg, 133 μmol), ^{t}Bu$_3$P (265 μL, 265 μmol, 1.0 M solution in toluene), ^{i}Pr$_2$NH (492 mg, 4.86 mmol), TIPSA (excess), 1,4-dioxane (40 mL), 21 d, 75°C, flash-chromatography (silica gel, PE / EA = 60:1).

Formula: C$_{24}$H$_{33}$NSi [363.61].

Yield: 1.41 g (3.88 mmol) **88 %** of a yellow solid.

^{1}H-NMR (400 MHz, (CD$_3$)$_2$CO): δ / ppm = 7.52 (s, 1 H, H-9), 7.32 (AA´, 2 H, H-6), 7.14–7.06 (AA´ + BB´, 4 H, H-12 a. H-7), 7.00 (BB´, 2 H, H-11), 2.27 (s, 3 H, H-14), 1.14–1.13 (-, 21 H, H-1 a. H-2).

^{13}C-NMR (100 MHz, (CD$_3$)$_2$CO): δ / ppm = 146.3 (quart.), 140.6 (quart.), 133.9 (tert.), 131.9 (quart.), 130.6 (tert.), 120.4 (tert.), 115.9 (tert.), 113.9 (quart.), 109.4 (quart.), 87.7 (quart.), 20.7 (prim.), 19.0 (prim.), 12.1 (tert.).

ESI-MS pos (high resolution)**:** [M$^{\bullet+}$]

<div style="text-align:center">

calc.   m/z = 363.23767

found. m/z = 363.23768 Δ = 0.03 ppm

</div>

Compound 30[346]
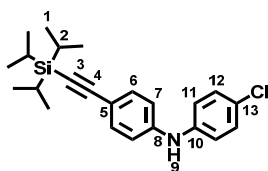
According to general procedure GP2:

27 (2.57 g, 9.10 mmol), CuI (36.0 mg, 191 μmol), Pd(PhCN)$_2$Cl$_2$ (105 mg, 273 μmol), ^{t}Bu$_3$P (546 μL, 546 μmol, 1.0 M solution in toluene), ^{i}Pr$_2$NH (1.01 g, 10.0 mmol), TIPSA (excess), 1,4-dioxane (80 mL), 10 d, 75°C, flash-chromatography (silica gel, PE / EA = 80:1).

Formula: $C_{23}H_{30}ClNSi$ [384.03].

Yield: 2.85 g (7.42 mmol) **82 %** of a colourless solid.

^{1}H-NMR (400 MHz, $(CD_3)_2CO$): δ / ppm = 7.77 (s, 1 H, H-9), 7.36 (AA´, 2 H, H-6), 7.27 (AA´, 2 H, H-12), 7.17 (BB´, 2 H, H-7), 7.07 (BB´, 2 H, H-11), 1.14-1.13 (-, 21 H, H-1 a. H-2).

^{13}C-NMR (100 MHz, $(CD_3)_2CO$): δ / ppm = 144.9 (quart.), 142.4 (quart.), 134.0 (tert.), 129.9 (tert.), 126.0 (quart.), 120.4 (tert.), 117.0 (tert.), 115.2 (quart.), 109.0 (quart.), 88.3 (quart.), 19.0 (prim.), 12.1 (tert).

ESI-MS pos (high resolution)**:** [M$^{•+}$]

$\qquad\qquad$ calc.$\quad$ m/z = 383.18305

$\qquad\qquad$ found.$\ $ m/z = 383.18252 $\qquad\qquad$ Δ = 1.38 ppm

Compound 31[346]
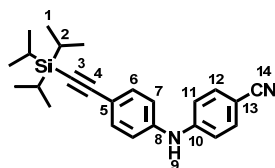
According to general procedure GP2:

28 (2.19 g, 8.04 mmol), CuI (31.0 mg, 161 μmol), Pd(PhCN)$_2$Cl$_2$ (93.0 mg, 241 μmol), ^{t}Bu$_3$P (483 μL, 483 μmol, 1.0 M solution in toluene), ^{i}Pr$_2$NH (895 mg, 8.85 mmol), TIPSA (excess), 1,4-dioxane (40 mL), 14 d, 75°C, flash-chromatography (silica gel, PE / EA = 10:1).

Formula: $C_{24}H_{30}N_2Si$ [374.59].

Yield: 2.69 g (7.18 mmol) **89 %** of a yellow solid.

^{1}H-NMR (400 MHz, $(CD_3)_2CO$): δ / ppm = 8.28 (s, 1 H, H-9), 7.58 (AA´, 2 H, H-12 o. H-6), 7.45 (AA´, 2 H, H-12 o. H-6), 7.24-7.02 (BB´ + BB´, 4 H, H-11 a. H-7), 1.14 (-, 21 H, H-1 a. H-2).

^{13}C-NMR (100 MHz, $(CD_3)_2CO$): δ / ppm = 148.2 (quart.), 142.5 (quart.), 134.4 (tert), 133.9 (tert.), 120.0 (quart.), 119.7 (tert.), 117.5 (quart.), 116.7 (tert.), 108.4 (quart.), 102.7 (quart.), 89.4 (quart.), 19.0 (prim.), 12.0 (tert.).

MALDI-TOF pos: [M•+]

<div align="center">

calc.   m/z = 374.217

found. m/z = 374.215

</div>

Compound 32[346]
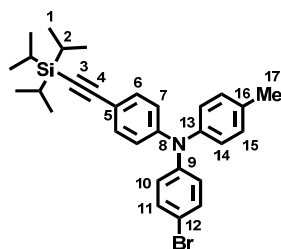
According to general procedure GP4:

29 (1.19 g, 3.28 mmol), 1-bromo-4-iodobenzene (1.39 g, 4.92 mmol), dried K_2CO_3 (2.26 g, 16.4 mmol), 18-crown-6-ether (108 mg, 410 μmol), activated copper (552 mg, 8.21 mmol), o-DCB (60 mL), 4 d, flash-chromatography (silica gel, PE).

Formula: $C_{30}H_{36}BrNSi$ [518.60].

Yield: 788 mg (1.52 mmol) **46 %** of a yellow solid.

¹H-NMR (400 MHz, $(CD_3)_2CO$): δ / ppm = 7.42 (AA´, 2 H, H-11), 7.36 (AA´, 2 H, H-6), 7.17 (AA´, 2 H, H-15), 7.00 (BB´, 2 H, H-14), 6.98 (BB´, 2 H, H-10), 6.94 (BB´, 2 H, H-7), 2.31 (s, 3 H, H-17), 1.14 (-, 21 H, H-1 a. H-2).

¹³C-NMR (100 MHz, $(CD_3)_2CO$): δ / ppm = 148.7 (quart.), 147.5 (quart.), 144.9 (quart.), 135.1 (quart.), 133.8 (tert.), 133.1 (tert.), 131.2 (tert.), 126.6 (tert.), 126.4 (tert.), 122.9 (tert.), 117.3 (quart.), 115.8 (quart.), 108.4 (quart.), 89.5 (quart.), 20.9 (prim.), 19.0 (prim.), 12.0 (tert.).

MALDI-TOF pos: [M•+]

<div align="center">

calc.   m/z = 517.179

found. m/z = 517.126

</div>

Compound 33[346]
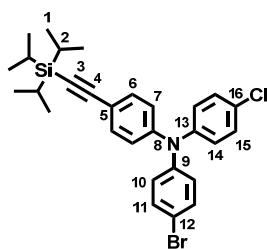
According to general procedure GP4:

30 (5.96 g, 14.8 mmol), 1-bromo-4-iodobenzene (6.29 g, 22.2 mmol), dried K_2CO_3 (10.2 g, 74.1 mmol), 18-crown-6-ether (490 mg, 1.85 mmol), activated copper (2.35 mg, 37.0 mmol), o-DCB (80 mL), 4 d, flash-chromatography (silica gel, PE).

Formula: $C_{29}H_{33}BrClNSi$ [539.02].

Yield: 3.45 g (6.40 mmol) **43 %** of a yellow solid.

^{1}H-NMR (400 MHz, $(CD_3)_2CO$): δ / ppm = 7.46 (AA´, 2 H, H-11), 7.40 (AA´, 2 H, H-6), 7.33 (AA´, 2 H, H-15), 7.09 (BB´, 2 H, H-14), 7.04-6.98 (BB´ + BB´, 4 H, H-7 a. H-10), 1.14 (-, 21 H, H-1 a. H-2).

^{13}C-NMR (100 MHz, $(CD_3)_2CO$): δ / ppm = 148.2 (quart.), 147.1 (quart.), 146.5 (quart.), 134.0 (tert.), 133.4 (tert.), 130.5 (tert.), 129.3 (quart.), 127.1 (tert.), 127.0 (tert.), 123.9 (tert.), 118.3 (quart.), 116.7 (quart.), 108.2 (quart.), 90.0 (quart.), 19.0 (prim.), 12.0 (tert.).

Compound 34[346]
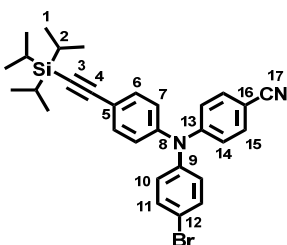
According to general procedure GP4:

31 (5.02 g, 13.4 mmol), 1-bromo-4-iodobenzene (5.69 g, 20.1 mmol), dried K_2CO_3 (9.27 g, 67.1 mmol), 18-crown-6-ether (443 mg, 1.67 mmol), activated copper (2.13 mg, 33.5 mmol), o-DCB (80 mL), 4 d, flash-chromatography (silica gel, PE / EA = 30:1).

Formula: $C_{30}H_{33}BrN_2Si$ [529.58].

Yield: 4.81 g (9.08 mmol) **68 %** of a yellow solid.

¹H-NMR (400 MHz, $(CD_3)_2CO$): δ / ppm = 7.62 (AA´, 2 H, H-11), 7.56 (AA´, 2 H, H-6), 7.49 (AA´, 2 H, H-15), 7.15 (BB´ + BB´, 2 H + 2 H, H-7 a. H-14), 7.11 (BB´, 2 H, H-10), 1.14 (-, 21 H, H-1 a. H-2).

¹³C-NMR (100 MHz, $(CD_3)_2CO$): δ / ppm = 151.7 (quart,), 147.1 (quart.), 146.1 (quart.), 139.9 (tert.), 134.34 (tert.), 134.33 (tert.), 133.8 (quart.), 128.8 (tert.), 126.1 (tert.), 122.3 (tert.), 120.3 (quart.), 119.6 (quart.), 118.6 (quart.), 107.8 (quart.), 90.6 (quart.), 19.0 (prim.), 12.0 (tert.).

MALDI-TOF pos: [M•⁺]

> calc.   m/z = 528.159
> found. m/z = 528.141

Compound 35[346]
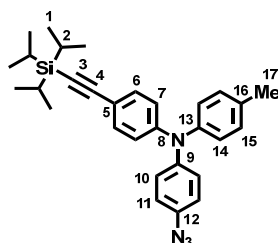
According to general procedure GP1:

32 (1.84 g, 3.56 mmol), NaN_3 (463 mg, 7.13 mmol), L(+)-sodium ascorbate (35.0 mg, 178 μmol), CuI (68.0 mg, 356 μmol), DMAP (47.0 mg, 535 μmol), nitrogen degassed ⁱPrOH/H_2O 7:3 (70 mL), flash-chromatography (silica gel, n-hexane → PE).

Formula: $C_{30}H_{36}N_4Si$ [480.72].

Yield: 1.56 mg (3.25 mmol) **91 %** of a brown solid.

¹H-NMR (400 MHz, $(CD_3)_2CO$): δ / ppm = 7.34 (AA´, 2 H, H-6), 7.16 (AA´, 2 H, H-15), 7.12 (AA´, 2 H, H-11), 7.04 (BB´, 2 H, H-10), 7.00 (BB´, 2 H, H-14), 6.90 (BB´, 2 H, H-7), 2.31 (s, 3 H, H-17), 1.13 (-, 21 H, H-2 a. H-1).

^{13}C-NMR (100 MHz, $(CD_3)_2CO$): δ / ppm = 149.1 (quart.), 145.3 (quart.), 145.2 (quart.), 135.8 (quart.), 134.8 (quart.), 133.7 (tert.), 131.1 (tert.), 127.0 (tert.), 126.3 (tert.), 122.1 (tert.), 121.0 (tert.), 116.6 (quart.), 108.6 (quart.), 89.3 (quart.), 20.8 (prim.), 19.0 (prim.), 12.1 (tert.).

MALDI-TOF pos: [M[·+] - N_2, -Me, + 2 H]

<div align="center">

calc.   m/z = 439.356

found. m/z = 439.215

</div>

Compound 36[346]
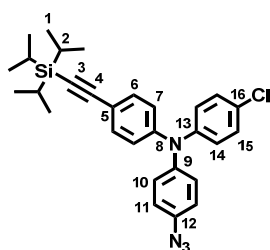
According to general procedure GP1:

33 (299 mg, 554 μmol), NaN_3 (72.0 mg, 1.10 mmol), *L*(+)-sodium ascorbate (5.49 mg, 280 μmol), CuI (10.5 mg, 550 μmol), DMAP (7.32 mg, 83.0 μmol), nitrogen degassed [i]PrOH/H_2O 7:3 (70 mL), flash-chromatography (silica gel, PE → PE / EA = 30:1).

Formula: $C_{29}H_{33}ClN_4Si$ [501.14].

Yield: 140 mg (279 μmol) **50 %** of a brown solid.

^{1}H-NMR (400 MHz, $(CD_3)_2CO$): δ / ppm = 7.38 (AA´, 2 H, H-6), 7.32 (AA´, 2 H, H-15), 7.15 (AA´, 2 H, H-11), 7.09-7.05 (BB´ + BB´, 2 H + 2 H, H-14 a. H-10), 6.97 (BB´, 2 H, H-7), 1.14 (-, 21 H, H-1 a. H-2).

^{13}C-NMR (100 MHz, $(CD_3)_2CO$): δ / ppm = 148.5 (quart.), 146.7 (quart.), 144.7 (quart.), 136.5 (quart.), 133.9 (tert.), 130.4 (tert.), 128.9 (quart.), 127.5 (tert.), 126.6 (tert.), 123.2 (tert.), 121.2 (tert.), 117.8 (quart.), 108.3 (quart.), 89.8 (quart.), 19.0 (prim.), 12.0 (tert.).

MALDI-TOF pos: [M[·+] + K]

<div align="center">

calc.   m/z = 539.179

found. m/z = 539.024

</div>

Compound 37[346]
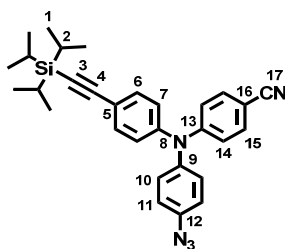
According to general procedure GP1:

34 (1.28 g, 2.43 mmol), NaN$_3$ (316 mg, 4.87 mmol), *L*(+)-sodium ascorbate (24.0 mg, 122 μmol), CuI (46.0 mg, 243 μmol), DMAP (32.0 mg, 365 μmol), nitrogen degassed *^{i}*PrOH/H$_2$O 7:3 (70 mL), flash-chromatography (silica gel, PE).

Formula: C$_{30}$H$_{33}$N$_5$Si [491.70].

Yield: 940 mg (1.91 mmol) **79 %** of a brown solid.

^{1}H-NMR (400 MHz, (CD$_3$)$_2$CO): δ / ppm = 7.59 (AA´, 2 H, H-6), 7.48 (AA´, 2 H, H-15), 7.25 (AA´, 2 H, H-11), 7.16–7.12 (BB´ + BB´, 2 H+ 2H, H-14 a. H-10), 7.07 (BB´, 2 H, H-7), 1.15 (-, 21 H, H-1 a. H-2).

^{13}C-NMR (100 MHz, (CD$_3$)$_2$CO): δ / ppm = 151.8 (quart.), 147.2 (quart.), 143.6 (quart.), 138.0 (quart.), 134.3 (tert.), 134.2 (tert.), 129.0 (tert.), 125.8 (tert.), 121.7 (tert.), 121.5 (tert.), 120.0 (quart.), 119.6 (quart.), 107.9 (quart.), 104.7 (quart.), 90.8 (quart.), 19.0 (prim.), 12.0 (tert.).

MALDI-TOF pos: [M$^{+\cdot}$ - N$_2$]

calc.   m/z = 463.243

found. m/z = 463.311

5.2.3.1.1   **Cascades**

Compound 41
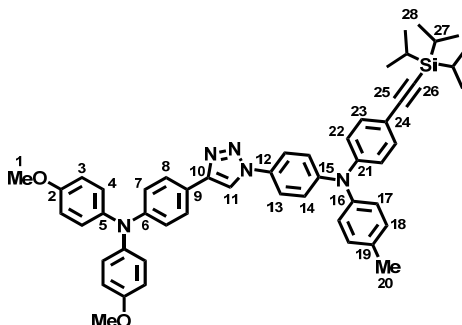
Compound **19** (75.0 mg, 228 μmol) and **35** (55.0 mg, 114 μmol) were dissolved in dry THF (30 mL) and the solution was degassed with nitrogen. After addition of DIPEA (15.0 mg, 114 μmol) and $(PPh_3)_3CuBr$ (21.0 mg, 23.0 μmol) the solution was stirred for 16 d at 65°C under preclusion of light. The solvent was evaporated *in vacuo* and the residue was purified by flash-chromatography (silica gel, PE / EA = 10:1 → 1:1). The product was further purified by recycling GPC in $CHCl_3$ and the product was obtained as a brownish solid.

Formula: $C_{52}H_{55}N_5O_2Si$ [810.11].

**Yield:** 26.1 mg (32.2 μmol) **28 %** of a brownish solid.

^{1}H-NMR (400 MHz, CD_2Cl_2): δ / ppm = 8.06 (s, 1 H, H-11), 7.67 (AA′, 2 H, H-8), 7.61 (AA′, 2 H, H-13), 7.35 (AA′, 2 H, H-23), 7.18–7.14 (AA′ + BB′, 2 H + 2 H, H-18 a. H-14), 7.08 (AA′, 4 H, H-4), 7.04 (BB′, 2 H, H-17), 7.00 (BB′, 2 H, H-22), 6.95 (BB′, 2 H, H-7), 6.86 (BB′, 4 H, H-3), 3.79 (s, 6 H, H-1), 2.34 (s, 3 H, H-20), 1.13 (-, 21 H, H-27 a. H-28).

^{13}C-NMR (100 MHz, CD_2Cl_2): δ / ppm = 156.7 (quart.), 149.4 (quart.), 148.5 (quart.), 148.2 (quart.), 147.9 (quart.), 144.4 (quart.), 141.0 (quart.), 135.0 (quart.), 133.4 (tert.), 132.0 (quart.), 130.7 (tert.), 127.2 (tert.), 126.7 (tert.), 126.2 (tert.), 124.2 (tert.), 123.1 (tert.), 122.6 (quart.), 121.8 (tert.), 120.5 (tert.), 117.5 (quart.), 117.0 (tert.), 115.1 (tert.), 107.5 (quart.), 90.1 (quart.), 55.8 (prim.), 21.0 (prim.), 18.8 (prim.), 11.8 (tert.).

MALDI-TOF pos: [M$^{•+}$]

calc.   m/z = 809.411

found. m/z = 809.404

Compound 42
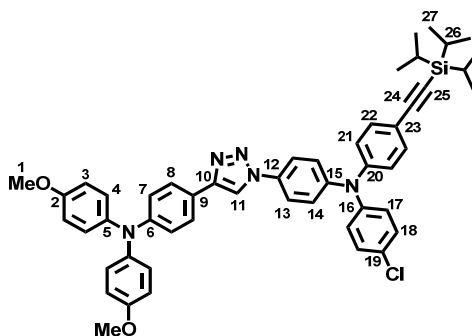
Compound **19** (154 mg, 467 μmol) and **36** (100 mg, 200 μmol) were dissolved in dry THF (20 mL) and the solution was degassed with nitrogen. After addition of DIPEA (26.0 mg, 200 μmol) and (PPh$_3$)$_3$CuBr (37.0 mg, 40.0 μmol) the solution was stirred for 15 d at 65°C under preclusion of light. The solvent was evaporated *in vacuo* and the residue was purified by flash-chromatography (silica gel, PE / EA = 1:2). The product fraction was further purified by recycling GPC in CHCl$_3$.

Formula: C$_{51}$H$_{52}$ClN$_5$O$_2$Si [830.53].

Yield: 85.0 mg (102 μmol) **51 %** of a brown solid.

^{1}H-NMR (400 MHz, CD$_2$Cl$_2$)**:** δ / ppm = 8.06 (s, 1 H, H-11), 7.69–7.63 (AA´+ AA´, 2 H + 2 H, H-8 a. H-13), 7.39 (AA´, 2 H, H-22), 7.28 (AA, 2 H, H-17), 7.20 (BB´, 2 H, H-14), 7.10–7.06 (AA´+ BB´, 4 H + 2 H, H-4 a. H-18), 7.03 (BB´, 2 H, H-21), 6.95 (BB´, 2 H, H-7), 6.86 (BB´, 4 H, H-3), 3.79 (s, 6 H, H-1), 1.13 (-, 21 H, H-26 a. H-27).

^{13}C-NMR (100 MHz, CD$_2$Cl$_2$)**:** δ / ppm = 156.7 (quart.), 149.4 (quart.), 148.5 (quart.), 147.6 (quart.), 147.4 (quart.), 145.8 (quart.), 140.9 (quart.), 133.6 (tert.), 132.7 (quart.), 130.0 (tert.), 129.4 (quart.), 127.3 (tert.), 126.7 (tert.), 126.6 (tert.), 124.9 (tert.), 123.8 (tert.), 122.5 (quart.), 122.0 (tert.), 120.4 (tert.), 118.5 (quart.), 117.0 (tert.), 115.1 (tert.), 107.2 (quart.), 90.6 (quart.), 55.8 (prim.), 18.8 (prim.), 11.7 (tert.).

MALDI-TOF pos: [M$^{\bullet+}$]

calc.   m/z = 829.357

found. m/z = 829.142

Compound 43
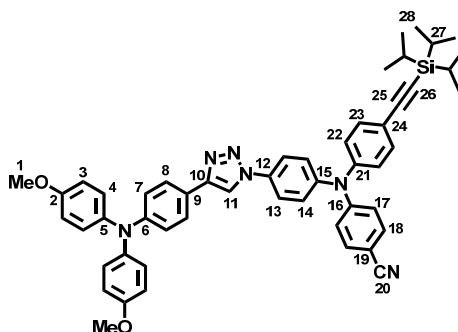
Compound **19** (101 mg, 307 μmol) and **37** (70.0 mg, 142 μmol) were dissolved in dry THF (20 mL) and the solution was degassed with nitrogen. After addition of DIPEA (6.67 mg, 52.0 μmol) and (PPh$_3$)$_3$CuBr (48.0 mg, 52.0 μmol) the solution was stirred for 9 d at 65°C under preclusion of light. The solvent was evaporated *in vacuo* and the residue was purified by recycling GPC in CHCl$_3$.

Formula: C$_{52}$H$_{52}$N$_6$O$_2$Si [821.09].

Yield: 18.7 mg (23.0 μmol) **16 %** of a brown solid.

^{1}H-NMR (400 MHz, CD$_2$Cl$_2$)**:** δ / ppm = 8.09 (s, 1 H, H-11), 7.73 (AA´, 2 H, H-13), 7.68 (AA´, 2 H, H-8), 7.51 (AA´, 2 H, H-18), 7.45 (AA´, 2 H, H-23), 7.27 (BB´, 2 H, H-14), 7.12–7.07 (AA´ + BB´+ BB´, 4 H + 2 H + 2 H, H-4 a. H-22 a. H-17), 6.96 (BB´, 2 H, H-7), 6.86 (BB´, 4 H, H-3), 3.79 (s, 6 H, H-1), 1.13 (-, 21 H, H-27 a. H-28).

^{13}C-NMR (100 MHz, CD$_2$Cl$_2$)**:** δ / ppm = 156.7 (quart.), 151.0 (quart.), 149.5 (quart.), 148.7 (quart.), 146.5 (quart.), 146.2 (quart.), 140.9 (quart.), 134.1 (quart.), 133.9 (tert.), 133.8 (tert.), 127.3 (tert.), 126.9 (tert.), 126.8 (quart.), 125.6 (tert.), 122.3 (quart.), 122.2 (tert.), 122.1 (tert.), 120.4 (tert.), 120.3 (tert.), 119.5 (quart.), 117.0 (tert.), 115.1 (tert.), 106.8 (quart.), 105.0 (quart.), 91.5 (quart.), 55.8 (prim.), 18.8 (prim.), 11.7 (tert.).

MALDI-TOF pos: [M$^{•+}$]

calc.   m/z = 820.391

found. m/z = 820.397

Compound 44
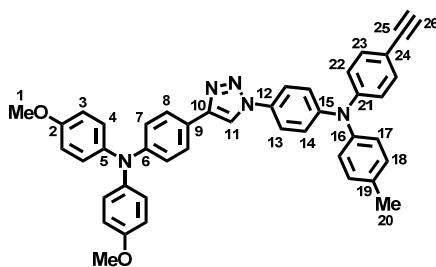
According to general procedure GP3:

41 (40.4 mg, 50.0 μmol), TBAF trihydrate (17.3 mg, 55.0 μmol), DCM (12 mL), 3 h, flash-chromatography (silica gel, DCM → EA). Furthermore the pure product was solved in DCM, washed once with a saturated aqueous $Na_2S_2O_3$-solution and the solvent was evaporated.

Formula: $C_{43}H_{35}N_5O_2$ [653.77].

Yield: 28.0 mg (42.8 μmol) **86 %** of a beige solid.

^{1}H-NMR (600 MHz, CD_2Cl_2): δ / ppm = 8.06 (s, 1 H, H-11), 7.67 (AA´, 2 H, H-8), 7.62 (AA´, 2 H, H-13), 7.36 (AA´, 2 H, H-23), 7.18 (BB´, 2 H, H-14), 7.16 (AA´, 2 H, H-18), 7.08 (AA´, 4 H, H-4), 7.05 (BB´, 2 H, H-17), 7.01 (BB´, 2 H, H-22), 6.95 (BB´, 2 H, H-7), 6.85 (BB´, 4 H, H-3), 3.78 (s, 6 H, H-1), 3.09 (s, 1 H, H-26), 2.34 (s, 3 H, H-20).

^{13}C-NMR (150 MHz, CD_2Cl_2): δ / ppm = 156.5 (quart.), 149.3 (quart.), 148.4 (quart.), 148.2 (quart.), 148.0 (quart.), 144.2 (quart.), 140.8 (quart.), 135.1 (quart.), 133.4 (tert.), 132.1 (quart.), 130.7 (tert.), 127.2 (tert.), 126.6 (tert.), 126.3 (tert.), 124.4 (tert.), 122.7 (tert.), 122.4 (quart.), 121.8 (tert.), 120.3 (tert.), 117.0 (tert.), 115.7 (quart.), 115.0 (tert.), 83.9 (tert.), 76.7 (quart.), 55.8 (prim.), 21.0 (prim.).

MALDI-TOF pos: [M$^{•+}$]

calc.   m/z = 653.278

found. m/z = 653.229

Compound 45
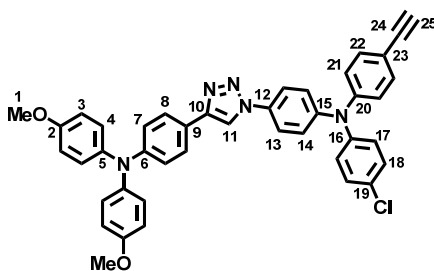
According to general procedure GP3:

42 (52.0 mg, 63.0 μmol), TBAF trihydrate (21.7 mg, 69.0 μmol), DCM (10 mL), 3 h, flash-chromatography (silica gel, DCM → EA). Furthermore the pure product was solved in DCM, washed once with a saturated aqueous $Na_2S_2O_3$-solution and the solvent was evaporated.

Formula: $C_{42}H_{32}ClN_5O_2$ [674.19].

Yield: 42.1 mg (62.4 μmol) **>99 %** of a beige solid.

^{1}H-NMR (400 MHz, CD_2Cl_2): δ / ppm = 8.07 (s, 1 H, H-11), 7.69–7.64 (AA´+ AA´, 2 H + 2 H, H-8 a. H-13), 7.40 (AA´, 2 H, H-22), 7.29 (AA, 2 H, H-17), 7.21 (BB´, 2 H, H-14), 7.10–7.06 (AA´+ BB', 4 H + 2 H, H-4 a. H-18), 7.03 (BB´, 2 H, H-21), 6.95 (BB´, 2 H, H-7), 6.86 (BB´, 4 H, H-3), 3.79 (s, 6 H, H-1), 3.11 (s, 1 H, H-25).

^{13}C-NMR (100 MHz, CD_2Cl_2): δ / ppm = 156.7 (quart.), 149.4 (quart.), 148.5 (quart.), 147.8 (quart.), 147.5 (quart.), 145.7 (quart.), 140.9 (quart.), 133.7 (tert.), 132.8 (quart.), 130.1 (tert.), 129.5 (tert.), 127.2 (tert.), 126.79 (tert.), 126.77 (tert.), 125.1 (tert.), 123.5 (tert.), 122.5 (quart.), 122.0 (quart.), 120.4 (tert.), 117.0 (tert.), 116.7 (quart.), 115.1 (tert.), 83.7 (tert.), 77.1 (quart.), 55.8 (prim).

MALDI-TOF pos: [M$^{•+}$]

	calc.	m/z = 673.223
	found.	m/z = 673.252

Compound 46
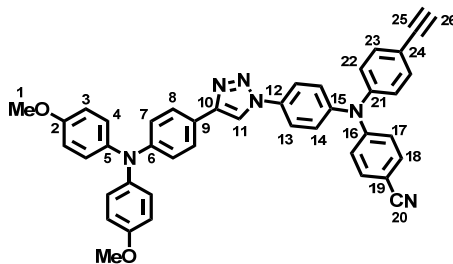
According to general procedure GP3:

43 (18.7 mg, 23.0 μmol), TBAF trihydrate (7.90 mg, 25.0 μmol), DCM (10 mL), 2 h, flash-chromatography (silica gel, DCM → EA).

Formula: $C_{43}H_{32}N_6O_2$ [664.75].

Yield: 15.0 mg (22.6 μmol) **98 %** of a yellow solid.

^{1}H-NMR (400 MHz, CD_2Cl_2): δ / ppm = 8.09 (s, 1 H, H-11), 7.74 (AA′, 2 H, H-13), 7.68 (AA′, 2 H, H-8), 7.52 (AA′, 2 H, H-18), 7.47 (AA′, 2 H, H-23), 7.28 (BB′, 2 H, H-14), 7.13–7.06 (BB′+ BB′+ AA′, 2 H + 2 H + 4 H, H-17 a. H-22 a. H-4), 6.96 (BB′, 2 H, H-7), 6.86 (BB′, 4 H, H-3), 3.79 (s, 6 H, H-1), 3.15 (s, 1 H, H-26).

^{13}C-NMR (100 MHz, CD_2Cl_2): δ / ppm = 156.7 (quart.), 151.0 (quart.), 149.5 (quart.), 148.7 (quart.), 146.6 (quart.), 146.4 (quart.), 140.9 (quart.), 134.1 (quart.), 134.0 (tert.), 133.8 (tert.), 127.3 (tert.), 127.0 (tert.), 126.8 (tert.), 125.5 (tert.), 122.27 (2 x tert.), 122.25 (tert.), 120.4 (tert.), 119.4 (quart.), 118.7 (quart.), 117.0 (tert.), 115.1 (quart.), 105.2 (quart.), 83.3 (tert.), 77.8 (quart.), 55.8 (prim.).

MALDI-TOF pos: [M$^{•+}$]

calc.   m/z = 664.258

found. m/z = 664.224

Compound Da[346]
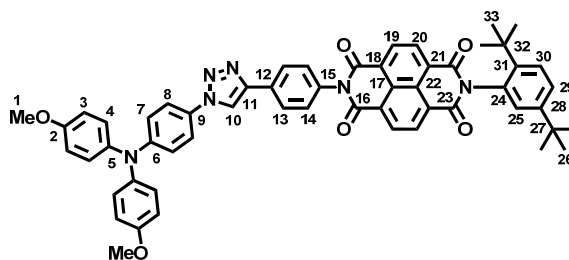
Compound **19** (70.0 mg, 126 μmol) and **8** (131 mg, 379 μmol) were dissolved in dry THF (40 mL) and the solution was degassed with nitrogen. After addition of DIPEA (16.0 mg, 122 μmol) and (PPh$_3$)$_3$CuBr (23.0 mg, 24.0 μmol) the solution was stirred for 7 d at 60°C under preclusion of light. The solvent was evaporated in vacuum and the residue was purified by flash-chromatography (silica gel, PE / DCM = 1:1 → DCM). The product fraction was further purified by recycling GPC in CHCl$_3$.

Formula: C$_{56}$H$_{48}$N$_6$O$_6$ [901.02].

Yield: 85.6 mg (95.0 μmol) **75 %** of a brownish solid.

^{1}H-NMR (600 MHz, CDCl$_3$): δ / ppm = 8.86 (-, 4 H, H-19 a. H-20), 8.16 (s, 1 H, H-10), 8.11 (AA´, 2 H, H-13), 7.61 (d, ^3J = 8.6, 1 H, H-30), 7.54 (AA´, 2 H, H-8), 7.49 (dd, ^3J = 8.6, ^4J = 2.3, 1 H, H-29), 7.43 (BB´, 2 H, H-14), 7.11 (AA´, 4 H, H-4), 7.03–7.02 (BB´ a. m, 2 H + 1 H, H-7 a. H-25), 6.88 (BB´, 4 H, H-3), 3.82 (s, 6 H, H-1), 1.33 (s, 9 H, H-26), 1.28 (s, 9 H, H-33).

^{13}C-NMR (150 MHz, CD$_2$Cl$_2$): δ / ppm = 163.9 (quart.), 163.1 (quart.), 156.6 (quart.), 150.5 (quart.), 149.6 (quart.), 147.2 (quart.), 143.8 (quart.), 140.2 (quart.), 134.4 (quart.), 132.1 (quart.), 131.7 (tert.), 131.6 (tert.), 129.3 (quart.), 129.2 (tert. a. quart.), 129.1 (tert.), 127.6 (tert.), 127.5 (quart.), 127.4 (quart.), 127.3 (quart.), 127.2 (tert.), 127.1 (quart.), 127.0 (tert.), 126.8 (tert.), 121.7 (tert.), 120.0 (tert.), 118.2 (tert.), 115.0 (tert.), 55.6 (prim.), 35.7 (quart.), 34.4 (quart.), 31.8 (prim.), 31.3 (prim.).

ESI-MS pos (high resolution): [M$^{\bullet+}$]

        calc.   m/z = 900.36298

        found.   m/z = 900.36241 Δ = 0.63 ppm

Compound Db
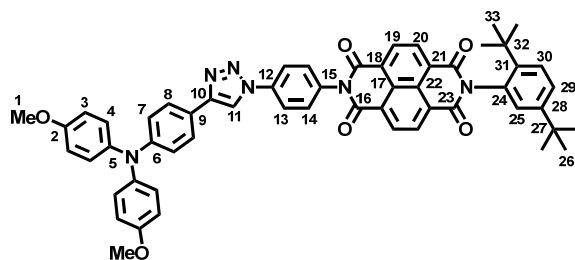
Compound **22** (70.0 mg, 122 μmol) and **6** (40.0 mg, 122 μmol) were dissolved in dry THF (20 mL) and the solution was degassed with nitrogen. After addition of DIPEA (16.0 mg, 122 μmol) and (PPh$_3$)$_3$CuBr (23.0 mg, 24.0 μmol) the solution was stirred for 38 d at 65°C under preclusion of light. The solvent was evaporated *in vacuo* and the residue was purified by flash-chromatography (silica gel, PE / EA = 6:1 → 5:1). The product fraction was further purified by recycling GPC in CHCl$_3$.

Formula: C$_{56}$H$_{48}$N$_6$O$_6$ [901.02].

Yield: 38.5 mg (43.0 μmol) **35 %** of a yellow solid.

^{1}H-NMR (600 MHz, CD$_2$Cl$_2$)**:** δ / ppm = 8.87–8.84 (-, 4 H, H-19 a. H-20), 8.23 (s, 1 H, H-11), 8.03 (AA′, 2 H, H-13), 7.72 (AA′, 2 H, H-8), 7.63 (d, ^3J = 8.6, 1 H, H-30), 7.56 (BB′, 2 H, H-14), 7.53 (dd, ^3J = 8.6, ^4J = 2.3, 1 H, H-29), 7.10 (AA′, 4 H, H-4), 7.05 (d, ^4J = 2.3, 1 H, H-25), 6.98 (BB′, 2 H, H-7), 6.87 (BB′, 4 H, H-3), 3.79 (s, 6 H, H-1), 1.33 (s, 9 H, H-26), 1.27 (s, 9 H, H-33).

^{13}C-NMR (150 MHz, CD$_2$Cl$_2$)**:** δ / ppm = 164.2 (quart.), 163.3 (quart.), 156.6 (quart.), 150.9 (quart.), 149.5 (quart.), 148.9 (quart.), 144.5 (quart.), 140.8 (quart.), 137.7 (quart.), 135.2 (quart.), 132.9 (quart.), 131.8 (tert.), 131.7 (tert.), 130.6 (tert.), 129.4 (tert.), 127.9 (tert.), 127.72 (quart.), 127.70 (2 x quart.), 127.3 (tert.), 127.2 (quart.), 126.9 (tert.), 126.8 (tert.), 122.1 (quart.), 121.5 (tert.), 120.3 (tert.), 117.0 (tert.), 115.0 (tert.), 55.8 (prim.), 35.8 (quart.), 34.5 (quart.), 31.8 (prim.), 31.2 (prim.).

ESI-MS pos (high resolution)**:** [M$^{•+}$]

calc.   m/z = 900.36298

found. m/z = 900.36265 Δ = 0.36 ppm

Compound T-Me
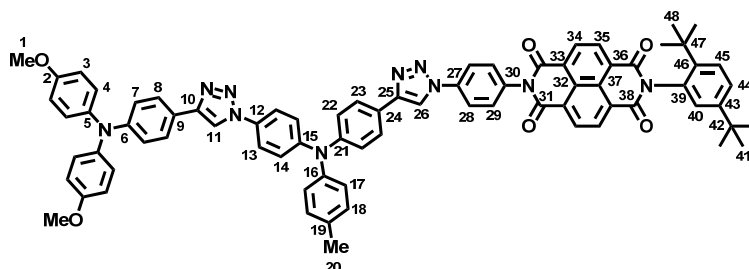
Compound **8** (17.1 mg, 30.0 μmol) and **44** (16.3 mg, 25.0 μmol) were dissolved in dry THF (15 mL) and the solution was degassed with nitrogen. After addition of DIPEA (3.22 mg, 25.0 μmol) and (PPh₃)₃CuBr (4.64 mg, 4.99 μmol) the solution was stirred for 13 d at 65°C under preclusion of light. The solvent was evaporated *in vacuo* and the residue was purified by recycling GPC in $CHCl_3$.

Formula: $C_{77}H_{64}N_{10}O_6$ [1225.40].

Yield: 11.9 mg (9.71 μmol) **39 %** of a brownish solid.

¹H-NMR (600 MHz, CD_2Cl_2): δ / ppm = 8.87–8.84 (-, 4 H, H-33 a. H-34), 8.31 (s, 1 H, H-26), 8.07 (s, 1 H, H-11), 8.04 (AAʹ, 2 H, H-28), 7.85 (AAʹ, 2 H, H-23), 7.68 (AAʹ, 2 H, H-8), 7.64–7.62 (AAʹ + m, 2 H + 1 H, H-13 a. H-45), 7.57 (BBʹ, 2 H, H-29), 7.53 (dd, ^3J = 8.6, ^4J = 2.3, 1 H, H-44), 7.24–7.20 (BBʹ + BBʹ, 2 H + 2 H, H-14 a. H-22), 7.18 (AAʹ, 2 H, H-18), 7.11 (BBʹ, 2 H, H-17), 7.08 (AAʹ, 4 H, H-4), 7.05 (d, ^4J = 2.3, 1 H, H-40), 6.95 (BBʹ, 2 H, H-7), 6.85 (BBʹ, 4 H, H-3), 3.78 (s, 6 H, H-1), 2.36 (s, 3 H, H-20), 1.33 (s, 9 H, H-41), 1.27 (s, 9 H, H-48).

¹³C-NMR (150 MHz, CD_2Cl_2): δ / ppm = 164.2 (quart.), 163.3 (quart.), 156.5 (quart.), 150.9 (quart.), 149.3 (quart.), 148.5 (quart.), 148.4 (quart.), 148.3 (quart.), 148.0 (quart.), 144.6 (quart.), 144.5 (quart.), 140.9 (quart.), 137.7 (quart.), 135.3 (quart.), 134.7 (quart.), 132.9 (quart.), 131.8 (tert.), 131.7 (tert.), 131.6 (quart.), 130.7 (tert.), 130.6 (tert.), 129.4 (tert.), 127.9 (tert.), 127.72 (2 x quart.), 127.71 (quart.), 127.23 (tert.), 127.20 (quart. + tert.), 126.8 (tert.), 126.6 (tert.), 126.1 (tert.), 125.0 (quart.), 124.2 (tert.), 123.7 (tert.), 122.5 (quart.), 121.8 (tert.), 121.5 (tert.), 120.4 (tert.), 117.6 (tert.), 117.0 (tert.), 115.0 (tert.), 55.8 (prim.), 35.8 (quart.), 34.5 (quart.), 31.8 (prim.), 31.2 (prim.), 21.0 (prim.).

ESI-MS pos (high resolution)**:** [M•+ + H]

$$\text{calc.} \quad m/z = 1224.50048$$

$$\text{found.} \quad m/z = 1224.50063 \qquad \Delta = 0.12 \text{ ppm}$$

Compound T-Cl

Compound **8** (58.0 mg, 101 μmol) and **45** (42.1 mg, 62.0 μmol) were dissolved in dry THF (15 mL) and the solution was degassed with nitrogen. After addition of DIPEA (8.26 mg, 64.0 μmol) and (PPh$_3$)$_3$CuBr (12.0 mg, 13.0 μmol) the solution was stirred for 13 d at 65°C under preclusion of light. The solvent was evaporated *in vacuo* and the residue was purified by recycling GPC in CHCl$_3$. The product fraction was further purified by dropping a concentrated solution in DCM into *n*-hexane. The solid was filtered off and washed with *n*-hexane.

Formula: C$_{76}$H$_{61}$ClN$_{10}$O$_6$ [1245.81].

Yield: 52.6 mg (42.2 μmol) **68 %** of a brownish solid.

^{1}H-NMR (600 MHz, CD$_2$Cl$_2$): δ / ppm = 8.87–8.84 (-, 4 H, H-33 + H-34), 8.32 (s, 1 H, H-25), 8.09 (s, 1 H, H-11), 8.04 (AA′, 2 H, H-27), 7.88 (AA′, 2 H, H-22), 7.69–7.66 (AA′ + AA′, 2 H + 2 H, H-8 a. H-13), 7.63 (d, ^3J = 8.6, 1 H, H-44), 7.58 (BB′, 2 H, H-28), 7.53 (dd, ^3J = 8.6, ^4J = 2.3, 1 H, H-43), 7.30 (AA′, 2 H, H-18), 7.26 (BB′, 2 H, H-14), 7.23 (BB′, 2 H, H-21), 7.14 (BB′, 2 H, H-17), 7.08 (AA′, 4 H, H-4), 7.05 (d, ^4J = 2.3, 1 H, H-39), 6.95 (BB′, 2 H, H-7), 6.85 (BB′, 4 H, H-3), 3.78 (s, 6 H, H-1), 1.33 (s, 9 H, H-40), 1.27 (s, 9 H, H-47).

^{13}C-NMR (150 MHz, CD$_2$Cl$_2$): δ / ppm = 164.2 (quart.), 163.3 (quart.), 156.6 (quart.), 150.9 (quart.), 149.3 (quart.), 148.4 (quart.), 148.3 (quart.), 147.8 (quart.), 147.4 (quart.), 146.0 (quart.), 144.5 (quart.), 140.8 (quart.), 137.6 (quart.), 135.4 (quart.), 132.9 (quart.), 132.4 (quart.), 131.8 (tert.), 131.7 (tert.), 130.7 (tert.), 129.9 (tert.), 129.4 (tert.), 129.0 (quart.), 127.9 (tert.), 127.72 (2 x quart.), 127.70 (quart.), 127.3 (tert.), 127.2 (tert.), 127.1 (quart.), 126.8 (tert.), 126.6 (tert.), 126.4 (tert.), 125.8 (quart.), 124.9 (tert.), 124.6 (tert.), 122.4 (quart.), 121.9 (tert.),

121.6 (tert.), 120.3 (tert.), 117.7 (tert.), 117.0 (tert.), 115.0 (tert.), 55.8 (prim.), 35.8 (quart.), 34.5 (quart.), 31.8 (prim.), 31.2 (prim.).

ESI-MS pos (high resolution)**:** [M$^{\bullet+}$ + H]

$$\text{calc.} \quad m/z = 1245.45368$$
$$\text{found.} \quad m/z = 1245.45604 \qquad \Delta = 1.89 \text{ ppm}$$

Compound T-CN
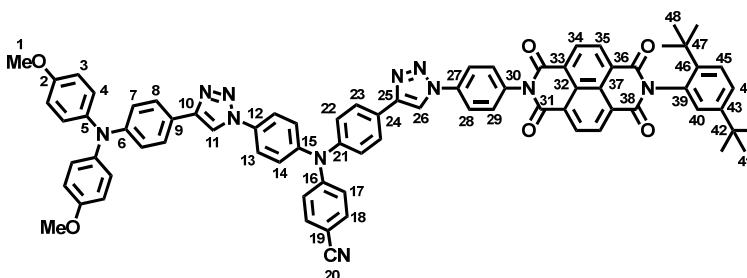
Compound **8** (15.0 mg, 27.0 μmol) and **46** (15.0 mg, 23.0 μmol) were dissolved in dry THF (20 mL) and the solution was degassed with nitrogen. After addition of DIPEA (2.92 mg, 23.0 μmol) and (PPh$_3$)$_3$CuBr (4.20 mg, 4.51 μmol) the solution was stirred for 34 d at 65°C under preclusion of light. The solvent was evaporated *in vacuo* and the residue was purified by flash-chromatography (silica gel, DCM / EA = 1:1). The product fraction was further purified by recycling GPC in CHCl$_3$.

Formula: C$_{77}$H$_{61}$N$_{11}$O$_6$ [1236.38].

Yield: 11.1 mg (8.98 μmol) **39 %** beige solid.

^{1}H-NMR (600 MHz, CD$_2$Cl$_2$)**:** δ / ppm = 8.87–8.84 (-, 4 H, H-34 a. H-35), 8.35 (s, 1 H, H-26), 8.12 (s, 1 H, H-11), 8.05 (AA′, 2 H, H-28), 7.96 (AA′, 2 H, H-23), 7.76 (AA′, 2 H, H-13), 7.68 (AA′, 2 H, H-8), 7.63 (d, ^3J = 8.6, 1 H, H-45), 7.59 (BB′, 2 H, H-29), 7.55–7.52 (AA′ + m, 2 H + 1 H, H-18 a. H-44), 7.25 (BB′, 2 H, H-14), 7.30 (BB′, 2 H, H-22), 7.15 (BB′, 2 H, H-17), 7.08 (AA′, 4 H, H-4), 7.05 (d, ^4J = 2.3, 1 H, H-40), 6.96 (BB′, 2 H, H-7), 6.86 (BB′, 4 H, H-3), 3.79 (s, 6 H, H-1), 1.33 (s, 9 H, H-41), 1.27 (s, 9 H, H-48).

^{13}C-NMR (150 MHz, CD$_2$Cl$_2$)**:** δ / ppm = 164.2 (quart.), 163.3 (quart.), 156.6 (quart.), 151.2 (quart.), 150.9 (quart.), 149.4 (quart.), 148.6 (quart.), 148.1 (quart.), 146.5 (quart.), 146.2 (quart.), 144.5 (quart.), 140.8 (quart.), 137.6 (quart.), 135.5 (quart.), 133.9 (quart.), 133.8 (tert.),

132.9 (quart.), 131.8 (tert.), 131.7 (tert.), 130.7 (tert.), 129.4 (tert.), 127.9 (tert.), 127.74 (quart.), 127.72 (quart.), 127.71 (quart. a. tert.), 127.5 (quart.), 127.2 (tert.), 127.1 (quart.), 126.8 (tert.), 126.78 (tert.), 126.73 (tert.), 126.6 (tert.), 122.2 (quart.), 122.1 (tert.), 121.7 (tert.), 121.6 (tert.), 120.3 (tert.), 119.6 (quart.), 118.1 (tert.), 116.9 (tert.), 115.0 (tert.), 104.6 (quart.), 55.8 (prim.), 35.8 (quart.), 34.5 (quart.), 31.8 (prim.), 31.2 (prim.).

ESI-MS pos (high resolution)**:** [M$^{\bullet+}$]

calc. m/z = 1235.48008

found. m/z = 1235.48040 Δ = 0.26 ppm

Chapter 7

LITERATURE

[1]   Balzani, V.; Credi, A.; Venturi, M. *ChemSusChem* **2008**, *1*, 26-58.

[2]   Ciamician, G. *Science* **1912**, *36*, 385-394.

[3]   Speiser, S. *Chem. Rev.* **1996**, *96*, 1953-1976.

[4]   Scholes, G. D. *Annu. Rev. Phys. Chem.* **2003**, *54*, 57-87.

[5]   Scholes, G. D.; Ghiggino, K. P. *J. Phys. Chem.* **1994**, *98*, 4580-4590.

[6]   Dale, R. E. *Biophys. J.* **1980**, *30*, 365-365.

[7]   Dale, R. E.; Eisinger, J.; Blumberg, W. E. *Biophys. J.* **1979**, *26*, 161-193.

[8]   Lakowicz, J. R. *Principles of Fluorescence Spectroscopy*. 3rd ed.; Springer: Berlin, **2006**.

[9]   Lin, S. H. *Mol. Phys.* **1971**, *21*, 853-863.

[10]   Förster, T. *Discuss. Faraday Soc.* **1959**, *27*, 7-17.

[11]   van der Meer, B. W.; Coker, G.; Chen, S. Y. S. *Resonance Energy Transfer: Theory and Data*. Wiley: Weinheim, **1994**.

[12]   Förster, T. *Ann. Physik* **1948**, *2*, 55-75.

[13]   Braslavsky, S. E.; Fron, E.; Rodríguez, H. B.; San Román, E.; Scholes, G. D.; Schweitzer, G.; Valeur, B.; Wirz, J. *Photochem. Photobiol. Sci.* **2008**, *7*, 1444-1448.

[14]   Stryer, L. *Annu. Rev. Biochem.* **1978**, *47*, 819-846.

[15]   Steinberg, I. Z. *Annu. Rev. Biochem.* **1971**, *40*, 83-114.

[16]   Dexter, D. L. *J. Chem. Phys.* **1953**, *21*, 836-850.

[17]   Kasha, M. *Radiat. Res.* **1963**, *20*, 55-70.

[18]   McRae, E. G.; Kasha, M. *Phys. Process. Radiation Biol., Proc. Intern. Symp.* **1964**, 23-42.

[19]   Kasha, M.; Rawls, H. R.; El-Bayoumi, M. A. *Pure Appl. Chem.* **1965**, *11*, 371-392.

[20]   Eisfeld, A.; Briggs, J. S. *Chem. Phys.* **2006**, *324*, 376-384.

[21]   Eisfeld, A.; Briggs, J. S. *Phys. Rev. Lett.* **2006**, *96*, 113003.

[22]   Jelley, E. E. *Nature* **1936**, *138*, 1009-1010.

[23]   Würthner, F.; Kaiser, T. E.; Saha-Möller, C. R. *Angew. Chem., Int. Ed.* **2011**, *50*, 3376-3410.

[24]   Watarai, H.; Adachi, K. *Anal. Bioanal. Chem.* **2009**, *395*, 1033-1046.

[25]   Liptay, W. *Z. Naturforsch.* **1965**, *20a*, 1441-1471.

[26]   Ecoffet, C.; Markovitsi, D.; Millié, P.; Lemaistre, J.-P. *Chem. Phys.* **1993**, *177*, 629-643.

[27]   Tanaka, F.; Mataga, N. *Chem. Phys.* **1998**, *236*, 277-289.

[28]   Waluk, J.; Thulstrup, E. W. *Chem. Phys. Lett.* **1987**, *135*, 515-520.

[29] Jameson, D. M.; Ross, J. A. *Chem. Rev.* **2010**, *110*, 2685-2708.

[30] Wynne, K.; Hochstrasser, R. M. *Chem. Phys.* **1993**, *171*, 179-188.

[31] Knox, R. S.; Gülen, D. *Photochem. Photobiol.* **1993**, *57*, 40-43.

[32] Knox, R. S.; Gülen, D.; Lotterhos, K. E. *Chem. Phys. Lett.* **2002**, *361*, 285-290.

[33] Galli, C.; Wynne, K.; LeCours, S. M.; Therien, M. J.; Hochstrasser, R. M. *Chem. Phys. Lett.* **1993**, *206*, 493-499.

[34] Matro, A.; Cina, J. A. *J. Phys. Chem.* **1995**, *99*, 2568-2582.

[35] Azumi, T.; McGlynn, S. P. *J. Chem. Phys.* **1962**, *37*, 2413-2420.

[36] Chen, R. F.; Bowman, R. L. *Science* **1965**, *147*, 729-732.

[37] Bajzer, Ž.; Moncrieffe, M. C.; Penzar, I.; Prendergast, F. G. *Biophys. J.* **2001**, *81*, 1765-1775.

[38] Bialik, C. N.; Wolf, B.; Rachofsky, E. L.; Alexander Ross, J. B.; Laws, W. R. *Biophys. J.* **1998**, *75*, 2564-2573.

[39] Ranasinghe, M. I.; Varnavski, O. P.; Pawlas, J.; Hauck, S. I.; Louie, J.; Hartwig, J. F.; Goodson, T., III *J. Am. Chem. Soc.* **2002**, *124*, 6520-6521.

[40] Goodson, T., III *Annu. Rev. Phys. Chem.* **2005**, *56*, 581-603.

[41] Guo, M.; Varnavski, O.; Narayanan, A.; Mongin, O.; Majoral, J.-P.; Blanchard-Desce, M.; Goodson, T., III *J. Phys. Chem. A* **2009**, *113*, 4763-4771.

[42] Zieschang, F.; Schmiedel, A.; Holzapfel, M.; Ansorg, K.; Engels, B.; Lambert, C. *J. Phys. Chem. C* **2013**, *117*, 19816-19831.

[43] Heckmann, A.; Lambert, C. *Angew. Chem., Int. Ed.* **2012**, *51*, 326-392.

[44] Marcus, R. A. *J. Chem. Phys.* **1956**, *24*, 966-978.

[45] Marcus, R. A. *J. Electroanal. Chem.* **1997**, *438*, 251-259.

[46] Marcus, R. A. *Pure Appl. Chem.* **1997**, *69*, 13-29.

[47] Marcus, R. A. *Discuss. Faraday Soc.* **1960**, *29*, 21-31.

[48] Marcus, R. A.; Sutin, N. *Biochim. Biophys. Acta* **1985**, *811*, 265-322.

[49] Paddon-Row, M. N. *Aust. J. Chem.* **2003**, *56*, 729-748.

[50] Lambert, C.; Nöll, G. *J. Chem. Soc., Perkin Trans. 2* **2002**, 2039-2043.

[51] Verhoeven, J. W.; van Ramesdonk, H. J.; Groeneveld, M. M.; Benniston, A. C.; Harriman, A. *ChemPhysChem* **2005**, *6*, 2251-2260.

[52] Bolton, J. R.; Archer, M. D. *Adv. Chem. Ser.* **1991**, 7-23.

[53] Nelsen, S. F.; Chang, H.; Wolff, J. J.; Adamus, J. *J. Am. Chem. Soc.* **1993**, *115*, 12276-12289.

[54] Nelsen, S. F.; Blackstock, S. C.; Kim, Y. *J. Am. Chem. Soc.* **1987**, *109*, 677-682.

[55]   Greenfield, S. R.; Svec, W. A.; Gosztola, D.; Wasielewski, M. R. *J. Am. Chem. Soc.* **1996**, *118*, 6767-6777.

[56]   Thu Ba, T. *J. Phys. Chem.* **1984**, *88*, 3906-3913.

[57]   Vauthey, E.; Suppan, P.; Haselbach, E. *Helv. Chim. Acta* **1988**, *71*, 93-99.

[58]   Miller, J. R.; Calcaterra, L. T.; Closs, G. L. *J. Am. Chem. Soc.* **1984**, *106*, 3047-3049.

[59]   Verhoeven, J. W. *J. Photochem. Photobiol. C: Photochem. Rev.* **2006**, *7*, 40-60.

[60]   Marcus, R. A. *Faraday Discuss.* **1982**, *74*, 7-15.

[61]   Ulstrup, J.; Jortner, J. *J. Chem. Phys.* **1975**, *63*, 4358-4368.

[62]   Sumi, H. In *Electron Transfer in Chemistry*; Wiley-VCH Verlag GmbH: **2008**, 64-108.

[63]   Jortner, J.; Bixon, M. *J. Chem. Phys.* **1988**, *88*, 167-170.

[64]   Jortner, J. *J. Chem. Phys.* **1976**, *64*, 4860-4867.

[65]   Bixon, M.; Jortner, J. *J. Chem. Phys.* **1968**, *48*, 715-726.

[66]   Cortés, J.; Heitele, H.; Jortner, J. *J. Phys. Chem.* **1994**, *98*, 2527-2536.

[67]   Brunschwig, B. S.; Sutin, N. *Coord. Chem. Rev.* **1999**, *187*, 233-254.

[68]   Brunschwig, B. S.; Creutz, C.; Sutin, N. *Chem. Soc. Rev.* **2002**, *31*, 168-184.

[69]   Hush, N. S. *Electrochim. Acta* **1968**, *13*, 1005-1023.

[70]   Hush, N. S. *Coord. Chem. Rev.* **1985**, *64*, 135-157.

[71]   Creutz, C.; Newton, M. D.; Sutin, N. *J. Photochem. Photobiol. A* **1994**, *82*, 47-59.

[72]   Sutin, N. *Prog. Inorg. Chem.* **1983**, *30*, 441-498.

[73]   Chako, N. Q. *J. Chem. Phys.* **1934**, *2*, 644-653.

[74]   Gould, I. R.; Young, R. H.; Mueller, L. J.; Albrecht, A. C.; Farid, S. *J. Am. Chem. Soc.* **1994**, *116*, 8188-8199.

[75]   Cave, R. J.; Newton, M. D. *Chem. Phys. Lett.* **1996**, *249*, 15-19.

[76]   Cave, R. J.; Newton, M. D. *J. Chem. Phys.* **1997**, *106*, 9213-9226.

[77]   Nelsen, S. F.; Newton, M. D. *J. Phys. Chem. A* **2000**, *104*, 10023-10031.

[78]   Nelsen, S. F.; Trieber II, D. A.; Ismagilov, R. F.; Teki, Y. *J. Chem. Soc.* **2001**, *123*, 5684-5694.

[79]   Day, P. *Endeavour* **1970**, *29*, 45-49.

[80]   Robin, M. B.; Day, P. In *Advances in Inorganic Chemistry and Radiochemistry*; Academic Press: New York and London, **1968**, Vol. 10, 247-422.

[81]   Szeghalmi, A. V.; Erdmann, M.; Engel, V.; Schmitt, M.; Amthor, S.; Kriegisch, V.; Nöll, G.; Stahl, R.; Lambert, C.; Leusser, D. *et al. J. Am. Chem. Soc.* **2004**, *126*, 7834-7845.

[82]   Lambert, C.; Risko, C.; Coropceanu, V.; Schelter, J.; Amthor, S.; Gruhn, N. E.; Durivage, J. C.; Brédas, J.-L. *J. Am. Chem. Soc.* **2005**, *127*, 8508-8516.

[83]   Wagenknecht, H.-A. *Chem. Unserer Zeit* **2002**, *36*, 318-330.

[84]   Davis, W. B.; Wasielewski, M. R.; Ratner, M. A.; Mujica, V.; Nitzan, A. *J. Phys. Chem. A* **1997**, *101*, 6158-6164.

[85]   Lambert, C.; Nöll, G.; Schelter, J. *Nat. Mater.* **2002**, *1*, 69-73.

[86]   Newton, M. D. *Chem. Rev.* **1991**, *91*, 767-792.

[87]   McConnell, H. M. *J. Chem. Phys.* **1961**, *35*, 508-515.

[88]   Fischer, M.; Vögtle, F. *Angew. Chem., Int. Ed.* **1999**, *38*, 884-905.

[89]   Tomalia, D. A.; Naylor, A. M.; Goddard III, W. A. *Angew. Chem., Int. Ed.* **1990**, *29*, 138-175.

[90]   Hawker, C. J.; Fréchet, J. M. J. *J. Chem. Soc., Chem. Commun.* **1990**, 1010-1013.

[91]   Buhleier, E.; Wehner, W.; Vögtle, F. *Synthesis* **1978**, 155-158.

[92]   Denkewalter, R. G. K., J.; Lukasavage, W. J. *U.S. Pat. 4*, 289 872, **1981**.

[93]   Tomalia, D. A.; Baker, H.; Dewald, J. R.; Hall, M.; Kallos, G.; Martin, S.; Roeck, J.; Ryder, J.; Smith, P. *Polym. J.* **1985**, *17*, 117-132.

[94]   Newkome, G. R.; Yao, Z.; Baker, G. R.; Gupta, V. K. *J. Org. Chem.* **1985**, *50*, 2003-2004.

[95]   Zeng, F.; Zimmerman, S. C. *Chem. Rev.* **1997**, *97*, 1681-1712.

[96]   Nantalaksakul, A.; Reddy, D. R.; Bardeen, C.; Thayumanavan, S. *Photosynth. Res.* **2006**, *87*, 133-150.

[97]   Varnavski, O.; Yan, X.; Mongin, O.; Blanchard-Desce, M.; Goodson, T., III *J. Phys. Chem. C* **2007**, *111*, 149-162.

[98]   Grage, M. M. L.; Zaushitsyn, Y.; Yartsev, A.; Chachisvilis, M.; Sundström, V.; Pullerits, T. *Phys. Rev. B* **2003**, *67*, 205207.

[99]   Yang, X.; Dykstra, T. E.; Scholes, G. D. *Phys. Rev. B* **2005**, *71*, 045203.

[100]   Beenken, W. J. D.; Pullerits, T. *J. Phys. Chem. B* **2004**, *108*, 6164-6169.

[101]   Wang, Y.; Ranasinghe, M. I.; Goodson, T. *J. Am. Chem. Soc.* **2003**, *125*, 9562-9563.

[102]   Bar-Haim, A.; Klafter, J.; Kopelman, R. *J. Am. Chem. Soc.* **1997**, *119*, 6197-6198.

[103]   Bar-Haim, A.; Klafter, J. *J. Phys. Chem. B* **1998**, *102*, 1662-1664.

[104]   Bar-Haim, A.; Klafter, J. *J. Lumin.* **1998**, *76–77*, 197-200.

[105]   Hagedorn, K. V.; Varnavski, O.; Hartwig, J.; Goodson, T., III *J. Phys. Chem. C* **2008**, *112*, 2235-2238.

[106]   Devadoss, C.; Bharathi, P.; Moore, J. S. *J. Am. Chem. Soc.* **1996**, *118*, 9635-9644.

[107]   Hirao, Y.; Ino, H.; Ito, A.; Tanaka, K.; Kato, T. *J. Phys. Chem. A* **2006**, *110*, 4866-4872.

[108]   Bronk, K.; Thayumanavan, S. *J. Org. Chem.* **2003**, *68*, 5559-5567.

[109]   Bronk, K.; Thayumanavan, S. *Org. Lett.* **2001**, *3*, 2057-2060.

[110]   Selby, T. D.; Blackstock, S. C. *J. Am. Chem. Soc.* **1998**, *120*, 12155-12156.

[111]   Justin Thomas, K. R.; Thompson, A. L.; Sivakumar, A. V.; Bardeen, C. J.; Thayumanavan, S. *J. Am. Chem. Soc.* **2004**, *127*, 373-383.

[112] Baranoff, E.; Dixon, I. M.; Collin, J.-P.; Sauvage, J.-P.; Ventura, B.; Flamigni, L. *Inorg. Chem.* **2004**, *43*, 3057-3066.

[113] Flamigni, L.; Baranoff, E.; Collin, J.-P.; Sauvage, J.-P. *Chem. - Eur. J.* **2006**, *12*, 6592-6606.

[114] Imahori, H.; Guldi, D. M.; Tamaki, K.; Yoshida, Y.; Luo, C.; Sakata, Y.; Fukuzumi, S. *J. Am. Chem. Soc.* **2001**, *123*, 6617-6628.

[115] Imahori, H.; Tamaki, K.; Araki, Y.; Sekiguchi, Y.; Ito, O.; Sakata, Y.; Fukuzumi, S. *J. Am. Chem. Soc.* **2002**, *124*, 5165-5174.

[116] Guldi, D. M.; Imahori, H.; Tamaki, K.; Kashiwagi, Y.; Yamada, H.; Sakata, Y.; Fukuzumi, S. *J. Phys. Chem. A* **2004**, *108*, 541-548.

[117] Guldi, D. M. *Chem. Soc. Rev.* **2002**, *31*, 22-36.

[118] Kashiwagi, Y.; Ohkubo, K.; McDonald, J. A.; Blake, I. M.; Crossley, M. J.; Araki, Y.; Ito, O.; Imahori, H.; Fukuzumi, S. *Org. Lett.* **2003**, *5*, 2719-2721.

[119] Fukuzumi, S. *Bull. Chem. Soc. Jpn.* **2006**, *79*, 177-195.

[120] Kaiser, C.; Schmiedel, A.; Holzapfel, M.; Lambert, C. *J. Phys. Chem. C* **2012**, *116*, 15265-15280.

[121] Guldi, D. M. *Angew. Chem., Int. Ed.* **2010**, *49*, 7844-7846.

[122] Miura, T.; Scott, A. M.; Wasielewski, M. R. *J. Phys. Chem. C* **2010**, *114*, 20370-20379.

[123] Liddell, P. A.; Kodis, G.; de la Garza, L.; Bahr, J. L.; Moore, A. L.; Moore, T. A.; Gust, D. *Helv. Chim. Acta* **2001**, *84*, 2765-2783.

[124] Di Valentin, M.; Bisol, A.; Agostini, G.; Liddell, P. A.; Kodis, G.; Moore, A. L.; Moore, T. A.; Gust, D.; Carbonera, D. *J. Phys. Chem. B* **2005**, *109*, 14401-14409.

[125] Kolb, H. C.; Finn, M. G.; Sharpless, K. B. *Angew. Chem., Int. Ed.* **2001**, *40*, 2004-2021.

[126] Michael, A. *J. Prakt. Chem.* **1893**, *48*, 94-95.

[127] Huisgen, R.; Szeimies, G.; Möbius, L. *Chem. Ber.* **1967**, *100*, 2494-2507.

[128] Huisgen, R. *Helv. Chim. Acta* **1967**, *50*, 2421-2439.

[129] Huisgen, R. *Angew. Chem., Int. Ed.* **1963**, *2*, 565-598.

[130] Meldal, M.; Tornøe, C. W. *Chem. Rev.* **2008**, *108*, 2952-3015.

[131] Hein, J. E.; Fokin, V. V. *Chem. Soc. Rev.* **2010**, *39*, 1302-1315.

[132] Bock, V. D.; Hiemstra, H.; van Maarseveen, J. H. *Eur. J. Org. Chem.* **2006**, 51-68.

[133] Rostovtsev, V. V.; Green, L. G.; Fokin, V. V.; Sharpless, K. B. *Angew. Chem., Int. Ed.* **2002**, *41*, 2596-2599.

[134] Tornøe, C. W.; Christensen, C.; Meldal, M. *J. Org. Chem.* **2002**, *67*, 3057-3064.

[135] Himo, F.; Lovell, T.; Hilgraf, R.; Rostovtsev, V. V.; Noodleman, L.; Sharpless, K. B.; Fokin, V. V. *J. Am. Chem. Soc.* **2005**, *127*, 210-216.

[136] Worrell, B. T.; Malik, J. A.; Fokin, V. V. *Science* **2013**, *340*, 457-460.

[137] Hou, J.; Liu, X.; Shen, J.; Zhao, G.; Wang, P. G. *Expert Opin. Drug Discov.* **2012**, *7*, 489-501.

[138] van Steenis, D. J. V. C.; David, O. R. P.; van Strijdonck, G. P. F.; van Maarseveen, J. H.; Reek, J. N. H. *Chem. Commun.* **2005**, 4333-4335.

[139] Calvo-Losada, S.; Pino, M.; Quirante, J. *J. Mol. Model.* **2014**, *20*, 1-7.

[140] Hein, J. E.; Tripp, J. C.; Krasnova, L. B.; Sharpless, K. B.; Fokin, V. V. *Angew. Chem., Int. Ed.* **2009**, *48*, 8018-8021.

[141] Zhang, L.; Chen, X.; Xue, P.; Sun, H. H. Y.; Williams, I. D.; Sharpless, K. B.; Fokin, V. V.; Jia, G. *J. Am. Chem. Soc.* **2005**, *127*, 15998-15999.

[142] Goodall, G. W.; Hayes, W. *Chem. Soc. Rev.* **2006**, *35*, 280-312.

[143] Ozkal, E.; Pericàs, M. A. *Adv. Synth. Catal.* **2014**, *356*, 711-717.

[144] Chanda, K.; Rej, S.; Huang, M. H. *Chem. - Eur. J.* **2013**, *19*, 16036-16043.

[145] Claes, D.; Holzapfel, M.; Clausen, N.; Maison, W. *Eur. J. Org. Chem.* **2013**, *2013*, 6361-6371.

[146] Brik, A.; Wu, C.-Y.; Wong, C.-H. *Org. Biomol. Chem.* **2006**, *4*, 1446-1457.

[147] Groth, T.; Renil, M.; Meinjohanns, E. *Comb. Chem. High Throughput Screening* **2003**, *6*, 589-610.

[148] Evans, M. J.; Cravatt, B. F. *Chem. Rev.* **2006**, *106*, 3279-3301.

[149] Kolb, H. C.; Sharpless, K. B. *Drug Discovery Today* **2003**, *8*, 1128-1137.

[150] Xu, L.; Li, Y.; Li, Y. *Asian J. Org. Chem.* **2014**, *3*, 582-602.

[151] Binder, W. H.; Sachsenhofer, R. *Macromol. Rapid Commun.* **2007**, *28*, 15-54.

[152] Lutz, J.-F. *Angew. Chem., Int. Ed.* **2007**, *46*, 1018-1025.

[153] Laughlin, S. T.; Baskin, J. M.; Amacher, S. L.; Bertozzi, C. R. *Science* **2008**, *320*, 664-667.

[154] de Miguel, G.; Wielopolski, M.; Schuster, D. I.; Fazio, M. A.; Lee, O. P.; Haley, C. K.; Ortiz, A. L.; Echegoyen, L.; Clark, T.; Guldi, D. M. *J. Am. Chem. Soc.* **2011**, *133*, 13036-13054.

[155] Wu, P.; Feldman, A. K.; Nugent, A. K.; Hawker, C. J.; Scheel, A.; Voit, B.; Pyun, J.; Fréchet, J. M. J.; Sharpless, K. B.; Fokin, V. V. *Angew. Chem., Int. Ed.* **2004**, *43*, 3928 –3932.

[156] Joralemon, M. J.; O'Reilly, R. K.; Matson, J. B.; Nugent, A. K.; Hawker, C. J.; Wooley, K. L. *Macromolecules* **2005**, *38*, 5436-5443.

[157] Ornelas, C.; Ruiz Aránzaes, J.; Cloutet, E.; Alves, S.; Astruc, D. *Angew. Chem., Int. Ed.* **2007**, *46*, 872-877.

[158] Franc, G.; Kakkar, A. *Chem. Commun.* **2008**, 5267-5276.

[159] Parent, M.; Mongin, O.; Kamada, K.; Katan, C.; Blanchard-Desce, M. *Chem. Commun.* **2005**, 2029-2031.

[160] Shirota, Y.; Kageyama, H. *Chem. Rev.* **2007**, *107*, 953-1010.

[161] Yen, H.-J.; Liou, G.-S. *Polymer Chemistry* **2012**, *3*, 255-264.

[162] Ning, Z.; Tian, H. *Chem. Comm.* **2009**, 5483-5495.

[163] Thelakkat, M. *Macromol. Mater. Eng.* **2002**, *287*, 442-461.

[164] Lambert, C.; Schelter, J.; Fiebig, T.; Mank, D.; Trifonov, A. *J. Am. Chem. Soc.* **2005**, *127*, 10600-10610.

[165] Lin, B. C.; Cheng, C. P.; Lao, Z. P. M. *J. Phys. Chem. A* **2003**, *107*, 5241-5251.

[166] Cias, P.; Slugovc, C.; Gescheidt, G. *J. Phys. Chem. A* **2011**, *115*, 14519-14525.

[167] Strehmel, B.; Amthor, S.; Schelter, J.; Lambert, C. *ChemPhysChem* **2005**, *6*, 893-896.

[168] Amthor, S.; Noller, B.; Lambert, C. *Chem. Phys.* **2005**, *316*, 141-152.

[169] Zhao, H.; Tanjutco, C.; Thayumanavan, S. *Tetrahedron Lett.* **2001**, *42*, 4421-4424.

[170] Holzapfel, M.; Lambert, C. *J. Phys. Chem. C* **2007**, *112*, 1227-1243.

[171] Dapperheld, S.; Steckhan, E.; Brinkhaus, K.-H. G.; Esch, T. *Chem. Ber.* **1991**, *124*, 2557-2567.

[172] Schmidt, W.; Steckhan, E. *Chem. Ber.* **1980**, *113*, 577-585.

[173] Andric, G.; Boas, J. F.; Bond, A. M.; Fallon, G. D.; Ghiggino, K. P.; Hogan, C. F.; Hutchison, J. A.; Lee, M. A. P.; Langford, S. J.; Pilbrow, J. R. *et al. Aust. J. Chem.* **2004**, *57*, 1011-1019.

[174] Ganesan, P.; Baggerman, J.; Zhang, H.; Sudhölter, E. J. R.; Zuilhof, H. *J. Phys. Chem. A* **2007**, *111*, 6151-6156.

[175] Klein, J. H.; Sunderland, T. L.; Kaufmann, C.; Holzapfel, M.; Schmiedel, A.; Lambert, C. *Phys. Chem. Chem. Phys.* **2013**, *15*, 16024-16030.

[176] Geng, Y.; Wu, S.-X.; Li, H.-B.; Tang, X.-D.; Wu, Y.; Su, Z.-M.; Liao, Y. *J. Mater. Chem.* **2011**, *21*, 15558-15566.

[177] Gawrys, P.; Djurado, D.; Rimarčík, J. n.; Kornet, A.; Boudinet, D.; Verilhac, J.-M.; Lukeš, V. r.; Wielgus, I.; Zagorska, M.; Pron, A. *J. Phys. Chem. B* **2010**, *114*, 1803-1809.

[178] Würthner, F.; Ahmed, S.; Thalacker, C.; Debaerdemaeker, T. *Chem. Eur. J.* **2002**, *8*, 4742-4750.

[179] Bergami, G.; Marchi, E.; Ceroni, P.; Balzani, V. In *Designing Dendrimers*; Wiley: **2012**, 341.

[180] Saragi, T. P. I.; Spehr, T.; Siebert, A.; Fuhrmann-Lieker, T.; Salbeck, J. *Chem. Rev.* **2007**, *107*, 1011-1065.

[181] Naito, K.; Miura, A. *J. Phys. Chem.* **1993**, *97*, 6240-6248.

[182] Naito, K. *Chem. Mater.* **1994**, *6*, 2343-2350.

[183] Kielkowski, P.; Macíčková-Cahová, H.; Pohl, R.; Hocek, M. *Angew. Chem., Int. Ed.* **2011**, *50*, 8727-8730.

[184] Yang, X.; Matsuo, D.; Suzuma, Y.; Fang, J.-K.; Xu, F.; Orita, A.; Otera, J.; Kajiyama, S.; Koumura, N.; Hara, K. *Synlett* **2011**, *2011*, 2402-2406.

[185] Al-Badri, Z. M.; Tew, G. N. *Macromolecules* **2008**, *41*, 4173-4179.

[186] Onitsuka, K.; Fujimoto, M.; Kitajima, H.; Ohshiro, N.; Takei, F.; Takahashi, S. *Chem. - Eur. J.* **2004**, *10*, 6433-6446.

[187] Ernst, A.; Gobbi, L.; Vasella, A. *Tetrahedron Lett.* **1996**, *37*, 7959-7962.

[188] Low, W.; Kang, J.; DiGruccio, M.; Kirby, D.; Perrin, M.; Fischer, W. *J. Am. Soc. Mass Spectrom.* **2004**, *15*, 1156-1160.

[189] Gritsan, N. P.; Tigelaar, D.; Platz, M. S. *J. Phys. Chem. A* **1999**, *103*, 4465-4469.

[190] Onitsuka, K.; Ohara, N.; Takei, F.; Takahashi, S. *Dalton Trans.* **2006**, 3693-3698.

[191] Hundertmark, T.; Littke, A. F.; Buchwald, S. L.; Fu, G. C. *Org. Lett.* **2000**, *12*, 1729-1731.

[192] Yuan, S.; Kirklin, S.; Dorney, B.; Liu, D.-J.; Yu, L. *Macromolecules* **2009**, *42*, 1554-1559.

[193] Goodbrand, H. B.; Hu, N.-X. *J. Org. Chem.* **1999**, *64*, 670-674.

[194] Andersen, J.; Madsen, U.; Björkling, F.; Liang, X. *Synlett* **2005**, *14*, 2209–2213.

[195] Carmieli, R.; Mi, Q.; Ricks, A. B.; Giacobbe, E. M.; Mickley, S. M.; Wasielewski, M. R. *J. Am. Chem. Soc.* **2009**, *131*, 8372-8373.

[196] Hartwig, J. F. *Handbook of Organopalladium Chemistry for Organic Synthesis*. John Wiley & Sons, Inc.: New York, **2002**.

[197] Bastug, G.; Nolan, S. P. *Organometallics* **2014**.

[198] Hoi, K. H.; Çalimsiz, S.; Froese, R. D. J.; Hopkinson, A. C.; Organ, M. G. *Chem. - Eur. J.* **2012**, *18*, 145-151.

[199] Surry, D. S.; Buchwald, S. L. *Chem. Sci.* **2011**, *2*, 27-50.

[200] Hassan, J.; Sévignon, M.; Gozzi, C.; Schulz, E.; Lemaire, M. *Chem. Rev.* **2002**, *102*, 1359-1470.

[201] Beletskaya, I. P.; Cheprakov, A. V. *Coord. Chem. Rev.* **2004**, *248*, 2337-2364.

[202] Karastatiris, P.; Mikroyannidis, J. A.; Spiliopoulos, I. K. *J. Polym. Sci., Part A: Polym. Chem.* **2008**, *46*, 2367-2378.

[203] Zhang, Q.; Ning, Z. J.; Tian, H. *Dyes Pigm.* **2009**, *81*, 80-84.

[204] Tanaka, K.; Kageyama, C.; Fukase, K. *Tetrahedron Lett.* **2007**, *48*, 6475-6479.

[205] Winnewisser, M.; Vogt, J.; Ahlbrecht, H. *J. Chem. Res., Synop.* **1978**, 298-299.

[206] Compernolle, F.; Dekeirel, M. *Org. Mass Spectrom.* **1971**, *5*, 427-436.

[207] Gilchrist, T. L.; Gymer, G. E.; Rees, C. W. *J. Chem. Soc., Perkin Trans. 1* **1975**, 1-8.

[208] Gilchrist, T. L.; Rees, C. W.; Thomas, C. *J. Chem. Soc., Perkin Trans. 1* **1975**, 8-11.

[209] Doherty, S.; Smyth, C. H.; Harrington, R. W.; Clegg, W. *Organometallics* **2009**, *28*, 5273-5276.

[210] Nishiyama, M.; Yamamoto, T.; Koie, Y. *Tetrahedron Lett.* **1998**, *39*, 617-620.

[211] Yamamoto, T.; Nishiyama, M.; Koie, Y. *Tetrahedron Lett.* **1998**, *39*, 2367-2370.

[212] Hill, L. L.; Crowell, J. L.; Tutwiler, S. L.; Massie, N. L.; Hines, C. C.; Griffin, S. T.; Rogers, R. D.; Shaughnessy, K. H.; Grasa, G. A.; Johansson Seechurn, C. C. C. *et al. J. Org. Chem.* **2010**, *75*, 6477-6488.

[213] Chaudhuri, M. K.; Khan, A. T.; Patel, B. K.; Dey, D.; Kharmawophlang, W.; Lakshmiprabha, T. R.; Mandal, G. C. *Tetrahedron Lett.* **1998**, *39*, 8163-8166.

[214] Buckland, D.; Bhosale, S. V.; Langford, S. J. *Tetrahedron Lett.* **2011**, *52*, 1990-1992.

[215] Guha, S.; Saha, S. *J. Am. Chem. Soc.* **2010**, *132*, 17674-17677.

[216] Suraru, S.-L.; Würthner, F. *J. Org. Chem.* **2013**, *78*, 5227-5238.

[217] Ajayakumar, M. R.; Hundal, G.; Mukhopadhyay, P. *Chem. Comm.* **2013**, *49*, 7684-7686.

[218] Rudolph, M.; Feldberg, S. W. DigiSim 3.03a, Bioanalytical Systems Inc., **1994-2002**.

[219] Zhou, Z.; Fahrni, C. J. *J. Am. Chem. Soc.* **2004**, *126*, 8862-8863.

[220] Nagarjuna, G.; Yurt, S.; Jadhav, K. G.; Venkataraman, D. *Macromolecules* **2010**, *43*, 8045-8050.

[221] Zieschang, F. Diploma Thesis, University of Würzburg, **2009**.

[222] Lambert, C.; Gaschler, W.; Schmälzlin, E.; Meerholz, K.; Bräuchle, C. *J. Chem. Soc., Perkin Trans. 2* **1999**, 577-588.

[223] Werner, U.; Sakaguchi, Y.; Hayashi, H.; Nohya, G.; Yoneshima, R.; Nakajima, S.; Osuka, A. *J. Phys. Chem.* **1995**, *99*, 13930-13937.

[224] Amthor, S.; Lambert, C.; Dümmler, S.; Fischer, I.; Schelter, J. *J. Phys. Chem. A* **2006**, *110*, 5204-5214.

[225] Strehmel, B.; Sarker, A. M.; Detert, H. *ChemPhysChem* **2003**, *4*, 249-259.

[226] Dörr, F. *Angew. Chem., Int. Ed.* **1966**, *78*, 457-474.

[227] Hall, R. D.; Valeur, B.; Weber, G. *Chem. Phys. Lett.* **1985**, *116*, 202-205.

[228] Frisch, M. J.; Trucks, G. W.; Schlegel, H. B.; Scuseria, G. E.; Robb, M. A.; Cheeseman, J. R.; Scalmani, G.; Barone, V.; Mennucci, B.; Petersson, G. A. *et al.* Gaussian 09, Revision B.01, Gaussian, Inc., **2010**.

[229] Demidov, A. A.; Andrews, D. L. *Photochem. Photobiol.* **1996**, *63*, 39-52.

[230] Verbouwe, W.; Van der Auweraer, M.; De Schryver, F. C.; Piet, J. J.; Warman, J. M. *J. Am. Chem. Soc.* **1998**, *120*, 1319-1324.

[231] Valeur, B.; Weber, G. *J. Chem. Phys.* **1978**, *69*, 2393-2400.

[232] Leroy, E.; Lami, H. *Chem. Phys. Lett.* **1976**, *41*, 373-377.

[233] Steeger, M.; Lambert, C. *Chem. - Eur. J.* **2012**, *18*, 11937-11948.

[234] Lambert, C.; Ehbets, J.; Rausch, D.; Steeger, M. *J. Org. Chem.* **2012**, *77*, 6147-6154.

[235] Sissa, C.; Painelli, A.; Blanchard-Desce, M.; Terenziani, F. *J. Phys. Chem. B* **2011**, *115*, 7009-7020.

[236] Cross, A. J.; Fleming, G. R. *Biophys. J.* **1984**, *46*, 45-56.

[237] Papenhuijzen, J.; Visser, A. J. W. G. *Biophys. Chem.* **1983**, *17*, 57-65.

[238] van Stokkum, I. H. M.; Larsen, D. S.; van Grondelle, R. *Biochim. Biophys. Acta, Bioenerg.* **2004**, *1657*, 82-104.

[239] van Veldhoven, E.; Zhang, H.; Glasbeek, M. *J. Phys. Chem. A* **2001**, *105*, 1687-1692.

[240] Glasbeek, M.; Zhang, H. *Chem. Rev.* **2004**, *104*, 1929-1954.

[241] Maroncelli, M. *J. Mol. Liq.* **1993**, *57*, 1-37.

[242] Fleming, G. R.; Cho, M. *Annu. Rev. Phys. Chem.* **1996**, *47*, 109-134.

[243] Fee, R. S.; Maroncelli, M. *Chem. Phys.* **1994**, *183*, 235-247.

[244] Horng, M. L.; Gardecki, J. A.; Papazyan, A.; Maroncelli, M. *J. Phys. Chem.* **1995**, *99*, 17311-17337.

[245] Toele, P.; Van Gorp, J. J.; Glasbeek, M. *J. Phys. Chem. A* **2005**, *109*, 10479-10487.

[246] van Veldhoven, E.; Zhang, H.; Rettig, W.; Brown, R. G.; Hepworth, J. D.; Glasbeek, M. *Chem. Phys. Lett.* **2002**, *363*, 189-197.

[247] van der Meer, M. J.; Zhang, H.; Glasbeek, M. *J. Chem. Phys.* **2000**, *112*, 2878-2887.

[248] Schanz, R.; Kovalenko, S. A.; Kharlanov, V.; Ernsting, N. P. *Appl. Phys. Lett.* **2001**, *79*, 566-568.

[249] Tkačenko, N. V. *Optical Spectroscopy: Methods And Instrumentations, Chapter 11 - Pump-Probe*. Elsevier Science & Technology Books: Amsterdam, **2006**.

[250] Liu, C.; Tang, K.-C.; Zhang, H.; Pan, H.-A.; Hua, J.; Li, B.; Chou, P.-T. *J. Phys. Chem. A* **2012**, *116*, 12339-12348.

[251] Fakis, M.; Giannetas, V.; Mikroyannidis, J. *Dyes Pigm.* **2010**, *87*, 44-48.

[252] Tretiak, S.; Saxena, A.; Martin, R. L.; Bishop, A. R. *Phys. Rev. Lett.* **2002**, *89*, 097402.

[253] Westenhoff, S.; Beenken, W. J. D.; Friend, R. H.; Greenham, N. C.; Yartsev, A.; Sundström, V. *Phys. Rev. Lett.* **2006**, *97*, 166804.

[254] Di Paolo, R. E.; de Melo, S. J.; Pina, J.; Burrows, H. D.; Morgado, J.; Maçanita, A. L. *ChemPhysChem* **2007**, *8*, 2657-2664.

[255] Busby, E.; Carroll, E. C.; Chinn, E. M.; Chang, L.; Moulé, A. J.; Larsen, D. S. *J. Phys. Chem. Lett.* **2011**, *2*, 2764-2769.

[256] Ghiggino, K. P.; Yeow, E. K. L.; Haines, D. J.; Scholes, G. D.; Smith, T. A. *J. Photochem. Photobiol., A* **1996**, *102*, 81-86.

[257] Beljonne, D.; Curutchet, C.; Scholes, G. D.; Silbey, R. J. *J. Phys. Chem. B* **2009**, *113*, 6583-6599.

[258] May, V. *Dalton Trans.* **2009**, *45*, 10086-10105.

[259] Hwang, I.; Scholes, G. D. *Chem. Mater.* **2011**, *23*, 610-620.

[260] May, V.; Kühn, O. In *Charge and Energy Transfer Dynamics in Molecular Systems*; Wiley VCH: Weinheim, **2011**.

[261] Klan, P.; Wirz, J. *Photochemistry of Organic Compounds*. Wiley: Chichester, **2009**; Vol. 3.

[262] Thompson, A. L.; Gaab, K. M.; Xu, J. J.; Bardeen, C. J.; Martínez, T. J. *J. Phys. Chem. A* **2004**, *108*, 671-682.

[263] Leegwater, J. A. *J. Phys. Chem.* **1996**, *100*, 14403-14409.

[264] Liptay, W.; Wortmann, R.; Schaffrin, H.; Burkhard, O.; Reitinger, W.; Detzer, N. *Chem. Phys.* **1988**, *120*, 429-438.

[265] Marcus, R. A. *J. Phys. Chem.* **1989**, *93*, 3078-3086.

[266] Jortner, J. *J. Chem. Phys.* **1976**, *64*, 4860-4867.

[267] Gould, I. R.; Noukakis, D.; Gomez-Jahn, L.; Young, R. H.; Goodman, J. L.; Farid, S. *Chem. Phys.* **1993**, *176*, 439-456.

[268] Kim, Y. H.; Jeong, D. H.; Kim, D.; Jeoung, S. C.; Cho, H. S.; Kim, S. K.; Aratani, N.; Osuka, A. *J. Am. Chem. Soc.* **2001**, *123*, 76-86.

[269] Kimura, A.; Kakitani, T.; Yamato, T. *J. Phys. Chem. B* **2000**, *104*, 9276-9287.

[270] Raghavan, S.; Knox, R. S.; Eberly, J. H. *Chem. Phys. Lett.* **2000**, *326*, 207-211.

[271] Kim, Y. R.; Share, P.; Pereira, M.; Sarisky, M.; Hochstrasser, R. M. *J. Chem. Phys.* **1989**, *91*, 7557-7562.

[272] PyMOL 1.5.0.3, Schrödinger, LLC, **2011**.

[273] Korth, M.; Pitoňák, M.; Řezáč, J.; Hobza, P. *J. Chem. Theory Comput.* **2010**, *6*, 344-352.

[274] Řezáč, J.; Fanfrlík, J.; Salahub, D.; Hobza, P. *J. Chem. Theory Comput.* **2009**, *5*, 1749-1760.

[275] Stewart, J. J. P. MOPAC 13.064L, Stewart Computational Chemistry, **2012**.

[276] Brodard, P.; Matzinger, S.; Vauthey, E.; Mongin, O.; Papamicaël, C.; Gossauer, A. *J. Phys. Chem. A* **1999**, *103*, 5858-5870.

[277] Morandeira, A.; Vauthey, E.; Schuwey, A.; Gossauer, A. *J. Phys. Chem. A* **2004**, *108*, 5741-5751.

[278] Yoon, M.-C.; Yoon, Z. S.; Cho, S.; Kim, D.; Takagi, A.; Matsumoto, T.; Kawai, T.; Hori, T.; Peng, X.; Aratani, N. *et al. J. Phys. Chem. A* **2007**, *111*, 9233-9239.

[279] Yeow, E. K. L.; Ghiggino, K. P.; Reek, J. N. H.; Crossley, M. J.; Bosman, A. W.; Schenning, A. P. H. J.; Meijer, E. W. *J. Phys. Chem. B* **2000**, *104*, 2596-2606.

[280] Wachsstock, D. TENUA 2.0, **2005**.

[281] Reynolds, L.; Gardecki, J. A.; Frankland, S. J. V.; Horng, M. L.; Maroncelli, M. *J. Phys. Chem.* **1996**, *100*, 10337-10354.

[282] Megerle, U.; Selmaier, F.; Lambert, C.; Riedle, E.; Lochbrunner, S. *Phys. Chem. Chem. Phys.* **2008**, *10*, 6245-6251.

[283] Heckmann, A.; Amthor, S.; Lambert, C. *Chem. Comm.* **2006**, 2959-2961.

[284] Fiedler, J.; Zališ, S.; Klein, A.; Hornung, F. M.; Kaim, W. *Inorg. Chem.* **1996**, *35*, 3039-3043.

[285] Ballester, M.; Riera, J.; Castañer, J.; Rodriguez, A.; Rovira, C.; Veciana, J. *J. Org. Chem.* **1982**, *47*, 4498-4505.

[286] Lambert, C.; Amthor, S.; Schelter, J. *J. Phys. Chem. A* **2004**, *108*, 6474-6486.

[287] Seibt, J.; Schaumlöffel, A.; Lambert, C.; Engel, V. *J. Phys. Chem. A* **2008**, *112*, 10178-10184.

[288] Kattnig, D. R.; Mladenova, B.; Grampp, G.; Kaiser, C.; Heckmann, A.; Lambert, C. *J. Phys. Chem. C* **2009**, *113*, 2983-2995.

[289] Potratz, S.; Mishra, A.; Bäuerle, P. *Beilstein J. Org. Chem.* **2012**, *8*, 683-692.

[290] Lambert, C.; Nöll, G.; Hampel, F. *J. Phys. Chem. A* **2001**, *105*, 7751-7758.

[291] Bonvoisin, J.; Launay, J.-P.; Van der Auweraer, M.; De Schryver, F. C. *J. Phys. Chem.* **1994**, *98*, 5052-5057.

[292] Bonvoisin, J.; Launay, J.-P.; Van der Auweraer, M.; De Schryver, F. C. *J. Phys. Chem.* **1996**, *100*, 18006-18006.

[293] Jarowski, P. D.; Wu, Y.-L.; Schweizer, W. B.; Diederich, F. *Org. Lett.* **2008**, *10*, 3347-3350.

[294] Devaraj, N. K.; Decreau, R. A.; Ebina, W.; Collman, J. P.; Chidsey, C. E. D. *J. Phys. Chem. B* **2006**, *110*, 15955-15962.

[295] Katan, C.; Blanchard-Desce, M.; Tretiak, S. *J. Chem. Theory Comput.* **2010**, *6*, 3410-3426.

[296] Natali, M.; Ravaglia, M.; Scandola, F.; Boixel, J.; Pellegrin, Y.; Blart, E.; Odobel, F. *J. Phys. Chem. C* **2013**, *117*, 19334-19345.

[297] Qin, A.; Lam, J. W. Y.; Tang, B. Z. *Chem. Soc. Rev.* **2010**, *39*, 2522-2544.

[298] Harriman, A.; Elliott, K. J.; Alamiry, M. A. H.; Pleux, L. L.; Séverac, M.; Pellegrin, Y.; Blart, E.; Fosse, C.; Cannizzo, C.; Mayer, C. R. *et al. J. Phys. Chem. C* **2009**, *113*, 5834-5842.

[299] Tabakovic, I.; Kunugi, Y.; Canavesi, A.; Miller, L. L. *Acta Chem. Scand.* **1998**, *52*, 131-136.

[300] Amthor, S.; Lambert, C. *J. Phys. Chem. A* **2005**, *110*, 1177-1189.

[301] Matuszná, K.; Breza, M.; Pálszegi, T. *J. Mol. Struct.: THEOCHEM* **2008**, *851*, 277-283.

[302] Ventura, B.; Barbieri, A.; Degli Esposti, A.; Seneclauze, J. B.; Ziessel, R. *Inorg. Chem.* **2012**, *51*, 2832-2840.

[303] Jahng, Y.; Rahman, A. F. M. M. *Bull. Chem. Soc. Jpn.* **2010**, *83*, 672-677.

[304] Katsis, D.; Geng, Y. H.; Ou, J. J.; Culligan, S. W.; Trajkovska, A.; Chen, S. H.; Rothberg, L. J. *Chem. Mater.* **2002**, *14*, 1332-1339.

[305] Johansson, N.; dos Santos, D. A.; Guo, S.; Cornil, J.; Fahlman, M.; Salbeck, J.; Schenk, H.; Arwin, H.; Brédas, J. L.; Salanek, W. R. *J. Chem. Phys.* **1997**, *107*, 2542-2549.

[306] Weisburger, J. H.; Weisburger, E. K.; Ray, F. E. *J. Am. Chem. Soc.* **1950**, *72*, 4253-4255.

[307] ChemBio3D Ultra 12.0.2, CambridgeSoft, **2010**.

[308] Simmons, H. E.; Fukunaga, T. *J. Am. Chem. Soc.* **1967**, *89*, 5208-5215.

[309] Boo, B. H.; Choi, Y. S.; Kim, T.-S.; Kang, S. K.; Kang, Y. H.; Lee, S. Y. *J. Mol. Struct.* **1996**, *377*, 129-136.

[310] Gleiter, R.; Haider, R.; Spanget-Larsen, J.; Bischof, P. *Tetrahedron Lett.* **1983**, *24*, 1149-1152.

[311] Spangetlarsen, J.; Gleiter, R.; Haider, R. *Helv. Chim. Acta* **1983**, *66*, 1441-1455.

[312] Kolosov, D.; English, D. S.; Bulovic, V.; Barbara, P. F.; Forrest, S. R.; Thompson, M. E. *J. Appl. Phys.* **2001**, *90*, 3242-3247.

[313] Ke, L.; Chen, P.; Chua, S. *J. Appl. Phys. Lett.* **2002**, *80*, 697-699.

[314] Shirota, Y. *J. Mater. Chem.* **2000**, *10*, 1-25.

[315] Katsuma, K.; Shirota, Y. *Adv. Mater.* **1998**, *10*, 223-226.

[316] Shirota, Y.; Kuwabara, Y.; Okuda, D.; Okuda, R.; Ogawa, H.; Inada, H.; Wakimoto, T.; Nakada, H.; Yonemoto, Y.; Kawami, S. *et al. J. Lumin.* **1997**, *72-4*, 985-991.

[317] Saragi, T. P. I.; Fuhrmann-Lieker, T.; Salbeck, J. *Adv. Funct. Mater.* **2006**, *16*, 966-974.

[318] Cammenga, H. K.; Epple, M. *Angew. Chem.* **1995**, *107*, 1284-1301.

[319] Höhne, G. W. H.; Cammenga, H. K.; Eysel, W.; Gmelin, E.; Hemminger, W. *Thermochim. Acta* **1990**, *160*, 1-12.

[320] Moynihan, C. T.; Easteal, A. J.; Wilder, J.; Tucker, J. *J. Phys. Chem.* **1974**, *78*, 2673-2677.

[321] Louie, J.; Hartwig, J. F.; Fry, A. J. *J. Am. Chem. Soc.* **1997**, *119*, 11695-11696.

[322] Miyasaka, H.; Masuhara, H.; Mataga, N. *J. Phys. Chem.* **1985**, *89*, 1631-1636.

[323] Miyasaka, H.; Masuhara, H.; Mataga, N. *J. Phys. Chem.* **1990**, *94*, 3577-3582.

[324] Barros, T. C.; Brochsztain, S.; Toscano, V. G.; Berci, P.; Politi, M. J. *J. Photochem. Photobiol., A* **1997**, *111*, 97-104.

[325] Weller, A. *Z. Phys. Chem.* **1982**, *133*, 93-98.

[326] Rogers, J. E.; Kelly, L. A. *J. Am. Chem. Soc.* **1999**, *121*, 3854-3861.

[327] Green, S.; Fox, M. A. *J. Phys. Chem.* **1995**, *99*, 14752-14757.

[328] Hayashi, H.; Nagakura, S. *Bull. Chem. Soc. Jpn.* **1984**, *57*, 322-328.

[329] Klumpp, T.; Linsenmann, M.; Larson, S. L.; Limoges, B. R.; Bürssner, D.; Krissinel, E. B.; Elliott, C. M.; Steiner, U. E. *J. Am. Chem. Soc.* **1999**, *121*, 1076-1087.

[330] Rawls, M. T.; Kollmannsberger, G.; Elliott, C. M.; Steiner, U. E. *J. Phys. Chem. A* **2007**, *111*, 3485-3496.

[331] Mori, Y.; Sakaguchi, Y.; Hayashi, H. *J. Phys. Chem. A* **2002**, *106*, 4453-4467.

[332] Steiner, U. E.; Ulrich, T. *Chem. Rev.* **1989**, *89*, 51-147.

[333] Anderson, P. W. *Phys. Rev.* **1959**, *115*, 2-13.

[334] Weiss, E. A.; Ahrens, M. J.; Sinks, L. E.; Ratner, M. A.; Wasielewski, M. R. *J. Am. Chem. Soc.* **2004**, *126*, 9510-9511.

[335] Weiss, E. A.; Ratner, M. A.; Wasielewski, M. R. *J. Phys. Chem. A* **2003**, *107*, 3639-3647.

[336] MacQueen, D. B.; Schanze, K. S. *J. Am. Chem. Soc.* **1991**, *113*, 7470-7479.

[337] Veldman, D.; Chopin, S. M. A.; Meskers, S. C. J.; Janssen, R. A. J. *J. Phys. Chem. A* **2008**, *112*, 8617-8632.

[338] Jeon, J.; Kim, H. J. *J. Phys. Chem. A* **2000**, *104*, 9812-9815.

[339] Mataga, N.; Chosrowjan, H.; Taniguchi, S.; Shibata, Y.; Yoshida, N.; Osuka, A.; Kikuzawa, T.; Okada, T. *J. Phys. Chem. A* **2002**, *106*, 12191-12201.

[340] Velapoldi, R. A.; Mielenz, K. D. *A Fluorescence Standard Reference Material: Quinine Sulfate Dihydrate.*; National Bureau of Standards: Washington, DC, **1980**.

[341] Kahlow, M. A.; Jarzeba, W.; DuBruil, T. P.; Barbara, P. F. *Rev. Sci. Instrum.* **1988**, *59*, 1098-1109.

[342] Xu, J.; Knutson, J. R. *Methods Enzymol.* **2008**, *450*, 159-183.

[343] Leonard, J.; Lygo, B.; Procter, G. *Praxis der Organischen Chemie. VCH-Weinheim Weinheim* **1996**; Vol. *1. Aufl.,*.

[344] Thesen, M. W.; Höfer, B.; Debeaux, M.; Janietz, S.; Wedel, A.; Köhler, A.; Johannes, H.-H.; Krueger, H. *J. Polym. Sci., Part A: Polym. Chem.* **2010**, *48*, 3417-3430.

[345] Xie, J.; Zhu, X.; Huang, M.; Meng, F.; Chen, W.; Wan, Y. *Eur. J. Org. Chem.* **2010**, *2010*, 3219-3223.

[346] Schreck, M. Bachelor Thesis, University of Würzburg, **2011**.

TABLE OF FORMULAS

1

2

3

4

5

6

7

8

9

10

11
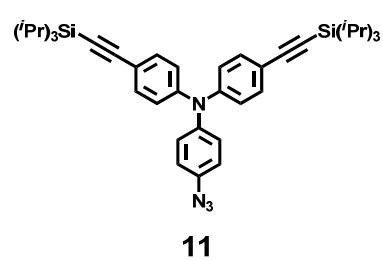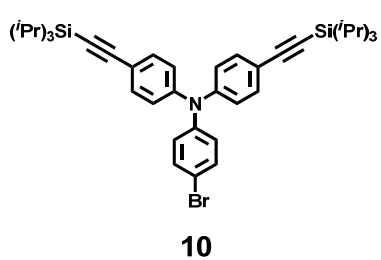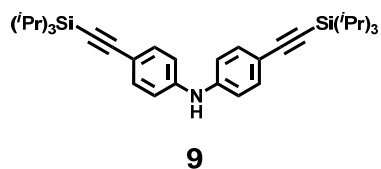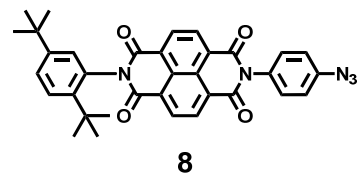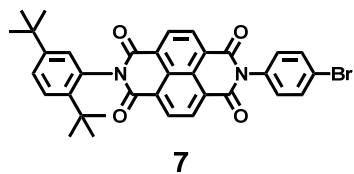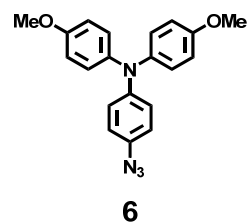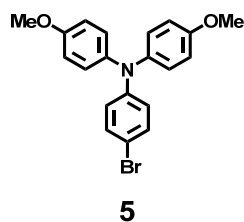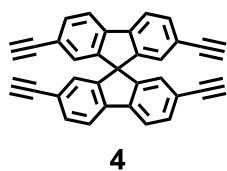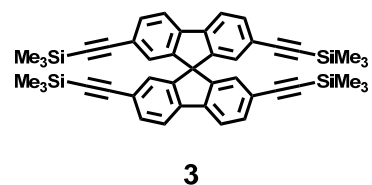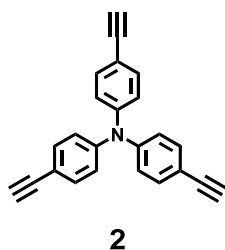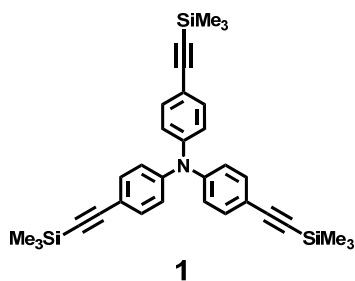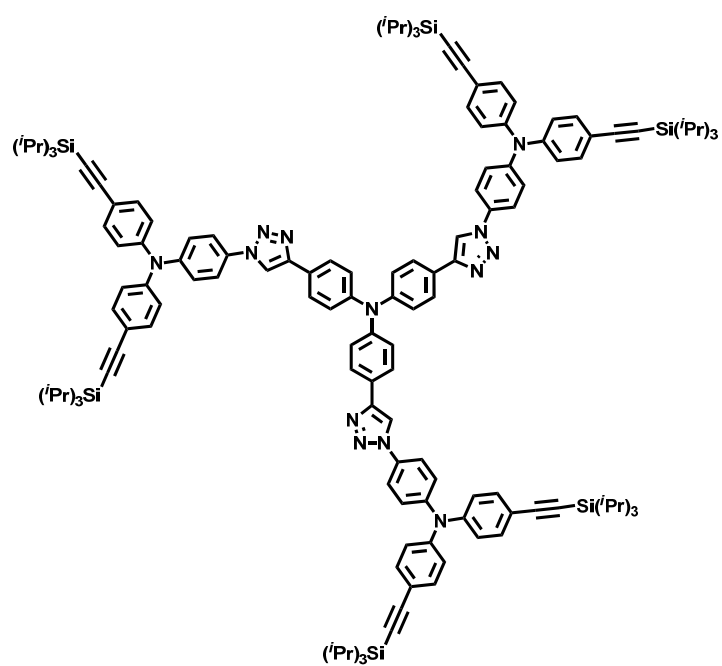
12
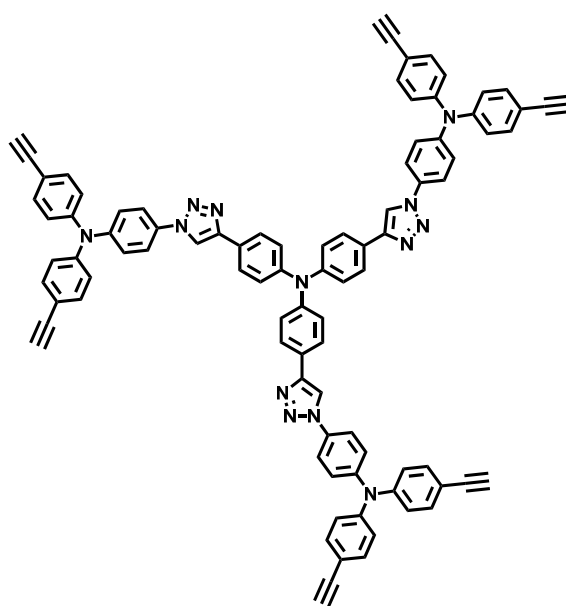
13
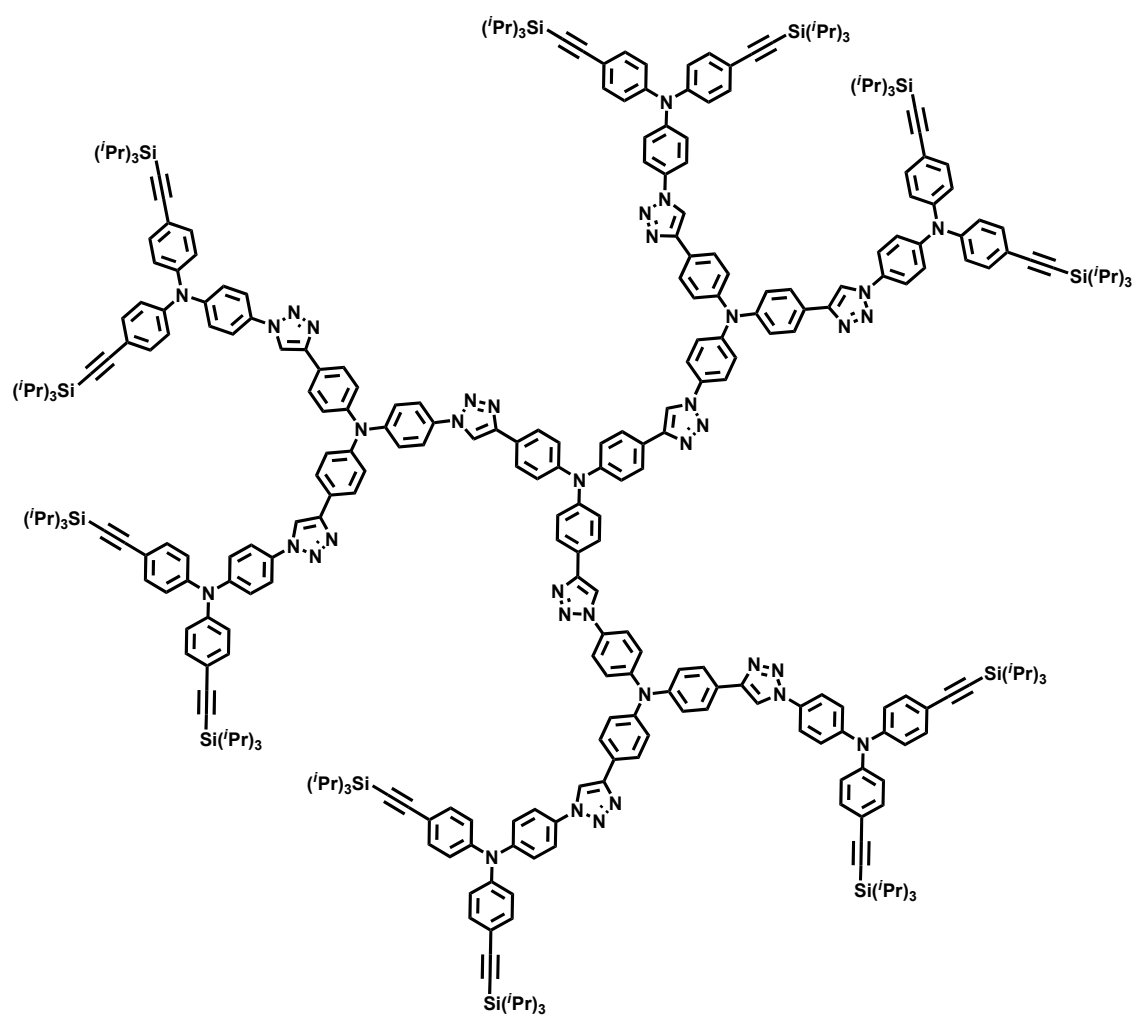
14
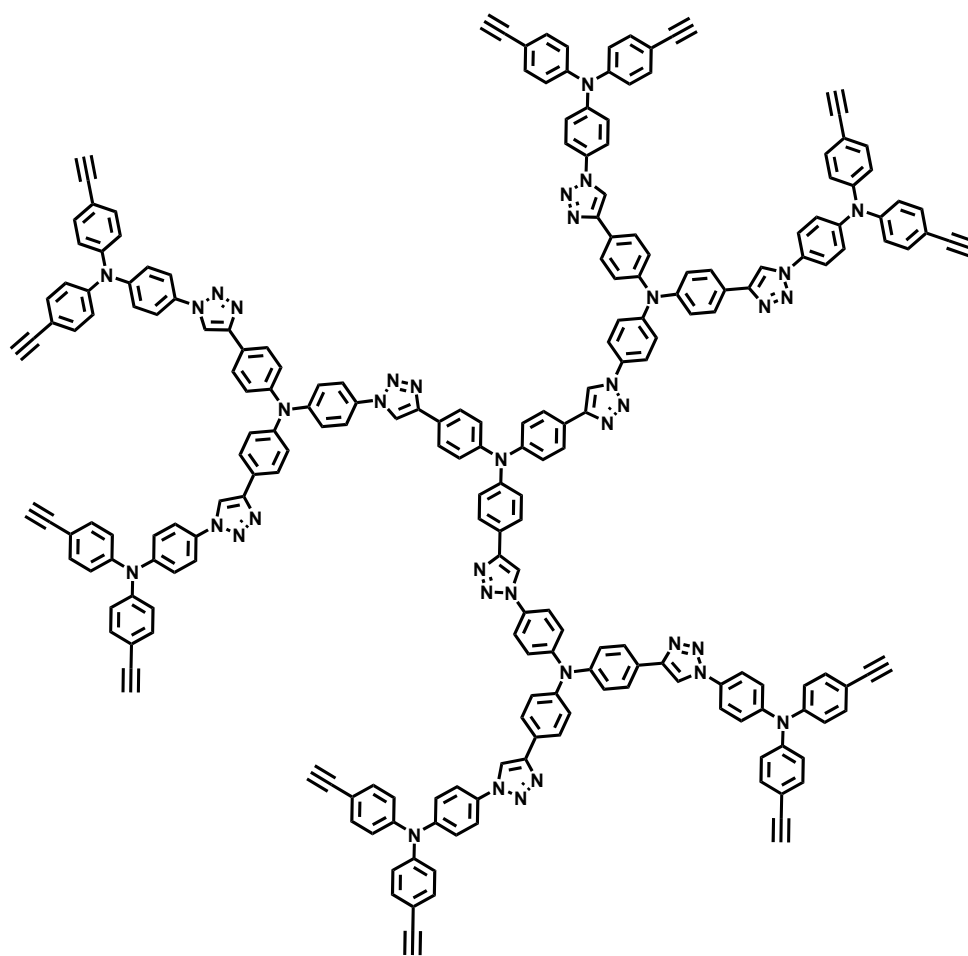
15
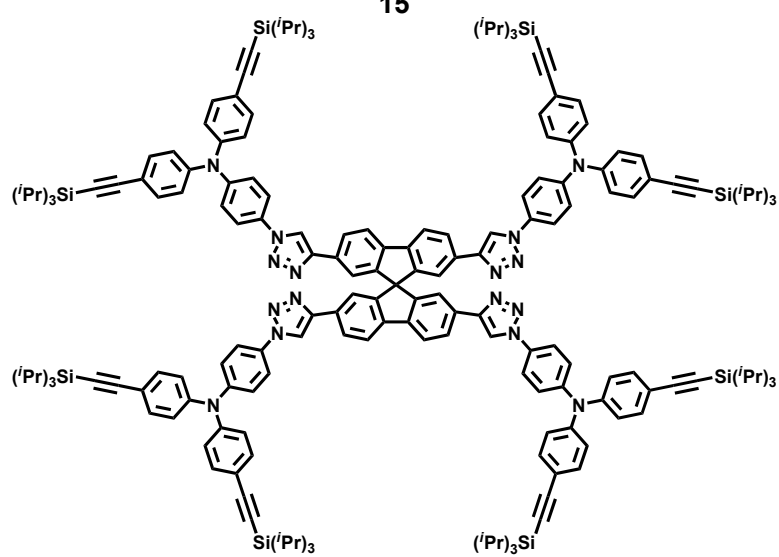
16
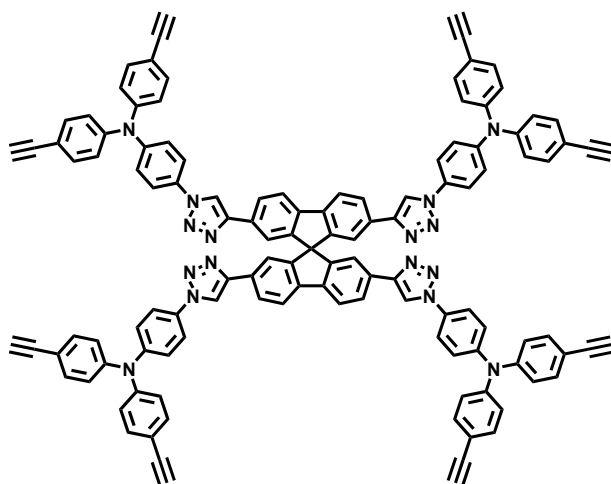
17
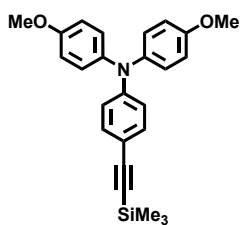
18

19

20

21

22

23

24

25

26

27

28

29

30

31

32

33

34

35

36

37

41

42

43

44

45

46
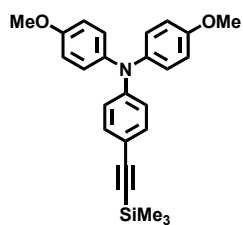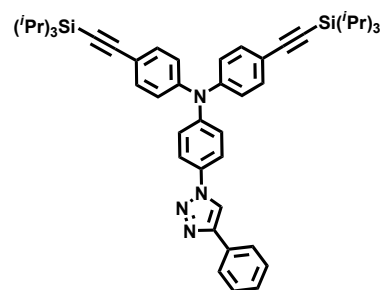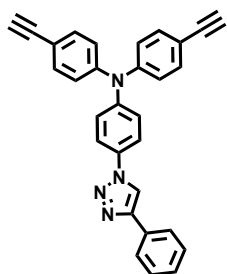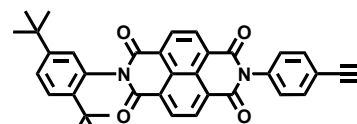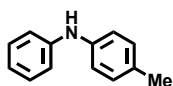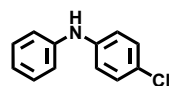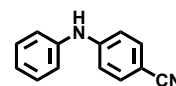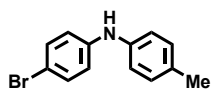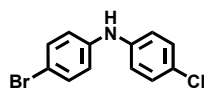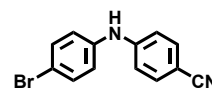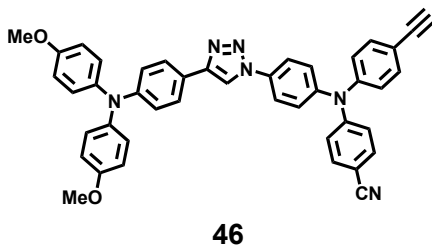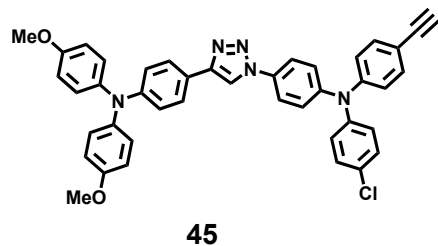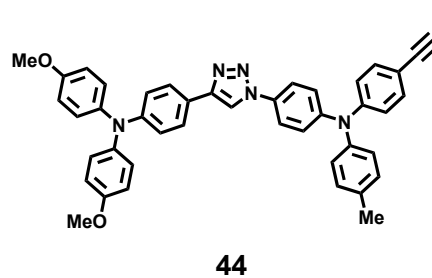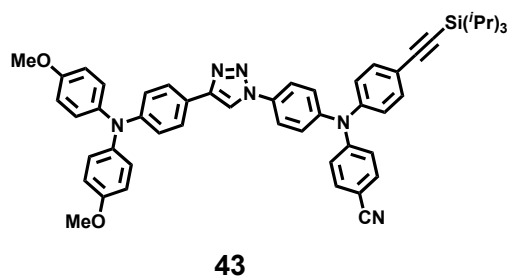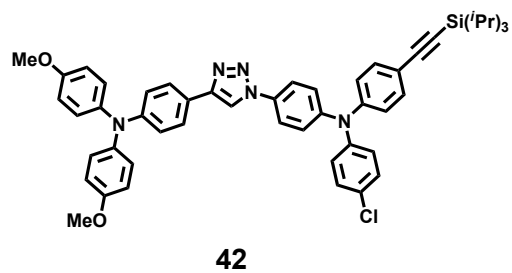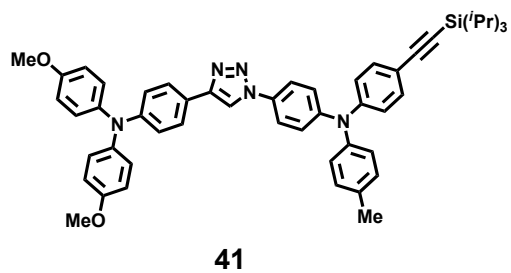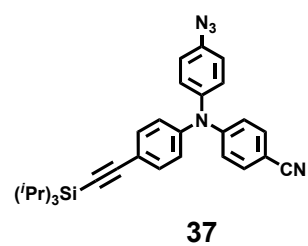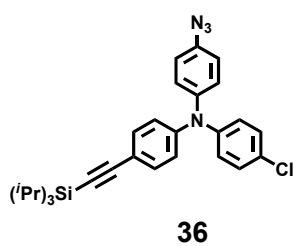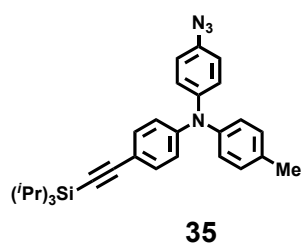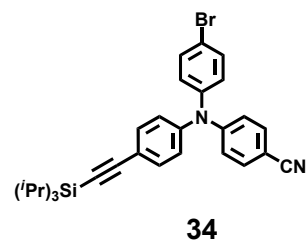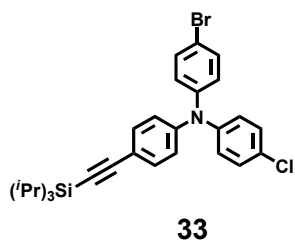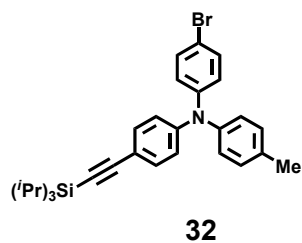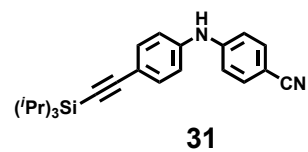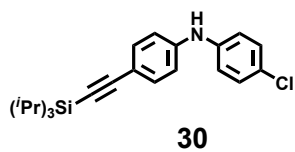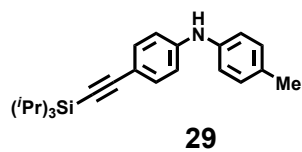
Dendrimers

G1

G2
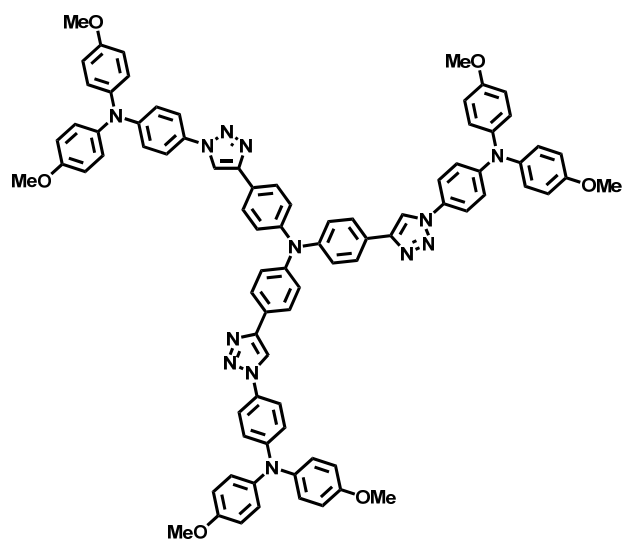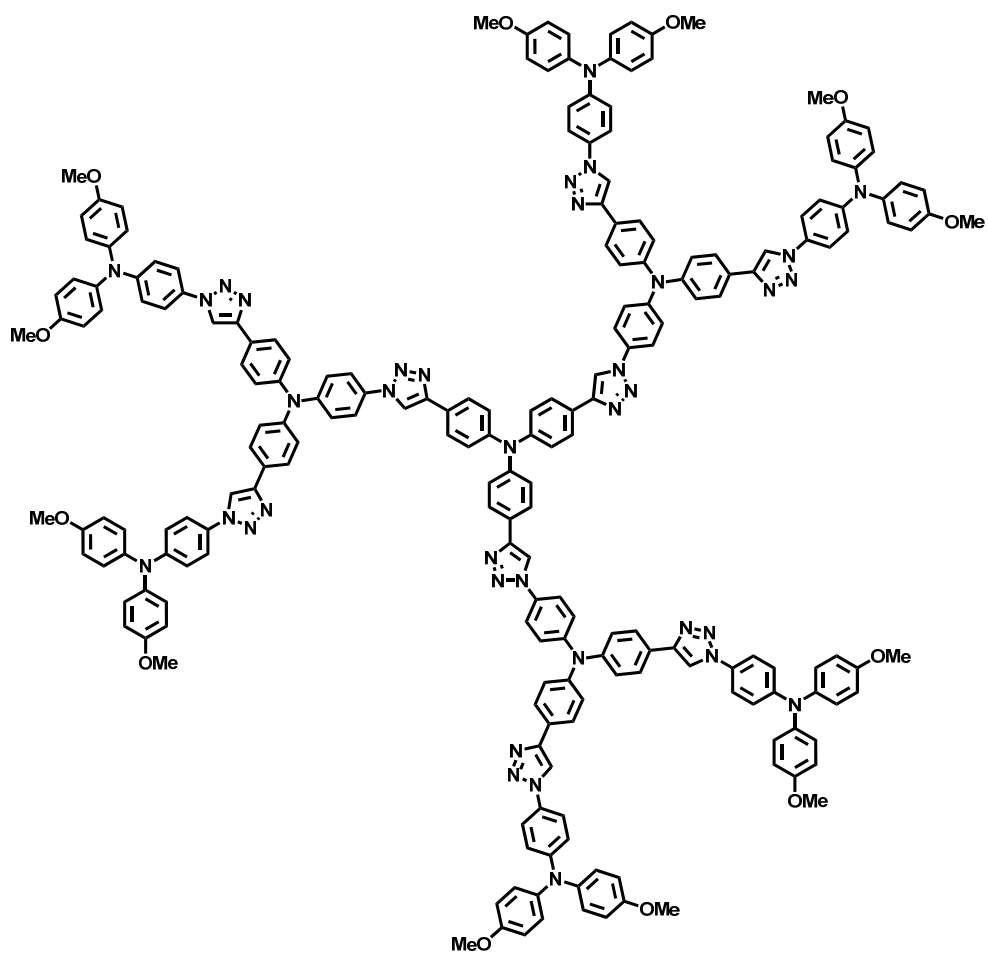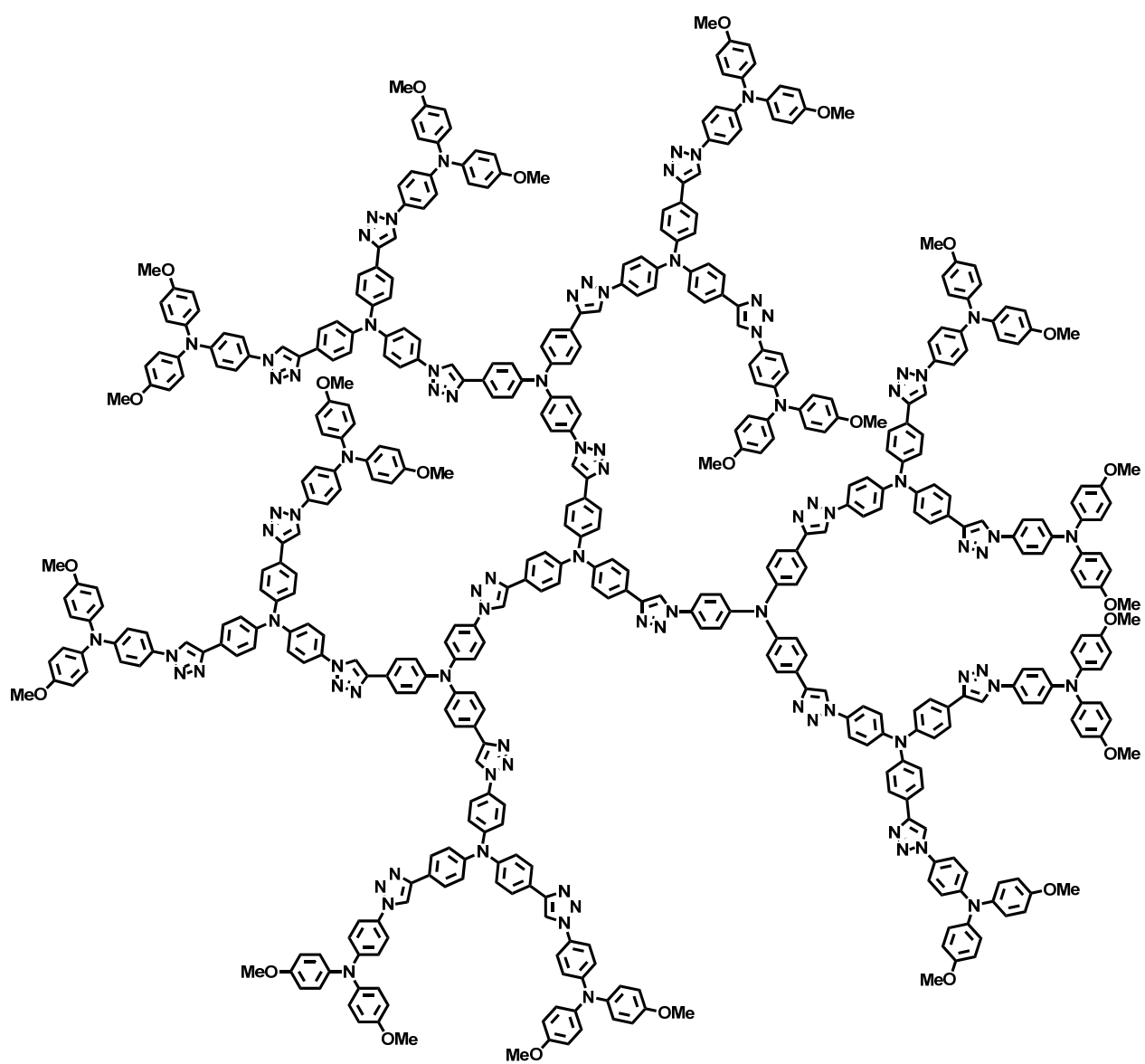
G3
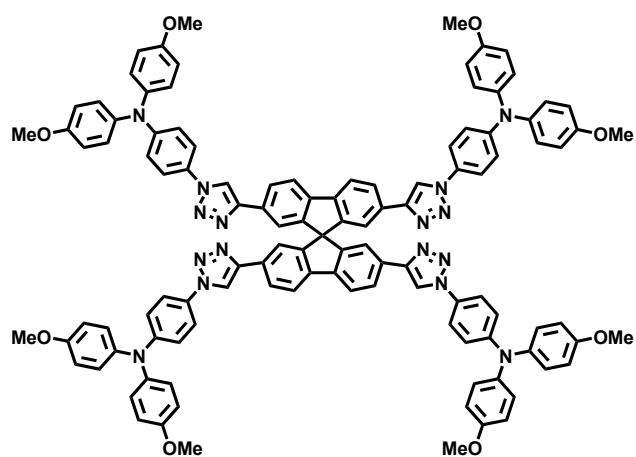
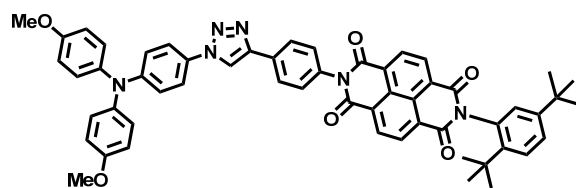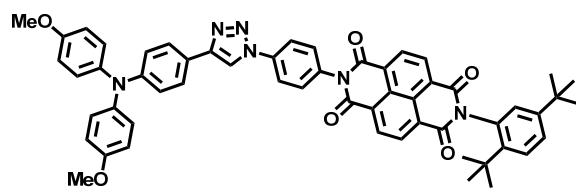**spiro-G1**
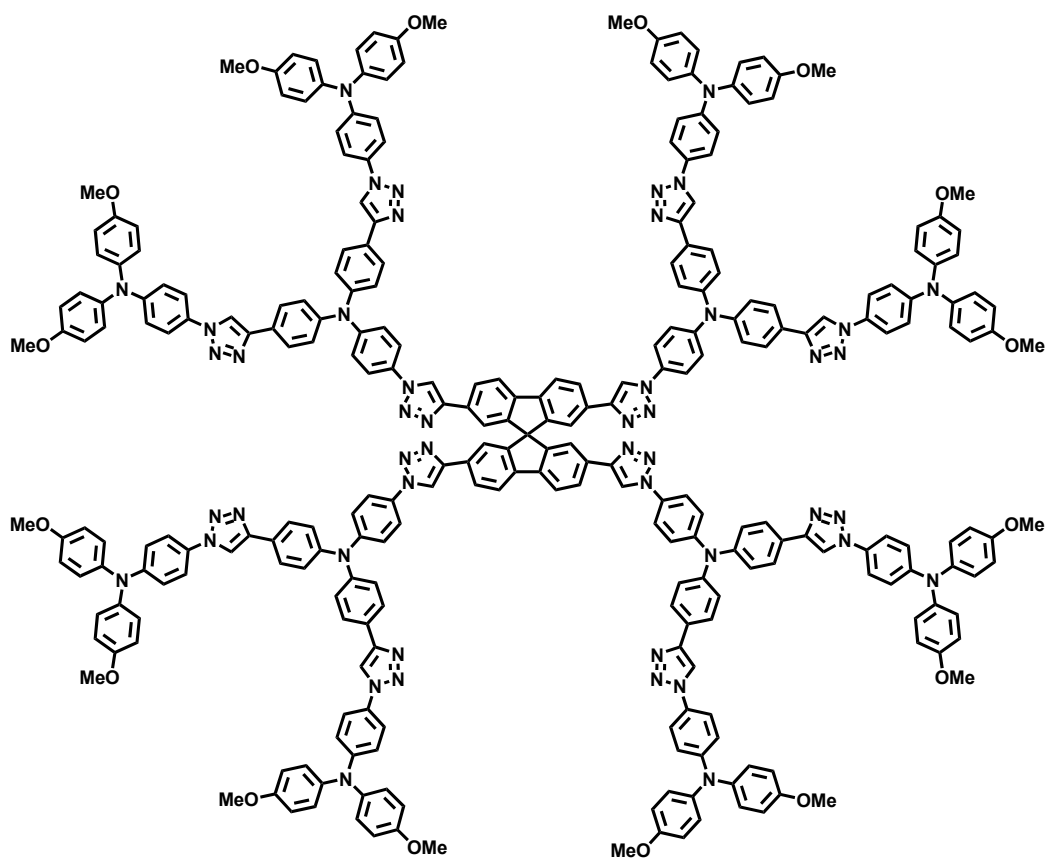
spiro-G2
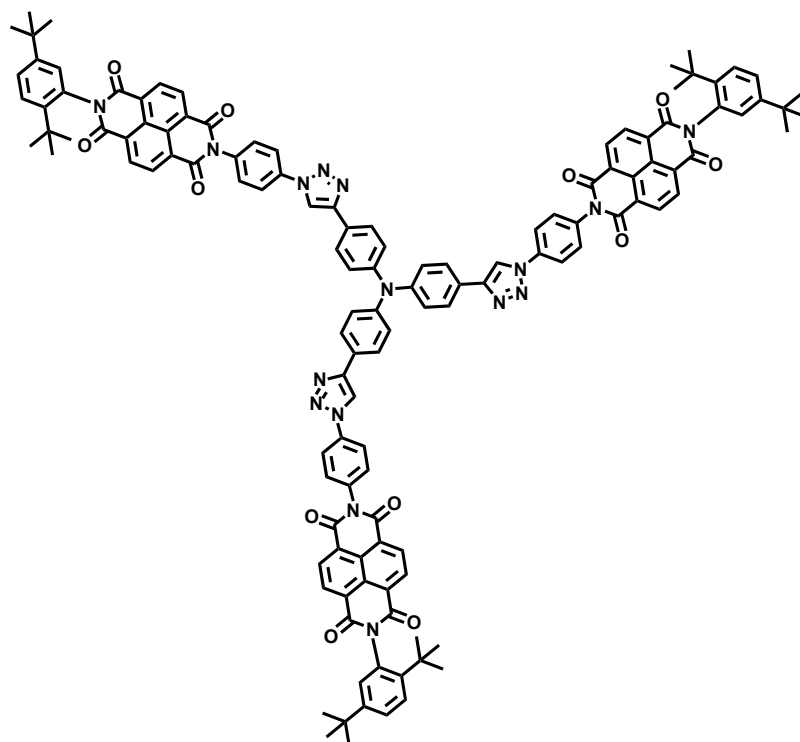
D-A-G1

Model Compounds
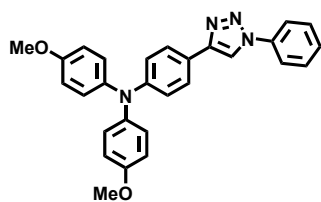
C-M
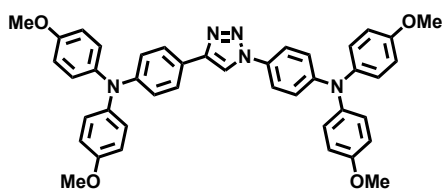
M
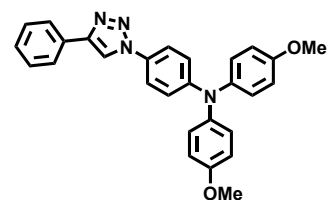
N-M
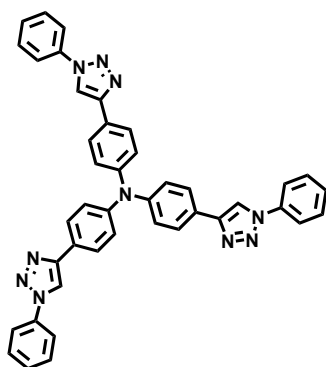
core-M
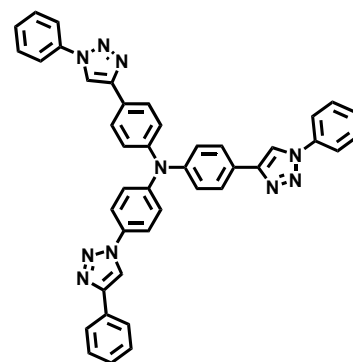
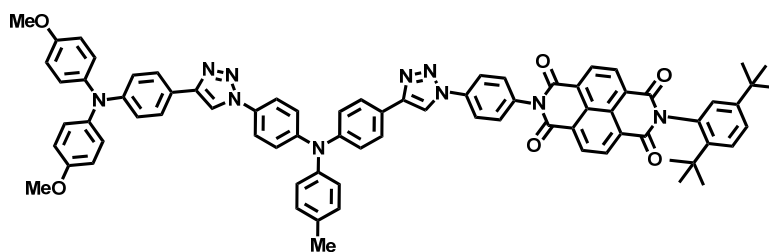**branch-M**
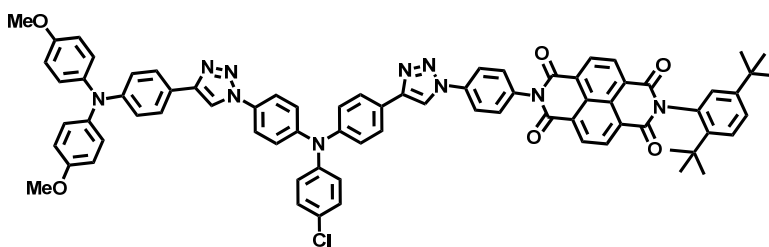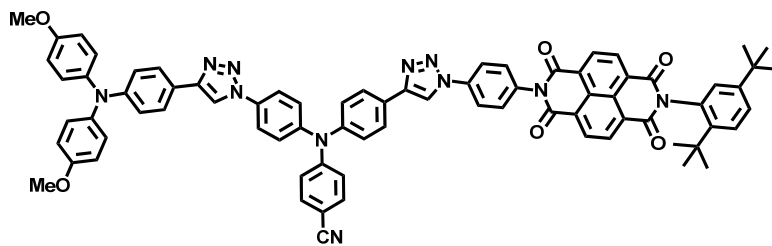
Cascades

Da

Db

T-Me

T-Cl

T-CN

Chapter 9

ZUSAMMENFASSUNG

Im Rahmen dieser Arbeit wurde die Synthese sowohl von dendritischen Makromolekülen als auch von kleineren Donor-Akzeptor-Systemen realisiert. Des Weiteren wurden diese Verbindungen bezüglich ihrer Energie- und Elektron-Transfer-Eigenschaften untersucht.

In allen untersuchten Systemen wurden die eingebauten Chromophore durch Triazole miteinander verknüpft. Dabei sind die Triazole das Ergebnis einer Kupfer(I)-katalysierten 1,3-dipolaren Cycloaddition zwischen einem terminalen Alkin und einem Azid. Für die Darstellung der vorgestellten Verbindungen wurde ein synthetisches Konzept auf der Basis von molekularen Bausteinen entwickelt, das den Austausch aller elementaren Komponenten ermöglicht. Die so erhaltenen Systeme bestehen aus Dendrimeren, die auschließlich aus Triarylaminen (TAA) aufgebaut sind (**G1**-**G3**), Dendrimeren mit einem Spirobifluoren-Gerüst als Kern (**spiro-G1** und **spiro-G2**) und dem Donor-Akzeptor Dendrimer (**D-A-G1**), in dem Naphthalindiimid-Akzeptoren (NDI) als Endgruppen fungieren.

Zusätzlich wurde eine Reihe von Modellverbindung verwirklicht, um mit ihrer Hilfe ein besseres Verständnis der photophysikalischen Prozesse in den Dendrimeren zu erlangen.

Durch eine Modifikation des synthetischen Baukastensystems, welches den Zugang zu den Dendrimeren ermöglichte, wurde außerdem die Darstellung einer Reihe von Donor-Akzeptor-Triaden (**T-Me**, **T-Cl** und **T-CN**) verwirklicht. Diese Triaden bestehen dabei aus zwei TAA-Donoren und einem NDI-Akzeptor. Mit Hilfe der Cyclovoltammetrie konnte ein abwärtsgerichteter Redoxgradient vom NDI zum endständigen TAA in den Triaden bestätigt werden. Realisiert wurde dieser Redoxgradient, indem das Redoxpotential des mittleren TAAs durch geeignete Substitutenten in der „freien" p-Position des TAAs gezielt beeinflusst wurde. Des Weiteren wurden zwei Dyaden (**Da** und **Db**) synthetisiert, die sich nur in der Verknüpfung des TAAs bzw. des NDIs an das Triazol unterscheiden. In all diesen Kaskaden sorgen sowohl eine Knotenebene entlang der N-N-Achse des NDIs als auch ein großer Verdrillungswinkel zwischen dem NDI-Kerngerüst und dem N-Arylsubstituenten für eine kleine elektronische Kopplung.

Bei den Untersuchungen der photophysikalischen Eigenschaften der Dendrimere lag der Schwerpunkt auf der Untersuchung der TAA-Dendrimere **G1**-**G3** bezüglich ihrer Homo-Energie-Transfer-Eigenschaften. Die Beobachtung eines starken *Stokes* Shifts in der Fluoreszenz dieser

Makromoleküle ist das Ergbnis einer Emission aus einem polaren Ladungs-Transfer-Zustand und einer großen Reorganisationsenergie λ. Dadurch gibt es im Lösungsmittel-relaxierten Zustand nur ein kleines Überlapp-Integral zwischen der Absorption des Akzeptors und der Emission des Donors. Gerade dieses Überlapp-Integral bestimmt gemäß der *Förster*-Theorie maßgeblich die Geschwindigkeitskontante des Energie-Transfers. In Untersuchungen auf der Basis der Fluoreszenz-Aufkonversion wurde eine starke und schnelle Abnahme der Anfangsfluoreszenzanisotropie beobachtet, gefolgt von einem deutlich langsameren Abfall auf der längeren Zeitskala. Demnach kommt es zunächst zu einem schnellen Energie-Transfer in den ersten 2 ps nach der Anregung und anschließend zu einem langsameren Energie-Hüpfen. Zeitaufgelöster Emissionsspektren (TRES) der Modellverbindung **M** haben gezwigt, dass die Lösungsmittel-Relaxation auf derselben Zeitskala wie der schnelle Energie-Transfer stattfindet. Nach einer Abschätzung der Geschwindigkeitskonstanten für den Energie-Transfer in **G1** auf Grundlage der *Förster*-Theorie findet der schnelle Energie-Transfer im Schwingungs-relaxierten Zustand statt, noch bevor die Lösungsmittel-Relaxation beginnt. Für diese Abschätzung wurde ein Fluorezenzspektrum von **G1** in Cyclohexan als Spektrum zum Zeitnullpunkt verwendet. Der Analyse zur Folge konkurrieren in den ersten 2 ps nach der Anregung sowohl die Lösungsmittel-Relaxation als auch der schnelle Energie-Transfer-Prozess miteinander. Daher ist es unerlässlich zwischen dem Energie-Transfer im *Franck-Condon-* und im Lösungsmittel-relaxierten Zustand zu unterscheiden. Außerdem konnte gezeigt werden, dass ein schneller Energie-Transfer auch in Ladungs-Transfer-Systemen möglich ist, in denen ein großer *Stokes* Shift einen effektiven spektralen Überlapp verhindert, wenn ein ausreichend großer spektraler Überlapp vor der Lösungsmittel-Relaxation vorliegt.

Auch in den Spiro-Dendrimeren **spiro-G1** und **spiro-G2** konnte ein Energie-Transfer nach der Anregung mit Hilfe von stationären Emissions-Anisotropie-Experimenten beobachtet werden. Dabei wurde angenommen, dass die Anregungsenergie in **spiro-G1** über das gesammte Molekül verteilt ist. Eine stärker polarisierte Fluoreszenz in **spiro-G2** im Vergleich zu **spiro-G1** legt den Schluss nahe, dass die Energie in **spiro-G2** wahrscheinlich nur über einen einzelnen Ast verteilt ist. Um dieser Fragestellung nachzugehen sind allerdings weiter Untersuchungen der Energie-Transfer-Prozesse durch z.B. zeitaufgelöste Emissions-Anisotropie-Messungen notwendig.

Zudem wurden stationäre Absorptionsspektroskopie-Messungen an den Radikal-Kationen von **G1**-**G2**, **spiro-G1** und **spiro-G2** und **M** durchgeführt, um die Elektron-Transfer-Eigenschaften von TAA-Triazol-Systemen zu untersuchen. Laut dieser Messungen erlaubt die Verwendung von Triazolen als Brückeneinheit in den Verbindungen in denen Elektron-Transfer-Prozesse untersucht wurden nur eine geringe elektronische Kommunikation zwischen den verknüpften Redox-Zentren.

Allerdings ist die elektronische Kopplung genügend groß, um einen effektiven Elektronen-Transfer zwischen den Zentren zu ermöglichen.

Sowohl die Dyaden (**Da** und **Db**) und Triaden (**T-Me**, **T-Cl** und **T-CN**) als auch das Donor-Akzeptor Dendrimer **D-A-G1** wurden in Bezug auf ihre Eigenschaften in photoinduzierten Elektron-Transfer-Prozessen untersucht, insbesondere die Faktoren, die die Prozesse von Ladungsseparation und Ladungsrekombination beeinflussen.

Der stationären Absorptionspektroskopie zur Foelge stellen die Absorptionsspekten der Kaskaden eine Superposition der Absorptionsspektren der einzelnen Chromophore dar. Demnach wechselwirken die einzelnen Chromophore in den Kaskaden im elektronischen Grundzustand nicht miteinander.

Des Weiteren wurden für die Kaskaden zeitaufgelöste ns- und fs-transiente Absorptionsspektroskopie-Messungen in Toluol und MeCN als Lösungsmittel durchgeführt. Diese Messungen zeigten, dass der Anregung bei einer Energie von 28200 cm^{-1} (355 nm) beziehungsweise 26300 cm^{-1} (380 nm) ein Elektron-Transfer vom TAA zum NDI folgt und ein ladungsgetrennter (CS) Zustand gebildet wird. Dabei wird in den Triaden zunächst ein ladungsgetrennter (CS1) Zustand populiert, in dem das NDI reduziert und das mittlere TAA oxidiert vorliegt. Nachfolgend wird duch einen zusätzlichen Elektronen-Transfer vom endständigen TAA zum mittleren TAA der CS2-Zustand generiert. Die energetisch niedrigsten CS-Zustände sowohl der Triaden als auch der Dyaden weisen Lebenzeiten auf der ns-Zeitskala auf. Im Gegensatz dazu besitzt der CS-Zustand von **Db** in MeCN nur eine Lebenszeit von etwa 43 ps auf. Zudem konnte hier die Bildung eines ^{3}NDI-Zustands beobachtet werden. Alle anderen CS-Zustände zeigen einen biexpontiellen Abfall, als Folge der Ausbildung sowohl eines ^{1}CS- als auch eines ^{3}CS-Zustands. In magnetfeld-abhängigen Messungen wurde für **Db** kein nennenswerter Effekt beobacht, was auf eine große Singulett-Triplett-Aufspaltung in den Dyaden zurückzuführen ist. Die Triaden besitzen eine deutlich kleinere Singulett-Triplett-Aufspaltung. Daher zeigte **T-CN** eine starke Abhängigkeit vom angelegten Magnetfeld, was zudem ein Beleg für die ^{1}CS/^{3}CS-Zuordnung darstellt. An dieser Stelle sind weitere Analysen der Singlet-Triplett-Dynamiken notwendig, die gegenwärtig durchgeführt werden.

Die Ladungsrekombination findet für alle Systeme in Toluol in der *Marcus invertierten* Region und in MeCN in der *Marcus normalen* Region statt. Allerdings konnte nur für **Db** ein ausgeprägter *invertierte* Region-Effekt beobachtet werden. In den Triaden sind die Geschwindigkeitskonstanten für die Ladungsrekombination in der *normalen* und in der *invertierten* Region wahrscheinlich nah am Scheitelpunkt der *Marcus* Parabel. Somit ist der *invertierte* Region-Effekt bei ihnen nur sehr

gering ausgeprägt und die Geschwindigkeitskonstanten für die Ladungsrekombination befinden sich in derselben Größenordnung. Im Vergleich mit den Geschwindigkeitskonstanten für die Ladungsrekombination von **Db** führt die größere räumliche Distanz der beiden Ladungen im CS2-Zustand in den Triaden zu verringerten Geschwindigkeitskonstanten für die Ladungsrekombination von ca. einer Größenordnung.

Allerdings ist die Gesamtlebensdauer der CS-Zustände wichtiger als eine kleine Geschwindigkeitskonstante für die Ladungsrekombination. Gerade diese Lebensdauer kann maßgeblich durch die Population des ^{3}CS-Zustandes verlängert werden. Die vorgestellten Ergebnisse zeigen, dass die größere Singulett-Triplett-Aufspaltung in den Dyaden zu einer Lebensdauer des CS-Zustands von mehreren μs führt, während sich die Lebensdauern der CS-Zustände in den Triaden im ns-Zeitbereich befinden. Des Weiteren konnte eine Lösungsmittelabhängigkeit der Singulett-Triplett-Aufspaltung in den Triaden beobachtet werden. Dies stellt einen vielversprechenden Ansatzpunkt für weitere Studien bezüglich der Singulett-Triplett-Aufspaltung dar.

Das Donor-Akzeptor-Dendrimer **D-A-G1** zeigt ähnliche Eigenschaften wie die beiden Dyaden (**Da** und **Db**). Durch das deutliche Auftreten einer NDI-Radikal-Anion-Bande im transienten Absorptionsspektrum kann auch nach der Anregung von **D-A-G1** die Bildung eines CS-Zustandes angenommen werden. Bemerkenswerterweise wurde die transiente Absorptionsbande des TAA-Radikal-Kation für **D-A-G1** in Toluol nicht beobachtet. Eine *Bixon-Jortner*-Analyse lieferte eine elektronische Kopplung für **D-A-G1**, die der für die Dyaden (**Da** und **Db**) vergleichbar ist. Durch einen energetisch höherliegenden CS-Zustand in **D-A-G1**, der die Ladungsrekombination in der *invertierten* Region verlangsamt, ist die Geschwindigkeitskonstante für die Ladungsrekombination bei **D-A-G1** kleiner als bei **Db**. In Kombination mit einer Singulett-Triplett-Aufspaltung vergleichbar mit der, der Dyaden, führt dies zu einer verlängerten Lebensdauer des CS-Zustands bis zu 14 μs in verdünnter Lösung. Beide Charakteristiken führen zu verbesserten Eigenschaften von **D-A-G1** hinsichtlich einer möglichen Verwendung als System für die Energieumwandlung von Sonnenlicht. Daher stellt **D-A-G1** eine vielversprechende Leitstruktur für weitere Untersuchungen bezüglich Lichtsammelsysteme dar. In einer zukünftigen Studie könnte das Donor-Akzteptor-Dendrimer zweiter Generation **D-A-G2** von Interesse sein. Synthetisch wäre es über eine "Click-Reaktion" zwischen **13** und **8** realisierbar. Den cyclovoltammetrischen Untersuchungen von **G1**-**G3** zur Folge, sollte in **D-A-G2** ein abwährtsgerichteter Gradient an CS-Zuständen vorliegen.

APPENDIX

Publications

Solvent Controlled Energy Transfer Processes in Triarylamine-Triazole Based Dendrimers, Zieschang, F.; Schmiedel, A.; Holzapfel, M.; Ansorg, K.; Engels, B.; Lambert, C. *J. Phys. Chem. C* **2013**, *117*, 19816-19831. DOI: 10.1021/jp404708x

Talks

ENERGY MIGRATION IN TAA MACROMOLECULES. "GRK1221 – Herbsttagung", Bad Staffelstein, Germany, 2013.

OPTICAL AND ELECTROCHEMICAL STUDIES OF FRACTAL TRIARYLAMINE MACROMOLECULES, "The 11th International Symposium on Functional π-Electron Systems" (Fpi11), Arcachon, France, 2013

Poster Contributions

OPTICAL AND ELECTROCHEMICAL INVESTIGATIONS OF TRIARYLAMINE DENDRIMERS. Zieschang, F.; Schmiedel, A.; Holzapfel, M.; Lambert, C. "Nanosystems for Solar Energy Conversion", Munich, Germany, **2013**.

ULTRA FAST DYNAMICS IN MULTIBRANCHED MACROMOLECULES. Zieschang, F.; Schmiedel, A.; Holzapfel, M.; Lambert, C. "Solar Technologies go Hybrid – Workshop", Bad Staffelstein, Germany, **2013**.

OPTICAL AND ELECTROCHEMICAL INVESTIAGTIONS OF TRIGONAL DENDRIMERS BASED ON TRIARYLAMINES. Zieschang, F.; Lambert, C. "Photochemie 2012", Potsdam, Germany, **2012**.

OPTICAL AND ELECTROCHEMICAL INVESTIGATIONS OF TRIARYLAMINE BASED DENDRIMERS. Zieschang, F.; Lambert, C. "XXIV IUPAC Symposium of Photochemistry", Coimbra, Portugal, **2012**.

OPTICAL AND ELECTROCHEMICAL PROPERTIES OF DENDRITIC SYSTEMS BASED ON TRIARYLAMNIES AND TRIAZOLES. Zieschang, F.; Lambert, C. "International Symposium on Functional π-Electron Systems (Fpi10), Beijing, China, **2011**.

DENDRITIC SYSTEMS BASED ON TRIARYLAMINE BUILDING BLOCKS: OPTICAL AND ELECTROCHEMICAL PROPERTIES. Zieschang, F.; Lambert, C. "Electronic Properties of pi-conjugated Materials II", Würzburg, Germany, **2011**.

TRIARYLAMINE-CONTAINING TRIGONAL DENDRIMERS: OPTICAL AND ELECTROCHEMICAL PROPERTIES. Zieschang, F.; Lambert, C. "22nd Lecture Conference of the GDCh-division of Photochemie", Erlangen, Germany, **2010**.

OPTICAL AND ELECTROCHEMICAL PROPERTIES OF A STARBURST TRIARYLAMINE. Zieschang, F.; Lambert, C. "XXIII IUPAC Symposium of Photochemistry", Ferrara, Italy, **2010**.

Simulation of the Decay Curves with TENUA

The decays of the ns-transient absorption measurements were simulated with the TENUA[280] program by adapting the following script (given for **Db**) for each compound.

For the simulation:

The ^{1}CS state (SCS) is in equilibrium with ^{3}CS state (TCS) with the related rate constants k_{TS} (k(-1)) and k_{ST} (k(+1)) and SCS is in equilibrium with S0 with the related rate constants k_S (k(+2)) and k_{-s} (k(-2)). SCS is the concentration of the singlet CS state and TCS is the concentration of the triplet CS state.

For the experimental data:

The state A is in equilibrium with state B with the related rate constants k(+3) as the $1/\tau_1$ and k(-3) = 0. State C is in equilibrium with state D with the related rate constants k(+4) as the $1/\tau_2$ and k(-4) = 0. A is the concentration of the state A ($1/a_1$) and C is the concentration of the state C ($1/a_2$).

```
SCS <-> TCS; SCS <-> S0;
A <-> B; C <-> D;
k(-1)=(1/3)*k(+1);
k(+1) : 3.516E5;
k(+2) : 1.8E8;
k(-2) : 0.0;
k(+3) : 118049;
k(-3) : 0.0;
k(+4) : 18422991;
k(-4) : 0.0;
SCS : 0.9323;
TCS :(1)-SCS;
A : 0.070;
C : 0.929;
*output
sum=1/(1)*(SCS+TCS);
sum2=1/(1)*(A+C);
```